frontiers | Research Topics

Structural immunology of molecular innate immunity

Edited by
Hyun Ho Park, Qian Yin and Jun Hyuck Lee

Published in
Frontiers in Immunology

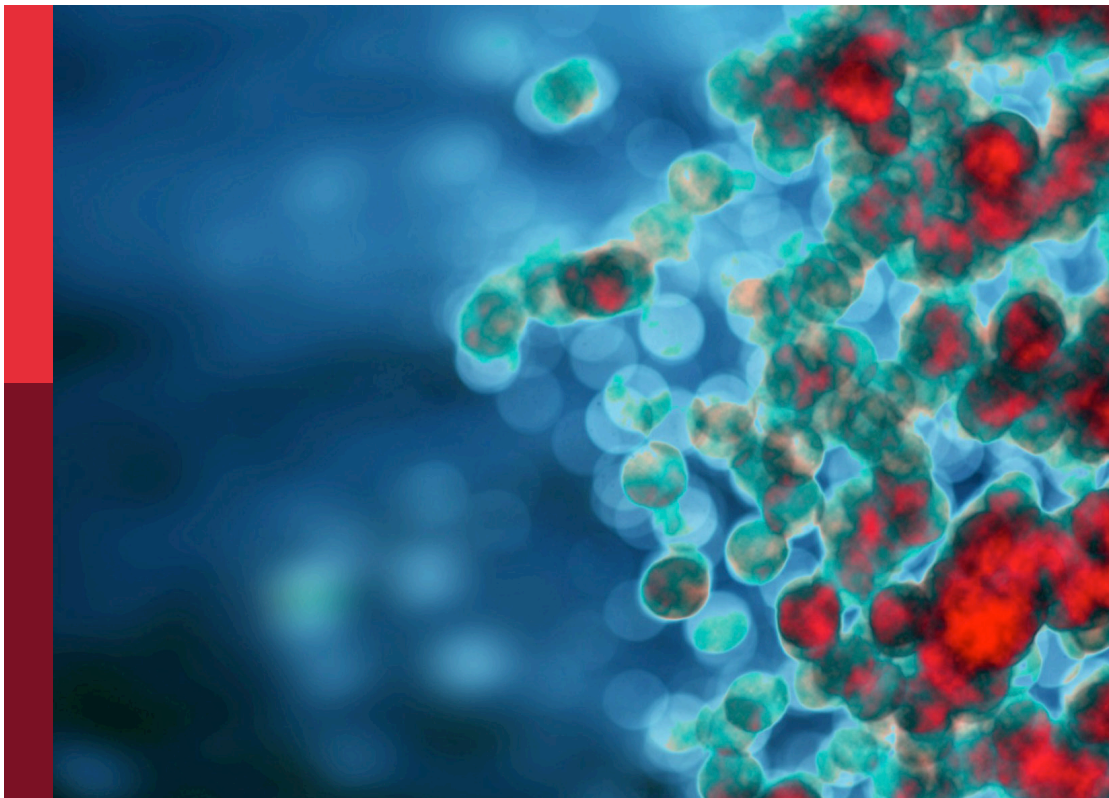

ISSN 1664-8714
ISBN 978-2-8325-3518-9
DOI 10.3389/978-2-8325-3518-9

About Frontiers

Frontiers is more than just an open access publisher of scholarly articles: it is a pioneering approach to the world of academia, radically improving the way scholarly research is managed. The grand vision of Frontiers is a world where all people have an equal opportunity to seek, share and generate knowledge. Frontiers provides immediate and permanent online open access to all its publications, but this alone is not enough to realize our grand goals.

Frontiers journal series

The Frontiers journal series is a multi-tier and interdisciplinary set of open-access, online journals, promising a paradigm shift from the current review, selection and dissemination processes in academic publishing. All Frontiers journals are driven by researchers for researchers; therefore, they constitute a service to the scholarly community. At the same time, the *Frontiers journal series* operates on a revolutionary invention, the tiered publishing system, initially addressing specific communities of scholars, and gradually climbing up to broader public understanding, thus serving the interests of the lay society, too.

Dedication to quality

Each Frontiers article is a landmark of the highest quality, thanks to genuinely collaborative interactions between authors and review editors, who include some of the world's best academicians. Research must be certified by peers before entering a stream of knowledge that may eventually reach the public - and shape society; therefore, Frontiers only applies the most rigorous and unbiased reviews. Frontiers revolutionizes research publishing by freely delivering the most outstanding research, evaluated with no bias from both the academic and social point of view. By applying the most advanced information technologies, Frontiers is catapulting scholarly publishing into a new generation.

What are Frontiers Research Topics?

Frontiers Research Topics are very popular trademarks of the *Frontiers journals series*: they are collections of at least ten articles, all centered on a particular subject. With their unique mix of varied contributions from Original Research to Review Articles, Frontiers Research Topics unify the most influential researchers, the latest key findings and historical advances in a hot research area.

Find out more on how to host your own Frontiers Research Topic or contribute to one as an author by contacting the Frontiers editorial office: frontiersin.org/about/contact

Structural immunology of molecular innate immunity

Topic editors

Hyun Ho Park — Chung-Ang University, Republic of Korea

Qian Yin — Florida State University, United States

Jun Hyuck Lee — Korea Polar Research Institute, Republic of Korea

Citation

Park, H. H., Yin, Q., Lee, J. H., eds. (2023). *Structural immunology of molecular innate immunity*. Lausanne: Frontiers Media SA. doi: 10.3389/978-2-8325-3518-9

Table of contents

frontiers | Frontiers in Immunology

TYPE Editorial
PUBLISHED 06 September 2023
DOI 10.3389/fimmu.2023.1284121

OPEN ACCESS

EDITED AND REVIEWED BY
Francesca Granucci,
University of Milano-Bicocca, Italy

*CORRESPONDENCE
Hyun Ho Park
xrayleox@cau.ac.kr

RECEIVED 28 August 2023
ACCEPTED 30 August 2023
PUBLISHED 06 September 2023

CITATION
Lee JH, Yin Q and Park HH (2023) Editorial: Structural immunology of molecular innate immunity. *Front. Immunol.* 14:1284121. doi: 10.3389/fimmu.2023.1284121

Editorial: Structural immunology of molecular innate immunity

Jun Hyuck Lee[1], Qian Yin[2] and Hyun Ho Park[3]*

[1]Unit of Research for Practical Application, Korea Polar Research Institute, Incheon, Republic of Korea, [2]Department of Biological Science, Florida State University, Tallahassee, FL, United States, [3]College of Pharmacy, Chung-Ang University, Seoul, Republic of Korea

KEYWORDS

cGAS-STING, complement receptors, innate immunity, structure, TLR

Editorial on the Research Topic
Structural immunology of molecular innate immunity

In the early stages of the host defense response, innate immunity plays a crucial role due to its ability to promptly recognize pathogenic or danger signals through various receptors located on cell surfaces or within the cytoplasm (1). This initial recognition event is subsequently followed by signal transduction processes involving a range of adaptor and effector molecules. The primary goals of the innate immune system include identifying and eliminating invading pathogens, recruiting diverse immune cells to the infection site, and facilitating preparations for the adaptive immune response (2). Over several decades, extensive investigations have been conducted to unravel the intricacies of the innate immune system, leading to an increasingly detailed comprehension of its molecular foundations (3–5).

The Research Topic "*Structural Immunology of Molecular Innate Immunity*" highlights 13 recent studies that delve into the process of innate immunity at the molecular level, with a specific focus on toll-like receptor (TLR)-mediated immune responses, cGAS-STING-mediated innate immunity, GTPase-mediated antiviral processes, the structural biology of the complement system, and Janus kinase as a drug for inflammatory diseases.

Toll-like receptors (TLRs) are well-established pattern recognition receptors responsible for recognizing pathogens and triggering innate immune responses. Since their discovery, TLRs have ushered in a new era in immunology, bridging the gap between initial pathogen recognition by innate immune cells and the subsequent initiation of the adaptive immune response. Recent investigations have further revealed that TLR signaling directly controls T cell activation, proliferation, differentiation, developmental processes, and overall function, covering a wide array of physiological scenarios. Duan et al. reviewed the multifaceted roles of TLR signaling, both through direct and indirect mechanisms, in governing cell-mediated immunity. They discussed the significance of TLR signaling in the host's defense mechanisms against a spectrum of challenges, including infectious diseases, autoimmune disorders, and cancer. Another group, Zheng and Dong, also reviewed the role of TLRs in pathogen detection *in vivo*. They summarized recent findings of TLRs' contributions to the differentiation of naïve CD4+ T cells into T helper (Th) cells, initiation of immune responses, and active participation in the pathogenic mechanisms underlying autoimmune and allergic disorders.

A couple of research groups reported original research in the field of TLR biology. Wildum et al. evaluated the therapeutic effect, host immune reactions, and safety of

RG7854, an oral double prodrug of a toll-like receptor 7 (TLR7) agonist, for developing medication for chronic hepatitis B (CHB). Based on their evaluation, they concluded that TLR7 agonists hold promise as immunotherapeutic avenues for achieving a functional cure in CHB patients. Jiang et al. highlighted the important role of surfactant protein D (SP-D), a well-known innate immune molecule. This study revealed that SP-D engages with the TLR4/MD-2 complex to suppress TLR4-mediated PI3K/Akt and NF-κB signaling activation within chondrocytes. These insights underscore the chondroprotective attributes of SP-D, relying on TLR4-mediated PI3K/Akt and NF-κB signaling pathways.

This Research Topic also includes four papers on cGAS-STING, a sensing axis related to innate immunity that has recently garnered significant attention. Cyclic GMP-AMP synthase (cGAS) identifies double-stranded DNA (dsDNA) from invading pathogens, initiating an interferon response by activating the downstream adaptor protein stimulator of interferon genes (STING). This represents the classic and fundamental biological role of the cGAS-STING signaling pathway, crucial for preventing the invasion of pathogenic microorganisms. Additionally, cGAS can interact with various types of nucleic acids, such as cDNA, DNA: RNA hybrids, and circular RNA, contributing to a diverse range of biological functions. A growing body of research has unveiled a significant connection between the cGAS-STING signaling pathway and autophagy, cellular senescence, antitumor immunity, inflammation, and autoimmune diseases. Wang et al. thoroughly reviewed the action mechanism of cGAS as it interacts with different types of nucleic acids, its multifaceted biological functions, and the potential for targeting this pathway to treat various diseases. Shi et al. conducted an evaluation of research on the cGAS-STING pathway, predicting the hotspots and emerging trends in the field using bibliometric analysis. This analysis revealed a shift in research focus from understanding how cGAS senses dsDNA and how cGAMP binds to STING to exploring the roles of the cGAS-STING pathway in various pathological states

The global prevalence of obesity, prediabetes, and diabetes is increasing, and these metabolic disorders are closely intertwined with neurodegenerative conditions, particularly Alzheimer's disease and related dementias. The connection between these disorders is shaped by innate inflammatory signaling, potentially involving the early activation of the cGAS/STING pathway. Elzinga et al. uncovered acute systemic changes in metabolic and inflammatory responses, marked by impaired glucose tolerance, insulin resistance, and shifts in the composition of peripheral immune cell populations. In the central nervous system, noticeable inflammatory changes manifested as microglial activation within a pro-inflammatory environment, occurring concurrently with cGAS-STING pathway activation. Notably, experiments involving neuron-microglial co-cultures demonstrated that blocking gap junctions led to a substantial reduction in cGAS-STING activation. The research also reported on the precise downstream signaling events of the cGAS-STING pathway. Xia et al. systematically analyzed porcine STING (pSTING), revealing its capability to induce IFN, autophagy, and apoptosis. The investigation unveiled distinct dynamics governing the three downstream events associated with pSTING, underscoring the emergence of IFN-independent triggers for autophagy and apoptosis. Furthermore, the study explored the regulatory influence of autophagy on pSTING-induced IFN and apoptosis.

The significance of GTPases in innate immunity has been highlighted by a couple of research groups. Zhang et al. presented their original research article concerning the function and mechanism of grass carp ADP ribosylation factor 1 (gcARF1) in viral infection. They confirmed that the small GTPase domain of gcARF1 is essential for promoting grass carp reovirus (GCRV) replication and infection, with the inhibition of gcARF1 GTPase activity resulting in a significant reduction in the number of VIBs. Their study demonstrated the indispensable role of gcARF1's GTPase activity in facilitating efficient GCRV replication. Ha et al. provided insights into the activation mechanism of immunity-related GTPase B10 (IRGB10) by presenting the crystal structures of GppNHp-bound and nucleotide-free IRGB10. These structures revealed that IRGB10 exists as a monomer in both nucleotide-free and GTP binding states. Furthermore, they determined that GTP hydrolysis plays a critical role in dimer formation and subsequent oligomerization of IRGB10. Building upon these findings, they proposed a mechanistic model to explain the operational mechanism of IRGB10 during the disruption of pathogen membranes.

The complement system assumes pivotal roles in a diverse array of immune and inflammatory processes and is often implicated as a causative or exacerbating factor in various human ailments, ranging from asthma to cancer. Complement receptors consist of no fewer than eight proteins categorized into four structural classes. These receptors coordinate complement-mediated humoral and cellular effector responses, while concurrently orchestrating intricate communication between the innate and adaptive arms of immunity. Santos-Lopez et al. reviewed a comprehensive overview of the current understanding of the structural biology underpinning complement receptors and their interactions with natural agonists and pharmacological antagonists. The review accentuates fundamental principles and delineates the unresolved areas where challenges and uncertainties persist, including the identification of research gaps. In the field of the complement system, Navas-Yuste et al. reported a structural study. They successfully deciphered the X-ray crystallographic structure of the glyceraldehyde-3-phosphate dehydrogenase (GAPDH) enzyme from L. interrogans. GAPDH is an enzyme involved in glycolysis and has been shown to serve additional functions in various pathogenic organisms, bolstering their infectivity and immune evasion capabilities. With this structural information, they established the interaction between L. interrogans GAPDH and the human innate immune anaphylatoxin C5a through *in vitro* experiments. These findings suggest L. interrogans GAPDH as a potential immune evasion factor targeting the complement system. Additionally, Kwon provided a review on Janus kinase (JAK). The Janus kinase (JAK) family of enzymes represents a class of non-receptor tyrosine kinases crucial for phosphorylating cytokine receptors and signaling transducer and activator of transcription (STAT) proteins within the JAK-STAT signaling pathway. JAKs have emerged as attractive drug targets to counteract aberrant JAK-STAT signaling. This review delves into the multifaceted roles of

JAKs within the JAK-STAT signaling pathway, providing an in-depth analysis of JAK structures and their conformational alterations critical for catalytic activity.

While advanced biological techniques have unveiled the molecular understanding of innate immunity, there is still much to learn about the molecular processes underlying innate immunity. In general, this Research Topic presents timely articles highlighting the current understanding of innate immunity at the molecular level. The authors express their gratitude to all contributors for sharing their discoveries and to the referees for their careful and insightful reviews. It is believed that the included articles will be of great interest to researchers studying innate immunity at the molecular level.

Author contributions

JL: Conceptualization, Writing – original draft. QY: Conceptualization, Writing – original draft. HP: Conceptualization, Funding acquisition, Project administration, Supervision, Writing – original draft, Writing – review & editing.

Funding

This research was supported by the National Research Foundation of Korea (NRF) grants funded by the Government of Korea (NRF- 2021R1A2C3003331). This research is a part of the project titled 'Development of potential antibiotic compounds using polar organism resources (KOPRI Grant PM23030)', funded by the Ministry of Oceans and Fisheries, Korea.

Acknowledgments

We would like to thank the authors, reviewers, and editors for their essential contribution to this exciting and unexplored Research Topic, as well as of the members of the Frontiers in Immunology Editorial Office.

Conflict of interest

The authors declare that the research was conducted in the absence of any commercial or financial relationships that could be construed as a potential conflict of interest.

Publisher's note

References

1. Medzhitov R, Janeway C Jr. Innate immunity. *N Engl J Med* (2000) 343:338–44. doi: 10.1056/NEJM200008033430506

2. Akira S, Uematsu S, Takeuchi O. Pathogen recognition and innate immunity. *Cell* (2006) 124:783–801. doi: 10.1016/j.cell.2006.02.015

3. Kagan JC, Magupalli VG, Wu H. SMOCs: supramolecular organizing centres that control innate immunity. *Nat Rev Immunol* (2014) 14:821–6. doi: 10.1038/nri3757

4. Shi M, Zhang PF, Vora SM, Wu H. Higher-order assemblies in innate immune and inflammatory signaling: a general principle in cell biology. *Curr Opin Cell Biol* (2020) 63:194–203. doi: 10.1016/j.ceb.2020.03.002

5. Fu J, Wu H. Structural mechanisms of NLRP3 inflammasome assembly and activation. *Annu Rev Immunol* (2023) 41:301–16. doi: 10.1146/annurev-immunol-081022-021207

frontiers in Immunology

REVIEW
published: 04 February 2022
doi: 10.3389/fimmu.2022.826880

A Variety of Nucleic Acid Species Are Sensed by cGAS, Implications for Its Diverse Functions

Dawei Wang, Heng Zhao, Yangkun Shen and Qi Chen**

Fujian Key Laboratory of Innate Immune Biology, Biomedical Research Center of South China, Fujian Normal University, Fuzhou, China

Cyclic GMP-AMP synthase (cGAS) recognizes double-stranded DNA (dsDNA) derived from invading pathogens and induces an interferon response *via* activation of the key downstream adaptor protein stimulator of interferon genes (STING). This is the most classic biological function of the cGAS-STING signaling pathway and is critical for preventing pathogenic microorganism invasion. In addition, cGAS can interact with various types of nucleic acids, including cDNA, DNA : RNA hybrids, and circular RNA, to contribute to a diverse set of biological functions. An increasing number of studies have revealed an important relationship between the cGAS-STING signaling pathway and autophagy, cellular senescence, antitumor immunity, inflammation, and autoimmune diseases. This review details the mechanism of action of cGAS as it interacts with different types of nucleic acids, its rich biological functions, and the potential for targeting this pathway to treat various diseases.

Keywords: cGAS, STING, Interferon, Nucleic acid recognition, Disease treatment strategy

OPEN ACCESS

Edited by:
Caroline Jefferies, Cedars Sinai Medical Center, United States

Reviewed by:
Spyridon Stavrou, University at Buffalo, United States
Helene Minyi Liu, National Taiwan University, Taiwan

****Correspondence:***
Yangkun Shen
shenyk@fjnu.edu.cn
Qi Chen
chenqi@fjnu.edu.cn

Specialty section:
This article was submitted to Molecular Innate Immunity, a section of the journal Frontiers in Immunology

Received: *01 December 2021*
Accepted: *20 January 2022*
Published: *04 February 2022*

Citation:
Wang D, Zhao H, Shen Y and Chen Q (2022) A Variety of Nucleic Acid Species Are Sensed by cGAS, Implications for Its Diverse Functions. Front. Immunol. 13:826880. doi: 10.3389/fimmu.2022.826880

INTRODUCTION

In the 1980s, researchers already understood the correlation between bacterial DNA and immune activation *in vitro* (1), i.e., they knew that exposing macrophages to bacterial DNA could stimulate the expression of interferon-alpha (IFN-α) and interferon-beta (IFN-β), and induce the activation of natural killer cells and the release of interferon-gamma (IFN-γ) (1, 2). Further studies showed that the immune activation induced by bacterial DNA is related to its large number of unmethylated CpG motifs, which are different from the DNA motifs in humans and mice (3, 4). When bacteria-derived DNA invades human cells, the host will recognize its pathogen-associated molecular patterns and trigger an immune response (3, 5, 6). Similarly, when a virus infects a host cell, the nucleic acid released into the cell triggers the intracellular immune response, causing antiviral immunity (7–9). Thus, identifying nucleic acids derived from pathogens is an important task for a host cell to mount an immune response and eliminate them.

Host cells have evolved different recognition patterns for different types of nucleic acids, *via* various pattern recognition receptors (PRRs). PRRs include mainly Toll-like receptors (TLR) (10), NOD-like receptors (NLRs) (11), C-type lectin receptors (CLRs) (12), RIG-I-like receptors (RLRs) (13), and DNA receptors/sensors (14). Among these, DAI (15), IFI16 (16, 17), DDX41 (18), MRE11 (19), LSm14A (20), DHX9 (21), hnRNPA2B1 (22), and cGAS (23–25) are considered DNA receptors/sensors.

cGAS is a cytoplasmic nucleic acid sensor with the widest recognition ability for double-stranded DNA (dsDNA); it binds dsDNA in a manner independent of sequence specificity (23). cGAS can also recognize other types of nucleic acids that trigger other important functions dependent on its subcellular location. The classic function of cGAS is to activate the downstream adaptor protein STING to induce IFN production and release. While the cGAS-STING signaling pathway plays a critical role in resisting pathogen invasion, excessive activation of this pathway can cause chronic inflammation, autoimmune disease, and cancer. Therefore, cGAS-STING signaling must be tightly regulated.

cGAS-MEDIATED SIGNALING PATHWAYS

cGAS-STING signaling presents an evolutionarily highly conserved mechanism of immunity (26, 27). Upon recognition of cytoplasmic DNA, cGAS uses ATP and GTP as substrates to synthesize cyclin GMP-AMP (cGAMP), which act as a second messenger to activate STING (28, 29). Activation of STING is critical for initiating the downstream immune cascade (30). Translocation of STING from the endoplasmic reticulum (ER) to the Golgi apparatus is a prerequisite condition for downstream signal transduction and transcriptional regulation of type I interferons (IFN-I). STING activation requires the palmitoylation of Cys88 and Cys91, which takes place in the Golgi (31). Palmitoylation may also promote the oligomerization of STING and the activation of TANK-binding kinase 1 (TBK1). Activated STING can recruit and activate inhibitor of nuclear factor kappa-B kinase (IKK) and TBK1, but recruiting TBK1 is not sufficient to activate interferon regulatory factor 3 (IRF3) (32). Phosphorylation of STING at Ser366 by TBK1 allows it to interact with IRF3, and facilitate TBK1 phosphorylation of IRF3 (33). Phosphorylated IRF3 forms a dimer and transfers to the nucleus, where it acts together with nuclear factor-κB (NF-κB) to initiate the expression of IFN-I and other cytokines (**Figure 1**) (33, 34). After STING is activated, the "unfolded protein response (UPR) motif" at the C-terminus triggers the ER stress response and autophagy by activating the formation of the Unc-51-like

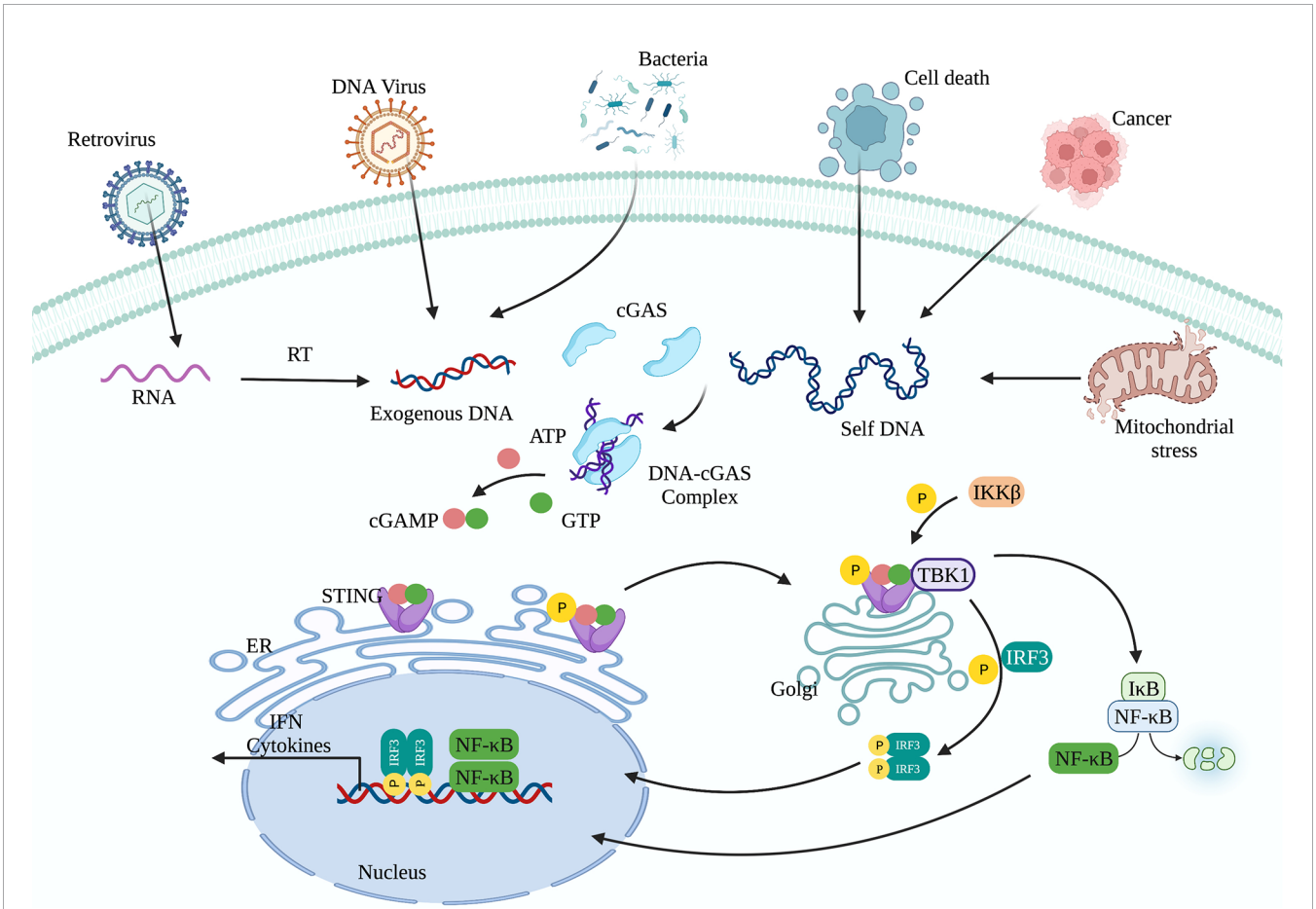

FIGURE 1 | The cGAS-STING signaling pathway. cGAS can recognize exogenous DNA from pathogens or self-DNA (from the mitochondria and nucleus). After cGAS recognizes DNA, it synthesizes the second messenger 2'3'-cGAMP, which activates STING. The translocation of STING from the endoplasmic reticulum to the Golgi apparatus is a prerequisite for participating in the downstream signal transduction and regulating IFN-I transcription. Activated STING can recruit and activate IKK and TBK1. TBK1 phosphorylates IRF3. Subsequently, phosphorylated IRF3 forms a dimer and translocates to the nucleus, where it acts together with NF-κB to initiate the expression of IFN-I and other immune regulatory factors.

autophagy activating kinase (ULK1) complex and the Beclin-1-class III phosphatidylinositol-3 kinase (PI3KC3) complex (35, 36). cGAS can also trigger autophagy through direct interaction with the Beclin-1-PI3KC3 complex (37). Autophagy mediated by the cGAS-STING pathway can spread to the whole cell, helping to remove pathogenic microorganisms (38) as well as excessive inflammatory factors and cytoplasmic DNA to prevent overactivation of the inflammatory response (39). Autophagy thus acts as negative feedback mechanism to limit continuous activation of the cGAS-STING signaling pathway.

Structural Basis for cGAS Binding dsDNA

The structure of cGAS with or without bound dsDNA has been resolved in various species (40–44). cGAS is inactive and maintains a U-shaped conformation until DNA binding induces a conformational change that remodels the enzyme active site into activated state (42, 45). Human cGAS contains 522 amino acid residues and adopts the characteristic bi-lobal fold of the nucleotidyltransferase family (42). The N-terminal lobe is a non-structural, positively charged domain, which consists of two helices and a highly twisted beta-sheet; all catalytic residues are located on the central beta-sheet (46). The C-terminal lobe is a helix bundle that contains a conserved zinc finger motif and a leucine residue (41, 46). The zinc finger motif mediates DNA binding and cGAS dimerization (46), and the leucine residue acts as a conservative structural switch that strictly regulates cGAMP production in response to dsDNA binding (41). The cleft between the N- and C-terminal lobes constitutes the substrate binding site of the enzyme (**Figure 2**) (42). The C-terminal domain of cGAS is highly conserved whereas the amino acid sequence homology of the N-terminal domain is low, though the residues that play decisive functional roles are relatively conserved (47).

A positively charged patch, located in the groove on the backside of the substrate binding cleft, is the major DNA binding site in cGAS (44). The activation loop, containing residues 210 to 220, among which Gly212 and Ser213 are highly conserved, is located near the DNA binding surface of cGAS and undergoes a conformational change similar to a switch after DNA binding (42). Meanwhile, Asn210 is critical for the enzymatic activity of cGAS. Deamination of Asn210 affects cGAMP synthesis, but does not weaken the self-dimerization, dsDNA-binding, or nucleotide-binding activity of cGAS (48). Upon DNA binding, the DNA binding site clashes with the activation loop, causing the loop to move inward and expose the binding site to the donor substrate. In contrast, modeling of the cGAS structures bound to dsRNA shows that the activation loop inserts into the major groove of dsRNA and does not cause detectable conformational changes, which may explain why dsRNA is unable to activate cGAS (42). In addition to the conformational changes in the activation loop, DNA binding induces a reorganization of the two loops at the entrance of the catalytic site in the N-terminal lobe of cGAS (44). These conformational changes promote enzyme activation by configuring the active site for Mg^{2+} ion binding and enhancing accessibility of the active site to the substrate (46).

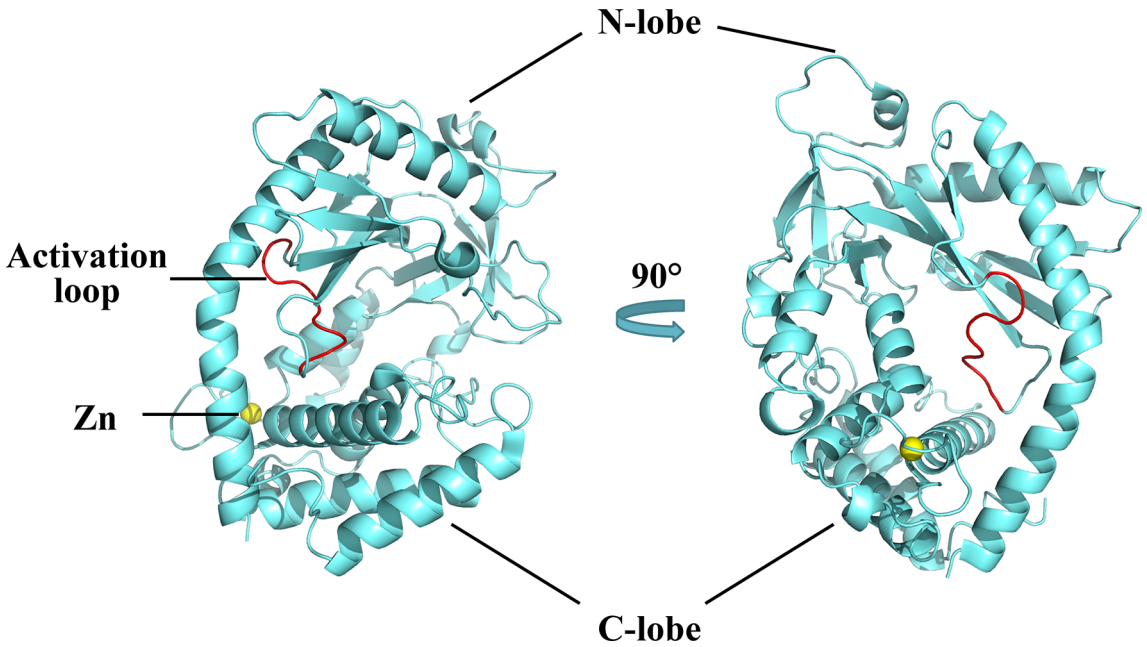

FIGURE 2 | Structures of human cGAS in the apo state. Human cGAS consists of two lobes. The N-terminal lobe consists of two helices and a highly twisted beta-sheet, and the C-terminal lobe is a helix bundle, which contains a conserved zinc finger motif and a leucine residue. Between the two lobes is a large cleft, which is the catalytic site for substrate binding. In the apo state, cGAS maintains an autoinhibitory U-shaped conformation (Structure of human cGAS adopted from PDB:4KM5).

cGAS-DNA Complex and Phase Separation

cGAS and DNA binding is primarily mediated by the interaction between positively charged residues on cGAS with the sugar-phosphate backbone of DNA, which explains the lack of sequence specificity of the interaction (46, 49). cGAS-DNA binding forms a droplet structure, resulting in phase separation, the degree of which can be enhanced by increasing the N-terminal binding valence (50). Through X-ray diffraction technology, it was found that long-stranded DNA can activate cGAS better than short-stranded DNA because the cGAS-DNA interaction forms a ladder-like complex; the longer the DNA chain, the more stable the structure of the complex, which implies a correlation between DNA length and binding efficiency (51). The formation of 2:2 cGAS-DNA complex is arranged into two DNA molecules in a roughly parallel manner, such that each complex has enhanced ability to bind subsequent cGAS dimers, thereby promoting a high degree of synergy in cGAS recruitment and activation (52). Once the cGAS-DNA complex is formed, a catalytic and accessible nucleotide-binding pocket is formed, the intermediate product pppGpA is synthesized, and subsequently cGAMP is generated (40).

Cellular Localization of cGAS

cGAS was first identified as a cytoplasmic DNA sensor abundantly present in the cytoplasm of L929 and THP1 cells (23). The physical barrier between cGAS and self-DNA formed by the mitochondrial membrane and nuclear envelope is regarded as an important regulatory strategy that prevents self-DNA recognition and autoimmune activation. However, further research revealed additional subcellular localization of cGAS, including at the plasma membrane and in the nucleus (24, 25, 53–55). A recent study showed that cGAS is located in the plasma membrane through its N-terminal phosphoinositide binding domain, which selectively interacts with phosphatidylinositol 4,5-bisphosphate; cGAS lacking the N-terminal domain is mislocalized to the cytoplasmic and nuclear compartments (24). Membrane localization may help cGAS more rapidly detect viral DNA that enters cells through endocytosis, while also preventing cGAS from interacting with endogenous DNA (24). Nuclear localization of cGAS is found in epithelial cells, long-term hematopoietic stem cells (LT-HSC), and certain cancer cells (25, 54, 56, 57), and nuclear cGAS has additional functions (see below) (53, 55, 58, 59). Together, studies suggest that the cellular localization of cGAS varies greatly across cell types, which may be linked to specific functions of cGAS.

In addition, the cellular localization of cGAS appears to change during the cell cycle or under conditions of cellular stress. cGAS is mainly located in the cytoplasm during the interphase, and rapidly transfers to the chromosomes when the nuclear membrane disappears in metaphase (60). One study described that a gradual decrease in cGAS Y215 phosphorylation is accompanied by an increase in cGAS nuclear translocation in response to cell damage caused by DNA damaging agents (55). Another study found that in migrating mammalian cells, the nuclear membrane opens at a high frequency during interphase, which allows cytoplasmic cGAS translocation to chromatin (61).

A VARIETY OF NUCLEIC ACID SPECIES ARE SENSED BY cGAS

cGAS Recognizes Pathogen-Derived dsDNA

DNA immune recognition mediated by cGAS-STING signaling plays a vital role in preventing pathogenic microbial infection (62). cGAS recognizes pathogen-derived DNA to activate innate immunity and antiviral immune responses (63).

Herpes simplex virus 1 (HSV-1) is the first DNA virus shown to activate the cGAS-STING signaling pathway *in vitro* and *in vivo* (64, 65). *In vitro*, acetyltransferase KAT5 mediates cGAS acetylation upon HSV-1 infection, which enhances the affinity of cGAS binding to viral DNA and is thought to enhance antiviral immunity (66). *In vivo*, *cGas*$^{-/-}$ mice developed ataxia and paralysis and had a higher mortality rate upon HSV-1 infection; high titers of HSV-1 were also detected in the knockout mouse brain (67). This phenomenon has also been verified in *sting*$^{-/-}$ mice (68). In contrast, wildtype mice were less likely to develop symptoms or die after HSV-1 infection (67). In addition to HSV-1, Kaposi's sarcoma-associated herpes virus (KSHV) can also activate the cGAS-STING signaling pathway (69). Compared with wildtype controls, cGAS or STING knockdown inhibited the expression of IFN-β in endothelial cells, and caused an increase in KSHV gene transcription and genomic copy number (69). DNA viruses such as human papillomavirus (70), cytomegalovirus (71), adenovirus (72), and vaccinia virus (73) have all been shown to activate cGAS and induce a host immune response to resist viral infection (74).

Many Gram-negative and positive bacteria can also activate the cGAS-STING signaling pathway. *Listeria monocytogenes* can replicate in the cytoplasm of human bone marrow cells, and its dsDNA is a major trigger of IFN-β expression dependent on IFI16, cGAS and STING (75). *Neisseria gonorrhoeae* induces the production of IFN through TLR4 and further enhances the IFN response by activating cGAS after it invades the cytoplasm of bone marrow-derived macrophages (76). In addition, the DNA derived from pathogenic microorganisms including *Mycobacteria*, *Legionella*, *Shigella*, *Francisella*, group B *streptococcus*, and *Chlamydia* can all be recognized by cGAS and activate STING to induce the body's immune response to eliminate the invading pathogenic microorganisms (32).

Thus, recognizing pathogen-derived dsDNA by cGAS is a key event for the host to perceive pathogen invasion and induce a response. Although other PRRs can recognize pathogen-derived nucleic acids and activate an immune response, activation of the cGAS-STING signaling pathway plays an indispensable role in helping the host to resist pathogenic microorganism invasion.

cGAS Recognizes Plasmid DNA

Plasmid transfection is used as a transient gene delivery system to express a foreign protein in the cell. Interestingly, a study

found that after cells were transfected with foreign plasmids, the ability of host cells to prevent viral infections improved, suggesting that activation of cGAS-STING signaling may ready the cell for subsequently fighting viral infections (77).

In addition, our research group found that inhibition of cGAS by gene knockout or chemical inhibition can increase transgene expression at the transcriptional level, and that this increase is negatively correlated with IFN and interferon-stimulated gene (ISG) expression (78). Thus, targeting the cGAS-STING signaling pathway is likely an effective strategy for gene therapy and nucleic acid drug development.

cGAS Recognizes Endogenous dsDNA

DNA is mainly stored in the nucleus; however, mitochondria, the organelles that supply energy to cells, also contain DNA molecules, namely mitochondrial DNA (mtDNA). Under normal circumstances, no (or little) free DNA is present in the cytoplasm and other organelles. Mitochondrial or nuclear damage caused by physical, chemical, and other factors can cause mtDNA or nuclear DNA to leak into the cytoplasm where it is recognized by cGAS, leading to the immune activation (59, 79, 80). Excessive activation of cGAS-STING signaling by endogenous dsDNA is related to the development of inflammatory and autoimmune diseases, including systemic lupus erythematosus (SLE), Aicardi-Goutières syndrome (AGS), and neurodegenerative diseases (81–83).

cGAS Recognizes dsDNA Derived From Mitochondria

Cells have many ways to maintain mitochondrial homeostasis. When mitochondria respond to stress, mtDNA is released into the cytoplasm through the Bax/Bak channel on the outer mitochondrial membrane. Subsequent activation of the mtDNA-cGAS-STING pathway induces the production of IFN-I (84).

Human mitochondrial transcription factor A (TFAM) is a type of mtDNA binding protein that controls mtDNA separation, abundance, and nucleoid structure (85). Genetic deletion of TFAM causes abnormal accumulation of mtDNA in the cytoplasm, leading to the activation of the cGAS-STING signaling pathway and production of IFN-I and ISGs (86). TDP-43, a nuclear DNA/RNA binding protein, is present in patients with Alzheimer's disease (87) and amyotrophic lateral sclerosis (ALS) (88). The inflammatory response triggered by TDP-43 depends on the cGAS-STING signaling pathway. In ALS, after TDP-43 enters the mitochondria of neuronal cells, it triggers mtDNA release into the cytoplasm through the mitochondrial permeability transition pore (mPTP), leading to the release of inflammatory factors and IFN-I mediated by the cGAS-STING signaling pathway (**Figure 3**) (89). Mitochondrial DNA can also be released from dying cells, which then triggers release of pro-inflammatory factors and IFN-I that acts on hematopoietic stem cells and has a profound impact on cell function (90, 91).

A study conducted in a cohort of White adults found that plasma mtDNA levels gradually increased after the age of 50 years; levels of tumor necrosis factor-α (TNF-α) and interleukin-6 (IL-6) were positively associated with plasma mtDNA levels, suggesting a possible correlation between the level of blood mtDNA and age-associated mild chronic inflammation (92). Although the detailed mechanism is unclear, these pro-inflammatory and apoptotic factors may increase through the mtDNA-cGAS-STING pathway. In addition, the internalized bacterial endotoxin lipopolysaccharide activated Gasdermin D, which promotes the formation of mitochondrial pores and induces mtDNA release into the cytosol of endothelial cells (93). The released mtDNA was recognized by cGAS, leading to the synthesis of cGAMP, which suppressed endothelial cell proliferation by down-regulating the YAP1 signaling pathway (93). In the inflammatory lung injury model, cGAS deficiency can restore the regeneration capacity of endothelial cells, suggesting that targeting the Gasdermin D-activated cGAS-YAP signaling pathway may be a new strategy for restoring endothelial function after inflammatory injury (93). Furthermore, viral infection also induces mtDNA release, for example, cGAS senses the virus by detecting the release of mtDNA during dengue virus infection (94), and viroporin activity of influenza virus M2 is essential for mtDNA release into the cytosol in a MAVS-dependent manner (95). mtDNA stress promotes cGAS-dependent cytoplasmic mtDNA recognition, enhancing antiviral signaling and IFN-I responses during infection by activating STING-TBK1-IRF3 signaling (86).

Overactivation of the mtDNA-cGAS-STING axis is an important factor in inflammation caused by mtDNA leakage. Conversely, mtDNA released in response to stress in tumor cells induces autophagy-dependent ferroptosis through cGAS-STING signaling pathway activation (96). Therefore, regulating the activation of cGAS-STING in response to mtDNA leakage could be a disease treatment strategy.

cGAS Recognizes Nuclear-Derived dsDNA in the Cytoplasm

Nuclear DNA leakage, which forms micronuclei in the cytoplasm, is the main source for abnormal accumulation of cytoplasmic DNA (97). In normal cells, DNA double-strand breaks can be precisely repaired by homologous recombination to maintain genome stability and inhibit tumorigenesis (98). In contrast, widespread instability of the tumor cell genome could lead to chromosome pulverization that generates micronuclei during mitosis (99). The nuclear membrane of micronuclei is unstable and easy to rupture, causing micronucleus-derived DNA to activate cGAS and induce IFN-I (**Figure 4**) (100).

DNA damage and the expression of senescence-associated secretory phenotype (SASP) factors, including pro-inflammatory factors, are the key signs of cellular senescence (101, 102). Once cells enter the senescence process, nuclear membrane damage occurs, causing nuclear DNA leakage. The nuclear-derived DNA activates cGAS, which in turn increases SASP expression (101). Deletion of cGAS eliminates SASP gene expression and other cellular senescence markers, suggesting a key role of cGAS in regulating the effect of DNA damage, SASP expression, and cellular senescence (101).

cGAS Enters the Nucleus to Recognize Genomic DNA

cGAS has been reported to be abundantly present in the nucleus of certain cells, including HeLa and MEF cells (103), which raises

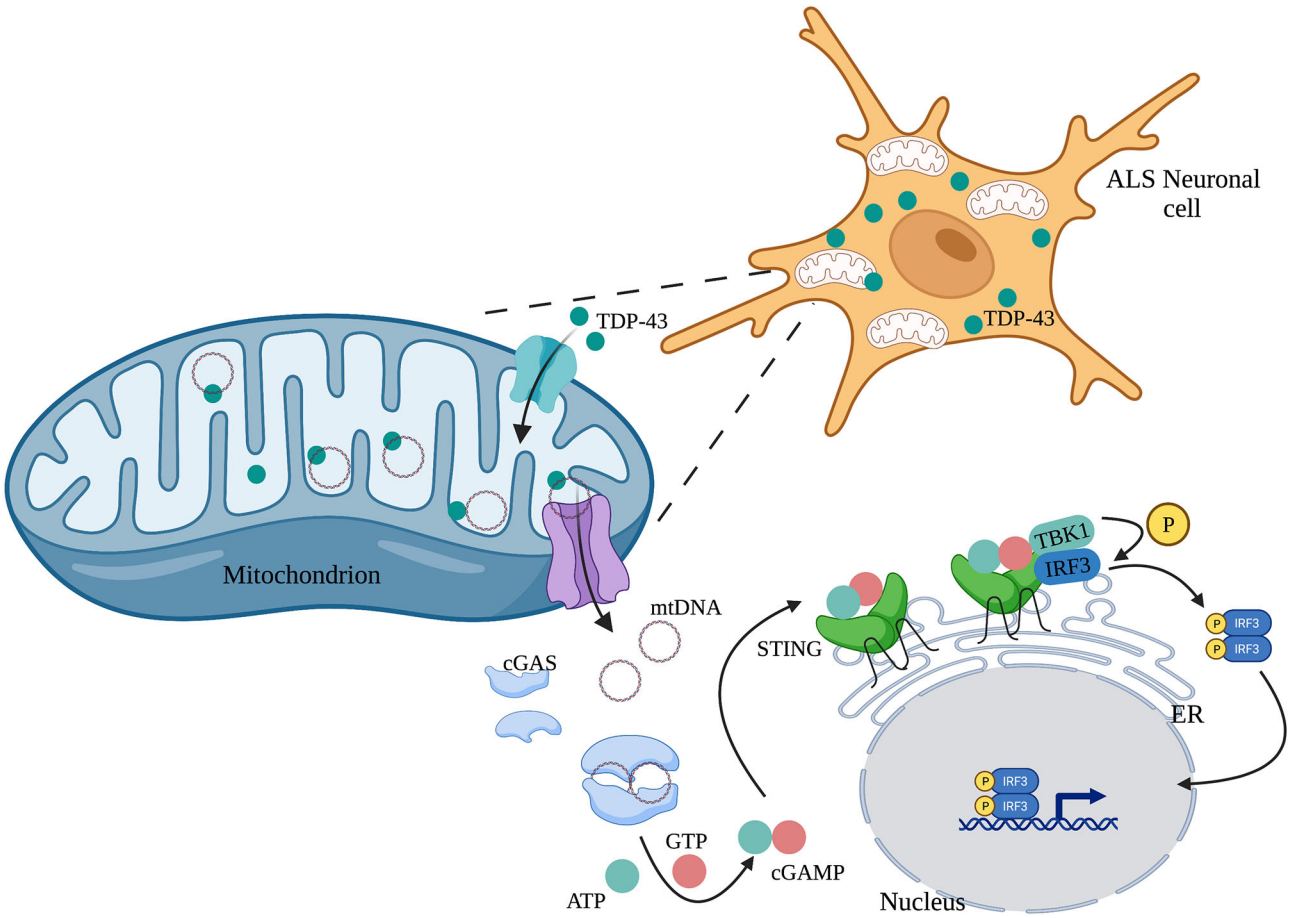

FIGURE 3 | TDP-43 induces mtDNA leakage in ALS neuronal cells. A large amount of TDP-43 protein is present in the neuronal cells of patients with ALS, which causes mtDNA release into the cytoplasm through the mPTP pathway. mtDNA leakage in turn activates the cGAS-STING signaling pathway and induces the production of inflammatory factors.

two issues that need to be addressed. First, it is unclear whether there are functional differences between nuclear-localized cGAS and cytoplasmic cGAS. Second, if nuclear-localized cGAS can also recognize DNA, what mechanism is involved? Indeed, nuclear-localized cGAS displays non-canonical functions independent of STING. One study found that cGAS slows down the replication fork by interacting with replication fork proteins in a DNA binding-dependent manner (58). Another study revealed that nuclear cGAS recruits protein arginine methyltransferase 5 to the enhancer of antiviral genes and enhances antiviral gene transcription through histone modification, thereby inducing innate immune responses (53). In addition, during DNA damage, nuclear translocation of cGAS is induced in a manner that is dependent on importin-α (55). In the nucleus, cGAS is recruited to DNA double-strand breaks and interacts with PARP1 through poly (ADP-ribose), which hinders the formation of PARP1-Timeless complex and inhibits the homologous recombination of broken double strands to promote tumorigenesis (55). In addition to the above non-canonical functions, activation of the IFN pathway by cGAS is inhibited during mitosis. Recent research revealed a critical mechanism underlying cGAS inactivation in mitosis: nuclear cGAS is tethered tightly by a salt-resistant interaction, which maintains the quiescent state of cGAS and prevents autoreactivity (25). Barrier-to-autointegration factor 1 (BAF), a chromatin-binding protein, can also inhibit cGAS activity through competitive binding with dsDNA, thereby inhibiting the formation of cGAS-DNA complexes during mitosis (104). Another study found that nuclear cGAS binds to the negatively charged acidic plaques formed by histones H2A and H2B through its second DNA binding site, which blocks the binding of cGAS and dsDNA and maintains nuclear cGAS in an inactive conformation (103, 105). In addition, two studies revealed that during mitotic entry, the CDK1-cyclin B complex hyperphosphorylates human cGAS at S305 (or mouse cGAS at S291), which inhibits its ability to synthesize cGAMP. Upon mitotic exit, type 1 phosphatase dephosphorylates cGAS to restore its DNA sensing ability (60, 106).

In summary, cells utilize several ingenious molecular mechanisms to mitigate the potential immune activation

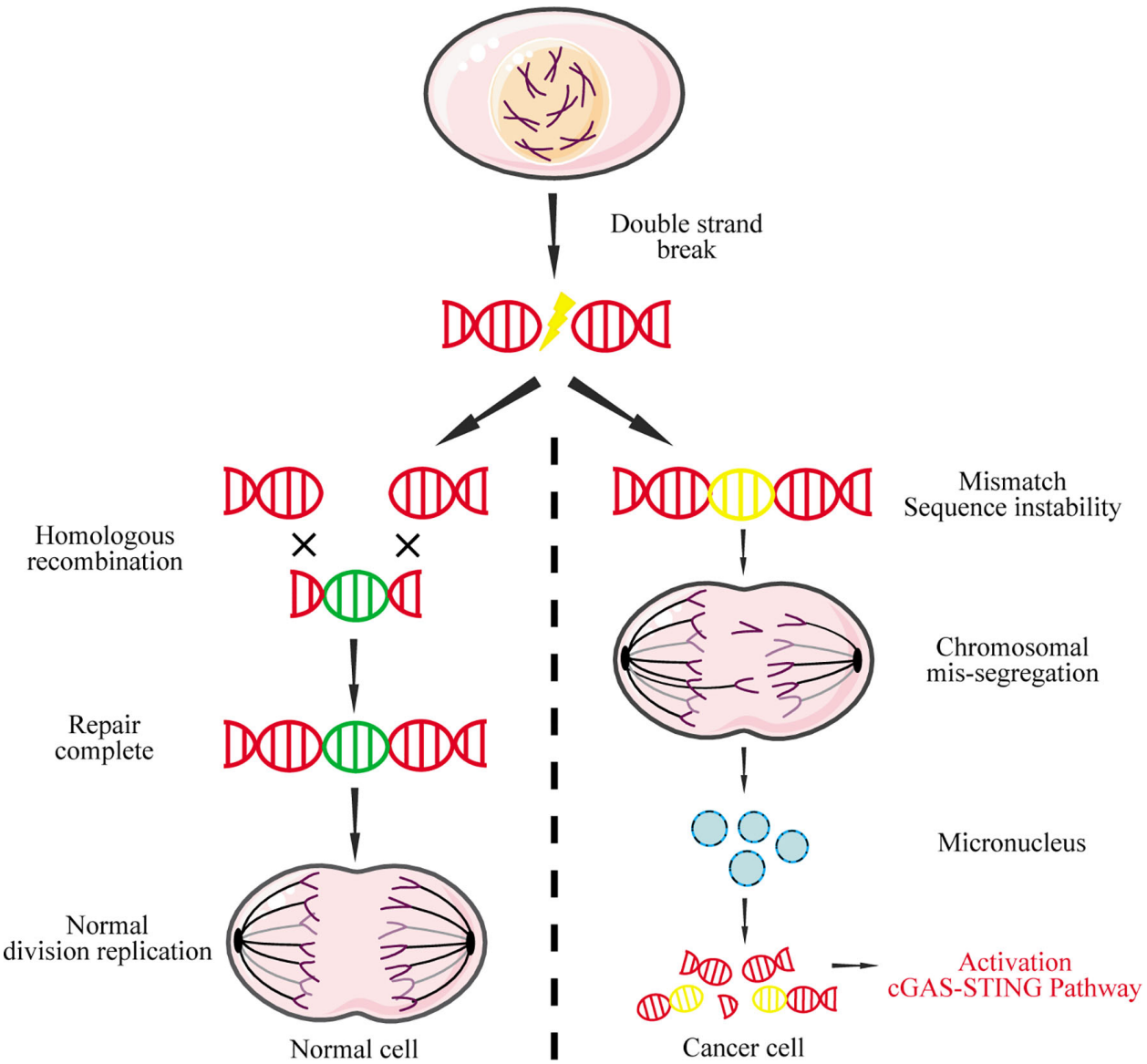

FIGURE 4 | Micronucleus-derived DNA activates the cGAS-STING signaling pathway. DNA double-strand breaks caused by physical or chemical factors during mitosis can be repaired by homologous recombination in normal cells. However, due to the instability of the cancer genome, chromosomal missegregation is often caused during mitosis, resulting in the formation of micronuclei. The nuclear membrane of these micronuclei is fragile and easily ruptured, causing the DNA to leak into the cytoplasm, which in turn activates the cGAS-STING signaling pathway.

caused by the recognition of nuclear DNA by cGAS, thereby ensuring cGAS perform its biological functions normally. When these regulatory mechanisms fail, cGAS misrecognition of nuclear DNA can lead to various cellular dysfunctional processes, including cellular senescence, inflammation, and tumorigenesis (17, 97, 107–109).

cGAS Associates With Telomeric DNA

Telomeres are protective structures at the end of chromosomes that gradually shorten with cell division (110). When telomeres are shortened to the limit, DNA damage signaling will be activated, triggering replicative senescence (111). A recent study showed that cGAS binds to telomeric/subtelomeric and recruits CDK1, which blocks the recruitment of RNF8 and avoids inappropriate DNA damage repair during mitosis (111). cGAS deficiency will cause chromosome end-to-end fusion between short telomeres to form dicentric chromosomes, hindering the initiation of cellular replicative senescence, resulting in genomic instability and increasing the probability of cell cancerization (111). In addition, telomere dysfunction leads to production of extrachromosomal DNA fragments that promote autophagy by activating the cGAS-STING signaling pathway (112).

Telomerase activity is significantly elevated in cancer cells. However, there is another mechanism to maintain extrachromosomal telomere repeats (ECTR) DNA sequence in cancer cells called alternative lengthening of telomeres (ALT) (113, 114). Studies have confirmed that induction of ECTRs in normal human fibroblasts activates the cGAS-STING signaling pathway, which in turn induces IFN-β production and leads to cell proliferation defect (114). Given that IFN-β has the function of activating immunity (115), *in vivo*, ECTR-induced IFN-β produced by ALT-induced cancer cells may exert anticancer functions. However, cGAS and STING expression are lost in most ALT cancer cell lines (114). Therefore, specific activation of the cGAS-STING signaling pathway in ALT-induced cancers may become a new therapeutic option.

cGAS Recognizes cDNA

cGAS can also recognize cDNA (ssDNA) reverse-transcribed from HIV-1 virus, causing a cascade of immune responses and inducing IRF3 activation and IFN production; these effects are inhibited in the absence of or by knocking down cGAS-STING signaling (116, 117). A subsequent study found that ssDNA is a predominantly cytosolic DNA species in the early stage of HIV infection. Stem-loop structures in primary HIV-1 cDNA, similar to the Y-form structure, activate cGAS in a sequence-specific manner (118). These phenomena were also observed for other retroviruses, including HIV-2 (119), mouse leukemia virus, and simian immunodeficiency virus (116).

Hepatitis B virus (HBV) is an enveloped virus containing partially double-stranded DNA, belonging to the Hepadnaviridae family. The mechanism for induction of innate immunity in response to HBV has been controversial (120–122). However, a recent study showed that HBV RNA does not cause immune stimulation in immunologically active bone marrow cells, while naked HBV DNA can (123). It was shown that the relaxed circular DNA (rcDNA) produced during HBV replication can be recognized by cGAS, thereby inducing an immune response (123).

Long interspersed element-1 (LINE1) is a type of retrotransposon (124). In the human genome, the vast majority of LINE1 are silent, but their overactivation can cause a variety of age-related pathologies, such as neurodegenerative diseases and cancer (125). SIRT6 is an ADP-ribose transferase enzyme/deacetylase involved in the regulation of LINE1 (126, 127). In *sirt6*$^{-/-}$ mice, the activity of LINE1 and the levels of IFN-I were significantly increased along with many aging-related characteristics, including growth retardation and a significantly shortened lifespan (128). *In vivo*, the use of nucleoside reverse transcriptase inhibitors (NRTIs) to target LINE1 can significantly extend the lifespan of *sirt6*$^{-/-}$mice; *in vitro*, inhibiting LINE1 with siRNA or NRTIs can eliminate IFN-I production. The number of detectable DNA damage markers in the cytoplasm is also significantly reduced (128). Interestingly, cGAS expression was also elevated in *sirt6*$^{-/-}$ MEF cells. Knockdown of cGAS in *sirt6*$^{-/-}$ MEF cells resulted in a decrease of IFN-I in the cytoplasm. Further evidence shows that cGAS can induce IFN-I by recognizing the cDNA transcribed from LINE1 (128).

Potential Functional Relationships Between cGAS and RNA

Virus-Derived RNA

Current research shows that the expression of IFNs induced by cGAS is stimulated by dsDNA, not RNA binding. The induction of IFN-β by dsRNA analogs poly(I:C) and poly(dA:dT) depends on the classic RIG-I-like receptor, not cGAS (129). Sendai virus is a known RNA virus that activates the RIG-I pathway and induces IFN-β expression, which is not affected by cGAS or STING deletion (67). However, not all RNA viruses follow the classic receptor recognition pathway. Some RNA virus infections seem to be affected by cGAS. West Nile virus is a single-stranded RNA virus, but *cGas*$^{-/-}$ mice are significantly more susceptible to infection compared to wildtype controls (130). Chikungunya virus (CHIKV) is another positive-sense single-stranded RNA virus. A study reported that the CHIKV capsid protein could induce cGAS degradation, thereby inhibiting DNA-dependent IFN-β transcription, whereas the cGAS-STING signaling pathway restrained CHIKV replication in fibroblasts and immune cells (131). Therefore, cGAS deficiency may downregulate certain antiviral genes, making cells more susceptible to some RNA viruses.

Interestingly, cGAS can recognize DNA : RNA hybrids and efficiently synthesize cGAMP in THP1 cells, although the induced cGAMP is less than that induced by dsDNA (132). In one protein-nucleic acid interaction model, RNA : DNA hybrids could bind the cGAS cleft in the same way as dsDNA, regardless of the orientation of the RNA and DNA strands. The structural comparison of dsDNA and RNA : DNA hybrids shows that they have similar double-stranded helical conformations, and their small and large grooves have similar shapes (132). Therefore, the mechanism by which RNA : DNA hybrids activate cGAS may be similar to that used by dsDNA to activate cGAS. Though the cGAS-STING signaling pathway responds to some RNA virus infections, the detailed underlying mechanism needs further investigation.

Circular RNAs (circRNAs)

circRNAs are a widespread form of non-coding RNA in eukaryotes, with tissue-specific and cell-specific expression patterns, whose biogenesis is regulated by specific cis-acting elements and trans-acting factors (133).

Under homeostasis, most hematopoietic stem cells in the bone marrow are quiescent and maintain the potential for self-renewal and differentiation (134). Disrupting the balance between self-renewal and differentiation of hematopoietic stem cells can cause bone marrow failure or hematological malignancies (135). A recent study found a circRNA derived from the D430042O09Rik gene transcript in mice, cia-cGAS, regulates the long-term homeostasis of hematopoietic stem cells (57). cia-cGAS is highly expressed in the nucleus of LT-HSC. IFN-I expression is increased in the bone marrow of cia-cGAS deficient mice, which in turn causes hematopoietic stem cells to exit the G0 phase and enter the active phase until exhaustion (57). Under homeostasis, cia-cGAS binds to cGAS in the nucleus, inhibits its enzymatic activity, and protects LT-HSC in the

dormant phase from cGAS-mediated "cell exhaustion". Furthermore, the binding affinity of cia-cGAS to cGAS is stronger than self-DNA to cGAS, which inhibits the production of IFN-I mediated by cGAS in LT-HSC, thereby maintaining the steady-state of LT-HSC (57).

This study provided an interesting new avenue for exploring the correlation and interaction between cGAS and circRNA, suggesting a potential new function of cGAS that is distinct from its role as a DNA sensor.

cGAS SIGNALING IN CELLULAR DYSFUNCTION

cGAS Signaling and Cellular Senescence

Cellular senescence is a state of irreversible growth arrest caused by various factors including oxidative stress, oncogenic stress, and telomere shortening. Although the causes and phenotypes of cellular senescence are diverse, a persistent DNA damage response is considered to be an important feature of cellular senescence (136).

Multiple studies provide strong evidence that cGAS plays an important role in promoting cellular senescence (101, 137, 138). With successive passaging of primary MEFs, most of the cells eventually senesce, and only a small fraction overcome the growth crisis and become immortal. Indepth studies have found that cGAS deletion accelerates the spontaneous immortalization of MEF cells, because the absence of cGAS eliminates SASP induced by spontaneous immortalization or DNA damaging agents (101). In addition, cGAS is activated by cytosolic chromatin fragments in senescent cells, which triggers the production of SASP factors through STING, thereby promoting paracrine senescence (137). These studies provided new insight into the mechanism of cellular senescence by establishing the cGAS-STING signaling pathway as an intermediate bridge between senescence and the SASP.

cGAS Signaling and Inflammation

The aberrant activation of the cGAS-STING signaling pathway has been implicated in a variety of inflammatory diseases.

Myocardial infarction (MI) involves a strong inflammatory response in related tissues. One study found that cGAS activation by self-DNA from apoptotic cells is the main cause of MI-related IFN-I production (139). In this model, ischemic myocardial injury causes cardiomyocyte damage and nucleic acid release, which activates the cGAS-STING axis. Compared to wildtype littermates, the survival rate of cGAS-deficient mice after MI is significantly higher, with the mice also showing reduced pathological remodeling including ventricular rupture, enhanced angiogenesis, and maintenance of myocardial contractile function (140).

Aicardi-Goutières syndrome (AGS) is a rare genetic disease characterized by systemic inflammation that most commonly affects the brain and skin. Patients with this disease often develop severe physical and mental disorders, chronic aseptic lymphocytosis, and elevated IFN-I levels (82). Studies have confirmed that the loss-of-function mutation of trex1 exonuclease is related to the development of AGS (141, 142). Similar to human AGS patients, trex1-deficient mice develop autoimmune disorders and fatal inflammatory phenotypes associated with high expression of ISGs (143, 144), which can be rescued by cGAS gene knockout (145). Elevated cGAMP can be detected in tissues from *trex1*$^{-/-}$ mice, demonstrating that cGAS is activated in these mice (142).

Systemic lupus erythematosus (SLE) is a serious chronic inflammatory disease that can affect most of the body's tissues and organs, including the skin, joints, kidneys, blood cells, and nervous system. Although the phenotype and course of SLE vary greatly, the disease is associated with a systemic increase of IFN-I and a defect in apoptotic cell clearance (81). A recent study showed that the expression of cGAS in peripheral blood mononuclear cells of patients with SLE was significantly higher than that of the control group; the higher the cGAMP level, the higher the disease activity in patients with SLE (146). Loss of trex1 can lead to accumulation of cytoplasmic DNA and the development of autoimmune diseases, including AGS and SLE. Our research group constructed *trex1*$^{D18N/D18N}$ mice, which show similar disease phenotypes as in patients with AGS and SLE. In these mice, we verified that cGAS deletion reduces multiple organ inflammation (147). Together, ours and others' studies indicate that cGAS is a key mediator of autoimmune diseases related to trex1 dysfunction.

In conclusion, several studies strongly support a central role of the cGAS-cGAMP-STING pathway in the pathogenesis of various IFN-I-mediated inflammatory diseases. Therefore, the development of drugs that target this pathway may provide new hope for the treatment of such inflammatory diseases.

cGAS Signaling and Tumorigenesis

The link between DNA damage and cancer has long been established. While this means that cells with DNA damage will be recognized and eliminated by immune cells, genomic instability itself is an important driver of cancer. Given the importance of cGAS in the DNA recognition pathway, it plays a crucial role in both aspects of cancer. Although the activation of the cGAS-STING signaling pathway has been tested as a potential cancer immunotherapy (see *Therapeutic Strategies in Tumor Immunotherapy*), the potential negative tumorigenic effects of overactivation of the cGAS signaling cannot be ignored.

7,12-dimethylbenz[a]anthracene (DMBA) is a known carcinogen. It activates the cGAS-STING signaling pathway by inducing DNA breaks and promotes skin carcinogenesis in mice. Interestingly, unlike other cancer models, DMBA-treated *sting*$^{-/-}$ mice were found to be more resistant to DMBA-induced skin cancer growth (148). Brain metastatic cells contain cytoplasmic dsDNA, which activate cGAS and produce large amounts of cGAMP. The connexin 43-based functional gap junctions between cancer cells and astrocytes allow the transfer of cGAMP to astrocytes, where it activates TBK1 and IRF3 and induces the production of IFN-α and TNF-α. These cytokines activate STAT1 and NF-κB signaling pathways in brain metastatic cells to support the growth and survival of cancer cells under the pressure of chemotherapy (149). Furthermore, the DNA damage

caused by etoposide, camptothecin, and H_2O_2 treatment can induce nuclear translocation of cGAS. The nuclear cGAS significantly suppresses the repair of DNA damage mediated by homologous recombination, and induces transformation of the damaged cells leading to tumorigenesis (55).

THERAPEUTIC STRATEGIES TARGETING THE cGAS PATHWAY

Therapeutic Strategies in Inflammatory Diseases

Given that the cGAS pathway is involved in a variety of inflammatory diseases, inhibitors or antagonists targeting the cGAS-STING signaling pathway are being considered as potential therapeutics. At present, a variety of effective inhibitors/antagonists of cGAS have been developed. 2-amino pyridine ring (G150) blocks the binding of dsDNA and cGAS by occupying the ATP and GTP binding active sites on cGAS (150). Suramin replaces the DNA bound to cGAS to block the downstream immune response. *In vitro*, adding suramin to THP1 cells can effectively reduce the expression levels of IFN-β mRNA and protein (151). RU.521 selectively binds to cGAS, thereby inhibiting cGAMP induced by dsDNA and reducing expression of IFN in a dose-dependent manner, without affecting other inflammatory pathways independent of the cGAS pathway (152). Aspirin is a common non-steroidal anti-inflammatory drug. It can acetylate cyclooxygenase, including cGAS, thereby inactivating cGAS. One study confirmed that aspirin can effectively inhibit autoimmunity induced by self-DNA in the cells of patients with AGS and AGS mouse models (153).

Therapeutic Strategies in Tumor Immunotherapy

Radiotherapy is a conventional cancer treatment method; damage of cancer cells triggers the release of pro-inflammatory factors and increases the infiltration of immune cells in the tumor (154). Studies have found that radiotherapy induces IFN-I in tumors and IFN-I receptors on immune cells (especially $CD8^+$ T cells), which are critical to its therapeutic effectiveness (155, 156). Meanwhile, cGAS deficiency in dendritic cells (DC) is sufficient to eliminate antitumor immunity *in vitro* (157). Subsequent studies have shown that the cGAS-STING signaling pathway is an important contributor to antitumor immunity after radiotherapy by detecting DNA damage in tumor cells and promoting the recognition of tumor-derived DNA in immune cells (158, 159). Additional studies have shown that cGAS is essential for the antitumor effect of immune checkpoint blockade in mice (160). Antibodies against the immune checkpoint inhibitor PD1/PD-L1 can effectively slow the growth rate of mouse B16 melanoma (161). Intramuscular injection of cGAMP also inhibits the growth of melanoma and prolongs the survival of tumor-bearing mice, as cGAMP activates DC and enhances the cross-presentation of tumor-associated antigens to CD8 T cells. The combination of the PD-L1 antibodies and cGAMP has a synergistic effect beyond each treatment alone (160). These studies show that the activation of the cGAS pathway is important in anti-tumor immunotherapy; however, given that the cGAS pathway also has a tumor-promoting effect, unchecked activation of the cGAS signaling pathway in tumor cells is not a therapeutic option.

CONCLUSIONS AND FUTURE DIRECTIONS

The discovery of the cGAS-STING signaling pathway provides a comprehensive functional network for activation of the dsDNA-dependent innate immune response, and plays a particularly important role in activating the immune response against DNA viruses. The cGAS-STING signaling pathway also modulates cell transfection and gene delivery, and may be harnessed to enhance the development of new antiviral therapies and nucleic acid vaccines (68, 162). However, the recognition of self-DNA by cGAS can cause various diseases, including inflammatory and autoimmune diseases, largely due to the overexpression of IFN. Therefore, inhibitors targeting cGAS may be a promising treatment approach for such diseases. Given that STING is the most important adaptor protein mediating cGAS-mediated IFN expression, inhibitors targeting STING may also have therapeutic applications (**Figure 5**).

At the same time, researchers have also found that the cGAS-STING signaling pathway is inhibited in various cancer cells ranging from melanoma (163) to ovarian cancer (164), and colorectal carcinoma (165). The mechanisms underlying this phenomenon have yet to be uncovered. Our group recently used zebularine (a demethylating agent) to activate the cGAS-STING signaling pathway in tumor cells (166). In our mouse tumor models, zebularine enhanced STING expression by reducing DNA methylation on the STING gene promoter. Administration of zebularine alone reduced tumor burden and extended mouse survival; its combination with cGAMP or immune checkpoint inhibitors had a synergistic anti-tumor effect (166). Thus, activating the cGAS-STING signaling pathway in tumor cells can significantly enhance tumor immunotherapy effects (**Figure 5**).

In addition, the ability of cGAS to sense cDNA, DNA : RNA hybrids, and circRNA, as well as the functional differences related to its subcellular localization, indicates that cGAS has multifaceted biological functions. Although no research has shown whether dsDNA, cDNA, DNA : RNA hybrids, and circRNA have similar characteristics, it is conceivable that the nucleic acid-sensing ability of cGAS may depend on the modulation of its structural flexibility and the interaction between cGAS and the elaborate structures of these different nucleic acid species.

In summary, research on cGAS has expanded our understanding of its roles, beyond a traditional cytoplasmic nucleic acid sensor, and has clarified the mechanisms that cGAS uses to recognize different types of nucleic acids. These studies have shed light on the relationship between cGAS and antiviral immunity, tumor immunity, inflammatory response,

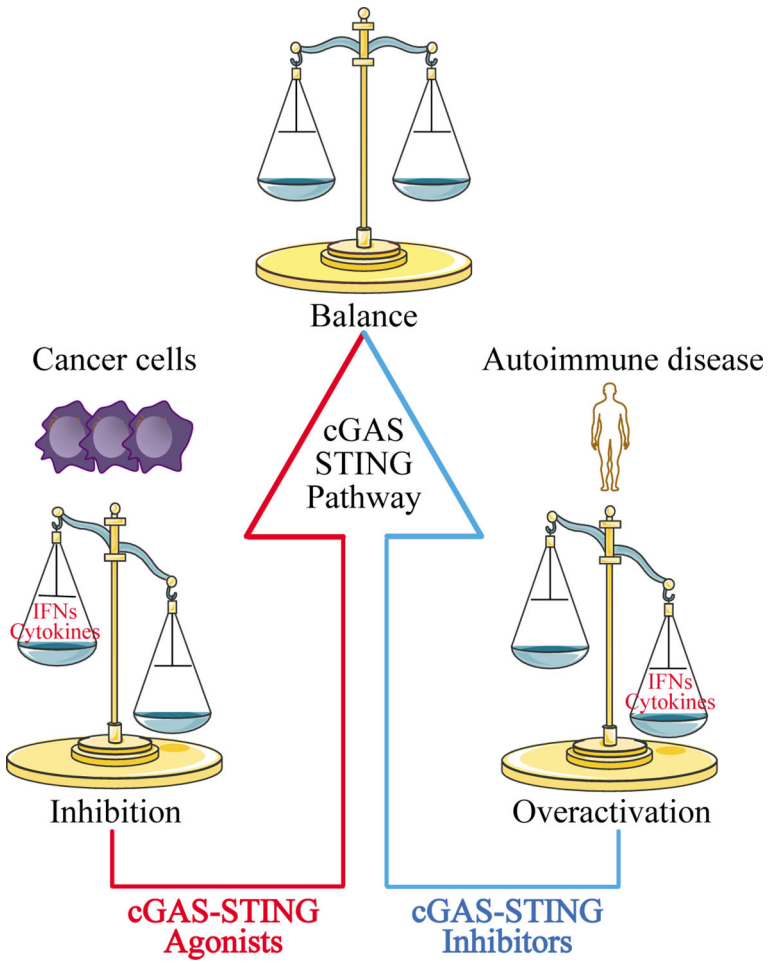

FIGURE 5 | Disease treatment strategies targeting the cGAS-STING signaling pathway. For cancer cells with low expression of cGAS-STING, using cGAS-STING agonists to activate the pathway is one approach to restoring immune surveillance and enhancing immune cell infiltration into tumors. For autoimmune diseases and inflammatory diseases caused by overactivation of the cGAS-STING signaling pathway, blocking the pathway with cGAS-STING inhibitors may provide an effective therapeutic strategy.

and autoimmune diseases. The cGAS-STING signaling pathway may be a promising drug target for inflammatory and autoimmune diseases or inform the design of effective nucleic acid drugs to treat various diseases.

AUTHOR CONTRIBUTIONS

DW and YS conceived the manuscript. DW and HZ drafted the manuscript. QC revised the manuscript. All authors contributed to manuscript revision, read, and approved the submitted version.

FUNDING

This work was supported by the National Natural Science Foundation of China (Grant No. 81770222).

ACKNOWLEDGMENTS

We sincerely thank colleagues in the QC lab for discussion and support.

REFERENCES

1. Yamamoto S, Kuramoto E, Shimada S, Tokunaga T. *In Vitro* Augmentation of Natural Killer Cell Activity and Production of Interferon-Alpha/Beta and -Gamma With Deoxyribonucleic Acid Fraction From Mycobacterium Bovis BCG. *Jpn J Cancer Res* (1988) 79:866–73. doi: 10.1111/j.1349-7006.1988.tb00049.x
2. Cowdery JS, Chace JH, Yi AK, Krieg AM. Bacterial DNA Induces NK Cells to Produce IFN-Gamma *In Vivo* and Increases the Toxicity of Lipopolysaccharides. *J Immunol* (1996) 156:4570–5.

3. Krieg AM, Yi AK, Matson S, Waldschmidt TJ, Bishop GA, Teasdale R, et al. CpG Motifs in Bacterial DNA Trigger Direct B-Cell Activation. *Nature* (1995) 374:546–9. doi: 10.1038/374546a0
4. Hemmi H, Takeuchi O, Kawai T, Kaisho T, Sato S, Sanjo H, et al. A Toll-Like Receptor Recognizes Bacterial DNA. *Nature* (2000) 408:740–5. doi: 10.1038/35047123
5. Hornung V, Latz E. Intracellular DNA Recognition. *Nat Rev Immunol* (2010) 10:123–30. doi: 10.1038/nri2690
6. Akira S, Uematsu S, Takeuchi O. Pathogen Recognition and Innate Immunity. *Cell* (2006) 124:783–801. doi: 10.1016/j.cell.2006.02.015
7. Cavlar T, Ablasser A, Hornung V. Induction of Type I IFNs by Intracellular DNA-Sensing Pathways. *Immunol Cell Biol* (2012) 90:474–82. doi: 10.1038/icb.2012.11
8. Yoneyama M, Fujita T. Recognition of Viral Nucleic Acids in Innate Immunity. *Rev Med Virol* (2010) 20:4–22. doi: 10.1002/rmv.633
9. Nakhaei P, Genin P, Civas A. Hiscott J.RIG-I-Like Receptors: Sensing and Responding to RNA Virus Infection. *Semin Immunol* (2009) 21:215–22. doi: 10.1016/j.smim.2009.05.001
10. Kawai T, Akira S. Toll-Like Receptors and Their Crosstalk With Other Innate Receptors in Infection and Immunity. *Immunity* (2011) 34:637–50. doi: 10.1016/j.immuni.2011.05.006
11. Kim YK, Shin JS, Nahm MH. NOD-Like Receptors in Infection, Immunity, and Diseases. *Yonsei Med J* (2016) 57:5–14. doi: 10.3349/ymj.2016.57.1.5
12. Sancho D, Reis e Sousa C. Signaling by Myeloid C-Type Lectin Receptors in Immunity and Homeostasis. *Annu Rev Immunol* (2012) 30:491–529. doi: 10.1146/annurev-immunol-031210-101352
13. Rehwinkel J, Gack MU. RIG-I-Like Receptors: Their Regulation and Roles in RNA Sensing. *Nat Rev Immunol* (2020) 20:537–51. doi: 10.1038/s41577-020-0288-3
14. Briard B, Place DE, Kanneganti TD. DNA Sensing in the Innate Immune Response. *Physiology (Bethesda)* (2020) 35:112–24. doi: 10.1152/physiol.00022.2019
15. Takaoka A, Wang Z, Choi MK, Yanai H, Negishi H, Ban T, et al. DAI (DLM-1/ZBP1) Is a Cytosolic DNA Sensor and an Activator of Innate Immune Response. *Nature* (2007) 448:501–5. doi: 10.1038/nature06013
16. Unterholzner L, Keating SE, Baran M, Horan KA, Jensen SB, Sharma S, et al. IFI16 is an Innate Immune Sensor for Intracellular DNA. *Nat Immunol* (2010) 11:997–1004. doi: 10.1038/ni.1932
17. Zhang F, Yuan Y, Ma F. Function and Regulation of Nuclear DNA Sensors During Viral Infection and Tumorigenesis. *Front Immunol* (2021) 11:624556. doi: 10.3389/fimmu.2020.624556
18. Zhang Z, Yuan B, Bao M, Lu N, Kim T, Liu YJ. The Helicase DDX41 Senses Intracellular DNA Mediated by the Adaptor STING in Dendritic Cells. *Nat Immunol* (2011) 12:959–65. doi: 10.1038/ni.2091
19. Kondo T, Kobayashi J, Saitoh T, Maruyama K, Ishii KJ, Barber GN, et al. DNA Damage Sensor MRE11 Recognizes Cytosolic Double-Stranded DNA and Induces Type I Interferon by Regulating STING Trafficking. *Proc Natl Acad Sci U S A* (2013) 110:2969–74. doi: 10.1073/pnas.1222694110
20. Li Y, Chen R, Zhou Q, Xu Z, Li C, Wang S, et al. LSm14A is a Processing Body-Associated Sensor of Viral Nucleic Acids That Initiates Cellular Antiviral Response in the Early Phase of Viral Infection. *Proc Natl Acad Sci U S A* (2012) 109:11770–5. doi: 10.1073/pnas.1203405109
21. Kim T, Pazhoor S, Bao M, Zhang Z, Hanabuchi S, Facchinetti V, et al. Aspartate-Glutamate-Alanine-Histidine Box Motif (DEAH)/RNA Helicase A Helicases Sense Microbial DNA in Human Plasmacytoid Dendritic Cells. *Proc Natl Acad Sci U S A* (2010) 107:15181–6. doi: 10.1073/pnas.1006539107
22. Wang L, Wen M, Cao X. Nuclear Hnrnpa2b1 Initiates and Amplifies the Innate Immune Response to DNA Viruses. *Science* (2019) 365:eaav0758. doi: 10.1126/science.aav0758
23. Sun L, Wu J, Du F, Chen X, Chen ZJ. Cyclic GMP-AMP Synthase is a Cytosolic DNA Sensor That Activates the Type I Interferon Pathway. *Science* (2013) 339:786–91. doi: 10.1126/science.1232458
24. Barnett KC, Coronas-Serna JM, Zhou W, Ernandes MJ, Cao A, Kranzusch PJ, et al. Phosphoinositide Interactions Position cGAS at the Plasma Membrane to Ensure Efficient Distinction Between Self- and Viral DNA. *Cell* (2019) 176:1432–46.e11. doi: 10.1016/j.cell.2019.01.049
25. Volkman HE, Cambier S, Gray EE, Stetson DB. Tight Nuclear Tethering of cGAS is Essential for Preventing Autoreactivity. *Elife* (2019) 8:e47491. doi: 10.7554/eLife.47491
26. Wischnewski M, Ablasser A. Interplay of cGAS With Chromatin. *Trends Biochem Sci* (2021) 46:822–31. doi: 10.1016/j.tibs.2021.05.011
27. Kwon J, Bakhoum SF. The Cytosolic DNA-Sensing cGAS-STING Pathway in Cancer. *Cancer Discov* (2020) 10:26–39. doi: 10.1158/2159-8290.CD-19-0761
28. Wu J, Sun L, Chen X, Du F, Shi H, Chen C, et al. Cyclic GMP-AMP is an Endogenous Second Messenger in Innate Immune Signaling by Cytosolic DNA. *Science* (2013) 339:826–30. doi: 10.1126/science.1229963
29. Zhang X, Shi H, Wu J, Zhang X, Sun L, Chen C, et al. Cyclic GMP-AMP Containing Mixed Phosphodiester Linkages is an Endogenous High-Affinity Ligand for STING. *Mol Cell* (2013) 51:226–35. doi: 10.1016/j.molcel.2013.05.022
30. Ishikawa H, Barber GN. STING is an Endoplasmic Reticulum Adaptor That Facilitates Innate Immune Signalling. *Nature* (2008) 455:674–8. doi: 10.1038/nature07317
31. Mukai K, Konno H, Akiba T, Uemura T, Waguri S, Kobayashi T, et al. Activation of STING Requires Palmitoylation at the Golgi. *Nat Commun* (2016) 7:11932. doi: 10.1038/ncomms11932
32. Chen Q, Sun L, Chen ZJ. Regulation and Function of the cGAS-STING Pathway of Cytosolic DNA Sensing. *Nat Immunol* (2016) 17:1142–9. doi: 10.1038/ni.3558
33. Liu S, Cai X, Wu J, Cong Q, Chen X, Li T, et al. Phosphorylation of Innate Immune Adaptor Proteins MAVS, STING, and TRIF Induces IRF3 Activation. *Science* (2015) 347:aaa2630. doi: 10.1126/science.aaa2630
34. Tanaka Y, Chen ZJ. STING Specifies IRF3 Phosphorylation by TBK1 in the Cytosolic DNA Signaling Pathway. *Sci Signal* (2012) 5:ra20. doi: 10.1126/scisignal.2002521
35. Moretti J, Roy S, Bozec D, Martinez J, Chapman JR, Ueberheide B, et al. STING Senses Microbial Viability to Orchestrate Stress-Mediated Autophagy of the Endoplasmic Reticulum. *Cell* (2017) 171:809–23.e813. doi: 10.1016/j.cell.2017.09.034
36. Saxton RA, Sabatini DM. mTOR Signaling in Growth, Metabolism, and Disease. *Cell* (2017) 168:960–76. doi: 10.1016/j.cell.2017.02.004
37. Liang Q, Seo GJ, Choi YJ, Kwak MJ, Ge J, Rodgers MA, et al. Crosstalk Between the cGAS DNA Sensor and Beclin-1 Autophagy Protein Shapes Innate Antimicrobial Immune Responses. *Cell Host Microbe* (2014) 15:228–38. doi: 10.1016/j.chom.2014.01.009
38. Watson RO, Manzanillo PS, Cox JS. Extracellular M. Tuberculosis DNA Targets Bacteria for Autophagy by Activating the Host DNA-Sensing Pathway. *Cell* (2012) 150:803–15. doi: 10.1016/j.cell.2012.06.040
39. Lan YY, Londoño D, Bouley R, Rooney MS, Hacohen N. Dnase2a Deficiency Uncovers Lysosomal Clearance of Damaged Nuclear DNA *via* Autophagy. *Cell Rep* (2014) 9:180–92. doi: 10.1016/j.celrep.2014.08.074
40. Gao P, Ascano M, Wu Y, Barchet W, Gaffney BL, Zillinger T, et al. Cyclic [G(2',5')pA(3',5')p] is the Metazoan Second Messenger Produced by DNA-Activated Cyclic GMP-AMP Synthase. *Cell* (2013) 153:1094–107. doi: 10.1016/j.cell.2013.04.046
41. Kato K, Ishii R, Goto E, Ishitani R, Tokunaga F, Nureki O. Structural and Functional Analyses of DNA-Sensing and Immune Activation by Human cGAS. *PloS One* (2013) 8:e76983. doi: 10.1371/journal.pone.0076983
42. Zhang X, Wu J, Du F, Xu H, Sun L, Chen Z, et al. The Cytosolic DNA Sensor cGAS Forms an Oligomeric Complex With DNA and Undergoes Switch-Like Conformational Changes in the Activation Loop. *Cell Rep* (2014) 6:421–30. doi: 10.1016/j.celrep.2014.01.003
43. Kranzusch PJ, Lee AS, Berger JM, Doudna JA. Structure of Human cGAS Reveals a Conserved Family of Second-Messenger Enzymes in Innate Immunity. *Cell Rep* (2013) 3:1362–8. doi: 10.1016/j.celrep.2013.05.008
44. Civril F, Deimling T, de Oliveira Mann CC, Ablasser A, Moldt M, Witte G, et al. Structural Mechanism of Cytosolic DNA Sensing by cGAS. *Nature* (2013) 498:332–7. doi: 10.1038/nature12305
45. Ding C, Song Z, Shen A, Chen T, Zhang A. Small Molecules Targeting the Innate Immune cGAS–STING–TBK1 Signaling Pathway. *Acta Pharm Sin B* (2020) 10:2272–98. doi: 10.1016/j.apsb.2020.03.001
46. Zhang X, Bai XC, Chen ZJ. Structures and Mechanisms in the cGAS-STING Innate Immunity Pathway. *Immunity* (2020) 53:43–53. doi: 10.1016/j.immuni.2020.05.013
47. Tao J, Zhang XW, Jin J, Du XX, Lian T, Yang J, et al. Nonspecific DNA Binding of cGAS N Terminus Promotes cGAS Activation. *J Immunol* (2017) 198:3627–36. doi: 10.4049/jimmunol.1601909

48. Zhang J, Zhao J, Xu S, Li J, He S, Zeng Y, et al. Species-Specific Deamidation of cGAS by Herpes Simplex Virus UL37 Protein Facilitates Viral Replication. *Cell Host Microbe* (2018) 24:234–48.e235. doi: 10.1016/j.chom.2018.07.004
49. Hu MM, Shu HB. Innate Immune Response to Cytoplasmic DNA: Mechanisms and Diseases. *Annu Rev Immunol* (2020) 38:79–98. doi: 10.1146/annurev-immunol-070119-115052
50. Du M, Chen ZJ. DNA-Induced Liquid Phase Condensation of cGAS Activates Innate Immune Signaling. *Science* (2018) 361:704–9. doi: 10.1126/science.aat1022
51. Andreeva L, Hiller B, Kostrewa D, Lässig C, de Oliveira Mann CC, Jan Drexler D, et al. cGAS Senses Long and HMGB/TFAM-Bound U-Turn DNA by Forming Protein-DNA Ladders. *Nature* (2017) 549:394–8. doi: 10.1038/nature23890
52. Zhou W, Whiteley AT, de Oliveira Mann CC, Morehouse BR, Nowak RP, Fischer ES, et al. Structure of the Human cGAS-DNA Complex Reveals Enhanced Control of Immune Surveillance. *Cell* (2018) 174:300–11.e311. doi: 10.1016/j.cell.2018.06.026
53. Cui S, Yu Q, Chu L, Cui Y, Ding M, Wang Q, et al. Nuclear cGAS Functions Non-Canonically to Enhance Antiviral Immunity *via* Recruiting Methyltransferase Prmt5. *Cell Rep* (2020) 33:108490. doi: 10.1016/j.celrep.2020.108490
54. Gentili M, Lahaye X, Nadalin F, Nader GPF, Puig Lombardi E, Herve S, et al. The N-Terminal Domain of cGAS Determines Preferential Association With Centromeric DNA and Innate Immune Activation in the Nucleus. *Cell Rep* (2019) 26:2377–93.e2313. doi: 10.1016/j.celrep.2019.01.105
55. Liu H, Zhang H, Wu X, Ma D, Wu J, Wang L, et al. Nuclear cGAS Suppresses DNA Repair and Promotes Tumorigenesis. *Nature* (2018) 563:131–6. doi: 10.1038/s41586-018-0629-6
56. Zierhut C, Yamaguchi N, Paredes M, Luo JD, Carroll T, Funabiki H. The Cytoplasmic DNA Sensor cGAS Promotes Mitotic Cell Death. *Cell* (2019) 178:302–15.e323. doi: 10.1016/j.cell.2019.05.035
57. Xia P, Wang S, Ye B, Du Y, Li C, Xiong Z, et al. A Circular RNA Protects Dormant Hematopoietic Stem Cells From DNA Sensor cGAS-Mediated Exhaustion. *Immunity* (2018) 48:688–701.e687. doi: 10.1016/j.immuni.2018.03.016
58. Chen H, Chen H, Zhang J, Wang Y, Simoneau A, Yang H, et al. cGAS Suppresses Genomic Instability as a Decelerator of Replication Forks. *Sci Adv* (2020) 6:eabb8941. doi: 10.1126/sciadv.abb8941
59. Bai J, Liu F. Nuclear cGAS: Sequestration and Beyond. *Protein Cell* (2021) 13:90–101. doi: 10.1007/s13238-021-00869-0
60. Zhong L, Hu MM, Bian LJ, Liu Y, Chen Q, Shu HB. Phosphorylation of cGAS by CDK1 Impairs Self-DNA Sensing in Mitosis. *Cell Discov* (2020) 6:26. doi: 10.1038/s41421-020-0162-2
61. Raab M, Gentili M, de Belly H, Thiam HR, Vargas P, Jimenez AJ, et al. ESCRT III Repairs Nuclear Envelope Ruptures During Cell Migration to Limit DNA Damage and Cell Death. *Science* (2016) 352:359–62. doi: 10.1126/science.aad7611
62. Hopfner KP, Hornung V. Molecular Mechanisms and Cellular Functions of cGAS-STING Signalling. *Nat Rev Mol Cell Biol* (2020) 21:501–21. doi: 10.1038/s41580-020-0244-x
63. Ablasser A, Hur S. Regulation of cGAS- and RLR-Mediated Immunity to Nucleic Acids. *Nat Immunol* (2020) 21:17–29. doi: 10.1038/s41590-019-0556-1
64. Huang J, You H, Su C, Li Y, Chen S, Zheng C. Herpes Simplex Virus 1 Tegument Protein VP22 Abrogates cGAS/STING-Mediated Antiviral Innate Immunity. *J Virol* (2018) 92:e00841–18. doi: 10.1128/JVI.00841-18
65. Barber GN. STING-Dependent Cytosolic DNA Sensing Pathways. *Trends Immunol* (2014) 35:88–93. doi: 10.1016/j.it.2013.10.010
66. Song ZM, Lin H, Yi XM, Guo W, Hu MM, Shu HB. KAT5 Acetylates cGAS to Promote Innate Immune Response to DNA Virus. *Proc Natl Acad Sci USA* (2020) 117:21568–75. doi: 10.1073/pnas.1922330117
67. Li XD, Wu J, Gao D, Wang H, Sun L, Chen ZJ. Pivotal Roles of cGAS-cGAMP Signaling in Antiviral Defense and Immune Adjuvant Effects. *Science* (2013) 341:1390–4. doi: 10.1126/science.1244040
68. Ishikawa H, Ma Z, Barber GN. STING Regulates Intracellular DNA-Mediated, Type I Interferon-Dependent Innate Immunity. *Nature* (2009) 461:788–92. doi: 10.1038/nature08476
69. Ma Z, Jacobs SR, West JA, Stopford C, Zhang Z, Davis Z, et al. Modulation of the cGAS-STING DNA Sensing Pathway by Gammaherpesviruses. *Proc Natl Acad Sci U S A* (2015) 112:E4306–15. doi: 10.1073/pnas.1503831112
70. Lau L, Gray EE, Brunette RL, Stetson DB. DNA Tumor Virus Oncogenes Antagonize the cGAS-STING DNA-Sensing Pathway. *Science* (2015) 350:568–71. doi: 10.1126/science.aab3291
71. Paijo J, Döring M, Spanier J, Grabski E, Nooruzzaman M, Schmidt T, et al. cGAS Senses Human Cytomegalovirus and Induces Type I Interferon Responses in Human Monocyte-Derived Cells. *PloS Pathog* (2016) 12:e1005546. doi: 10.1371/journal.ppat.1005546
72. Lam E, Falck-Pedersen E. Unabated Adenovirus Replication Following Activation of the cGAS/STING-Dependent Antiviral Response in Human Cells. *J Virol* (2014) 88:14426–39. doi: 10.1128/JVI.02608-14
73. El-Jesr M, Teir M, Maluquer de Motes C. Vaccinia Virus Activation and Antagonism of Cytosolic DNA Sensing. *Front Immunol* (2020) 11:568412. doi: 10.3389/fimmu.2020.568412
74. Tan X, Sun L, Chen J, Chen ZJ. Detection of Microbial Infections Through Innate Immune Sensing of Nucleic Acids. *Annu Rev Microbiol* (2018) 72:447–78. doi: 10.1146/annurev-micro-102215-095605
75. Hansen K, Prabakaran T, Laustsen A, Jørgensen SE, Rahbæk SH, Jensen SB, et al. Listeria Monocytogenes Induces Ifnβ Expression Through an IFI16-, cGAS- and STING-Dependent Pathway. *EMBO J* (2014) 33:1654–66. doi: 10.15252/embj.201488029
76. Andrade WA, Agarwal S, Mo S, Shaffer SA, Dillard JP, Schmidt T, et al. Type I Interferon Induction by Neisseria Gonorrhoeae: Dual Requirement of Cyclic GMP-AMP Synthase and Toll-Like Receptor 4. *Cell Rep* (2016) 15:2438–48. doi: 10.1016/j.celrep.2016.05.030
77. Langereis MA, Rabouw HH, Holwerda M, Visser LJ, van Kuppeveld FJ. Knockout of cGAS and STING Rescues Virus Infection of Plasmid DNA-Transfected Cells. *J Virol* (2015) 89:11169–73. doi: 10.1128/JVI.01781-15
78. Fu Y, Fang Y, Lin Z, Yang L, Zheng L, Hu H, et al. Inhibition of cGAS-Mediated Interferon Response Facilitates Transgene Expression. *iScience* (2020) 23:101026. doi: 10.1016/j.isci.2020.101026
79. Riley JS, Tait SW. Mitochondrial DNA in Inflammation and Immunity. *EMBO Rep* (2020) 21:e49799. doi: 10.15252/embr.201949799
80. Maekawa H, Inoue T, Ouchi H, Jao TM, Inoue R, Nishi H, et al. Mitochondrial Damage Causes Inflammation *via* cGAS-STING Signaling in Acute Kidney Injury. *Cell Rep* (2019) 29:1261–73.e1266. doi: 10.1016/j.celrep.2019.09.050
81. Crowl JT, Gray EE, Pestal K, Volkman HE, Stetson DB. Intracellular Nucleic Acid Detection in Autoimmunity. *Annu Rev Immunol* (2017) 35:313–36. doi: 10.1146/annurev-immunol-051116-052331
82. Crow YJ. Type I Interferonopathies: Mendelian Type I Interferon Up-Regulation. *Curr Opin Immunol* (2015) 32:7–12. doi: 10.1016/j.coi.2014.10.005
83. Sliter DA, Martinez J, Hao L, Chen X, Sun N, Fischer TD, et al. Parkin and PINK1 Mitigate STING-Induced Inflammation. *Nature* (2018) 561:258–62. doi: 10.1038/s41586-018-0448-9
84. Rongvaux A, Jackson R, Harman CC, Li T, West AP, de Zoete MR, et al. Apoptotic Caspases Prevent the Induction of Type I Interferons by Mitochondrial DNA. *Cell* (2014) 159:1563–77. doi: 10.1016/j.cell.2014.11.037
85. Kasashima K, Sumitani M, Endo H. Human Mitochondrial Transcription Factor A is Required for the Segregation of Mitochondrial DNA in Cultured Cells. *Exp Cell Res* (2011) 317:210–20. doi: 10.1016/j.yexcr.2010.10.008
86. West AP, Khoury-Hanold W, Staron M, Tal MC, Pineda CM, Lang SM, et al. Mitochondrial DNA Stress Primes the Antiviral Innate Immune Response. *Nature* (2015) 520:553–7. doi: 10.1038/nature14156
87. Shih YH, Tu LH, Chang TY, Ganesan K, Chang WW, Chang PS, et al. TDP-43 Interacts With Amyloid-β, Inhibits Fibrillization, and Worsens Pathology in a Model of Alzheimer's Disease. *Nat Commun* (2020) 11:5950. doi: 10.1038/s41467-020-19786-7
88. Saberi S, Stauffer JE, Schulte DJ, Ravits J. Neuropathology of Amyotrophic Lateral Sclerosis and Its Variants. *Neurol Clin* (2015) 33:855–76. doi: 10.1016/j.ncl.2015.07.012
89. Yu CH, Davidson S, Harapas CR, Hilton JB, Mlodzianoski MJ, Laohamonthonkul P, et al. TDP-43 Triggers Mitochondrial DNA Release *via* mPTP to Activate cGAS/STING in ALS. *Cell* (2020) 183:636–49.e618. doi: 10.1016/j.cell.2020.09.020
90. Banoth B, Cassel SL. Mitochondria in Innate Immune Signaling. *Transl Res* (2018) 202:52–68. doi: 10.1016/j.trsl.2018.07.014

91. White MJ, McArthur K, Metcalf D, Lane RM, Cambier JC, Herold MJ, et al. Apoptotic Caspases Suppress mtDNA-Induced STING-Mediated Type I IFN Production. *Cell* (2014) 159:1549–62. doi: 10.1016/j.cell.2014.11.036
92. Pinti M, Cevenini E, Nasi M, De Biasi S, Salvioli S, Monti D, et al. Circulating Mitochondrial DNA Increases With Age and is a Familiar Trait: Implications for "Inflamm-Aging". *Eur J Immunol* (2014) 44:1552–62. doi: 10.1002/eji.201343921
93. Huang LS, Hong Z, Wu W, Xiong S, Zhong M, Gao X, et al. mtDNA Activates cGAS Signaling and Suppresses the YAP-Mediated Endothelial Cell Proliferation Program to Promote Inflammatory Injury. *Immunity* (2020) 52:475–86.e475. doi: 10.1016/j.immuni.2020.02.002
94. Aguirre S, Luthra P, Sanchez-Aparicio MT, Maestre AM, Patel J, Lamothe F, et al. Dengue Virus NS2B Protein Targets cGAS for Degradation and Prevents Mitochondrial DNA Sensing During Infection. *Nat Microbiol* (2017) 2:17037. doi: 10.1038/nmicrobiol.2017.37
95. Moriyama M, Koshiba T, Ichinohe T. Influenza A Virus M2 Protein Triggers Mitochondrial DNA-Mediated Antiviral Immune Responses. *Nat Commun* (2019) 10:4624. doi: 10.1038/s41467-019-12632-5
96. Li C, Zhang Y, Liu J, Kang R, Klionsky DJ, Tang D. Mitochondrial DNA Stress Triggers Autophagy-Dependent Ferroptotic Death. *Autophagy* (2021) 17:948–60. doi: 10.1080/15548627.2020.1739447
97. Li T, Chen ZJ. The cGAS-cGAMP-STING Pathway Connects DNA Damage to Inflammation, Senescence, and Cancer. *J Exp Med* (2018) 215:1287–99. doi: 10.1084/jem.20180139
98. Wright WD, Shah SS, Heyer WD. Homologous Recombination and the Repair of DNA Double-Strand Breaks. *J Biol Chem* (2018) 293:10524–35. doi: 10.1074/jbc.TM118.000372
99. Crasta K, Ganem NJ, Dagher R, Lantermann AB, Ivanova EV, Pan Y, et al. DNA Breaks and Chromosome Pulverization From Errors in Mitosis. *Nature* (2012) 482:53–8. doi: 10.1038/nature10802
100. Hatch EM, Fischer AH, Deerinck TJ, Hetzer MW. Catastrophic Nuclear Envelope Collapse in Cancer Cell Micronuclei. *Cell* (2013) 154:47–60. doi: 10.1016/j.cell.2013.06.007
101. Yang H, Wang H, Ren J, Chen Q, Chen ZJ. cGAS is Essential for Cellular Senescence. *Proc Natl Acad Sci U S A* (2017) 114:E4612–20. doi: 10.1073/pnas.1705499114
102. Coppé JP, Desprez PY, Krtolica A, Campisi J. The Senescence-Associated Secretory Phenotype: The Dark Side of Tumor Suppression. *Annu Rev Pathol* (2010) 5:99–118. doi: 10.1146/annurev-pathol-121808-102144
103. Zhao B, Xu P, Rowlett CM, Jing T, Shinde O, Lei Y, et al. The Molecular Basis of Tight Nuclear Tethering and Inactivation of cGAS. *Nature* (2020) 587:673–7. doi: 10.1038/s41586-020-2749-z
104. Guey B, Wischnewski M, Decout A, Makasheva K, Kaynak M, Sakar MS, et al. BAF Restricts cGAS on Nuclear DNA to Prevent Innate Immune Activation. *Science* (2020) 369:823–8. doi: 10.1126/science.aaw6421
105. Pathare GR, Decout A, Glück S, Cavadini S, Makasheva K, Hovius R, et al. Structural Mechanism of cGAS Inhibition by the Nucleosome. *Nature* (2020) 587:668–72. doi: 10.1038/s41586-020-2750-6
106. Li T, Huang T, Du M, Chen X, Du F, Ren J, et al. Phosphorylation and Chromatin Tethering Prevent cGAS Activation During Mitosis. *Science* (2021) 371:eabc5386. doi: 10.1126/science.abc5386
107. Loo TM, Miyata K, Tanaka Y, Takahashi A. Cellular Senescence and Senescence-Associated Secretory Phenotype *via* the cGAS-STING Signaling Pathway in Cancer. *Cancer Sci* (2020) 111:304–11. doi: 10.1111/cas.14266
108. Wan D, Jiang W, Hao J. Research Advances in How the cGAS-STING Pathway Controls the Cellular Inflammatory Response. *Front Immunol* (2020) 11:615. doi: 10.3389/fimmu.2020.00615
109. Zheng J, Mo J, Zhu T, Zhuo W, Yi Y, Hu S, et al. Comprehensive Elaboration of the cGAS-STING Signaling Axis in Cancer Development and Immunotherapy. *Mol Cancer* (2020) 19:133. doi: 10.1186/s12943-020-01250-1
110. Turner KJ, Vasu V, Griffin DK. Telomere Biology and Human Phenotype. *Cells* (2019) 8:73. doi: 10.3390/cells8010073
111. Li X, Li X, Xie C, Cai S, Li M, Jin H, et al. cGAS Guards Against Chromosome End-to-End Fusions During Mitosis and Facilitates Replicative Senescence. *Protein Cell* (2021) 13:47–64. doi: 10.1007/s13238-021-00879-y
112. Nassour J, Radford R, Correia A, Fusté JM, Schoell B, Jauch A, et al. Autophagic Cell Death Restricts Chromosomal Instability During Replicative Crisis. *Nature* (2019) 565:659–63. doi: 10.1038/s41586-019-0885-0
113. Henson JD, Neumann AA, Yeager TR, Reddel RR. Alternative Lengthening of Telomeres in Mammalian Cells. *Oncogene* (2002) 21:598–610. doi: 10.1038/sj.onc.1205058
114. Chen YA, Shen YL, Hsia HY, Tiang YP, Sung TL, Chen LY. Extrachromosomal Telomere Repeat DNA is Linked to ALT Development *via* cGAS-STING DNA Sensing Pathway. *Nat Struct Mol Biol* (2017) 24:1124–31. doi: 10.1038/nsmb.3498
115. Zitvogel L, Galluzzi L, Kepp O, Smyth MJ, Kroemer G. Type I Interferons in Anticancer Immunity. *Nat Rev Immunol* (2015) 15:405–14. doi: 10.1038/nri3845
116. Gao D, Wu J, Wu YT, Du F, Aroh C, Yan N, et al. Cyclic GMP-AMP Synthase is an Innate Immune Sensor of HIV and Other Retroviruses. *Science* (2013) 341:903–6. doi: 10.1126/science.1240933
117. Sumner RP, Harrison L, Touizer E, Peacock TP, Spencer M, Zuliani-Alvarez L, et al. Disrupting HIV-1 Capsid Formation Causes cGAS Sensing of Viral DNA. *EMBO J* (2020) 39:e103958. doi: 10.15252/embj.2019103958
118. Herzner AM, Hagmann CA, Goldeck M, Wolter S, Kübler K, Wittmann S, et al. Sequence-Specific Activation of the DNA Sensor cGAS by Y-Form DNA Structures as Found in Primary HIV-1 cDNA. *Nat Immunol* (2015) 16:1025–33. doi: 10.1038/ni.3267
119. Lahaye X, Satoh T, Gentili M, Cerboni S, Conrad C, Hurbain I, et al. The Capsids of HIV-1 and HIV-2 Determine Immune Detection of the Viral cDNA by the Innate Sensor cGAS in Dendritic Cells. *Immunity* (2013) 39:1132–42. doi: 10.1016/j.immuni.2013.11.002
120. Thomsen MK, Nandakumar R, Stadler D, Malo A, Valls RM, Wang F, et al. Lack of Immunological DNA Sensing in Hepatocytes Facilitates Hepatitis B Virus Infection. *Hepatology* (2016) 64:746–59. doi: 10.1002/hep.28685
121. Guo F, Tang L, Shu S, Sehgal M, Sheraz M, Liu B, et al. Activation of Stimulator of Interferon Genes in Hepatocytes Suppresses the Replication of Hepatitis B Virus. *Antimicrob Agents Chemother* (2017) 61:e00771–17. doi: 10.1128/AAC.00771-17
122. Cheng X, Xia Y, Serti E, Block PD, Chung M, Chayama K, et al. Hepatitis B Virus Evades Innate Immunity of Hepatocytes But Activates Cytokine Production by Macrophages. *Hepatology* (2017) 66:1779–93. doi: 10.1002/hep.29348
123. Lauterbach-Rivière L, Bergez M, Mönch S, Qu B, Riess M, Vondran FWR, et al. Hepatitis B Virus DNA is a Substrate for the cGAS/STING Pathway But is Not Sensed in Infected Hepatocytes. *Viruses* (2020) 12:592. doi: 10.3390/v12060592
124. An W, Dai L, Niewiadomska AM, Yetil A, O'Donnell KA, Han JS, et al. Characterization of a Synthetic Human LINE-1 Retrotransposon ORFeus-Hs. *Mob DNA* (2011) 2:2. doi: 10.1186/1759-8753-2-2
125. Hancks DC, Kazazian HHJr. Active Human Retrotransposons: Variation and Disease. *Curr Opin Genet Dev* (2012) 22:191–203. doi: 10.1016/j.gde.2012.02.006
126. Kuang J, Chen L, Tang Q, Zhang J, Li Y, He J. The Role of Sirt6 in Obesity and Diabetes. *Front Physiol* (2018) 9:135. doi: 10.3389/fphys.2018.00135
127. Van Meter M, Kashyap M, Rezazadeh S, Geneva AJ, Morello TD, Seluanov A, et al. SIRT6 Represses LINE1 Retrotransposons by Ribosylating KAP1 But This Repression Fails With Stress and Age. *Nat Commun* (2014) 5:5011. doi: 10.1038/ncomms6011
128. Simon M, Van Meter M, Ablaeva J, Ke Z, Gonzalez RS, Taguchi T, et al. LINE1 Derepression in Aged Wild-Type and SIRT6-Deficient Mice Drives Inflammation. *Cell Metab* (2019) 29:871–85.e875. doi: 10.1016/j.cmet.2019.02.014
129. Yoneyama M, Kikuchi M, Natsukawa T, Shinobu N, Imaizumi T, Miyagishi M, et al. The RNA Helicase RIG-I has an Essential Function in Double-Stranded RNA-Induced Innate Antiviral Responses. *Nat Immunol* (2004) 5:730–7. doi: 10.1038/ni1087
130. Schoggins JW, MacDuff DA, Imanaka N, Gainey MD, Shrestha B, Eitson JL, et al. Pan-Viral Specificity of IFN-Induced Genes Reveals New Roles for cGAS in Innate Immunity. *Nature* (2014) 505:691–5. doi: 10.1038/nature12862
131. Webb LG, Veloz J, Pintado-Silva J, Zhu T, Rangel MV, Mutetwa T, et al. Chikungunya Virus Antagonizes cGAS-STING Mediated Type-I Interferon Responses by Degrading cGAS. *PloS Pathog* (2020) 16:e1008999. doi: 10.1371/journal.ppat.1008999

132. Mankan AK, Schmidt T, Chauhan D, Goldeck M, Höning K, Gaidt M, et al. Cytosolic RNA:DNA Hybrids Activate the cGAS-STING Axis. *EMBO J* (2014) 33:2937–46. doi: 10.15252/embj.201488726
133. Kristensen LS, Andersen MS, Stagsted LVW, Ebbesen KK, Hansen TB, Kjems J. The Biogenesis, Biology and Characterization of Circular RNAs. *Nat Rev Genet* (2019) 20:675–91. doi: 10.1038/s41576-019-0158-7
134. Singh S, Jakubison B, Keller JR. Protection of Hematopoietic Stem Cells From Stress-Induced Exhaustion and Aging. *Curr Opin Hematol* (2020) 27:225–31. doi: 10.1097/MOH.0000000000000586
135. Ficara F, Murphy MJ, Lin M, Cleary ML. Pbx1 Regulates Self-Renewal of Long-Term Hematopoietic Stem Cells by Maintaining Their Quiescence. *Cell Stem Cell* (2008) 2:484–96. doi: 10.1016/j.stem.2008.03.004
136. Mohamad Kamal NS, Safuan S, Shamsuddin S, Foroozandeh P. Aging of the Cells: Insight Into Cellular Senescence and Detection Methods. *Eur J Cell Biol* (2020) 99:151108. doi: 10.1016/j.ejcb.2020.151108
137. Glück S, Guey B, Gulen MF, Wolter K, Kang TW, Schmacke NA, et al. Innate Immune Sensing of Cytosolic Chromatin Fragments Through cGAS Promotes Senescence. *Nat Cell Biol* (2017) 19:1061–70. doi: 10.1038/ncb3586
138. Dou Z, Ghosh K, Vizioli MG, Zhu J, Sen P, Wangensteen KJ, et al. Cytoplasmic Chromatin Triggers Inflammation in Senescence and Cancer. *Nature* (2017) 550:402–6. doi: 10.1038/nature24050
139. King KR, Aguirre AD, Ye YX, Sun Y, Roh JD, Ng RPJr, et al. IRF3 and Type I Interferons Fuel a Fatal Response to Myocardial Infarction. *Nat Med* (2017) 23:1481–7. doi: 10.1038/nm.4428
140. Cao DJ, Schiattarella GG, Villalobos E, Jiang N, May HI, Li T, et al. Cytosolic DNA Sensing Promotes Macrophage Transformation and Governs Myocardial Ischemic Injury. *Circulation* (2018) 137:2613–34. doi: 10.1161/CIRCULATIONAHA.117.031046
141. Crow YJ, Rehwinkel J. Aicardi-Goutieres Syndrome and Related Phenotypes: Linking Nucleic Acid Metabolism With Autoimmunity. *Hum Mol Genet* (2009) 18:R130–136. doi: 10.1093/hmg/ddp293
142. Gao D, Li T, Li XD, Chen X, Li QZ, Wight-Carter M, et al. Activation of Cyclic GMP-AMP Synthase by Self-DNA Causes Autoimmune Diseases. *Proc Natl Acad Sci U S A* (2015) 112:E5699–705. doi: 10.1073/pnas.1516465112
143. Crow YJ, Hayward BE, Parmar R, Robins P, Leitch A, Ali M, et al. Mutations in the Gene Encoding the 3'-5' DNA Exonuclease TREX1 Cause Aicardi-Goutières Syndrome at the AGS1 Locus. *Nat Genet* (2006) 38:917–20. doi: 10.1038/ng1845
144. Ahn J, Ruiz P, Barber GN. Intrinsic Self-DNA Triggers Inflammatory Disease Dependent on STING. *J Immunol* (2014) 193:4634–42. doi: 10.4049/jimmunol.1401337
145. Gray EE, Treuting PM, Woodward JJ, Stetson DB. Cutting Edge: cGAS Is Required for Lethal Autoimmune Disease in the Trex1-Deficient Mouse Model of Aicardi-Goutières Syndrome. *J Immunol* (2015) 195:1939–43. doi: 10.4049/jimmunol.1500969
146. An J, Durcan L, Karr RM, Briggs TA, Rice GI, Teal TH, et al. Expression of Cyclic GMP-AMP Synthase in Patients With Systemic Lupus Erythematosus. *Arthritis Rheumatol* (2017) 69:800–7. doi: 10.1002/art.40002
147. Xiao N, Wei J, Xu S, Du H, Huang M, Zhang S, et al. cGAS Activation Causes Lupus-Like Autoimmune Disorders in a TREX1 Mutant Mouse Model. *J Autoimmun* (2019) 100:84–94. doi: 10.1016/j.jaut.2019.03.001
148. Ahn J, Xia T, Konno H, Konno K, Ruiz P, Barber GN. Inflammation-Driven Carcinogenesis is Mediated Through STING. *Nat Commun* (2014) 5:5166. doi: 10.1038/ncomms6166
149. Chen Q, Boire A, Jin X, Valiente M, Er EE, Lopez-Soto A, et al. Carcinoma-Astrocyte Gap Junctions Promote Brain Metastasis by cGAMP Transfer. *Nature* (2016) 533:493–8. doi: 10.1038/nature18268
150. Lama L, Adura C, Xie W, Tomita D, Kamei T, Kuryavyi V, et al. Development of Human cGAS-Specific Small-Molecule Inhibitors for Repression of dsDNA-Triggered Interferon Expression. *Nat Commun* (2019) 10:2261. doi: 10.1038/s41467-019-08620-4
151. Wang M, Sooreshjani MA, Mikek C, Opoku-Temeng C, Sintim HO. Suramin Potently Inhibits cGAMP Synthase, cGAS, in THP1 Cells to Modulate IFN-β Levels. *Future Med Chem* (2018) 10:1301–17. doi: 10.4155/fmc-2017-0322
152. Vincent J, Adura C, Gao P, Luz A, Lama L, Asano Y, et al. Small Molecule Inhibition of cGAS Reduces Interferon Expression in Primary Macrophages From Autoimmune Mice. *Nat Commun* (2017) 8:750. doi: 10.1038/s41467-017-00833-9
153. Dai J, Huang YJ, He X, Zhao M, Wang X, Liu ZS, et al. Acetylation Blocks cGAS Activity and Inhibits Self-DNA-Induced Autoimmunity. *Cell* (2019) 176:1447–60.e1414. doi: 10.1016/j.cell.2019.01.016
154. McLaughlin M, Patin EC, Pedersen M, Wilkins A, Dillon MT, Melcher AA, et al. Inflammatory Microenvironment Remodelling by Tumour Cells After Radiotherapy. *Nat Rev Cancer* (2020) 20:203–17. doi: 10.1038/s41568-020-0246-1
155. Burnette BC, Liang H, Lee Y, Chlewicki L, Khodarev NN, Weichselbaum RR, et al. The Efficacy of Radiotherapy Relies Upon Induction of Type I Interferon-Dependent Innate and Adaptive Immunity. *Cancer Res* (2011) 71:2488–96. doi: 10.1158/0008-5472
156. Lee Y, Auh SL, Wang Y, Burnette B, Wang Y, Meng Y, et al. Therapeutic Effects of Ablative Radiation on Local Tumor Require CD8+ T Cells: Changing Strategies for Cancer Treatment. *Blood* (2009) 114:589–95. doi: 10.1182/blood-2009-02-206870
157. Deng L, Liang H, Xu M, Yang X, Burnette B, Arina A, et al. STING-Dependent Cytosolic DNA Sensing Promotes Radiation-Induced Type I Interferon-Dependent Antitumor Immunity in Immunogenic Tumors. *Immunity* (2014) 41:843–52. doi: 10.1016/j.immuni.2014.10.019
158. Schadt L, Sparano C, Schweiger NA, Silina K, Cecconi V, Lucchiari G, et al. Cancer-Cell-Intrinsic cGAS Expression Mediates Tumor Immunogenicity. *Cell Rep* (2019) 29:1236–48.e1237. doi: 10.1016/j.celrep.2019.09.065
159. Marcus A, Mao AJ, Lensink-Vasan M, Wang L, Vance RE, Raulet DH. Tumor-Derived cGAMP Triggers a STING-Mediated Interferon Response in Non-Tumor Cells to Activate the NK Cell Response. *Immunity* (2018) 49:754–63.e4. doi: 10.1016/j.immuni.2018.09.016
160. Wang H, Hu S, Chen X, Shi H, Chen C, Sun L, et al. cGAS is Essential for the Antitumor Effect of Immune Checkpoint Blockade. *Proc Natl Acad Sci U S A* (2017) 114:1637–42. doi: 10.1073/pnas.1621363114
161. Zou W, Wolchok JD, Chen L. PD-L1 (B7-H1) and PD-1 Pathway Blockade for Cancer Therapy: Mechanisms, Response Biomarkers, and Combinations. *Sci Transl Med* (2016) 8:328rv324. doi: 10.1126/scitranslmed.aad7118
162. Ishii KJ, Kawagoe T, Koyama S, Matsui K, Kumar H, Kawai T, et al. TANK-Binding Kinase-1 Delineates Innate and Adaptive Immune Responses to DNA Vaccines. *Nature* (2008) 451:725–9. doi: 10.1038/nature06537
163. Xia T, Konno H, Barber GN. Recurrent Loss of STING Signaling in Melanoma Correlates With Susceptibility to Viral Oncolysis. *Cancer Res* (2016) 76:6747–59. doi: 10.1158/0008-5472.CAN-16-1404
164. de Queiroz N, Xia T, Konno H, Barber GN. Ovarian Cancer Cells Commonly Exhibit Defective STING Signaling Which Affects Sensitivity to Viral Oncolysis. *Mol Cancer Res* (2019) 17:974–86. doi: 10.1158/1541-7786.MCR-18-0504
165. Xia T, Konno H, Ahn J, Barber GN. Deregulation of STING Signaling in Colorectal Carcinoma C Onstrains DNA Damage Responses and Correlates With Tumorigenesis. *Cell Rep* (2016) 14:282–97. doi: 10.1016/j.celrep.2015.12.029
166. Lai J, Fu Y, Tian S, Huang S, Luo X, Lin L, et al. Zebularine Elevates STING Expression and Enhances cGAMP Cancer Immunotherapy in Mice. *Mol Ther* (2021) 29:1758–71. doi: 10.1016/j.ymthe.2021.02.00

Conflict of Interest: The authors declare that the research was conducted in the absence of any commercial or financial relationships that could be construed as a potential conflict of interest.

frontiers in Immunology

REVIEW
published: 03 March 2022
doi: 10.3389/fimmu.2022.812774

Toll-Like Receptor Signaling and Its Role in Cell-Mediated Immunity

Tianhao Duan[1], *Yang Du*[1], *Changsheng Xing*[1], *Helen Y. Wang*[1,2] *and Rong-Fu Wang*[1,2,3*]

[1] Department of Medicine, Keck School of Medicine, University of Southern California, Los Angeles, CA, United States, [2] Department of Pediatrics, Children's Hospital Los Angeles, Keck School of Medicine, University of Southern California, Los Angeles, CA, United States, [3] Norris Comprehensive Cancer Center, Keck School of Medicine, University of Southern California, Los Angeles, CA, United States

Innate immunity is the first defense system against invading pathogens. Toll-like receptors (TLRs) are well-defined pattern recognition receptors responsible for pathogen recognition and induction of innate immune responses. Since their discovery, TLRs have revolutionized the field of immunology by filling the gap between the initial recognition of pathogens by innate immune cells and the activation of the adaptive immune response. TLRs critically link innate immunity to adaptive immunity by regulating the activation of antigen-presenting cells and key cytokines. Furthermore, recent studies also have shown that TLR signaling can directly regulate the T cell activation, growth, differentiation, development, and function under diverse physiological conditions. This review provides an overview of TLR signaling pathways and their regulators and discusses how TLR signaling, directly and indirectly, regulates cell-mediated immunity. In addition, we also discuss how TLR signaling is critically important in the host's defense against infectious diseases, autoimmune diseases, and cancer.

Keywords: toll-like receptors, cell-mediated immunity, T cells, signaling pathway, infectious diseases, autoimmune diseases, cancer

OPEN ACCESS

Edited by:
Subhasis Chattopadhyay, National Institute of Science Education and Research (NISER), India

Reviewed by:
Subhransu Sekhar Sahoo, Purdue University, United States
Sarang Tartey, IGM Biosciences, United States

***Correspondence:**
Rong-Fu Wang
rongfuwa@usc.edu

Specialty section:
This article was submitted to T Cell Biology, a section of the journal Frontiers in Immunology

Received: *10 November 2021*
Accepted: *08 February 2022*
Published: *03 March 2022*

Citation:
Duan T, Du Y, Xing C, Wang HY and Wang R-F (2022) Toll-Like Receptor Signaling and Its Role in Cell-Mediated Immunity. Front. Immunol. 13:812774. doi: 10.3389/fimmu.2022.812774

INTRODUCTION

The innate immune system is the first line of defense against infectious pathogens and cancer by sensing and responding to the structure-conserved molecules of the pathogens (pathogen-associated molecular patterns, or PAMPs) as well as the endogenous ligands released from damaged cells (damage-associated molecular patterns, or DAMPs). The pattern recognition receptors (PRRs) are a key element of the immune system, including Toll-like receptors (TLRs), RIG-I-like receptors, Nod-like receptors (NLRs), AIM2-like receptors, C-type lectin receptors, and intracellular DNA and RNA sensors (1–3). Upon the recognition of their specific ligands from the invasive pathogens or damaged cells, PRRs initiate a variety of downstream signaling cascades, including nuclear factor kappa B (NF-κB), type I interferon (IFN) and inflammasome signaling pathways, leading to the production of corresponding proinflammatory or antiviral cytokines and chemokines (2, 4). The activation of TLR signaling is also crucial to the induction of antigen-specific adaptive immune responses by promoting the maturation of dendritic cells (DCs) and activating the adaptive immune cells for the clearance of invading pathogens (4–6).

TLRs belong to the family of Type I integral membrane glycoproteins characterized by the extracellular domains containing variable numbers of leucine-rich-repeat (LRR) motifs and a

cytoplasmic Toll/interleukin 1 (IL-1) receptor (TIR) homology domain (7). Toll was identified initially as a gene controlling dorsoventral axis formation of the *Drosophila* embryo in the 1980s (8), and its crucial anti-fungal function in *Drosophila* was demonstrated in 1996 (9). The mammalian homolog of the Toll receptor (now termed TLR4) was first discovered in 1997 to play a critical role the in innate immunity by inducing the expression of inflammatory responses-related genes (10). These findings revolutionized our understanding of the immune system and triggered an explosion of research in PRRs. To date, 10 TLRs have been identified in humans (TLR1–TLR10) and 12 in mice (TLR1–TLR9 and TLR11–TLR13). TLR1–TLR10 are conserved between mice and humans, although mouse TLR10 is not functional, while TLR11–TLR13 are expressed only in mice but not in humans. These receptors are localized on the cell surface (TLR1, TLR2, TLR4, and TLR5) or in intracellular compartments, such as the endoplasmic reticulum, endosome, lysosome, or endolysosome (TLR3, TLR7, TLR8, and TLR9) (6).

Cell surface TLRs mainly recognize membrane components of the microorganisms such as lipids, lipoproteins, and proteins (2). For example, TLR4 recognizes lipopolysaccharide (LPS). TLR2 forms a heterodimer with either TLR1 or TLR6 and recognizes different PAMPs of pathogens (including lipoproteins, peptidoglycans, lipoteichoic acids, zymosan, mannan, and glycosylphosphatidylinositol-anchored mucin-like glycoproteins from Trypanosoma cruzi trypomastigotes) (11). TLR5 recognizes the flagellin of bacteria (2). Human TLR10 can homodimerize or heterodimerize with TLR1, TLR2, and TLR6 (12), and sense HIV proteins (13). Intracellular TLRs mainly recognize nucleic acids derived from pathogens or self-nucleic acids in a disease condition. TLR3 recognizes double-stranded viral RNA and self RNAs derived from damaged cells; TLR7, TLR8, and TLR13 recognize fragments of single-stranded RNA with distinct sequence preferences, and TLR7 is predominantly expressed in plasmacytoid dendritic cells (pDCs). In addition, TLR9 recognizes single-stranded DNA containing unmethylated cytidine-phosphateguanosine (CpG) motifs from bacteria or viruses (6, 14). TLR10 was recently identified to sense HIV-1 gp41 protein but its biological functions in humans haven't been fully elucidated (12, 13).

Each TLR contains a similar cytoplasmic portion known as the TIR domain, which is highly similar to that of the IL-1 receptor family. The extracellular portion of TLRs is the ectodomain, with LRRs displayed as a horseshoe-like structure. The characteristic feature of these LRRs is the consensus sequence motif—$L(X_2)LXL(X_2)NXL(X_2)L(X_7)L(X_2)$—in which X can be any amino acid (15). The ectodomain of TLRs forms a homo- or hetero-dimer along with a co-receptor or accessory molecule to interact with their respective PAMPs or DAMPs (16). TLRs are expressed on all the innate immune cells and a large majority of non-hematopoietic cells, such as macrophages, neutrophils, DCs, natural killer cells, mast cells, basophils, eosinophil, and epithelial cells (4, 17). Importantly, TLRs can also be detected on adaptive immune cells, including T and B cells (18, 19).

Adaptive immunity consists of humoral immunity and cell-mediated immunity, which are mainly mediated by B lymphocytes and T lymphocytes, respectively. Cell-mediated immunity (also called cellular immunity) is responsible for generating a cluster of differentiation 8 $(CD8)^+$ cytotoxic T-lymphocytes (CTLs) and an antigen-specific cluster of differentiation 4 $(CD4)^+$ T helper (Th) cells, which help B cells produce antibodies. CTLs recognize and produce molecules that directly kill infected host cells. In contrast, Th cells release various cytokines that influence the function of other cells involved in both adaptive and innate immune responses (20). To induce efficient activation and clonal expansion of antigen-specific T cells, antigen presentation and co-stimulatory signaling are essential, which must be simultaneously provided by the antigen-presenting cells (APCs) to T cells. Importantly, the production of cytokines, expression of costimulatory molecules, and antigen-presenting activity in APCs are induced or enhanced by microbe-derived adjuvants, which are recognized by TLRs expressed on APCs and boost the APC signaling to promote activation of immune responses in T cells (21). Therefore, TLRs play a critical role in linking the innate immunity and cell-mediated immunity. This review article mainly summarizes the recent progress on TLR signaling pathways and their crucial role in cell-mediated immunity.

TLR SIGNALING PATHWAYS

Innate immunity was formerly thought to be a nonspecific immune response. However, the discovery of TLRs led to the realization of the considerable specificity of innate immunity and its capability to discriminate between self and nonself (22–24). Cell surface TLRs (TLR1, TLR2, TLR4, TLR5, TLR6, and TLR11) mainly recognize microbial membrane components to induce an inflammatory response (11). By contrast, intracellular TLRs (TLR3, TLR7, TLR8, and TLR9) mainly recognize microbial nucleic acids derived from bacteria or viruses and induce Type I IFN responses and inflammatory responses. However, the misrecognition of self-nucleic acids may cause autoimmune diseases (25).

Upon binding by specific ligands, ligand-mediated dimerization of TLR ectodomains results in the coordinate dimerization of the cytosolic TIR domains of each TLR (26). Dimerized receptor TIR domains are detected by two receptor-proximal membrane adaptor proteins: the TIR domain-containing adapter protein (TIRAP; also known as MAL) (27, 28) and the TIRAP-inducing IFN-β (TRIF)-related adaptor molecule (TRAM) (29, 30). These peripheral membrane proteins survey the inner leaflets of the plasma and endosomal membranes through the actions of an N-terminal phosphoinositide binding domain of TIRAP or a bipartite localization domain of TRAM consisting of an N-terminal myristoylation motif and a phosphoinositide-binding motif (31–33).

TIRAP and TRAM can further recruit myeloid differentiation primary response protein 88 (MyD88) and TRIF, respectively (34), and stimulate the assembly of a large oligomeric scaffold called Myddosome or Triffosome (35). These supramolecular complexes consist of downstream signaling components and

kinase enzymes. Increased local concentrations of signaling molecules promote the intrinsically weak allosteric interactions and initiate cytosolic signaling transduction (36). Depending on the distinct supramolecular complexes formed, TLR signaling pathways can be mainly classified as either MyD88-dependent pathways, which drive the induction of inflammatory cytokines, or TRIF-dependent pathways, which are responsible for the induction of Type I IFN as well as inflammatory cytokines (2) (**Figure 1**).

MYD88-DEPENDENT PATHWAY

MyD88 is the first identified member of the TIR family; it is commonly used by all the TLRs except TLR3, and it activates the NF-κB signaling pathway (11). Upon activation by specific ligands, MyD88 recruits IL-1 receptor-associated kinases (IRAK)—IRAK4, IRAK1, IRAK2, and IRAK-M—which form a complex with IRAK kinase family members, referred to as the Myddosome (37–39). During Myddosome formation, IRAK4 is activated initially by MyD88 through its N-terminal death domain, which is also contained in IRAK4. Similar to MyD88, IRAK4 is also essential for the activation of NF-κB and mitogen-activated protein kinases (MAPKs) in the MyD88-dependent pathway (40, 41). The activated IRAK4 can sequentially activate IRAK1 and IRAK2, which are then autophosphorylated at several sites (42). Although activation of both kinases is required for robust activation of TLR-induced NF-κB and MAPK signaling, the relative importance of IRAK1 and IRAK2 may differ in humans and mice (43).

Activated IRAK1 can interact with tumor necrosis factor (TNF) receptor-associated factors 6 (TRAF6), an E3 ligase that catalyzes the synthesis of Lys63 (K63)-linked polyubiquitin, resulting in activation of TRAF6. TRAF6, along with E2 ubiquitin-conjugating enzymes Ubc13 and Uev1A, generates the K63-linked polyubiquitin chains and promotes K63-linked polyubiquitination of both TRAF6 itself and IRAK1. Early studies suggested that K63-linked polyubiquitination of TRAF6 and IRAK1 might serve as a platform for activation of downstream TGFβ-activated protein kinase 1 (TAK1) or IκB kinase (IKK) (44–48). However, the direct biochemical evidence is missing and the conflicting results have been reported that

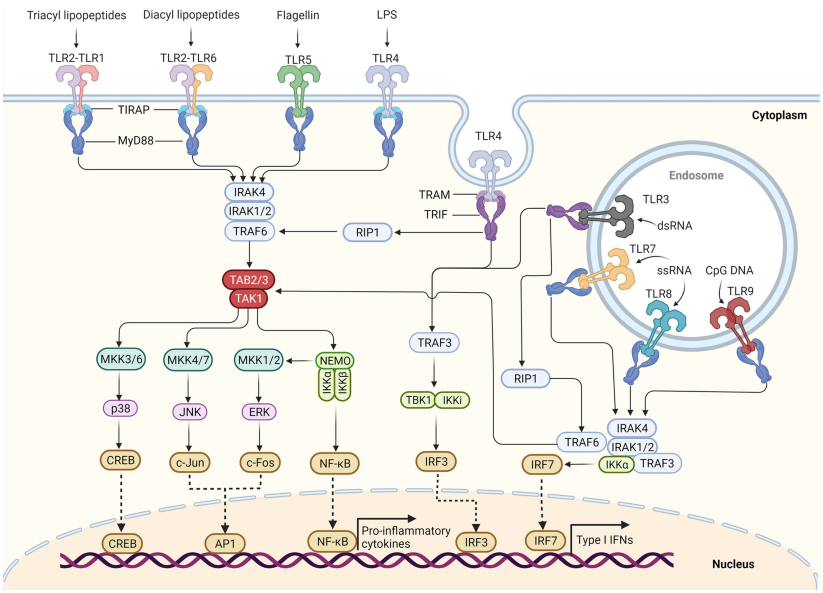

FIGURE 1 | TLR signaling pathway in innate immune cells. TLR5, TLR4, and the heterodimers of TLR2–TLR1 or TLR2–TLR6 prefer to recognize the membrane components of pathogens at the cell surface, whereas TLR3, TLR7–TLR8, and TLR9 localize to the endosomes, where they recognize the nucleic acids from both the host and foreign microorganisms. TLR4 localizes at the plasma membrane, but it is endocytosed into endosomes upon activation. Upon binding to their respective ligands, TLR signaling is initiated by dimerization of receptors, leading to the engagement of TIR domains of TLRs with TIRAP and MyD88 (or directly interact with MyD88) or with TRAM and TRIF (or directly interact with TRIF). The TLR4 signaling switches from MyD88 to TRIF once TLR4 moves to the endosomes. Engagement of MyD88 recruits the downstream signaling molecules to form Myddosome, which is based on MyD88 and contains IRAK4 and IRAK1/2. IRAK1 further activates the E3 ubiquitin ligase-TRAF6 to synthesize the K63-linked polyubiquitin chains, leading to the recruitment and activation of the TAK1 complex. The activated TAK1 further phosphorylates and activates the canonical IKK complex, ultimately leading to the activation factor NF-κB. The activation of TAK1 also leads to the activation of MAPKs, including MKK4/7 and MKK3/6, which further activate JNK and p38, respectively. The activation of IKKβ also leads to the activation of MKK1 and MKK2, which further activate ERK1/2. The activation of these MAPKs leads to some important transcription factor activations, such as CREB, AP1. These transcription factors cooperate with NF-κB to promote the induction of pro-inflammatory cytokines. Engagement of TRIF recruits the TRAF6 and TRAF3. Activated TRAF6 can recruit the kinase RIP1 and activate the TAK1 complex and IKK complex, leading to the activation of NF-κB and MAPKs. TRIF also promotes the TRAF3-dependent activation of the TBK1 and IKKε (originally IKKi), which further phosphorylates and activates IRF3. Among TLR7, TLR8, and TLR9 signaling in pDCs, IRF7 can bind to the Myddosome and is directly activated by IRAK1 and IKKε. Activation of IRF3 and IRF7 leads to the induction of Type I IFN.

ubiquitination of TRAF6 may be dispensable for the downstream protein kinase activation (49). Therefore, whether the K63-linked polyubiquitination of TRAF6 and IRAK1 can directly activate downstream protein kinases or it just serves as a marker of signaling pathway activation still requires further investigations. Recent biochemical studies revealed that the free K63 polyubiquitin chains synthesized by TRAF6 and Ubc13/Uev1A, which are not conjugated to any cellular protein, could directly activate TAK1 *in vitro* by binding to the novel zinc finger-type ubiquitin-binding domain of TAB2 and TAB3 (50), leading to close proximity-dependent transphosphorylation of TAK1 at Thr-187 (50, 51). However, whether and how these free polyubiquitin chains activate downstream protein kinases *in vivo* remains to be determined. Phosphorylated TAK1 then activates the IKK complex-NF-κB pathway and -MAPK pathway (6).

The IKK complex is comprised of the catalytic subunits IKKα and IKKβ and the regulatory subunit nuclear factor-κB essential modulator (NEMO) (also called IKKγ) (44). K63 polyubiquitin chains might bridge TAK1 to form a complex with IKK, thus allowing TAK1 to phosphorylate IKKβ through its close proximity to the IKK complex, which leads to activation of the IKK complex (52–54). Recently, Met1-linked ubiquitin dimers (also known as linear ubiquitin dimers) were shown to bind with 100-fold higher affinity to NEMO compared with K63-linked ubiquitin (55, 56), indicating that linear ubiquitination, catalyzed by the linear ubiquitin chain assembly complex (LUBAC), also contributes to the activation of IKK (57–63). The activated IKK complex can further phosphorylate the NF-κB inhibitory protein IκBα, which undergoes proteasome degradation, allowing NF-κB to translocate into the nucleus to induce proinflammatory gene expression (6).

In the MAPK pathway, the activated TAK1 simultaneously activates the MAPK family members Jun N-terminal kinases (JNKs) and p38 by inducing the phosphorylation of MAPK kinases 4/7 (MKK4/7) and MKK3/6. The IKKβ also catalyzes the phosphorylation of p105 to cause its degradation by the Skp1-Cul1-F-box ubiquitin ligase ($SCF^{\beta TrCP}$) complex, producing p50 and releasing tumor progression locus 2 (TPL2) to activate MKK1/2, which further phosphorylates and activates extracellular signal –regulated protein kinase 1 (ERK1) and ERK2. These MAPKs then phosphorylate cyclic AMP-responsive element-binding protein (CREB) and activator protein 1 (AP-1) transcription factors consisted of a heterodimer of c-Fos and c-Jun subunits to regulate inflammatory responses (44). TAK1 is a central component of MyD88-dependent NF-κB and MAPK signaling pathways. An earlier study suggested that TAK1 is required for the activation of the NF-κB and MAPK signaling pathway in both mouse embryonic fibroblast cells, B cells and T cells (64–68). However, we found that TAK1 serves as a negative regulator in mouse neutrophils (69, 70). By contrast, TAK1 might serve as a positive regulator in human neutrophils (71), suggesting a cell type-specific role for TAK1 in TLR-induced signaling (72). Interestingly, we recently found that *Tak1* deficiency in mice alters the intestinal microbiome, which can drive protective immunity against colitis and colorectal cancer (73).

Among TLR7, TLR8, and TLR9 signaling in pDCs, MyD88 also activates NF-κB signaling and interacts with interferon regulatory factor (IRF)-5 and IRF-7 for the induction of proinflammatory cytokines or Type I IFN (IFN-α and IFN-β) responses (74–76). IRF7 is highly expressed by pDCs, which can bind to the Myddosome containing IRAK4, TRAF6, TRAF3, IRAK1, and IKKα (77). IRAK1 and IKKα further phosphorylate the IRF7 protein, leading to its dissociation from the Myddosome and dimerization. The IRF7 homodimer translocates into the nucleus and drives IFNα expression (11). By contract, IRF5 is phosphorylated by IKKβ on Ser462 and contributes to proinflammatory cytokine transcription but not IFNα production (76, 78–80).

TRIF-DEPENDENT PATHWAY

In macrophages and conventional DCs (cDCs), TLR3- or TLR4-induced IFN expression is not dependent on MyD88 but instead is driven by TRIF as well as the proteins TRAM and TRAF3 (29, 30, 81, 82). Upon detection of dimerized TLR4 in endosomes, TRAM is thought to interact with TRIF to induce the formation of the putative Triffosome (35), in which TRIF interacts with TRAF6 and TRAF3. Activated TRAF6 can recruit the kinase receptor-interacting protein 1 (RIP1), which in turn recruits and activates the TAK1 complex and IKK complex, leading to activation of NF-κB and MAPKs and the induction of inflammatory cytokines (6). An earlier study suggested that TRAF6 might mediate RIP1 ubiquitination (83). However, TRAF6 has also been reported to be dispensable for TRIF-dependent TLR signaling (84), suggesting that additional E3(s) might be responsible for RIP1 ubiquitination. Recently, an E3 ubiquitin ligase Peli1 was found to facilitate TRIF-dependent TLR signaling and proinflammatory cytokine production by inducing the ubiquitination of RIP1 (85), indicating that Peli1 might share a redundant role with TRAF6.

TRIF also promotes the TRAF3-dependent activation of the IKK-related kinase TANK-binding kinase 1 (TBK1). TRAF3 activates the TBK1 and inhibitor of NF-κB kinase (IKKi) along with NEMO for phosphorylation and dimerization of the IFN-inducing transcription factor IFN regulatory factor 3 (IRF3). Subsequently, the IRF3 homodimer translocates into the nucleus from the cytoplasm, where it drives the expression of Type I IFN genes and IFN-stimulated genes (ISGs) (86–88). Recently, a 39-amino-acid pLxIS motif was identified within TRIF (but not MyD88), which can be phosphorylated by TBK1. The phosphorylated motif can recruit IRF3, leading to the phosphorylation and activation of IRF3 by TBK1 (89, 90). Therefore, the TLR4 uses TRIF but not MyD88 to promote IRF3-induced IFN expression in the endosome. Unlike TLR4, TRAM cannot interact with TLR3 or regulate TLR3 signaling (29), indicating that TLR3 might directly interact with TRIF or use another sorting adaptor to link TRIF to TLR3.

TLR-MEDIATED REGULATION OF APCS

TLR-mediated activation and maturation of DCs and macrophages are critical links between innate and adaptive

immunity (21). DCs are professional APCs and play a central role in inducing the activation and differentiation of naïve T cells into Th type 1 (Th1) cells, Th2 cells, and CTL effectors (91). Once DCs take up the antigen, the activated DCs can migrate to local lymphoid tissues to present the antigenic peptides on the relevant major histocompatibility complex (MHC) molecules (4). This process is regulated by recognizing pathogens *via* the variety of PRRs expressed by DCs. Among these PRRs, TLR family members play a critical role in generating effector T cell responses (4, 92, 93). The production of "innate" cytokines (type I IFN, IL-1, IL-6, IL-12, TNF-α), up-regulation of costimulatory molecules (CD40, CD80, and CD86), and altered expression of chemokine receptors (CCR2, CCR5, and CCR7) are the characteristics of DC maturation (21), which can be induced by ligands of TLRs, including LPS, lipoproteins, and CpG DNA (4, 75, 81, 94–96) (**Figure 2**).

Moreover, TLR signals can also facilitate peptide loading onto MHC molecules or the cross-presentation of exogenous antigens for the stimulation of $CD8^+$ T cell responses by promoting the acidification of endosomes or the fusion of MHC Class I-containing endosomes with phagosomes in DCs (97–99). In addition, LPS-induced TLR signaling can promote the redistribution of MHC Class I and II molecules to the surface of DCs (100). TLR4 activation on DCs promotes cytosolic routing of dendritic cell-specific intercellular adhesion molecule-3-grabbing non-integrin (DC-SIGN)-targeted antigens for presentation on MHC Class I and increased $CD8^+$ T cell activation (101). Recently, TLR3, TLR4, and TLR9 ligands were reported to induce autocrine C3a receptor and C5a receptor (C3ar1/C5ar1) signaling in DCs, which causes the expansion of effector T cells and instability of regulatory T cells and contributes to T cell-dependent transplant rejection (102). IFN-γ combined with TLR ligation TLR2, TLR4, or TLR9 agonists can enhance DC activation and function to increase antigen-specific T cell responses (103).

Interestingly, TLR2 seems more critical than TLR4 in mouse DC-derived IL-10 responses to schistosome antigens (104). TLR2 signaling activation on DCs can promote higher frequency effector and memory $CD4^+$ T cell responses than TLR4 signaling activation. The novel TLR2 agonist SUP3 also showed a heightened ability to enhance DC-mediated antigen presentation and T cell activation (105). By contrast, the TLR5 ligand flagellin was most effective at activating neonatal lung APCs by inducing significantly higher expression of maturation markers on $CD103^+$ (cDC1) and $CD11b^+$ (cDC2) subsets (106). Monocyte-derived DCs stimulated with TLR4 and TLR7/8 ligands induce naive allogeneic $CD4^+$ T cells to secrete IL-10 and IFN-γ sequentially and eventually IL-17A (107). The activation of TLR9 and IL-12 pathways in $CD8\alpha^+$ DCs can drive $CD4^+$ T cells to act as Th cells or induce rapid polyclonal conversion to immunosuppressive Treg during *Listeria* infection (108). Interestingly, although all TLRs on DCs are able to induce $CD8^+$ T cell activation *in vitro*, the abilities of surface and endosomal TLRs to activate $CD8^+$ T cells might be different *in vivo*. The nucleic acid recognizing endosomal TLRs potently induce $CD8^+$ T cell activation, whereas the bacterial ligands recognizing surface TLRs were incapable of inducing $CD8^+$ T cell priming. Moreover, surface TLRs might have a dominant effect of inhibiting $CD8^+$ T cell expansion induced by activation of endosomal TLRs (109).

Based on the particular cell surface markers, DCs can be divided into different subsets, including myeloid DCs, pDCs,

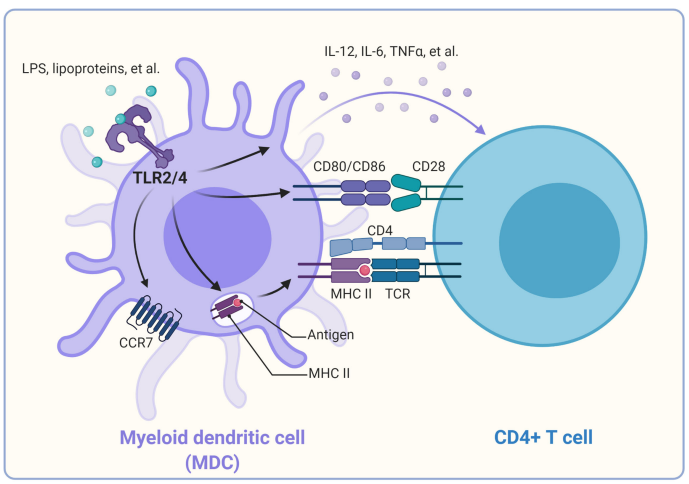

FIGURE 2 | Promotion of $CD4^+$ T cell activation by TLRs on dendritic cells. Once TLR2/4 recognize their individual ligands, they can alter the expression of chemokine receptors (CCR2, CCR5, and CCR7), leading to DC migration from the infected tissue to the draining lymph node, where naïve T cells are stimulated. TLR2/4 signaling can promote the antigen process and bind to the major histocompatibility complex II and be presented to the $CD4^+$ T cells, thus providing the first signal for activation of the $CD4^+$ T cells. In addition, TLR signaling triggers the up-regulation of costimulatory molecules on the cell surface of DCs, which provide the second signal to activate the antigen-specific $CD4^+$ T cells. TLR signaling can also induce the production of cytokines such as IL-12, TNF-α in DCs. These cytokines function as "instructive" cytokines and drive the activation and differentiation of $CD4^+$ T cells.

$CD8\alpha^+$ DCs, and $CD11b^+$ DCs (4). Human pDCs express TLR7 and TLR9, whereas $CD11c^+$ human myeloid DCs express TLR1, TLR2, TLR3, TLR5, TLR6, and TLR8 (110–112). Human blood monocytes express TLR1, TLR2, TLR4, and TLR5, but progressively lose these receptors and acquire the expression of TLR3 as they differentiate into mature DCs in the presence of granulocyte-macrophage colony-stimulating factor and IL-4 (113). Mice splenic DC subsets express TLR1, TLR2, TLR4, TLR6, TLR8, and TLR9, but not TLR3 (114). Interestingly, freshly isolated mouse splenic DC subsets or macrophages only express low amounts of TLR4 and do not respond to LPS stimulation. By contrast, bone marrow-derived DCs or macrophages have high expression of TLR4 and respond robustly to LPS (115).

Since different DC subsets express subset-specific PRRs, DCs are functionally heterogeneous (110, 114, 116). Different DC subsets respond to different stimuli and activate distinct signaling pathways, leading to the release of specific cytokines, which in turn determine the specific Th cell subsets that are generated and activated (117). pDCs express TLR7 and TLR9, which recognize ssRNA and CpG DNA, respectively, but pDCs do not express other TLRs that detect bacterial cell wall components. Therefore, pDCs are thought to specifically detect viral infections to induce Type I IFNs and control antiviral immunity (35, 116).

TLR-MEDIATED REGULATION OF T CELLS

TLR signaling in innate immune cells indirectly regulates T cell differentiation and proliferation by promoting DC maturation and regulatory cytokine production (118). Since T cells also express different TLRs, recent studies have revealed that TLR-mediated signaling can directly regulate effector T cells and Treg cells (119).

$CD4^+$ Th cells play a critical role in initiating and maintaining adaptive immune responses against cancer (120). $CD4^+$ Th cells are required for the expansion and maintenance of memory $CD8^+$ T cells (121). Naïve murine or human $CD4^+$ T cells can express TLR2 after their stimulation (122, 123). TLR2 signaling can promote the proliferation and production of IFNγ in Th1 cells (124). Costimulation of TCR and TLR2 in naïve murine $CD4^+$ T cells increases their differentiation to proinflammatory Th1 cells and secretion of cytokines and chemokines (122, 125). Costimulation of neonatal $CD4^+$ T cells with TLR2 ligand and anti-CD3 also show an increased proinflammatory Th1 immune response (IFN-γ and TNF-α production) and IL-2 production (126). Moreover, TLR2 signaling on $CD4^+$ T cells exerts a protective action by increasing the population of *Mycobacterium tuberculosis* Ag-specific T cells during mycobacterial tuberculosis (127).

Similarly, TLR2 signaling can also regulate the immune response of the $CD8^+$ T cell. TLR2 agonists can enhance cell survival, proliferation, IFN-γ production, and memory cell formation of $CD8^+$ T cells in response to a suboptimal TCR signal by reducing the threshold for costimulatory signals from APCs (128–130). The TLR2/MyD88-dependent signaling pathway in $CD8^+$ T cells also can increase their survival, clonal expansion, and differentiation into long-lived memory T cells by activating the phosphatidylinositol 3-kinase (PI3K)-Akt pathway during vaccinia virus infection (130). Interestingly, MyD88-dependent signaling is also essential for $CD4^+$ T cell-promoted IFN-γ production and hematopoietic progenitor cell expansion during intracellular bacterial infection (131). In addition, MyD88-dependent signaling in the host can protect against acute allogenic graft versus host disease after bone marrow transplantation (132). However, activating the MyD88 signaling pathway in donor $CD4^+$ T cells promotes the survival and differentiation of T cells toward Th1, Tc1, and Th17. It increased the severity of graft versus host disease in a mouse model of allogeneic hematopoietic stem cell transplantation (133). MyD88-dependent signaling is also reported to promote differentiation and proliferation of $CD4^+$ T cells toward Th17 cells by linking IL-1 and IL-23 signaling and sustaining mTOR signaling (134).

Besides TLR2, TLR4 is also expressed on $CD4^+$ T cells, and the TLR4 ligation could enhance both the *in vitro* cell proliferation and survival of $CD4^+$ T cells (135). However, the activation of TLR4 signaling could affect the phenotype and ability of $CD4^+$ T cells to provoke the intestinal inflammation, through the induction of MAPK phosphatase 3 (MKP-3) to inhibit TCR stimulation-induced activation of ERK1/2 (136). Moreover, LPS can induce the adhesion of human T cells to fibronectin and the up-regulated expression of suppressor of cytokine signaling 3 (SOCS3), which further led to the inhibition of T cell chemotaxis toward the chemokine stromal cell-derived factor 1α (CXCL12) (137, 138). By contrast, $CD4^+$ T cells are pathologic and contribute to an exaggerated immune activation in the mice that is absence of functional Tregs, resulting in the mortality to a nonlethal dose of LPS or *Escherichia coli* challenge (139). Recently, it was reported that the TLR4 expression on T cells goes down during TCR and mitogenic activation (140). However, the VIPER peptide (VP), an established inhibitor of TLR4 signaling, restores TLR4 expression and regulates the activation of naive T cell, indicating that TLR4 responses might be associated with the acute-stage T cell responses (140).

The agonist of TLR9 (CpG-ODNs) was found to promote the release of IL-8 in purified $CD8^+$ T cells (110). Additionally, the expression of TLR7 is increased in the mesenteric lymph node $CD4^+$ and $CD8^+$ T cells after *Schistosoma japonicum* infection. The TLR7 agonist can enhance the production of IFN-γ in $CD8^+$ T cells from mesenteric lymph node T cells in infected mice (141). Moreover, TLR7/MyD88-dependent signaling activation in $CD8^+$ T cells can promote cellular glycolysis and enhance T cell effector functions (142). TLR3 is constitutively expressed on $CD8^+$ T effector cells. Furthermore, the TLR3 agonist polyinosinic-polycytidylic acid [Poly (I:C)] increases IFN-γ production in Ag-specific $CD8^+$ T cells (143). Poly (I:C) treatment significantly increases the IL-2 and IFN-γ production of chimeric antigen receptor-modified T (CAR T) cells along with improving their lytic action against tumor or cancer cells (144). CAR T cells also show an increased anti-tumor action against refractory or relapsed B cell acute lymphoblastic

leukemia upon co-stimulation with TLR2 signaling by introducing the TIR domain of TLR2 into the CAR construct (145). The third-generation anti-CD19 CAR T cells incorporated with the intracellular signaling domains of CD28 and TLR2 are under clinical trial for relapsed or refractory B-cell non-Hodgkin's lymphoma (146).

TLR-MEDIATED REGULATION OF REGULATORY T CELLS

Treg cells are critical for maintaining peripheral tolerance, preventing autoimmune diseases, and limiting chronic inflammatory diseases by suppressing host immune responses and inducing self-tolerance (147). $CD4^+$ Treg cells are a small subset (5–6%) of the overall $CD4^+$ T cell population (121). Foxp3 is a specific marker of $CD4^+$ Treg cells in both mice and humans (148–152). In previous studies, the elevated proportion of $CD4^+$ $CD25^+$ Treg cells in the total $CD4^+$ T cell population was observed in several different human cancers, including lung, breast, and ovarian tumors (153–155). We also demonstrated the presence of antigen-specific $CD4^+$ Treg cells at tumor sites (152, 156). We showed that Treg cells could suppress the proliferation of naive $CD4^+$ T cells and inhibit IL-2 secretion of $CD4^+$ effector cells upon activation by tumor-specific antigens (157). In addition, we identified $CD8^+$ Treg and γδ-TCR Treg cells in prostate and breast cancer (158, 159). Notably, the $CD8^+$ Treg cells expressed Foxp3 molecules, while the γδ-TCR Treg cells did not. Like $CD4^+$ Treg cells, both of these $CD8^+$ and γδ-TCR Treg cell subtypes have immune suppression ability and inhibit anti-tumor immunity.

To abrogate Treg cell-mediated immune suppression, we sought to identify the TLR ligands that could reverse Treg cell suppressive activity. We found that Poly-G10 oligonucleotides can directly change their suppressive function in the absence of DCs. The TLR8-MyD88 signaling pathway is required to reverse Treg cell function by Poly-G oligonucleotides (158, 160). Moreover, we found that the natural ligands for human TLR8—ssRNA40 and ssRNA33, which are derived from HIV viral sequences (161)—could completely reverse the suppressive function of Treg cells, indicating that activation of the TLR8-dependent signaling pathway is critical for the reversal of Treg-suppressive functions. Besides different subsets of $CD4^+$ Treg cells, we found that the $CD8^+$ Treg cells and γδ-TCR Treg cells in prostate and breast cancer also express a low level of human TLR8 molecules (158, 159). Interestingly, we demonstrated that Poly-G oligonucleotide treatment could also reverse the suppressive function of $CD8^+$ Treg cells and γδ-TCR Treg cells, suggesting that these cells might share the same TLR8/MyD88 signaling pathway-mediated mechanism with previously characterized $CD4^+$ Treg cell subsets (158, 159).

Recent studies show that TLR8 stimulation in humans reverses Tregs' immunosuppressive function and enhances their anti-tumor function by inhibiting glycolysis and glucose uptake (162). $CD4^+$ T cells stimulation with TLR8 ligand ssRNA 40 in a co-culture system with ovarian cancer cells (SKOV3) inhibited the glycolysis metabolism and downregulated the percentage of Treg cells (163). Therefore, the TLR8 signaling pathway may regulate Treg by reprogramming the glycolysis metabolism. These findings raise an intriguing possibility that the activation of the TLR8 signaling pathway could block the suppressive function of different subsets of Treg cells to improve the efficacy of cancer immunotherapy.

Since TLR8 is non-functional in mice (164), Poly-G oligonucleotides cannot reverse the suppressive activity of murine Treg cells. However, recent studies showed that other TLR signaling in mice could also mediate the regulation of Treg cells. TLR2-deficient mice showed a reduced number of $CD4^+$ $CD25^+$ Treg cells (165). Additionally, stimulation of mouse Treg cells with TLR2 ligand Pam3Cys increased its proliferation and temporarily reversed its suppressive function (166, 167). The activation of TLR9 signaling has been reported to inhibit the immunosuppressive function of Treg through direct MyD88-dependent costimulation of effector $CD4^+$ T cells (168). However, another study showed that human $CD4^+$ $CD25^+$ Treg or effector Th1 and Th2 cells did not highly express TLR9 naturally, but 25-dihydroxyvitamin D3 (1α25VitD3)—the active form of Vitamin D—could induce it (169). Stimulation of 1α25VitD3-induced IL-10–secreting Treg with TLR9 agonists showed a decreased IL-10 and IFN-γ production, indicating the reduction of their immunoregulatory function (169). In contrast, stimulation of human Treg cells with the TLR5 ligand flagellin increased rather than reversed their suppressive function (170). The TLR4 ligand LPS was also reported to induce proliferation and enhance the suppressive function of Treg cells (171).

REGULATORS IN TLR SIGNALING

Uncontrolled TLR signaling activation can be harmful or even fatal (172). Therefore, the stringent and precise regulation of TLR signaling pathways is essential to maintaining immune balance in the host. In the last few years, many positive and negative regulators have been identified to control TLR-induced NF-κB signaling pathways at multiple levels through different mechanisms (173). These regulators include co-receptors, such as CD14 (174, 175); soluble receptors, such as sTLR (176, 177); transmembrane proteins, such as ST2L (178), SIGIRR (179, 180), and TRAILR (181); and intracellular regulators, such as SOCS-1 (182, 183), MyD88s (184, 185), TOLLIP (186), IRAK-M (187), A20 (188, 189), CYLD (the familial cylindromatosis tumor suppressor gene) (190–194), Nrdp1 (195), regulatory Nod proteins (196–206), TRIAD3A (207), and tripartite motif-containing proteins (TRIMs) (208). These molecules maintain the balance between activation and inhibition of TLR signaling in response to diverse PAMPs (172).

We also participated in the identification of some critical regulators of TLRs and the NF-κB signaling pathway. NLRs were originally believed to function as pathogen sensors and cellular danger signals. However, alongside other groups, we recently found that several NLRs, known as regulatory NLRs, negatively

regulate TLR and RIG-I-like receptor signaling. NLR family member X1 (NLRX1) is the first NLR that was identified to negatively modulate RIG-I-mediated antiviral responses by binding to mitochondrial antiviral-signaling protein (MAVS) and disrupting RIG-I-MAVS (209). Then, we found that it could also negatively regulate TLR-induced NF-κB signaling by targeting the TRAF6 and IKKα/β-NEMO complex (199, 201). Besides NLRX1, NLR family CARD domain containing 5 (NLRC5) is another member of the NLR protein family that is recognized as a novel regulator of both adaptive and innate immune responses (210). We identified NLRC5 as a negative regulator of both NF-κB and Type I IFN signaling (196, 200, 202, 203, 206). NLRC5 inhibits IKK phosphorylation and NF-κB signaling by interacting with IKKα/β but not NEMO. NLRC5 inhibits Type I IFN signaling by targeting RIG-I/MDA5 after viral infection and blocking the RIG-I–MAVS interaction. We recently identified NLR family pyrin domain-containing 11 (NLRP11) as a regulatory NLR to attenuate TLR signaling by targeting TRAF6 for degradation *via* the ubiquitin ligase RNF19A (205).

Besides the NLR family, we also discovered some regulators from the LRR-containing (LRRC) family, ubiquitin-specific protease (USP) family, and tripartite motif family (TRIM) family. We found that LRRC25 negatively regulates the TLR-induced NF-κB signaling pathway by promoting p65/RelA for autophagic degradation (211). Interestingly, LRRC25 also inhibits Type I IFN signaling by targeting IFN-stimulated gene 15 (ISG15)-associated RIG-I for autophagic degradation (212). We found that USP38 could also negatively regulate TLR and RIG-I signaling through different mechanisms (213, 214). In contrast, TRIM14 functions as a positive regulator in the noncanonical NF-κB signaling pathway and cGAS- and RIG-I-mediated Type I IFN signaling pathway (215–218).

TLR-MEDIATED IMMUNITY IN CANCER

Deidier observed that patients infected with syphilis had remission of malignant tumors, revealing the correlation between immune system activation triggered by infection and cancer remission (219). Studies on TLRs involved in cancer have shown that TLR signaling has not only anti-tumor effects but also pro-tumor functions on carcinogenesis, which is dependent on the individual TLR and cancer type (220, 221). TLR stimulation enhances the anti-tumor immune response either through immune cells or directly targeting tumor cells to induce apoptosis. In murine models of hepatocellular carcinoma, TLR2-deficient mice showed a decrease in the expression of IFN-γ, TNF-α, (IL)-1α/β, IL-6, and Cxcl-2, which attenuate p21- and p16/pRb-dependent senescence, leading to the increased proliferation of tumor cells (222). We found that TLR8 ligand treatment suppresses prostate and breast cancer by reversing the function of $CD8^+$ Treg cells and γδ-TCR Treg cells (160). Shanshan Qi et al. (223) generated hTLR8 mice by replacing exon 3 of mouse *Tlr8* with human *TLR8* to analyze the role of TLR8 in tumor progression. They found that the MC38 tumor grew slower in hTLR8 mice compared with naïve mice. hTLR8 mice also exhibit increased IFN-γ and TNF-α positive $CD4^+$ T cells and effector T cells (223).

In addition, a synthetic bacterial lipoprotein (a TLR1/TLR2 agonist) was reported to reduce the suppressive function of $Foxp3^+$ Treg cells and enhance the cytotoxicity of tumor-specific CTL (224). Combination treatment with the TLR1/2 ligand Pam_3CSK_4 and anti-CTLA4 mAb improved the anti-tumor immunity compared with anti-CTLA4 mAb alone. This study showed that TLR1/2 increased FcgR IV expression in macrophages, which led to Treg cell depletion and augmentation of T cell/Treg ratios within the tumor (225). Besides their anti-tumor effects, TLRs have also shown pro-tumor functions. Stimulation of TLR4 by LPS promoted immunosuppressive cytokine production, resulting in tumor immune evasion in lung cancer cells (226). In breast cancer, a stimulation expressed-TLR4 tumor with LPS promoted cancer cell proliferation *via* upregulation of IL-8 and IL-6 production (227, 228). Interestingly, TLR6 signaling was recently reported to prevent the inflammation by impacting the composition of microbiota during inflammation-induced colorectal cancer (229). Besides TLRs, MyD88 is also involved in cancer development. MyD88-dependent signaling is reported to control the expression of several key modifier genes of intestinal tumorigenesis and play a crucial role in both spontaneous and carcinogen-induced tumor development (230). Besides, diethylnitrosamine (DEN) administration induced higher serum interleukin-6 (IL-6) production in males than it did in females in DEN-induced hepatocellular carcinoma model. Further study showed that DEN exposure promoted the production of IL-6 in Kupffer cells (KCs) in a MyD88-dependent manner and depletion of MyD88 protected male mice from DEN-induced hepatocarcinogenesis (231). In the activated B-cell-like (ABC) subtype of diffuse large B-cell lymphoma (DLBCL), MyD88 L265P is reported to contribute to the constitutive NF-κB and JAK kinase signaling, which promotes malignant cell survival in these lymphomas (232). MyD88 L265P somatic mutation is identified as a commonly recurring mutation in patients with Waldenström's macroglobulinemia (233). 69% of patients with cutaneous diffuse large B cell lymphoma (CBCL) carry MyD88 L265P mutation, which is significantly associated with shorter disease-specific survival (234). In addition, the MyD88/IL1 receptor (IL1R) axis upregulates programmed cell death (PD)-1 expression on tumor-associated macrophages (TAMs) *via* promoting recruitment of NF-κB to the Pdcd1 promoter, which sustains their immunosuppressive function in melanoma (235). Based on the critical role of TLRs and TLRs-mediated signaling pathways in cancer development, researchers have taken advantage of agonists and antagonists of TLRs to treat some types of cancer **(Table 1)**. Various agonists of TLRs are currently under investigation in clinical trials for cancer treatments **(Table 2)**. Due to the double-edged role of TLRs in tumor biology, it is essential to understand how TLRs manipulate the immune system and tumor cell characteristics, which may provide us with new therapeutic strategies against cancer.

TABLE 1 | TLR agonists, antagonists and cancer.

TLR	Agonist/Antagonist	Cancer and Model	Observation	Reference
TLR1/2	Bacterial lipoprotein, Pam3CSK4	Lung carcinoma, leukemia, and melanoma	Inhibits the suppressive function of Foxp3+ Tregs and enhance the cytotoxicity of tumor-specific CTL; depletion of tumor-infiltrating Treg cells	(224, 225)
TLR2/TLR4	OM-174 (synthetic derivative of lipid A), bacille Calmette-Guérin (BCG)	Melanoma, bladder cancer	Increases natural killer cell and CTL activity; prolongs survival of bladder cancer patients	(236, 237)
TLR3	Poly I:C, poly-ICLC(Hiltonol)	B16 melanoma cells, facial embryonal rhabdomyosarcoma	IFN-γ plus poly I:C reduces the expression of PD-L1; shows tumor regression and prolonged survival	(238, 239)
TLR4	MPLA	Breast and ovarian cancer models	MPLA + IFNγ repolarizes TAMs to tumoricidal macrophages and activates cytotoxic T cells	(240)
TLR4	TAK-242 (resatorvid), Eritoran	Breast cancer, colorectal cancer	Inhibits breast cancer cell viability, inhibits the proliferation of breast cancer cells, induces G2/M cell cycle arrest in breast cancer cells and induces apoptosis of breast cancer cells; blocks LPS-enhanced-AKT phosphorylation in colorectal cancer cells	(241, 242)
TLR5	Entolimod	Murine colon and mammary metastatic cancer models	Restrains liver metastases and facilitates the formation of $CD8^+$ T cell memory	(243)
TLR7	Imiquimod	Various cutaneous malignancies	Induces apoptosis, induces production of various cytokines, and stimulates cell-mediated immune response	(244)
TLR7/8	MEDI9197	B16-OVA melanoma tumor model	Localized administration of TLR7/8 agonism polarizes anti-tumor immunity towards a Th1 response and activates natural killer cells and $CD8^+$ T cells	(245)
TLR7/TLR9	Chloroquine	Hepatocellular carcinoma	Downregulate the level of phosphoralated-AKT and inhibit HuH7 cell proliferation;	(246)
TLR9	CpG	Colon cancer animal model, head and neck cancer animal model, melanoma	Reverses resistance to PD-1 blockade therapy by expending $CD8^+$ T cells; enhances the efficacy of anti-PD-1 therapy; expands tumor antigen-specific $CD8^+$ T cells	(247–249)

TLR-MEDIATED IMMUNITY IN AUTOIMMUNE DISEASE

TLRs are supposed to sense pathogenic components and initiate the immune response that contributes to host homeostasis. However, in the specific scenario, TLRs are improperly activated by self-antigens, leading to chronic systemic inflammatory disorders and the occurrence of autoimmunity. Numerous studies have demonstrated that TLRs are involved in the pathogenesis of various autoimmune diseases such as

TABLE 2 | Clinical trials of TLR agonists TLR in cancer.

TLR	TLR agonist	Cancer type	Status	Reference
TLR3	poly-IC12U (Ampligen)	Colorectal cancer	Phase II	NCT04119830 NCT03403634
		Melanoma	Phase II	NCT04093323
		Prostate cancer	Phase II	NCT03899987
	poly-ICLC (Hiltonol)	Non-Hodgkin's Lymphoma, breast cancer, head and neck squamous cell carcinoma	Phase I/II	NCT03789097
		Melanoma	Phase I/II	NCT03617328
		Mesothelioma	Phase I	NCT04525859
		Prostate cancer	Phase I	NCT03835533
TLR4	MPLA	Melanoma, ovarian cancer, lung cancer	Phase I/II	NCT01584115
	GLA-SE	Stage III adult soft tissue sarcoma, stage IV adult soft tissue sarcoma	Phase I	NCT02180698
		Follicular low grade non-Hodgkin's lymphoma	Phase I/II	NCT02501473
TLR5	Mobilan	Prostate cancer	Phase I	NCT02844699
	Entolimod	Advanced or metastatic solid tumors cancers	Phase I	NCT01527136
TLR7	Imiquimod	Superficial basal cell carcinoma	Phase III	NCT00189306
		Malignant melanoma	Phase I	NCT00142454
		High-risk melanoma	Phase II	NCT00273910
TLR7/8	Resiquimod	Stage II, Stage III, or Stage IV Melanoma	Phase I	NCT00470379
TLR9	MGN1703	Metastatic colorectal carcinoma	Phase III	NCT02077868
	SD-101	Non-Hodgkin lymphoma	Phase I	NCT03410901

rheumatoid arthritis (RA), systemic lupus erythematosus (SLE), multiple sclerosis, and Crohn's disease (250) **(Table 3)**. RA is an autoimmune disorder that affects the synovial joints, causing chronic and persistent inflammation and the destruction of articular tissues. MyD88 also has been demonstrated to be crucial for the production of MMPs (the major enzymes involved in joint tissue destruction) in RA synovial membrane cultures (275). TLR2 and TLR4 expression were reported to be associated with the levels of IL-12 and IL-8 in the synovial tissue of RA patients (251). The surface expression of TLR4 on $CD8^+$ T cells directly correlates with the disease severity of RA. And the TLR4-expressing $CD8^+$ T cells can respond to LPS and express robust amounts of cytolytic and inflammatory molecules including TNFα and IFNγ (256). Besides RA, TLR2 and TLR4 are also involved in heat shock proteins-associated atherosclerosis (257, 258). Moreover, emerging evidence indicates that TLR2 is strongly associated with diabetes (259–261).

SLE is characterized by the presence of autoantibodies triggered by CpG DNA and ssRNA-associated self-antigens. In endosomes, the self-antigens are sensed by TLR7 and TLR9. TLR7 is essential for generating the germinal center and drives the extrafollicular pathway, which is associated with pathogenic antibody secretion. Notably, TLR9 has been demonstrated to have a protective function in SLE by limiting the stimulatory activity of TLR7 (262). Genetic studies have shown that copy number variation of TLR7 is associated with SLE development (263, 264). Additionally, TLR7 localizes on the X chromosome escapes X inactivation in B cells and myeloid cells in females, resulting in the gender difference in TLR7 expression (265), leading to a higher incidence in women than men. Moreover, SLE patients with increased expression of TLR7 showed significant expansion of $CD19^+$ IgD^+CD38^{++} transitional B cells and increased IgG auto-Ab production (266). Recent data show that the expression of *TLR7* in mild and severe lupus-prone models is dependent on the activity of IRAK4 (the TLR7-downstream signaling molecule) and the pathogenic environment. Impairments of IRAK4 signaling refrain from all pathological characteristics associated with murine lupus. These data suggest a feedback loop of TLR7 expression and pathological changes in SLE patients (267).

A study in experimental autoimmune encephalomyelitis (EAE) mice models showed that deficiency of MyD88 conferred complete resistance to EAE in mice, indicating that a TLR-mediated immune response is required to induce EAE (276). Consistently, depletion of TLR4 solely in $CD4^+$ T cells impairs Th17 and markedly abolishes the disease symptoms (135). In addition, accumulating evidence suggests that TLR8 contributes to autoimmune diseases as well. It is reported that human monocytes that lack CD14 ($CD14^{dim}$) and express CD16 do not produce cytokines in response to bacterial cues that are sensed by cell-surface TLRs. Instead, they trigger the production of TNF-α, IL-1β, and C-C motif chemokine ligand 3 in response to viruses through the TLR7-TLR8-MyD88-MEK pathway. Further study showed that these $CD14^{dim}$ monocytes recognize self-nucleic acids and drive the production of inflammatory cytokines in patients with lupus (268).

Cristiana et al. (277) used human *TLR8*-transgenic mice to show that high copy number chimeras developed the multiorgan inflammatory syndrome through DC-intrinsic huTLR8 activation and subsequent T cell activation. The severity of the inflammation was associated with the expression level of huTLR8. They observed spontaneous arthritis in high-expressing human *TLR8* mice. Furthermore, they demonstrated that *TLR8* mRNA expression was much higher in blood from both SoJIA and Still's disease donors than healthy donors. Finally, the mRNA level of *TLR8* was associated with the transcription level of inflammatory cytokines in these patients.

In addition, the ectopic expression of TLR8 on pDCs in systemic sclerosis patients induces the production of CXCL4, which in turn enhances TLR8- and TLR9-induced IFN production by pDCs. Both CXCL4 and IFNs are the featured cytokines in systemic sclerosis (269). These data suggest that TLR8 is the key RNA-sensing TLR in the pathogenesis of autoimmune disease, demonstrating the potential of TLR8 for clinical development. Emerging evidence suggests numerous autoimmune diseases are triggered by the dysregulation of TLR. Some TLR antagonists have already been applied to autoimmune disease treatment in mice models. Due to redundancy between different TLRs in different disease-affected tissues, it is crucial to dissect the detailed molecular mechanism and cell-mediated immune regulation in the specific disease context to facilitate drug development for clinic treatments.

TLR-MEDIATED IMMUNITY IN INFECTIOUS DISEASE

TLRs play an essential role in host immune responses to various invading pathogens, including bacteria, fungi, viruses, and parasites **(Table 4)**. TLR1 is crucial for the induction of mucosal Th17 immunity and IgA responses during *Yersinia enterocolitica* infection (316, 317). The I602S mutant of TLR1

TABLE 3 | TLRs implicated in autoimmune diseases.

Autoimmune diseases	TLR	Reference
Rheumatoid arthritis	TLR2, TLR4, TLR3/7, TLR9	(251–256)
Atherosclerosis	TLR2, TLR4	(257, 258)
Diabetes	TLR2	(259–261)
Systemic lupus erythematosus	TLR7, TLR8, TLR9	(262–268)
Systemic sclerosis	TLR2, TLR8	(269–271)
Myositis	TLR3, TLR4, TLR7, TLR9	(272–274)

TABLE 4 | TLRs and infectious diseases.

TLR	Class of Pathogen Recognized	Infectious Agent	Reference
TLR1/2	Bacteria	Mycobacteria	(278–280)
TLR2	Bacteria	*Staphylococcus aureus*	(281, 282)
		Listeria monocytogenes	
	ssRNA viruses	SARS-CoV-2	(283)
TLR2/3	Protozoa	*Neospora caninum*	(284)
TLR3	DNA viruses	HSV	(285)
	Retroviruses	HIV	(286–290)
	ssRNA viruses	Respiratory syncytial virus	(291–294)
	Protozoa	*Neospora caninum*	(295)
TLR4	Bacteria	*Staphylococcus aureus*	(281, 296)
	ssRNA viruses	Syncytial virus	(297)
		Rabies virus	(298, 299)
	Bacteria	Mycobacteria	(300)
TLR5	Bacteria	*Burkholderia pseudomallei*	(301)
TLR2/6	ssRNA viruses	Dengue virus	(302)
TLR6	Bacteria	*Legionella pneumophila*	(303)
TLR7	Protozoa	*Leishmania*	(304)
TLR7/8	ssRNA viruses	Influenza A	(305)
	Retroviruses	HIV-1	(306–308)
TLR8	Retroviruses	HIV-1	(309)
	Bacteria	*Staphylococcus aureus*	(310)
TLR9	DNA viruses	HSV-1, HSV-2	(311)
		HPV	(312)
		Adenovirus	(313–315)

results in the deficiency of TLR1 trafficking from the cytosol to the cell surface, potentially impairing blood monocytes' immune functions against pathogenic *Mycobacterium tuberculosis* (318). Recently, it was reported that mice deficient in both TLR2 and TLR4 were highly susceptible to intracellular *Salmonella typhimurium* infection (319). However, *Tlr2/4*-deficient mice lacking additional TLR9 involved in *S. typhimurium* recognition were less susceptible to infection (319). Notably, TLR2 was also reported to recognize the envelope (E) protein of SARS-CoV-2 to induce a hyperinflammatory response in mice bone-marrow-derived macrophages (283). Besides TLR2, TLR4 was also reported to recognize the spike (S) protein of SARS-CoV-2 and activate the NF-κB signaling to produce IL-1β (320).

Numerous studies have shown that TLR4 is also involved in various infectious diseases. Infants carrying D299G and T399I polymorphisms are more vulnerable to respiratory syncytial virus infection (321). The single nucleotide polymorphism rs11536889 of TLR4 is involved in organ failure in sepsis patients (322). However, the effects of TLR4 remain controversial during *M. tuberculosis* infection. It was reported that *Tlr4*-deficient mice exhibited the same sensitivity compared to congenic control mice (323). By contrast, another study found that TLR4 mutant mice showed reduced macrophage recruitment and failure to develop a protective immune response against chronic *M. tuberculosis* infection (324). Melioidosis is a high-mortality infectious disease caused by *Burkholderia pseudomallei*, a flagellated, Gram-negative bacterium. TLR5 c.1174C>T (a TLR5 variant carrying a nonsense mutation) is associated with lower IL-10 and TNF-α production and prolonged survival in human melioidosis.

Influenza A virus is a contagious agent that causes respiratory disease. TLR7 is responsible for influenza A virus sensing in the endosome, while RIG-I senses influenza A virus in the cytosol (161, 325–327). The sensing mechanisms for TLR7 and RIG-I are different. TLR7 directly recognizes virus ssRNA in a virus-replication-independent manner. By contrast, RIG-I recognizes the viral replication intermediates in certain cell types (328). Both signaling pathways move toward the activation of IRF3/7 and NF-κB to trigger the production of Type I IFN and proinflammatory cytokines and downstream IFN-stimulated genes (1). Furthermore, it has been shown that intranasal administration of the TLR7 agonist (imiquimod) can significantly reduce airway and pulmonary inflammation in mice during influenza A virus infection (329).

Different single nucleotide polymorphisms of TLR8 and TLR9 confer varying degrees of risk in the development of tuberculosis, suggesting that TLR8 and TLR9 are involved in tuberculosis (330). The most characteristic role of TLRs is sensing the PAMPs from pathogens and initiating immune responses against infectious agents. Notably, in certain scenarios, TLRs may be subverted by the pathogens to alter the host cytokine pattern for their own benefit (319, 331). Thus, further studies on the interplay between pathogen evasion and TLR subversion will have implications for human health.

CONCLUSION AND PERSPECTIVES

This review provides an updated overview of TLR signaling and its critical role in cell-mediated immunity. The fundamental mechanisms of TLR signaling transduction have been identified by cell biological and biochemical approaches, as well as loss-of-function genetic analysis. Significant progress has also been made in the structural elucidation of TLRs and their downstream

signaling supramolecular complex (332, 333). The essential role of TLR signaling in activating innate immune cells to initiate adaptive immunity was illustrated. Importantly, the direct regulatory roles of TLR signaling in effector T cells and Treg cells have been identified. In addition, the individual TLRs signaling involved in infectious disease, autoimmune disease and cancer have been extensively studied (**Figure 3**).

Despite the rapid advancement of our knowledge, there are still large gaps in our understanding of TLR signaling. For example, although free unanchored K63-Ub chains have been demonstrated as a kind of indispensable "second messenger" to activate downstream protein kinases during TLR-induced NF-κB signaling activation by biochemical experiments, how and whether these free unanchored K63-Ub chains activate downstream protein kinases in cells is still unknown. Especially, how to control the activation specificity if these chains are just free in the cytoplasm still remains elusive. Therefore, the detailed mechanisms of how these polyubiquitin chains activate the kinase complex during TLR signaling pathway activation warrant further investigation.

Due to the vital role of TLR signaling in T cell activation, growth, differentiation, and function, it would be necessary to dissect the T cell-specific TLR signaling pathway. In the past few years, T cell-based cancer immunotherapy has made significant progress (334). The Food Drug Administration (FDA) has approved four CD19-CAR-engineered T cell products for blood cancer. Cancer vaccines along with TLR signaling activation could become a more effective therapeutic approach to inhibiting or even eliminating cancer cells. Cancer vaccines along with TLR signaling activation could become a more effective therapeutic approach to inhibiting or even eliminating cancer cells (335).

Besides cancer immunity, TLRs are also involved in many infectious diseases by recognizing the PAMPs of pathogens, initiating inflammatory responses, and eliminating invasive microorganisms at the early stage. However, prolonged or excessive inflammatory responses are harmful or even fatal for the host at the late stage. In the current COVID-19 pandemic, fatal hyperinflammation, but not SARS-CoV-2 directly, is the primary cause of mortality in severe COVID-19 patients. Therefore, drugs targeting viral replication might be ineffective for severe COVID-19 patients since most hospitalized patients are at the late stage of disease. In this case, drugs targeting TLR-dependent inflammatory signaling pathways might be more effective in reducing the mortality of severe COVID-19 patients.

As the field has developed, multidisciplinary approaches have been used in the study of TLR signaling pathways. Integrated methods, combined with transcriptomics, genetic/chemical perturbations, and phosphoproteomics, have been used to systematically discover TLR signaling regulatory components. The m6A RNA sequence technique led to the discovery that mRNA stability is an essential mechanism for regulating TLR-dependent innate immune responses. The single-cell sequencing (scRNA-seq) approach is used to dissect the characteristics of TLR-mediated immune responses at the single-cell level. The development of super-resolution single-molecule localization microscopy empowers the ability to directly observe the supramolecular signaling complex during TLR signaling activation at the single-molecule level. Finally, the advances in cryo-electron microscopy have facilitated our understanding how TLRs recognize their ligands and initiate immune signaling at the atom level. These recent advancements markedly increase our ability to understand TLR signaling pathways and develop new therapeutic strategies against various infectious, autoimmune diseases, and cancers.

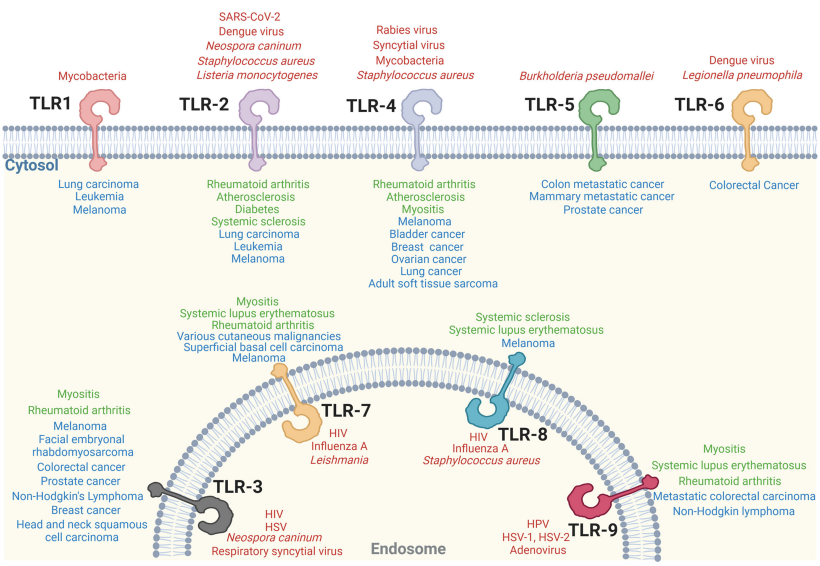

FIGURE 3 | Individual TLR singaling involves in various diseases. Individual TLR-associated infectious diseases (red), autoimmune diseases (green) and cancer (blue) are shown.

AUTHOR CONTRIBUTIONS

R-FW, TD, and YD designed and wrote the manuscript. TD, YD, CX, HW, and R-FW discussed and revised the manuscript. All authors contributed to the article and approved the submitted version.

FUNDING

This work was in part supported by grants from the NCI, NIH (R01CA101795, R01CA246547 and U54CA210181), Department of Defense (DoD) CDMRP BCRP (BC151081) and LCRP (LC200368) to R-FW.

REFERENCES

1. Takeuchi O, Akira S. Pattern Recognition Receptors and Inflammation. *Cell* (2010) 140(6):805–20. doi: 10.1016/j.cell.2010.01.022
2. Akira S, Uematsu S, Takeuchi O. Pathogen Recognition and Innate Immunity. *Cell* (2006) 124(4):783–801. doi: 10.1016/j.cell.2006.02.015
3. Cai X, Chiu YH, Chen ZJ. The cGAS-cGAMP-STING Pathway of Cytosolic DNA Sensing and Signaling. *Mol Cell* (2014) 54(2):289–96. doi: 10.1016/j.molcel.2014.03.040
4. Iwasaki A, Medzhitov R. Toll-Like Receptor Control of the Adaptive Immune Responses. *Nat Immunol* (2004) 5(10):987–95. doi: 10.1038/ni1112
5. Hayden MS, Ghosh S. NF-kappaB in Immunobiology. *Cell Res* (2011) 21 (2):223–44. doi: 10.1038/cr.2011.13
6. Kawasaki T, Kawai T. Toll-Like Receptor Signaling Pathways. *Front Immunol* (2014) 5:461. doi: 10.3389/fimmu.2014.00461
7. Wang HY, Wang R-F. Innate Immune Signaling and Negative Regulators in Cancer. In: R Wang, editor. *Innate Immune Regulation and Cancer Immunotherapy*. New York, NY: Springer New York (2012). doi: 10.1007/978-1-4419-9914-6_6
8. Anderson KV, Jürgens G, Nüsslein-Volhard C. Establishment of Dorsal-Ventral Polarity in the Drosophila Embryo: Genetic Studies on the Role of the Toll Gene Product. *Cell* (1985) 42(3):779–89. doi: 10.1016/0092-8674(85)90274-0
9. Lemaitre B, Nicolas E, Michaut L, Reichhart J-M, Hoffmann JA. The Dorsoventral Regulatory Gene Cassette Spätzle/Toll/cactus Controls the Potent Antifungal Response in Drosophila Adults. *Cell* (1996) 86(6):973–83. doi: 10.1016/S0092-8674(00)80172-5
10. Medzhitov R, Preston-Hurlburt P, Janeway CA. A Human Homologue of the Drosophila Toll Protein Signals Activation of Adaptive Immunity. *Nature* (1997) 388(6640):394–7. doi: 10.1038/41131
11. Kawai T, Akira S. The Role of Pattern-Recognition Receptors in Innate Immunity: Update on Toll-Like Receptors. *Nat Immunol* (2010) 11(5):373–84. doi: 10.1038/ni.1863
12. Fore F, Indriputri C, Mamutse J, Nugraha J. TLR10 and Its Unique Anti-Inflammatory Properties and Potential Use as a Target in Therapeutics. *Immune Netw* (2020) 20(3):e21–1. doi: 10.4110/in.2020.20.e21
13. Henrick BM, Yao X-D, Zahoor MA, l. Abimiku A, Osawe S, Rosenthal KL. TLR10 Senses HIV-1 Proteins and Significantly Enhances HIV-1 Infection. *Front Immunol* (2019) 10:482. doi: 10.3389/fimmu.2019.00482
14. Lind NA, Rael VE, Pestal K, Liu B, Barton GM. Regulation of the Nucleic Acid-Sensing Toll-Like Receptors. *Nat Rev Immunol* (2021) 16:1–12. doi: 10.1038/s41577-021-00577-0
15. Medzhitov R. Toll-Like Receptors and Innate Immunity. *Nat Rev Immunol* (2001) 1(2):135–45. doi: 10.1038/35100529
16. Botos I, Segal DM, Davies DR. The Structural Biology of Toll-Like Receptors. *Structure* (2011) 19(4):447–59. doi: 10.1016/j.str.2011.02.004
17. McClure R, Massari P. TLR-Dependent Human Mucosal Epithelial Cell Responses to Microbial Pathogens. *Front Immunol* (2014) 5:386. doi: 10.3389/fimmu.2014.00386
18. Sutmuller RPM, Morgan ME, Netea MG, Grauer O, Adema GJ. Toll-Like Receptors on Regulatory T Cells: Expanding Immune Regulation. *Trends Immunol* (2006) 27(8):387–93. doi: 10.1016/j.it.2006.06.005
19. Hua Z, Hou B. TLR Signaling in B-Cell Development and Activation. *Cell Mol Immunol* (2013) 10(2):103–6. doi: 10.1038/cmi.2012.61
20. Bhagavan NV, Ha C-E. Chapter 33 - Immunology. In: NV Bhagavan and C-E Ha, editors. *Essentials of Medical Biochemistry*. San Diego: Academic Press (2011). doi: 10.1016/B978-0-12-095461-2.00033-3
21. Akira S, Takeda K, Kaisho T. Toll-Like Receptors: Critical Proteins Linking Innate and Acquired Immunity. *Nat Immunol* (2001) 2(8):675–80. doi: 10.1038/90609
22. Medzhitov R, Janeway CA. Innate Immunity: The Virtues of a Nonclonal System of Recognition. *Cell* (1997) 91(3):295–8. doi: 10.1016/S0092-8674(00)80412-2
23. Hoffmann JA, Kafatos FC, Janeway CA, Ezekowitz RAB. Phylogenetic Perspectives in Innate Immunity. *Science* (1999) 284(5418):1313–8. doi: 10.1126/science.284.5418.1313
24. Aderem A, Ulevitch RJ. Toll-Like Receptors in the Induction of the Innate Immune Response. *Nature* (2000) 406(6797):782–7. doi: 10.1038/35021228
25. Blasius AL, Beutler B. Intracellular Toll-Like Receptors. *Immunity* (2010) 32 (3):305–15. doi: 10.1016/j.immuni.2010.03.012
26. Latz E, Verma A, Visintin A, Gong M, Sirois CM, Klein DCG, et al. Ligand-Induced Conformational Changes Allosterically Activate Toll-Like Receptor 9. *Nat Immunol* (2007) 8(7):772–9. doi: 10.1038/ni1479
27. Fitzgerald KA, Palsson-McDermott EM, Bowie AG, Jefferies CA, Mansell AS, Brady G, et al. Mal (MyD88-Adapter-Like) Is Required for Toll-Like Receptor-4 Signal Transduction. *Nature* (2001) 413(6851):78–83. doi: 10.1038/35092578
28. Horng T, Barton GM, Medzhitov R. TIRAP: An Adapter Molecule in the Toll Signaling Pathway. *Nat Immunol* (2001) 2(9):835–41. doi: 10.1038/ni0901-835
29. Yamamoto M, Sato S, Hemmi H, Uematsu S, Hoshino K, Kaisho T, et al. TRAM is Specifically Involved in the Toll-Like Receptor 4-Mediated MyD88-Independent Signaling Pathway. *Nat Immunol* (2003) 4(11):1144–50. doi: 10.1038/ni986
30. Fitzgerald KA, Rowe DC, Barnes BJ, Caffrey DR, Visintin A, Latz E, et al. LPS-TLR4 Signaling to IRF-3/7 and NF-Kappa B Involves the Toll Adapters TRAM and TRIF. *J Exp Med* (2003) 198(7):1043–55. doi: 10.1084/jem.20031023
31. Kagan JC, Su T, Horng T, Chow A, Akira S, Medzhitov R. TRAM Couples Endocytosis of Toll-Like Receptor 4 to the Induction of Interferon-Beta. *Nat Immunol* (2008) 9(4):361–8. doi: 10.1038/ni1569
32. Rowe DC, McGettrick AF, Latz E, Monks BG, Gay NJ, Yamamoto M, et al. The Myristoylation of TRIF-Related Adaptor Molecule Is Essential for Toll-Like Receptor 4 Signal Transduction. *Proc Natl Acad Sci USA* (2006) 103 (16):6299–304. doi: 10.1073/pnas.0510041103
33. Kagan JC, Medzhitov R. Phosphoinositide-Mediated Adaptor Recruitment Controls Toll-Like Receptor Signaling. *Cell* (2006) 125(5):943–55. doi: 10.1016/j.cell.2006.03.047
34. O'Neill LA, Bowie AG. The Family of Five: TIR-Domain-Containing Adaptors in Toll-Like Receptor Signalling. *Nat Rev Immunol* (2007) 7 (5):353–64. doi: 10.1038/nri2079
35. Fitzgerald KA, Kagan JC. Toll-Like Receptors and the Control of Immunity. *Cell* (2020) 180(6):1044–66. doi: 10.1016/j.cell.2020.02.041
36. Kagan JC, Magupalli VG, Wu H. SMOCs: Supramolecular Organizing Centres That Control Innate Immunity. *Nat Rev Immunol* (2014) 14 (12):821–6. doi: 10.1038/nri3757
37. Lin SC, Lo YC, Wu H. Helical Assembly in the MyD88-IRAK4-IRAK2 Complex in TLR/IL-1R Signalling. *Nature* (2010) 465(7300):885–U2. doi: 10.1038/nature09121
38. Motshwene PG, Moncrieffe MC, Grossmann JG, Kao C, Ayaluru M, Sandercock AM, et al. An Oligomeric Signaling Platform Formed by the Toll-Like Receptor Signal Transducers MyD88 and IRAK-4. *J Biol Chem* (2009) 284(37):25404–11. doi: 10.1074/jbc.M109.022392
39. Bonham KS, Orzalli MH, Hayashi K, Wolf AI, Glanemann C, Weninger W, et al. A Promiscuous Lipid-Binding Protein Diversifies the Subcellular Sites

of Toll-Like Receptor Signal Transduction. *Cell* (2014) 156(4):705–16. doi: 10.1016/j.cell.2014.01.019
40. Cao ZD, Henzel WJ, Gao XO. IRAK: A Kinase Associated With the Interleukin-1 Receptor. *Science* (1996) 271(5252):1128–31. doi: 10.1126/science.271.5252.1128
41. Li SY, Strelow A, Fontana EJ, Wesche H. IRAK-4: A Novel Member of the IRAK Family With the Properties of an IRAK-Kinase. *Proc Natl Acad Sci USA* (2002) 99(8):5567–72. doi: 10.1073/pnas.082100399
42. Kollewe C, Mackensen AC, Neumann D, Knop J, Cao P, Li SU, et al. Sequential Autophosphorylation Steps in the Interleukin-1 Receptor-Associated Kinase-1 Regulate its Availability as an Adapter in Interleukin-1 Signaling. *J Biol Chem* (2004) 279(7):5227–36. doi: 10.1074/jbc.M309251200
43. Sun J, Li N, Oh KS, Dutta B, Vayttaden SJ, Lin B, et al. Comprehensive RNAi-Based Screening of Human and Mouse TLR Pathways Identifies Species-Specific Preferences in Signaling Protein Use. *Sci Signal* (2016) 9 (409):ra3. doi: 10.1126/scisignal.aab2191
44. Clark K, Nanda S, Cohen P. Molecular Control of the NEMO Family of Ubiquitin-Binding Proteins. *Nat Rev Mol Cell Biol* (2013) 14(10):673–85. doi: 10.1038/nrm3644
45. Windheim M, Stafford M, Peggie M, Cohen P. Interleukin-1 (IL-1) Induces the Lys63-Linked Polyubiquitination of IL-1 Receptor-Associated Kinase 1 to Facilitate NEMO Binding and the Activation of IkappaBalpha Kinase. *Mol Cell Biol* (2008) 28(5):1783–91. doi: 10.1128/MCB.02380-06
46. Gottipati S, Rao NL, Fung-Leung WP. IRAK1: A Critical Signaling Mediator of Innate Immunity. *Cell Signal* (2008) 20(2):269–76. doi: 10.1016/j.cellsig.2007.08.009
47. Conze DB, Wu CJ, Thomas JA, Landstrom A, Ashwell JD. Lys63-Linked Polyubiquitination of IRAK-1 is Required for Interleukin-1 Receptor- and Toll-Like Receptor-Mediated NF-kappaB Activation. *Mol Cell Biol* (2008) 28 (10):3538–47. doi: 10.1128/MCB.02098-07
48. Lamothe B, Besse A, Campos AD, Webster WK, Wu H, Darnay BG. Site-Specific Lys-63-Linked Tumor Necrosis Factor Receptor-Associated Factor 6 Auto-Ubiquitination is a Critical Determinant of I Kappa B Kinase Activation. *J Biol Chem* (2007) 282(6):4102–12. doi: 10.1074/jbc.M609503200
49. Walsh MC, Kim GK, Maurizio PL, Molnar EE, Choi Y. TRAF6 Autoubiquitination-Independent Activation of the Nfκb and MAPK Pathways in Response to IL-1 and RANKL. *PloS One* (2008) 3(12):e4064. doi: 10.1371/journal.pone.0004064
50. Hu L, Xu J, Xie X, Zhou Y, Tao P, Li H, et al. Oligomerization-Primed Coiled-Coil Domain Interaction With Ubc13 Confers Processivity to TRAF6 Ubiquitin Ligase Activity. *Nat Commun* (2017) 8(1):814. doi: 10.1038/s41467-017-01290-0
51. Xia ZP, Sun L, Chen X, Pineda G, Jiang X, Adhikari A, et al. Direct Activation of Protein Kinases by Unanchored Polyubiquitin Chains. *Nature* (2009) 461(7260):114–9. doi: 10.1038/nature08247
52. Ea C-K, Deng L, Xia Z-P, Pineda G, Chen ZJ. Activation of IKK by TNFα Requires Site-Specific Ubiquitination of RIP1 and Polyubiquitin Binding by NEMO. *Mol Cell* (2006) 22(2):245–57. doi: 10.1016/j.molcel.2006.03.026
53. Wu C-J, Conze DB, Li T, Srinivasula SM, Ashwell JD. Sensing of Lys 63-Linked Polyubiquitination by NEMO is a Key Event in NF-κB Activation. *Nat Cell Biol* (2006) 8(4):398–406. doi: 10.1038/ncb1384
54. Bhoj VG, Chen ZJ. Ubiquitylation in Innate and Adaptive Immunity. *Nature* (2009) 458(7237):430–7. doi: 10.1038/nature07959
55. Lo Y-C, Lin S-C, Rospigliosi CC, Conze DB, Wu C-J, Ashwell JD, et al. Structural Basis for Recognition of Diubiquitins by NEMO. *Mol Cell* (2009) 33(5):602–15. doi: 10.1016/j.molcel.2009.01.012
56. Rahighi S, Ikeda F, Kawasaki M, Akutsu M, Suzuki N, Kato R, et al. Specific Recognition of Linear Ubiquitin Chains by NEMO is Important for NF-kappaB Activation. *Cell* (2009) 136(6):1098–109. doi: 10.1016/j.cell.2009.03.007
57. Tokunaga F, Sakata SI, Saeki Y, Satomi Y, Kirisako T, Kamei K, et al. Involvement of Linear Polyubiquitylation of NEMO in NF-κb Activation. *Nat Cell Biol* (2009) 11(2):123–32. doi: 10.1038/ncb1821
58. Fujita H, Rahighi S, Akita M, Kato R, Sasaki Y, Wakatsuki S, et al. Mechanism Underlying IkappaB Kinase Activation Mediated by the Linear Ubiquitin Chain Assembly Complex. *Mol Cell Biol* (2014) 34 (7):1322–35. doi: 10.1128/MCB.01538-13
59. Tokunaga F. Linear Ubiquitination-Mediated NF-κb Regulation and its Related Disorders. *J Biochem* (2013) 154(4):313–23. doi: 10.1093/jb/mvt079
60. Noad J, von der Malsburg A, Pathe C, Michel MA, D. Komander and F. Randow: LUBAC-Synthesized Linear Ubiquitin Chains Restrict Cytosol-Invading Bacteria by Activating Autophagy and NF-KappaB. *Nat Microbiol* (2017) 2:17063. doi: 10.1038/nmicrobiol.2017.63
61. Shimizu Y, Taraborrelli L, Walczak H. Linear Ubiquitination in Immunity. *Immunol Rev* (2015) 266(1):190–207. doi: 10.1111/imr.12309
62. Sasaki K, Iwai K. Roles of Linear Ubiquitinylation, a Crucial Regulator of NF-κb and Cell Death, in the Immune System. *Immunol Rev* (2015) 266 (1):175–89. doi: 10.1111/imr.12308
63. Iwai K, Fujita H, Sasaki Y. Linear Ubiquitin Chains: NF-κb Signalling, Cell Death and Beyond. *Nat Rev Mol Cell Biol* (2014) 15(8):503–8. doi: 10.1038/nrm3836
64. Sato S, Sanjo H, Takeda K, Ninomiya-Tsuji J, Yamamoto M, Kawai T, et al. Essential Function for the Kinase TAK1 in Innate and Adaptive Immune Responses. *Nat Immunol* (2005) 6(11):1087–95. doi: 10.1038/ni1255
65. Schuman J, Chen Y, Podd A, Yu M, Liu H-H, Wen R, et al. A Critical Role of TAK1 in B-Cell Receptor–Mediated Nuclear Factor κb Activation. *Blood* (2009) 113(19):4566–74. doi: 10.1182/blood-2008-08-176057
66. Liu H-H, Xie M, Schneider MD, Chen ZJ. Essential Role of TAK1 in Thymocyte Development and Activation. *Proc Natl Acad Sci* (2006) 103 (31):11677. doi: 10.1073/pnas.0603089103
67. Sato S, Sanjo H, Tsujimura T, Ninomiya-Tsuji J, Yamamoto M, Kawai T, et al. TAK1 is Indispensable for Development of T Cells and Prevention of Colitis by the Generation of Regulatory T Cells. *Int Immunol* (2006) 18 (10):1405–11. doi: 10.1093/intimm/dxl082
68. Wan YY, Chi H, Xie M, Schneider MD, Flavell RA. The Kinase TAK1 Integrates Antigen and Cytokine Receptor Signaling for T Cell Development, Survival and Function. *Nat Immunol* (2006) 7(8):851–8. doi: 10.1038/ni1355
69. Ajibade AA, Wang QF, Cui J, Zou J, Xia XJ, Wang MJ, et al. TAK1 Negatively Regulates NF-Kappa B and P38 MAP Kinase Activation in Gr-1(+)CD11b(+) Neutrophils. *Immunity* (2012) 36(1):43–54. doi: 10.1016/j.immuni.2011.12.010
70. Lamothe B, Lai YJ, Hur L, Orozco NM, Wang J, Campos AD, et al. Deletion of TAK1 in the Myeloid Lineage Results in the Spontaneous Development of Myelomonocytic Leukemia in Mice. *PloS One* (2012) 7(12):e51228. doi: 10.1371/journal.pone.0051228
71. Ear T, Fortin CF, Simard FA, McDonald PP. Constitutive Association of TGF-β–Activated Kinase 1 With the IκB Kinase Complex in the Nucleus and Cytoplasm of Human Neutrophils and Its Impact on Downstream Processes. *J Immunol* (2010) 184(7):3897–906. doi: 10.4049/jimmunol.0902958
72. Ajibade AA, Wang HY, Wang RF. Cell Type-Specific Function of TAK1 in Innate Immune Signaling. *Trends Immunol* (2013) 34(7):307–16. doi: 10.1016/j.it.2013.03.007
73. Xing C, Wang M, Ajibade AA, Tan P, Fu C, Chen L, et al. Microbiota Regulate Innate Immune Signaling and Protective Immunity Against Cancer. *Cell Host Microbe* (2021) 29(6):959–974.e7. doi: 10.1016/j.chom.2021.03.016
74. Honda K, Ohba Y, Yanai H, Negishi H, Mizutani T, Takaoka A, et al. Spatiotemporal Regulation of MyD88–IRF-7 Signalling for Robust Type-I Interferon Induction. *Nature* (2005) 434(7036):1035–40. doi: 10.1038/nature03547
75. Honda K, Yanai H, Negishi H, Asagiri M, Sato M, Mizutani T, et al. IRF-7 is the Master Regulator of Type-I Interferon-Dependent Immune Responses. *Nature* (2005) 434(7034):772–7. doi: 10.1038/nature03464
76. Takaoka A, Yanai H, Kondo S, Duncan G, Negishi H, Mizutani T, et al. Integral Role of IRF-5 in the Gene Induction Programme Activated by Toll-Like Receptors. *Nature* (2005) 434(7030):243–9. doi: 10.1038/nature03308
77. Kawai T, Akira S. Toll-Like Receptor and RIG-1-Like Receptor Signaling. *Ann N Y Acad Sci* (2008) 1143(1):1–20. doi: 10.1196/annals.1443.020
78. Ren JY, Chen X, Chen ZJJ. IKK Beta is an IRF5 Kinase That Instigates Inflammation. *Proc Natl Acad Sci USA* (2014) 111(49):17438–43. doi: 10.1073/pnas.1418516111
79. Lopez-Pelaez M, Lamont DJ, Peggie M, Shpiro N, Gray NS, Cohen P. Protein Kinase IKK Beta-Catalyzed Phosphorylation of IRF5 at Ser462 Induces its

Dimerization and Nuclear Translocation in Myeloid Cells. *Proc Natl Acad Sci USA* (2014) 111(49):17432–7. doi: 10.1073/pnas.1418399111
80. Schoenemeyer A, Barnes BJ, Mancl ME, Latz E, Goutagny N, Pitha PM, et al. The Interferon Regulatory Factor, IRF5, Is a Central Mediator of Toll-Like Receptor 7 Signaling. *J Biol Chem* (2005) 280(17):17005–12. doi: 10.1074/jbc.M412584200
81. Yamamoto M, Sato S, Hemmi H, Hoshino K, Kaisho T, Sanjo H, et al. Role of Adaptor TRIF in the MyD88-Independent Toll-Like Receptor Signaling Pathway. *Science* (2003) 301(5633):640–3. doi: 10.1126/science.1087262
82. Hoebe K, Janssen EM, Kim SO, Alexopoulou L, Flavell RA, Han JH, et al. Upregulation of Costimulatory Molecules Induced by Lipopolysaccharide and Double-Stranded RNA Occurs by Trif-Dependent and Trif-Independent Pathways. *Nat Immunol* (2003) 4(12):1223–9. doi: 10.1038/ni1010
83. Cusson-Hermance N, Khurana S, Lee TH, Fitzgerald KA, Kelliher MA. Rip1 Mediates the Trif-Dependent Toll-Like Receptor 3- and 4-Induced NF-κB Activation But Does Not Contribute to Interferon Regulatory Factor 3 Activation*. *J Biol Chem* (2005) 280(44):36560–6. doi: 10.1074/jbc.M506831200
84. Gohda J, Matsumura T, Inoue J-I. Cutting Edge: TNFR-Associated Factor (TRAF) 6 Is Essential for MyD88-Dependent Pathway But Not Toll/IL-1 Receptor Domain-Containing Adaptor-Inducing IFN-β (TRIF)-Dependent Pathway in TLR Signaling. *J Immunol* (2004) 173(5):2913. doi: 10.4049/jimmunol.173.5.2913
85. Chang M, Jin W, Sun S-C. Peli1 Facilitates TRIF-Dependent Toll-Like Receptor Signaling and Proinflammatory Cytokine Production. *Nat Immunol* (2009) 10(10):1089–95. doi: 10.1038/ni.1777
86. McWhirter SM, Fitzgerald KA, Rosains J, Rowe DC, Golenbock DT, Maniatis T. IFN-Regulatory Factor 3-Dependent Gene Expression is Defective in Tbk1-Deficient Mouse Embryonic Fibroblasts. *Proc Natl Acad Sci USA* (2004) 101(1):233–8. doi: 10.1073/pnas.2237236100
87. Sharma S, tenOever BR, Grandvaux N, Zhou GP, Lin RT, Hiscott J. Triggering the Interferon Antiviral Response Through an IKK-Related Pathway. *Science* (2003) 300(5622):1148–51. doi: 10.1126/science.1081315
88. Fitzgerald KA, McWhirter SM, Faia KL, Rowe DC, Latz E, Golenbock DT, et al. IKK Epsilon and TBK1 are Essential Components of the IRF3 Signaling Pathway. *Nat Immunol* (2003) 4(5):491–6. doi: 10.1038/ni921
89. Liu SQ, Cai X, Wu JX, Cong Q, Chen X, Li T, et al. Phosphorylation of Innate Immune Adaptor Proteins MAVS, STING, and TRIF Induces IRF3 Activation. *Science* (2015) 347(6227):1217–U17. doi: 10.1126/science.aaa2630
90. Zhao B, Shu C, Gao X, Sankaran B, Du F, Shelton CL, et al. Structural Basis for Concerted Recruitment and Activation of IRF-3 by Innate Immune Adaptor Proteins. *Proc Natl Acad Sci* (2016) 113(24):E3403. doi: 10.1073/pnas.1603269113
91. Banchereau J, Steinman RM. Dendritic Cells and the Control of Immunity. *Nature* (1998) 392(6673):245–52. doi: 10.1038/32588
92. Schnare M, Barton GM, Holt AC, Takeda K, Akira S, Medzhitov R. Toll-Like Receptors Control Activation of Adaptive Immune Responses. *Nat Immunol* (2001) 2(10):947–50. doi: 10.1038/ni712
93. Palliser D, Ploegh H, Boes M. Myeloid Differentiation Factor 88 Is Required for Cross-Priming *In Vivo*. *J Immunol* (2004) 172(6):3415. doi: 10.4049/jimmunol.172.6.3415
94. Hoshino K, Sugiyama T, Matsumoto M, Tanaka T, Saito M, Hemmi H, et al. IκB Kinase-α is Critical for Interferon-α Production Induced by Toll-Like Receptors 7 and 9. *Nature* (2006) 440(7086):949–53. doi: 10.1038/nature04641
95. Ito T, Amakawa R, Kaisho T, Hemmi H, Tajima K, Uehira K, et al. Interferon-α and Interleukin-12 Are Induced Differentially by Toll-Like Receptor 7 Ligands in Human Blood Dendritic Cell Subsets. *J Exp Med* (2002) 195(11):1507–12. doi: 10.1084/jem.20020207
96. Reis e Sousa C, Sher A, Kaye P. The Role of Dendritic Cells in the Induction and Regulation of Immunity to Microbial Infection. *Curr Opin Immunol* (1999) 11(4):392–9. doi: 10.1016/S0952-7915(99)80066-1
97. Nair-Gupta P, Baccarini A, Tung N, Seyffer F, Florey O, Huang YJ, et al. TLR Signals Induce Phagosomal MHC-I Delivery From the Endosomal Recycling Compartment to Allow Cross-Presentation. *Cell* (2014) 158(3):506–21. doi: 10.1016/j.cell.2014.04.054
98. Blander JM, Medzhitov R. Toll-Dependent Selection of Microbial Antigens for Presentation by Dendritic Cells. *Nature* (2006) 440(7085):808–12. doi: 10.1038/nature04596
99. Trombetta ES, Ebersold M, Garrett W, Pypaert M, Mellman I. Activation of Lysosomal Function During Dendritic Cell Maturation. *Science* (2003) 299 (5611):1400–3. doi: 10.1126/science.1080106
100. Turley SJ, Inaba K, Garrett WS, Ebersold M, Unternaehrer J, Steinman RM, et al. Transport of Peptide-MHC Class II Complexes in Developing Dendritic Cells. *Science* (2000) 288(5465):522–7. doi: 10.1126/science.288.5465.522
101. Horrevorts SK, Duinkerken S, Bloem K, Secades P, Kalay H, Musters RJ, et al. Toll-Like Receptor 4 Triggering Promotes Cytosolic Routing of DC-SIGN-Targeted Antigens for Presentation on MHC Class I. *Front Immunol* (2018) 9. doi: 10.3389/fimmu.2018.01231
102. Sheen J-H, Strainic MG, Liu J, Zhang W, Yi Z, Medof ME, et al. TLR-Induced Murine Dendritic Cell (DC) Activation Requires DC-Intrinsic Complement. *J Immunol* (2017) 199(1):278–91. doi: 10.4049/jimmunol.1700339
103. Sheng K-C, Day S, Wright MD, Stojanovska L, Apostolopoulos V. Enhanced Dendritic Cell-Mediated Antigen-Specific CD4+ T Cell Responses: IFN-Gamma Aids TLR Stimulation. *J Drug Deliv* (2013) 2013:516749. doi: 10.1155/2013/516749
104. Gao Y, Zhang M, Chen L, Hou M, Ji M, Wu G. Deficiency in TLR2 But Not in TLR4 Impairs Dendritic Cells Derived IL-10 Responses to Schistosome Antigens. *Cell Immunol* (2012) 272(2):242–50. doi: 10.1016/j.cellimm.2011.10.007
105. Guo X, Wu N, Shang Y, Liu X, Wu T, Zhou Y, et al. The Novel Toll-Like Receptor 2 Agonist SUP3 Enhances Antigen Presentation and T Cell Activation by Dendritic Cells. *Front Immunol* (2017) 8:158. doi: 10.3389/fimmu.2017.00158
106. Sharma P, Levy O, Dowling DJ. The TLR5 Agonist Flagellin Shapes Phenotypical and Functional Activation of Lung Mucosal Antigen Presenting Cells in Neonatal Mice. *Front Immunol* (2020) 11:171. doi: 10.3389/fimmu.2020.00171
107. Lombardi V, Van Overtvelt L, Horiot S, Moingeon P. Human Dendritic Cells Stimulated *via* TLR7 and/or TLR8 Induce the Sequential Production of Il-10, IFN-γ, and IL-17A by Naive CD4+ T Cells. *J Immunol* (2009) 182(6):3372–9. doi: 10.4049/jimmunol.0801969
108. Dolina JS, Lee J, Griswold RQ, Labarta-Bajo L, Kannan S, Greenbaum JA, et al. TLR9 Sensing of Self-DNA Controls Cell-Mediated Immunity to Listeria Infection *via* Rapid Conversion of Conventional CD4+ T Cells to Treg. *Cell Rep* (2020) 31(1):107249. doi: 10.1016/j.celrep.2020.01.040
109. Mandraju R, Murray S, Forman J, Pasare C. Differential Ability of Surface and Endosomal TLRs to Induce CD8 T Cell Responses *In Vivo*. *J Immunol (Baltimore Md 1950)* (2014) 192(9):4303–15. doi: 10.4049/jimmunol.1302244
110. Hornung V, Rothenfusser S, Britsch S, Krug A, Jahrsdörfer B, Giese T, et al. Quantitative Expression of Toll-Like Receptor 1–10 mRNA in Cellular Subsets of Human Peripheral Blood Mononuclear Cells and Sensitivity to CpG Oligodeoxynucleotides. *J Immunol* (2002) 168(9):4531. doi: 10.4049/jimmunol.168.9.4531
111. Jarrossay D, Napolitani G, Colonna M, Sallusto F, Lanzavecchia A. Specialization and Complementarity in Microbial Molecule Recognition by Human Myeloid and Plasmacytoid Dendritic Cells. *Eur J Immunol* (2001) 31(11):3388–93. doi: 10.1002/1521-4141(200111)31:11<3388::AID-IMMU3388>3.0.CO;2-Q
112. Kadowaki N, Ho S, Antonenko S, Malefyt RW, Kastelein RA, Bazan F, et al. Subsets of Human Dendritic Cell Precursors Express Different Toll-Like Receptors and Respond to Different Microbial Antigens. *J Exp Med* (2001) 194(6):863–9. doi: 10.1084/jem.194.6.863
113. Visintin A, Mazzoni A, Spitzer JH, Wyllie DH, Dower SK, Segal DM. Regulation of Toll-Like Receptors in Human Monocytes and Dendritic Cells. *J Immunol* (2001) 166(1):249. doi: 10.4049/jimmunol.166.1.249
114. Edwards AD, Diebold SS, Slack EMC, Tomizawa H, Hemmi H, Kaisho T, et al. Toll-Like Receptor Expression in Murine DC Subsets: Lack of TLR7 Expression by CD8 Alpha(+) DC Correlates With Unresponsiveness to Imidazoquinolines. *Eur J Immunol* (2003) 33(4):827–33. doi: 10.1002/eji.200323797

115. Boonstra A, Asselin-Paturel C, Gilliet M, Crain C, Trinchieri G, Liu Y-J, et al. Flexibility of Mouse Classical and Plasmacytoid-Derived Dendritic Cells in Directing T Helper Type 1 and 2 Cell Development: Dependency on Antigen Dose and Differential Toll-Like Receptor Ligation. *J Exp Med* (2003) 197 (1):101–9. doi: 10.1084/jem.20021908
116. Merad M, Sathe P, Helft J, Miller J, Mortha A. The Dendritic Cell Lineage: Ontogeny and Function of Dendritic Cells and Their Subsets in the Steady State and the Inflamed Setting. *Annu Rev Immunol* (2013) 31. doi: 10.1146/annurev-immunol-020711-074950
117. Anderson DA, Murphy KM. Models of Dendritic Cell Development Correlate Ontogeny With Function. *Adv Immunol* (2019) 143. doi: 10.1016/bs.ai.2019.09.001
118. Mills KH. TLR-Dependent T Cell Activation in Autoimmunity. *Nat Rev Immunol* (2011) 11(12):807–22. doi: 10.1038/nri3095
119. Kumar V. Toll-Like Receptors in Adaptive Immunity. *Handb Exp Pharmacol* (2021) 225(3):510–9. doi: 10.1007/164_2021_543
120. Wang RF. The Role of MHC Class II-Restricted Tumor Antigens and CD4 (+) T Cells in Antitumor Immunity. *Trends Immunol* (2001) 22(5):269–76. doi: 10.1016/s1471-4906(01)01896-8
121. Wang RF, Miyahara Y, Wang HY. Toll-Like Receptors and Immune Regulation: Implications for Cancer Therapy. *Oncogene* (2008) 27(2):181–9. doi: 10.1038/sj.onc.1210906
122. Karim AF, Reba SM, Li Q, Boom WH, Rojas RE. Toll Like Receptor 2 Engagement on CD4(+) T Cells Promotes TH9 Differentiation and Function. *Eur J Immunol* (2017) 47(9):1513–24. doi: 10.1002/eji.201646846
123. Komai-Koma M, Jones L, Ogg GS, Xu DM, Liew FY. TLR2 is Expressed on Activated T Cells as a Costimulatory Receptor. *Proc Natl Acad Sci USA* (2004) 101(9):3029–34. doi: 10.1073/pnas.0400171101
124. Imanishi T, Hara H, Suzuki S, Suzuki N, Akira S, Saito T. Cutting Edge: TLR2 Directly Triggers Th1 Effector Functions. *J Immunol* (2007) 178(11):6715–9. doi: 10.4049/jimmunol.178.11.6715
125. Biswas A, Banerjee P, Biswas T. Porin of Shigella Dysenteriae Directly Promotes Toll-Like Receptor 2-Mediated CD4(+) T Cell Survival and Effector Function. *Mol Immunol* (2009) 46(15):3076–85. doi: 10.1016/j.molimm.2009.06.006
126. Sinnott BD, Park B, Boer MC, Lewinsohn DA, Lancioni CL. Direct TLR-2 Costimulation Unmasks the Proinflammatory Potential of Neonatal CD4(+) T Cells. *J Immunol* (2016) 197(1):68–77. doi: 10.4049/jimmunol.1501297
127. Reba SM, Li Q, Onwuzulike S, Ding XD, Karim AF, Hernandez Y, et al. TLR2 Engagement on CD4+T Cells Enhances Effector Functions and Protective Responses to Mycobacterium Tuberculosis. *Eur J Immunol* (2014) 44 (5):1410–21. doi: 10.1002/eji.201344100
128. Cottalorda A, Verschelde C, Marcais A, Tomkowiak M, Musette P, Uematsu S, et al. TLR2 Engagement on CD8 T Cells Lowers the Threshold for Optimal Antigen-Induced T Cell Activation. *Eur J Immunol* (2006) 36(7):1684–93. doi: 10.1002/eji.200636181
129. Lee S-M, Joo Y-D, Seo S-K. Expression and Function of TLR2 on CD4 Versus CD8 T Cells. *Immune Netw* (2009) 9(4):127–32. doi: 10.4110/in.2009.9.4.127
130. Mercier BC, Cottalorda A, Coupet CA, Marvel J, Bonnefoy-Berard N. TLR2 Engagement on CD8 T Cells Enables Generation of Functional Memory Cells in Response to a Suboptimal TCR Signal. *J Immunol* (2009) 182 (4):1860–7. doi: 10.4049/jimmunol.0801167
131. Zhang Y, Jones M, McCabe A, Winslow GM, Avram D, MacNamara KC. MyD88 Signaling in CD4 T Cells Promotes IFN-γ Production and Hematopoietic Progenitor Cell Expansion in Response to Intracellular Bacterial Infection. *J Immunol (Baltimore Md 1950)* (2013) 190(9):4725–35. doi: 10.4049/jimmunol.1203024
132. Xing S, Zhang X, Liu JH, Huang X, Zhou P. Host MyD88 Signaling Protects Against Acute Graft-Versus-Host Disease After Allogeneic Bone Marrow Transplantation. *Clin Exp Immunol* (2019) 195(1):121–31. doi: 10.1111/cei.13215
133. Satomi M, Daigo H, Masanori K, Hiroyuki O, Eiko H, Emi Y, et al. Myeloid Differentiation Factor 88 Signaling in Donor T Cells Accelerates Graft-Versus-Host Disease. *Haematologica* (2020) 105(1):226–34. doi: 10.3324/haematol.2018.203380
134. Chang J, Burkett PR, Borges CM, Kuchroo VK, Turka LA, Chang C-H. MyD88 is Essential to Sustain mTOR Activation Necessary to Promote T Helper 17 Cell Proliferation by Linking IL-1 and IL-23 Signaling. *Proc Natl Acad Sci USA* (2013) 110(6):2270–5. doi: 10.1073/pnas.1206048110
135. Reynolds JM, Martinez GJ, Chung Y, Dong C. Toll-Like Receptor 4 Signaling in T Cells Promotes Autoimmune Inflammation. *Proc Natl Acad Sci USA* (2012) 109(32):13064–9. doi: 10.1073/pnas.1120585109
136. González-Navajas JM, Fine S, Law J, Datta SK, Nguyen KP, Yu M, et al. TLR4 Signaling in Effector CD4+ T Cells Regulates TCR Activation and Experimental Colitis in Mice. *J Clin Invest* (2010) 120(2):570–81. doi: 10.1172/JCI40055
137. Zanin-Zhorov A, Tal-Lapidot G, Cahalon L, Cohen-Sfady M, Pevsner-Fischer M, Lider O, et al. Cutting Edge: T Cells Respond to Lipopolysaccharide Innately *via* TLR4 Signaling. *J Immunol* (2007) 179 (1):41. doi: 10.4049/jimmunol.179.1.41
138. Cohen I, Zanin-Zhorov A. Signaling *via* TLR2 and TLR4 Directly Down-Regulates T Cell Effector Functions: The Regulatory Face of Danger Signals. *Front Immunol* (2013) 4:211. doi: 10.3389/fimmu.2013.00211
139. Okeke EB, Okwor I, Uzonna JE. Regulatory T Cells Restrain CD4<sup< +</sup< T Cells From Causing Unregulated Immune Activation and Hypersensitivity to Lipopolysaccharide Challenge. *J Immunol* (2014) 193 (2):655. doi: 10.4049/jimmunol.1303064
140. Sahoo SS, Pratheek BM, Meena VS, Nayak TK, Kumar PS, Bandyopadhyay S, et al. VIPER Regulates Naive T Cell Activation and Effector Responses: Implication in TLR4 Associated Acute Stage T Cell Responses. *Sci Rep* (2018) 8(1):7118. doi: 10.1038/s41598-018-25549-8
141. Qu J, Yu X, Jin C, Feng Y, Xie S, Xie H, et al. TLR7 Modulated T Cell Response in the Mesenteric Lymph Node of *Schistosoma Japonicum*-Infected C57BL/6 Mice. *J Immunol Res* (2019) 2019:2691808. doi: 10.1155/2019/2691808
142. Li Q, Yan Y, Liu J, Huang X, Zhang X, Kirschning C, et al. Toll-Like Receptor 7 Activation Enhances CD8+ T Cell Effector Functions by Promoting Cellular Glycolysis. *Front Immunol* (2019) 10:2191(2191). doi: 10.3389/fimmu.2019.02191
143. Tabiasco J, Devêvre E, Rufer N, Salaun B, Cerottini J-C, Speiser D, et al. Human Effector $CD8^+$ T Lymphocytes Express TLR3 as a Functional Coreceptor. *J Immunol* (2006) 177(12):8708–13. doi: 10.4049/jimmunol.177.12.8708
144. Di S, Zhou M, Pan Z, Sun R, Chen M, Jiang H, et al. Combined Adjuvant of Poly I:C Improves Antitumor Effects of CAR-T Cells. *Front Oncol* (2019) 9:241. doi: 10.3389/fonc.2019.00241
145. Lai Y, Weng J, Wei X, Qin L, Lai P, Zhao R, et al. Toll-Like Receptor 2 Costimulation Potentiates the Antitumor Efficacy of CAR T Cells. *Leukemia* (2018) 32(3):801–8. doi: 10.1038/leu.2017.249
146. George P, Dasyam N, Giunti G, Mester B, Bauer E, Andrews B, et al. Third-Generation Anti-CD19 Chimeric Antigen Receptor T-Cells Incorporating a TLR2 Domain for Relapsed or Refractory B-Cell Lymphoma: A Phase I Clinical Trial Protocol (ENABLE). *BMJ Open* (2020) 10(2):e034629. doi: 10.1136/bmjopen-2019-034629
147. Vignali DAA, Collison LW, Workman CJ. How Regulatory T Cells Work. *Nat Rev Immunol* (2008) 8(7):523–32. doi: 10.1038/nri2343
148. Walker MR, Kasprowicz DJ, Gersuk VH, Benard A, Van Landeghen M, Buckner JH, et al. Induction of FoxP3 and Acquisition of T Regulatory Activity by Stimulated Human CD4(+)CD25(-) T Cells. *J Clin Invest* (2003) 112(9):1437–43. doi: 10.1172/jci200319441
149. Khattri R, Cox T, Yasayko SA, Ramsdell F. An Essential Role for Scurfin in CD4(+)CD25(+) T Regulatory Cells. *Nat Immunol* (2003) 4(4):337–42. doi: 10.1038/ni909
150. Hori S, Nomura T, Sakaguchi S. Control of Regulatory T Cell Development by the Transcription Factor Foxp3. *Science* (2003) 299(5609):1057–61. doi: 10.1126/science.1079490
151. Fontenot JD, Gavin MA, Rudensky AY. Foxp3 Programs the Development and Function of CD4(+)CD25(+) Regulatory T Cells. *Nat Immunol* (2003) 4 (4):330–6. doi: 10.1038/ni904
152. Wang HY, Lee DA, Peng GY, Guo Z, Li YC, Kiniwa Y, et al. Tumor-Specific Human CD4(+) Regulatory T Cells and Their Ligands: Implications for Immunotherapy. *Immunity* (2004) 20(1):107–18. doi: 10.1016/s1074-7613(03)00359-5
153. Curiel TJ, Coukos G, Zou LH, Alvarez X, Cheng P, Mottram P, et al. Specific Recruitment of Regulatory T Cells in Ovarian Carcinoma Fosters Immune

Privilege and Predicts Reduced Survival. *Nat Med* (2004) 10(9):942–9. doi: 10.1038/nm1093
154. Liyanage UK, Moore TT, Joo HG, Tanaka Y, Herrmann V, Doherty G, et al. Prevalence of Regulatory T Cells is Increased in Peripheral Blood and Tumor Microenvironment of Patients With Pancreas or Breast Adenocarcinoma. *J Immunol* (2002) 169(5):2756–61. doi: 10.4049/jimmunol.169.5.2756
155. Woo EY, Chu CS, Goletz TJ, Schlienger K, Yeh H, Coukos G, et al. Regulatory CD4(+)CD25(+) T Cells in Tumors From Patients With Early-Stage non-Small Cell Lung Cancer and Late-Stage Ovarian Cancer. *Cancer Res* (2001) 61(12):4766–72.
156. Wang HY, Peng GY, Guo Z, Shevach EM, Wang RF. Recognition of a New ARTC1 Peptide Ligand Uniquely Expressed in Tumor Cells by Antigen-Specific CD4(+) Regulatory T Cells. *J Immunol* (2005) 174(5):2661–70. doi: 10.4049/jimmunol.174.5.2661
157. Wang HY, Wang RF. Regulatory T Cells and Cancer. *Curr Opin Immunol* (2007) 19(2):217–23. doi: 10.1016/j.coi.2007.02.004
158. Peng G, Wang HY, Peng W, Kiniwa Y, Seo KH, Wang RF. Tumor-Infiltrating Gamma Delta T Cells Suppress T and Dendritic Cell Function *via* Mechanisms Controlled by a Unique Toll-Like Receptor Signaling Pathway. *Immunity* (2007) 27(2):334–48. doi: 10.1016/j.immuni.2007.05.020
159. Kiniwa Y, Miyahara Y, Wang HY, Peng W, Peng G, Wheeler TM, et al. CD8+ Foxp3+ Regulatory T Cells Mediate Immunosuppression in Prostate Cancer. *Clin Cancer Res* (2007) 13(23):6947–58. doi: 10.1158/1078-0432.ccr-07-0842
160. Peng GY, Guo Z, Kiniwa Y, Voo KS, Peng WY, Fu TH, et al. Toll-Like, Receptor 8-Mediated Reversal of CD4(+) Regulatory T Cell Function. *Science* (2005) 309(5739):1380–4. doi: 10.1126/science.1113401
161. Heil F, Hemmi H, Hochrein H, Ampenberger F, Kirschning C, Akira S, et al. Species-Specific Recognition of Single-Stranded RNA *via* Toll-Like Receptor 7 and 8. *Science* (2004) 303(5663):1526–9. doi: 10.1126/science.1093620
162. Li L, Liu X, Sanders KL, Edwards JL, Ye J, Si F, et al. TLR8-Mediated Metabolic Control of Human Treg Function: A Mechanistic Target for Cancer Immunotherapy. *Cell Metab* (2019) 29(1):103–123.e5. doi: 10.1016/j.cmet.2018.09.020
163. Shang W, Xu R, Xu T, Wu M, Xu J, Wang F. Ovarian Cancer Cells Promote Glycolysis Metabolism and TLR8-Mediated Metabolic Control of Human CD4+ T Cells. *Front Oncol* (2020) 10:570899(1956). doi: 10.3389/fonc.2020.570899
164. Jurk M, Heil F, Vollmer J, Schetter C, Krieg AM, Wagner H, et al. Human TLR7 or TLR8 Independently Confer Responsiveness to the Antiviral Compound R-848. *Nat Immunol* (2002) 3(6):499–9. doi: 10.1038/ni0602-499
165. Netea MG, Sutmuller R, Hermann C, van der Graaf CAA, van der Meer JWM, van Krieken JH, et al. Toll-Like Receptor 2 Suppresses Immunity Against Candida Albicans Through Induction of IL-10 and Regulatory T Cells. *J Immunol* (2004) 172(6):3712–8. doi: 10.4049/jimmunol.172.6.3712
166. Sutmuller RPM, den Brok M, Kramer M, Bennink EJ, Toonen LWJ, Kullberg BJ, et al. Toll-Like Receptor 2 Controls Expansion and Function of Regulatory T Cells. *J Clin Invest* (2006) 116(2):485–94. doi: 10.1172/jci25439
167. Liu H, Komai-Koma M, Xu D, Liew FY. Toll-Like Receptor 2 Signaling Modulates the Functions of CD4+ CD25+ Regulatory T Cells. *Proc Natl Acad Sci USA* (2006) 103(18):7048–53. doi: 10.1073/pnas.0601554103
168. LaRosa DF, Gelman AE, Rahman AH, Zhang J, Turka LA, Walsh PT. CpG DNA Inhibits CD4+CD25+ Treg Suppression Through Direct MyD88-Dependent Costimulation of Effector CD4+ T Cells. *Immunol Lett* (2007) 108(2):183–8. doi: 10.1016/j.imlet.2006.12.007
169. Urry Z, Xystrakis E, Richards DF, McDonald J, Sattar Z, Cousins DJ, et al. Ligation of TLR9 Induced on Human IL-10-Secreting Tregs by 1alpha,25-Dihydroxyvitamin D3 Abrogates Regulatory Function. *J Clin Invest* (2009) 119(2):387–98. doi: 10.1172/JCI32354
170. Crellin NK, Garcia RV, Hadisfar O, Allan SE, Steiner TS, Levings MK. Human CD4(+) T Cells Express TLR5 and its Ligand Flagellin Enhances the Suppressive Capacity and Expression of FOXP3 in CD4(+)CD25(+) T Regulatory Cells. *J Immunol* (2005) 175(12):8051–9. doi: 10.4049/jimmunol.175.12.8051
171. Caramalho I, Lopes-Carvalho T, Ostler D, Zelenay S, Haury M, Demengeot J. Regulatory T Cells Selectively Express Toll-Like Receptors and are Activated by Lipopolysaccharide. *J Exp Med* (2003) 197(4):403–11. doi: 10.1084/jem.20021633
172. Liew FY, Xu DM, Brint EK, O'Neill LAJ. Negative Regulation of Toll-Like Receptor-Mediated Immune Responses. *Nat Rev Immunol* (2005) 5(6):446–58. doi: 10.1038/nri1630
173. Cui J, Chen YJ, Wang HY, Wang RF. Mechanisms and Pathways of Innate Immune Activation and Regulation in Health and Cancer. *Hum Vaccines Immunother* (2014) 10(11):3270–85. doi: 10.4161/21645515.2014.979640
174. Zanoni I, Ostuni R, Marek LR, Barresi S, Barbalat R, Barton GM, et al. CD14 Controls the LPS-Induced Endocytosis of Toll-Like Receptor 4. *Cell* (2011) 147(4):868–80. doi: 10.1016/j.cell.2011.09.051
175. Baumann CL, Aspalter IM, Sharif O, Pichlmair A, Bluml S, Grebien F, et al. CD14 is a Coreceptor of Toll-Like Receptors 7 and 9. *J Exp Med* (2010) 207(12):2689–701. doi: 10.1084/jem.20101111
176. LeBouder E, Rey-Nores JE, Rushmere NK, Grigorov M, Lawn SD, Affolter M, et al. Soluble Forms of Toll-Like Receptor (TLR)2 Capable of Modulating TLR2 Signaling are Present in Human Plasma and Breast Milk. *J Immunol* (2003) 171(12):6680–9. doi: 10.4049/jimmunol.171.12.6680
177. Iwami K, Matsuguchi T, Masuda A, Kikuchi T, Musikacharoen T, Yoshikai Y. Cutting Edge: Naturally Occurring Soluble Form of Mouse Toll-Like Receptor 4 Inhibits Lipopolysaccharide Signaling. *J Immunol* (2000) 165(12):6682–6. doi: 10.4049/jimmunol.165.12.6682
178. Brint EK, Xu DM, Liu HY, Dunne A, McKenzie ANJ, O'Neill LAJ, et al. ST2 is an Inhibitor of Interleukin 1 Receptor and Toll-Like Receptor 4 Signaling and Maintains Endotoxin Tolerance. *Nat Immunol* (2004) 5(4):373–9. doi: 10.1038/ni1050
179. Garlanda C, Riva F, Polentarutti N, Buracchi C, Sironi M, De Bortoli M, et al. Intestinal Inflammation in Mice Deficient in Tir8, an Inhibitory Member of the IL-1 Receptor Family. *Proc Natl Acad Sci USA* (2004) 101(10):3522–6. doi: 10.1073/pnas.0308680101
180. Wald D, Qin JZ, Zhao ZD, Qian YC, Naramura M, Tian LP, et al. SIGIRR, a Negative Regulator of Toll-Like Receptor-Interleukin 1 Receptor Signaling. *Nat Immunol* (2003) 4(9):920–7. doi: 10.1038/ni968
181. Diehl GE, Yue HH, Hsieh K, Kuang AA, Ho M, Morici LA, et al. TRAIL-R as a Negative Regulator of Innate Immune Cell Responses. *Immunity* (2004) 21(6):877–89. doi: 10.1016/j.immuni.2004.11.008
182. Nakagawa R, Naka T, Tsutsui H, Fujimoto M, Kimura A, Abe T, et al. SOCS-1 Participates in Negative Regulation of LPS Responses. *Immunity* (2002) 17(5):677–87. doi: 10.1016/s1074-7613(02)00449-1
183. Kinjyo I, Hanada T, Inagaki-Ohara K, Mori H, Aki D, Ohishi M, et al. SOCS1/JAB is a Negative Regulator of LPS-Induced Macrophage Activation. *Immunity* (2002) 17(5):583–91. doi: 10.1016/s1074-7613(02)00446-6
184. Burns K, Janssens S, Brissoni B, Olivos N, Beyaert R, Tschopp J. Inhibition of Interleukin 1 Receptor/Toll-Like Receptor Signaling Through the Alternatively Spliced, Short Form of MyD88 is Due to its Failure to Recruit IRAK-4. *J Exp Med* (2003) 197(2):263–8. doi: 10.1084/jem.20021790
185. Janssens S, Burns K, Tschopp J, Beyaert R. Regulation of Interleukin-1-and Lipopolysaccharide-Induced NF-Kappa B Activation by Alternative Splicing of Myd88. *Curr Biol* (2002) 12(6):467–71. doi: 10.1016/s0960-9822(02)00712-1
186. Zhang GL, Ghosh S. Negative Regulation of Toll-Like Receptor-Mediated Signaling by Tollip. *J Biol Chem* (2002) 277(9):7059–65. doi: 10.1074/jbc.M109537200
187. Kobayashi K, Hernandez LD, Galan JE, Janeway CA, Medzhitov R, Flavell RA. IRAK-M is a Negative Regulator of Toll-Like Receptor Signaling. *Cell* (2002) 110(2):191–202. doi: 10.1016/s0092-8674(02)00827-9
188. Shembade N, Ma A, Harhaj EW. Inhibition of NF-Kappa B Signaling by A20 Through Disruption of Ubiquitin Enzyme Complexes. *Science* (2010) 327(5969):1135–9. doi: 10.1126/science.1182364
189. Boone DL, Turer EE, Lee EG, Ahmad RC, Wheeler MT, Tsui C, et al. The Ubiquitin-Modifying Enzyme A20 is Required for Termination of Toll-Like Receptor Responses. *Nat Immunol* (2004) 5(10):1052–60. doi: 10.1038/ni1110
190. Lee AJ, Zhou XF, Chang M, Hunzeker J, Bonneau RH, Zhou DP, et al. Regulation of Natural Killer T-Cell Development by Deubiquitinase CYLD. *EMBO J* (2010) 29(9):1600–12. doi: 10.1038/emboj.2010.31
191. Reiley WW, Jin W, Lee AJ, Wright A, Wu XF, Tewalt EF, et al. Deubiquitinating Enzyme CYLD Negatively Regulates the Ubiquitin-Dependent Kinase Tak1 and Prevents Abnormal T Cell Responses. *J Exp Med* (2007) 204(6):1475–85. doi: 10.1084/jem.20062694

192. Reiley WW, Zhang MY, Jin W, Losiewicz M, Donohue KB, Norbury CC, et al. Regulation of T Cell Development by the Deubiquitinating Enzyme CYLD. *Nat Immunol* (2006) 7(4):411–7. doi: 10.1038/ni1315
193. Trompouki E, Hatzivassiliou E, Tsichritzis T, Farmer H, Ashworth A, Mosialos G. CYLD Is a Deubiquitinating Enzyme That Negatively Regulates NF-Kappa B Activation by TNFR Family Members. *Nature* (2003) 424(6950):793–6. doi: 10.1038/nature01803
194. Kovalenko A, Chable-Bessia C, Cantarella G, Israel A, Wallach D, Courtois G. The Tumour Suppressor CYLD Negatively Regulates NF-Kappa B Signalling by Deubiquitination. *Nature* (2003) 424(6950):801–5. doi: 10.1038/nature01802
195. Wang C, Chen TY, Zhang J, Yang MJ, Li N, Xu XF, et al. The E3 Ubiquitin Ligase Nrdp1 'Preferentially' Promotes TLR-Mediated Production of Type I Interferon. *Nat Immunol* (2009) 10(7):744–U100. doi: 10.1038/ni.1742
196. Tong YZ, Cui J, Li QT, Zou J, Wang HY, Wang RF. Enhanced TLR-Induced NF-Kappa B Signaling and Type I Interferon Responses in NLRC5 Deficient Mice. *Cell Res* (2012) 22(5):822–35. doi: 10.1038/cr.2012.53
197. Schneider M, Zimmermann AG, Roberts RA, Zhang L, Swanson KV, Wen HT, et al. The Innate Immune Sensor NLRC3 Attenuates Toll-Like Receptor Signaling *via* Modification of the Signaling Adaptor TRAF6 and Transcription Factor NF-Kappa B. *Nat Immunol* (2012) 13(9):823–31. doi: 10.1038/ni.2378
198. Anand PK, Malireddi RKS, Lukens JR, Vogel P, Bertin J, Lamkanfi M, et al. NLRP6 Negatively Regulates Innate Immunity and Host Defence Against Bacterial Pathogens. *Nature* (2012) 488(7411):389–+. doi: 10.1038/nature11250
199. Xia XJ, Cui J, Wang HLY, Zhu L, Matsueda S, Wang QF, et al. NLRX1 Negatively Regulates TLR-Induced NF-Kappa B Signaling by Targeting TRAF6 and IKK. *Immunity* (2011) 34(6):843–53. doi: 10.1016/j.immuni.2011.02.022
200. Kumar H, Pandey S, Zou JA, Kumagai Y, Takahashi K, Akira S, et al. NLRC5 Deficiency Does Not Influence Cytokine Induction by Virus and Bacteria Infections. *J Immunol* (2011) 186(2):994–1000. doi: 10.4049/jimmunol.1002094
201. Allen IC, Moore CB, Schneider M, Lei Y, Davis BK, Scull MA, et al. NLRX1 Protein Attenuates Inflammatory Responses to Infection by Interfering With the RIG-I-MAVS and TRAF6-NF-Kappa B Signaling Pathways. *Immunity* (2011) 34(6):854–65. doi: 10.1016/j.immuni.2011.03.026
202. Cui J, Zhu L, Xia XJ, Wang HY, Legras X, Hong J, et al. NLRC5 Negatively Regulates the NF-Kappa B and Type I Interferon Signaling Pathways. *Cell* (2010) 141(3):483–96. doi: 10.1016/j.cell.2010.03.040
203. Benko S, Magalhaes JG, Philpott DJ, Girardin SE. NLRC5 Limits the Activation of Inflammatory Pathways. *J Immunol* (2010) 185(3):1681–91. doi: 10.4049/jimmunol.0903900
204. Tattoli I, Carneiro LA, Jehanno M, Magalhaes JG, Shu Y, Philpott DJ, et al. NLRX1 is a Mitochondrial NOD-Like Receptor That Amplifies NF-Kappa B and JNK Pathways by Inducing Reactive Oxygen Species Production. *EMBO Rep* (2008) 9(3):293–300. doi: 10.1038/sj.embor.7401161
205. Wu C, Su Z, Lin M, Ou J, Zhao W, Cui J, et al. NLRP11 Attenuates Toll-Like Receptor Signalling by Targeting TRAF6 for Degradation *via* the Ubiquitin Ligase RNF19A. *Nat Commun* (2017) 8(1):1977–7. doi: 10.1038/s41467-017-02073-3
206. Meng Q, Cai C, Sun T, Wang Q, Xie W, Wang R, et al. Reversible Ubiquitination Shapes NLRC5 Function and Modulates NF-κb Activation Switch. *J Cell Biol* (2015) 211(5):1025–40. doi: 10.1083/jcb.201505091
207. Chuang TH, Ulevitch RJ. Triad3A, an E3 Ubiquitin-Protein Ligase Regulating Toll-Like Receptors. *Nat Immunol* (2004) 5(5):495–502. doi: 10.1038/ni1066
208. Shi M, Deng WW, Bi EG, Mao KR, Ji YY, Lin GM, et al. TRIM30 Alpha Negatively Regulates TLR-Mediated NF-Kappa B Activation by Targeting TAB2 and TAB3 for Degradation. *Nat Immunol* (2008) 9(4):369–77. doi: 10.1038/ni1577
209. Moore CB, Bergstralh DT, Duncan JA, Lei Y, Morrison TE, Zimmermann AG, et al. NLRX1 is a Regulator of Mitochondrial Antiviral Immunity. *Nature* (2008) 451(7178):573–U8. doi: 10.1038/nature06501
210. Kobayashi KS, van den Elsen PJ. NLRC5: A Key Regulator of MHC Class I-Dependent Immune Responses. *Nat Rev Immunol* (2012) 12(12):813–20. doi: 10.1038/nri3339
211. Feng Y, Duan T, Du Y, Jin S, Wang M, Cui J, et al. LRRC25 Functions as an Inhibitor of NF-κb Signaling Pathway by Promoting P65/RelA for Autophagic Degradation. *Sci Rep* (2017) 7(1):13448–8. doi: 10.1038/s41598-017-12573-3
212. Du Y, Duan T, Feng Y, Liu Q, Lin M, Cui J, et al. LRRC25 Inhibits Type I IFN Signaling by Targeting ISG15-Associated RIG-I for Autophagic Degradation. *EMBO J* (2018) 37(3):351–66. doi: 10.15252/embj.201796781
213. Zhao Z, Su Z, Liang P, Liu D, Yang S, Wu Y, et al. USP38 Couples Histone Ubiquitination and Methylation *via* KDM5B to Resolve Inflammation. *Adv Sci (Weinheim Baden-Wurttemberg Germany)* (2020) 7(22):2002680–2002680. doi: 10.1002/advs.202002680
214. Lin M, Zhao Z, Yang Z, Meng Q, Tan P, Xie W, et al. USP38 Inhibits Type I Interferon Signaling by Editing TBK1 Ubiquitination Through NLRP4 Signalosome. *Mol Cell* (2016) 64(2):267–81. doi: 10.1016/j.molcel.2016.08.029
215. Chen M, Meng Q, Qin Y, Liang P, Tan P, He L, et al. TRIM14 Inhibits cGAS Degradation Mediated by Selective Autophagy Receptor P62 to Promote Innate Immune Responses. *Mol Cell* (2016) 64(1):105–19. doi: 10.1016/j.molcel.2016.08.025
216. Chen M, Zhao Z, Meng Q, Liang P, Su Z, Wu Y, et al. TRIM14 Promotes Noncanonical NF-κb Activation by Modulating P100/P52 Stability *via* Selective Autophagy. *Adv Sci (Weinheim Baden-Wurttemberg Germany)* (2019) 7(1):1901261–1901261. doi: 10.1002/advs.201901261
217. Tan P, He L, Cui J, Qian C, Cao X, Lin M, et al. Assembly of the WHIP-TRIM14-PPP6C Mitochondrial Complex Promotes RIG-I-Mediated Antiviral Signaling. *Mol Cell* (2017) 68(2):293–307.e5. doi: 10.1016/j.molcel.2017.09.035
218. Zhou Z, Jia X, Xue Q, Dou Z, Ma Y, Zhao Z, et al. TRIM14 is a Mitochondrial Adaptor That Facilitates Retinoic Acid-Inducible Gene-I–like Receptor-Mediated Innate Immune Response. *Proc Natl Acad Sci* (2014) 111(2):E245–54. doi: 10.1073/pnas.1316941111
219. Deidier A. Deux Dissertations Medecinales et Chirurgicales, L'une Sur La Maladie Venerienne, L'autre Sur La Nature & La Curation Des Tumeurs. Chez Charles Maurice d'Houry (1725).
220. Dajon M, Iribarren K, Cremer I. Toll-Like Receptor Stimulation in Cancer: A Pro- and Anti-Tumor Double-Edged Sword. *Immunobiology* (2017) 222(1):89–100. doi: 10.1016/j.imbio.2016.06.009
221. Urban-Wojciuk Z, Khan MM, Oyler BL, Fåhraeus R, Marek-Trzonkowska N, Nita-Lazar A, et al. The Role of TLRs in Anti-Cancer Immunity and Tumor Rejection. *Front Immunol* (2019) 10:2388(2388). doi: 10.3389/fimmu.2019.02388
222. Lin H, Yan J, Wang Z, Hua F, Yu J, Sun W, et al. Loss of Immunity-Supported Senescence Enhances Susceptibility to Hepatocellular Carcinogenesis and Progression in Toll-Like Receptor 2-Deficient Mice. *Hepatology* (2013) 57(1):171–82. doi: 10.1002/hep.25991
223. Qi S, Zhang H, Sun R, An A, Li H, Ouyang D. 245 Human TLR8 Knock-in Mice Potentiate Immunotherapy Responses of MC38 Syngeneic Tumors. *J Immunother Cancer* (2020) 8(Suppl 3):A146. doi: 10.1136/jitc-2020-SITC2020.0245
224. Zhang Y, Luo F, Cai Y, Liu N, Wang L, Xu D, et al. TLR1/TLR2 Agonist Induces Tumor Regression by Reciprocal Modulation of Effector and Regulatory T Cells. *J Immunol* (2011) 186(4):1963–9. doi: 10.4049/jimmunol.1002320
225. Sharma N, Vacher J, Allison JP. TLR1/2 Ligand Enhances Antitumor Efficacy of CTLA-4 Blockade by Increasing Intratumoral Treg Depletion. *Proc Natl Acad Sci USA* (2019) 116(21):10453–62. doi: 10.1073/pnas.1819004116
226. He W, Liu Q, Wang L, Chen W, Li N, Cao X. TLR4 Signaling Promotes Immune Escape of Human Lung Cancer Cells by Inducing Immunosuppressive Cytokines and Apoptosis Resistance. *Mol Immunol* (2007) 44(11):2850–9. doi: 10.1016/j.molimm.2007.01.022
227. Yang H, Zhou H, Feng P, Zhou X, Wen H, Xie X, et al. Reduced Expression of Toll-Like Receptor 4 Inhibits Human Breast Cancer Cells Proliferation and Inflammatory Cytokines Secretion. *J Exp Clin Cancer Res* (2010) 29:92. doi: 10.1186/1756-9966-29-92
228. Yang H, Wang B, Wang T, Xu L, He C, Wen H, et al. Toll-Like Receptor 4 Prompts Human Breast Cancer Cells Invasiveness *via* Lipopolysaccharide Stimulation and is Overexpressed in Patients With Lymph Node Metastasis. *PloS One* (2014) 9(10):e109980. doi: 10.1371/journal.pone.0109980

229. Kim J-H, Kordahi MC, Chac D, DePaolo RW. Toll-Like Receptor-6 Signaling Prevents Inflammation and Impacts Composition of the Microbiota During Inflammation-Induced Colorectal Cancer. *Cancer Prev Res* (2020) 13(1):25. doi: 10.1158/1940-6207.CAPR-19-0286
230. Rakoff-Nahoum S, Medzhitov R. Regulation of Spontaneous Intestinal Tumorigenesis Through the Adaptor Protein Myd88. *Science* (2007) 317: (5834):124–7. doi: 10.1126/science.1140488
231. Naugler WE, Sakurai T, Kim S, Maeda S, Kim K, Elsharkawy AM, et al. Gender Disparity in Liver Cancer Due to Sex Differences in MyD88-Dependent IL-6 Production. *Science* (2007) 317: (5834):121–4. doi: 10.1126/science.1140485
232. Ngo VN, Young RM, Schmitz R, Jhavar S, Xiao W, Lim K-H, et al. Oncogenically Active MYD88 Mutations in Human Lymphoma. *Nature* (2011) 470(7332):115–9. doi: 10.1038/nature09671
233. Treon SP, Xu L, Yang G, Zhou Y, Liu X, Cao Y, et al. MYD88 L265P Somatic Mutation in Waldenström's Macroglobulinemia. *N Engl J Med* (2012) 367: (9):826–33. doi: 10.1056/NEJMoa1200710
234. Pham-Ledard A, Beylot-Barry M, Barbe C, Leduc M, Petrella T, Vergier B, et al. High Frequency and Clinical Prognostic Value of MYD88 L265P Mutation in Primary Cutaneous Diffuse Large B-Cell Lymphoma, Leg-Type. *JAMA Dermatol* (2014) 150(11):1173–9. doi: 10.1001/jamadermatol.2014.821
235. Tartey S, Neale G, Vogel P, Malireddi RKS, Kanneganti T-D. A MyD88/IL1R Axis Regulates PD-1 Expression on Tumor-Associated Macrophages and Sustains Their Immunosuppressive Function in Melanoma. *J Cancer Res* (2021) 81(9):2358–72. doi: 10.1158/0008-5472.CAN-20-3510
236. D'Agostini C, Pica F, Febbraro G, Grelli S, Chiavaroli C, Garaci E. Antitumour Effect of OM-174 and Cyclophosphamide on Murine B16 Melanoma in Different Experimental Conditions. *Int Immunopharmacol* (2005) 5(7-8):1205–12. doi: 10.1016/j.intimp.2005.02.013
237. Morales A, Eidinger D, Bruce AW. Intracavitary Bacillus Calmette-Guerin in the Treatment of Superficial Bladder Tumors. *J Urol* (1976) 116(2):180–3. doi: 10.1016/s0022-5347(17)58737-6
238. Guinn ZP, Petro TM. IFN-Gamma Synergism With Poly I:C Reduces Growth of Murine and Human Cancer Cells With Simultaneous Changes in Cell Cycle and Immune Checkpoint Proteins. *Cancer Lett* (2018) 438:1–9. doi: 10.1016/j.canlet.2018.09.003
239. Salazar AM, Erlich RB, Mark A, Bhardwaj N, Herberman RB. Therapeutic *in Situ* Autovaccination Against Solid Cancers With Intratumoral Poly-ICLC: Case Report, Hypothesis, and Clinical Trial. *Cancer Immunol Res* (2014) 2 (8):720–4. doi: 10.1158/2326-6066.CIR-14-0024
240. Sun L, Kees T, Almeida AS, Liu B, He XY, Ng D, et al. Activating a Collaborative Innate-Adaptive Immune Response to Control Metastasis. *Cancer Cell* (2021) 39(10):1361–74.e9. doi: 10.1016/j.ccell.2021.08.005
241. Zandi Z, Kashani B, Bashash D, Poursani EM, Mousavi SA, Chahardoli B, et al. The Anticancer Effect of the TLR4 Inhibition Using TAK-242 (Resatorvid) Either as a Single Agent or in Combination With Chemotherapy: A Novel Therapeutic Potential for Breast Cancer. *J Cell Biochem* (2020) 121: (2):1623–34. doi: 10.1002/jcb.29397
242. Hsu RYC, Chan CHF, Spicer JD, Rousseau MC, Giannias B, Rousseau S, et al. LPS-Induced TLR4 Signaling in Human Colorectal Cancer Cells Increases β1 Integrin-Mediated Cell Adhesion and Liver Metastasis. *J Cancer Res* (2011) 71(5):1989–98. doi: 10.1158/0008-5472.CAN-10-2833
243. Brackett CM, Kojouharov B, Veith J, Greene KF, Burdelya LG, Gollnick SO, et al. Toll-Like Receptor-5 Agonist, Entolimod, Suppresses Metastasis and Induces Immunity by Stimulating an NK-Dendritic-CD8+ T-Cell Axis. *Proc Natl Acad Sci USA* (2016) 113(7):E874–83. doi: 10.1073/pnas.1521359113
244. Bubna AK. Imiquimod - Its Role in the Treatment of Cutaneous Malignancies. *Indian J Pharmacol* (2015) 47(4):354–9. doi: 10.4103/0253-7613.161249
245. Mullins SR, Vasilakos JP, Deschler K, Grigsby I, Gillis P, John J, et al. Intratumoral Immunotherapy With TLR7/8 Agonist MEDI9197 Modulates the Tumor Microenvironment Leading to Enhanced Activity When Combined With Other Immunotherapies. *J Immunother Cancer* (2019) 7 (1):244. doi: 10.1186/s40425-019-0724-8
246. Mohamed FE, Al-Jehani RM, Minogue SS, Andreola F, Winstanley A, Olde Damink SWM, et al. Effect of Toll-Like Receptor 7 and 9 Targeted Therapy to Prevent the Development of Hepatocellular Carcinoma. *Liver Int* (2015) 35: (3):1063–76. doi: 10.1111/liv.12626
247. Wang S, Campos J, Gallotta M, Gong M, Crain C, Naik E, et al. Intratumoral Injection of a CpG Oligonucleotide Reverts Resistance to PD-1 Blockade by Expanding Multifunctional CD8+ T Cells. *Proc Natl Acad Sci USA* (2016) 113(46):E7240–9. doi: 10.1073/pnas.1608555113
248. Sato-Kaneko F, Yao S, Ahmadi A, Zhang SS, Hosoya T, Kaneda MM, et al. Combination Immunotherapy With TLR Agonists and Checkpoint Inhibitors Suppresses Head and Neck Cancer. *JCI Insight* (2017) 2(18): e93397. doi: 10.1172/jci.insight.93397
249. Fourcade J, Kudela P, Andrade Filho PA, Janjic B, Land SR, Sander C, et al. Immunization With Analog Peptide in Combination With CpG and Montanide Expands Tumor Antigen-Specific CD8+ T Cells in Melanoma Patients. *J Immunother* (2008) 31(8):781–91. doi: 10.1097/CJI.0b013e318183af0b
250. Farrugia M, Baron B. The Role of Toll-Like Receptors in Autoimmune Diseases Through Failure of the Self-Recognition Mechanism. *Int J Inflam* (2017) 2017:8391230. doi: 10.1155/2017/8391230
251. Radstake TR, Roelofs MF, Jenniskens YM, Oppers-Walgreen B, van Riel PL, Barrera P, et al. Expression of Toll-Like Receptors 2 and 4 in Rheumatoid Synovial Tissue and Regulation by Proinflammatory Cytokines Interleukin-12 and Interleukin-18 *via* Interferon-Gamma. *Arthritis Rheum* (2004) 50 (12):3856–65. doi: 10.1002/art.20678
252. Roelofs MF, Wenink MH, Brentano F, Abdollahi-Roodsaz S, Oppers-Walgreen B, Barrera P, et al. Type I Interferons Might Form the Link Between Toll-Like Receptor (TLR) 3/7 and TLR4-Mediated Synovial Inflammation in Rheumatoid Arthritis (RA). *Ann Rheum Dis* (2009) 68 (9):1486–93. doi: 10.1136/ard.2007.086421
253. Li X, Xu T, Wang Y, Huang C, Li J. Toll-Like Receptor (TLR)-3: A Potent Driving Force Behind Rheumatoid Arthritis. *Clin Rheumatol* (2014) 33 (2):291–2. doi: 10.1007/s10067-013-2418-9
254. Kim W, Kim TH, Oh SJ, Kim HJ, Kim JH, Kim HA, et al. Association of TLR 9 Gene Polymorphisms With Remission in Patients With Rheumatoid Arthritis Receiving TNF-Alpha Inhibitors and Development of Machine Learning Models. *Sci Rep* (2021) 11(1):20169. doi: 10.1038/s41598-021-99625-x
255. Davis MLR, LeVan TD, Yu F, Sayles H, Sokolove J, Robinson W, et al. Associations of Toll-Like Receptor (TLR)-4 Single Nucleotide Polymorphisms and Rheumatoid Arthritis Disease Progression: An Observational Cohort Study. *Int Immunopharmacol* (2015) 24(2):346–52. doi: 10.1016/j.intimp.2014.12.030
256. Tripathy A, Khanna S, Padhan P, Smita S, Raghav S, Gupta B. Direct Recognition of LPS Drive TLR4 Expressing CD8+ T Cell Activation in Patients With Rheumatoid Arthritis. *Sci Rep* (2017) 7(1):933. doi: 10.1038/s41598-017-01033-7
257. Xu Q, Metzler B, Jahangiri M, Mandal K. Molecular Chaperones and Heat Shock Proteins in Atherosclerosis. *Am J Physiol Heart Circ Physiol* (2012) 302(3):H506–14. doi: 10.1152/ajpheart.00646.2011
258. Wick G, Jakic B, Buszko M, Wick MC, Grundtman C. The Role of Heat Shock Proteins in Atherosclerosis. *Nat Rev Cardiol* (2014) 11(9):516–29. doi: 10.1038/nrcardio.2014.91
259. Park Y, Park S, Yoo E, Kim D, Shin H. Association of the Polymorphism for Toll-Like Receptor 2 With Type 1 Diabetes Susceptibility. *Ann N Y Acad Sci* (2004) 1037:170–4. doi: 10.1196/annals.1337.028
260. Sepehri Z, Kiani Z, Nasiri AA, Kohan F. Toll-Like Receptor 2 and Type 2 Diabetes. *Cell Mol Biol Lett* (2016) 21:2. doi: 10.1186/s11658-016-0002-4
261. Guo Z, Zhang Y, Liu C, Youn JY, Cai H. Toll-Like Receptor 2 (TLR2) Knockout Abrogates Diabetic and Obese Phenotypes While Restoring Endothelial Function *via* Inhibition of NOX1. *Diabetes* (2021) 70(9):2107–19. doi: 10.2337/db20-0591
262. Fillatreau S, Manfroi B, Dorner T. Toll-Like Receptor Signalling in B Cells During Systemic Lupus Erythematosus. *Nat Rev Rheumatol* (2021) 17(2):98–108. doi: 10.1038/s41584-020-00544-4
263. Garcia-Ortiz H, Velazquez-Cruz R, Espinosa-Rosales F, Jimenez-Morales S, Baca V, Orozco L. Association of TLR7 Copy Number Variation With Susceptibility to Childhood-Onset Systemic Lupus Erythematosus in Mexican Population. *Ann Rheum Dis* (2010) 69(10):1861–5. doi: 10.1136/ard.2009.124313
264. Conrad DF, Pinto D, Redon R, Feuk L, Gokcumen O, Zhang Y, et al. Origins and Functional Impact of Copy Number Variation in the Human Genome. *Nature* (2010) 464(7289):704–12. doi: 10.1038/nature08516

265. Souyris M, Cenac C, Azar P, Daviaud D, Canivet A, Grunenwald S, et al. TLR7 Escapes X Chromosome Inactivation in Immune Cells. *Sci Immunol* (2018) 3(19):eaap8855. doi: 10.1126/sciimmunol.aap8855
266. Wang T, Marken J, Chen J, Tran VB, Li QZ, Li M, et al. High TLR7 Expression Drives the Expansion of CD19(+)CD24(hi)CD38(hi) Transitional B Cells and Autoantibody Production in SLE Patients. *Front Immunol* (2019) 10:1243:1243. doi: 10.3389/fimmu.2019.01243
267. Celhar T, Lu HK, Benso L, Rakhilina L, Lee HY, Tripathi S, et al. TLR7 Protein Expression in Mild and Severe Lupus-Prone Models Is Regulated in a Leukocyte, Genetic, and IRAK4 Dependent Manner. *Front Immunol* (2019) 10:1546:1546. doi: 10.3389/fimmu.2019.01546
268. Cros J, Cagnard N, Woollard K, Patey N, Zhang SY, Senechal B, et al. Human CD14dim Monocytes Patrol and Sense Nucleic Acids and Viruses *via* TLR7 and TLR8 Receptors. *Immunity* (2010) 33(3):375–86. doi: 10.1016/j.immuni.2010.08.012
269. Ah Kioon MD, Tripodo C, Fernandez D, Kirou KA, Spiera RF, Crow MK, et al. Plasmacytoid Dendritic Cells Promote Systemic Sclerosis With a Key Role for TLR8. *Sci Transl Med* (2018) 10(423):eaam8458. doi: 10.1126/scitranslmed.aam8458
270. Ciechomska M, O'Reilly S, Przyborski S, Oakley F, Bogunia-Kubik K, van Laar JM. Histone Demethylation and Toll-Like Receptor 8-Dependent Cross-Talk in Monocytes Promotes Transdifferentiation of Fibroblasts in Systemic Sclerosis *Via* Fra-2. *Arthritis Rheumatol* (2016) 68(6):1493–504. doi: 10.1002/art.39602
271. O'Reilly S, Cant R, Ciechomska M, Finnigan J, Oakley F, Hambleton S, et al. Serum Amyloid A Induces Interleukin-6 in Dermal Fibroblasts *via* Toll-Like Receptor 2, Interleukin-1 Receptor-Associated Kinase 4 and Nuclear Factor-Kappab. *Immunology* (2014) 143(3):331–40. doi: 10.1111/imm.12260
272. Zong M, Bruton JD, Grundtman C, Yang H, Li JH, Alexanderson H, et al. TLR4 as Receptor for HMGB1 Induced Muscle Dysfunction in Myositis. *Ann Rheum Dis* (2013) 72(8):1390–9. doi: 10.1136/annrheumdis-2012-202207
273. Tournadre A, Lenief V, Eljaafari A, Miossec P. Immature Muscle Precursors are a Source of Interferon-Beta in Myositis: Role of Toll-Like Receptor 3 Activation and Contribution to HLA Class I Up-Regulation. *Arthritis Rheum* (2012) 64(2):533–41. doi: 10.1002/art.33350
274. Cappelletti C, Baggi F, Zolezzi F, Biancolini D, Beretta O, Severa M, et al. Type I Interferon and Toll-Like Receptor Expression Characterizes Inflammatory Myopathies. *Neurology* (2011) 76(24):2079–88. doi: 10.1212/WNL.0b013e31821f440a
275. Sacre SM, Andreakos E, Kiriakidis S, Amjadi P, Lundberg A, Giddins G, et al. The Toll-Like Receptor Adaptor Proteins MyD88 and Mal/TIRAP Contribute to the Inflammatory and Destructive Processes in a Human Model of Rheumatoid Arthritis. *Am J Pathol* (2007) 170(2):518–25. doi: 10.2353/ajpath.2007.060657
276. Prinz M, Garbe F, Schmidt H, Mildner A, Gutcher I, Wolter K, et al. Innate Immunity Mediated by TLR9 Modulates Pathogenicity in an Animal Model of Multiple Sclerosis. *J Clin Invest* (2006) 116(2):456–64. doi: 10.1172/JCI26078
277. Guiducci C, Gong M, Cepika AM, Xu Z, Tripodo C, Bennett L, et al. RNA Recognition by Human TLR8 can Lead to Autoimmune Inflammation. *J Exp Med* (2013) 210(13):2903–19. doi: 10.1084/jem.20131044
278. Tapping RI, Tobias PS. Mycobacterial Lipoarabinomannan Mediates Physical Interactions Between TLR1 and TLR2 to Induce Signaling. *J Endotoxin Res* (2003) 9(4):264–8. doi: 10.1179/096805103225001477
279. Misch EA, Macdonald M, Ranjit C, Sapkota BR, Wells RD, Siddiqui MR, et al. Human TLR1 Deficiency Is Associated With Impaired Mycobacterial Signaling and Protection From Leprosy Reversal Reaction. *PloS Negl Trop Dis* (2008) 2(5):e231. doi: 10.1371/journal.pntd.0000231
280. Elass E, Aubry L, Masson M, Denys A, Guerardel Y, Maes E, et al. Mycobacterial Lipomannan Induces Matrix Metalloproteinase-9 Expression in Human Macrophagic Cells Through a Toll-Like Receptor 1 (TLR1)/TLR2- and CD14-Dependent Mechanism. *Infect Immun* (2005) 73 (10):7064–8. doi: 10.1128/IAI.73.10.7064-7068.2005
281. Stenzel W, Soltek S, Sanchez-Ruiz M, Akira S, Miletic H, Schluter D, et al. Both TLR2 and TLR4 are Required for the Effective Immune Response in Staphylococcus Aureus-Induced Experimental Murine Brain Abscess. *Am J Pathol* (2008) 172(1):132–45. doi: 10.2353/ajpath.2008.070567
282. Nguyen BN, Chavez-Arroyo A, Cheng MI, Krasilnikov M, Louie A, Portnoy DA. TLR2 and Endosomal TLR-Mediated Secretion of IL-10 and Immune Suppression in Response to Phagosome-Confined Listeria Monocytogenes. *PloS Pathog* (2020) 16(7):e1008622. doi: 10.1371/journal.ppat.1008622
283. Zheng M, Karki R, Williams EP, Yang D, Fitzpatrick E, Vogel P, et al. TLR2 Senses the SARS-CoV-2 Envelope Protein to Produce Inflammatory Cytokines. *Nat Immunol* (2021) 22(7):829–38. doi: 10.1038/s41590-021-00937-x
284. Zhang X, Li X, Gong P, Wang X, Zhang N, Chen M, et al. Host Defense Against Neospora Caninum Infection *via* IL-12p40 Production Through TLR2/TLR3-AKT-ERK Signaling Pathway in C57BL/6 Mice. *Mol Immunol* (2021) 139:140–52. doi: 10.1016/j.molimm.2021.08.019
285. Zhang SY, Jouanguy E, Ugolini S, Smahi A, Elain G, Romero P, et al. TLR3 Deficiency in Patients With Herpes Simplex Encephalitis. *Science* (2007) 317 (5844):1522–7. doi: 10.1126/science.1139522
286. Fujimoto C, Nakagawa Y, Ohara K, Takahashi H. Polyriboinosinic Polyribocytidylic Acid [Poly(I:C)]/TLR3 Signaling Allows Class I Processing of Exogenous Protein and Induction of HIV-Specific CD8+ Cytotoxic T Lymphocytes. *Int Immunol* (2004) 16(1):55–63. doi: 10.1093/intimm/dxh025
287. Sironi M, Biasin M, Cagliani R, Forni D, De Luca M, Saulle I, et al. A Common Polymorphism in TLR3 Confers Natural Resistance to HIV-1 Infection. *J Immunol* (2012) 188(2):818–23. doi: 10.4049/jimmunol.1102179
288. Huik K, Avi R, Pauskar M, Kallas E, Jogeda EL, Karki T, et al. Association Between TLR3 Rs3775291 and Resistance to HIV Among Highly Exposed Caucasian Intravenous Drug Users. *Infect Genet Evol* (2013) 20:78–82. doi: 10.1016/j.meegid.2013.08.008
289. Cheng L, Wang Q, Li G, Banga R, Ma J, Yu H, et al. TLR3 Agonist and CD40-Targeting Vaccination Induces Immune Responses and Reduces HIV-1 Reservoirs. *J Clin Invest* (2018) 128(10):4387–96. doi: 10.1172/JCI99005
290. Liu H, Zhou RH, Liu Y, Guo L, Wang X, Hu WH, et al. HIV Infection Suppresses TLR3 Activation-Mediated Antiviral Immunity in Microglia and Macrophages. *Immunology* (2020) 160(3):269–79. doi: 10.1111/imm.13181
291. Rudd BD, Smit JJ, Flavell RA, Alexopoulou L, Schaller MA, Gruber A, et al. Deletion of TLR3 Alters the Pulmonary Immune Environment and Mucus Production During Respiratory Syncytial Virus Infection. *J Immunol* (2006) 176(3):1937–42. doi: 10.4049/jimmunol.176.3.1937
292. Huang S, Wei W, Yun Y. Upregulation of TLR7 and TLR3 Gene Expression in the Lung of Respiratory Syncytial Virus Infected Mice. *Wei Sheng Wu Xue Bao* (2009) 49(2):239–45.
293. Wu J, Wang Z, Guo YN, Dong LQ. Activation of TLR3 Pathway in the Pathogenesis of Nephrotic Syndrome Induced by Respiratory Syncytial Virus in Rat Model. *Sichuan Da Xue Xue Bao Yi Xue Ban* (2010) 41(4):600–3, 625.
294. Satkunanathan S, Kumar N, Bajorek M, Purbhoo MA, Culley FJ. Respiratory Syncytial Virus Infection, TLR3 Ligands, and Proinflammatory Cytokines Induce CD161 Ligand LLT1 Expression on the Respiratory Epithelium. *J Virol* (2014) 88(5):2366–73. doi: 10.1128/JVI.02789-13
295. Miranda VDS, Franca FBF, da Costa MS, Silva VRS, Mota CM, Barros P, et al. Toll-Like Receptor 3-TRIF Pathway Activation by Neospora Caninum RNA Enhances Infection Control in Mice. *Infect Immun* (2019) 87(4): e00739-18. doi: 10.1128/IAI.00739-18
296. Chantratita N, Tandhavanant S, Seal S, Wikraiphat C, Wongsuvan G, Ariyaprasert P, et al. TLR4 Genetic Variation is Associated With Inflammatory Responses in Gram-Positive Sepsis. *Clin Microbiol Infect* (2017) 23(1):47 e1–47 e10. doi: 10.1016/j.cmi.2016.08.028
297. Kurt-Jones EA, Popova L, Kwinn L, Haynes LM, Jones LP, Tripp RA, et al. Pattern Recognition Receptors TLR4 and CD14 Mediate Response to Respiratory Syncytial Virus. *Nat Immunol* (2000) 1(5):398–401. doi: 10.1038/80833
298. Tang HB, Lu ZL, Wei XK, Zhong TZ, Zhong YZ, Ouyang LX, et al. Viperin Inhibits Rabies Virus Replication *via* Reduced Cholesterol and Sphingomyelin and is Regulated Upstream by TLR4. *Sci Rep* (2016) 6:30529. doi: 10.1038/srep30529
299. Chen C, Zhang C, Li H, Wang Z, Yuan Y, Zhou M, et al. TLR4 Regulates Rabies Virus-Induced Humoral Immunity Through Recruitment of cDC2 to Lymph Organs. *J Virol* (2021) 95(24):JVI0082921. doi: 10.1128/JVI.00829-21
300. Zhang ZM, Zhang AR, Xu M, Lou J, Qiu WQ. TLR-4/miRNA-32-5p/FSTL1 Signaling Regulates Mycobacterial Survival and Inflammatory Responses in

Mycobacterium Tuberculosis-Infected Macrophages. *Exp Cell Res* (2017) 352 (2):313–21. doi: 10.1016/j.yexcr.2017.02.025

301. Chaichana P, Chantratita N, Brod F, Koosakulnirand S, Jenjaroen K, Chumseng S, et al. A Nonsense Mutation in TLR5 is Associated With Survival and Reduced IL-10 and TNF-Alpha Levels in Human Melioidosis. *PloS Negl Trop Dis* (2017) 11(5):e0005587. doi: 10.1371/journal.pntd.0005587
302. Chen J, Ng MM, Chu JJ. Activation of TLR2 and TLR6 by Dengue NS1 Protein and Its Implications in the Immunopathogenesis of Dengue Virus Infection. *PloS Pathog* (2015) 11(7):e1005053. doi: 10.1371/journal.ppat.1005053
303. Misch EA, Verbon A, Prins JM, Skerrett SJ, Hawn TR. A TLR6 Polymorphism is Associated With Increased Risk of Legionnaires' Disease. *Genes Immun* (2013) 14(7):420–6. doi: 10.1038/gene.2013.34
304. Regli IB, Passelli K, Martinez-Salazar B, Amore J, Hurrell BP, Muller AJ, et al. TLR7 Sensing by Neutrophils Is Critical for the Control of Cutaneous Leishmaniasis. *Cell Rep* (2020) 31(10):107746. doi: 10.1016/j.celrep.2020.107746
305. Pang IK, Pillai PS, Iwasaki A. Efficient Influenza A Virus Replication in the Respiratory Tract Requires Signals From TLR7 and RIG-I. *Proc Natl Acad Sci USA* (2013) 110(34):13910–5. doi: 10.1073/pnas.1303275110
306. Valencia Pacheco GJ, Pinzon Herrera F, Cruz Lopez JJ, Vera Gamboa Ldel C, Pavia Ruiz N, Santos Rivero A, et al. Expression and Activation of Intracellular Receptors TLR7, TLR8 and TLR9 in Peripheral Blood Monocytes From HIV-Infected Patients. *Colomb Med (Cali)* (2013) 44 (2):92–9. doi: 10.25100/cm.v44i2.1183
307. Cardoso EC, Pereira NZ, Mitsunari GE, Oliveira LM, Ruocco RM, Francisco RP, et al. TLR7/TLR8 Activation Restores Defective Cytokine Secretion by Myeloid Dendritic Cells But Not by Plasmacytoid Dendritic Cells in HIV-Infected Pregnant Women and Newborns. *PloS One* (2013) 8(6):e67036. doi: 10.1371/journal.pone.0067036
308. Pietrobon AJ, Yoshikawa FSY, Oliveira LM, Pereira NZ, Matozo T, de Alencar BC, et al. Antiviral Response Induced by TLR7/TLR8 Activation Inhibits HIV-1 Infection in Cord Blood Macrophages. *J Infect Dis* (2021) 225 (3):510–9. doi: 10.1093/infdis/jiab389
309. Gringhuis SI, van der Vlist M, van den Berg LM, den Dunnen J, Litjens M, Geijtenbeek TB. HIV-1 Exploits Innate Signaling by TLR8 and DC-SIGN for Productive Infection of Dendritic Cells. *Nat Immunol* (2010) 11(5):419–26. doi: 10.1038/ni.1858
310. Greulich W, Wagner M, Gaidt MM, Stafford C, Cheng Y, Linder A, et al. TLR8 Is a Sensor of RNase T2 Degradation Products. *Cell* (2019) 179 (6):1264–1275 e13. doi: 10.1016/j.cell.2019.11.001
311. Ma Y, He B. Recognition of Herpes Simplex Viruses: Toll-Like Receptors and Beyond. *J Mol Biol* (2014) 426(6):1133–47. doi: 10.1016/j.jmb.2013.11.012
312. Lai ZZ, Ni Z, Pan XL, Song L. Toll-Like Receptor 9 (TLR9) Gene Polymorphisms Associated With Increased Susceptibility of Human Papillomavirus-16 Infection in Patients With Cervical Cancer. *J Int Med Res* (2013) 41(4):1027–36. doi: 10.1177/0300060513483398
313. Basner-Tschakarjan E, Gaffal E, O'Keeffe M, Tormo D, Limmer A, Wagner H, et al. Adenovirus Efficiently Transduces Plasmacytoid Dendritic Cells Resulting in TLR9-Dependent Maturation and IFN-Alpha Production. *J Gene Med* (2006) 8(11):1300–6. doi: 10.1002/jgm.964
314. Pahl JH, Verhoeven DH, Kwappenberg KM, Vellinga J, Lankester AC, van Tol MJ, et al. Adenovirus Type 35, But Not Type 5, Stimulates NK Cell Activation *via* Plasmacytoid Dendritic Cells and TLR9 Signaling. *Mol Immunol* (2012) 51(1):91–100. doi: 10.1016/j.molimm.2012.02.119
315. Zang J, Zheng MH, Cao XL, Zhang YZ, Zhang YF, Gao XY, et al. Adenovirus Infection Promotes the Formation of Glioma Stem Cells From Glioblastoma Cells Through the TLR9/NEAT1/STAT3 Pathway. *Cell Commun Signal* (2020) 18(1):135. doi: 10.1186/s12964-020-00598-7
316. DePaolo RW, Kamdar K, Khakpour S, Sugiura Y, Wang W, Jabri B. A Specific Role for TLR1 in Protective T(H)17 Immunity During Mucosal Infection. *J Exp Med* (2012) 209(8):1437–44. doi: 10.1084/jem.20112339
317. Sugiura Y, Kamdar K, Khakpour S, Young G, Karpus WJ, DePaolo RW. TLR1-Induced Chemokine Production is Critical for Mucosal Immunity Against Yersinia Enterocolitica. *Mucosal Immunol* (2013) 6(6):1101–9. doi: 10.1038/mi.2013.5
318. Johnson CM, Lyle EA, Omueti KO, Stepensky VA, Yegin O, Alpsoy E, et al. Cutting Edge: A Common Polymorphism Impairs Cell Surface Trafficking and Functional Responses of TLR1 But Protects Against Leprosy. *J Immunol* (2007) 178(12):7520–4. doi: 10.4049/jimmunol.178.12.7520
319. Arpaia N, Godec J, Lau L, Sivick KE, McLaughlin LM, Jones MB, et al. TLR Signaling is Required for Salmonella Typhimurium Virulence. *Cell* (2011) 144(5):675–88. doi: 10.1016/j.cell.2011.01.031
320. Zhao Y, Kuang M, Li J, Zhu L, Jia Z, Guo X, et al. SARS-CoV-2 Spike Protein Interacts With and Activates TLR41. *Cell Res* (2021) 31(7):818–20. doi: 10.1038/s41422-021-00495-9
321. Awomoyi AA, Rallabhandi P, Pollin TI, Lorenz E, Sztein MB, Boukhvalova MS, et al. Association of TLR4 Polymorphisms With Symptomatic Respiratory Syncytial Virus Infection in High-Risk Infants and Young Children. *J Immunol* (2007) 179(5):3171–7. doi: 10.4049/jimmunol.179.5.3171
322. Mansur A, von Gruben L, Popov AF, Steinau M, Bergmann I, Ross D, et al. The Regulatory Toll-Like Receptor 4 Genetic Polymorphism Rs11536889 is Associated With Renal, Coagulation and Hepatic Organ Failure in Sepsis Patients. *J Transl Med* (2014) 12:177. doi: 10.1186/1479-5876-12-177
323. Reiling N, Holscher C, Fehrenbach A, Kroger S, Kirschning CJ, Goyert S, et al. Cutting Edge: Toll-Like Receptor (TLR)2- and TLR4-Mediated Pathogen Recognition in Resistance to Airborne Infection With Mycobacterium Tuberculosis. *J Immunol* (2002) 169(7):3480–4. doi: 10.4049/jimmunol.169.7.3480
324. Abel B, Thieblemont N, Quesniaux VJ, Brown N, Mpagi J, Miyake K, et al. Toll-Like Receptor 4 Expression is Required to Control Chronic Mycobacterium Tuberculosis Infection in Mice. *J Immunol* (2002) 169 (6):3155–62. doi: 10.4049/jimmunol.169.6.3155
325. Lund JM, Alexopoulou L, Sato A, Karow M, Adams NC, Gale NW, et al. Recognition of Single-Stranded RNA Viruses by Toll-Like Receptor 7. *Proc Natl Acad Sci USA* (2004) 101(15):5598–603. doi: 10.1073/pnas.0400937101
326. Diebold SS, Kaisho T, Hemmi H, Akira S, Reis e Sousa C. Innate Antiviral Responses by Means of TLR7-Mediated Recognition of Single-Stranded RNA. *Science* (2004) 303(5663):1529–31. doi: 10.1126/science.1093616
327. Pichlmair A, Schulz O, Tan CP, Naslund TI, Liljestrom P, Weber F, et al. RIG-I-Mediated Antiviral Responses to Single-Stranded RNA Bearing 5'-Phosphates. *Science* (2006) 314(5801):997–1001. doi: 10.1126/science.1132998
328. Iwasaki A, Medzhitov R. Regulation of Adaptive Immunity by the Innate Immune System. *Science* (2010) 327(5963):291–5. doi: 10.1126/science.1183021
329. To EE, Erlich J, Liong F, Luong R, Liong S, Bozinovski S, et al. Intranasal and Epicutaneous Administration of Toll-Like Receptor 7 (TLR7) Agonists Provides Protection Against Influenza A Virus-Induced Morbidity in Mice. *Sci Rep* (2019) 9(1):2366. doi: 10.1038/s41598-019-38864-5
330. Wang MG, Zhang MM, Wang Y, Wu SQ, Zhang M, He JQ. Association of TLR8 and TLR9 Polymorphisms With Tuberculosis in a Chinese Han Population: A Case-Control Study. *BMC Infect Dis* (2018) 18(1):561. doi: 10.1186/s12879-018-3485-y
331. Jude BA, Pobezinskaya Y, Bishop J, Parke S, Medzhitov RM, Chervonsky AV, et al. Subversion of the Innate Immune System by a Retrovirus. *Nat Immunol* (2003) 4(6):573–8. doi: 10.1038/ni926
332. Asami J, Shimizu T. Structural and Functional Understanding of the Toll-Like Receptors. *Protein Sci* (2021) 30(4):761–72. doi: 10.1002/pro.4043
333. Behzadi P, García-Perdomo HA, Karpiński TM. Toll-Like Receptors: General Molecular and Structural Biology. *J Immunol Res* (2021) 2021:9914854. doi: 10.1155/2021/9914854
334. Wang R-F, Wang HY. Immune Targets and Neoantigens for Cancer Immunotherapy and Precision Medicine. *Cell Res* (2017) 27(1):11–37. doi: 10.1038/cr.2016.155
335. Luchner M, Reinke S, Milicic A. TLR Agonists as Vaccine Adjuvants Targeting Cancer and Infectious Diseases. *Pharmaceutics* (2021) 13(2):142. doi: 10.3390/pharmaceutics13020142

Conflict of Interest: The authors declare that the research was conducted in the absence of any commercial or financial relationships that could be construed as a potential conflict of interest.

this article, or claim that may be made by its manufacturer, is not guaranteed or endorsed by the publisher.

frontiers | Frontiers in Immunology

REVIEW
published: 19 April 2022
doi: 10.3389/fimmu.2022.843891

Role of Toll-Like Receptors and Th Responses in Viral Myocarditis

Shi-Yue Zheng[1] *and Jian-Zeng Dong*[1,2]*

[1] Department of Cardiology, Beijing Anzhen Hospital, Capital Medical University, Beijing, China, [2] Department of Cardiology, The First Affiliated Hospital of Zhengzhou University, Zhengzhou, China

Myocarditis is the common cause of sudden cardiac death, dilated cardiomyopathy (DCM) and heart failure (HF) in young adults. The most common type of myocarditis is viral myocarditis (VMC). Toll-like receptors (TLRs) are vital to identify pathogens *in vivo*. TLRs promote the differentiation of naive $CD4^+$T cells to T helper (Th) cells, activate the immune response, and participate in the pathogenesis of autoimmune and allergic diseases. Although the pathogenesis of VMC is unclear, autoimmune responses have been confirmed to play a significant role; hence, it could be inferred that VMC is closely related to TLRs and Th responses. Some drugs have been found to improve the prognosis of VMC by regulating the immune response through activated TLRs. In this review, we discuss the role of TLRs and Th responses in VMC.

Keywords: viral myocarditis, TLRs, Th cells, regulatory T cell, immune response

OPEN ACCESS

Edited by:
Steven O'Reilly,
STipe Therapeutics, Denmark

Reviewed by:
Sally A. Huber,
University of Vermont, United States
Katelyn Ann Bruno,
Mayo Clinic Florida, United States

***Correspondence:**
Jian-Zeng Dong
jzdong@ccmu.edu.cn

Specialty section:
This article was submitted to Molecular Innate Immunity, a section of the journal Frontiers in Immunology

Received: *04 January 2022*
Accepted: *24 March 2022*
Published: *19 April 2022*

Citation:
Zheng SY and Dong JZ (2022) Role of Toll-Like Receptors and Th Responses in Viral Myocarditis. Front. Immunol. 13:843891. doi: 10.3389/fimmu.2022.843891

INTRODUCTION

Myocarditis is a myocardial inflammation resulted from infectious, idiopathic, or autoimmune causes, of which the most popular is viral infection brought by enterovirus, Epstein-Barr (EB) virus, or human herpesvirus 6. Besides, myocarditis is the primary cause of dilated cardiomyopathy (DCM) and gradually becomes a cause of sudden cardiovascular death among young people (< 40-year-old) (1). Most patients with myocarditis can recover fully; however, some (up to 20%) develop chronic myocarditis, eventually resulting in DCM and heart failure (HF) (2). Myocarditis is diagnosed by combining clinical presentation, biomarkers, electrocardiogram (ECG), echocardiography, cardiac magnetic resonance imaging (CMRI), and endocardial biopsy (EMB). Tissue taken from EMB should be combined with the results of histology, immunohistochemistry and viral polymerase chain reaction (PCR) for the diagnosis of myocarditis (3). The EMB histology of myocarditis showed a value of leukocytes>14/mm^2 with T lymphocytes>7/mm^2, while immunohistochemistry showed an increase in the number of $CD3^+$T cells or $CD68^+$macrophages or $CD163^+$M2 macrophages and virus genome could be detected by viral PCR (4, 5). EMB is a non-targeted operation, with low sensitivity as its main shortcoming, which may occur false-negative results when VMC is multifocal, focal, or localized (4). Therefore, the sensitivity of EMB in fulminant myocarditis with extensive inflammatory infiltration is increased, while that in focal myocarditis is relatively low, which may lead to false-negative results. In addition, although the virus can replicate in the myocardium, it does not cause enough myocardial inflammation, and EMB detection of the virus genome may also show false-negative results. The diagnostic criteria of CMRI for myocarditis are based on the 'Lake-Louise' criteria (6, 7). Therefore, in order to improve the sensitivity of EMB in diagnosis of myocarditis, we can determine the sampling site by combining

CMRI and obtain myocardial tissue from three different sites. Chronic myocarditis also has persistent myocardial inflammation, which is the intermediate stage between acute myocarditis and chronic inflammatory cardiomyopathy. However, there is no detectable inflammation due to myocardial fibrosis in patients with chronic inflammatory cardiomyopathy, which renders diagnosis and treatment rather challenging (8).

Although the pathogenesis of myocarditis is yet unclear, the role of immune response in its process is under intensive focus. Under physiological conditions, a small number of immune cells are detected in the myocardium. After the onset of infections or autoimmune disorders, numerous immune cells and cytokines gather in the myocardial tissue to initiate inflammatory reactions. This process requires the initiation and maintenance of congenital and adaptive immune systems. Toll-like receptors (TLRs) recognize endogenous and exogenous ligands and are expressed on various cells, such as macrophages, neutrophils, dendritic cells (DCs), mast cells, and natural killer (NK) cells (9). They transmit signals to downstream pathways to stimulate innate and adaptive immunity after identifying the ligands involved in the pathogenesis of various autoimmune diseases, such as systemic lupus erythematosus (SLE), rheumatoid arthritis (RA), multiple sclerosis (MS), experimental autoimmune encephalitis (EAE), and experimental autoimmune myocarditis (EAM) (10). TLR1-TLR10 mRNA can be detected in normal peripheral blood T cells, but only TLR2-TLR5 and TLR9 expression can be detected at the protein level. TLR1, TLR2, and TLR7 are overexpressed on mRNA level in patients with myocarditis (9, 11). In addition, the inflammatory factors produced after TLRs activation, including interferon-gamma (IFN- γ), interleukin (IL)-6, and tumor growth factor-beta (TGF-β), can also stimulate native CD4+T cells to differentiate into T helper (Th) cells and participate in immune response to aggravate myocarditis. This study reviewed the role of TLRs and Th responses in viral myocarditis (VMC).

VMC

VMC is the most common myocarditis caused by various viruses, including enterovirus, adenovirus, influenza virus, EB virus, and parvovirus; the most common is Coxsackievirus B3 (CVB3) that belongs to enterovirus (12). CVB3 may be cleared by innate immune response or stimulate the immune system to produce autoantibodies against the infection. The condition can be cured or progressed to DCM and HF (13). According to the clinical characteristics, VMC can be classified into fulminant, acute, subacute, or chronic myocarditis and localized or diffuse inflammatory infiltration can be observed in myocardial pathology. Fulminant myocarditis is rare and characterized by diffuse inflammatory infiltration in myocardial tissue, which has multiple active lesions and can be completely relieved, die, or progress to chronic myocarditis. Acute or chronic myocarditis progresses latently, resulting in DCM or HF (14). The pathological progression of VMC has three phases at the cellular and tissue level: the acute phase caused by viral entry and replication, the subacute phase characterized by inflammatory cell infiltration, and the chronic phase characterized by cardiac remodeling (15). VMC can be diagnosed by combining biomarkers, ECG, echocardiography, CMRI, and EMB (16). With the continuous update and development of technology, viruses in patients with VMC can be detected by polymerase chain technology, but EMB is still the gold standard for the diagnosis of myocarditis (3, 17, 18). VMC can be divided into eosinophilic, lymphocytic, giant cell, and granulomatous myocarditis based on the histological types observed by EMB. The most common type is lymphocytic myocarditis, wherein the main infiltration is by $CD4^+$T and $CD8^+$T lymphocytes, accompanied by $CD68^+$ macrophages and few B lymphocytes (19, 20). However, only 38% of patients with VMC present viral genomes in their EMB samples (21). Hence, a close correlation is established between virus infection and immune response in the pathogenic process of VMC, while many studies have confirmed that the core of innate immunity and adaptive immunity is related to TLRs (22).

TLRs

TLRs were first discovered as *Drosophila* gene and related to the human immune response (23). They are vital receptors on cells to recognize pathogens and belong to the pattern recognition receptor family (PRRs). They can detect pathogen-associated molecular patterns (PAMPs), such as unmethylated cytosine-phosphate-guanine DNA (CpGor TLR3, TLR7, TLR8, and TLR9 transport) and PRAT4A (responsible for TLR1, TLR2, TLR4, and TLR7 transport). These TLRs can only be functional after transport to the internal lysosome (24). Moreover, TLRs can also be heterodimerized, which expands the range of cognitive ligands. Different TLRs correspond to various endogenous ligands that are TLR4 and TLR2 agonists. The abnormal activation of TLRs may lead to unrestricted inflammatory response (25).

CHARACTERISTICS OF TLRs

Hitherto, 11 TLRs have been found in humans (**Table 1**) (26). TLRs, such as TLR1, TLR2, TLR4, TLR6, and TLR10, are expressed on the cell surface and can recognize microbial membrane components, such as p-DNA), single-stranded RNA (ssRNA), double-stranded RNA (dsRNA), lipopolysaccharide (LPS), and flagellin and initiate immune response (27). In addition to the above exogenous ligands, TLRs can also recognize endogenous ligands, including high mobility group box 1 (HMGB1), heat shock proteins (HSP), human cardiac myosin (HCM) peptides S2-16, and HCM S2-28 (28, 29). Moreover, TLRs activate various types of cells and are highly expressed in most immune cells, chondrocytes, endothelial cells, and fibroblasts (30). All TLRs consist of an amino-terminal domain and a carboxyl-terminal Toll/interleukin-1 receptor (TIR) domain. The TIR domain interacts with the junction proteins, including myeloid differentiation factor 88 (MyD88), MyD88 adaptor-like (Mal, also known as TIR domain-containing

TABLE 1 | Characteristics of TLRs.

TLRs	Localization	Ligands	Signaling pathways	Cytokines
TLR1 (with TLR2)	Cell surface	Triacylated lipopeptides	MyD88/TIRAP-NF-κB	TNF-α, IL-8
TLR2	Cell surface	HSP, HMGB1, HCM	MyD88/TIRAP-NF-κB	TNF-α, IL-8, IFN-γ, IL-12, IL-6
TLR3	Intracellular vesicle	Virus dsRNA	TRIF-IRF-3/NF-κB/AP-1	IFN-α/β
TLR4	Cell surface	HSP, Gp96, HMGB1	Mal/MyD88-NF-κB and TRIF/TRAM-type 1 IFN	IL-1β, TGF-β, TNF-α, IL-12 p40, IFN-α/β
TLR5	Cell surface	Flagellin	MyD88-NF-κB and p38 MAPK	IL-8, TNF-α
TLR6 (with TLR2)	Cell surface	Diacylated lipopeptides	MyD88/TIRAP-NF-κB	IFN-γ, IL-12, IL-6
TLR7	Intracellular vesicle	Virus ssRNA	MyD88-IRF-7	TNF-α, IL-12 p40
TLR8	Intracellular vesicle	Virus ssRNA, HCM	MyD88-NF-κB and MyD88-IRF-1/4/7	IL-1β, TNF-α, IL-6, IL-12, IFN-α/β
TLR9	Intracellular vesicle	Unmethylated CpG-DNA	MyD88	NF-κB, IL-1β, IL-18, IFN-α/β
TLR10	Cell surface	Lipopeptides	(–)	Inhibit IL-6, IL-10, TNF α, IL-1β

adapter protein (TIRAP)), TIR domain-containing adaptor inducing IFN-β (TRIF), TRIF-related adaptor molecule (TRAM), and sterile a- and armadillo motif-containing protein (SARM), stimulating nuclear factor-kappa B (NF-κB) and the production of various proinflammatory cytokines, thereby initiating an immune response (31). Some TLRs, including TLR1, TLR2, TLR4, TLR5, TLR6, and TLR10, are expressed on the cell surface, while others, including TLR3, TLR7, TLR8, and TLR9, are expressed on the intracellular vesicles (32). Intracellular TLRs exist in the endoplasmic reticulum (ER) and are transported by ER resident proteins to the plasma membrane or lysosomes after stimulation: UNC93B (responsible f proteins, lipids, and participate in the recognition of virus proteins (33).

TLR2 forms heterodimers with TLR1 or TLR6 and recognizes different TLR ligands, resulting in different functions: dimers combined with TLR1 can recognize triacylated lipopeptides from bacteria while diacylated lipopeptides with TLR6 (34). Both TLR1/2 and TLR2/6 signaling pathways activate downstream inflammatory cytokines, tumor necrosis factor-alpha (TNF-α), (IL-8, IFN-γ, IL-12, and IL-6, through MyD88/Mal-NF-κB signaling pathway (35–37). When recognizing dsRNA, TLR3 transmits signals through TRIF and activates the transcription factor interferon regulatory factor 3 (IRF-3), NF-κB, and AP-1 (the complex of transcription factor 2 and jun), inducing the production of IFN-α/β, cytokines, or chemokines and the maturation of DCs (38, 39). TLR4 is the first molecule identified among TLRs and is mainly expressed in myeloid immune cells and in some non-immune such as endothelial cells (40). TLR4 can recognize heat shock protein, oxidized phospholipid, heparan sulfate, fibrinogen, fibronectin, tendon protein-C, and hyaluronic acid (41). Similar to other TLRs, TLR4 interacts with the intracellular TIR domain responsible for signal transduction (42). It mainly recruits Mal and MyD88 to activate NF-κB and utilizes TRIF and TRAM to activate type 1 IFN to produce proinflammatory factors, such as IL-1β, TGF-β, TNF-α, and IL-12 p40, to eliminate bacteria (43, 44). TLR5 activates the innate immune response against flagella by inducing a MyD88-dependent signaling pathway that stimulates the proinflammatory transcription factor NF-κB in epithelial cells, monocytes, and DCs (45). IL-8 and TNF-α can also be induced by the p38 mitogen-activated protein kinase (MAPK) signaling pathway in response to flagellin infection (46). TLR7 and TLR8 are homologous and located on the X chromosome. Both recognize virus ssRNA and are expressed in various immune cells (47). TLR7 is mainly expressed in plasma-like DCs and B cells, while TLR8 is mainly expressed in monocytes or macrophages, myeloid DCs, and neutrophils (48). Inflammatory factors, such as TNF-α and IL-12 p40 are activated through the MyD88-IRF-7 pathway after TLR7 activation, promoting the innate immune cells to perceive endosomal ssRNA, detecting RNA virus infection (49, 50). However, the overexpression or overactivation of TLR7 promotes the reduction of B cells producing IL-10 in an IFN-γ signal transduction-dependent manner and suppresses the immune response (51). TLR8 induces NF-κB through MyD88 signal transduction and promotes the expression of inflammatory factors, such as IL-1β, TNF-α, IL-6, and IL-12 after recognizing ssRNA. It also induces the production of IFN-α/β through IRAK4, IRAK1, and IRF-7 in response to viral infection (52). TLR9 was first cloned and identified as the receptor of unmethylated CpG-DNA in 2000. It induces the expression of IFN-α/β and proinflammatory cytokines (NF-κB, IL-1β, and IL-18) and activates the immune response only by recruiting MyD88 (53). TLR8 modulates the function of TLR7 on DCs, and TLR9 restrains the response of TLR7 on B cells. TLR7 crosstalk with TLR8 and TLR9 and play a critical role in the immune response of the body (54). Intriguingly, TLR10 is known as an orphan receptor because it lacks classical downstream signaling pathway. It is also an inhibitory receptor, homologous to TLR1 and TLR6, and hence, can form heterodimers with TLR2 and inhibit the production of proinflammatory cytokines, such as IL-6, IL-10, TNF-α, and IL-1β (46). It also inhibits monocyte differentiation, reduces the ability of DCs to stimulate T cells, and suppresses the immune response (55). The human *TLR11* gene has no function due to the presence of a stop codon (25).

TLRs AND Th RESPONSES

Naive $CD4^+$T cells can differentiate into different subtypes of $CD4^+$Th cells under the stimulus of cytokines. $CD4^+$Th cells direct the immune response and play key roles in pathogenic infection, chronic inflammation, autoimmune diseases, and cancer. Some studies have found a variety of $CD4^+$Th cells, such as Th1, Th2, Th17, and regulatory T (Treg) cells (**Figure 1**) (56). Naive $CD4^+$T

cells differentiate into Th1 cells post-stimulation of IL-2 and IFN–γ and expression of transcription factors T-bet and secrete IFN-γ, IL-2 and TNF. Th1 cells enhance cell-mediated inflammation and participate in type 1 immune response to intracellular pathogens, such as mycobacteria and viruses (57). Th2 cells are activated by IL-4 and IL-2 and are defined by the expression of transcription factor GATA3, subsequently secreting IL-4, IL-5, IL-6, IL-10, and IL-13. The Th2 cells also participate in type 2 immune response against large extracellular pathogens, such as worms, and play a role in the production of antibodies and allergic reactions (58). Th17 cells, stimulated by TGF-β, IL-6, IL-21, and IL-23 and the expression of transcription factor ROR-γt, produce IL-17, IL-17F, IL-22, and IL-21, which leads to tissue inflammation and promotes participation in type 3 immune response of extracellular pathogens, including bacteria and fungi. Different from other Th cells, Tregs differentiate under the stimulation of IL-10 and TGF-β and the expression of transcription factor Foxp3 to produce anti-inflammatory cytokines, IL-10 and TGF-β (59). Moreover, Tregs inhibit autoimmune diseases and regulate immune response to maintain immune cell homeostasis. Type 1 and 3 immune responses mediate autoimmune diseases, such as SLE, RA, and MES, while type 2 immune responses can lead to allergic diseases, such as asthma (60). Cytokines crosslink each other to maintain Th cells balance. IFN-γ and IL-4 antagonize each other at different levels, and hence the development of Th1 and Th2 cells is mutually exclusive (61). Th17 cells can promote the development of autoimmunity, while Treg cells inhibit autoimmunity; thus, the imbalance of Th17/Treg cells in the body is considered the leading mechanism underlying autoimmune diseases (62).

The activation of TLRs has been shown to bridge innate immunity and acquired immunity. In addition to expression in antigen-presenting cells (DCs and macrophages), TLRs are also expressed in T cells playing a costimulatory role in T cell activation and inducing Th cell differentiation (**Figure 2**) (63). TLR2 promotes the differentiation of Th17 cells and immune response by disrupting the balance of Th17/Treg cells (64). TLR2/6 ligand is a bacterial lipopeptide that can induce DC tolerance and promote the differentiation of IL-10-producing Tregs through the c-Jun N-terminal kinase (JNK) pathway both *in vivo* and *in vitro*. On the other hand, the activation of TLR2/1 promotes the DCs to produce a high level of IL-12 p40 and a low level of IL-10 through p38 MAPK signaling pathway, thereby triggering the differentiation of Th1 or Th 17 cells (65). TLR4 eliminates Th1 response through IRF1 and IFN-α/β receptor-dependent mechanisms. The lack of TLR4 promotes Th1 cell differentiation by enhancing STAT1 pathway, inhibits Th17 cell differentiation by inhibiting STAT3 pathway, and interferes with immune response (66, 67). Bacterial LPS also aggravates allergic inflammation through the production of Th2 cytokines and participates in the immune response of the body post-TLR4 activation (68). Soluble bacterial flagellin stimulates the body to induce Th2 response through TLR5 and inhibits Th1 response to bacterial infection (69). TLR5 promotes DCs in the intestinal tract to differentiate into Th17 cells and respond to pathogen invasion (70). TLR8 induces the expression of IL-12B and IL-23A, promotes the differentiation of IL-23-dependent Th17 cells, and produces immune responses after activating human neutrophils (71). The co-stimulation of TLR7/8 ligands and TLR4 or TLR3 ligands produce IL-12p70 that is the key cytokine to induce Th1 immune response (72). Therefore, ligand co-stimulation is crucial to induce Th1 response. TLR9 is essential in the production of proinflammatory cytokines and other inflammatory responses and to initiate Th1 response and B cell proliferation (73). The interaction between CpG-DNA and TLR9 rapidly activates DCs through the Toll/IL-1 receptor signaling pathway, promoting the differentiation of Th1 cells and the production of cytokines (IL-12 and IL-18) (74). TLR9

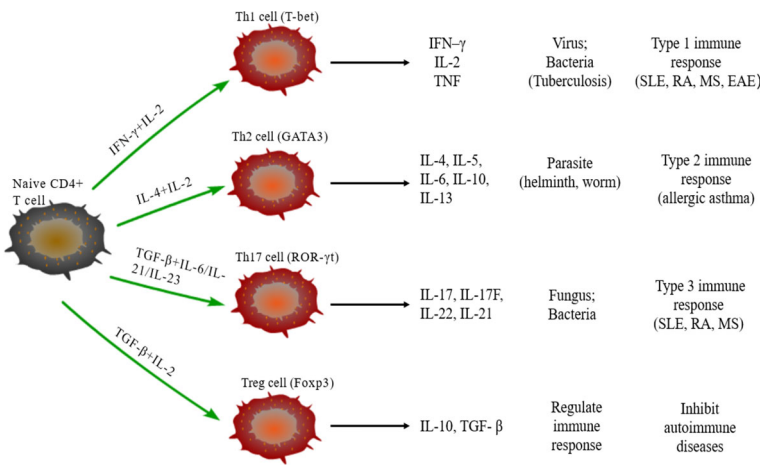

FIGURE 1 | Differentiation of naïve CD4$^+$T cells. Naive CD4$^+$T cells can differentiate into Th1 cells under the stimulus of IFN-γ and IL-2, secrete IFN-γ, IL-2, and TNF, and participate in type 1 immune response. Under the stimulus of IL-2 and IL-4, naive CD4$^+$T cells differentiate into Th2 cells that can secrete IL-4/5/6/10/13 and participate in type 2 immune response. The differentiation of Th17 cells need TGF-β, IL-6, IL-21, and IL-23, and participate in type 3 immune response through secreting IL-17/17F/21/22; TGF-β and IL-2 are required for naïve CD4$^+$T cells to differentiate into Treg cells that secrete IL-10 and TGF-β regulate the immune response.

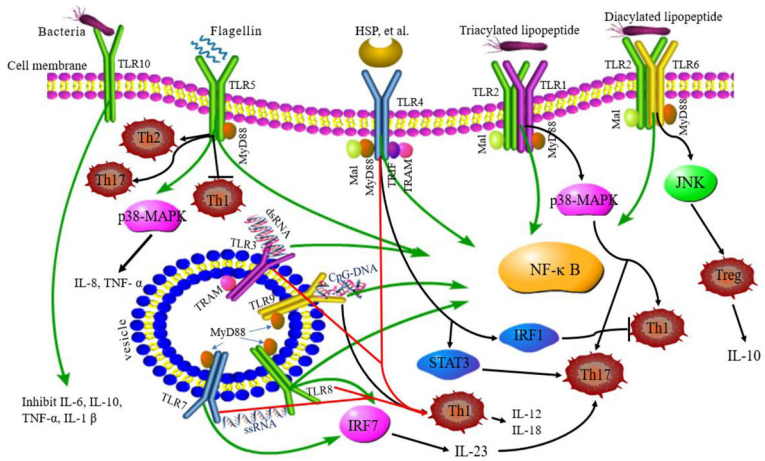

FIGURE 2 | TLRs signaling pathway and related Th responses. TLR1, TLR2, TLR4, TLR5, TLR6, and TLR10 are expressed on the cell surface, while TLR3, TLR7, TLR8, and TLR9 are expressed on intracellular vesicles. TLRs can recognize different ligands and recruit adapter proteins, MyD88, Mal, TRIF, or TRAM, activating the downstream signaling pathway. TLR10 is an orphan receptor and lacks a classical downstream signaling pathway. Some TLRs promote the differentiation of Th cells. TLR2/6 promotes Treg cell differentiation through the JNK pathway. TLR2/1 promotes Th1 and Th17 cell differentiation through p38 MAPK pathway. TLR4 eliminates the Th1 response through IRF1 and promotes Th17 cell differentiation by STAT3 pathway. TLR5 can stimulate the body to induce Th2 response, inhibit Th1 response, and promote DC differentiation into Th17 cells. TLR8 induces the expression of IL-12B and IL-23A, promotes the differentiation of IL-23-dependent Th17 cells. TLR9 promotes the differentiation of Th1 cells. Green lines: TLR signaling pathways; black lines: TLRs related to Th cell differentiation; red lines: co-stimulation of TLRs induced to Th1 cell.

ligands also bind to Th cells to promote the proliferation of cells and upregulate the cytokines (75). TLRs-induced immune response is involved in various diseases (9). Presently, several TLR agonists are being tested as adjuvants in the treatment of autoimmune diseases by balancing the immune response.

ROLE OF Th RESPONSES IN VMC

Th responses play an important role in the pathogenesis of VMC, but different Th responses have different effects on VMC, which may have opposite effects. Besides, the dominant Th responses are different in different stages of VMC.

Th1/Th2 RESPONSES

The imbalance of Th1/Th2 cells can be observed in the process of VMC (**Figure 3**). Fuse et al. (76) observed the changes in Th1/Th2 ratio of peripheral blood lymphocytes in a patient with acute VMC. In the acute inflammatory phase (day 6), Th1 cells were dominant, while in the recovery phase (days 13 and 20), the proportion of Th2 cells increased. The induction of VMC was related to the dominance of Th1 cells, while the recovery was related to the increased proportion of Th2 cells. However, Th2 immune response induces ventricular remodeling that promotes myocarditis to develop into DCM and HF in the pathogenesis of VMC, while Th1 response alleviates VMC by inhibiting Th2 response and virus replication, but increases acute myocardial inflammation (77). Therefore, when Th2 response begins to be active, the inflammation of VMC decreases, and if Th2 response persists, it will promote myocardial fibrosis and ventricular remodeling. The study also demonstrated that Suramin (a growth factor blocker) inhibits myocardial inflammation in myocarditis by regulating the environment of Th1/Th2 cytokines (78). Therefore, elucidating the Th1/Th2 response might help to understand the activity of VMC. Based on these results, several drugs, such as atorvastatin, tanshinone IIA, apigenin, and cyclooxygenase-2 inhibitors, have been shown to have protective effects on rat model of myocarditis by regulating Th1/Th2 balance (79–82). However, the above drugs can promote Th2 response, which may aggravate the progression of VMC to DMC or HF. Therefore, it is necessary to clarify the therapeutic effect of drugs in the stage from myocarditis to DCM or HF.

Th17/TREG RESPONSES

Th17 cells secreted IL-17, promoting myocardial fibrosis after myocarditis through protein kinase C β/extracellular signal-regulated kinases 1 and 2/NF-κB pathway, which is an indispensable link in the process of DCM (83). In addition, Tregs can protect mice from CVB3-induced myocarditis progression to cardiomyopathy (84). CVB3 infection stimulates the differentiation of Th17 cells and promotes the secretion of IL-17 by inhibiting the expression of Nucleoporin 98 and aggravating VMC (85). In the acute phase of VMC, Th17 cells stimulate B cells to produce autoantibodies and participate in humoral immune response. The Th2 cells participate in humoral

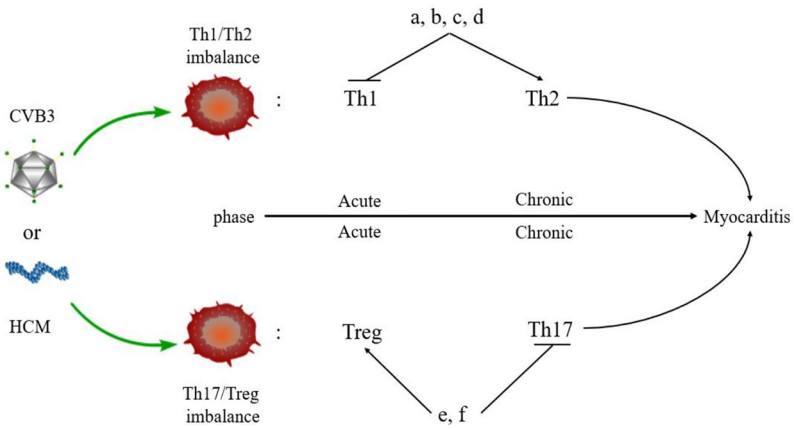

FIGURE 3 | Myocarditis and Th responses. An imbalance of Th cells is observed in the pathogenesis of myocarditis. Th1 and Treg cells are predominant in the acute phase of myocarditis, while Th2 and Th17 cells dominate the chronic phase of myocarditis. Some drugs regulate the balance of Th cells in myocarditis. **(A)** Atorvastatin; **(B)** Tanshinone IIA; **(C)** Apigenin; **(D)** Cyclooxygenase-2 inhibitors; **(E)**. Valproic acid; **(F)** Fenofibrate.

immune response at the late stage of VMC, which is consistent with the above conclusion (86). In the pathogenesis of VMC, the imbalance of Th17/Treg cells plays a critical role in the immune mechanism. MicroRNA-155 (miR-155) is a key regulator of the immune system and promotes the development of myocarditis *via* differentiation of Th17 cells leading to the imbalance of Th17/Treg cells. The inhibition of miR-155 relieves myocardial injury and the disease (87). Other drugs, such as valproic acid and fenofibrate have also been found to inhibit inflammation, reduce CVB3-induced VMC, and improve prognosis by directly inhibiting the differentiation of Th17 cells (88). Thus, VMC can be treated by promoting the differentiation of Treg cells and regulating the balance of Th17/Treg cells (89). In addition, estrogen inhibits the differentiation of Th17 cells that are mainly induced in males with CVB3 infection but less in females. Thus, Th17 cells show gender bias in myocarditis: the incidence of myocarditis has a male-to-female ratio of 2:1 (90). This indirectly indicates that Th17/Treg cell balance plays a key role in the epidemiological characteristics of myocarditis.

ROLE OF TLRs IN VMC

As key members of PRRs, TLRs participate in the upstream signaling pathway that activates innate immune cells and T cells, resulting in the production of proinflammatory cytokines and the activation of T cells. TLRs are considered to be the main factors in the development of autoimmunity, participating in and promoting the occurrence of autoimmune inflammatory diseases (91). The above observations indicate gender differences in the incidence of VMC. Roberts et al. (92) demonstrated that high expression of TLR2 in early infected female mice exerted a protective effect, while that of TLR4 in male mice was lethal. This differential expression between genders resulted in disease resistance in female mice and susceptibility in male mice (**Figure 4**). Hence, TLRs are deemed to play a critical role in gender difference with respect to myocarditis and understanding the underlying mechanisms would illuminate the epidemiological characteristic of myocarditis (93). TLR3 recognizes dsRNA intermediates produced during CVB3 replication and activates TRIF and TRAF6 to transmit signals to NF-κB (94). TLR3-TRIF signaling pathway helps the host to defend against CVB3 infection. The mechanism might be ascribed to the induction of type II IFN expression, rather than IFN-α/β, and TLR3-TRAF6-III IFN signaling pathway also has antiviral effects (95, 96). The lack of TLR3 increases virus replication and aggravates myocardial inflammation. It also worsens cardiac function and increases the susceptibility to CVB3 (97). The genetic variation of TLR3 affects the host's susceptibility facing VMC by inhibiting the signal transduction of NF-κB (21). These results proved that TLR3 has a protective effect on the myocardium in the process of virus infection. In addition, neutrophils also interact with and recognize CVB3 through TLR8, activating NF-κB and its downstream factors, resulting in VMC development (98). It also upregulates the expression of TLR4, promotes the expression of NF-κB, and induces myocarditis (99). Based on these results, astragalus polysaccharides have been shown to protect TLR4-induced myocardial injury and inflammation by inhibiting the CVB3-related signaling pathway (100), which provides a potential target to treat myocarditis. TLR7 preferentially promotes the differentiation of Th17 cells and the expression of inflammatory factors, such as IL-17 after CVB3 infection, while TLR8 promotes the production of Th1 cytokines and IFN-α/β response, which are involved in the pathogenesis of myocarditis (101). The potent autoantigen HCM is released from damaged heart during viral infection. HCM peptides S2-16 and S2-28, as an endogenous ligands, can bind to TLR2 and TLR8, and promote the release of pro-inflammatory factors such as IL-8, IL-6, IL-23 and TGF-β, which mainly induce the differentiation of Th17 cells and contribute to DCM or HF (29, 102). Although TLR9 can recognize various DNA viruses unlike the indirect way of recognizing RNA viruses,

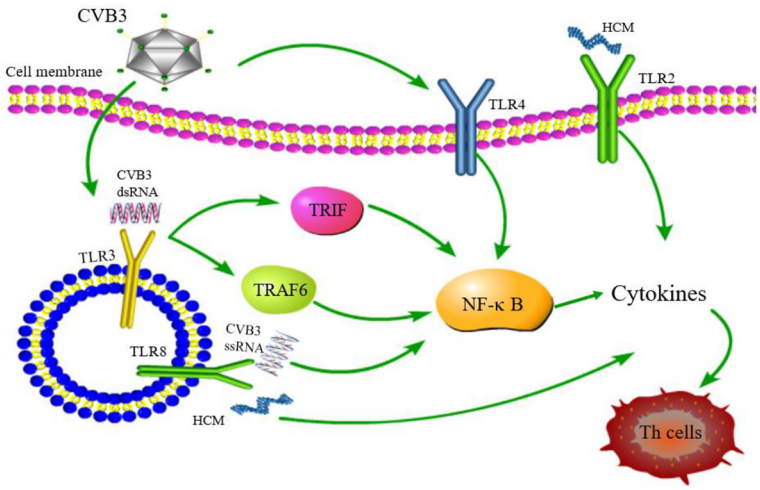

FIGURE 4 | TLR signaling pathway related to CVB3 infection. TLR4/NF-κB is activated after CVB3 infection; TLR3 recognizes CVB3 dsRNA and activates TRIF and TRAF6 to transmit signals to NF-κB; TLR8 recognizes CVB3 ssRNA and activates NF-κB signaling pathway. TLR2 and TLR8 recognizes HCM and promotes the differentiation of Th cells. Although other TLRs may be related to the pathogenesis of myocarditis, whether other TLRs can be activated and its downstream pathway after CVB3 infection has not been reported.

TLR9-MyD88 signaling pathway mediates myocardial injury in acute phase rather than chronic phase CVB3-induced myocarditis (103). Nonetheless, the mechanisms of other TLRs in myocarditis are yet to be clarified.

CONCLUSIONS

TLRs and Th responses play a critical role in the pathogenesis of VMC and have become the focus of current research. TLRs are a new class of innate immune receptors that mediate CD4+T cell differentiation, induce Th1 and Th2 immune responses, and participate in VMC pathogenesis. Except that CVB3 can directly bind to TLRs to promote Th responses, the release of HCM from damaged heart can also promote DCM or HF through TLRs and Th responses after viral infection. Blocking or activating a single TLR or regulating TLR signaling pathway may affect innate immunity, host resistance, and VMC pathogenesis, indicating that specific TLRs agonists or antagonists comprise new immunotherapy for VMC. In addition, some anti-inflammatory drugs have been found to reduce myocardial injury and improve VMC by interfering with TLR signaling pathways and Th immune responses. However, the role of other TLRs and Th responses in VMC has not yet been reported. Therefore, clarifying the role of TLRs and Th responses in VMC can provide novel ideas for the treatment of VMC.

AUTHOR CONTRIBUTIONS

All authors contributed to the article and approved the submitted version.

REFERENCES

1. Huber SA. Viral Myocarditis and Dilated Cardiomyopathy: Etiology and Pathogenesis. *Curr Pharm Des* (2016) 22:408–26. doi: 10.2174/1381612822666151222160500
2. Fujinami RS, von Herrath MG, Christen U, Whitton JL. Molecular Mimicry, Bystander Activation, or Viral Persistence: Infections and Autoimmune Disease. *Clin Microbiol Rev* (2006) 19:80–94. doi: 10.1128/CMR.19.1.80-94.2006
3. Caforio AL, Pankuweit S, Arbustini E, Basso C, Gimeno-Blanes J, Felix SB, et al. Current State of Knowledge on Aetiology, Diagnosis, Management, and Therapy of Myocarditis: A Position Statement of the European Society of Cardiology Working Group on Myocardial and Pericardial Diseases. *Eur Heart J* (2013) 34:2636–48, 48a-48d. doi: 10.1093/eurheartj/eht210
4. Ammirati E, Buono A, Moroni F, Gigli L, Power JR, Ciabatti M, et al. State-Of-the-Art of Endomyocardial Biopsy on Acute Myocarditis and Chronic Inflammatory Cardiomyopathy. *Curr Cardiol Rep* (2022). doi: 10.1007/s11886-022-01680-x
5. Basso C, Calabrese F, Angelini A, Carturan E, Thiene G. Classification and Histological, Immunohistochemical, and Molecular Diagnosis of Inflammatory Myocardial Disease. *Heart Fail Rev* (2013) 18:673–81. doi: 10.1007/s10741-012-9355-6
6. Friedrich MG, Sechtem U, Schulz-Menger J, Holmvang G, Alakija P, Cooper LT, et al. Cardiovascular Magnetic Resonance in Myocarditis: A JACC White Paper. *J Am Coll Cardiol* (2009) 53:1475–87. doi: 10.1016/j.jacc.2009.02.007
7. Luetkens JA, Homsi R, Sprinkart AM, Doerner J, Dabir D, Kuetting DL, et al. Incremental Value of Quantitative CMR Including Parametric Mapping for the Diagnosis of Acute Myocarditis. *Eur Heart J Cardiovasc Imaging* (2016) 17:154–61. doi: 10.1093/ehjci/jev246
8. Ammirati E, Frigerio M, Adler ED, Basso C, Birnie DH, Brambatti M, et al. Management of Acute Myocarditis and Chronic Inflammatory

Cardiomyopathy: An Expert Consensus Document. *Circ Heart Fail* (2020) 13:e007405. doi: 10.1161/CIRCHEARTFAILURE.120.007405
9. Vijay K. Toll-Like Receptors in Immunity and Inflammatory Diseases: Past, Present, and Future. *Int Immunopharmacol* (2018) 59:391–412. doi: 10.1016/j.intimp.2018.03.002
10. Takeda K, Akira S. Toll-Like Receptors. *Curr Protoc Immunol* (2015) 109:14121–141210. doi: 10.1002/0471142735.im1412s109
11. Heidecker B, Kittleson MM, Kasper EK, Wittstein IS, Champion HC, Russell SD, et al. Transcriptomic Biomarkers for the Accurate Diagnosis of Myocarditis. *Circulation* (2011) 123:1174–84. doi: 10.1161/CIRCULATIONAHA.110.002857
12. Lasrado N, Reddy J. An Overview of the Immune Mechanisms of Viral Myocarditis. *Rev Med Virol* (2020) 30:1–14. doi: 10.1002/rmv.2131
13. Narovlyanskaya O, Winokur EJ. Viral Myocarditis. *Dimens Crit Care Nurs* (2020) 39:75–80. doi: 10.1097/DCC.0000000000000402
14. Hare JM, Baughman KL. Fulminant and Acute Lymphocytic Myocarditis: The Prognostic Value of Clinicopathological Classification. *Eur Heart J* (2001) 22:269–70. doi: 10.1053/euhj.2000.2272
15. Fung G, Luo H, Qiu Y, Yang D, McManus B. Myocarditis. *Circ Res* (2016) 118:496–514. doi: 10.1161/CIRCRESAHA.115.306573
16. Olejniczak M, Schwartz M, Webber E, Shaffer A, Perry TE. Viral Myocarditis-Incidence, Diagnosis and Management. *J Cardiothorac Vasc Anesth* (2020) 34:1591–601. doi: 10.1053/j.jvca.2019.12.052
17. Kociol RD, Cooper LT, Fang JC, Moslehi JJ, Pang PS, Sabe MA, et al. Recognition and Initial Management of Fulminant Myocarditis: A Scientific Statement From the American Heart Association. *Circulation* (2020) 141: e69–92. doi: 10.1161/CIR.0000000000000745
18. Pollack A, Kontorovich AR, Fuster V, Dec GW. Viral Myocarditis–Diagnosis, Treatment Options, and Current Controversies. *Nat Rev Cardiol* (2015) 12:670–80. doi: 10.1038/nrcardio.2015.108
19. Imanaka-Yoshida K. Inflammation in Myocardial Disease: From Myocarditis to Dilated Cardiomyopathy. *Pathol Int* (2020) 70:1–11. doi: 10.1111/pin.12868
20. Seferovic PM, Tsutsui H, McNamara DM, Ristic AD, Basso C, Bozkurt B, et al. Heart Failure Association of the ESC, Heart Failure Society of America and Japanese Heart Failure Society Position Statement on Endomyocardial Biopsy. *Eur J Heart Fail* (2021) 23:854–71. doi: 10.1002/ejhf.2190
21. Gorbea C, Makar KA, Pauschinger M, Pratt G, Bersola JL, Varela J, et al. A Role for Toll-Like Receptor 3 Variants in Host Susceptibility to Enteroviral Myocarditis and Dilated Cardiomyopathy. *J Biol Chem* (2010) 285:23208–23. doi: 10.1074/jbc.M109.047464
22. Vidya MK, Kumar VG, Sejian V, Bagath M, Krishnan G, Bhatta R. Toll-Like Receptors: Significance, Ligands, Signaling Pathways, and Functions in Mammals. *Int Rev Immunol* (2018) 37:20–36. doi: 10.1080/08830185.2017.1380200
23. Muzio M, Polentarutti N, Bosisio D, Manoj Kumar PP, Mantovani A. Toll-Like Receptor Family and Signalling Pathway. *Biochem Soc Trans* (2000) 28:563–6. doi: 10.1042/bst0280563
24. Lim KH, Staudt LM. Toll-Like Receptor Signaling. *Cold Spring Harb Perspect Biol* (2013) 5:a011247. doi: 10.1101/cshperspect.a011247
25. Yu L, Wang L, Chen S. Endogenous Toll-Like Receptor Ligands and Their Biological Significance. *J Cell Mol Med* (2010) 14:2592–603. doi: 10.1111/j.1582-4934.2010.01127.x
26. Kumar V. Toll-Like Receptors in Adaptive Immunity. *Handb Exp Pharmacol* (2021). doi: 10.1007/164_2021_543
27. Wagner H. Endogenous TLR Ligands and Autoimmunity. *Adv Immunol* (2006) 91:159–73. doi: 10.1016/S0065-2776(06)91004-9
28. Rifkin IR, Leadbetter EA, Busconi L, Viglianti G, Marshak-Rothstein A. Toll-Like Receptors, Endogenous Ligands, and Systemic Autoimmune Disease. *Immunol Rev* (2005) 204:27–42. doi: 10.1111/j.0105-2896.2005.00239.x
29. Zhang P, Cox CJ, Alvarez KM, Cunningham MW. Cutting Edge: Cardiac Myosin Activates Innate Immune Responses Through TLRs. *J Immunol* (2009) 183:27–31. doi: 10.4049/jimmunol.0800861
30. Chen JQ, Szodoray P, Zeher M. Toll-Like Receptor Pathways in Autoimmune Diseases. *Clin Rev Allergy Immunol* (2016) 50:1–17. doi: 10.1007/s12016-015-8473-z
31. McGettrick AF, O'Neill LA. Localisation and Trafficking of Toll-Like Receptors: An Important Mode of Regulation. *Curr Opin Immunol* (2010) 22:20–7. doi: 10.1016/j.coi.2009.12.002
32. Noreen M, Arshad M. Association of TLR1, TLR2, TLR4, TLR6, and TIRAP Polymorphisms With Disease Susceptibility. *Immunol Res* (2015) 62:234–52. doi: 10.1007/s12026-015-8640-6
33. Zhou R, Liu L, Wang Y. Viral Proteins Recognized by Different TLRs. *J Med Virol* (2021) 93:6116–23. doi: 10.1002/jmv.27265
34. Deng Y, Yang J, Qian J, Liu R, Huang E, Wang Y, et al. TLR1/TLR2 Signaling Blocks the Suppression of Monocytic Myeloid-Derived Suppressor Cell by Promoting its Differentiation Into M1-Type Macrophage. *Mol Immunol* (2019) 112:266–73. doi: 10.1016/j.molimm.2019.06.006
35. Cervantes JL, Weinerman B, Basole C, Salazar JC. TLR8: The Forgotten Relative Revindicated. *Cell Mol Immunol* (2012) 9:434–8. doi: 10.1038/cmi.2012.38
36. Kim J, Durai P, Jeon D, Jung ID, Lee SJ, Park YM, et al. Phloretin as a Potent Natural TLR2/1 Inhibitor Suppresses TLR2-Induced Inflammation. *Nutrients* (2018) 10:868. doi: 10.3390/nu10070868
37. Marinho FA, de Paula RR, Mendes AC, de Almeida LA, Gomes MT, Carvalho NB, et al. Toll-Like Receptor 6 Senses Mycobacterium Avium and is Required for Efficient Control of Mycobacterial Infection. *Eur J Immunol* (2013) 43:2373–85. doi: 10.1002/eji.201243208
38. Matsumoto M, Seya T. TLR3: Interferon Induction by Double-Stranded RNA Including Poly(I:C). *Adv Drug Delivery Rev* (2008) 60:805–12. doi: 10.1016/j.addr.2007.11.005
39. Mukherjee S, Huda S, Sinha Babu SP. Toll-Like Receptor Polymorphism in Host Immune Response to Infectious Diseases: A Review. *Scand J Immunol* (2019) 90:e12771. doi: 10.1111/sji.12771
40. Ciesielska A, Matyjek M, Kwiatkowska K. TLR4 and CD14 Trafficking and its Influence on LPS-Induced Pro-Inflammatory Signaling. *Cell Mol Life Sci* (2021) 78:1233–61. doi: 10.1007/s00018-020-03656-y
41. Lai CY, Su YW, Lin KI, Hsu LC, Chuang TH. Natural Modulators of Endosomal Toll-Like Receptor-Mediated Psoriatic Skin Inflammation. *J Immunol Res* (2017) 2017:7807313. doi: 10.1155/2017/7807313
42. Kuzmich NN, Sivak KV, Chubarev VN, Porozov YB, Savateeva-Lyubimova TN, Peri F. TLR4 Signaling Pathway Modulators as Potential Therapeutics in Inflammation and Sepsis. *Vaccines (Basel)* (2017) 5:34. doi: 10.3390/vaccines5040034
43. Plociennikowska A, Hromada-Judycka A, Borzecka K, Kwiatkowska K. Co-Operation of TLR4 and Raft Proteins in LPS-Induced Pro-Inflammatory Signaling. *Cell Mol Life Sci* (2015) 72:557–81. doi: 10.1007/s00018-014-1762-5
44. Vaure C, Liu Y. A Comparative Review of Toll-Like Receptor 4 Expression and Functionality in Different Animal Species. *Front Immunol* (2014) 5:316. doi: 10.3389/fimmu.2014.00316
45. Yoon SI, Kurnasov O, Natarajan V, Hong M, Gudkov AV, Osterman AL, et al. Structural Basis of TLR5-Flagellin Recognition and Signaling. *Science* (2012) 335:859–64. doi: 10.1126/science.1215584
46. Yu Y, Zeng H, Lyons S, Carlson A, Merlin D, Neish AS, et al. TLR5-Mediated Activation of P38 MAPK Regulates Epithelial IL-8 Expression *Via* Posttranscriptional Mechanism. *Am J Physiol Gastrointest Liver Physiol* (2003) 285:G282–90. doi: 10.1152/ajpgi.00503.2002
47. Wang J, Shao Y, Bennett TA, Shankar RA, Wightman PD, Reddy LG. The Functional Effects of Physical Interactions Among Toll-Like Receptors 7, 8, and 9. *J Biol Chem* (2006) 281:37427–34. doi: 10.1074/jbc.M605311200
48. Eng HL, Hsu YY, Lin TM. Differences in TLR7/8 Activation Between Monocytes and Macrophages. *Biochem Biophys Res Commun* (2018) 497:319–25. doi: 10.1016/j.bbrc.2018.02.079
49. Diebold SS, Kaisho T, Hemmi H, Akira S, Sousa CR. Innate Antiviral Responses by Means of TLR7-Mediated Recognition of Single-Stranded RNA. *Science* (2004) 303:1529–31. doi: 10.1126/science.1093616
50. Javmen A, Szmacinski H, Lakowicz JR, Toshchakov VY. Frontline Science: Targeting the TLR7 Signalosome Assembly. *J Leukoc Biol* (2020) 108:1697–706. doi: 10.1002/JLB.2HI0819-180R
51. Chodisetti SB, Fike AJ, Domeier PP, Choi NM, Soni C, Rahman ZSM. TLR7 Negatively Regulates B10 Cells Predominantly in an IFNgamma Signaling Dependent Manner. *Front Immunol* (2020) 11:1632. doi: 10.3389/fimmu.2020.01632
52. Saruta M, Michelsen KS, Thomas LS, Yu QT, Landers CJ, Targan SR. TLR8-Mediated Activation of Human Monocytes Inhibits TL1A Expression. *Eur J Immunol* (2009) 39:2195–202. doi: 10.1002/eji.200939216

53. Muller T, Hamm S, Bauer S. TLR9-Mediated Recognition of DNA. *Handb Exp Pharmacol* (2008) 183:51–70. doi: 10.1007/978-3-540-72167-3_3
54. Desnues B, Macedo AB, Roussel-Queval A, Bonnardel J, Henri S, Demaria O, et al. TLR8 on Dendritic Cells and TLR9 on B Cells Restrain TLR7-Mediated Spontaneous Autoimmunity in C57BL/6 Mice. *Proc Natl Acad Sci USA* (2014) 111:1497–502. doi: 10.1073/pnas.1314121111
55. Hess NJ, Felicelli C, Grage J, Tapping RI. TLR10 Suppresses the Activation and Differentiation of Monocytes With Effects on DC-Mediated Adaptive Immune Responses. *J Leukoc Biol* (2017) 101:1245–52. doi: 10.1189/jlb.3A1116-492R
56. Zhu J. T Helper Cell Differentiation, Heterogeneity, and Plasticity. *Cold Spring Harb Perspect Biol* (2018) 10:a030338. doi: 10.1101/cshperspect.a030338
57. Gagliani N, Huber S. Basic Aspects of T Helper Cell Differentiation. *Methods Mol Biol* (2017) 1514:19–30. doi: 10.1007/978-1-4939-6548-9_2
58. Zhu X, Zhu J. CD4 T Helper Cell Subsets and Related Human Immunological Disorders. *Int J Mol Sci* (2020) 21:8011. doi: 10.3390/ijms21218011
59. Korn T, Bettelli E, Oukka M, Kuchroo VK. IL-17 and Th17 Cells. *Annu Rev Immunol* (2009) 27:485–517. doi: 10.1146/annurev.immunol.021908.132710
60. Annunziato F, Romagnani C, Romagnani S. The 3 Major Types of Innate and Adaptive Cell-Mediated Effector Immunity. *J Allergy Clin Immunol* (2015) 135:626–35. doi: 10.1016/j.jaci.2014.11.001
61. Cunningham MW. Cardiac Myosin and the TH1/TH2 Paradigm in Autoimmune Myocarditis. *Am J Pathol* (2001) 159:5–12. doi: 10.1016/S0002-9440(10)61665-3
62. Lee GR. The Balance of Th17 Versus Treg Cells in Autoimmunity. *Int J Mol Sci* (2018) 19:730. doi: 10.3390/ijms19030730
63. Jin B, Sun T, Yu XH, Yang YX, Yeo AE. The Effects of TLR Activation on T-Cell Development and Differentiation. *Clin Dev Immunol* (2012) 2012:836485. doi: 10.1155/2012/836485
64. Nyirenda MH, Sanvito L, Darlington PJ, O'Brien K, Zhang GX, Constantinescu CS, et al. TLR2 Stimulation Drives Human Naive and Effector Regulatory T Cells Into a Th17-Like Phenotype With Reduced Suppressive Function. *J Immunol* (2011) 187:2278–90. doi: 10.4049/jimmunol.1003715
65. Kamdar K, Nguyen V, DePaolo RW. Toll-Like Receptor Signaling and Regulation of Intestinal Immunity. *Virulence* (2013) 4:207–12. doi: 10.4161/viru.23354
66. Sacramento LA, Benevides L, Maruyama SR, Tavares L, Fukutani KF, Francozo M, et al. TLR4 Abrogates the Th1 Immune Response Through IRF1 and IFN-Beta to Prevent Immunopathology During L. infantum infection. *PloS Pathog* (2020) 16:e1008435. doi: 10.1371/journal.ppat.1008435
67. Xu QQ, Zhou Q, Xu LL, Lin H, Wang XJ, Ma WL, et al. Toll-Like Receptor 4 Signaling Inhibits Malignant Pleural Effusion by Altering Th1/Th17 Responses. *Cell Biol Int* (2015) 39:1120–30. doi: 10.1002/cbin.10485
68. Lee AJ, Ro M, Cho KJ, Kim JH. Lipopolysaccharide/TLR4 Stimulates IL-13 Production Through a MyD88-BLT2-Linked Cascade in Mast Cells, Potentially Contributing to the Allergic Response. *J Immunol* (2017) 199:409–17. doi: 10.4049/jimmunol.1602062
69. Flores-Langarica A, Bobat S, Marshall JL, Yam-Puc JC, Cook CN, Serre K, et al. Soluble Flagellin Coimmunization Attenuates Th1 Priming to Salmonella and Clearance by Modulating Dendritic Cell Activation and Cytokine Production. *Eur J Immunol* (2015) 45:2299–311. doi: 10.1002/eji.201545564
70. Liu H, Chen F, Wu W, Cao AT, Xue X, Yao S, et al. TLR5 Mediates CD172alpha(+) Intestinal Lamina Propria Dendritic Cell Induction of Th17 Cells. *Sci Rep* (2016) 6:22040. doi: 10.1038/srep22040
71. Tamassia N, Arruda-Silva F, Wright HL, Moots RJ, Gardiman E, Bianchetto-Aguilera F, et al. Human Neutrophils Activated *via* TLR8 Promote Th17 Polarization Through IL-23. *J Leukoc Biol* (2019) 105:1155–65. doi: 10.1002/JLB.MA0818-308R
72. Bekeredjian-Ding I, Roth SI, Gilles S, Giese T, Ablasser A, Hornung V, et al. T Cell-Independent, TLR-Induced IL-12p70 Production in Primary Human Monocytes. *J Immunol* (2006) 176:7438–46. doi: 10.4049/jimmunol.176.12.7438
73. Kumagai Y, Takeuchi O, Akira S. TLR9 as a Key Receptor for the Recognition of DNA. *Adv Drug Delivery Rev* (2008) 60:795–804. doi: 10.1016/j.addr.2007.12.004
74. Wagner H. Interactions Between Bacterial CpG-DNA and TLR9 Bridge Innate and Adaptive Immunity. *Curr Opin Microbiol* (2002) 5:62–9. doi: 10.1016/s1369-5274(02)00287-4
75. Sharma RK, Sehgal S, Sachdeva N, Kumar R, Gupta A. Direct Engagement of TLR9 Ligand With T Helper Cells Leads to Cell Proliferation & Up-Regulation of Cytokines. *Immunol Invest* (2019) 48:79–95. doi: 10.1080/08820139.2018.1515223
76. Fuse K, Kodama M, Aizawa Y, Yamaura M, Tanabe Y, Takahashi K, et al. Th1/Th2 Balance Alteration in the Clinical Course of a Patient With Acute Viral Myocarditis. *Jpn Circ J* (2001) 65:1082–4. doi: 10.1253/jcj.65.1082
77. Fairweather D, Stafford KA, Sung YK. Update on Coxsackievirus B3 Myocarditis. *Curr Opin Rheumatol* (2012) 24:401–7. doi: 10.1097/BOR.0b013e328353372d
78. Fuse K, Kodama M, Ito M, Okura Y, Kato K, Hanawa H, et al. Polarity of Helper T Cell Subsets Represents Disease Nature and Clinical Course of Experimental Autoimmune Myocarditis in Rats. *Clin Exp Immunol* (2003) 134:403–8. doi: 10.1111/j.1365-2249.2003.02312.x
79. Guo G, Zhao Q, Wang Q, Li E. Tanshinone IIA Ameliorate Coxsackie Virus B3-Induced Viral Myocarditis Through the Inhibition of Inflammation and Modulation T Helper 1/T Helper 2 Balance in Mice. *Pharmacology* (2019) 103:136–42. doi: 10.1159/000495755
80. Liu W, Li WM, Gao C, Sun NL. Effects of Atorvastatin on the Th1/Th2 Polarization of Ongoing Experimental Autoimmune Myocarditis in Lewis Rats. *J Autoimmun* (2005) 25:258–63. doi: 10.1016/j.jaut.2005.06.005
81. Suzuki J, Ogawa M, Futamatsu H, Kosuge H, Tanaka H, Isobe M. A Cyclooxygenase-2 Inhibitor Alters Th1/Th2 Cytokine Balance and Suppresses Autoimmune Myocarditis in Rats. *J Mol Cell Cardiol* (2006) 40:688–95. doi: 10.1016/j.yjmcc.2006.01.006
82. Zhang S, Liu X, Sun C, Yang J, Wang L, Liu J, et al. Apigenin Attenuates Experimental Autoimmune Myocarditis by Modulating Th1/Th2 Cytokine Balance in Mice. *Inflammation* (2016) 39:678–86. doi: 10.1007/s10753-015-0294-y
83. Liu Y, Zhu H, Su Z, Sun C, Yin J, Yuan H, et al. IL-17 Contributes to Cardiac Fibrosis Following Experimental Autoimmune Myocarditis by a PKCbeta/Erk1/2/NF-kappaB-Dependent Signaling Pathway. *Int Immunol* (2012) 24:605–12. doi: 10.1093/intimm/dxs056
84. Vdovenko D, Eriksson U. Regulatory Role of CD4(+) T Cells in Myocarditis. *J Immunol Res* (2018) 2018:4396351. doi: 10.1155/2018/4396351
85. Long Q, Liao YH, Xie Y, Liang W, Cheng X, Yuan J, et al. Coxsackievirus B3 Directly Induced Th17 Cell Differentiation by Inhibiting Nup98 Expression in Patients With Acute Viral Myocarditis. *Front Cell Infect Microbiol* (2016) 6:171. doi: 10.3389/fcimb.2016.00171
86. Yuan J, Cao AL, Yu M, Lin QW, Yu X, Zhang JH, et al. Th17 Cells Facilitate the Humoral Immune Response in Patients With Acute Viral Myocarditis. *J Clin Immunol* (2010) 30:226–34. doi: 10.1007/s10875-009-9355-z
87. Yan L, Hu F, Yan X, Wei Y, Ma W, Wang Y, et al. Inhibition of microRNA-155 Ameliorates Experimental Autoimmune Myocarditis by Modulating Th17/Treg Immune Response. *J Mol Med (Berl)* (2016) 94:1063–79. doi: 10.1007/s00109-016-1414-3
88. Jin H, Guo X. Valproic Acid Ameliorates Coxsackievirus-B3-Induced Viral Myocarditis by Modulating Th17/Treg Imbalance. *Virol J* (2016) 13:168. doi: 10.1186/s12985-016-0626-z
89. Cheng H, Xi Y, Chi X, Wu Y, Liu G. Fenofibrate Treatment of Rats With Experimental Autoimmune Myocarditis by Alleviating Treg/Th17 Disorder. *Cent Eur J Immunol* (2016) 41:64–70. doi: 10.5114/ceji.2016.58817
90. Li Z, Yue Y, Xiong S. Distinct Th17 Inductions Contribute to the Gender Bias in CVB3-Induced Myocarditis. *Cardiovasc Pathol* (2013) 22:373–82. doi: 10.1016/j.carpath.2013.02.004
91. Mills KH. TLR-Dependent T Cell Activation in Autoimmunity. *Nat Rev Immunol* (2011) 11:807–22. doi: 10.1038/nri3095
92. Roberts BJ, Dragon JA, Moussawi M, Huber SA. Sex-Specific Signaling Through Toll-Like Receptors 2 and 4 Contributes to Survival Outcome of Coxsackievirus B3 Infection in C57Bl/6 Mice. *Biol Sex Differ* (2012) 3:25. doi: 10.1186/2042-6410-3-25

93. Roberts BJ, Moussawi M, Huber SA. Sex Differences in TLR2 and TLR4 Expression and Their Effect on Coxsackievirus-Induced Autoimmune Myocarditis. *Exp Mol Pathol* (2013) 94:58–64. doi: 10.1016/j.yexmp.2012.06.005
94. Marchant D, Si X, Luo H, McManus B, Yang D. The Impact of CVB3 Infection on Host Cell Biology. *Curr Top Microbiol Immunol* (2008) 323:177–98. doi: 10.1007/978-3-540-75546-3_8
95. Negishi H, Osawa T, Ogami K, Ouyang X, Sakaguchi S, Koshiba R, et al. A Critical Link Between Toll-Like Receptor 3 and Type II Interferon Signaling Pathways in Antiviral Innate Immunity. *Proc Natl Acad Sci USA* (2008) 105:20446–51. doi: 10.1073/pnas.0810372105
96. Su R, Shereen MA, Zeng X, Liang Y, Li W, Ruan Z, et al. The TLR3/IRF1/Type III IFN Axis Facilitates Antiviral Responses Against Enterovirus Infections in the Intestine. *mBio* (2020) 11:e02540–20. doi: 10.1128/mBio.02540-20
97. Abston ED, Coronado MJ, Bucek A, Onyimba JA, Brandt JE, Frisancho JA, et al. TLR3 Deficiency Induces Chronic Inflammatory Cardiomyopathy in Resistant Mice Following Coxsackievirus B3 Infection: Role for IL-4. *Am J Physiol Regul Integr Comp Physiol* (2013) 304:R267–77. doi: 10.1152/ajpregu.00516.2011
98. Rivadeneyra L, Charo N, Kviatcovsky D, de la Barrera S, Gomez RM, Schattner M. Role of Neutrophils in CVB3 Infection and Viral Myocarditis. *J Mol Cell Cardiol* (2018) 125:149–61. doi: 10.1016/j.yjmcc.2018.08.029
99. Zhao Z, Cai TZ, Lu Y, Liu WJ, Cheng ML, Ji YQ. Coxsackievirus B3 Induces Viral Myocarditis by Upregulating Toll-Like Receptor 4 Expression. *Biochem (Mosc)* (2015) 80:455–62. doi: 10.1134/S0006297915040094
100. Liu T, Zhang M, Niu H, Liu J, Ruilian M, Wang Y, et al. Astragalus Polysaccharide From Astragalus Melittin Ameliorates Inflammation *Via* Suppressing the Activation of TLR-4/NF-kappaB P65 Signal Pathway and Protects Mice From CVB3-Induced Virus Myocarditis. *Int J Biol Macromol* (2019) 126:179–86. doi: 10.1016/j.ijbiomac.2018.12.207
101. de Marcken M, Dhaliwal K, Danielsen AC, Gautron AS, Dominguez-Villar M. TLR7 and TLR8 Activate Distinct Pathways in Monocytes During RNA Virus Infection. *Sci Signal* (2019) 12:eaaw1347. doi: 10.1126/scisignal.aaw1347
102. Myers JM, Cooper LT, Kem DC, Stavrakis S, Kosanke SD, Shevach EM, et al. Cardiac Myosin-Th17 Responses Promote Heart Failure in Human Myocarditis. *JCI Insight* (2016) 1:e85851. doi: 10.1172/jci.insight.85851
103. Riad A, Westermann D, Escher F, Becher PM, Savvatis K, Lettau O, et al. Myeloid Differentiation Factor-88 Contributes to TLR9-Mediated Modulation of Acute Coxsackievirus B3-Induced Myocarditis *In Vivo*. *Am J Physiol Heart Circ Physiol* (2010) 298:H2024–31. doi: 10.1152/ajpheart.01188.2009

Conflict of Interest: The authors declare that the research was conducted in the absence of any commercial or financial relationships that could be construed as a potential conflict of interest.

Publisher's Note: All claims expressed in this article are solely those of the authors and do not necessarily represent those of their affiliated organizations, or those of the publisher, the editors and the reviewers. Any product that may be evaluated in this article, or claim that may be made by its manufacturer, is not guaranteed or endorsed by the publisher.

frontiers | Frontiers in Immunology

ORIGINAL RESEARCH
published: 23 May 2022
doi: 10.3389/fimmu.2022.884113

Toll-Like Receptor 7 Agonist RG7854 Mediates Therapeutic Efficacy and Seroconversion in Woodchucks With Chronic Hepatitis B

Steffen Wildum[1], Kyle E. Korolowicz[2], Manasa Suresh[2], Guido Steiner[1], Lue Dai[3], Bin Li[2], Changsuek Yon[2], Maria Cristina De Vera Mudry[1], Franziska Regenass-Lechner[1], Xu Huang[2], Xupeng Hong[2], Marta G. Murreddu[2], Bhaskar V. Kallakury[4], John A. T. Young[1] and Stephan Menne[2]**

[1] Roche Pharma, Research and Early Development, Roche Innovation Center Basel, Basel, Switzerland, [2] Department of Microbiology and Immunology, Georgetown University Medical Center, Washington, DC, United States, [3] Roche Pharma, Research and Early Development, Roche Innovation Center Shanghai, Shanghai, China, [4] Department of Pathology, Georgetown University Medical Center, Washington, DC, United States

OPEN ACCESS

Edited by:
Ramesh Akkina,
Colorado State University,
United States

Reviewed by:
Shikha Shrivastava,
Walter Reed Army Institute of Research, United States
David Milich,
VLP Biotech, United States

***Correspondence:**
Steffen Wildum
steffen.wildum@roche.com
Stephan Menne
stephan.menne@georgetown.edu

Specialty section:
This article was submitted to Vaccines and Molecular Therapeutics, a section of the journal Frontiers in Immunology

Received: 25 February 2022
Accepted: 22 April 2022
Published: 23 May 2022

Citation:
Wildum S, Korolowicz KE, Suresh M, Steiner G, Dai L, Li B, Yon C, De Vera Mudry MC, Regenass-Lechner F, Huang X, Hong X, Murreddu MG, Kallakury BV, Young JAT and Menne S (2022) Toll-Like Receptor 7 Agonist RG7854 Mediates Therapeutic Efficacy and Seroconversion in Woodchucks With Chronic Hepatitis B. Front. Immunol. 13:884113. doi: 10.3389/fimmu.2022.884113

Conventional treatment of chronic hepatitis B (CHB) is rarely curative due to the immunotolerant status of patients. RG7854 is an oral double prodrug of a toll-like receptor 7 (TLR7) agonist that is developed for the treatment of CHB. The therapeutic efficacy, host immune response, and safety of RG7854 were evaluated in the woodchuck model of CHB. Monotreatment with the two highest RG7854 doses and combination treatment with the highest RG7854 dose and entecavir (ETV) suppressed viral replication, led to loss of viral antigens, and induced seroconversion in responder woodchucks. Since viral suppression and high-titer antibodies persisted after treatment ended, this suggested that a sustained antiviral response (SVR) was induced by RG7854 in a subset of animals. The SVR rate, however, was comparable between both treatment regimens, suggesting that the addition of ETV did not enhance the therapeutic efficacy of RG7854 although it augmented the proliferation of blood cells in response to viral antigens and magnitude of antibody titers. The induction of interferon-stimulated genes in blood by RG7854/ETV combination treatment demonstrated on-target activation of TLR7. Together with the virus-specific blood cell proliferation and the transient elevations in liver enzymes and inflammation, this suggested that cytokine-mediated non-cytolytic and T-cell mediated cytolytic mechanisms contributed to the SVR, in addition to the virus-neutralizing effects by antibody-producing plasma cells. Both RG7854 regimens were not associated with treatment-limiting adverse effects but accompanied by dose-dependent, transient neutropenia and thrombocytopenia. The study concluded that finite, oral RG7854 treatment can induce a SVR in woodchucks that is based on the retrieval of antiviral innate and adaptive immune responses. This supports future investigation of the TLR7 agonist as an immunotherapeutic approach for achieving functional cure in patients with CHB.

Keywords: chronic hepatitis B, woodchuck, TLR7 agonism, RG7854, functional cure, entecavir, innate immune response, adaptive immune response

INTRODUCTION

Chronic infection with hepatitis B virus (HBV) affects approximately 296 million individuals worldwide and results in 820,000 deaths every year due to HBV-associated liver disease, making this viral infection one of the most serious global health issues (1). Carriers of HBV have a high risk of developing chronic hepatitis B (CHB), liver cirrhosis, and hepatocellular carcinoma (HCC) and will die without therapeutic intervention and/or liver transplantation. The hallmarks of CHB are high levels of viremia (HBV DNA) and surface antigenemia (HBsAg) in the circulation, while antibodies to HBsAg (anti-HBs antibodies) are characteristically absent (2, 3). Several studies have shown the importance of these viral markers in the HBV-related disease outcome. Loss of HBsAg either mediated by antiviral treatment or induced spontaneously is associated with a lower risk of liver disease progression to HCC (4, 5), while development of anti-HBs antibodies after prophylactic vaccination or resolution of acute HBV infection offers lifelong immunity (6, 7). However, the currently approved drugs, including oral nucleos(t)ide analogues (NAs) and systemic (pegylated) interferon-alpha (IFN-α), rarely achieve immunological control of HBV or a functional cure, which is defined as sustained suppression of HBV DNA and loss of HBsAg after treatment discontinuation, with or without seroconversion to anti-HBs antibodies (8). The underlying reason is that NAs effectively suppress HBV DNA synthesis and reduce liver inflammation but require lifelong administration, since these direct-acting antivirals do not affect the persistent covalently-closed circular (ccc) viral DNA genome within the nucleus of infected hepatocytes, and viral relapse is typically observed after treatment cessation (8). IFN-α directly targets HBV cccDNA and suppresses its functions (9–12) and induces an antiviral immune response in patients, but is sometimes associated with severe side effects (8). The HBV cure rate accomplished with IFN-α is slightly higher than with NAs, and combination treatment with both drugs increases this rate to approximately 10% of patients (8, 13). Thus, novel therapeutics are urgently needed for use as single agents or for incorporation into already applied treatment regimens, with the overall goal to achieve HBV functional cure in a majority of patients after a finite course of treatment.

CHB in patients is associated with insufficient innate and adaptive immunity against HBV (3, 14–18). Unlike many other viruses, HBV avoids the induction of a type-I IFN-based host innate immune response during initial establishment of the infection, and thus displays a stealth-like behavior (19). During progression to chronic HBV infection, the high levels of viral proteins in the periphery and liver are thought to interfere with the pathway activation of pathogen recognition receptors (PRRs) (17, 20–24). Viral proteins further modulate innate immune cell subsets (25–27) although the altered function of dendritic cells (DCs) appears to correlate more with liver disease progression than with antigen load (28). Prolonged exposure to viral proteins rather than high antigen load during chronic HBV infection is further believed to be responsible for the functional impairment of HBV-specific T-cells and HBsAg-specific B-cells (29–32). These immunodeficiencies have shifted the focus of anti-HBV drug discovery to immunomodulation as a therapeutic strategy for reviving the impaired antiviral immunity in patients with CHB (8).

Since HBV is not actively or entirely inhibiting the function of PRRs (33, 34), small molecules stimulating selected receptors have been developed and several agonists were evaluated first in animal models of HBV and subsequently in patients (35, 36). Among these, agonists of toll-like receptor 7 (TLR7) appear promising therapeutics that may be able to overcome the HBV-associated immunodeficiencies present in patients. TLR7 is predominately expressed within the endosome of antigen presenting cells (APCs), including plasmacytoid (p) DCs and B-lymphocytes, and naturally recognizes viral single-stranded RNA (37). Following receptor activation, the downstream signaling cascade leads to the production of multiple type-I IFN isotypes and T-cell attractant chemokines, enhancement of antigen processing and presentation by APCs, and upregulation of costimulatory molecules critical for the cross-priming of cytotoxic T-cells (38, 39), all of which could be beneficial in restoring innate and adaptive immunity for subsequent HBV control. GS-9620, the first in-class oral TLR7 agonist developed for the treatment of CHB produced a long-lasting viral suppression in chimpanzees infected with HBV (40) and a sustained antiviral response (SVR) or functional cure in a subset of woodchucks infected with woodchuck hepatitis virus (WHV) (41). The unprecedented antiviral effect achieved in the latter animal model of HBV with any single agent therapy evaluated so far was due to an additional activation of woodchuck TLR8 by high GS-9620 dosage (42). However, GS-9620 treatment of patients failed to mediate therapeutic efficacy at tolerated doses when used alone or in combination with a NA (43, 44), but improved the responses of HBV-specific natural killer (NK) cells and T-cells (45). APR002, another oral TLR7 agonist, induced a functional cure in a subset of woodchucks, but only when administered together with the nucleoside analogue entecavir (ETV) (46).

Abbreviations: ALT, alanine aminotransferase; Anti-HBs, antibodies to hepatitis B virus surface antigen; Anti-WHe, antibodies to woodchuck hepatitis virus e antigen; Anti-WHs, antibodies to woodchuck hepatitis virus surface antigen; APC, antigen-presenting cell; APR002, a TLR7 agonist developed by Apros Therapeutics; AST, aspartate aminotransferase; cccDNA, covalently-closed circular DNA; CHB, chronic hepatitis B; CXCL10, IFN-γ induced protein 10 (IP-10); DC, dendritic cell; EOS, end of the study; ETV, entecavir; F, female; ge, genome equivalents or copy numbers; GGT, gamma-glutamyl transferase; GS-9620, a TLR7 agonist developed by Gilead Sciences; HBsAg, hepatitis B virus surface antigen; IFN, interferon; ISG, interferon-stimulated gene; ISG15, IFN-induced 17 kDa protein; LPS, lipopolysaccharide; M, male; MX1, IFN-induced guanosine triphosphate-binding protein; NA, nucleos(t)ide analogue; ND, not determined; NK, natural killer; NR, Non-Responders; OAS1, 2'-5'-oligoadenylate synthetase 1; PBMC, peripheral blood mononuclear cell; PR, Partial Responders; PRR, pathogen recognition receptor; QOD, every other day; R, Responders; RG7854, an oral double prodrug of the TLR7-specific agonist RO7011785; RI, replicative intermediate; RO7011785, a TLR7 agonist developed by F. Hoffmann-La Roche, Ltd.; RO7049389, capsid assembly modulator developed by F. Hoffmann-La Roche, Ltd.; SDH, sorbitol dehydrogenase; StdU, standard units; SVR, sustained antiviral response; TLR, toll-like receptor; WHcAg, woodchuck hepatitis virus core antigen; WHeAg, woodchuck hepatitis virus e antigen; WHsAg, woodchuck hepatitis virus surface antigen; WHV, woodchuck hepatitis virus.

The Eastern woodchuck (*Marmota monax*), chronically infected with WHV, is an established, immunocompetent animal model for studies of HBV pathogenesis and therapy. Like HBV, WHV is a member of the genus Orthohepadnavirus, and both viruses are closely related regarding their genome structure and replication mechanism (47). Host immune response to WHV and virus-induced liver disease progression in woodchucks parallel HBV infection in humans (35, 48–52). Woodchucks are applied in the assessment of the safety and therapeutic efficacy of new drugs developed for the treatment of CHB and HCC, and the preclinical use of this model is predictive of antiviral efficacy of NAs (53, 54) and immunomodulators against HBV in patients (42, 55).

We report here the evaluation of RG7854, an oral double prodrug of a TLR7-specific agonist developed by F. Hoffmann-La Roche, Ltd., in woodchucks with CHB. RG7854 is converted *in vivo* to its active metabolite RO7011785 *via* hydrolysis by mainly carboxylesterase 2 and oxidation by aldehyde oxidase (56). The initial dose-finding study in woodchucks assessed tolerability and potency of three increasing RG7854 doses. Since the safe and potent NAs are expected to remain the pillar of any future anti-HBV therapy, the subsequent combination treatment study in woodchucks assessed the antiviral benefit of high RG7854 dosage, when administered together with ETV. Like RG7854 monotreatment, RG7854/ETV combination treatment resulted in undetectable viral DNA, loss of WHV surface (WHsAg) and e antigens (WHeAg), and seroconversion to antibodies against both viral proteins (anti-WHs and anti-WHe antibodies) in a subset of woodchucks that was characterized by remarkably high titers of virus-neutralizing antibodies, but did not further enhance the rate of functional cure beyond that of RG7854 alone.

MATERIALS AND METHODS

Investigational Drugs

RG7854 and ETV were manufactured by F. Hoffmann-La Roche and provided as a dry powder. RG7854 was dissolved in vehicle (i.e., 2% (w/v) Klucel LF (hydroxypropylcellulose), 0.09% (w/v) methylparaben, and 0.01% (w/v) propylparaben in water). ETV was also dissolved in vehicle (i.e., ultrapure water). Drugs were mixed with woodchuck diet (Dyets, Inc., Bethlehem, PA) and orally administered to animals within 30 minutes after preparation using an aluminum luer lock tube with gavage needle. Control animals were administered placebo (i.e., vehicle) mixed with woodchuck diet.

Study Design

Woodchucks received humane care according to the criteria outlined in the Guide for the Care and Use of Laboratory Animals. Animal protocols including woodchucks were approved by the Institutional Animal Care and Use Committee of Northeastern Wildlife, Inc. (Harrison, ID) and Georgetown University (Washington, DC). All animals were born in captivity at the animal facilities of Northeastern Wildlife, Inc., infected with WHV at three days of age to model vertical HBV transmission in humans, and raised to adulthood prior to use in the RG7854 mono and RG7854/ETV combination treatment studies. Before study initiation, chronic WHV carrier woodchucks of both genders were confirmed positive for serum WHV DNA, WHsAg, and WHeAg, and negative for anti-WHs and anti-WHe antibodies. Woodchucks were allocated to three and two groups in the mono or combination treatment studies, respectively (**Figure 1**; **Supplementary Table 1**), and randomized within blocks (i.e., sex) and factors (i.e., body weight). If needed, animals were moved between the groups based on other parameters, including pretreatment serum WHV DNA and WHsAg loads and liver enzyme levels, for achieving comparable ranges within each group. Animal research staff was not blinded in regard to treatment administration and animal procedures. However, laboratory research staff was blinded to animal group/treatment allocation during sample processing and analysis. Woodchucks undergoing monotreatment were orally treated every other day (QOD) for 24 weeks with vehicle (Group 1; n=5) or RG7854 (30/120 or 60 mg/kg) (Group 2; n=5 or Group 3; n=6) and then followed for additional 11 weeks until the end of the study (EOS) at week 35. The RG7854 starting doses of 30

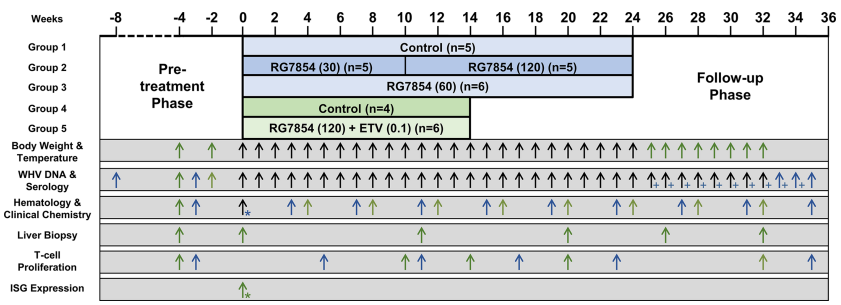

FIGURE 1 | Study design. In the monotreatment study (▬), woodchucks were dosed with vehicle or RG7854 (30/120 or 60 mg/kg orally, QOD) for 24 weeks and followed for another 11 weeks. Starting in week 10 of treatment, the 30 mg/kg dose was increased to 120 mg/kg in Group 2 and administered for 14 weeks. In the combination treatment study (▬), woodchucks were dosed with vehicle or RG7854 (120 mg/kg orally, QOD) together with ETV (0.1 mg/kg orally, once daily) for 14 weeks and followed for another 18 weeks. Arrows indicate the time of measurements for the specific parameters listed. Black arrows indicate parameters measured in both studies. * Pre-and post-dose samples were collected. + Only serum WHV DNA was measured.

and 60 mg/kg were selected to match the proportional increase in plasma exposure of the active form of the TLR7 agonist RO7011785 in WHV-naïve woodchucks after administration of single, oral doses ranging from 3 to 30 mg/kg (data not shown). Compared to the efficacious range of RG7854 determined previously in an HBV mouse model (57), both starting doses represented a targeted 2-3-fold higher plasma exposure in chronic WHV carrier woodchucks to account for differences in metabolic size (58). However, due to the absence of immediate antiviral effects after treatment initiation, the RG7854 dose in Group 2 was increased from 30 to 120 mg/kg starting in week 10 and continuing for additional 14 weeks of treatment. Woodchucks undergoing combination treatment were orally treated QOD for 14 weeks with vehicle (Group 4; n= 4) or RG7854 (120 mg/kg) together with daily ETV (0.1 mg/kg) (Group 5; n=6) and then followed for additional 18 weeks until the EOS at week 32. Thus, woodchucks of Groups 2 and 5 underwent high dose (120 mg/kg) RG7854 mono or combination treatment for 14 weeks and animals of Group 3 received intermediate dose (60 mg/kg) RG7854 monotreatment for 24 weeks. A control group undergoing ETV monotreatment was not included in this study due to the paucity of woodchucks with chronic WHV infection.

Drug Safety and Mortality

Clinical observations were made daily, while measurements of body weight and temperature were obtained weekly. Hematology and clinical chemistry markers were determined at regular intervals. Mortality associated with RG7854 and ETV was not observed. In the monotreatment study, woodchucks F7991 (Group 1), F7996 (Group 2), and F8226 (Group 3) were euthanized during treatment in weeks 18, 7, or 17, respectively. Woodchuck F7934 (Group 1) was found dead and M7979 (Group 2) was euthanized during the follow-up in weeks 25 or 26, respectively. Scheduled euthanasia or death were due to the development of end-stage HCC in all cases. In the combination treatment study, woodchuck F5008 died due to internal hemorrhage after the liver biopsy procedure in week 11.

Animals and Procedures

Woodchucks were pair-housed in stainless-steel cages with solid floors and aspen contact bedding. Animals received aspen woodblocks for enrichment. The temperature was maintained at 65 to 70°F (approximately 18 to 21°C) and lights were on a 12/12-hour cycle. Woodchucks were fed laboratory chow formulated and specifically pelleted for woodchucks (Dyets) and had access to tap water *ad libitum*. Woodchucks were not fasted for any procedure and all procedures were conducted during the light cycle. Procedures involving body weight and temperature measurements, blood collection, liver biopsy, liver ultrasonography, and euthanasia were performed under isoflurane inhalation and/or ketamine/xylazine intramuscular injection anesthesia. Blood samples for testing serology, hematology, and clinical chemistry were obtained *via* femoral venipuncture. Liver tissues for assessing WHV nucleic acids and histology were collected by ultrasound-guided, percutaneous liver biopsy. Blood and liver tissues were always obtained prior to drug and vehicle administration.

Serum WHV Markers

Serum WHV DNA load was assayed quantitatively by slot-blot hybridization and PCR (lower limit of detection (LLOD): 600 WHV genomic equivalents (ge) or copy numbers per mL serum), as described previously (58, 59). Serum WHsAg load was assayed quantitatively by ELISA (LLOD: 5 ng WHsAg/mL serum) comparable to the assay described previously (59, 60). Serum WHeAg load was assayed qualitatively using a cross-reactive ELISA (DiaSorin, Minneapolis, MN) by following the manufacturer's protocol. Results were obtained as an optical density read out, and a value of ≤0.060 optical density units (ODU) indicated absence of WHeAg. Serum anti-WHs antibodies were assayed quantitatively using an established enzyme immunoassay (LLOD: 100 standard units (StdU)/mL serum), as described previously (59, 60). Serum anti-WHe antibodies were assayed qualitatively using a cross-reactive ELISA (DiaSorin) by following the manufacturer's protocol. An ODU value of ≥2.33 (i.e., sample ODU value at pretreatment (T0) minus sample ODU value in a given study week) indicated presence of anti-WHe antibodies.

Liver WHV Markers

Intrahepatic levels of WHV DNA replicative intermediates (RI) and cccDNA were assayed quantitatively by Southern blot hybridization, while intrahepatic WHV RNA levels, consisting of pre-genomic and surface RNA molecules, were determined quantitatively by Northern blot hybridization, as described previously (58, 59). Woodchuck β-actin was used for the normalization of WHV nucleic acid concentrations. Both hybridization assays provided results spanning up to >1 and >2 orders of magnitude of detection for WHV RNA and WHV cccDNA or WHV DNA RI molecules, respectively (LLOD: 2 pg WHV DNA or WHV RNA/μg cellular nucleic acids).

Hematology and Clinical Chemistry Markers

Blood samples for hematology and serum clinical chemistry were analyzed at the Animal Health Diagnostic Center of Cornell University (Ithaca, NY) using parameters established for woodchucks (61, 62). Hematology markers included white blood cells, segmented neutrophils, banded neutrophils, lymphocytes, monocytes, eosinophils, basophils, red blood cells, hemoglobin, hematocrit, mean cell volume, mean cell hemoglobin, mean cell hemoglobin concentration, red cell distribution width, platelet count, and mean platelet volume. Clinical chemistry markers included alkaline phosphatase, alanine aminotransferase (ALT), aspartate aminotransferase (AST), gamma-glutamyl transferase (GGT), sorbitol dehydrogenase (SDH), sodium, potassium, chloride, bicarbonate, anion gap, sodium/potassium ratio, urea, creatinine, calcium, phosphate, magnesium, total protein, albumin, globulin, albumin/globulin ratio, glucose, total bilirubin, direct bilirubin, indirect bilirubin, amylase, cholesterol, creatine kinase, iron, total iron binding capacity, percent saturation, lipemia, hemolysis, and icterus.

Histology

Paraffin-embedded liver tissues were sectioned (5 microns) and stained with hematoxylin and eosin at the Histopathology & Tissue Shared Resource (HTSR) Laboratory of Georgetown University (Washington, DC). Tissue sections were examined by a board-certified pathologist (BVK). Liver disease progression, including portal and sinusoidal hepatitis, bile duct proliferation, steatosis, fibrosis, and necrosis, was assessed *via* criteria developed for woodchuck liver (63, 64), as well as by using the METAVIR scale for scoring human liver.

T-Cell Proliferation

Peripheral blood mononuclear cells (PBMCs) were isolated from whole blood by Ficoll-Paque density gradient centrifugation and cultured in AIM-V medium (Invitrogen/Thermo Fisher Scientific, Waltham, MA) in 96-well opaque plates (Sigma, St. Louis, MO), as described previously (65). PBMCs were stimulated with 0.02% (v/v) DMSO (Sigma, unstimulated medium control), 0.5 μg/mL lipopolysaccharide (LPS; Sigma, no-peptide control), and pools of peptides covering the entire WHV core antigen (WHcAg) or WHsAg (Invitrogen/Thermo Fisher Scientific). Peptides were dissolved in sterile saline for obtaining a final concentration of 10.0 μg/mL of each peptide in 0.02% (v/v) DMSO. T-cell proliferation was determined after five days with the CellTiter Glo One Solution assay (Promega, Madison, WI) by following the manufacturer's protocol. The derived luminescence signal of triplicate cultures was averaged and expressed as a fold-change by dividing the average signal in the presence of stimulator (LPS or WHcAg- or WHsAg-derived peptides) by that in the absence of stimulator (DMSO-containing medium). Results were further represented as a fold-change relative to the pretreatment baseline. A fold-change of ≥2.1 was considered a positive result for WHV-specific T-cell proliferation (66).

IFN-Stimulated Gene Induction

The induction of IFN-stimulated genes (ISGs) in blood was determined by using reverse transcription PCR and woodchuck-specific primers and probes (**Supplementary Table 2**), as described previously (55, 66). In brief, total RNA from whole blood collected in PAXgene blood tubes (Qiagen, Redwood City, CA) was isolated using the PAXgene Blood miRNA kit (Qiagen) with on-column DNase I digestion using RNase-free DNase by following the manufacturer's protocol. Messenger RNA in these samples was then reverse transcribed using oligo(dT) and the High-Capacity cDNA Reverse Transcription kit (Applied Biosystems, Foster City, CA). Expression changes of IFN-induced 17 kDa protein (*ISG15*), IFN-induced guanosine triphosphate-binding protein (*MX1*), 2'-5'-oligoadenylate synthetase 1 (*OAS1*), and IFN-γ induced protein 10 (*CXCL10* or IP-10) were determined on an ABI 7500 Real Time PCR System instrument (Applied Biosystems) by using the TaqMan Gene Expression Master mix (Applied Biosystems). Woodchuck 18S ribosomal RNA expression was used to normalize target gene expression. Transcript levels of ISGs were calculated as a fold-change relative to the pretreatment baseline level using the formula $2^{-\Delta Ct}$. A fold-change of ≥2.1 was considered a positive result for increased transcription (66).

Statistical Analysis

All experimental data was carefully inspected for consistency and completeness before statistical analysis. Values below detectable concentration or assay limit were replaced by either the minimum of all measured values (4 and 3 international units (IU)/L for serum ALT or GGT, respectively) or by the corresponding assay LLOD (600 ge/mL for serum WHV DNA, 5 ng/mL for serum WHsAg, 2 pg/μg for intrahepatic WHV DNA RI, cccDNA, and RNA). Data for serum WHV DNA, WHsAg, and anti-WHs antibodies were transformed to a $\log_{10}$ scale and arithmetically averaged prior to statistical analysis. Whenever appropriate, mean parameters (i.e., body weight and temperature, hematology, clinical chemistry, serum and liver WHV markers, blood host markers, and liver pathology) at each timepoint of the study were compared to the values at pretreatment and/or between the three or two groups undergoing RG7854 mono or RG7854/ETV combination treatment, respectively, using an unpaired Student's *t*-test with equal variance. $P< 0.05$ was considered statistically significant. Sex was not considered a factor in the statistical analysis.

RESULTS

RG7854 Treatment, Alone and Together With ETV, Induced Suppression of Serum Viremia and Antigenemia and Seroconversion in a Subset of Woodchucks

The antiviral efficacy of RG7854 was first evaluated in a dose-finding study in woodchucks with established chronic WHV infection (**Figure 1**). Sixteen woodchucks were assigned to repeat-dose monotreatment with either vehicle (Group 1; n=5) or RG7854 at doses of 30 mg/kg (Group 2; n=5) and 60 mg/kg (Group 3; n=6) for 24 weeks. Since an interim analysis indicated that both RG7854 doses did not induce marked declines in serum WHV markers or elicited antibodies in woodchucks immediately after treatment initiation (**Figures 2**–**4**; **Supplementary Figures 1, 2**), the dose in Group 2 was increased from 30 to 120 mg/kg in week 10 and administered for 14 weeks, while the original 60 mg/kg dose in Group 3 continued for 24 weeks.

In contrast to low dose (30 mg/kg) RG7854, the switch to high dose (120 mg/kg) RG7854 treatment produced a rapid decline in serum WHV DNA, WHsAg, and WHeAg in two of four woodchucks in Group 2 (i.e., F7981 and F8085) within 1-6 weeks (**Figures 2**-**4**; **Supplementary Figures 1, 2**). Both animals achieved a marked reduction in viremia and complete loss of detectable surface and e antigenemia, which was associated with emerging anti-WHs but not anti-WHe antibodies during treatment, and with a notably high anti-WHs antibody titer in F8085 that waned thereafter. The response to intermediate dose (60 mg/kg) RG7854 treatment in Group 3 was more varied, with two of five woodchucks

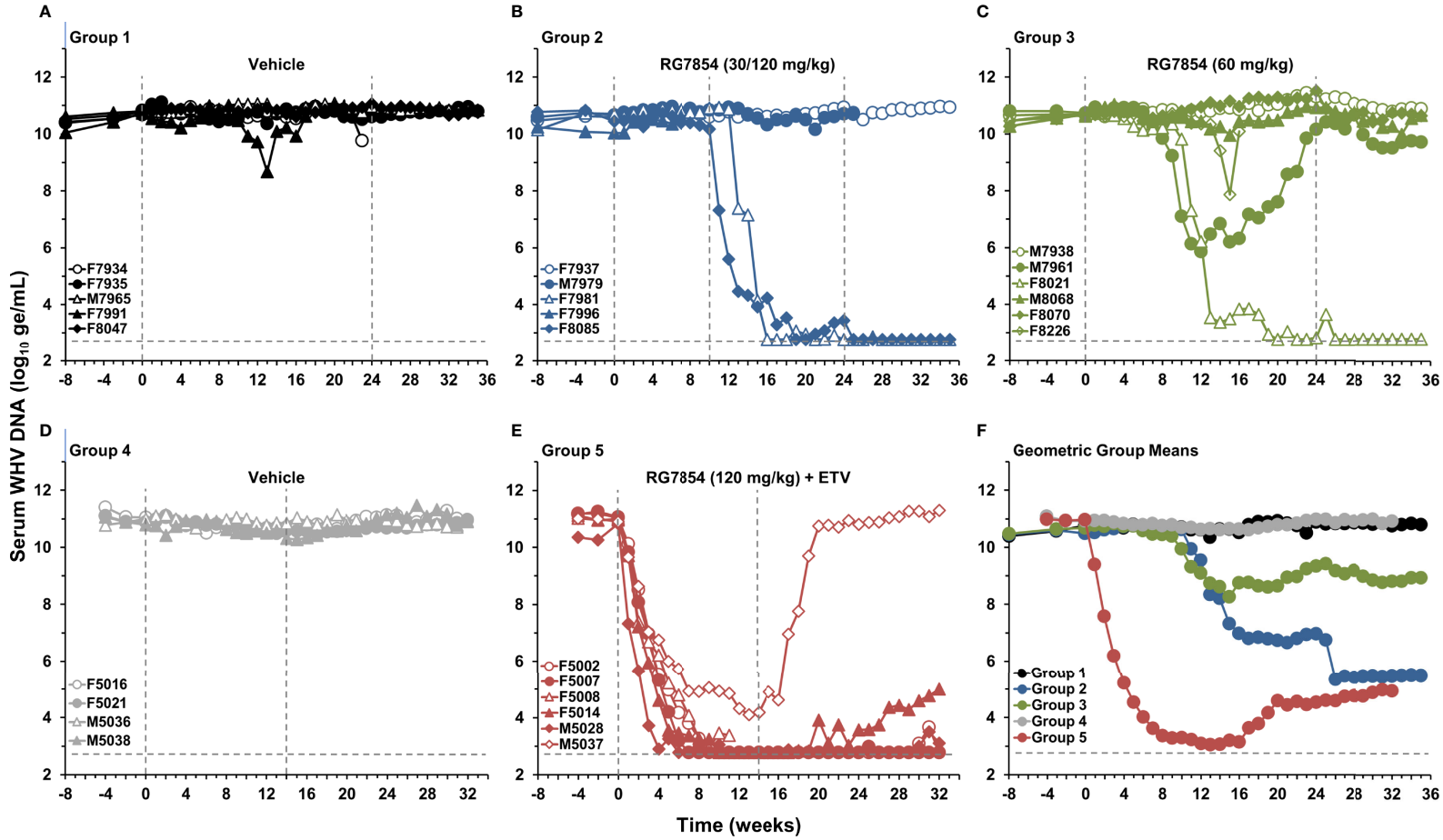

FIGURE 2 | Effect of RG7854, alone and together with ETV, on serum viremia levels. Kinetics of WHV DNA load in individual woodchucks administered **(A)** placebo or RG7854 at doses of **(B)** 30/120 mg/kg or **(C)** 60 mg/kg in the monotreatment study and **(D)** placebo or **(E)** RG7854 at a dose of 120 mg/kg plus ETV in the combination treatment study. **(F)** Geometric group mean WHV DNA loads. The outer vertical dotted lines represent the duration of 24-week monotreatment or 14-week combination treatment, while the inner vertical dotted line represents the switch from 30 to 120 mg/kg RG7854 in Group 2 during week 10 in this and the following figures. The horizontal dotted lines indicate the detection limit for WHV DNA by quantitative polymerase chain reaction (i.e., 600 ge/mL). The geometric mean WHV DNA load in Group 3 was significantly reduced compared to Group 1 at T0 and at week 7 ($P< 0.05$) (Student's *t*-test). Compared to Group 1, the geometric mean WHV DNA load in Group 2 was not significantly different ($P> 0.05$). The geometric mean WHV DNA load in Group 5 was significantly reduced compared to Group 4 during weeks 1-32 ($P< 0.05$). ge, genome equivalents or copy numbers.

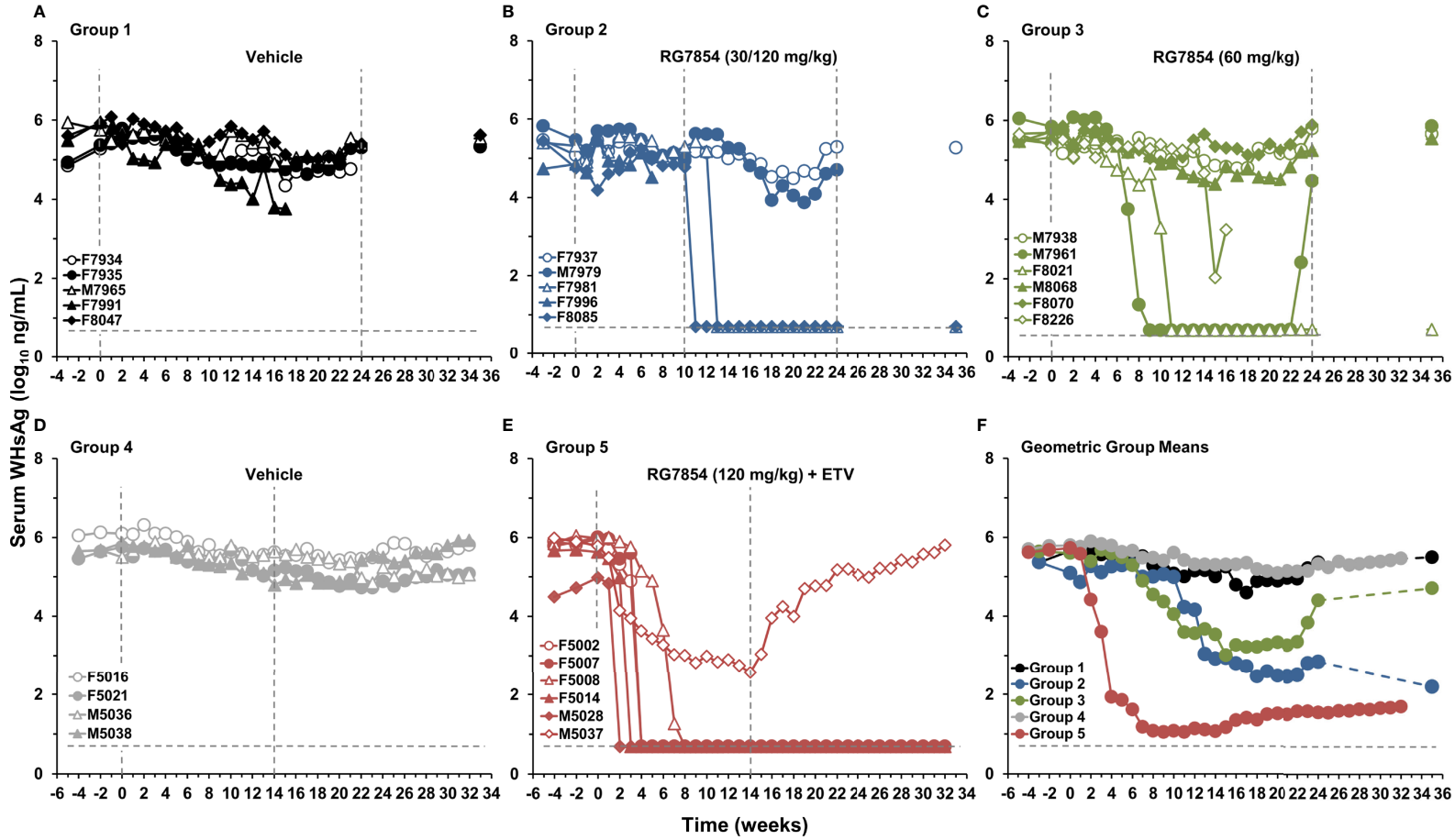

FIGURE 3 | Effect of RG7854, alone and together with ETV, on serum surface antigenemia levels. Kinetics of WHsAg load in individual woodchucks administered **(A)** placebo or RG7854 at doses of **(B)** 30/120 mg/kg or **(C)** 60 mg/kg in the monotreatment study and **(D)** placebo or **(E)** RG7854 at a dose of 120 mg/kg plus ETV in the combination treatment study. **(F)** Geometric group mean WHsAg loads. The horizontal dotted lines indicate the detection limit for WHsAg by quantitative enzyme-linked immunosorbent assay (i.e., 5 ng/mL). The geometric mean WHsAg loads in Group 2 and Group 3 were significantly reduced compared to Group 1 at T0 and at weeks 1, 6, 7, and 8 or at week 15, respectively ($P < 0.05$) (Student's *t*-test). Compared to Group 4, the geometric mean WHsAg load in Group 5 was significantly reduced during weeks 4-32 ($P < 0.05$).

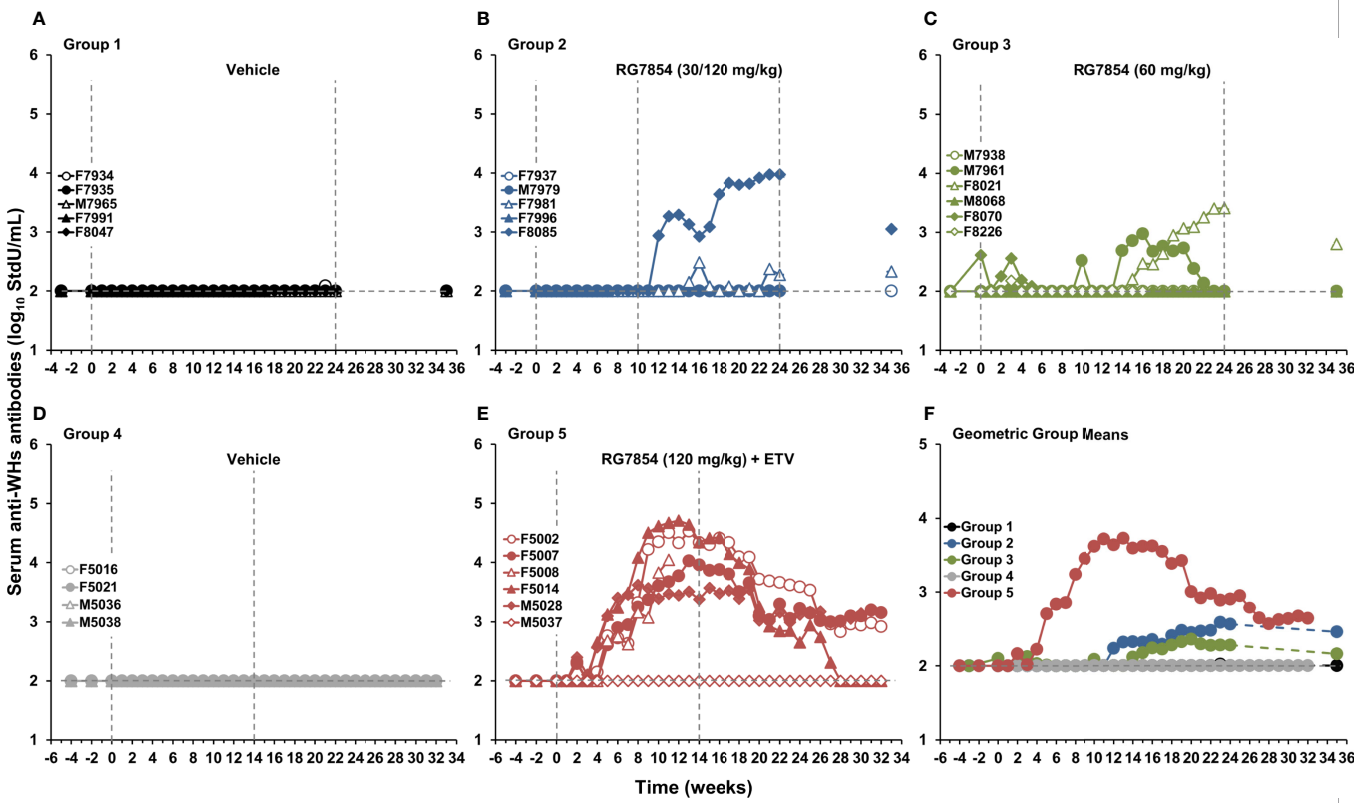

FIGURE 4 | Effect of RG7854 treatment, alone and together with ETV, on the elicitation of serum antibodies to WHsAg. Kinetics of anti-WHs antibody titer in individual woodchucks administered **(A)** placebo or RG7854 at doses of **(B)** 30/120 mg/kg or **(C)** 60 mg/kg in the monotreatment study and **(D)** placebo or **(E)** RG7854 at a dose of 120 mg/kg plus ETV in the combination treatment study. **(F)** Geometric group mean anti-WHs antibody titers. The horizontal dotted lines indicate the detection limit for anti-WHs antibodies by quantitative enzyme immunoassay (i.e., 100 StdU/mL). The geometric mean anti-WHs antibody titers in Group 2 and Group 3 were not significantly different to Group 1 ($P > 0.05$) (Student's *t*-test). Compared to Group 4, the geometric mean anti-WHs antibody titer in Group 5 was significantly increased during weeks 5-27 ($P < 0.05$). StdU, standard units.

displaying a more pronounced antiviral effect, starting 6-10 weeks after treatment initiation. F8021 achieved complete suppression of WHV DNA and loss of WHsAg and WHeAg, and elicited antibodies to both antigens during treatment. M7961 had transient reductions in WHV DNA and WHsAg, with minor changes in WHeAg and a transient induction of anti-WHs but not of anti-WHe antibodies, and experienced a gradual viral rebound towards the EOS that already started during treatment. A comparable antiviral response was not noted for other woodchucks in Groups 2 and 3, and marked changes in WHV markers and antibodies were absent in control animals of Group 1. Compared to Group 1, the declines in serum WHV DNA, WHsAg, and WHeAg loads and the increases in anti-WHs antibody titer and anti-WHe antibody level in Groups 2 and 3 were not significant during most of the study.

Since therapeutic efficacy was observed shortly after the switch to the high RG7854 dose, treatment with the TLR7 agonist at this dose in combination with ETV was subsequently tested in chronic WHV carrier woodchucks (**Figure 1**). Combination treatment with ETV was selected because most therapeutic interventions based on immunomodulation will likely be provided concurrently or as add-on to standard-of-care treatment with NAs. Thus, ten woodchucks were assigned to repeat-dose treatment with either vehicle (Group 4; n=4) or RG7854 (120 mg/kg) together with ETV (0.1 mg/kg) for 14 weeks (Group 5; n=6). The ETV dosage was selected based on another reported study in woodchucks (46).

Similar to high dose (120 mg/kg) RG7854 monotreatment, RG7854/ETV combination treatment produced rapid and marked declines in serum WHV DNA, WHsAg, and WHeAg within 1-5 weeks after initiation in four of five woodchucks in Group 5 (**Figures 2**, **3**; **Supplementary Figure 1**). F5002, F5007, and M5028 accomplished sustained suppression of viremia and loss of surface and e antigenemia, and elicited anti-WHs and anti-WHe antibodies immediately thereafter which persisted throughout the study (**Figure 4**; **Supplementary Figure 2**). Seroconversion was again associated with remarkable high levels of anti-WHs antibodies although titers started to wane at the end of treatment and more so during the follow-up. Anti-WHe levels waned as well but the decline was more gradual. F5014 also showed marked reductions in WHV DNA and WHeAg, loss of WHsAg, and a transient induction of anti-WHs but not of anti-WHe antibodies; however, this woodchuck experienced a relapse in viremia towards the EOS after treatment cessation. The treatment response in these four

animals was clearly different to the less pronounced and always transient declines in viremia and surface and e antigenemia noted for M5037, with absent antibody response to both antigens. Comparable changes in viral markers and antibodies were not present in control animals of Group 4, and the declines in serum WHV DNA, WHsAg, and WHeAg loads and the increase in anti-WHs antibody titer in woodchucks of Group 5 were significant during most of the study.

RG7854 Mono and Combination Treatment Resulted in a SVR in a Comparable Number of Woodchucks

Based on the above observations and for correlative analyses of the RG7854 mono and RG7854/ETV combination treatment responses, response groups were defined as the following: Responders (R) had serum WHV DNA $<10^3$ genomic equivalents (ge)/mL, WHsAg ≤5 ng/mL, and anti-WHs antibodies $>10^3$ standard units (StdU)/mL at the end of treatment. Non-Responders (NR) had minimum WHV DNA $>10^8$ ge/mL, minimum WHsAg $>10^3$ ng/mL, and absent anti-WHs antibodies (≤100 StdU/mL) at the end of treatment. Partial Responders (PR) had WHV DNA and WHsAg loads between Responders and Non-Responders and anti-WHs antibody titers >100 but $<10^3$ StdU/mL at the end of treatment (**Table 1**). This rather stringent definition revealed that F8021 of Group 3 was a Responder to 24-week intermediate RG7854 dose monotreatment, while F7981 and F8085 of Group 2 and M7961 of Group 3 were Partial Responders to 14-week high or 24-week intermediate RG7854 dose monotreatment, respectively. All other animals in both groups were Non-

TABLE 1 | Correlative analyses of RG7854 mono and RG7854/ETV combination treatment responses.

Treatment Group	Treatment	Animal Identification	Treatment Response Group[a]	Sustained Viral Response[b]	Baseline/Max. Decline Serum WHV DNA (log_{10} ge/mL)[c]	Baseline/Max. Decline Serum WHsAg (log_{10} ng/mL)[c]	Baseline/Max. Increase Serum Anti-WHs Antibodies (log_{10} StdU/mL)[d]
1	Vehicle	F7934	ND[††]		10.68/0.91	5.28/0.93	2.00/0.09
		F7935	NR	–	10.83/0.48	5.37/0.74	2.00/0.00
		M7965	NR	–	10.80/0.06	5.76/0.84	2.00/0.00
		F7991	ND[†]		10.73/2.06	5.96/2.20	2.00/0.00
		F8047	NR	–	10.76/0.15	5.93/0.99	2.00/0.00
2	RG7854 (30/120 mg/kg)	F7937	NR	–	10.60/0.10	5.08/0.60	2.00/0.00
		M7979	NR[††]		10.66/0.51	5.47/1.61	2.00/0.00
		F7981	PR	+	10.70/7.92[e]	5.32/4.62[f]	2.00/0.49
		F7996	ND[†]		10.03/0.00	4.85/0.33	2.00/0.00
		F8085	PR	+	10.45/7.67[e]	4.75/4.05[f]	2.00/1.98
3	RG7854 (60 mg/kg)	M7938	NR	–	10.67/0.07	5.42/0.63	2.00/0.00
		M7961	PR	–	10.73/4.87	5.84/5.14[f]	2.00/0.98
		F8021	R	+	10.63/7.85[e]	5.69/4.99[f]	2.00/1.41
		M8068	NR	–	10.68/0.72	5.57/1.18	2.00/0.00
		F8070	NR	–	10.70/0.28	5.72/0.77	2.61/-0.05
		F8226	ND[†]		10.70/2.83	5.36/3.33	2.00/0.18
4	Vehicle	F5016	NR	–	11.06/0.55	6.10/0.74	2.00/0.00
		F5021	NR	–	10.89/0.45	5.75/1.03	2.00/0.00
		M5036	NR	–	10.99/0.31	5.50/0.65	2.00/0.00
		M5038	NR	–	10.79/0.51	5.86/1.07	2.00/0.00
5	RG7854 (120 mg/kg) + ETV (0.1 mg/kg)	F5002	R	+	11.04/8.26[e]	5.97/5.28[f]	2.00/2.53
		F5007	R	+	11.07/8.29[e]	6.01/5.31[f]	2.00/2.03
		F5008	ND[†]		11.00/8.08	5.97/5.28[f]	2.00/2.05
		F5014	R	–	10.96/8.19[e]	5.63/4.93[f]	2.00/2.71
		M5028	R	+	10.83/8.05[e]	4.99/4.29[f]	2.00/1.62
		M5037	NR	–	10.91/6.80	5.79/3.22	2.00/0.00

[a]*Treatment response groups were defined as follows: R, Responders, serum WHV DNA $<10^3$ ge/mL, serum WHsAg ≤5 ng/mL, and anti-WHs antibodies $>10^3$ StdU/mL at the end of treatment; NR, Non-Responders, minimum serum WHV DNA $>10^8$ ge/mL, minimum serum WHsAg $>10^3$ ng/mL, and absent anti-WHs antibodies (≤100 StdU/mL) at the end of treatment; PR, Partial Responders, serum WHV DNA and WHsAg loads between Responders and Non-Responders and anti-WHs antibody titer >100 but $<10^3$ StdU/mL at the end of treatment.*

[b]*Sustained viral response was defined as serum WHV DNA $<10^3$ ge/mL, serum WHsAg ≤5 ng/mL, and anti-WHs antibodies present at the EOS.*

[c]*The maximum reductions in serum WHV DNA and WHsAg during treatment and/or follow-up were calculated relative to the week 0 (T0) timepoint (pretreatment baseline).*

[d]*The maximum increase in serum anti-WHs antibodies during treatment and/or follow-up was calculated relative to the week 0 (T0) timepoint (pretreatment baseline).*

[e]*Viremia in animals F7981, F8021, F8085, F5002, F5007, F5014, and M5028 was < lower limit of detection (LLOD; 600 ge/mL) at one or more timepoints; the LLOD was used to calculate the maximum WHV DNA decline in these animals.*

[f]*Antigenemia in animals M7961, F7981, F8021, F8085, F5002, F5007, F5008, F5014, and M5028 was < LLOD (5 ng/mL) at one or more timepoints; the LLOD was used to calculate the maximum WHsAg decline in these animals.*

[†]*Treatment response group was not determined (ND) as animal died during treatment: F7991 (Group 1), F7996 (Group 2), and F8226 (Group 3) were euthanized in weeks 18, 7, or 17, respectively, due to symptoms associated with end-stage HCC. F5008 (Group 5) died in week 11 due to liver biopsy-related hemorrhage.*

[††]*Treatment response group was ND as animal died during the follow-up: F7934 (Group 1) was found dead in week 25, cause of death was attributed to terminal HCC. M7979 (Group 2) was euthanized in week 26 due to symptoms associated with end-stage HCC.*

Responders. This definition further revealed that F5002, F5007, F5014, and M5028 of Group 5 were Responders to 14-week high RG7854 dose/ETV combination treatment, while M5037 was a Non-Responder.

For a further delineation of the RG7854 mono and combination treatment responses in regard to durability, a SVR was defined as serum WHV DNA $<10^3$ ge/mL, WHsAg ≤5 ng/mL, and anti-WHs antibodies present at the EOS (**Table 1**). Based on WHV DNA assayed between the end of monotreatment and the EOS and WHsAg and anti-WHs antibodies measured at the EOS in woodchucks of Groups 1-3, this suggested that a SVR was achieved in F7981, F8021, and F8085 of Groups 2 and 3 at the end of the study in week 35. Based on the viremia, antigenemia, and antibody data obtained between the end of combination treatment and the EOS, this further indicated that a SVR was accomplished in F5002, F5007, and M5028 of Group 5 at the end of the study in week 32. Thus, 1 out of 5 surviving woodchucks in Group 3 (20%), 2 out of 3 surviving animals in Group 2 (67%), and 3 out of 5 surviving animals in Group 5 (60%) achieved a SVR. Although a trend towards higher SVR percentage for combination over mono treatment (38% vs. 60%) may exist, the comparable percentage between animals receiving the high RG7854 dose during mono and combination treatment (67% vs. 60%) and the equal number of 3 woodchucks with SVR each in the mono and combination treatment regimens suggested no apparent added benefit of ETV in regard to the observed therapeutic efficacy.

RG7854/ETV Combination Treatment Produced Sustained Suppression of Viral Replication in the Liver of Woodchucks With SVR

For further confirming the SVR mediated by RG7854/ETV combination treatment, changes in intrahepatic WHV nucleic acids were assayed in sequential liver biopsies obtained during the study (**Figure 5**). Consistent with the effects on serum viremia and antigenemia, Responders in Group 5 had markedly reduced WHV DNA RI, cccDNA, and RNA loads in liver as early as week 11 of treatment. All WHV nucleic acids became undetectable six weeks after drug withdrawal in F5002, F5007, and M5028 with SVR, and stayed absent until the EOS. F5014, a Responder without SVR, experienced reductions in these viral markers during and following treatment as well, but the declines were more gradual and WHV nucleic acids relapsed at the EOS, as also observed for serum viremia. M5037, a Non-Responder, had the least decline in viral markers during treatment and WHV nucleic acids returned to baseline level after treatment cessation. Control animals in Group 4 had no comparable changes in intrahepatic WHV markers, and the declines in WHV DNA RI, cccDNA, and RNA loads in woodchucks of Group 5 were significant during most of the study.

The First Dose of RG7854/ETV Combination Treatment Induced ISGs in the Periphery of Woodchucks With SVR

In line with previous studies on TLR7 agonism (41, 46), RG7854 induced the transcription of ISGs and T-cell attractant chemokines in blood of woodchucks after the first dose in combination with ETV (**Figure 6**). While peak expression of *ISG15*, *MX1*, *OAS1*, and *CXCL10* was observed between 6- and 12-hours post-dose in most animals of Group 5, the transcription magnitude was quite varied. When compared to M5037, the sole Non-Responder, Responders and woodchucks with SVR often had marked expression changes in all four genes. This correlation was only observed partially for F5002 with a SVR, which presented with increased transcription of *ISG15* and *CXCL10* but not of *MX1* and *OAS1*. Since these expression changes were absent in control animals of Group 4 and typically are not observed during ETV monotreatment (46, 67), this indicated on-target activation of TLR7 in woodchucks by RG7854.

RG7854/ETV Combination Treatment Elicited Virus-Specific T-Cell Responses in the Periphery of Woodchucks With SVR

Changes in WHV-specific T-cell responses during RG7854 mono and combination treatment were assessed by stimulating PBMCs of woodchucks with peptides covering the entire WHcAg or WHsAg (**Figures 7**, **8**). RG7854 monotreatment induced transient WHcAg- and WHsAg-specific T-cell responses during treatment only in M7961 of Group 3, a Partial Responder, but not in other Partial Responders, Responders, or woodchucks with SVR in Groups 2 and 3, although an increasing trend to such responses was noted. This pattern was clearly different to RG7854/ETV treatment, as F5002, F5007, F5014, and M5028 of Group 5, all Responders and woodchucks with SVR, except for F5014, presented with pronounced and sometimes long-lasting WHV-specific T-cell responses during treatment that declined after drug withdrawal. Induction and augmentation of WHsAg-specific T-cell responses in these animals apparently correlated with absent surface antigenemia and detectable anti-WHs antibodies in serum (**Figures 3**, **4**). In M5037, the sole Non-Responder, absent WHsAg-specific T-cell response correlated with reduced albeit detectable surface antigen and absent anti-WHs antibodies. Stimulation of PBMCs with LPS as a no-peptide control revealed that the general cell proliferation in woodchucks was not affected by RG7854 mono or combination treatment (**Supplementary Figure 3**). Since ETV monotreatment does not significantly modify cellular responses in woodchucks (67), these results indicated that the inclusion of the NA into the treatment regimen facilitated an enhanced potential of WHV-specific T-cell responses by RG7854.

RG7854 Treatment, Alone and Together With ETV, Was Safe in Woodchucks

The RG7854 mono and combination treatment regimens were well-tolerated by woodchucks, and there were no signs of overt

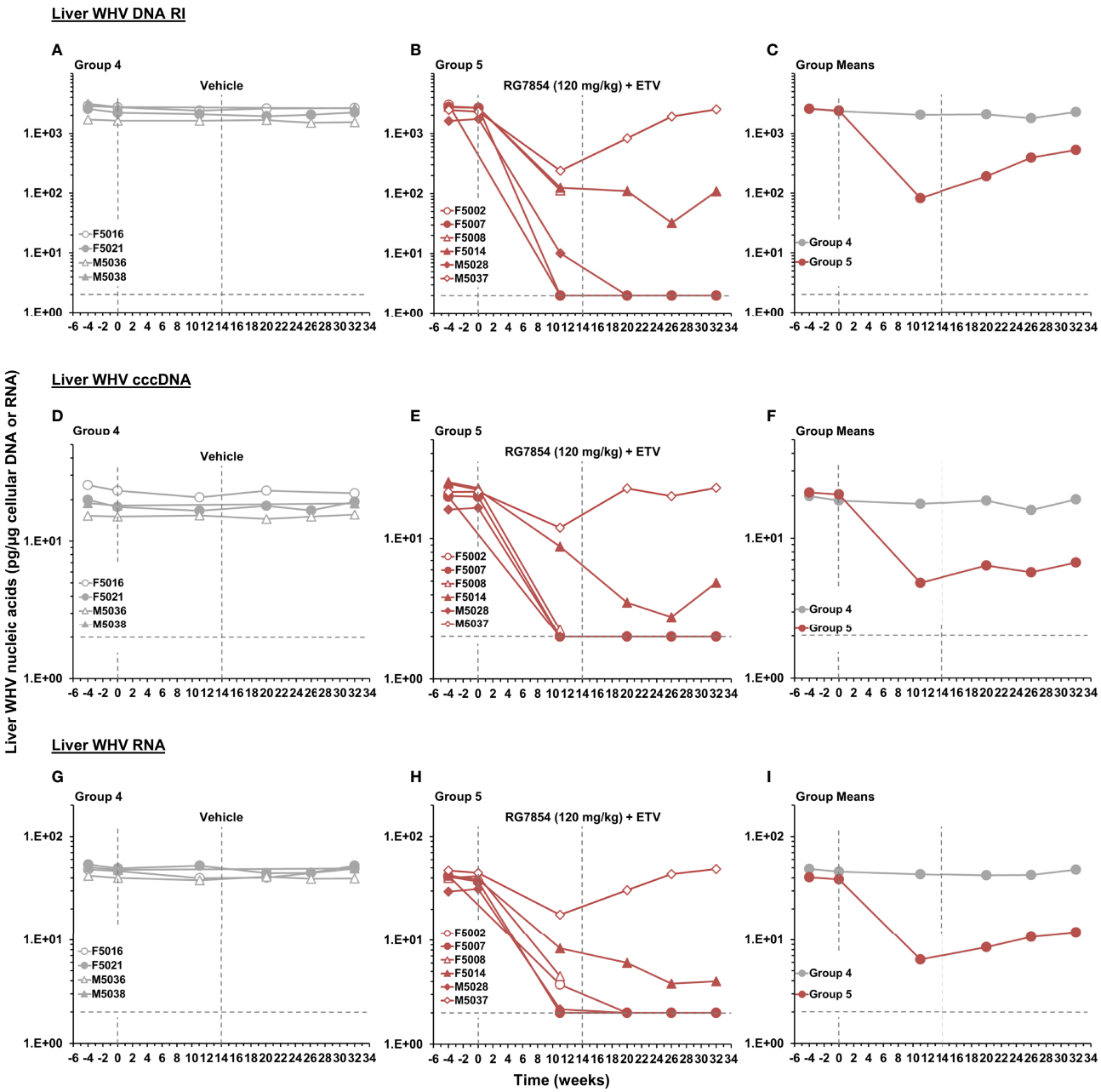

FIGURE 5 | Effect of RG7854 together with ETV on liver viremia levels. Kinetics of WHV DNA RI, cccDNA, and RNA loads in individual woodchucks administered **(A, D, G)** placebo or **(B, E, H)** RG7854 at a dose of 120 mg/kg plus ETV in the combination treatment study. **(C, F, I)** Group mean WHV nucleic acids. The vertical dotted lines represent the duration of 14-week combination treatment. The horizontal dotted lines indicate the detection limit for WHV nucleic acids by quantitative Southern and Northern blot hybridization (i.e., 2 pg/µg cellular DNA or RNA). The mean WHV DNA RI, cccDNA, and RNA loads in Group 5 were significantly reduced compared to Group 4 at weeks 11, 20 and 32, at weeks 11 and 32, or at weeks 11, 20, and 32, respectively ($P < 0.05$) (Student's *t*-test).

toxicity based on clinical observations, body weights and temperatures, most hematology and clinical chemistry markers, and necropsy observations. A trend to lower numbers of segmented neutrophils and significantly reduced numbers of platelets were noted in woodchucks of Group 2, especially after the switch to high dose RG7854 treatment, but neutropenia and thrombocytopenia reversed after drug withdrawal (data not shown). Likewise, all animals in Group 5 experienced significant neutropenia and thrombocytopenia during RG7854/ETV combination treatment that reversed immediately after treatment cessation or during treatment, respectively (data not shown).

In regard to liver enzymes, F7996 of Group 2 and F8226 of Group 3 had transiently elevated levels of ALT and AST during RG7854 monotreatment, but the rises were comparable to F7991

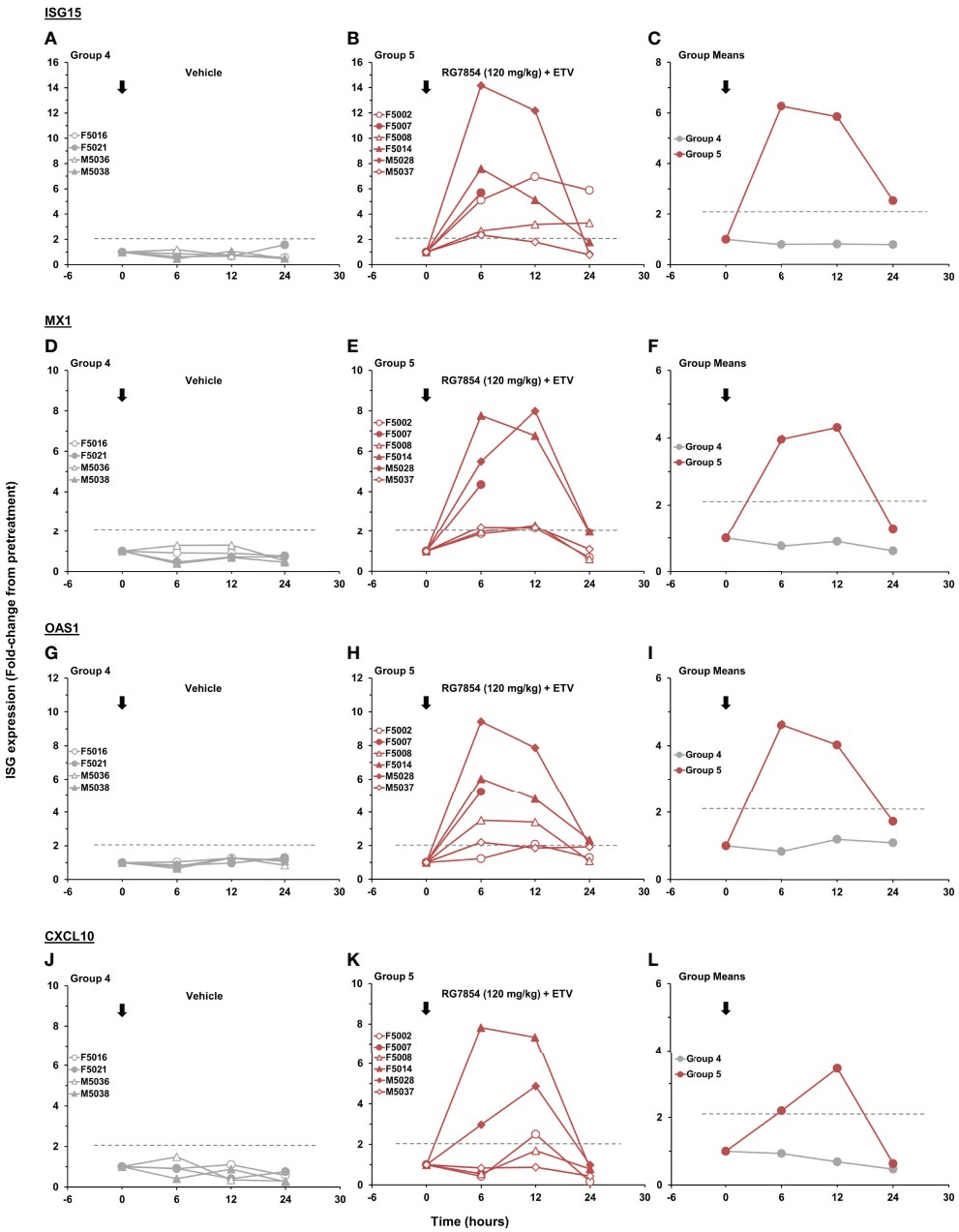

FIGURE 6 | Effect of the first dose of RG7854 together with ETV on peripheral ISG transcription. Kinetics of *ISG15*, *MX1*, *OAS1*, and *CXCL10* gene expression in individual woodchucks prior to (0 hours) and 6-, 12-, and 24-hours post administration of the first dose of **(A, D, G, J)** placebo or **(B, E, H, K)** RG7854 at 120 mg/kg plus ETV in the combination treatment study. **(C, F, I, L)** Group mean ISG transcription levels. The horizontal dotted lines indicate the cutoff for positive gene expression (i.e., ≥2.1-fold increase from the pretreatment baseline). The mean transcription levels of *ISG15*, *MX1*, and *OAS1* in Group 5 were significantly increased compared to Group 4 at 6 and 12 hours, at 6 hours, or at 6 hours, respectively ($P < 0.05$) (Student's *t*-test). The mean *CXCL10* transcription level in Group 5 was not significantly different to Group 4 ($P > 0.05$).

of Group 1 around the initiation of placebo treatment (**Figure 9** and **Supplementary Figure 4**). The transaminase increases appeared unrelated to RG7854, as they occurred during the progression to end-stage HCC and in parallel to rising GGT levels (**Supplementary Figure 5**), leading to the scheduled euthanasia of these three animals. Other woodchucks in Groups 1 and 3 had gradual increases in ALT, AST, and GGT levels towards the EOS, most likely due to the progression of WHV-induced liver disease. In contrast, F5002, F5007, and M5028 of Group 5 with SVR presented with varied and sometimes marked increases in transaminases during RG7854/ETV combination treatment, in addition to elevations in SDH

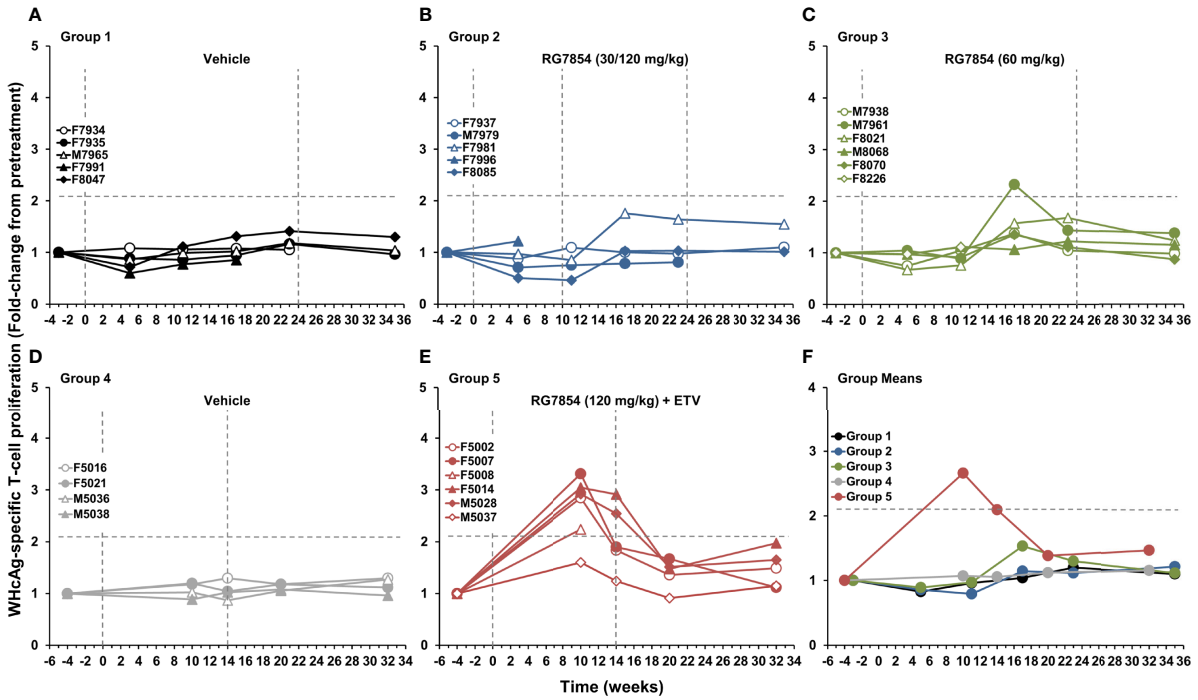

FIGURE 7 | Effect of RG7854, alone and together with ETV, on peripheral WHcAg-specific T-cell response. Kinetics of PBMC proliferation to stimulation with WHcAg-derived peptides of individual woodchucks administered **(A)** placebo or RG7854 at doses of **(B)** 30/120 mg/kg or **(C)** 60 mg/kg in the monotreatment study and **(D)** placebo or **(E)** RG7854 at a dose of 120 mg/kg plus ETV in the combination treatment study. **(F)** Group mean WHcAg-specific T-cell responses. The horizontal dotted lines indicate the cutoff for positive PBMC proliferation (i.e., ≥2.1-fold-change from the pretreatment baseline). The mean WHcAg-specific T-cell response in Groups 2 and 3 was not significantly different to Group 1 ($P > 0.05$) (Student's *t*-test). The mean WHcAg-specific T-cell response in Group 5 was significantly increased compared to Group 4 at weeks 10 and 14 ($P < 0.05$).

level (**Supplementary Figure 6**). Elevated liver enzymes coincided with the reductions and subsequent undetectability of serum viremia and antigenemia in these animals, but increases reversed thereafter and normalized during treatment or shortly after drug withdrawal. Furthermore, transient elevations in liver inflammation based on portal and sinusoidal hepatitis scores (**Supplementary Figure 7**) correlated temporally with these liver enzyme increases in woodchucks of Group 5 with SVR, but were also present in F5014, a Responder without SVR, and in M5037, a Non-Responder, albeit to a lesser degree. The rises in ALT, AST, and SDH or liver inflammation, respectively, were comparable to the elevations noted in M5036 and M5038 of Group 4 before the initiation of placebo treatment. Although liver enzyme increases in Group 5 were not significantly different to Group 4, these results suggested that, in contrast to RG7854 monotreatment, the SVR mediated by RG7854/ETV combination treatment was associated with transiently modulated liver enzymes (and likely liver inflammation) in individual woodchucks.

DISCUSSION

RG7854, an oral double prodrug of the TLR7-specific agonist RO7011785, is developed by F. Hoffmann-La Roche for increasing the HBV cure rate in patients with CHB by immunomodulation *via* TLR7 agonism. The prodrug approach is predicted to widen the therapeutic window of the agonist and to improve its overall tolerability by enhancing bioavailability and limiting intolerability of RO7011785 due to inadvertent TLR7 activation in the gastrointestinal tract (56). For testing therapeutic efficacy, host immune response, and safety, RG7854 was first evaluated in a dose-finding study in woodchucks with chronic WHV infection. Intermediate (60 mg/kg) and high (120 mg/kg) RG7854 dose administration for 24 or 14 weeks, respectively, produced dose-dependent antiviral effects and resulted in a SVR in a total of 3 out of 8 surviving woodchucks. Since these animals seroconverted to anti-WHs antibodies during treatment and WHV DNA and WHsAg remained undetectable at the EOS in week 35, this suggested that a functional cure was induced by RG7854 monotreatment. The SVR achieved in woodchucks is comparable to the durable antiviral effect in an HBV mouse model in which RG7854 dose-dependently reduced the levels of HBV DNA and HBsAg and promoted the emergence of anti-HBs antibodies (57). Because most immunotherapeutic approaches for CHB will be provided to patients on top of standard-of-care with NAs, RG7854 was subsequently evaluated together with ETV in chronic WHV carrier woodchucks. High (120 mg/kg) RG7854 dose administration for 14 weeks in combination with ETV

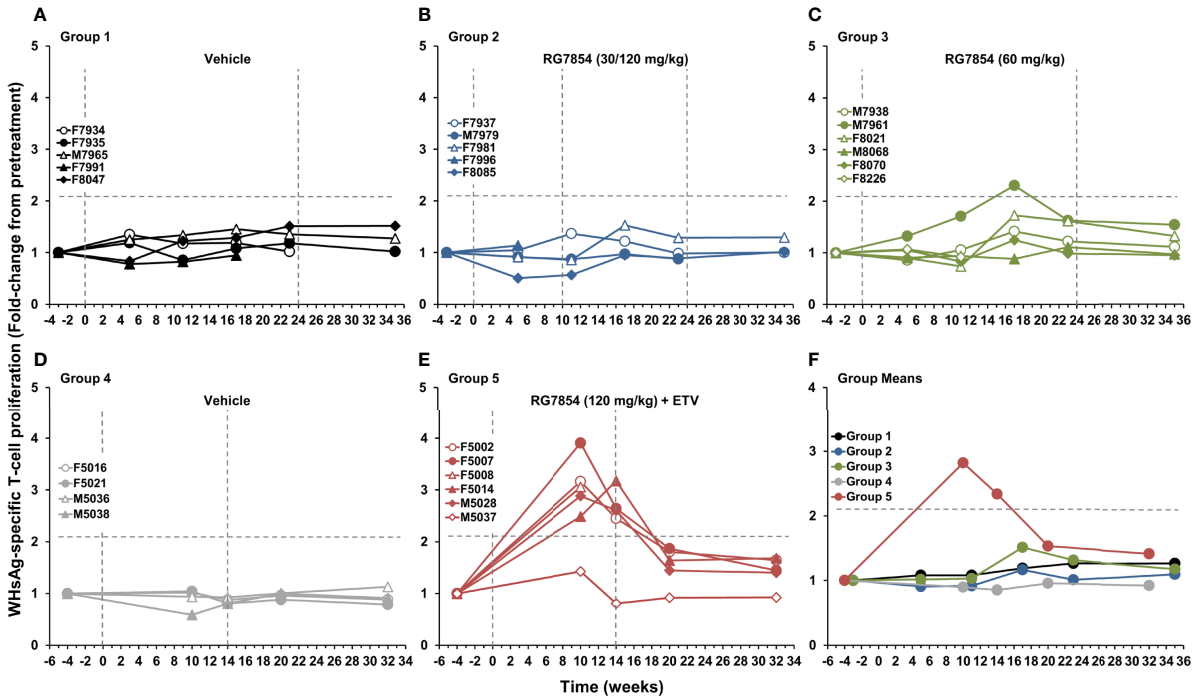

FIGURE 8 | Effect of RG7854, alone and together with ETV, on peripheral WHsAg-specific T-cell response. Kinetics of PBMC proliferation to stimulation with WHsAg-derived peptides of individual woodchucks administered **(A)** placebo or RG7854 at doses of **(B)** 30/120 mg/kg or **(C)** 60 mg/kg in the monotreatment study and **(D)** placebo or **(E)** RG7854 at a dose of 120 mg/kg plus ETV in the combination treatment study. **(F)** Group mean WHsAg-specific T-cell responses. The horizontal dotted lines indicate the cutoff for positive PBMC proliferation (i.e., ≥2.1-fold-change from the pretreatment baseline). The mean WHsAg-specific T-cell response in Groups 2 and 3 was not significantly different to Group 1 ($P > 0.05$) (Student's *t*-test). The mean WHsAg-specific T-cell response in Group 5 was significantly increased compared to Group 4 at weeks 10 and 14 ($P < 0.05$).

mediated a SVR in 3 out of surviving 5 woodchucks at the EOS in week 32. Based on equal animal numbers with functional cure after RG7854 mono and combination treatment, this indicated that concurrent NA administration did not further increase the therapeutic efficacy of the TLR7 agonist. The SVR in animals undergoing RG7854 combination treatment, including undetectable viral cccDNA in the liver, correlated with the development of innate and adaptive immunity, as determined by the induction of important ISGs at treatment initiation and the proliferation of virus-specific T-cells and production of high-titer, virus-neutralizing antibodies by plasma cells during treatment. Since suppression of WHV replication after initiation of high dose RG7854 mono and combination treatment occurred within 1-6 weeks, and in absence of a ETV monotreatment control group, the contribution of the NA to the therapeutic efficacy could not be differentiated from that of the TLR7 agonist but ETV administration was associated with more robust T- and B-cell responses, as well as transient elevations in liver enzymes and inflammation in some but not all woodchucks.

The SVR produced by RG7854, alone and together with ETV, is clearly different to the antiviral response typically obtained with NAs in woodchucks during comparable treatment durations (48). Although ETV monotreatment was not included as a control in the current study, studies have shown that the ETV-mediated antiviral effect in woodchucks using comparable dosage and treatment durations is transient and that viral relapse occurs after treatment cessation (59, 67), indicating that WHV suppression is dependent on the continued presence of this NA. ETV treatment can modulate WHsAg and WHeAg loads in woodchucks, but similar to patients with CHB undergoing NA treatment (8), it does not mediate loss of these antigens nor induces seroconversion to anti-WHs antibodies (46, 59, 67). The reason for the apparent inability of ETV to enhance the antiviral effect of RG7854 is unknown, but it can be speculated that the immune-mediated WHV suppression by the TLR7 agonist in Responders is rapid and sufficient and cannot be improved by further reduction of mainly viremia levels during parallel NA treatment. This finding is in agreement with the antiviral effect in the above HBV mouse model in which the addition of ETV also did not mediate a greater HBsAg decline than RG7854 alone (68). Since woodchucks are outbred, it can further be speculated that, in addition to genetic factors, Partial Responders and Non-Responders to RG7854 mono and combination treatment developed more severe immunodeficiencies during CHB progression which could not be overcome during the 14- to 24-week treatment duration. Importantly, continuous exposure to viral surface antigen in patients and woodchucks with CHB are implicated in the immunologic tolerance against HBV and WHV at the level of B- and T-cells (3, 14, 29, 30, 48, 69). Future

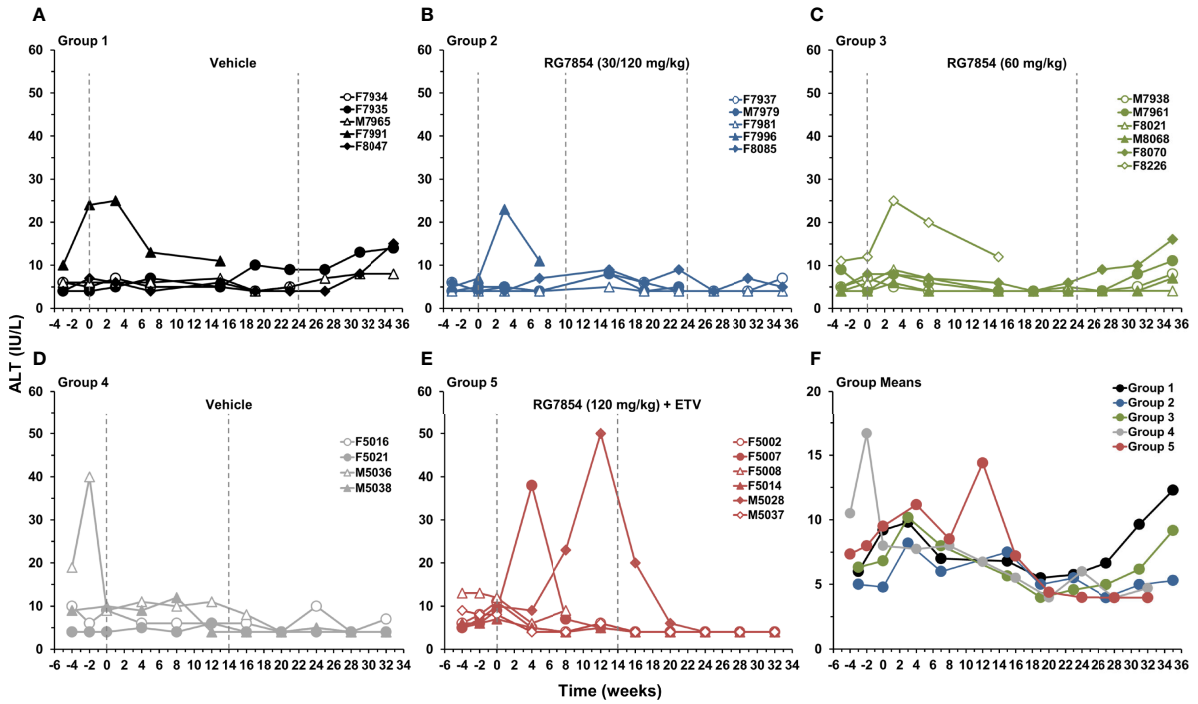

FIGURE 9 | Effect of RG7854, alone and together with ETV, on serum ALT. Kinetics of ALT level in individual woodchucks administered **(A)** placebo or RG7854 at doses of **(B)** 30/120 mg/kg or **(C)** 60 mg/kg in the monotreatment study and **(D)** placebo or **(E)** RG7854 at a dose of 120 mg/kg plus ETV in the combination treatment study. **(F)** Group mean ALT levels. The mean ALT level in Group 2 was significantly reduced compared to Group 1 at week 35 ($P < 0.05$) (Student's *t*-test). The mean ALT level in Group 5 was not significantly different to Group 4 ($P > 0.05$). IU, international units.

preclinical studies could assess if the therapeutic efficacy of RG7854 is augmentable by administering the TLR7 agonist on top of (prolonged) NA treatment for modelling the most likely treatment scenario in patients. In addition, targeting steps in the HBV lifecycle other than DNA synthesis by the viral polymerase may increase the therapeutic efficacy of RG7854, as indicated in the above HBV mouse model in which parallel treatment with RO7049389, a capsid assembly modulator, produced an antiviral effect that was superior over monotreatment with either compound (68).

Activation of a type-I IFN response in APCs by TLR7 agonists resulting in the production of antiviral cytokines is expected to inhibit HBV replication within hepatocytes by a non-cytolytic mechanism (39). Since assays for the measurement of serum IFN-α were not available, the pharmacodynamic response of woodchucks to the initial RG7854/ETV dose was tested by the IFN-α dependent expression of innate immune genes in blood of these animals. The three ISGs with antiviral effector functions (*ISG15*, *OAS1*, and *MX1*) and the one T-cell-attractant chemokine tested (*CXCL10*) were also recently evaluated in mice and woodchucks during TLR7 agonism (41, 46, 57). Comparable to these studies, ISG and chemokine induction in woodchucks was consistent with TLR7 activation by RG7854 and appeared to correlate partially with the subsequent SVR observed in Responders. Notably, the magnitude of ISG and chemokine induction in woodchucks was similar to those obtained with RG7854 in healthy volunteers at well-tolerated doses of 100 mg or higher, including a high individual variability (56).

Although not determined directly, the transient but sometimes pronounced elevations in liver enzymes and inflammation in Responders to RG7854/ETV combination treatment may indicate that a cytolytic mechanism is further involved in the immune-mediated WHV suppression. Besides antiviral cytokines, the cytotoxic activity of NK- and T-cells during TLR7 agonism were reported to be responsible for the therapeutic efficacy achieved with GS-9620 in woodchucks (41). These predicted mechanisms are supported by enhanced cytokine production of T-cells and increased activation and function of NK-cells in blood of patients with NA-suppressed HBV replication who received add-on GS-9620 treatment (45). Importantly, transient alterations in transaminases during SVR mediated by TLR7 agonism in woodchucks (41, 46) are also present in patients resolving chronic HBV infection while undergoing NA treatment (70). Thus, albeit hepatic flares are typically seen as a clinical perturbation, temporary elevations in liver enzymes (and inflammation) could also be considered as direct evidence for the antiviral activity of TLR7 agonists rather than an unwanted side effect (71).

From the study in the aforementioned HBV mouse model it is hypothesized that RG7854 stimulates TLR7 in pDCs within spleen and lymph nodes but not in the gastrointestinal tract, and that such activated cells prime T- and B-cells for generating an effective immune response against HBV (57). For determining

if RG7854-treated woodchucks developed a functional T-cell response, WHV-specific PBMC proliferation was tested longitudinally. In agreement with the recovery of HBV core and polymerase specific T-cells in patients after exposure to low antigen levels and subsequent control of viral replication mediated by NA treatment (72, 73), a WHcAg-specific T-cell response emerged especially in Responders to RG7854/ETV combination treatment. While HBsAg-specific T-cells are usually not retrieved in these patients (73), the recovery of WHsAg-specific T-cells in Responders could indicate that woodchucks with CHB still possess residual, quiescent T-cells directed against this viral antigen similar to young patients with CHB (74), and as expected for self or neoself-reactive T cells. Since WHV-specific T-cells were detected around the time of substantial declines in surface and e antigenemia, this suggested that the removal of tolerizing viral proteins from the system likely retrieved the antiviral functions of helper and cytolytic T-cells and/or activated these cells. The strength and/or duration of these T-cell responses in some Responders correlated with the temporary elevations in transaminases that are considered markers of immune clearance of HBV-infected hepatocytes (70). T-cell responses waned after the loss of WHsAg and WHeAg and were not detected after treatment cessation, indicating that these cells contributed to the RG7854-mediated WHV suppression.

WHV-specific humoral responses were further assessed for determining if RG7854-treated woodchucks developed a functional B-cell response. Responders to monotreatment and especially to RG7854/ETV combination treatment elicited antibodies to WHsAg (and often to WHeAg) that were characterized by remarkably high titers, as also noted for anti-HBs antibodies in the HBV mouse model following treatment with the TLR7 agonist and a capsid assembly modulator (68). Antibody emergence may indicate a reversal of impaired functions of DCs and B-cells in the setting of CHB in patients treated with NAs (30, 75) and in woodchucks treated with TLR agonists, alone and together with ETV (41, 42, 46). Since WHV-specific antibodies were detected immediately after the loss of WHsAg and WHeAg, this suggested again that the elimination of tolerizing viral antigens supported a restoration of B-cell functions and/or activation of these cells, as also reported for patients with NA treatment-induced seroconversion (75). Direct TLR7 stimulation in B-lymphocytes by RG7854 may further lead to polyclonal cell expansion and differentiation into immunoglobulin-secreting plasma cells (76) which could additionally explain the high anti-WHs and anti-HBs titers achieved in woodchucks and mice (68). These virus-neutralizing antibodies are important to prevent reinfection of already infected hepatocytes, as well as *de novo* infection of naïve hepatocytes that emerge during liver replenishment due to natural cell death or cytolytic elimination by T-cells, and of uninfected hepatocytes that arise from non-cytolytic viral elimination by cytokines. Because anti-WHs antibodies persisted until the EOS while WHsAg-specific T-cell responses became undetectable, the durable humoral response is apparently required for the continued suppression of WHV replication by residual virus and/or maintenance of the virus-free status. Altogether, the induction of ISGs and the development of WHV-specific B- and T-cell responses suggested that a crosslink between innate and adaptive immunity was induced by RG7854 mono and combination treatment in Responders with SVR.

RG7854 administration, alone and together with ETV, was not associated with treatment-limiting adverse effects, and repeated dosing for 14 to 24 weeks was well-tolerated by woodchucks. Sustained changes in clinical chemistry and most hematology parameters were not noted; however, RG7854 treatment at the highest dose was associated with thrombocytopenia, and additional neutropenia when combined with ETV. These adverse effects were transient and reversed immediately after treatment cessation or even during treatment, and the incidence and severity was reduced with lower RG7854 doses. The underlying mechanism(s) by which RG7854 causes reductions in neutrophils and platelets in woodchucks are unknown. However, neutropenia and thrombocytopenia appeared woodchuck-specific, since both parameters were not measured for RG7854 treatment in the HBV mouse model (57, 68) and, more importantly, were absent in healthy volunteers administered single and multiple RG7854 doses (56). Moreover, the drug posology for the current clinical phase 2 trial in patients with CHB (i.e., NCT04225715) has a starting RG7854 dose of slightly below 150 mg (56, 77) that is approximately 45-55 times lower than the 100 and 120 mg/kg efficacious doses in mice and woodchucks, and thus is not expected to induce these hematology changes. While the clinical outcome of RG7854 treatment is unknown at this time, it is expected that add-on administration to NA-treated patients in combination with a capsid assembly modulator (RO7049389) or small interfering RNA (RO7445482) will be safe and antiviral efficacious due to the chosen double prodrug approach for improving oral bioavailability and minimizing TLR7 activation in the gastrointestinal tract.

A comparison of therapeutic efficacy achieved in woodchucks with other TLR7 agonists suggested different pharmacokinetics and pharmacodynamics for GS-9620, APR002, and RG7854 (41, 46). As established in the aforementioned HBV mouse model, RG7854 targets spleen and lymph nodes following oral administration and activates pDCs leading to increased numbers of HBV-specific B- and T-cells in these secondary lymphoid organs (57), including upregulated germinal center B-cells (68), but the active metabolite is also detected in liver (data not shown). This overall is different to GS-9620 and APR002 that target gut-associated lymphoid tissues and/or liver after oral administration and intestinal absorption for activating resident pDCs (46, 78). Compared to GS-9620, APR002 is more hepatoselective due to the incorporation of a liver-targeting moiety into the TLR7 pharmacophore (46). Enhanced hepatic and limited systemic exposure of APR002 over GS-9620 is likely due to active uptake and high retainment of the TLR7 agonist in the liver *via* organic-anion-transporting polypeptide (OATP) transporters (46).

In conclusion, RG7854 treatment, alone and together with ETV, produced a SVR and anti-WHs antibody seroconversion in a subset of woodchucks with CHB. By analogy, these results suggest that oral treatment of patients with the double prodrug of the TLR7-specific agonist has the potential to induce sustained immunological control of chronic HBV infection and may present a new therapeutic option in the search for an HBV cure.

DATA AVAILABILITY STATEMENT

The original contributions presented in the study are included in the article/**Supplementary Material**. Further inquiries can be directed to the corresponding authors.

ETHICS STATEMENT

The animal study was reviewed and approved by Institutional Animal Care and Use Committee of Northeastern Wildlife, Inc. (Harrison, ID) and Georgetown University (Washington, DC).

AUTHOR CONTRIBUTIONS

Study concept and design: SW, MV, FR-L, JY, and SM; Acquisition of data: KK, MS, BL, CY, MV, XH, XPH, MD, and BK; Analysis and interpretation of data: SW, MS, GS, LD, MV, FR-L, and SM; Drafting of the manuscript: SW and SM; Critical revision of the manuscript for important intellectual content: SW, KK, MS, GS, LD, BL, CY, MV, FR-L, XH, XPH, MD, BK, JY, and SM; Statistical analysis: GS and SM; Obtained funding: JY; Administrative, technical, or material support: N/A; Study supervision: SW and SM. All authors contributed to the article and approved the submitted version.

ACKNOWLEDGMENTS

The authors gratefully acknowledge John Patterson, Erich Wolz, Gaurav Tyagi and David Moore (Pharmaceutical Sciences, Roche Pharma, Research and Early Development, Roche Innovation Center Basel, Switzerland) for their excellent assistance with the conduct of the in-life phase of the woodchuck study at Northeastern Wildlife, Inc., and Supti Sen, Vinona Muralidaran, and Dr. Deborah Berry (Histopathology and Tissue Shared Resources (HTSR), Georgetown University Medical Center, Washington, DC, United States) for their excellent assistance with the woodchuck liver tissues. The HTSR is partially supported by NIH/NCI grant P30 CA051008.

SUPPLEMENTARY MATERIAL

The Supplementary Material for this article can be found online at: https://www.frontiersin.org/articles/10.3389/fimmu.2022.884113/full#supplementary-material

REFERENCES

1. Organization WH. *Hepatitis B* (2021). Available at: https://wwwwhoint/news-room/fact-sheets/detail/hepatitis-b (Accessed February 15, 2022).
2. Ferrari C. HBV and the Immune Response. *Liver Int* (2015) 35 Suppl 1:121–8. doi: 10.1111/liv.12749
3. Tan A, Koh S, Bertoletti A. Immune Response in Hepatitis B Virus Infection. *Cold Spring Harb Perspect Med* (2015) 5(8):a021428. doi: 10.1101/cshperspect.a021428
4. Song C, Zhu J, Ge Z, Yu C, Tian T, Wang H, et al. Spontaneous Seroclearance of Hepatitis B Surface Antigen and Risk of Hepatocellular Carcinoma. *Clin Gastroenterol Hepatol* (2019) 17(6):1204–6. doi: 10.1016/j.cgh.2018.08.019
5. Yip TC, Wong GL, Chan HL, Tse YK, Lam KL, Lui GC, et al. HBsAg Seroclearance Further Reduces Hepatocellular Carcinoma Risk After Complete Viral Suppression With Nucleos(T)Ide Analogues. *J Hepatol* (2019) 70(3):361–70. doi: 10.1016/j.jhep.2018.10.014
6. Wright TL, Lau JY. Clinical Aspects of Hepatitis B Virus Infection. *Lancet* (1993) 342(8883):1340–4. doi: 10.1016/0140-6736(93)92250-W
7. Banatvala J, Van Damme P, Oehen S. Lifelong Protection Against Hepatitis B: The Role of Vaccine Immunogenicity in Immune Memory. *Vaccine* (2000) 19 (7-8):877–85. doi: 10.1016/S0264-410X(00)00224-3
8. Fanning GC, Zoulim F, Hou J, Bertoletti A. Therapeutic Strategies for Hepatitis B Virus Infection: Towards a Cure. *Nat Rev Drug Discov* (2019) 18(11):827–44. doi: 10.1038/s41573-019-0037-0
9. Wieland SF, Guidotti LG, Chisari FV. Intrahepatic Induction of Alpha/Beta Interferon Eliminates Viral RNA-Containing Capsids in Hepatitis B Virus Transgenic Mice. *J Virol* (2000) 74(9):4165–73. doi: 10.1128/JVI.74.9.4165-4173.2000
10. Lucifora J, Xia Y, Reisinger F, Zhang K, Stadler D, Cheng X, et al. Specific and Nonhepatotoxic Degradation of Nuclear Hepatitis B Virus cccDNA. *Science* (2014) 343(6176):1221–8. doi: 10.1126/science.1243462
11. Liu Y, Nie H, Mao R, Mitra B, Cai D, Yan R, et al. Interferon-Inducible Ribonuclease ISG20 Inhibits Hepatitis B Virus Replication Through Directly Binding to the Epsilon Stem-Loop Structure of Viral RNA. *PloS Pathog* (2017) 13(4):e1006296. doi: 10.1371/journal.ppat.1006296
12. Belloni L, Allweiss L, Guerrieri F, Pediconi N, Volz T, Pollicino T, et al. IFN-Alpha Inhibits HBV Transcription and Replication in Cell Culture and in Humanized Mice by Targeting the Epigenetic Regulation of the Nuclear cccDNA Minichromosome. *J Clin Invest* (2012) 122(2):529–37. doi: 10.1172/JCI58847
13. Likhitsup A, Lok AS. Understanding the Natural History of Hepatitis B Virus Infection and the New Definitions of Cure and the Endpoints of Clinical Trials. *Clin Liver Dis* (2019) 23(3):401–16. doi: 10.1016/j.cld.2019.04.002
14. Megahed FAK, Zhou X, Sun P. The Interactions Between HBV and the Innate Immunity of Hepatocytes. *Viruses* (2020) 12(3):285. doi: 10.3390/v12030285
15. Revill P, Yuan Z. New Insights Into How HBV Manipulates the Innate Immune Response to Establish Acute and Persistent Infection. *Antivir Ther* (2013) 18(1):1–15. doi: 10.3851/IMP2542
16. Kondo Y, Ninomiya M, Kakazu E, Kimura O, Shimosegawa T. Hepatitis B Surface Antigen Could Contribute to the Immunopathogenesis of Hepatitis B Virus Infection. *ISRN Gastroenterol* (2013) 2013:935295. doi: 10.1155/2013/935295
17. Lebosse F, Testoni B, Fresquet J, Facchetti F, Galmozzi E, Fournier M, et al. Intrahepatic Innate Immune Response Pathways are Downregulated in Untreated Chronic Hepatitis B. *J Hepatol* (2017) 66(5):897–909. doi: 10.1016/j.jhep.2016.12.024

18. Faure-Dupuy S, Lucifora J, Durantel D. Interplay Between the Hepatitis B Virus and Innate Immunity: From an Understanding to the Development of Therapeutic Concepts. *Viruses* (2017) 9(5):95. doi: 10.3390/v9050095
19. Wieland S, Thimme R, Purcell RH, Chisari FV. Genomic Analysis of the Host Response to Hepatitis B Virus Infection. *Proc Natl Acad Sci USA* (2004) 101 (17):6669–74. doi: 10.1073/pnas.0401771101
20. Visvanathan K, Skinner NA, Thompson AJ, Riordan SM, Sozzi V, Edwards R, et al. Regulation of Toll-Like Receptor-2 Expression in Chronic Hepatitis B by the Precore Protein. *Hepatology* (2007) 45(1):102–10. doi: 10.1002/hep.21482
21. Wang S, Chen Z, Hu C, Qian F, Cheng Y, Wu M, et al. Hepatitis B Virus Surface Antigen Selectively Inhibits TLR2 Ligand-Induced IL-12 Production in Monocytes/Macrophages by Interfering With JNK Activation. *J Immunol* (2013) 190(10):5142–51. doi: 10.4049/jimmunol.1201625
22. Vincent IE, Zannetti C, Lucifora J, Norder H, Protzer U, Hainaut P, et al. Hepatitis B Virus Impairs TLR9 Expression and Function in Plasmacytoid Dendritic Cells. *PloS One* (2011) 6(10):e26315. doi: 10.1371/journal.pone.0026315
23. Wu J, Meng Z, Jiang M, Pei R, Trippler M, Broering R, et al. Hepatitis B Virus Suppresses Toll-Like Receptor-Mediated Innate Immune Responses in Murine Parenchymal and Nonparenchymal Liver Cells. *Hepatology* (2009) 49(4):1132–40. doi: 10.1002/hep.22751
24. Wei C, Ni C, Song T, Liu Y, Yang X, Zheng Z, et al. The Hepatitis B Virus X Protein Disrupts Innate Immunity by Downregulating Mitochondrial Antiviral Signaling Protein. *J Immunol* (2010) 185(2):1158–68. doi: 10.4049/jimmunol.0903874
25. van der Molen RG, Sprengers D, Binda RS, de Jong EC, Niesters HG, Kusters JG, et al. Functional Impairment of Myeloid and Plasmacytoid Dendritic Cells of Patients With Chronic Hepatitis B. *Hepatology* (2004) 40(3):738–46. doi: 10.1002/hep.20366
26. Op den Brouw ML, Binda RS, van Roosmalen MH, Protzer U, Janssen HL, van der Molen RG, et al. Hepatitis B Virus Surface Antigen Impairs Myeloid Dendritic Cell Function: A Possible Immune Escape Mechanism of Hepatitis B Virus. *Immunology* (2009) 126(2):280–9. doi: 10.1111/j.1365-2567.2008.02896.x
27. Duan XZ, Wang M, Li HW, Zhuang H, Xu D, Wang FS. Decreased Frequency and Function of Circulating Plasmocytoid Dendritic Cells (pDC) in Hepatitis B Virus Infected Humans. *J Clin Immunol* (2004) 24(6):637–46. doi: 10.1007/s10875-004-6249-y
28. Gehring AJ, Ann D'Angelo J. Dissecting the Dendritic Cell Controversy in Chronic Hepatitis B Virus Infection. *Cell Mol Immunol* (2015) 12(3):283–91. doi: 10.1038/cmi.2014.95
29. Park JJ, Wong DK, Wahed AS, Lee WM, Feld JJ, Terrault N, et al. Hepatitis B Virus–Specific and Global T-Cell Dysfunction in Chronic Hepatitis B. *Gastroenterology* (2016) 150(3):684–95.e5. doi: 10.1053/j.gastro.2015.11.050
30. Burton AR, Pallett LJ, McCoy LE, Suveizdyte K, Amin OE, Swadling L, et al. Circulating and Intrahepatic Antiviral B Cells are Defective in Hepatitis B. *J Clin Invest* (2018) 128(10):4588–603. doi: 10.1172/JCI121960
31. Le Bert N, Gill US, Hong M, Kunasegaran K, Tan DZM, Ahmad R, et al. Effects of Hepatitis B Surface Antigen on Virus-Specific and Global T Cells in Patients With Chronic Hepatitis B Virus Infection. *Gastroenterology* (2020) 159(2):652–64. doi: 10.1053/j.gastro.2020.04.019
32. Le Bert N, Salimzadeh L, Gill US, Dutertre CA, Facchetti F, Tan A, et al. Comparative Characterization of B Cells Specific for HBV Nucleocapsid and Envelope Proteins in Patients With Chronic Hepatitis B. *J Hepatol* (2020) 72 (1):34–44. doi: 10.1016/j.jhep.2019.07.015
33. Suslov A, Boldanova T, Wang X, Wieland S, Heim MH. Hepatitis B Virus Does Not Interfere With Innate Immune Responses in the Human Liver. *Gastroenterology* (2018) 154(6):1778–90. doi: 10.1053/j.gastro.2018.01.034
34. Mutz P, Metz P, Lempp FA, Bender S, Qu B, Schoneweis K, et al. HBV Bypasses the Innate Immune Response and Does Not Protect HCV From Antiviral Activity of Interferon. *Gastroenterology* (2018) 154(6):1791–804.e22. doi: 10.1053/j.gastro.2018.01.044
35. Suslov A, Wieland S, Menne S. Modulators of Innate Immunity as Novel Therapeutics for Treatment of Chronic Hepatitis B. *Curr Opin Virol* (2018) 30:9–17. doi: 10.1016/j.coviro.2018.01.008
36. Meng Z, Chen Y, Lu M. Advances in Targeting the Innate and Adaptive Immune Systems to Cure Chronic Hepatitis B Virus Infection. *Front Immunol* (2019) 10:3127. doi: 10.3389/fimmu.2019.03127
37. Liu G, Gack MU. Distinct and Orchestrated Functions of RNA Sensors in Innate Immunity. *Immunity* (2020) 53(1):26–42. doi: 10.1016/j.immuni.2020.03.017
38. Miyake K, Shibata T, Ohto U, Shimizu T. Emerging Roles of the Processing of Nucleic Acids and Toll-Like Receptors in Innate Immune Responses to Nucleic Acids. *J Leukoc Biol* (2017) 101(1):135–42. doi: 10.1189/jlb.4MR0316-108R
39. Sepehri Z, Kiani Z, Alavian SM, Arababadi MK, Kennedy D. The Link Between TLR7 Signaling and Hepatitis B Virus Infection. *Life Sci* (2016) 158:63–9. doi: 10.1016/j.lfs.2016.06.026
40. Lanford RE, Guerra B, Chavez D, Giavedoni L, Hodara VL, Brasky KM, et al. GS-9620, an Oral Agonist of Toll-Like Receptor-7, Induces Prolonged Suppression of Hepatitis B Virus in Chronically Infected Chimpanzees. *Gastroenterology* (2013) 144(7):1508–17,17.e1-10. doi: 10.1053/j.gastro.2013.02.003
41. Menne S, Tumas DB, Liu KH, Thampi L, AlDeghaither D, Baldwin BH, et al. Sustained Efficacy and Seroconversion With the Toll-Like Receptor 7 Agonist GS-9620 in the Woodchuck Model of Chronic Hepatitis B. *J Hepatol* (2015) 62 (6):1237–45. doi: 10.1016/j.jhep.2014.12.026
42. Daffis S, Balsitis S, Chamberlain J, Zheng J, Santos R, Rowe W, et al. Toll-Like Receptor 8 Agonist GS-9688 Induces Sustained Efficacy in the Woodchuck Model of Chronic Hepatitis B. *Hepatology* (2021) 73(1):53–67. doi: 10.1002/hep.31255
43. Gane EJ, Lim YS, Gordon SC, Visvanathan K, Sicard E, Fedorak RN, et al. The Oral Toll-Like Receptor-7 Agonist GS-9620 in Patients With Chronic Hepatitis B Virus Infection. *J Hepatol* (2015) 63(2):320–8. doi: 10.1016/j.jhep.2015.02.037
44. Janssen HLA, Brunetto MR, Kim YJ, Ferrari C, Massetto B, Nguyen AH, et al. Safety, Efficacy and Pharmacodynamics of Vesatolimod (GS-9620) in Virally Suppressed Patients With Chronic Hepatitis B. *J Hepatol* (2018) 68(3):431–40. doi: 10.1016/j.jhep.2017.10.027
45. Boni C, Vecchi A, Rossi M, Laccabue D, Giuberti T, Alfieri A, et al. TLR7 Agonist Increases Responses of Hepatitis B Virus-Specific T Cells and Natural Killer Cells in Patients With Chronic Hepatitis B Treated With Nucleos(T)Ide Analogues. *Gastroenterology* (2018) 154(6):1764–77.e7. doi: 10.1053/j.gastro.2018.01.030
46. Korolowizc KE, Li B, Huang X, Yon C, Rodrigo E, Corpuz M, et al. Liver-Targeted Toll-Like Receptor 7 Agonist Combined With Entecavir Promotes a Functional Cure in the Woodchuck Model of Hepatitis B Virus. *Hepatol Commun* (2019) 3(10):1296–310. doi: 10.1002/hep4.1397
47. Summers J, Smolec JM, Snyder R. A Virus Similar to Human Hepatitis B Virus Associated With Hepatitis and Hepatoma in Woodchucks. *Proc Natl Acad Sci USA* (1978) 75(9):4533–7. doi: 10.1073/pnas.75.9.4533
48. Menne S, Cote PJ. The Woodchuck as an Animal Model for Pathogenesis and Therapy of Chronic Hepatitis B Virus Infection. *World J Gastroenterol* (2007) 13(1):104–24. doi: 10.3748/wjg.v13.i1.104
49. Tennant BC, Toshkov IA, Peek SF, Jacob JR, Menne S, Hornbuckle WE, et al. Hepatocellular Carcinoma in the Woodchuck Model of Hepatitis B Virus Infection. *Gastroenterology* (2004) 127(5 Suppl 1):S283–93. doi: 10.1053/j.gastro.2004.09.043
50. Kosinska AD, Liu J, Lu M, Roggendorf M. Therapeutic Vaccination and Immunomodulation in the Treatment of Chronic Hepatitis B: Preclinical Studies in the Woodchuck. *Med Microbiol Immunol* (2015) 204(1):103–14. doi: 10.1007/s00430-014-0379-5
51. Michalak TI. Diverse Virus and Host-Dependent Mechanisms Influence the Systemic and Intrahepatic Immune Responses in the Woodchuck Model of Hepatitis B. *Front Immunol* (2020) 11:853. doi: 10.3389/fimmu.2020.00853
52. Suresh M, Menne S. Application of the Woodchuck Animal Model for the Treatment of Hepatitis B Virus-Induced Liver Cancer. *World J Gastrointest Oncol* (2021) 13(6):509–35. doi: 10.4251/wjgo.v13.i6.509
53. Korba BE, Cote P, Hornbuckle W, Tennant BC, Gerin JL. Treatment of Chronic Woodchuck Hepatitis Virus Infection in the Eastern Woodchuck (Marmota Monax) With Nucleoside Analogues is Predictive of Therapy for Chronic Hepatitis B Virus Infection in Humans. *Hepatology* (2000) 31 (5):1165–75. doi: 10.1053/he.2000.5982
54. Colonno RJ, Genovesi EV, Medina I, Lamb L, Durham SK, Huang ML, et al. Long-Term Entecavir Treatment Results in Sustained Antiviral Efficacy and Prolonged Life Span in the Woodchuck Model of Chronic Hepatitis Infection. *J Infect Dis* (2001) 184(10):1236–45. doi: 10.1086/324003

55. Korolowicz KE, Iyer RP, Czerwinski S, Suresh M, Yang J, Padmanabhan S, et al. Antiviral Efficacy and Host Innate Immunity Associated With SB 9200 Treatment in the Woodchuck Model of Chronic Hepatitis B. *PloS One* (2016) 11(8):e0161313. doi: 10.1371/journal.pone.0161313
56. Luk A, Jiang Q, Glavini K, Triyatni M, Zhao N, Racek T, et al. A Single and Multiple Ascending Dose Study of Toll-Like Receptor 7 Agonist (RO7020531) in Chinese Healthy Volunteers. *Clin Transl Sci* (2020) 13(5):985–93. doi: 10.1111/cts.12791
57. Dai L, Yu X, Yu Y, Gu L, Zhao J, Zhu L, et al. Preclinical Mechanistic and Efficacy Evaluation of a Novel Small Molecule TLR7 Agonist RO7020531 for the Treatment of Chronic Hepatitis B. *J Hepatol* (2018) 68:S802–S3. doi: 10.1016/S0168-8278(18)31878-6
58. Menne S, Butler SD, George AL, Tochkov IA, Zhu Y, Xiong S, et al. Antiviral Effects of Lamivudine, Emtricitabine, Adefovir Dipivoxil, and Tenofovir Disoproxil Fumarate Administered Orally Alone and in Combination to Woodchucks With Chronic Woodchuck Hepatitis Virus Infection. *Antimicrob Agents Chemother* (2008) 52(10):3617–32. doi: 10.1128/AAC.00654-08
59. Korolowicz KE, Suresh M, Li B, Huang X, Yon C, Leng X, et al. Treatment With the Immunomodulator AIC649 in Combination With Entecavir Produces Antiviral Efficacy in the Woodchuck Model of Chronic Hepatitis B. *Viruses* (2021) 13(4):648. doi: 10.3390/v13040648
60. Cote PJ, Roneker C, Cass K, Schodel F, Peterson D, Tennant B, et al. New Enzyme Immunoassays for the Serologic Detection of Woodchuck Hepatitis Virus Infection. *Viral Immunol* (1993) 6(2):161–9. doi: 10.1089/vim.1993.6.161
61. Bellezza CA, Concannon PW, Hornbuckle WE, Roth L, Tennant BC. Woodchucks as Laboratory Animals. In: JG Fox, et al, editors. *Laboratory Animal Medicine*. Netherlands: Elsevier Science (2002). p. 309–28.
62. Hornbuckle WE, Graham ES, Roth L, Baldwin BH, Wickenden C, Tennant BC. Laboratory Assessment of Hepatic Injury in the Woodchuck (Marmota Monax). *Lab Anim Sci* (1985) 35(4):376–81.
63. Peek SF, Cote PJ, Jacob JR, Toshkov IA, Hornbuckle WE, Baldwin BH, et al. Antiviral Activity of Clevudine [L-FMAU, (1-(2-Fluoro-5-Methyl-Beta, L-Arabinofuranosyl) Uracil)] Against Woodchuck Hepatitis Virus Replication and Gene Expression in Chronically Infected Woodchucks (Marmota Monax). *Hepatology* (2001) 33(1):254–66. doi: 10.1053/jhep.2001.20899
64. Tennant BC, Baldwin BH, Graham LA, Ascenzi MA, Hornbuckle WE, Rowland PH, et al. Antiviral Activity and Toxicity of Fialuridine in the Woodchuck Model of Hepatitis B Virus Infection. *Hepatology* (1998) 28 (1):179–91. doi: 10.1002/hep.510280124
65. Menne S, Tennant BC, Gerin JL, Cote PJ. Chemoimmunotherapy of Chronic Hepatitis B Virus Infection in the Woodchuck Model Overcomes Immunologic Tolerance and Restores T-Cell Responses to Pre-S and S Regions of the Viral Envelope Protein. *J Virol* (2007) 81(19):10614–24. doi: 10.1128/JVI.00691-07
66. Suresh M, Czerwinski S, Murreddu MG, Kallakury BV, Ramesh A, Gudima SO, et al. Innate and Adaptive Immunity Associated With Resolution of Acute Woodchuck Hepatitis Virus Infection in Adult Woodchucks. *PloS Pathog* (2019) 15(12):e1008248. doi: 10.1371/journal.ppat.1008248
67. Menne S, Wildum S, Steiner G, Suresh M, Korolowicz K, Balarezo M, et al. Efficacy of an Inhibitor of Hepatitis B Virus Expression in Combination With Entecavir and Interferon-Alpha in Woodchucks Chronically Infected With Woodchuck Hepatitis Virus. *Hepatol Commun* (2020) 4(6):916–31. doi: 10.1002/hep4.1502
68. Dai L, Yu Y, Gu L, Zhao J, Zhu L, Yun H, et al. Combination Treatment of a TLR7 Agonist RO7020531and a Capsid Assembly Modulator RO7049389 Achieved Sustainable Viral Loadsuppression and HBsAg Loss in an AAV-HBV Mouse Model. *J Hepatol* (2018) 68:S17–S8. doi: 10.1016/S0168-8278(18)30253-8
69. Chiale C, Marchese AM, Robek MD. Innate Immunity and HBV Persistence. *Curr Opin Virol* (2021) 49:13–20. doi: 10.1016/j.coviro.2021.04.003
70. Wong D, Littlejohn M, Edwards R, Jackson K, Revill P, Gaggar A, et al. ALT Flares During Nucleotide Analogue Therapy are Associated With HBsAg Loss in Genotype A HBeAg-Positive Chronic Hepatitis B. *Liver Int* (2018) 38 (10):1760–9. doi: 10.1111/liv.13716
71. Bertoletti A, Le Bert N. Fine-Tuning TLR-7-Based Therapy for Functional HBV Cure. *Hepatol Commun* (2019) 3(10):1289–92. doi: 10.1002/hep4.1420
72. Boni C, Laccabue D, Lampertico P, Giuberti T, Vigano M, Schivazappa S, et al. Restored Function of HBV-Specific T Cells After Long-Term Effective Therapy With Nucleos(T)Ide Analogues. *Gastroenterology* (2012) 143 (4):963–73.e9. doi: 10.1053/j.gastro.2012.07.014
73. Rivino L, Le Bert N, Gill US, Kunasegaran K, Cheng Y, Tan DZ, et al. Hepatitis B Virus-Specific T Cells Associate With Viral Control Upon Nucleos(T)Ide-Analogue Therapy Discontinuation. *J Clin Invest* (2018) 128(2):668–81. doi: 10.1172/JCI92812
74. Kennedy PTF, Sandalova E, Jo J, Gill U, Ushiro-Lumb I, Tan AT, et al. Preserved T-Cell Function in Children and Young Adults With Immune-Tolerant Chronic Hepatitis B. *Gastroenterology* (2012) 143(3):637–45. doi: 10.1053/j.gastro.2012.06.009
75. Xu X, Shang Q, Chen X, Nie W, Zou Z, Huang A, et al. Reversal of B-Cell Hyperactivation and Functional Impairment is Associated With HBsAg Seroconversion in Chronic Hepatitis B Patients. *Cell Mol Immunol* (2015) 12(3):309–16. doi: 10.1038/cmi.2015.25
76. Bekeredjian-Ding IB, Wagner M, Hornung V, Giese T, Schnurr M, Endres S, et al. Plasmacytoid Dendritic Cells Control TLR7 Sensitivity of Naive B Cells *via* Type I IFN. *J Immunol* (2005) 174(7):4043–50. doi: 10.4049/jimmunol.174.7.4043
77. *ClinicalTrials.gov. NCT04225715* (2022). Available at: https://clinicaltrialsgov/ct2/show/NCT04225715 (Accessed February 15, 2022).
78. Fosdick A, Zheng J, Pflanz S, Frey CR, Hesselgesser J, Halcomb RL, et al. Pharmacokinetic and Pharmacodynamic Properties of GS-9620, a Novel Toll-Like Receptor 7 Agonist, Demonstrate Interferon-Stimulated Gene Induction Without Detectable Serum Interferon at Low Oral Doses. *J Pharmacol Exp Ther* (2014) 348(1):96–105. doi: 10.1124/jpet.113.207878

Conflict of Interest: SM has received grants from F. Hoffmann-La Roche, Ltd. and serves occasionally as a paid scientific consultant to Northeastern Wildlife, Inc. GS is employed by Roche, while LD is a former employee of Roche. SW, MV, FR-L, and JY own stock in and are employed by Roche.

The remaining authors declare that the research was conducted in the absence of any commercial or financial relationships that could be construed as a potential conflict of interest.

The authors declare that this work was funded by F. Hoffmann-La Roche, Ltd. (https://www.roche.com) who played a role in the design of the study, collection of data, analysis and interpretation of data, preparation of the manuscript, and in the decision to submit the manuscript for publication.

Publisher's Note: All claims expressed in this article are solely those of the authors and do not necessarily represent those of their affiliated organizations, or those of the publisher, the editors and the reviewers. Any product that may be evaluated in this article, or claim that may be made by its manufacturer, is not guaranteed or endorsed by the publisher.

frontiers | Frontiers in Immunology

ORIGINAL RESEARCH
published: 03 June 2022
doi: 10.3389/fimmu.2022.916383

A Bibliometric Analysis of the Innate Immune DNA Sensing cGAS-STING Pathway from 2013 to 2021

Xuan Shi†, *Sheng Wang*†, *Yutong Wu*†, *Quanfu Li*, *Tong Zhang*, *Keting Min*, *Di Feng*, *Meiyun Liu*, *Juan Wei*, *Lina Zhu*, *Wei Mo*, *Zhuoran Xiao*, *Hao Yang*, *Yuanli Chen** *and Xin Lv**

Department of Anesthesiology, Shanghai Pulmonary Hospital, School of Medicine, Tongji University, Shanghai, China

Background and aims: Cyclic guanosine monophosphate (GMP)-adenosine monophosphate (AMP) (cGAMP) synthase (cGAS) and stimulator of interferon genes (STING) are key components of the innate immune system. This study aims to evaluate the research of cGAS-STING pathway and predict the hotspots and developing trends in this field using bibliometric analysis.

Methods: We retrieved publications from Science Citation Index Expanded (SCI-expanded) of Web of Science Core Collection (WoSCC) in 1975-2021 on 16 March 2022. We examined the retrieved data by bibliometrix package in R software, VOSviewer and CiteSpace were used for visualizing the trends and hotspots of research on the cGAS-STING pathway.

Results: We identified 1047 original articles and reviews on the cGAS-STING pathway published between 1975 and 2021. Before 2016, the publication trend was increasing steadily, but there was a significant increase after 2016. The United States of America (USA) produced the highest number of papers (Np) and took the highest number of citations (Nc), followed by China and Germany. The University of Texas System and Frontiers in Immunology were the most prolific affiliation and journal respectively. In addition, collaboration network analysis showed that there were tight collaborations among the USA, China and some European countries, so the top 10 affiliations were all from these countries and regions. The paper published by Sun LJ in 2013 reached the highest local citation score (LCS). Keywords co-occurrence and co-citation cluster analysis revealed that inflammation, senescence, and tumor were popular terms related to the cGAS-STING pathway recently. Keywords burst detection suggested that STING-dependent innate immunity and NF-κB-dependent broad antiviral response were newly-emerged hotspots in this area.

OPEN ACCESS

Edited by:
Chaofeng Han,
Second Military Medical University, China

Reviewed by:
Degang Yang,
Tongji University, China
Yuelan Wang,
Shandong University, China
Mengshu Cao,
Nanjing Drum Tower Hospital, China
Zhengyu He,
Shanghai Jiao Tong University, China

****Correspondence:***
Xin Lv
xinlvg@126.com
Yuanli Chen
chenyuanli90@163.com

†These authors have contributed equally to this work

Specialty section:
This article was submitted to Molecular Innate Immunity, a section of the journal Frontiers in Immunology

Received: *09 April 2022*
Accepted: *09 May 2022*
Published: *03 June 2022*

Citation:
Shi X, Wang S, Wu Y, Li Q, Zhang T, Min K, Feng D, Liu M, Wei J, Zhu L, Mo W, Xiao Z, Yang H, Chen Y and Lv X (2022) A Bibliometric Analysis of the Innate Immune DNA Sensing cGAS-STING Pathway from 2013 to 2021. Front. Immunol. 13:916383. doi: 10.3389/fimmu.2022.916383

Conclusions: This bibliometric analysis shows that publications related to the cGAS-STING pathway tend to increase continuously. The research focus has shifted from the mechanism how cGAS senses dsDNA and cGAMP binds to STING to the roles of the cGAS-STING pathway in different pathological state.

Keywords: innate immunity, cGAS-STING pathway, bibliometrics, VOSviewer, CiteSpace

INTRODUCTION

Over the past two decades, in mammalian cells, recognition of pathogens' nucleic acids has been a key feature to sense microbial pathogens. In the field of sensing double-stranded DNA (dsDNA), cGAS is an important DNA-binding protein that represents the initiator of sensing dsDNA. Three strategies have been reported for cGAS to recognize pathogens efficiently. Firstly, cGAS is discovered in the cytoplasm, plasma membrane, and nucleus, it can rapidly recognize DNA and initiate the downstream immune response (1–4). Secondly, the recognition would be strengthened by high-mobility group box 1 protein (HMGB1), mitochondrial transcription factor A (TFAM) and modified by reactive oxygen species (ROS) (5, 6). Thirdly, the second messenger cyclic GMP-AMP (cGAMP) from these infected cells would show alarm to bystander cells to activate cGAS-STING pathway in these cells (7). When combined with dsDNA, the structure of cGAS would change and affect catalytic pockets. ATP and GTP in this pocket are catalyzed by cGAMP (8). As a second messenger, cGAMP is detected by STING, a cyclic-dinucleotide sensor (9, 10). Then STING is transported from the endoplasmic reticulum (ER) to Golgi through ER-Golgi intermediate compartment and sets off downstream signaling reaction (10, 11). STING is regarded as the central molecule of the downstream of I IFN (12, 13). STING is reported to enhance the activity of RIG-1-like receptors (RLR) signaling pathway (14) and the activity of interferons-β (IFN-β) which is dependent on interferon regulator factor 3 (IRF3) (15–17). In addition, the activation of STING can activate TANK-binding kinase 1 (TBK1) and IκB kinase (IKK). p-TBK1 phosphorylates interferon regulatory factor 3 (IRF3), and IRF3 translocated to the nucleus to transcript IFN-I (18). IKK is also recruited by STING, phosphorylates IκBα and induces NF-κB to translocate to nucleus. After that, lots of cytokines are transcribed to induce inflammatory and immune responses (19). In recent years, scholars have done lots of research about the cGAS-STING pathway. It is important to explore the hotspots and development trends of the cGAS-STING pathway in the past 10 years with CiteSpace and VOSviewer software.

Bibliometric analysis is a useful method by which scholars can evaluate the history, current, and future of publications and their quantity and quality (20). Bibliometrics can analyze publications (books, journals, and so on) by applying the literature system and metrology as objects. In addition, it can provide useful information to help to write the guideline, make decisions and treat diseases (21–23). In these years, many bibliometric analyses have been published in the biological field. However, bibliometric analysis on the cGAS-STING pathway remains a void. So the study aims to systematically analyze the research on the cGAS-STING pathway to digest the current state and the hotspots in this field.

MATERIALS AND METHODS

Data Collection

The Science Citation Index Expanded (SCI-expanded) of Web of Science Core Collection (WoSCC) in 1975-2021 was systematically searched from 1 January 1975 to 31 December 2021 and was downloaded in a single day (2022.03.17) to avoid deviations. The search terms were set as follows: TS = ("stimulator of interferon genes" OR "transmembrane protein 173" OR STING OR ERIS OR MITA OR MPYS OR NET23 OR TMEM173) AND TS = ("Mab-21 domain containing 1" OR "E330016A19Rik" OR "cyclic guanosine monophosphate-adenosine monophosphate synthase" OR "cGAMP synthase" OR "cyclic GMP-AMP synthase" OR "MB21D1" OR "cGAS"). Two reviewers (XS and YW) independently identified these data search and then discussed the potential differences, the final agreement reached 0.90 (24). These two reviewers then sent these original articles and reviews into Endnote for further validation. Finally, 1047 original articles and reviews written in English were included. **Figure 1** is the flowchart of literature selection.

Duplicate authors and misspelled elements were removed, and we used a thesaurus file to merge duplicates into one word, delete the useless words and correct the misspelled elements. Then, the clean data were imported to VOSviewer v.1.6.15.0, CiteSpace version 5.8.R3, and the "bibliometrix package 3.2.1" of R software (Version 4.1.3) for bibliometric analysis.

Bibliometric Analysis

We used the numbers of papers and citations to represent the bibliographic material as previously reported (25). The productivities of papers were represented by the numbers of publications (Np), the impacts were represented by the numbers of citations (without self-citations) (Nc) and the numbers of average citations (Na) were Nc/Np, which represented the qualities of publications. These elements were regarded as three main perspectives to evaluate the levels of researches. In some cases, H-index was also developed to evaluate individual academic achievements, the publication output of a region or a nation, an institution, or a journal (26). What's more, the impact factor (IF) from the latest version of Journal Citation Reports (JCR), and local citation score (LCS) also indicated the value of an article (27, 28).

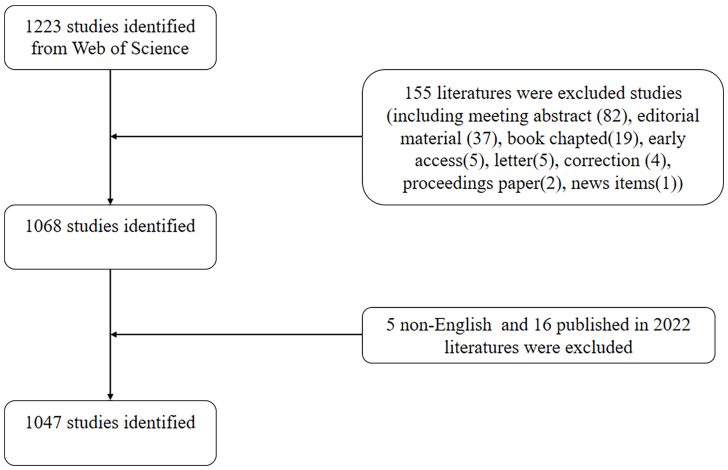

FIGURE 1 | Flowchart of the screening process.

VOSviewer, CiteSpace, and R (Version 4.1.3) are used for statistical computing and graphics. VOSviewer is a program to establish bibliometric maps by using the data collected from Web of Science Core Collection (29). It can provide a general comprehensive and detailed view of bibliometric maps based on collaborative data. CiteSpace is a program to analyze the potential knowledge contained in the scientific literature and visualize collected data (30). R software (Version 4.1.3) is the language and environment, which is wildly used for statistical computing and graphics (31). In this study, the bibliometrix package 3.2.1 in R was used to analyze data and perform a basic bibliometric analysis (32).

RESULTS

An Overview of Publications on the cGAS-STING Pathway

The number of original articles (785) and reviews (262) published was 1047, the total Nc for retrieved articles and reviews was 33357, the average Nc per article was 31.86. The H-index of all original articles and reviews was 102.

The Annual Trend of Paper Publication Quantity

The annual Np related to the cGAS-STING pathway was shown in **Figure 2A**. The numbers of annual papers rose rapidly from 16 in 2013 to 332 in 2021 and the correlation coefficient R^2 is 0.9863. The rapid increase indicated that more and more researchers were paying attention to this area.

From 2013 to 2021, the Np in the USA had increased steadily. When it comes to China, before 2019, the Np was at a low level and was almost as half as that in the USA. However, the Np in China had reached the first place in 2021. This might be related to the increased investments of the Chinese government in scientific research.

In **Figure 2B**, it was interesting to note that the number of annual publications can be divided into two stages. With the model of research development (33), we found that from 2013 to 2016 (period I), publications outputs were at a low level. Theories in this area were not completed and the cGAS-STING pathway just began to come into focus. From 2016 to now (period II), a rapid increase occurred and the publication outputs had been over 1000 in 2021, which represented that more scholars were conducting research in this field and theories about the cGAS-STING pathway were booming. Since the cGAS-STING pathway has attracted more attention, a spurt would occur shortly.

Analysis of Countries and Affiliations

A total of 1047 articles were published from 54 countries and regions. We ranked the top 10 output countries and regions of all authors according to the number of Np (**Table 1**). Because we used the bibliometrix package in R (Version 4.1.3) software to analyze all data, the data of England, Scotland, and Wales were merged automatically by the package in analysis of countries, and finally these were shown as UK. In **Figure 3A**, the Np in other countries was relatively at low levels and remained steady except the USA and China. China ranked first in Np in 2021 but the LCS of China was much lower than that of the USA (**Figure 3B**), representing that qualities of publications in China were still at a relative low level. The Np and LCS in the USA both increased rapidly, which means the publications about the cGAS-STING pathway in the USA were not only for quantity but also for quality. **Figure 3C** represents the distributions of publications in different countries and regions. Cooperation among different countries is an important driving force to promote the development of scientific research. To this point, close cooperation among different countries were shown in **Figure 3D**. The lines donated the cooperation between countries. The wider the lines, the closer the cooperation. However, most countries lacked lines, which means they lacked stable cooperation and communication.

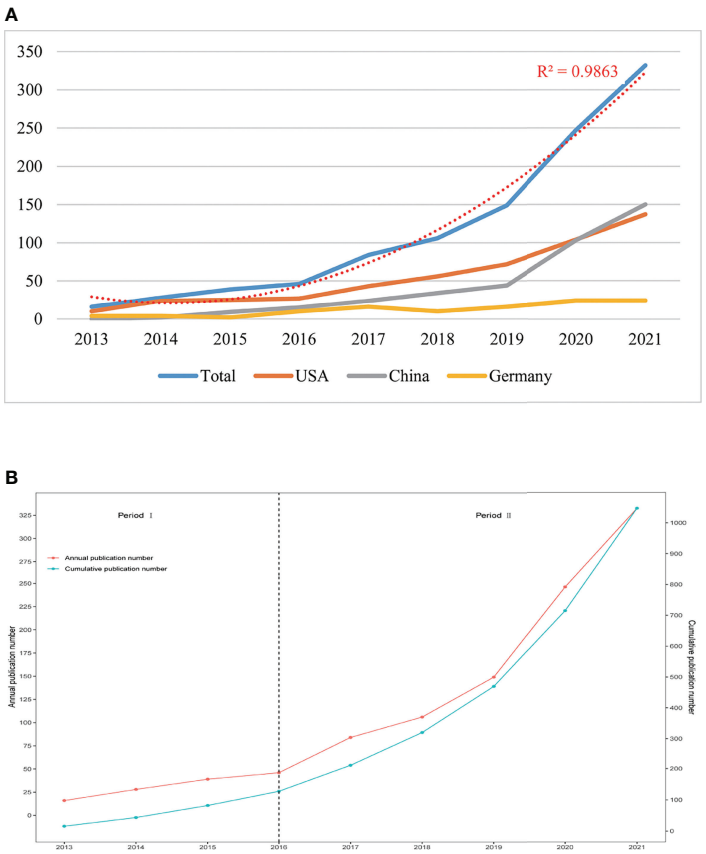

FIGURE 2 | **(A)** The total numbers of publications and top three countries from 2013 to 2021. **(B)** The numbers of publications by year and accumulation from 2013 to 2021.

Table 2 showed the top 10 affiliations with the highest number of publications related to the cGAS-STING pathway. University of Texas System had the highest Np (88, 8.40%) among all affiliations, which were almost as twice as Chinese Academy of Sciences (51, 4.87%). The team of Zhijian James Chen, who discovered cGAS for the first time and explained its function, is from University of Texas System. The publications from this team contributed a lot for the first place of University of Texas System. The Nps of affiliations ranking three to five were the same, Howard Hughes Medical Institute (48, 4.58%), University of California System (48, 4.58%), and Harvard University (48, 4.58%). Among the top 10 affiliations, half of them belonged to the USA. This was related to its high investment and strong technical strength. In addition, University of Texas System got the highest H-index (38) followed by Howard Hughes Medical Institute (37), scholars in this area should focus on their high-quality research notably.

TABLE 1 | Publications in the 10 most productive countries/regions.

Rank	Country/Region	(Np)	% of (1047)	(Nc)	(Na)	H-index
1	USA	493	47.09	28654	58.12	88
2	China	370	35.34	7574	20.47	48
3	Germany	110	10.51	6680	60.73	40
4	UK	82	7.83	5011	61.11	33
5	France	69	6.59	2845	41.23	25
6	Japan	53	5.06	2453	46.28	25
7	Denmark	42	4.01	2007	47.79	19
8	Italy	36	3.44	912	25.33	15
9	Australia	33	3.15	1846	55.94	17
10	Canada	33	3.15	1379	41.79	13

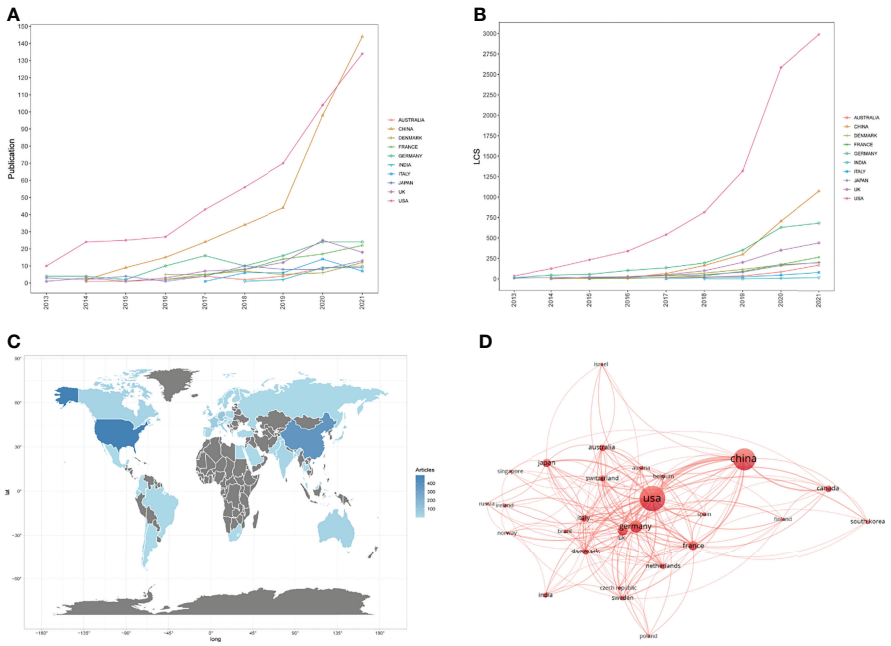

FIGURE 3 | **(A)** Publications in the 10 most productive countries/regions. **(B)** The yearly number of local citation scores (LCS) of the 10 most productive countries/regions. **(C)** Distributions of countries/regions of publications. **(D)** The cooperation map of countries involved in the cGAS-STING pathway.

Analysis of Journals

The 10 journals with the most research in cGAS-STING area, along with H-index and impact factor (IF) Eigenfactor Score as indicators of impact were listed in **Table 3**. These journals were more likely to accept articles on cGAS-STING pathway because they had produced the most publications on the related topics recently. Scholars in cGAS-STING area should focus on research published in these journals. The highest IF belonged to Nature (IF=49.926), followed by Immunity (IF=31.745), Cell Host & Microbe (IF=21.023), Nature Communication (IF=14.919) and Proceedings of the National Academy of Sciences of the United States of America (PNAS) (IF=11.205). The IF of these 5 journals were over 10 and they published over 1/10 papers in this area in the past, representing that cGAS-STING is a popular research orientation and it is not difficult for studies in cGAS-STING area to publish in top journals.

Analysis of Local Citation Score

The LCS analysis provided detailed information for articles with high local citations. The numbers of LCS per year for the top 15 articles were presented in **Figure 4A** and **S Table 1**. Interestingly, 8 of them were from the team of Zhijian James Chen, the pioneer and founder of the cGAS-STING area. These research outputs of Chen's lab were leading the trend and breakthrough in this area. The paper written by Sun LJ, the Ph.D. student in Chen's lab, got the highest LCS score (555). In this paper, the authors firstly discovered an enzyme named cyclic GMP–AMP synthase (cGAS), which can detect DNA and active I IFN signaling

TABLE 2 | The top 10 productive affiliations.

Rank	Affiliations	Country	(Np)	(Nc)	(Na)	H-index
1	UNIV OF TEXAS SYSTEM	USA	88	10905	123.92	38
2	CHINESE ACADEMY OF SCIENCES	China	51	1120	21.96	21
3	HOWARD HUGHES MEDICAL INSTITUTE	USA	48	12049	251.02	37
4	UNIV OF CALIFORNIA SYSTEM	USA	48	3151	65.65	24
5	HARVARD UNIV	USA	48	836	17.42	22
6	WUHAN UNIVERSITY	China	36	671	18.64	15
7	CENTRE NATIONAL DE LA RECHERCHE SCIENTIFIQUE CNRS	France	35	1130	32.29	18
8	INSTITUTION NATIONAL DE LA SANTE ET DE LA RECHERCHE MEDICALE INSERM	France	34	1900	55.88	17
9	AARHUS UNIVERSITY	Denmark	33	1715	51.97	18
10	NATIONAL INSTITUTES OF HEALTH NIH USA	USA	28	1591	56.82	14

TABLE 3 | The top 10 productive journals.

Rank	Journal	Np	H-index	Nc	Na	IF (2020)
1	FRONTIERS IN IMMUNOLOGY	55	10	338	6.15	7.561
2	JOURNAL OF IMMUNOLOGY	35	17	892	25.49	5.442
3	JOURNAL OF VIROLOGY	31	18	915	29.52	5.078
4	PLOS PATHOGENS	31	17	826	26.65	6.823
5	NATURE COMMUNICATIONS	29	18	2149	74.10	14.919
6	CELL REPORTS	27	18	1838	68.07	9.423
7	NATURE	27	24	6393	236.78	49.962
8	PNAS	25	17	1322	52.88	11.205
9	IMMUNITY	17	15	3159	185.82	31.745
10	CELL HOST MICROBE	13	13	1514	116.46	21.023

pathway (1). Apart from two reviews (Chen Q, 2016; Harding SM, 2017) (8, 34), the other 13 high LCS studies were all from 2013 to 2015, when the area just emerged. After 2016, scholars around the world are conducted more and more research based on these classical research. Visualization of the top 50 LCS articles was shown in **Figure 4B**. In this network, each node represented a cited article, the size of each node was proportional to the frequency of this article by the other 49 articles.

Analysis of Hotspots and Frontiers

By analyzing keywords, readers can easily summarize the topic of one study and explore the hotpots and directions in this area.

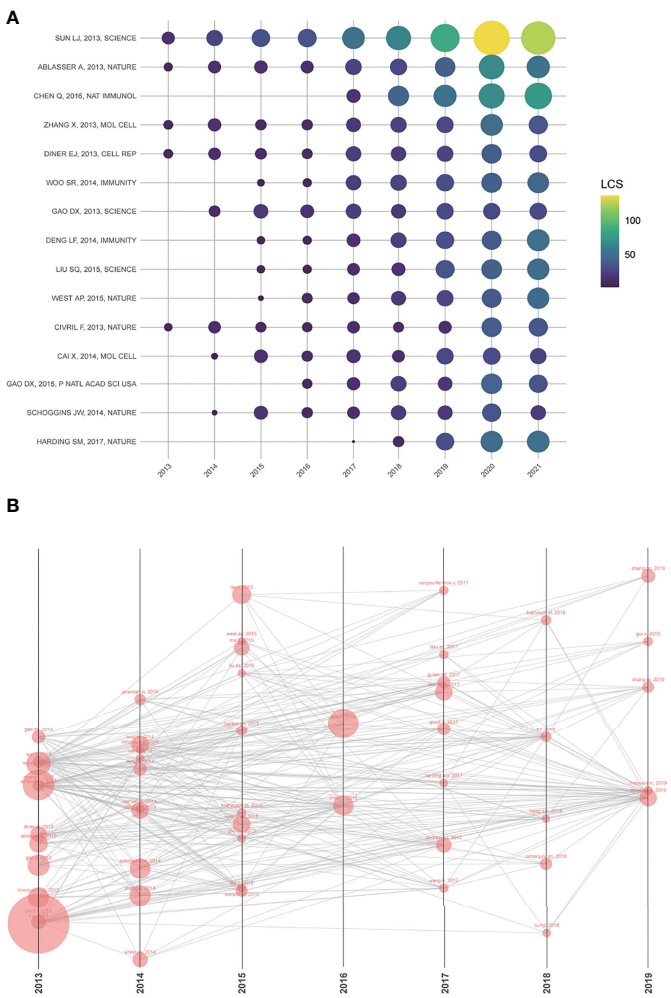

FIGURE 4 | **(A)** The yearly number of local citations of papers with high local citation scores (LCS). The size and colors of the circle present the LCS of papers in that year. **(B)** One paper cited by the other papers with the top 50 LCS. The size of each node is proportional to the frequency of this article by the other 49 articles.

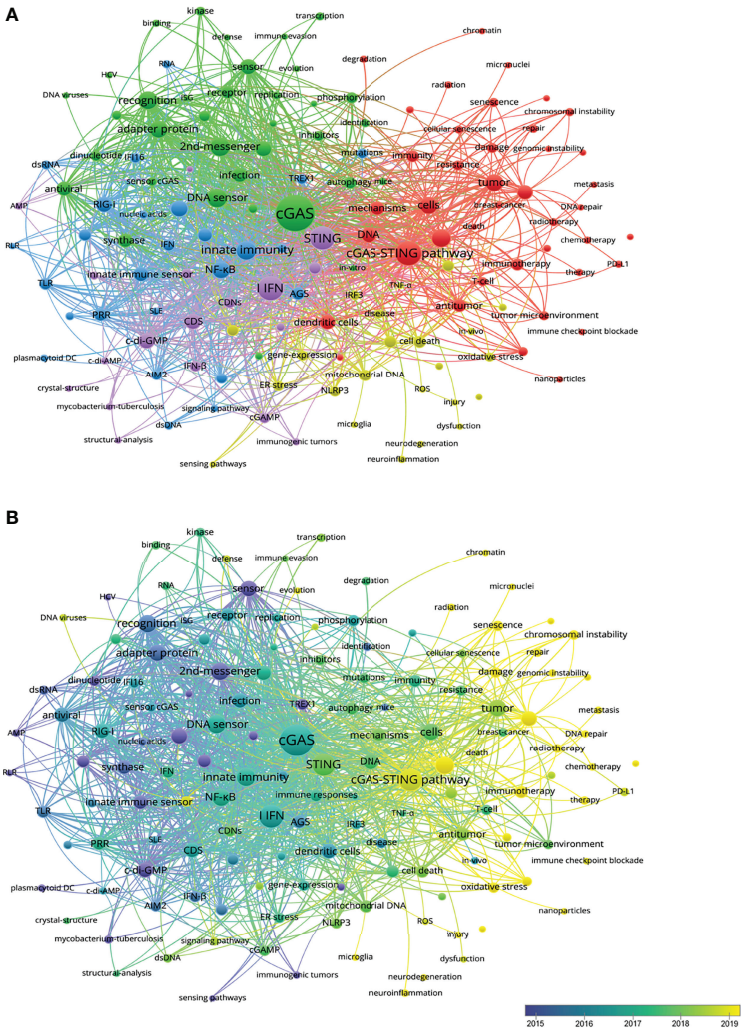

FIGURE 5 | **(A)** CiteSpace visualization map of keywords clustering analysis related to the cGAS-STING pathway. The size of each nodes represents the frequency of occurrences. **(B)** Visualization of keywords according to the average publication year. Keywords in yellow appeared later than that in blue.

Thus, co-occurrence analysis described of hot topics in this area (**Figure 5A**). There were five clusters: cGAS-STING pathway in inflammation and tumor immunology (red), cGAS-STING pathway sensing virus and its structure foundation (green), cGAS-STING pathway in innate immunity (purple), in ROS-induced inflammasome activation (yellow), and in autoimmune disease (blue). In overlay visualization, keywords were colored differently according to their average publication year (**Figure 5B**). For instance, 'DNA sensor' and '2nd-messenger' were appeared at the beginning of the discovery of this area, whereas keywords 'Inflammation' and 'Tumor' were more recent. Senescence (cluster1, APY: 2020.143), Cancer therapy (cluster2, 2020), Neuroinflammation (cluster3, APY: 2020.539), and Neurodegeneration (cluster3, APY: 2020.3) are colored in yellow, which indicated that these fields had grown in popularity recently and would become hotspots soon (**S Table 2**).

Co-cited Reference Clusters Analysis

A co-citation network is a network of references co-cited by one or more papers at the same time. Conceptual clusters were created when a set of manuscripts were cited repeatedly together. **Figure 6A** showed the different clusters of these co-cited references, and 15 clusters were divided by CiteSpace: STING agonist, dsDNA-induced oligomerization, genomic instability, interferon response, acute kidney injury, NF-κB-dependent broad antiviral response, DNA damage response, human cytomegalovirus tegument protein, STING-dependent innate immunity, small molecule, cGAS-STING pathway, STING-dependent cytosolic DNA, early stage, LRRC8 volume-regulated anion channel, and other retroviruses. A timeline view of distinct clusters was presented in **Figure 6B**. It showed that cluster 1, dsDNA-induced oligomerization, had the most citation burst. Moreover, the hotspots were shifting from dsDNA-induced

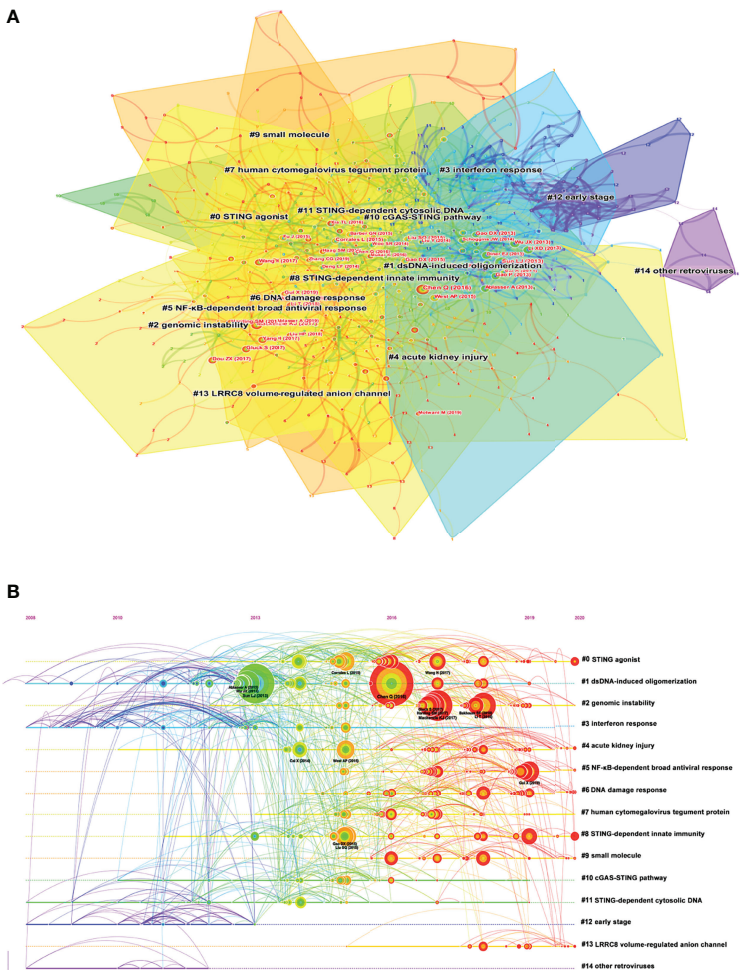

FIGURE 6 | **(A)** The clustered network map of co-cited references on the cGAS-STING pathway. **(B)** The timeline view of co-citation clusters with their cluster-labels on the right.

oligomerization to genomic instability, STING-dependent innate immunity, and NF-κB-dependent broad antiviral response.

Burst Detection

Burst detection is used to reveal the hot references with an abrupt increase over time. In **Figure 7**, nodes represented articles, those nodes with red circles represented burst articles in this area. **Figure 8** showed the most burst of co-cited references began in 2013, the year when the team of Zhijian James Chen discovered cGAS-STING pathway. 4 of 5 top strongest citation bursts were from the team of Zhijian James Chen, which also indicated his team's great influence in this field.

DISCUSSION

In this study, we analyzed the development trends and hotspots of research on the cGAS-STING pathway by VOSviewer, CiteSpace and R (Version 4.1.3) software. We retrieved 1047 original articles and reviews published in 2013-2021. The annual numbers of publications showed an overall upward tread. Interestingly, the Np rocketed up after 2016. These publications with high LCS published before 2016 were the main reason for the rapid growth of the annual Np after 2016.

Among the top countries/regions, the USA ranked first in Np (493, 47.09%), followed by China (370, 35.34%), indicating that the USA and China are the leading countries in the cGAS-STING area. This was closely related to the large research expenditures of the USA and China in recent years. However, the Np, Na, and H-index in the USA were all higher than those in China. This may be because the cGAS-STING pathway was initially proposed by Zhijian James Chen (1), and then deep and extensive research were conducted by Chen's team in the cGAS-STING area. What's more, five of the top ten affiliations and seven of the top ten journals were from the USA. Because of these, the USA prevails in the cGAS-STING area. When it comes to affiliations, the H-index of Chinese Academy of Sciences (21) and Wuhan University (15) were similar to the other top 10 affiliations except

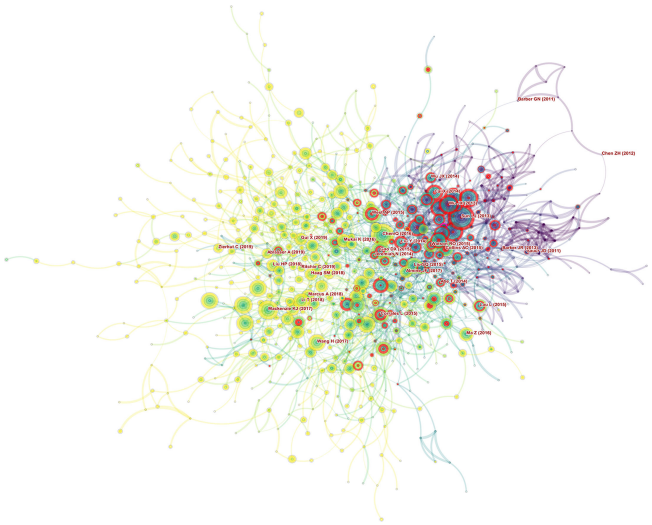

FIGURE 7 | Papers with the strongest citation bursts in original articles on the cGAS-STING pathway between 2013 and 2021.

for University of Texas System (38), but only one original study was included in the top 50 LCS (35), symbolizing that there were good studies in China which attracted the attention of international counterparts, but scholars and affiliations in China should make more efforts to promote the quality of their studies in this field. The other countries also made contributions to this field, although their influences of them were not as good as those in the USA and China.

As can be seen in the co-occurrence network, there were many lines from the USA and the line between the USA and

Top 45 References with the Strongest Citation Bursts

References	Year	Strength	Begin	End	2013 - 2021
Sun LJ, 2013, SCIENCE, V339, P786, DOI 10.1126/science.1232458, DOI	2013	76.82	2013	2018	
Wu JX, 2013, SCIENCE, V339, P826, DOI 10.1126/science.1229963, DOI	2013	49.92	2013	2018	
Ablasser A, 2013, NATURE, V498, P380, DOI 10.1038/nature12306, DOI	2013	36.27	2013	2018	
Gao P, 2013, CELL, V153, P1094, DOI 10.1016/j.cell.2013.04.046, DOI	2013	31.74	2013	2018	
Zhang X, 2013, MOL CELL, V51, P226, DOI 10.1016/j.molcel.2013.05.022, DOI	2013	31.05	2013	2018	
Diner EJ, 2013, CELL REP, V3, P1355, DOI 10.1016/j.celrep.2013.05.009, DOI	2013	30	2013	2018	
Paludan SR, 2013, IMMUNITY, V38, P870, DOI 10.1016/j.immuni.2013.05.004, DOI	2013	14.42	2013	2018	
Wu JX, 2014, ANNU REV IMMUNOL, V32, P461, DOI 10.1146/annurev-immunol-032713-120156, DOI	2014	12.12	2014	2019	
Conlon J, 2013, J IMMUNOL, V190, P5216, DOI 10.4049/jimmunol.1300097, DOI	2013	9.95	2013	2018	
Abe T, 2013, MOL CELL, V50, P5, DOI 10.1016/j.molcel.2013.01.039, DOI	2013	9.26	2013	2018	
Barber GN, 2014, TRENDS IMMUNOL, V35, P88, DOI 10.1016/j.it.2013.10.010, DOI	2014	7.99	2014	2019	
Barker JR, 2013, MBIO, V4, P0, DOI 10.1128/mBio.00018-13, DOI	2013	7.2	2013	2018	
Cavlar T, 2013, EMBO J, V32, P1440, DOI 10.1038/emboj.2013.86, DOI	2013	6.17	2013	2018	
Ablasser A, 2014, J IMMUNOL, V192, P5993, DOI 10.4049/jimmunol.1400737, DOI	2014	5.83	2014	2019	
Danilchanka O, 2013, CELL, V154, P962, DOI 10.1016/j.cell.2013.08.014, DOI	2013	3.08	2013	2018	
Li XD, 2013, SCIENCE, V341, P1390, DOI 10.1126/science.1244040, DOI	2013	36.62	2014	2018	
Gao DX, 2013, SCIENCE, V341, P903, DOI 10.1126/science.1240933, DOI	2013	33.22	2014	2018	
Tanaka Y, 2012, SCI SIGNAL, V5, P0, DOI 10.1126/scisignal.2002521, DOI	2012	24.36	2013	2017	
Civril F, 2013, NATURE, V498, P332, DOI 10.1038/nature12305, DOI	2013	22.01	2013	2017	
Deng LF, 2014, IMMUNITY, V41, P843, DOI 10.1016/j.immuni.2014.10.019, DOI	2014	21.39	2015	2019	
Cai X, 2014, MOL CELL, V54, P289, DOI 10.1016/j.molcel.2014.03.040, DOI	2014	20.39	2015	2019	
Schoggins JW, 2014, NATURE, V505, P691, DOI 10.1038/nature12862, DOI	2014	20.06	2015	2019	
Konno H, 2013, CELL, V155, P688, DOI 10.1016/j.cell.2013.09.049, DOI	2013	18.92	2014	2018	
Ablasser A, 2013, NATURE, V503, P530, DOI 10.1038/nature12640, DOI	2013	17.82	2014	2018	
Gao P, 2013, CELL, V154, P748, DOI 10.1016/j.cell.2013.07.023, DOI	2013	17.09	2014	2018	
Liu Y, 2014, NEW ENGL J MED, V371, P507, DOI 10.1056/NEJMoa1312625, DOI	2014	16.92	2015	2019	
Kranzusch PJ, 2013, CELL REP, V3, P1362, DOI 10.1016/j.celrep.2013.05.008, DOI	2013	16.73	2013	2017	
Li X, 2013, IMMUNITY, V39, P1019, DOI 10.1016/j.immuni.2013.10.019, DOI	2013	15.26	2014	2018	
Ahn J, 2012, P NATL ACAD SCI USA, V109, P19386, DOI 10.1073/pnas.1215006109, DOI	2012	15.14	2013	2017	
Gall A, 2012, IMMUNITY, V36, P120, DOI 10.1016/j.immuni.2011.11.018, DOI	2012	13.76	2013	2017	
Burdette DL, 2013, NAT IMMUNOL, V14, P19, DOI 10.1038/ni.2491, DOI	2013	12.36	2013	2017	
Rongvaux A, 2014, CELL, V159, P1563, DOI 10.1016/j.cell.2014.11.037, DOI	2014	11.93	2015	2019	
Ouyang SY, 2012, IMMUNITY, V36, P1073, DOI 10.1016/j.immuni.2012.03.019, DOI	2012	11	2013	2017	
Zhang X, 2014, CELL REP, V6, P421, DOI 10.1016/j.celrep.2014.01.003, DOI	2014	10.82	2014	2018	
Hansen K, 2014, EMBO J, V33, P1654, DOI 10.15252/embj.201488029, DOI	2014	10.65	2015	2019	
Liang QM, 2014, CELL HOST MICROBE, V15, P228, DOI 10.1016/j.chom.2014.01.009, DOI	2014	9.01	2015	2019	
Lahaye X, 2013, IMMUNITY, V39, P1132, DOI 10.1016/j.immuni.2013.11.002, DOI	2013	8.71	2014	2018	
Jakobsen MR, 2013, P NATL ACAD SCI USA, V110, P0, DOI 10.1073/pnas.1311669110, DOI	2013	8.71	2014	2018	
Goubau D, 2013, IMMUNITY, V38, P855, DOI 10.1016/j.immuni.2013.05.007, DOI	2013	7.25	2014	2018	
Lam E, 2014, J VIROL, V88, P974, DOI 10.1128/JVI.02702-13, DOI	2014	7.05	2014	2018	
Yin Q, 2012, MOL CELL, V46, P735, DOI 10.1016/j.molcel.2012.05.029, DOI	2012	6.87	2013	2017	
Kondo T, 2013, P NATL ACAD SCI USA, V110, P2969, DOI 10.1073/pnas.1222694110, DOI	2013	6.53	2014	2018	
Ahn J, 2014, CURR OPIN IMMUNOL, V31, P121, DOI 10.1016/j.coi.2014.10.009, DOI	2014	6.33	2015	2019	
Wu XM, 2014, NUCLEIC ACIDS RES, V42, P8243, DOI 10.1093/nar/gku569, DOI	2014	3.29	2015	2019	
Kranzusch PJ, 2014, CELL, V158, P1011, DOI 10.1016/j.cell.2014.07.028, DOI	2014	2.53	2015	2019	

FIGURE 8 | CiteSpace visualization map of the top 45 references with the strongest citation bursts involved in the cGAS-STING pathway.

China was the thickest, indicating that the collaboration between the USA and China was very close. Moreover, there were close collaborations between the USA and some countries in Europe, with 3 European affiliations listed in the top 10 affiliations. Therefore, institutions in the USA, China, and other countries should remove academic barriers, try to communicate to promote the development of the cGAS-STING pathway.

Notably, of the top 10 productive journals, the IFs of five were over 10, and the number of published papers in these journals accounted for 1/10 of that in the cGAS-STING area. This indicated that studies about the cGAS-STING pathway were of high quality. Frontiers in immunology (55, 5.33%) published the most articles in this area, followed by journal of immunology (35, 3.39%) and journal of virology (30, 2.91%), which reminded scholars to pay more attention to the roles of the cGAS-STING pathway in immunity and virus detection. In addition, the burst detection showed that STING-dependent innate immunity and NF-κB-dependent broad antiviral response were the hotspots recently. Scholars on this topic should pay more attention to these hotspots.

In the initial phase of one field, research is focused on the basic theories and mechanisms, which lay a solid foundation for further studies. Similarly, the hotspots of the cGAS-STING pathway have been changed from the mechanism to its roles in different diseases and translational medicine. In the first few years, scholars such as Zhijian James Chen and Veit Hornung discovered the role of cGAS in sensing dsDNA and activating the I IFN pathway. cGAS activates the second-messenger (36), which is essential for the STING activation (37–39). What's more, scholars analyzed the structural mechanism how cGAS senses cytosolic DNA (40, 41).

In the next stage, scholars started to study the roles of the cGAS-STING pathway in different diseases and the influences of the cGAS-STING pathway in cell life activities. Immunity published two studies to demonstrate the roles of the cGAS-STING pathway in immunogenic tumors (42, 43), initiating studies of the cGAS-STING pathway in diseases. In these studies, the STING pathway was regarded as a key regulator of tumor immune responses. Researchers found that tumor-derived DNA was the ligand of STING pathway and was associated with phosphorylation of TBK1 and IRF3 and STING-dependent IFN-β. In STING-deficient mice, most of the therapeutic effects for the immune inhibitory factors were lost. In 2015, the relationships between the cGAS-STING pathway and apoptosis, autophagy, and inflammasome activation were studied by scholars (44–46). Based on these mechanistic investigations, the team of Zhijian James Chen and Blossom Damania reviewed the roles of the cGAS-STING pathway in autoimmune, inflammatory disease, and virus infection, respectively (8, 47). These two reviews concluded the studies between 2013 and 2016 and thus got high LCS.

In recent years, the keywords have focused on the roles of the cGAS-STING pathway in the treatments of diseases. In this period (period II in **Figure 2B**), publications increased rapidly based on previous studies. Article keywords demonstrated that scholars in the fields of cancer and neuroscience should pay more attention to the cGAS-STING pathway because these were hotspots in recent years. Shannon Grabosch's study demonstrated that cisplatin activated the cGAS-STING pathway to modify tumor immunogenicity by increasing PD-L1, MHC I and calreticulin in tumor cells (48). In malignant tumors, scientists found that the expression of STING was positively correlated with immune cell infiltration (49). Inhibition of cGAS and STING in tomor cells can prevent tumor metastasis (50, 51). Scientists also found that cGAS-STING pathway promoted tumor progression in lewis lung cancer (LCC) (52), brain tumor (50), colon tumor (53), oral cancer (54), and tongue squamous cell carcinoma (55). In December 2017, Chukwuemika Aroh et al. firstly demonstrated that administration of cGAMP delivered by ultra-pH-sensitive nanoparticle can induce potent antiretroviral response against HIV-1 isolates (56). After that, more and more researchers paid attention to the nanoscience. Since the nanoparticle is a hotspot recently, with the development of interdisciplinary research, researchers should focus on the effects of the nanoparticle on diseases by interfering with the cGAS-STING pathway.

Based on VOSviewer, CiteSpace and R (Version 4.1.3) software, we analyzed and made the visualization of the literature, and revealed the development trends and the hotspots in this field. At the same time, we used LCS to find the important literature, which led to the development of the cGAS-STING area and scholars in this field should pay close attention to these literature. Moreover, this study provided a better insight into the evolving research foci and trends when compared with traditional reviews. However, there are still some limitations. Firstly, only English articles and reviews from SCI-expanded were included. Secondly, because VOSviewer could not analyze the full texts of the publications, it may omit some information. Lastly, the publications included were from 2013 to 2021, the influential studies published in 2022 with low Nc were excluded, but this limitation would not change the results in this study. Therefore, future work should expand the research base to include non-English studies and the latest outstanding publications.

CONCLUSION

This bibliometric analysis revealed that the research on the innate immune DNA sensing cGAS-STING pathway were developing rapidly at present. The USA and China were the leading countries, and the USA has made many outstanding breakthroughs in this field. About 10% studies were published in high-quality journals. From 2013 to 2021, the foci of research on the cGAS-STING pathway has changed from the basic mechanism to treatments of diseases *via* the cGAS-STING pathway, especially cancer and nanoparticle, these would be hotspots of research recently and in the near future.

DATA AVAILABILITY STATEMENT

The raw data supporting the conclusions of this article will be made available by the authors, without undue reservation.

AUTHOR CONTRIBUTIONS

XS and SW conceived the study. XS, YW, QL, TZ, KM, DF, ML, and JW were involved in the data collection and analysis. LZ, WM, ZX, and HY re-examined the data. XS and SW drafted the manuscript. YC and XL revised the manuscript. All authors have provided final approval of the version to be submitted. XS, SW, and YW contributed equally to this work.

FUNDING

This work was supported by grants from the National Natural Science Foundation of China (No.81871601, No.82100090, and No.82000085), grants from the Program of Shanghai Academic Research Leader (No.21XD1402800), grants from the Shanghai "Rising Stars of Medical Talent" Youth Development Program: Outstanding Youth Medical Talents, grants from the Shanghai Natural Science Foundation (22ZR1452200), grants from the Shanghai Sailing Program (21YF1438400).

SUPPLEMENTARY MATERIAL

The Supplementary Material for this article can be found online at: https://www.frontiersin.org/articles/10.3389/fimmu.2022.916383/full#supplementary-material

REFERENCES

1. Sun L, Wu J, Du F, Chen X, Chen ZJ. Cyclic GMP-AMP Synthase is a Cytosolic DNA Sensor That Activates the Type I Interferon Pathway. *Science* (2013) 339(6121):786–91. doi: 10.1126/science.1232458
2. Barnett KC, Coronas-Serna JM, Zhou W, Ernandes MJ, Cao A, Kranzusch PJ, et al. Phosphoinositide Interactions Position cGAS at the Plasma Membrane to Ensure Efficient Distinction Between Self- and Viral DNA. *Cell* (2019) 176 (6):1432–46.e1411. doi: 10.1016/j.cell.2019.01.049
3. Gentili M, Lahaye X, Nadalin F, Nader GPF, Puig Lombardi E, Herve S, et al. The N-Terminal Domain of cGAS Determines Preferential Association With Centromeric DNA and Innate Immune Activation in the Nucleus. *Cell Rep* (2019) 26(9):2377–93.e2313. doi: 10.1016/j.celrep.2019.01.105. Erratum in: *Cell Rep.* 2019 Mar 26;26(13):3798.
4. Mackenzie KJ, Carroll P, Martin CA, Murina O, Fluteau A, Simpson DJ, et al. cGAS Surveillance of Micronuclei Links Genome Instability to Innate Immunity. *Nature* (2017) 548(7668):461–5. doi: 10.1038/nature23449
5. Andreeva L, Hiller B, Kostrewa D, Lässig C, de Oliveira Mann CC, Jan Drexler D, et al. cGAS Senses Long and HMGB/TFAM-Bound U-Turn DNA by Forming Protein-DNA Ladders. *Nature* (2017) 549(7672):394–8. doi: 10.1038/nature23890
6. Gehrke N, Mertens C, Zillinger T, Wenzel J, Bald T, Zahn S, et al. Oxidative Damage of DNA Confers Resistance to Cytosolic Nuclease TREX1 Degradation and Potentiates STING-Dependent Immune Sensing. *Immunity* (2013) 39(3):482–95. doi: 10.1016/j.immuni.2013.08.004
7. Zhou C, Chen X, Planells-Cases R, Chu J, Wang L, Cao L, et al. Transfer of cGAMP Into Bystander Cells *via* LRRC8 Volume-Regulated Anion Channels Augments STING-Mediated Interferon Responses and Anti-Viral Immunity. *Immunity* (2020) 52(5):767–81.e766. doi: 10.1016/j.immuni.2020.03.016
8. Chen Q, Sun L, Chen Z. Regulation and Function of the cGAS-STING Pathway of Cytosolic DNA Sensing. *Nat Immunol* (2016) 17(10):1142–9. doi: 10.1038/ni.3558
9. Zhong B, Yang Y, Li S, Wang Y, Li Y, Diao F, et al. The Adaptor Protein MITA Links Virus-Sensing Receptors to IRF3 Transcription Factor Activation. *Immunity* (2008) 29(4):538–50. doi: 10.1016/j.immuni.2008.09.003
10. Ishikawa H, Ma Z, Barber G. STING Regulates Intracellular DNA-Mediated, Type I Interferon-Dependent Innate Immunity. *Nature* (2009) 461 (7265):788–92. doi: 10.1038/nature08476
11. Abe T, Barber G. Cytosolic-DNA-Mediated, STING-Dependent Proinflammatory Gene Induction Necessitates Canonical NF-κb Activation Through TBK1. *J Virol* (2014) 88(10):5328–41. doi: 10.1128/JVI.00037-14
12. Paludan SR, Bowie AG. Immune Sensing of DNA. *Immunity* (2013) 38 (5):870–80. doi: 10.1016/j.immuni.2013.05.004
13. West AP, Shadel GS, Ghosh S. Mitochondria in Innate Immune Responses. *Nat Rev Immunol* (2011) 11(6):389–402. doi: 10.1038/nri2975
14. Ishikawa H, Barber GN. STING is an Endoplasmic Reticulum Adaptor That Facilitates Innate Immune Signalling. *Nature* (2008) 455(7213):674–8. doi: 10.1038/nature07317
15. Kawai T, Takahashi K, Sato S, Coban C, Kumar H, Kato H, et al. IPS-1, an Adaptor Triggering RIG-I- and Mda5-Mediated Type I Interferon Induction. *Nat Immunol* (2005) 6(10):981–8. doi: 10.1038/ni1243
16. Bhatia R, Shaffer TH, Hossain J, Fisher AO, Horner LM, Rodriguez ME, et al. Surfactant Administration Prior to One Lung Ventilation: Physiological and Inflammatory Correlates in a Piglet Model. *Pediatr Pulmonol* (2011) 46 (11):1069–78. doi: 10.1002/ppul.21485
17. Liu HM, Loo YM, Horner SM, Zornetzer GA, Katze MG, Gale MJr. The Mitochondrial Targeting Chaperone 14-3-3ε Regulates a RIG-I Translocon That Mediates Membrane Association and Innate Antiviral Immunity. *Cell Host Microbe* (2012) 11(5):528–37. doi: 10.1016/j.chom.2012.04.006
18. Zhang C, Shang G, Gui X, Zhang X, Bai XC, Chen ZJ. Structural Basis of STING Binding With and Phosphorylation by TBK1. *Nature* (2019) 567 (7748):394–8. doi: 10.1038/s41586-019-1000-2
19. Fitzgerald KA, McWhirter SM, Faia KL, Rowe DC, Latz E, Golenbock DT, et al. IKKepsilon and TBK1 are Essential Components of the IRF3 Signaling Pathway. *Nat Immunol* (2003) 4(5):491–6. doi: 10.1038/ni921
20. Cancino CA, Merigo JM, Coronado F, Dessouky Y, Dessouky M. Forty Years of Computers & Industrial Engineering: A Bibliometric Analysis. *Comput Ind Eng* (2017) 113:614–29. doi: 10.1016/j.cie.2017.08.033
21. Narotsky D, Green P, Lebwohl B. Temporal and Geographic Trends in Celiac Disease Publications: A Bibliometric Analysis. *Eur J Gastroenterol Hepatol* (2012) 24(9):1071–7. doi: 10.1097/MEG.0b013e328355a4ab
22. Seriwala H, Khan M, Shuaib W, Shah S. Bibliometric Analysis of the Top 50 Cited Respiratory Articles. *Expert Rev Respir Med* (2015) 9(6):817–24. doi: 10.1586/17476348.2015.1103649
23. Khan M, Ullah W, Riaz I, Bhulani N, Manning W, Tridandapani S, et al. Top 100 Cited Articles in Cardiovascular Magnetic Resonance: A Bibliometric Analysis. *J Cardiovasc Magn Reson: Off J Soc Cardiovasc Magn Reson* (2016) 18(1):87. doi: 10.1186/s12968-016-0303-9
24. Landis J, Koch G. The Measurement of Observer Agreement for Categorical Data. *Biometrics* (1977) 33(1):159–74. doi: 10.2307/2529310
25. Wang S, Zhou H, Zheng L, Zhu W, Zhu L, Feng D, et al. Global Trends in Research of Macrophages Associated With Acute Lung Injury Over Past 10 Years: A Bibliometric Analysis. *Front Immunol* (2021) 12:669539. doi: 10.3389/fimmu.2021.669539
26. Hirsch J. An Index to Quantify an Individual's Scientific Research Output. *Proc Natl Acad Sci USA* (2005) 102(46):16569–72. doi: 10.1073/pnas.0507655102
27. Jones T, Huggett S, Kamalski J. Finding a Way Through the Scientific Literature: Indexes and Measures. *World Neurosurg* (2011) 76:36–8. doi: 10.1016/j.wneu.2011.01.015
28. Roldan-Valadez E, Salazar-Ruiz S, Ibarra-Contreras R, Rios C. Current Concepts on Bibliometrics: A Brief Review About Impact Factor, Eigenfactor Score, CiteScore, SCImago Journal Rank, Source-Normalised Impact Per Paper, H-Index, and Alternative Metrics. *Irish J Med Sci* (2019) 188(3):939–51. doi: 10.1007/s11845-018-1936-5
29. van Eck N, Waltman L. Software Survey: VOSviewer, a Computer Program for Bibliometric Mapping. *Scientometrics* (2010) 84(2):523–38. doi: 10.1007/s11192-009-0146-3
30. Chen C. Searching for Intellectual Turning Points: Progressive Knowledge Domain Visualization. *Proc Natl Acad Sci USA* (2004) 101(Suppl 1):5303–10. doi: 10.1073/pnas.0307513100

31. Aria M, Cuccurullo C. Bibliometrix: An R-Tool for Comprehensive Science Mapping Analysis. *J Informetr* (2017) 11(4):959–75. doi: 10.1016/j.joi.2017.08.007
32. Hao X, Liu Y, Li X, Zheng J. Visualizing the History and Perspectives of Disaster Medicine: A Bibliometric Analysis. *Disaster Med Public Health Preparedness* (2019) 13:966–73. doi: 10.1017/dmp.2019.31
33. Frame JD, Baum JJ, Card M. Information Approach to Examining Developments in an Energy Technology - Coal-Gasification. *J Am Soc Inf Sci* (1979) 30(4):193–201. doi: 10.1002/asi.4630300404
34. Harding S, Benci J, Irianto J, Discher D, Minn A, Greenberg R. Mitotic Progression Following DNA Damage Enables Pattern Recognition Within Micronuclei. *Nature* (2017) 548(7668):466–70. doi: 10.1038/nature23470
35. Liu H, Zhang H, Wu X, Ma D, Wu J, Wang L, et al. Nuclear cGAS Suppresses DNA Repair and Promotes Tumorigenesis. *Nature* (2018) 563(7729):131–6. doi: 10.1038/s41586-018-0629-6
36. Kranzusch P, Lee A, Berger J, Doudna J. Structure of Human cGAS Reveals a Conserved Family of Second-Messenger Enzymes in Innate Immunity. *Cell Rep* (2013) 3(5):1362–8. doi: 10.1016/j.celrep.2013.05.008
37. Ablasser A, Schmid-Burgk J, Hemmerling I, Horvath G, Schmidt T, Latz E, et al. Cell Intrinsic Immunity Spreads to Bystander Cells *via* the Intercellular Transfer of cGAMP. *Nature* (2013) 503(7477):530–4. doi: 10.1038/nature12640
38. Gao P, Ascano M, Zillinger T, Wang W, Dai P, Serganov A, et al. Structure-Function Analysis of STING Activation by C[G(2',5')Pa(3',5')P] and Targeting by Antiviral DMXAA. *Cell* (2013) 154(4):748–62. doi: 10.1016/j.cell.2013.07.023
39. Zhang X, Shi H, Wu J, Zhang X, Sun L, Chen C, et al. Cyclic GMP-AMP Containing Mixed Phosphodiester Linkages is an Endogenous High-Affinity Ligand for STING. *Mol Cell* (2013) 51(2):226–35. doi: 10.1016/j.molcel.2013.05.022
40. Civril F, Deimling T, de Oliveira Mann C, Ablasser A, Moldt M, Witte G, et al. Structural Mechanism of Cytosolic DNA Sensing by cGAS. *Nature* (2013) 498(7454):332–7. doi: 10.1038/nature12305
41. Zhang X, Wu J, Du F, Xu H, Sun L, Chen Z, et al. The Cytosolic DNA Sensor cGAS Forms an Oligomeric Complex With DNA and Undergoes Switch-Like Conformational Changes in the Activation Loop. *Cell Rep* (2014) 6(3):421–30. doi: 10.1016/j.celrep.2014.01.003
42. Woo S, Fuertes M, Corrales L, Spranger S, Furdyna M, Leung M, et al. STING-Dependent Cytosolic DNA Sensing Mediates Innate Immune Recognition of Immunogenic Tumors. *Immunity* (2014) 41(5):830–42. doi: 10.1016/j.immuni.2014.10.017
43. Deng L, Liang H, Xu M, Yang X, Burnette B, Arina A, et al. STING-Dependent Cytosolic DNA Sensing Promotes Radiation-Induced Type I Interferon-Dependent Antitumor Immunity in Immunogenic Tumors. *Immunity* (2014) 41(5):843–52. doi: 10.1016/j.immuni.2014.10.019
44. White M, McArthur K, Metcalf D, Lane R, Cambier J, Herold M, et al. Apoptotic Caspases Suppress mtDNA-Induced STING-Mediated Type I IFN Production. *Cell* (2014) 159(7):1549–62. doi: 10.1016/j.cell.2014.11.036
45. Watson R, Bell S, MacDuff D, Kimmey J, Diner E, Olivas J, et al. The Cytosolic Sensor cGAS Detects Mycobacterium Tuberculosis DNA to Induce Type I Interferons and Activate Autophagy. *Cell Host Microbe* (2015) 17(6):811–9. doi: 10.1016/j.chom.2015.05.004
46. Man S, Karki R, Malireddi R, Neale G, Vogel P, Yamamoto M, et al. The Transcription Factor IRF1 and Guanylate-Binding Proteins Target Activation of the AIM2 Inflammasome by Francisella Infection. *Nat Immunol* (2015) 16(5):467–75. doi: 10.1038/ni.3118
47. Ma Z, Damania B. The cGAS-STING Defense Pathway and Its Counteraction by Viruses. *Cell Host Microbe* (2016) 19(2):150–8. doi: 10.1016/j.chom.2016.01.010
48. Grabosch S, Bulatovic M, Zeng F, Ma T, Zhang L, Ross M, et al. Cisplatin-Induced Immune Modulation in Ovarian Cancer Mouse Models With Distinct Inflammation Profiles. *Oncogene* (2019) 38(13):2380–93. doi: 10.1038/s41388-018-0581-9
49. An X, Zhu Y, Zheng T, Wang G, Zhang M, Li J, et al. An Analysis of the Expression and Association With Immune Cell Infiltration of the cGAS/STING Pathway in Pan-Cancer. *Mol Ther Nucleic Acids* (2019) 14:80–9. doi: 10.1016/j.omtn.2018.11.003
50. Chen Q, Boire A, Jin X, Valiente M, Er EE, Lopez-Soto A, et al. Carcinoma-Astrocyte Gap Junctions Promote Brain Metastasis by cGAMP Transfer. *Nature* (2016) 533(7604):493–8. doi: 10.1038/nature18268
51. Bakhoum SF, Ngo B, Laughney AM, Cavallo JA, Murphy CJ, Ly P, et al. Chromosomal Instability Drives Metastasis Through a Cytosolic DNA Response. *Nature* (2018) 553(7689):467–72. doi: 10.1038/nature25432
52. Lemos H, Mohamed E, Huang L, Ou R, Pacholczyk G, Arbab AS, et al. STING Promotes the Growth of Tumors Characterized by Low Antigenicity *via* IDO Activation. *Cancer Res* (2016) 76(8):2076–81. doi: 10.1158/0008-5472.CAN-15-1456
53. Liang H, Deng L, Hou Y, Meng X, Huang X, Rao E, et al. Host STING-Dependent MDSC Mobilization Drives Extrinsic Radiation Resistance. *Nat Commun* (2017) 8(1):1736. doi: 10.1038/s41467-017-01566-5
54. Cheng AN, Cheng LC, Kuo CL, Lo YK, Chou HY, Chen CH, et al. Mitochondrial Lon-Induced mtDNA Leakage Contributes to PD-L1-Mediated Immunoescape *via* STING-IFN Signaling and Extracellular Vesicles. *J Immunother Cancer* (2020) 8(2):e001372. doi: 10.1136/jitc-2020-001372
55. Liang D, Xiao-Feng H, Guan-Jun D, Er-Ling H, Sheng C, Ting-Ting W, et al. Activated STING Enhances Tregs Infiltration in the HPV-Related Carcinogenesis of Tongue Squamous Cells *via* the C-Jun/CCL22 Signal. *Biochim Biophys Acta* (2015) 1852(11):2494–503. doi: 10.1016/j.bbadis.2015.08.011
56. Aroh C, Wang Z, Dobbs N, Luo M, Chen Z, Gao J, et al. Innate Immune Activation by cGMP-AMP Nanoparticles Leads to Potent and Long-Acting Antiretroviral Response Against HIV-1. *J Immunol* (2017) 199(11):3840–8. doi: 10.4049/jimmunol.1700972

Conflict of Interest: The authors declare that the research was conducted in the absence of any commercial or financial relationships that could be construed as a potential conflict of interest.

The reviewer, DY, declared a shared affiliation with the authors to the handling editor at the time of review.

Publisher's Note: All claims expressed in this article are solely those of the authors and do not necessarily represent those of their affiliated organizations, or those of the publisher, the editors and the reviewers. Any product that may be evaluated in this article, or claim that may be made by its manufacturer, is not guaranteed or endorsed by the publisher.

frontiers | Frontiers in Immunology

ORIGINAL RESEARCH
published: 05 July 2022
doi: 10.3389/fimmu.2022.913901

Innate/Inflammatory Bioregulation of Surfactant Protein D Alleviates Rat Osteoarthritis by Inhibiting Toll-Like Receptor 4 Signaling

Huanyu Jiang[1,2†], *Yubiao Zhang*[1,2†], *Geliang Hu*[1†], *Xiaobin Shang*[1], *Jianghua Ming*[1], *Ming Deng*[1], *Yaming Li*[1], *Yonggang Ma*[1], *Shiqing Liu*[1] *and Yan Zhou*[1,2*]

[1] *Department of Orthopedics, Renmin Hospital of Wuhan University, Wuhan, China,* [2] *Central Laboratory, Renmin Hospital of Wuhan University, Wuhan, China*

OPEN ACCESS

Edited by:
Kari Ann Shirey, University of Maryland, Baltimore, United States

Reviewed by:
Daniel Prantner, University of Maryland, Baltimore, United States
Eloi Franco-Trepat, Health Research Institute of Santiago de Compostela (IDIS), Spain

***Correspondence:**
Yan Zhou
yanzhou0827@whu.edu.cn

†These authors have contributed equally to this work

Specialty section:
This article was submitted to Inflammation, a section of the journal Frontiers in Immunology

Received: *06 April 2022*
Accepted: *10 June 2022*
Published: *05 July 2022*

Citation:
Jiang H, Zhang Y, Hu G, Shang X, Ming J, Deng M, Li Y, Ma Y, Liu S and Zhou Y (2022) Innate/Inflammatory Bioregulation of Surfactant Protein D Alleviates Rat Osteoarthritis by Inhibiting Toll-Like Receptor 4 Signaling. Front. Immunol. 13:913901. doi: 10.3389/fimmu.2022.913901

Osteoarthritis (OA) is a deteriorating disease of cartilage tissues mainly characterized as low-grade inflammation of the joint. Innate immune molecule surfactant protein D (SP-D) is a member of collectin family of collagenous Ca^{2+}-dependent defense lectins and plays a vital role in the inflammatory and innate immune responses. The present study investigated the SP-D-mediated innate/inflammatory bioregulation in OA and explored the underlying molecular mechanism. Transcriptome analysis revealed that SP-D regulated genes were strongly enriched in the inflammatory response, immune response, cellular response to lipopolysaccharide (LPS), PI3K-Akt signaling, Toll-like receptor (TLR) signaling, and extracellular matrix (ECM)-receptor interaction pathways. Knockdown of the SP-D gene by the recombinant adeno-associated virus promoted the macrophage specific markers of CD68, F4/80 and TLR4 in the articular cartilage *in vivo*. SP-D alleviated the infiltration of synovial macrophages and neutrophils, and inhibited TLR4, TNF-α and the phosphorylation of PI3K, Akt and NF-κB p65 in cartilage. SP-D suppressed cartilage degeneration, inflammatory and immune responses in the rat OA model, whilst TAK-242 strengthened this improvement. In *in vitro* conditions, SP-D pre-treatment inhibited LPS-induced overproduction of inflammation-correlated cytokines such as IL-1β and TNF-α, and suppressed the overexpression of TLR4, MD-2 and NLRP3. SP-D prevented the LPS-induced degradation of ECM by down-regulating MMP-13 and up-regulating collagen II. Blocking of TLR4 by TAK-242 further enhanced these manifestations. We also demonstrated that SP-D binds to the TLR4/MD-2 complex to suppress TLR4-mediated PI3K/Akt and NF-κB signaling activation in chondrocytes. Taken together, these findings indicate that SP-D has chondroprotective properties dependent on TLR4-mediated PI3K/Akt and NF-κB signaling and that SP-D has an optimal bioregulatory effect on the inflammatory and innate responses in OA.

Keywords: surfactant protein D, osteoarthritis, inflammation, innate immunity, chondrocyte, toll-like receptor 4

INTRODUCTION

Osteoarthritis (OA) is a deteriorating disease of cartilage tissues, and inflammation plays a leading role in its pathogenesis (1). The pathogenesis of OA involves not only the destruction of cartilage tissues but also the remodeling of subchondral bones, formation of ectopic bones, articular cartilage hypertrophy, and inflammation of the synovial lining (2). OA affects the whole joint and causes inflammation and other clinical manifestations. The inflammation in OA is chronic, relatively mild, and mediated primarily by the innate immune system (3).

Surfactant protein D (SP-D) is a member of the soluble C-type lectin family called collectins. This protein acts as a link between innate immunity and adaptive immunity and prevents infection, allergy, and inflammation (4, 5). The lung stabilizing effect of SP-D is widely known. Still, its stabilizing roles in extra-pulmonary tissues such as articular cartilage, brain, testes, heart, kidneys, and pancreas are poorly understood. In addition, SP-D is expressed at different levels in the synovial fluid of rheumatoid arthritis patients and is involved in the pathogenesis of rheumatoid arthritis (6–8). Our previous studies have shown that SP-D is highly expressed in the cartilage and regulates chondrocyte apoptosis (9, 10).

SP-D modulates the immune function by interacting with Toll-like receptors (TLRs), which are a type of pattern recognition receptors (PRRs) (11, 12). TLR4 activates the innate immune response by recognizing danger-associated molecular patterns (DAMPs) that are mainly endogenous signals for cell death and tissue damage. Lipopolysaccharide (LPS), an outer surface component of Gram-negative bacteria, is an exogenous TLR4 agonist, while high mobility group box 1 and heat shock proteins are endogenous TLR4 agonists (13). Opioid-induced non-stereoselective activation of TLR4 and increased activation of TLR4 signaling by the release of DAMPs, may act as a critical trigger for continuous NOD-like receptor protein 3 (NLRP3) inflammasome activation (14). Studies have shown that SP-D can inhibit the activation of alveolar macrophages and dendritic cells *via* mite allergen-induced TLR4 signaling. The inhibition by SP-D depends on the binding of carbohydrate recognition domain (CRD) to the extracellular domain of TLR4 (15). OA-associated inflammation has been linked to the innate immune response *via* different mechanisms including the activation of TLRs (16). TLRs are members of a highly conserved family of receptors that recognize either pathogen or DAMPs, which are host-derived molecules released as a response to tissue stress and injury (17). TLR4 is involved in the production of innate immune factors that increase synovitis, cartilage degradation and osteoarthritis (18).

In this study, we explored the functional relevance of SP-D to better understand its role as a suppressor of OA-associated immune responses and inflammation in chondrocytes. We further analyzed the impact of SP-D on the signal transmission potential of the TLR4-mediated signaling in osteoarthritic chondrocytes. All these findings suggest that SP-D may be a potential target for OA treatment.

MATERIALS AND METHODS

Reagents and Antibodies

F4/80 (#SAB5500103) was obtained from Sigma-Aldrich (St. Louis, MO, USA). The TLR4 inhibitor TAK-242 (#614316) was obtained from Calbiochem (San Diego, CA, USA). The PI3K inhibitor wortmannin (#HY-10197) was obtained from MedChemExpress (New Jersey, USA). Collagen II (#28459-1-AP) was obtained from Proteintech Group (Wuhan, China). TLR4 (#AF7017), CD68 (#DF7518), PI3K (#DF6069) antibodies were obtained from Affinity Biosciences (Cincinnati, OH, USA). SP-D (#ab220422), MD-2 (#ab24182), TNF-α (#ab66579), glyceraldehyde-3-phosphate dehydrogenase (GAPDH) (#ab181602), MMP-13 (#ab84594), and NLRP3 (ab263899) antibodies were obtained from Abcam (Cambridge, UK). Antibodies for NF-κB p65 (#8242), phospho-p65 (p-p65) (#3033), p-Akt (#4060) and Akt (#9272) were procured from Cell Signaling Technology (Boston, MA, USA). Recombinant human SP-D (rhSP-D) (#CSB-YP021175HU) was purchased from Huamei Biotech Co., Ltd (Wuhan, China). ELISA Kits of rat IL-1β (#ELK1272) and TNF-α (#ELK1396) were purchased from ELK Biotechnology (Wuhan, China). SNP (#1008) was purchased from Youcare Pharmaceutical Group Co., Ltd (Beijing, China). All of the other chemicals and reagents were of analytical grade.

Cell Culture, RNA Isolation and Sample Preparation

Primary chondrocytes were isolated from the knee joint of Sprague-Dawley (SD) newborn rats. The 0.5-1 mm^3 pieces of cartilage were digested with 0.25% trypsin and 0.02% EDTA for 1 h. The samples were transferred to a dish containing 0.2% type II collagenase and incubated for 4 - 5 h at 37°C. The suspended cells were carefully collected by pipette aspiration. Cells were washed and resuspended in complete Dulbecco's modified Eagle's medium/F12 (Hyclone, USA), supplemented with 10% fetal bovine serum and penicillin/streptomycin. The primary cells were frozen and stored for subsequent cell experiments.

Third generation of rat chondrocytes were seeded in 6-well culture plates for 12 h. The complete cDNA length of the SP-D gene was cloned into the pcDNA3.1 vector (Youbio Biotech Changsha, PRC) using the hot fusion method designed with CE Design V1.04 (Vazyme Biotech Co., Ltd). Each primer comprises of a fragment of gene specific sequence and a 17-30 bp sequence of the pcDNA3.1 vector. This vector also harbored a FLAG tag (Sigma), which was fused to the 3' end of SP-D and used as a labeled protein. After the cells grew to about 80% confluence, the medium was removed, and the cells were co-treated by lipofectamine transfected pcDNA3.1 empty plasmid and pcDNA3.1-SP-D plasmid (1 μg/μL). The media was changed after 6 h, and the samples were collected at 48 h. The culture medium was removed at the specified time point, and the total RNA of cartilage tissue cells was isolated using the GenElute™ Mammalian Total RNA Miniprep kit (Sigma). The total RNA was resolved with DNAse I (Qiagen, Hilden, Germany). The concentration and consistency of RNA were determined with a

2100 Microbial Detector (Agilent Technologies). TaqMan reverse transcription reagents and a hexamer (Applied Biosystems, Foster City, CA, USA) were used to reverse transcribe the RNA (150 ng/test sample) into cDNA for RT-PCR.

RNA-Sequencing and Bioinformatics Analysis

RNA-Sequencing was carried out using RNA samples to ensure sufficient RNA quantity and less variation. The process involved total RNA isolation, cDNA library preparation, and RNA transcriptome sequencing (Illumina HiSeq 4000). These procedures were carried out by Shenzhen BGI Tech Co., Ltd. Both pcDNA3.1-SP-D and control chondrocytes had three biological replicates. There were six RNA-seq samples (SP-D_1st, SP-D_2nd, SP-D_3rd, Ctrl_1st, Ctrl_2nd, and Ctrl_3rd). The fragments per kilobase of transcript per million fragments mapped (FPKM) was used to present the level of gene expression. The features of RNA were verified by Agilent 2100 Microbial Detector (Labx, Midland, Canada). During RNA-sequencing, a template with RNA Concordance Number > 6.5 was used. After sequencing the transcriptome, low-quality, environmental pollutants from the power adapter and high-component unidentified base (N) noise readings were filtered out. Bowtie 2 (18) (http://bowtie-bio.sourceforge.net/Bowtie2/index.html) was then used to align the reads to the reference gene (NCBI Rnor 6.0). Subsequently, DEseq2 was used to test the differential expression genes (DEGs). The fold change was > 2, and the adjusted P value was < 0.05. A heat map was created using MeV (https://sourceforge.net/projects/mev-tm4/) to assess the performance levels of DEGs. To determine the gene functions, DEGs were used as inputs to the Gene Ontology (GO) and Kyoto Encyclopedia of Genes and Genomes (KEGG) databases.

Recombinant Adeno-Associated Virus (rAAV) Construction and Animal Studies

ShRNAs specific for SP-D/scrambled controls were cloned into the GV478 AAV vector (Shanghai Genechem Co., Ltd), and co-transfected into AAV-293 cells with pAAV-RC and pHelper vectors. rAAV particles were isolated from cell supernatants, concentrated and purified for *in vivo* studies.

Adult male Sprague-Dawley (SD) rats were procured from Wuhan University Clinical Experiment Management Center/ABSL-III laboratory. The animal studies were approved by the Federation of Small Animal Care and Application of Wuhan University Medical College. In the rAAV serotype study of small animals with normal bones and joints, rats were injected with rAAV encoded SP-D-specific shRNA intra-articularly [1×10^{10} deoxyribonuclease resistant particle (drp)/25 μl/knee joint] for 10 consecutive days (**Table 1**). The rats were sacrificed at the fourth week of the first injection, and no other intervention was carried out during this time.

All the rats were fed under the standard conditions for one week to acclimatize them to the laboratory conditions. The rats were randomly divided into five groups (n = 5): sham operation group, OA-induction group, OA + TAK-242 group, OA + rhSP-D group, and OA + rhSP-D + TAK-242 group. OA was induced through transection of the anterior cruciate ligament of the knee joint and resection of the medial meniscus (ACLT + MMx), followed by active movement of the rats in the electronic rotating cage (19, 20). The joint cavity injection dose was kept as 40 μl TAK-242 (4 μM) and 40 μg/mL rhSP-D once per week, and the administration of the dose started fourth-week post-surgery. Phosphate buffered saline (PBS) was injected in the sham operation group rats and OA induction group rats (**Table 1**). At 10 weeks post-operation, the animals were euthanized by cardiac exsanguination.

Histological Analysis

The knee joints of the rats were separated, fixed with 4% paraformaldehyde for 24 h, decalcified for 6 weeks, and embedded with paraffin wax. 5 μm sagittal sections were prepared and stained with toluidine blue-O and hematoxylin-eosin (H&E). The pathophysiology was analyzed by two blind observers according to the modified Mankin scoring system (21). In addition, the levels of proteoglycan in the cartilage tissues were determined by Safranin-O-Fast Green staining.

Examination of Immune Cell Infiltration in Synovial Tissues

The synovial tissue samples were collected from the side of the iliac tendon and fixed in 2.5% glutaraldehyde in 0.1 M PBS (pH 7.3). The test samples were washed with PBS, treated with 1% osmium oxide at 4°C, and immobilized for 3 h. The samples were rinsed in dH_2O, dried with alcohol and toluene concentration gradient, and embedded in epoxy resin. The sliced sections were two-way colored and imaged with a transmission electron microscope (TEM) (HITACHI, H-600IV, Japan).

TABLE 1 | The treatments in each group.

Group	PBS	rAAV-GFP	rAAV-SP-D shRNA	TAK-242	rhSP-D
Control group	+	–	–	–	–
rAAV-GFP + Control group	–	+	–	–	–
rAAV-SP-D + Control group	–	–	+	–	–
Sham operation group	+	–	–	–	–
OA-induction group	+	–	–	–	–
OA + TAK-242 group	–	–	–	+	–
OA + rhSP-D group	–	–	–	–	+
OA + rhSP-D + TAK-242 group	–	–	–	+	+

Immunohistochemistry and Immunofluorescence Analysis

The TLR4, F4/80, TNF-α, SP-D, and CD68 expressions in articular cartilage were evaluated by immunohistochemistry, and SP reaction was carried out according to the manufacturer's protocol. Briefly, cartilage sections were treated with a moderate primary antibody and visualized using an optical microscope. The percentage of positively immunostained cells was measured. The immunofluorescent mean densities of p-PI3K, p-Akt and p-p65 in cartilage samples were assessed by Image-Pro Plus 6.0 image analysis software (Media Cybernetics Co., USA). The tissue sections were incubated with a fluorescent-conjugated secondary antibody (Boster Biological Engineering, Wuhan, China) under dark conditions for 1 h and visualized using fluorescence microscopy (AX10, Carl Zeiss).

Cell Stimulation

Primary chondrocytes from SD newborn rats were resuscitated and cultured. The cells were grown inside a humidified 5% CO2 incubator at 37°C and passed down until 80% converged. After reaching the third generation, cells were seeded in 6-well culture plates for 12 h, the medium was removed and pre-treated with a series of rhSP-D concentrations, pcDNA3.1-SP-D (1 μg/μL), TLR4 inhibitor TAK-242 (1 μM), and wortmannin (3 nM) for 2 h before LPS (1 μg/mL) co-treatment for 24 h.

Western Blotting

The chondrocyte proteins were isolated using the total protein extraction kit according to the manufacturer's instructions. The protein samples were separated by SDS-PAGE, transferred to PVDF membrane, and blocked with 5% (w/v) skimmed milk powder diluted with TBST for 1 h. The primary antibodies against collagen II, MMP-13, NLRP3, TLR4, MD-2, p65, p-p65, p-PI3K, PI3K, p-Akt, Akt, and GAPDH were then used to probe the blots at 4°C overnight. The blots were washed in TBST [50 ml TrisHCL (1 M, pH7.5), 8g Nacl, 0.2 g Kcl, 0.5 ml Tween 20, in 1L distilled water], incubated with HRP-conjugated secondary antibodies for 1 h, treated with enhanced electrochemiluminescence detection reagent (Amersham Biosciences, USA), and visualized using Odyssey infrared imager protein detection system software (LI-COR Bioscience, NE, UK). The relative expression level of the target protein was normalized to the band intensity of GAPDH.

ELISA Analysis

The levels of IL-1β and TNF-α were determined in the culture supernatant, collected at the experimental endpoint. IL-1β and TNF-α levels were measured using rat ELISA kits according to the manufacturers' protocol (technical duplicates were measured and mean values were used). Absorbance values were determined at 450 nm using a microplate reader and standard curves relating concentration to absorbance values were plotted.

Immunofluorescence

The chondrocytes were allowed to grow and develop to 70% confluence on the 6-well plate and subjected to a serum protein starvation period before the test. The cells were immobilized in 4% paraformaldehyde for 20 minutes, infiltrated in 0.5% Triton X-100 for 5 minutes, and blocked in 1% BSA for 10 minutes. The cells were then incubated for 2 h with rabbit antibodies against PI3K and NF-κB p65. The cells were washed again and incubated with Cy3 coupling reaction secondary antibody (Bost Bioengineering, Wuhan, China) for 1 h. DAPI was then used for nuclear staining, and the cells were imaged using a fluorescence microscope (AX10, Carl Zeiss).

Molecular Docking

The X-ray crystal structures of TLR4/MD-2 homodimer complex (PDB code: 3VQ2, screen resolution: 2.48 Å) were downloaded from the RCSB protein data bank (http://www.rcsb.org/). Based on the Tripos force field and G-asteiger-Huckel charge in the Sybyl package, the chemical structure of SP-D was constructed. The Surflex-Dock program flow was used to simulate the molecular interactions between SP-D and TLR4/MD-2. Finally, UCSF PyMoL was used to transform the output into a 3D image for visualization.

Statistical Analysis

Data are presented as mean ± standard error of the mean (SEM). Student's t-test and one-way analysis of variance (ANOVA) with Spearman rank correlation test were used for two-group and multi-group comparisons, respectively. All statistical analyses were performed by SPSS version 15.0 and GraphPad Prism 5 software (San Diego, Florida, UK). A P value of < 0.05 was considered statistically significant.

RESULTS

SP-D Overexpression Broadly Affected the Gene Expression Profile of Chondrocytes

To explore the targets regulated by SP-D in OA, the expression of SP-D was overexpressed in chondrocytes by transfection of pcDNA3.1-SP-D plasmid. Compared with control plasmid, pcDNA3.1-SP-D effectively promoted protein expression of SP-D (**Figure 1A**). Then, RNA-Sequencing was used to detect the gene expression profiles of SP-D overexpression and control chondrocytes. The amount of the cleaned reads that were mapped to the human genome averaged 73 million per sample and the amount of uniquely mapped reads averaged 62 million (**Supplementary Table S1**).

Based on the FPKM values of each expressed gene, a correlation matrix was constructed for the six samples that were used for unsupervised hierarchical clustering. As shown, there was a clear separation of the pcDNA3.1-SP-D and control samples, with the three biological replicates clustered together (**Figure 1B**). This result demonstrated that SP-D overexpression obviously changed the gene expression profile of chondrocytes.

The differential gene cluster map showed a close relationship between the gene expression pattern and cluster of the samples. The heatmap plot of the FPKM values of all DEGs showed a clear separation between the pcDNA3.1-SP-D and control group, and a

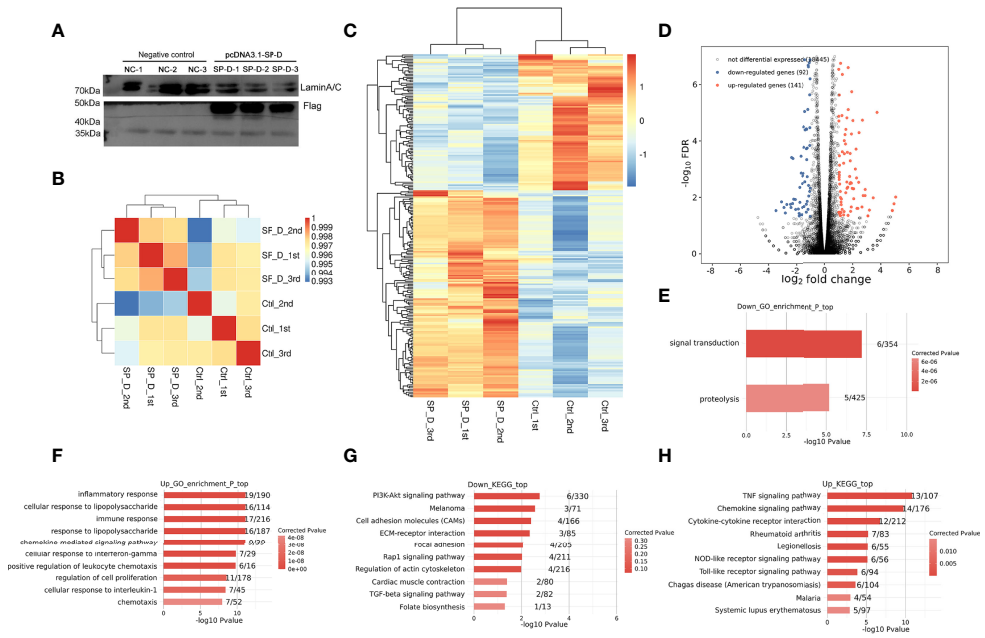

FIGURE 1 | Effects of SP-D overexpression on the gene expression profile of chondrocytes. **(A)** Chondrocytes were co-treated by lipofectamine transfected pcDNA3.1 empty plasmid and pcDNA3.1-SP-D plasmid (1 μg/μL). The protein expression of SP-D was assessed *via* western blotting. **(B)** The clustering analysis of samples showed high similarity, which confirmed the correctness of the experimental design and sample sampling. **(C)** The heat map showed that the gene expression patterns and clustering relationships of the samples were similar. **(D)** Comparisons between samples showed the number of differentially expressed genes. **(E, F)** GO analysis showed that the biological processes such as regulation of 'inflammatory responses', 'immune response' and 'response to LPS' were associated with SP-D in chondrocytes. **(G, H)** KEGG pathway analyses revealed these genes to be significantly linked to pathways including the 'PI3K-Akt signaling pathway', 'ECM-receptor interaction', 'TLR signaling pathway', and 'TNF signaling pathway'.

high consistency among three replicates of the same groups (**Figure 1C**). On comparison of DEGs among various samples, we found that 141 genes were significantly up-regulated and 92 genes were down-regulated (**Figure 1D**). All the results above supported a conclusion that SP-D shows a significantly higher capacity of up-regulating than down-regulating gene expression. We used GO analysis to better understand the role of SP-D and related genes. All molecular processes, including the inflammatory responses, immune responses, LPS responses (**Figures 1E, F**), extracellular space, and chemokine activity (**Supplementary Figure 1**) were related to SP-D in chondrocytes. The KEGG pathway analyses revealed that these genes were significantly related to PI3K-Akt signaling, TLR signaling, ECM-receptor interactions, and Rap1 signaling pathways (**Figures 1G, H**). These results indicated that SP-D regulates the expression of many genes associated with inflammatory and immune responses, TLR and PI3K-Akt signalings.

In Vivo Transfection of Chondrocytes with rAAV Vectors Reduced SP-D Expression and Promoted Inflammatory Immune Responses in Joint Cartilage

The intra-articular cartilage was treated with rAAV-SP-D shRNA to analyze its ability to change the SP-D expression in the cartilage. H&E staining showed that the morphology of articular cartilage did not change after SP-D silencing. Compared with the control animals, rAAV-SP-D shRNA-treated animals had reduced SP-D expression in the cartilage tissues (**Figures 2A, B**). Western blot analysis showed that a loss of SP-D in rAAV-SP-D shRNA-treated synovium and cartilage compared to control animals was observed (**Supplementary Figure 2**). Furthermore, we evaluated the changes in the expression of macrophage specific markers. The levels of CD63, F4/80 and TLR4 in the cartilage tissue treated with rAAV-SP-D shRNA were significantly increased as compared to the cartilage tissues in the control and rAAV-GFP-treated animals (**Figures 2C–E**). These results indicated that SP-D exerts a protective effect on articular cartilage by regulating the expression of immune-inflammatory proteins in articular cartilage tissue.

Inhibition of the Infiltration of Synovial Immune Cells by SP-D and Its Chondroprotective Effects *In Vivo*

The timeline of OA modeling, intervention and sampling was shown in **Figure 3A**. Macroscopic observations were shown in **Figure 3B**. The femoral condyles cartilage in the sham group was smooth and free of osteophytes, while cartilage lesions developed on femoral condyles and the cartilage surface gloss was severely corroded in the OA-induction group. The cartilage tissue destruction was ameliorated after intra-articular injection of rhSP-D and TLR4 signaling antagonist (TAK-242). We evaluated the cellular immune infiltration in the synovial

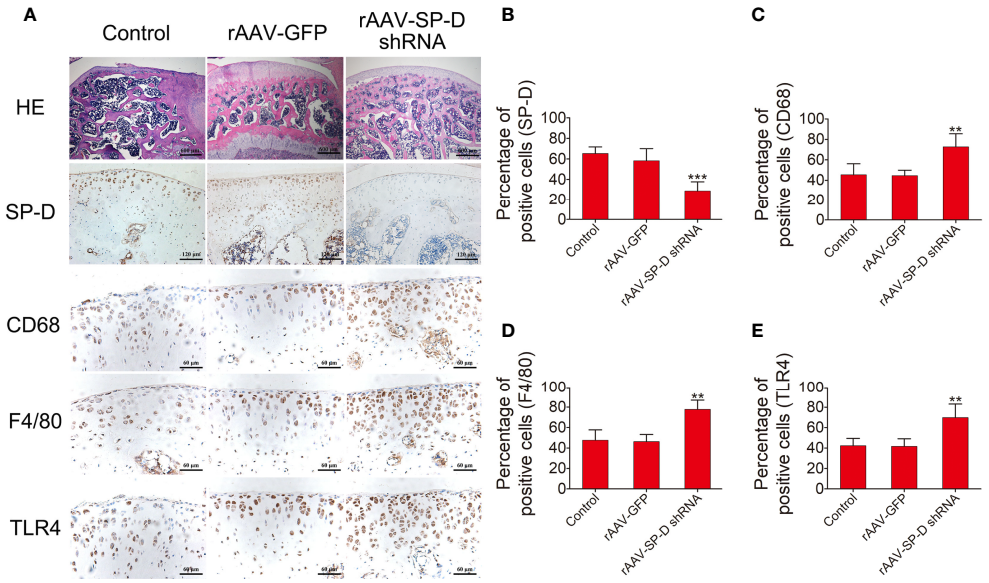

FIGURE 2 | RAAV-mediated SP-D gene was transferred into the rat knee joints. **(A)** Rats were injected intra-articularly with rAAV encoding SP-D-specific shRNA for 10 consecutive days and sacrificed at the fourth week of the first injection. H&E staining and immunohistochemical staining of SP-D, CD68, F4/80, and TLR4 protein levels in cartilage were assessed following rAAV-GFP or rAAV-SP-D shRNA injection into the rat knee joints. The ratios of immunoreactive cells of SP-D **(B)**, CD68 **(C)**, F4/80 **(D)**, and TLR4 **(E)** were analyzed. Data were expressed as mean ± SEM (n = 5). **P < 0.01 and ***P < 0.001 vs. rAAV-GFP group.

tissues using TEM (**Figure 3B**). The sham group animals showed collagen fibers with standard structures, while the OA-induction group animals showed irregular collagen fibers, and macrophages and neutrophils infiltration. This cellular immunity recruited many lysosomes and other immune-reactive substances. In the OA + rhSP-D group, the infiltration of macrophages was reduced, with a few neutrophils and lymphocytes. In the OA + TAK-242 + rhSP-D group, immune cells infiltration had significantly decreased, and the morphology of synovial fibroblasts could be observed.

To investigate the involvement of SP-D in the regulation of inflammatory responses, the inflammatory cytokines of TLR4 and TNF-α in the surgical OA model were determined by immunohistochemical analysis. The immunoreactivity expressed by TLR4 and TNF-α in the articular cartilage zone of the OA-induction group animals was significantly higher than that of the sham-operated animals (**Figure 3C**). Intra-articular injections of rhSP-D significantly inhibited the expression of TLR4 and TNF-α in cartilage derived from the rat OA model, while TAK-242 had a synergistic effect and enhanced the inhibitory effect of rhSP-D.

We studied the pathology of the surface layer of cartilage tissue in the slices stained with H&E, Toluidine blue-O and Safranin O stains. A certain degree of cartilage defects and loss of hyaline cartilage was observed in the OA-induction group (**Figure 4A**). The severity of cartilage degeneration in the rhSP-D and TAK-242 treatment groups was much lesser than that of the OA-induction group, as indicated by the cartilage thickness and surface regularity. rhSP-D and TAK-242 maintained cartilage tissues and avoided cartilage deterioration, as indicated by the low modified Mankin scores as compared with the OA-induction group (**Figure 4B**). The modified Mankin score of the OA + TAK-242 + rhSP-D group was significantly lower than that of the OA + rhSP-D group. These results indicated that SP-D was involved in the inhibition of synovial immune cells infiltration, and SP-D synergistically delayed cartilage degeneration along with TLR4 inhibitor TAK-242.

SP-D Modulated Inflammatory Responses by Suppressing TLR4-Mediated PI3K/Akt Activation and NF-κB Signaling

To investigate whether SP-D could regulate PI3K/Akt and NF-κB p65 transcription, we examined the phosphorylation levels of PI3K, Akt and NF-κB p65 in the cartilage of ACLT + MMx surgically induced rat OA model by immunofluorescence (**Figures 5–7**). The percentages of p-PI3K, p-Akt and p-p65-positive cells in the OA-induced group were significantly higher than those in the sham-operation group. The staining of p-PI3K, p-Akt and p-p65 were significantly concentrated in the cytoplasm and nucleus of chondrocytes in the cartilage of the OA-induced group. We found that rhSP-D reduced phosphorylation levels of PI3K, Akt and NF-κB p65 in cartilage derived from rats with surgically induced OA. We injected TLR4 inhibitor TAK-242, which inhibited the expression of p-PI3K, p-Akt and p-p65 in comparison with the OA-induced group. When we injected both rhSP-D and TAK-242 together, the inhibitory effect of rhSP-D was increased. Similar results were obtained when we evaluated the phosphorylation of PI3K, Akt and NF-κB p65 expression in synovial tissues (**Supplementary Figures 3–5**). Together, these data indicated that SP-D modulates inflammatory responses

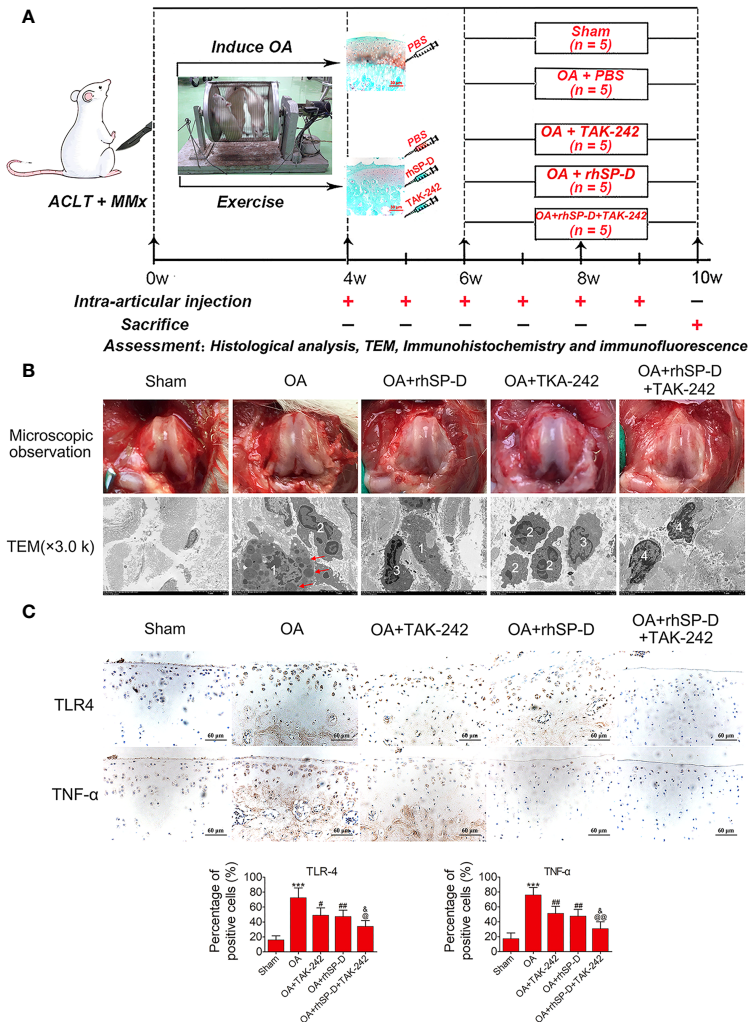

FIGURE 3 | An overview of study timelines and suppression of inflammatory and immune responses by SP-D in the rat OA model. **(A)** The ACLT + MMx rats were put into an electronic rotator cage for 30 min per day as a means of inducing OA model beginning 1 week post-surgery. At 4 weeks post-surgery, animals were injected intra-articularly with different concentrations of rhSP-D and TAK-242 once per week. PBS was used as controls in sham and OA model animals. At 10 weeks post-operation, the animals were euthanized by cardiac exsanguination. Histological staining, immunohistochemistry, immunofluorescence, and TEM were used for detection. **(B)** Microscopic observation and synovial immune cells infiltration were assessed *via* TEM (3,000 ×). 1 = macrophage;2 = neutrophil;3 = lymphocyte;4 = synovial fibroblast;The red arrows represented lysosomes. **(C)** Immunohistochemical staining of TLR4 and TNF-α in ACLT + MMx-induced OA rats with the administration of rhSP-D and TAK-242. The ratios of immunoreactive cells were quantified. Data were expressed as mean ± SEM (n = 5). ***P < 0.001 vs. the sham-operated group; $^{\#}$P < 0.05 and $^{\#\#}$P < 0.01 vs. the OA-induction group; $^{\&}$P < 0.05 vs. OA + rhSP-D group; $^{@}$P < 0.05 and $^{@@}$P < 0.01 vs. OA + TAK-242 group.

by suppressing TLR4-mediated downstream PI3K/Akt and NF-κB signalings.

SP-D Reduced Chondrocyte Inflammatory Responses Induced by LPS

To investigate the involvement of SP-D in the regulation of inflammatory responses, LPS-induced inflammatory cytokines in rat chondrocytes were determined by ELISA analysis. The levels of IL-1β and TNF-α in chondrocytes were monitored. As shown in **Figures 8A, B**, the expression levels of IL-1β and TNF-α were induced by LPS, while transfection of pcDNA3.1-SP-D plasmid in chondrocytes led to the reduction of IL-1β and TNF-α. Pretreated with rhSP-D significantly abolished the elevation of IL-1β and TNF-α induced by LPS. These data suggest that SP-D protected chondrocytes from LPS-induced inflammatory cell responses.

SP-D Suppressed the TLR4-Mediated PI3K/Akt Activation and NF-κB Signaling in LPS-Stimulated Chondrocytes

To determine whether SP-D inhibits TLR4 mediated PI3K/Akt activation and NF-κB p65 signaling, we treated chondrocytes with rhSP-D and/or TLR4 inhibitor TAK-242 and PI3K inhibitor

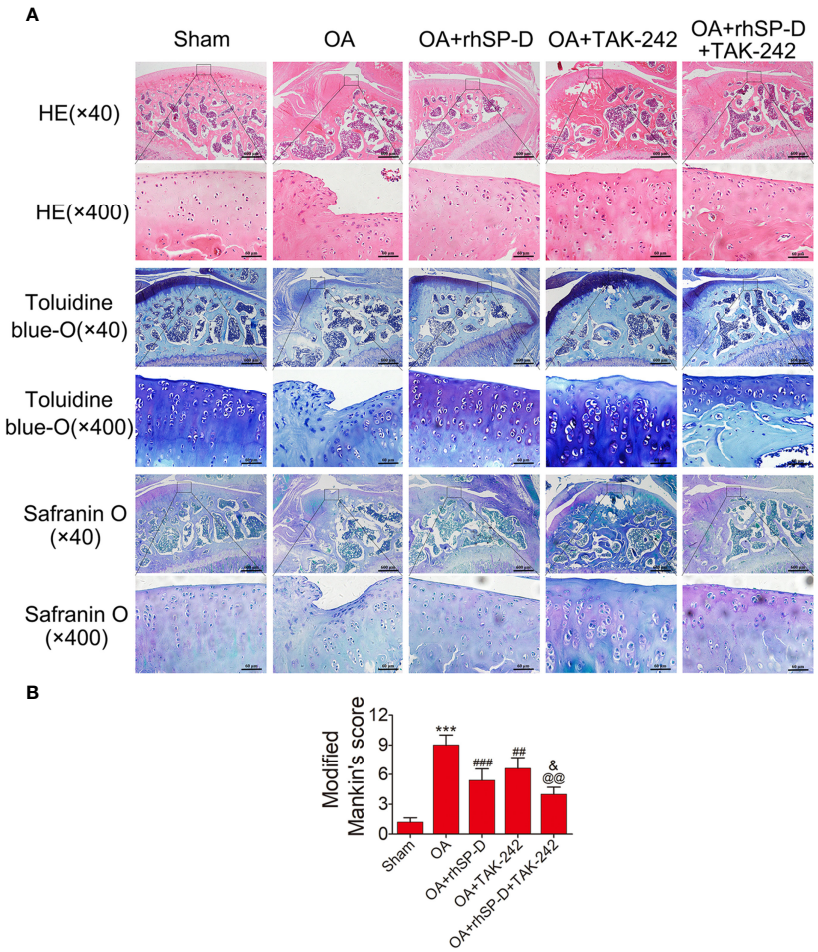

FIGURE 4 | The rescue of cartilage degeneration by SP-D in rat OA model. **(A)** H&E, Safranin O and toluidine blue O-stained tissue histology in rat articular cartilage at 10 weeks post-surgery. **(B)** The modified Mankin scores were assigned to tissue samples. Data were expressed as mean ± SEM (n = 5). ***P < 0.001 vs. the sham-operated group; ##P < 0.01 and ###P < 0.001 vs. the OA-induction group; &P < 0.05 vs. OA + rhSP-D group; @@P < 0.01. vs. OA + TAK-242 group.

wortmannin. Immunofluorescence staining was carried out to determine the expression of PI3K and NF-κB p65 in chondrocytes. As shown in **Figures 8C–F**, LPS promoted the expression of PI3K and p65, and rhSP-D inhibited the effects of LPS on the expression of PI3K and NF-κB p65 in chondrocytes. Moreover, pre-treatment with TAK-242 and wortmannin significantly enhanced the rhSP-D-mediated decrease in the densities of PI3K and p65 subunits. Western blot analysis showed that the expression levels of MMP-13 and NLRP3 in LPS-stimulated chondrocytes were significantly higher, while the level of collagen II was significantly lower than the control group (**Figures 9A, D–F**). We found that rhSP-D treatment and transfection of pcDNA3.1-SP-D plasmid significantly reduced the expression levels of MMP-13 and NLRP3, and increased the expression level of collagen II in LPS-induced chondrocytes, while TAK-242 and wortmannin enhanced the effect of rhSP-D on LPS-induced chondrocytes. The expression of TLR4, MD-2, p-p65, p-PI3K, and p-Akt increased in the LPS-stimulated group (**Figures 9B, C, G–K**). The administration of rhSP-D and transfection of pcDNA3.1-SP-D plasmid blocked the LPS-induced increase in TLR4, MD-2, p-p65, p-PI3K, and p-Akt. TAK-242 and wortmannin enhanced rhSP-D-mediated reduction in the expression of TLR4, MD-2, p-p65, p-PI3K, and p-Akt. Overall, SP-D inhibited the LPS-induced degradation of ECM and reduced LPS-induced chondrocyte inflammation by suppressing TLR4-mediated PI3K/Akt transcription factors and NF-κB activation.

Molecular Binding Capacity of the SP-D and TLR4/MD-2 Complex

Since SP-D inhibited the transcription factor of TLR4 and MD-2 receptors in chondrocytes, we performed docking calculations to explore the interactions between SP-D and TLR4/MD-2 complex (**Figures 10A–C**). As per the spatial filling model, the carbohydrate recognition domain of SP-D was completely inserted in the inhibitory pocket of the recombinant soluble

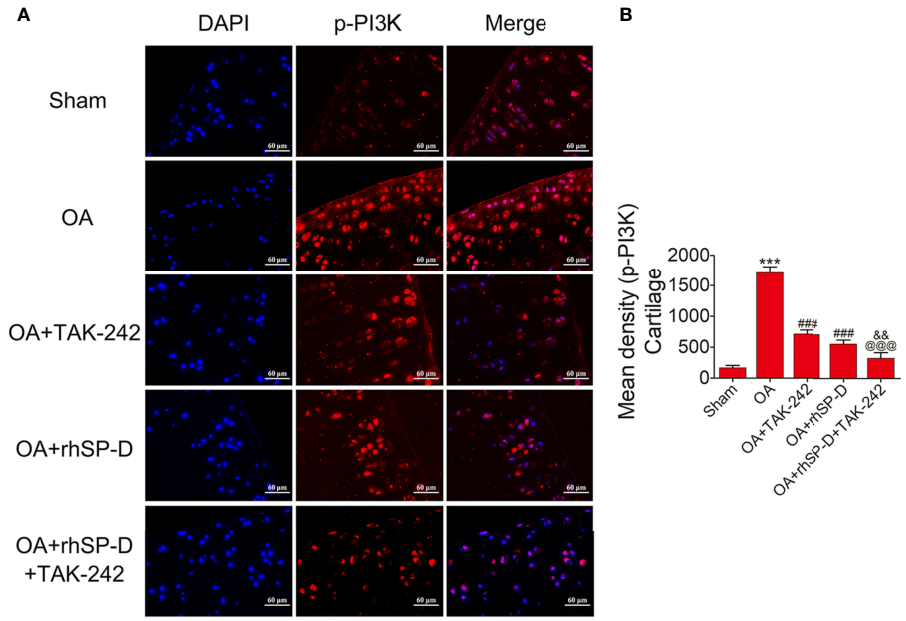

FIGURE 5 | Suppression of TLR4-mediated PI3K signaling by SP-D treatment *in vivo*. **(A)** Immunofluorescence with an antibody to p-PI3K in articular cartilage from the ACLT + MMx-induced OA rats with rhSP-D and TAK-242 treatment at 10 weeks post-surgery. **(B)** The ratios of immunoreactive cells were quantified in articular cartilage according to immunofluorescence. Data were expressed as mean ± SEM (n = 5). ***P < 0.001 vs. the sham-operated group; $^{###}$P < 0.001 vs. the OA-induction group; $^{\&\&}$P < 0.01 vs. OA + rhSP-D group; $^{@@@}$P < 0.001 vs. OA + TAK-242 group.

forms of TLR4 and MD-2 homodimer complex. The surface layer of SP-D was fused with TLR4/MD-2 homodimer complex with average generalized born score of -25.03 kcal/mol and average poisson-boltzmann of -46.87 kcal/mol.

DISCUSSION

In this study, we demonstrated that SP-D suppresses OA-related immune responses and chondrocyte inflammation by inhibiting

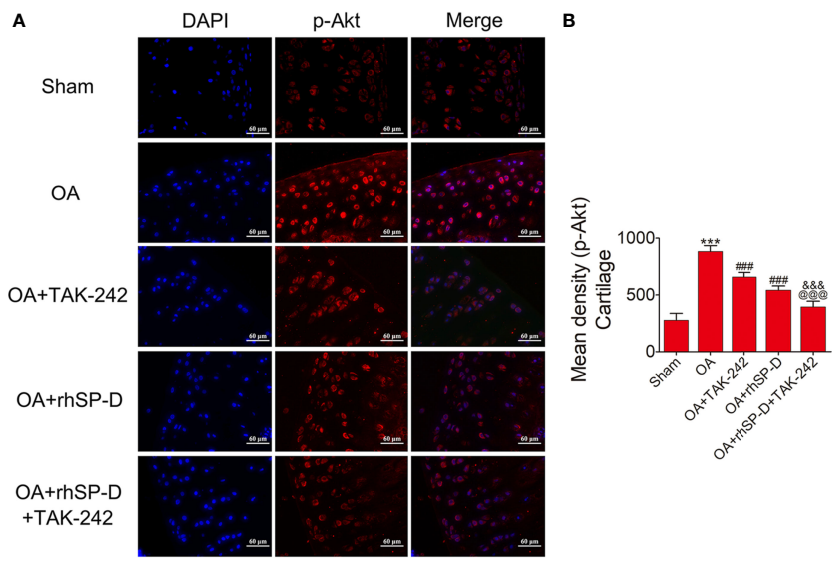

FIGURE 6 | SP-D modulated TLR4-mediated Akt signaling *in vivo*. **(A)** Immunofluorescence with an antibody to p-Akt in articular cartilage from the ACLT + MMx -induced OA rats with rhSP-D and TAK-242 treatment at 10 weeks post-surgery. **(B)** The ratios of immunoreactive cells were quantified in articular cartilage according to immunofluorescence. Data were expressed as mean ± SEM (n = 5). ***P < 0.001 vs. the sham-operated group; $^{###}$P < 0.001 vs. the OA-induction group; $^{\&\&\&}$P < 0.001 vs. OA + rhSP-D group; $^{@@@}$P < 0.001 vs. OA + TAK-242 group.

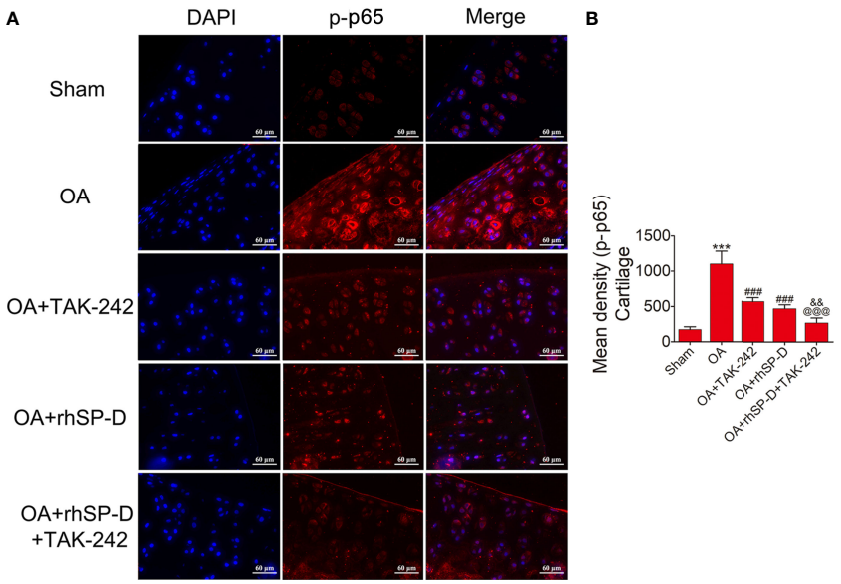

FIGURE 7 | SP-D regulated TLR4-mediated NF-κB pathway *in vivo*. **(A)** Immunofluorescence with an antibody to p-p65 in articular cartilage from the ACLT + MMx-induced OA rats with rhSP-D and TAK-242 treatment at 10 weeks post-surgery. **(B)** The ratios of immunoreactive cells were quantified in articular cartilage according to immunofluorescence. Data were expressed as mean ± SEM (n = 5). ***P < 0.001 vs. the sham-operated group; $^{###}$P < 0.001 vs. the OA-induction group; $^{\&\&}$P < 0.01 vs. OA + rhSP-D group; $^{@@@}$P < 0.001 vs. OA + TAK-242 group.

TLR4-mediated PI3K/Akt transcription and NF-κB activation. Firstly, transcriptome analysis revealed that SP-D overexpression broadly affects inflammatory response, immune response, and PI3K-Akt and TLR signaling in chondrocytes. Secondly, SP-D knockdown by rAAV injection resulted in the induction of inflammatory and innate responses in joint cartilage; however, these responses were not sufficient to promote disease progression. Finally, SP-D binds to TLR4/MD-2 complex to

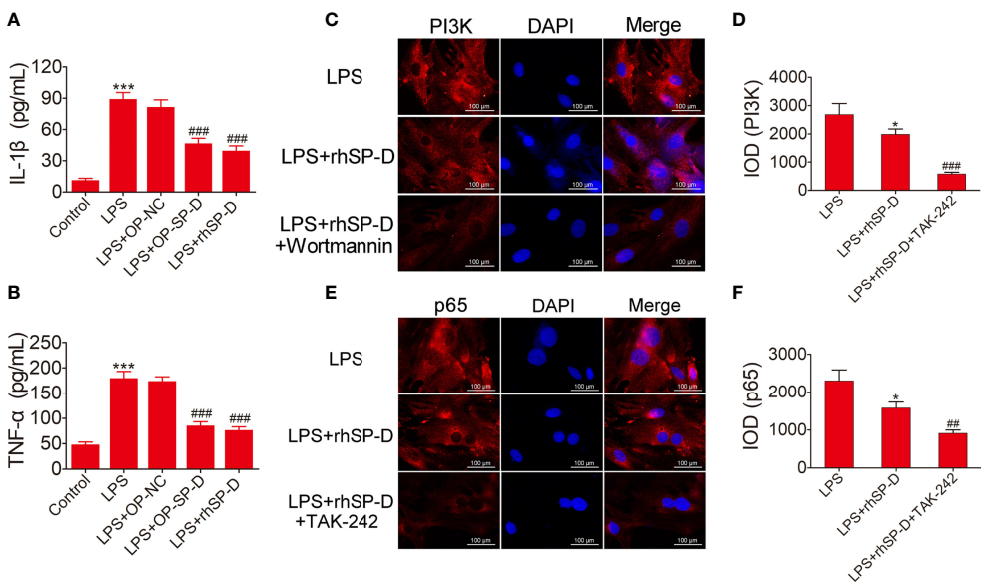

FIGURE 8 | Suppression of inflammatory response and the PI3K and NF-κB pathways by SP-D treatment *in vitro*. **(A, B)** Chondrocytes were pre-incubated with rhSP-D and transfection of pcDNA3.1-SP-D plasmid for 2 h before LPS co-treatment for 24 h. The concentrations of IL-1β and TNF-α were determined by ELISA. Data were expressed as mean ± SEM (n = 3). ***P < 0.001 vs. control group; $^{###}$P < 0.001 vs. LPS group. **(C–F)** Immunofluorescence with antibodies to PI3K and p65 in chondrocytes, and the fluorescence images of PI3K and p65-Tracker Red in chondrocytes. The IOD was quantified according to immunofluorescence. Data were expressed as mean ± SEM (n = 3). *P < 0.05 vs. LPS group; $^{##}$P < 0.01 and $^{###}$P < 0.001 vs. LPS + rhSP-D group.

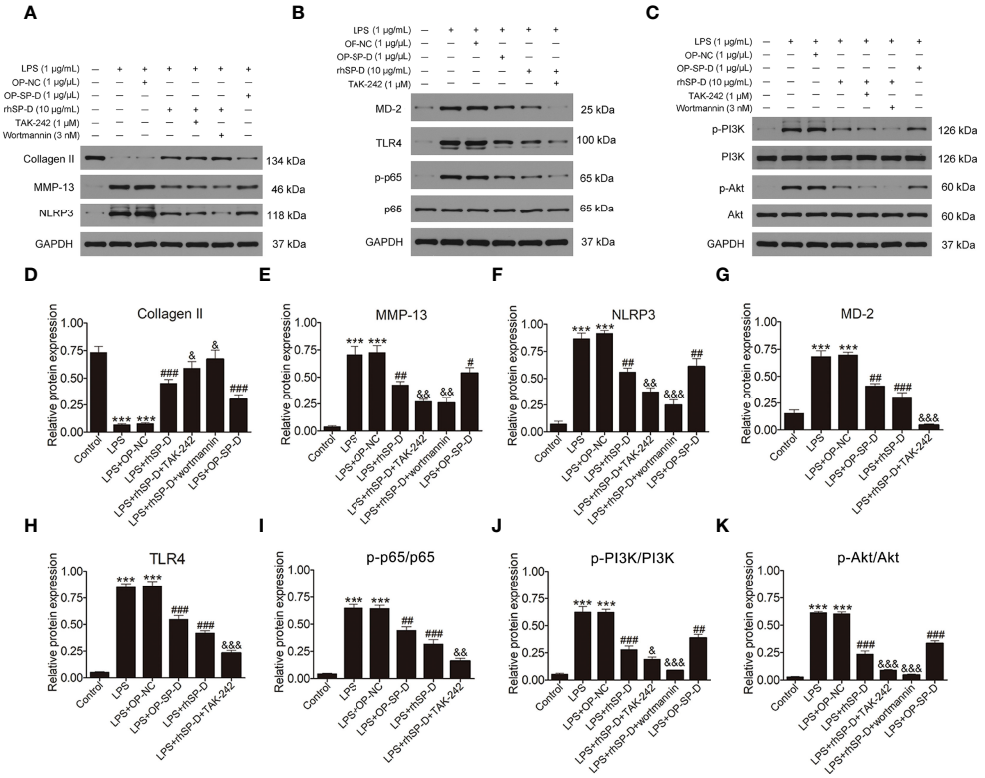

FIGURE 9 | Effects of SP-D on inflammation and ECM by suppressing TLR4-mediated PI3k/Akt and NF-κB signalings in chondrocytes. **(A–C)** The protein expression of Collagen II, MMP-13, NLRP3, p-PI3K, PI3K, p-Akt, Akt, MD-2, TLR4, p-p65, and p65 were assessed *via* western blotting with GAPDH as a loading control. **(D–K)** The ratios of Collagen II, MMP-13, NLRP3, MD-2, and TLR4 to GAPDH, and p-PI3K/PI3K, p-Akt/Akt, p-p65/p65 were analyzed. Data were expressed as mean ± SEM (n = 3). ***P < 0.001 vs. the control group; $^{\#\#}$P < 0.01 and $^{\#\#\#}$P < 0.001 vs. the LPS group; $^{\&}$P < 0.05, $^{\&\&}$P < 0.01 and $^{\&\&\&}$P < 0.001 vs. the LPS + rhSP-D group. OP-SP-D, SP-D overexpressing plasmid; OP-NC, Negative control plasmid.

suppress TLR4-mediated PI3K/Akt and NF-κB signaling activation in osteoarthritic chondrocytes. All these data show that SP-D plays a functional role in OA and highlight its potential value in the treatment of OA.

The activation of the innate immune system is associated with tissue damage or chronic inflammation (22). The level of TLR4, an innate immune system mediator, rises in the cartilage tissues in surgically induced OA (23). Several strategies have been proposed to manipulate the signal transmission of the protein kinase in chondrocytes. Targeting TLRs and/or their downstream signaling pathways may inhibit the progression of OA. The modulation of SP-D involves various pathological inflammatory manifestations including subacute inflammation, which is the basis of this disease (24, 25). Previous reports indicate that the production of TLR4 and MD-2 complex is particularly important for LPS signaling, and the interaction between SP-D and the receptor complex may harm LPS signal transmission (26, 27).

To understand the molecular mechanisms underlying the therapeutic efficacy of SP-D against OA, we conducted a whole-genome transcriptome analysis using chondrocytes of rat cartilage. Gene expression analysis based on RNA-sequencing revealed that many genes are differentially controlled by SP-D. These genes were closely related to the critical pathways associated with inflammatory responses, cellular responses to LPS, immune responses, and cell proliferation. The analysis of the basic functions and pathways involving SP-D and those related to DEGs revealed that the OA pathways are highly involved in the PI3K-Akt signaling, ECM-receptor interactions, and TLR signaling. These findings direct for further research on the mechanism of SP-D underlying the modulation of inflammatory and immune responses of cartilage tissues.

To validate the anti-inflammatory effect of SP-D, we stimulated the chondrocytes with LPS and analyzed LPS-stimulated inflammatory responses. Among inflammatory cytokines, the interleukin family, particularly IL-1β and TNF-α, play a leading role in the pathological progression of OA (28, 29). During the pathological process of OA, inflammatory mediators, especially IL-1β, induce the release of other pro-inflammatory cytokines, thereby promoting the catabolic response and destroying the structure of the articular cartilage in chondrocytes. MMP-13 promotes the degradation of cartilage tissues, dissolves the components of ECM, and plays a role during the inflammation period of OA (30). The pro-inflammatory cytokines not only cause direct damage to cartilage, but also degrade the ECM and collagen II, destroying

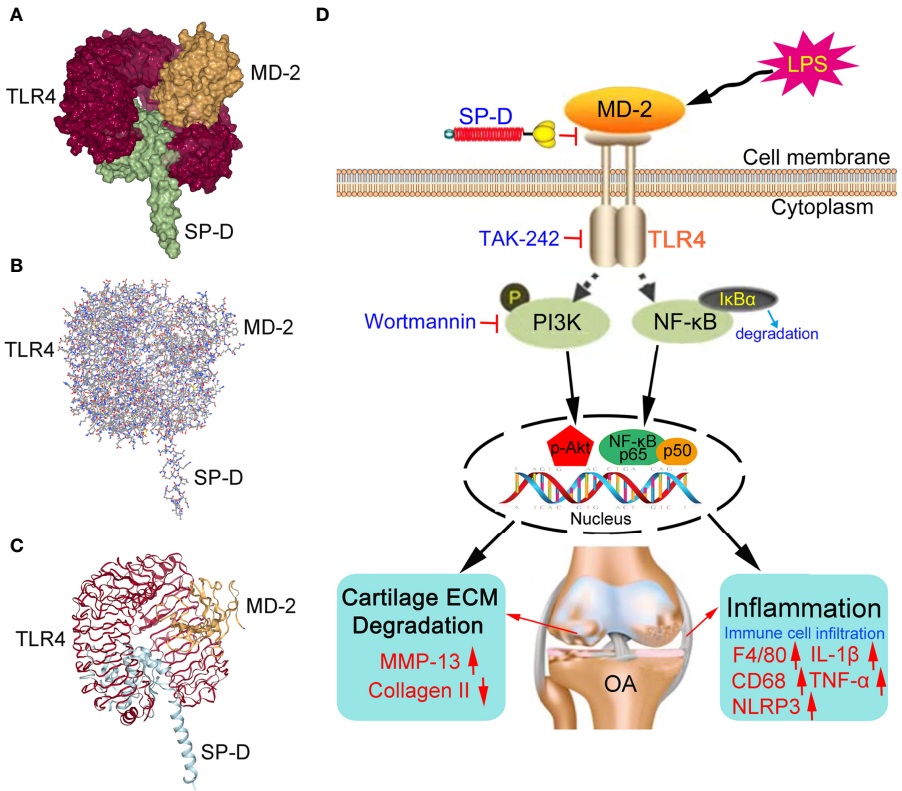

FIGURE 10 | Proposed mechanisms of SP-D interference with OA chondrocyte inflammatory response and cartilage degradation. **(A–C)** The spatial filling model illustrated that SP-D was fully embedded in the inhibitory pocket of TLR4/MD-2 homodimer complex. The surface of SP-D binds to TLR4/MD-2 homodimer complex with average generalized born score of -25.03 kcal/mol and average poisson-boltzmann of -46.87 kcal/mol. **(D)** SP-D as a modulator of inflammatory response *via* inhibition of TLR4-mediated NF-κB activation and PI3K/Akt pathways.

the joint cartilage. Therefore, molecules capable of targeting LPS-induced inflammation may have the potential to be therapeutic drug candidates for OA. In the present study, we found that SP-D suppressed the increase in MMP-13, NLRP3, IL-1β, and TNF-α in LPS-induced chondrocytes. The anti-inflammatory effect of SP-D was related to the inhibition of TLR4 expression. SP-D is known to bind to several carbohydrate ligands, including LPS from different strains of bacteria *via* its lectin domains. Further, LPS induced chondrocyte inflammation; SP-D pre-incubated with LPS inhibited LPS induced inflammation. The LPS-sensing receptor, TLR4, plays a pivotal role in cell survival and inflammation. Activation of TLR4 triggered the release of pro-inflammatory cytokines such as IL-1β and TNF-α, resulting in damage to the host cells. These findings partially suggest that SP-D plays a negative role in inflammatory responses and prevents the degradation of ECM by regulating the function of TLR4.

To explore the regulatory function of SP-D in innate immunity, we disrupted the expression of SP-D by injecting rAAV into the knee joints of rats. In the present study, we observed that SP-D disruption in all normal knee joints does not cause the deterioration of cartilage tissues in the long term. In addition, SP-D knockdown led to the increased expression of F4/80, CD68, TLR4 and other innate immune response proteins, indicating that endogenous SP-D is likely to modulate the immune responses in all normal cartilage tissues. Although we observed no structural changes and degeneration of articular cartilage during the onset and early development of OA, we found reduced expression of SP-D on the cartilage surface. The increased levels of inflammatory factors damaged the defense barrier of cartilage, leading to cartilage degeneration and the onset of OA. We reduced the level of SP-D in normal cartilage tissues through artificial intervention, including an intra-articular injection of rAAV. The expression of inflammatory factors in cartilage tissue increased, and the natural immune function of cartilage was gradually affected. Under such conditions, we assumed that even minor triggers can lead to the onset of OA. Meanwhile, SP-D suppressed the hyperplasia of the synovial membrane and infiltration of immune cells. These results suggested that endogenous SP-D promotes innate immunity in rat articular cartilage and synovial tissues. Absence of SP-D in the knocked-down animals is associated with higher intrinsic pro-inflammatory status. Therefore, the higher level of CD68, F4/80 and TLR4 could be a consequence of many factors other than SP-D knockdown. These findings are consistent with previous reports, demonstrating that endogenous SP-D manipulates the cellular immunomodulation checkpoint in chondrocytes, joint articular cartilage, and synovial membrane (31).

The inflammatory microenvironment of the OA joint is found to be orchestrated by macrophages, neutrophils, and multiple inflammatory cytokines. Previous studies have demonstrated the importance of macrophages and neutrophils in driving inflammatory and destructive responses in OA (32, 33). These results indicated there is a triggering low-grade inflammatory cycle that leads to the infiltration of macrophages and neutrophils and further induce structural changes in the synovial tissues of OA rats. We established the rat OA model and injected TLR4 inhibitor TAK-242 to investigate whether SP-D participates in the inhibition of cartilage and synovial inflammation by inactivating TLR4 signaling. Surgical OA modeling leads to the decrease of SP-D activity, promotes the infiltration of immune cells in the synovial tissues and activates TLR4 signaling, leading to the release of IL-1β and TNF-α. SP-D reduced inflammatory cytokines and immune cells (neutrophils and macrophages) *via* modulating the TLR4 signaling. Based on these findings, we postulate that SP-D is a barrier to cartilage surfactant homeostasis and inhibits the innate immune responses and maintains the stability of the joint structure.

The endogenous molecules released from the injured tissues and inflammatory cells activate pro-inflammatory responses by interacting with TLR4. The analysis of the KEGG pathway revealed that these genes were significantly related to PI3K-Akt signaling and TLR signaling. We selected the PI3K-Akt signaling pathway that ranked high and was closely related to the regulation of inflammation. The PI3K/Akt signaling pathway is one of the most crucial cell survival pathways that participates in the modulation of inflammatory responses, cellular activation, and apoptosis (34, 35). The induction of PI3K/Akt signaling reduces the pro-inflammatory response of the NF-κB pathway (36). LPS stimulates TLR4 and promotes the expression of cell survival genes by activating the NF-κB pathway (37, 38). Pre-treatment with a moderate amount of LPS protects human dendritic cells or myocytes from apoptosis *via* PI3K/Akt and NF-κB dependent sensory system of TLR4 (39, 40). In the present study, pretreatment with LPS enhanced the activation of PI3K/Akt and NF-κB signaling in chondrocytes. These manifestations were abrogated by SP-D, and TAK-242 enhanced the inhibitory effect of SP-D. These findings suggest that crosstalk may exist between TLR4/NF-κB and PI3K/Akt signaling pathways in the regulation of inflammation in chondrocytes pretreated with LPS. However, despite proving that SP-D could exert its anti-inflammatory effects *via* the PI3K/Akt and NF-κB signalings, its potential upstream and downstream cascading effects should be studied further. Previous studies revealed that TLR4 signaling is currently one of the most widely studied upstream cascades, and the concentration of TLR4 in PI3K/Akt and NF-κB activation and that the OA development has received increasing attention (41, 42). We further explored whether SP-D targets the TLR4/MD-2 complex. TLR4/MD-2/LPS complex formation results in the intracellular domain of TLR4 being cascaded. SP-D exerted anti-inflammatory activities by affecting the proper assembly of the TLR4/MD-2/LPS ternary complex, the activation of which is associated with OA. We simulated the potential interaction between SP-D and TLR4/MD-2 complex using docking approaches, and found that SP-D specifically binds to the MD-2 inhibitory pocket and interferes with the formation of the TLR4/MD-2 complex. Using docking approaches, we further simulated the underlying mechanism of SP-D interacting with TLR4/MD-2 and found that SP-D specifically interferes with the formation of the TLR4/MD-2 complex. Therefore, SP-D binds to the TLR4 and MD-2 complex and suppresses inflammation and innate immune responses by decreasing the PI3K/Akt mediated activation of the TLR4 receptor and NF-κB transcription factors (**Figure 10D**).

In conclusion, SP-D suppresses LPS-induced inflammatory and innate responses in rat articular chondrocytes by inhibiting TLR4-mediated PI3K/Akt activation and NF-κB signalings. Therefore, SP-D may be considered as a potential therapeutic intervention to prevent the progression of OA. Meanwhile, SP-D knockout mice should be used in future study, which could further demonstrate the critical role of SP-D in OA.

DATA AVAILABILITY STATEMENT

The datasets presented in this study can be found in online repositories. The name of the repository and accession number can be found below: NCBI Sequence Read Archive; PRJNA836943.

ETHICS STATEMENT

This study was approved by the Animal Care and Use Committee of Medical School, Wuhan University (WDRM 20160104). Written informed consent was obtained from the owners for the participation of their animals in this study.

AUTHOR CONTRIBUTIONS

YZ, HJ, YuZ, and GH initiated the study, designed experiments and wrote the paper. YuZ, MD, YL, and YM performed experiments. YZ, JM, and XS analyzed and interpreted the data. YZ, YL, and SL reviewed the manuscript and wrote the paper. All authors have critically reviewed the manuscript and approved the final manuscript.

FUNDING

This project was funded by National Natural Science Foundation of China (grant number: 81802203), Fundamental Research Funds for the Central Universities (grant number: 2042018kf0123), Guiding Fund of Renmin Hospital of Wuhan University (grant number: RMYD2018M43).

SUPPLEMENTARY MATERIAL

The Supplementary Material for this article can be found online at: https://www.frontiersin.org/articles/10.3389/fimmu.2022.913901/full#supplementary-material

Supplementary Table 1 | Summary of sample names, description, the RNA-seq sequencing information, and mapping results in each sample.

Supplementary Figure 1 | DEGs were annotated to GO database to detect the gene function. **(A–D)** GO analysis showed that the biological processes such as regulation of 'extracellular space', 'protein binding' and 'chemokine activity' were associated with SP-D in chondrocytes.

Supplementary Figure 2 | RAAV-mediated SP-D gene was transferred into the rat knee joints. **(A)** SD rats received an intra-articular injection of rAAV encoding SP-D-specific shRNA for SP-D or GFP into the knee for 10 consecutive days. SP-D expression in synovium and cartilage was assessed *via* western blotting. **(B)** The ratios of SP-D in synovium and cartilage were analyzed. Data were expressed as mean ± SEM (n = 3). $^{***}P < 0.001$ versus the rAAV-GFP group.

Supplementary Figure 3 | Suppression of TLR4 mediated PI3K signaling by SP-D treatment in OA synovium. **(A)** Immunofluorescence with an antibody to p-PI3K in synovium. **(B)** The ratios of immunoreactive cells were quantified in synovium according to immunofluorescence. Data were expressed as mean ± SEM (n = 5). $^{###}P < 0.001$ vs. the OA-induction group; $^{&&&}P < 0.001$ vs. OA + rhSP-D group.

Supplementary Figure 4 | Suppression of TLR4 mediated Akt signaling by SP-D treatment in OA synovium. **(A)** Immunofluorescence with an antibody to p-Akt in synovium. **(B)** The ratios of immunoreactive cells were quantified in synovium. Data were expressed as mean ± SEM (n = 5). $^{###}P < 0.001$ vs. the OA-induction group; $^{&&&}P < 0.001$ vs. OA + rhSP-D group.

Supplementary Figure 5 | Suppression of TLR4 mediated NF-κB signaling by SP-D treatment in OA synovium. **(A)** Immunofluorescence with an antibody to p-p65 in synovium. **(B)** The ratios of immunoreactive cells were quantified in synovium. Data were expressed as mean ± SEM (n = 5). $^{##}P < 0.01$ vs. the OA-induction group; $^{&&}P < 0.01$ vs. OA + rhSP-D group.

REFERENCES

1. Urban H, Little CB. The Role of Fat and Inflammation in the Pathogenesis and Management of Osteoarthritis. *Rheumatol (Oxford England)* (2018) 57: iv10–21. doi: 10.1093/rheumatology/kex399
2. Mobasheri A, Rayman MP, Gualillo O, Sellam J, van der Kraan P, Fearon U. The Role of Metabolism in the Pathogenesis of Osteoarthritis. *Nat Rev Rheumatol* (2017) 13:302–11. doi: 10.1038/nrrheum.2017.50
3. Griffin TM, Scanzello CR. Innate Inflammation and Synovial Macrophages in Osteoarthritis Pathophysiology. *Clin Exp Rheumatol* (2019) 37 Suppl 120:57–63.
4. Colmorten KB, Nexoe AB, Sorensen GL. The Dual Role of Surfactant Protein-D in Vascular Inflammation and Development of Cardiovascular Disease. *Front Immunol* (2019) 10:2264. doi: 10.3389/fimmu.2019.02264
5. Hsieh IN, De Luna X, White MR, Hartshorn KL. The Role and Molecular Mechanism of Action of Surfactant Protein D in Innate Host Defense Against Influenza a Virus. *Front Immunol* (2018) 9:1368. doi: 10.3389/fimmu.2018.01368
6. Kankavi O. Increased Expression of Surfactant Protein a and D in Rheumatoid Arthritic Synovial Fluid (RASF). *Croat Med J* (2006) 47:155–61.
7. Christensen AF, Sørensen GL, Hørslev-Petersen K, Holmskov U, Lindegaard HM, Junker K, et al. Circulating Surfactant Protein -D is Low and Correlates Negatively With Systemic Inflammation in Early, Untreated Rheumatoid Arthritis. *Arthritis Res Ther* (2010) 12:R39. doi: 10.1186/ar2948
8. Christensen AF, Sorensen GL, Junker K, Revald PH, Varnum C, Sorensen FB, et al. Localization of Surfactant Protein-D in the Rheumatoid Synovial Membrane. *APMIS* (2018) 126:9–13. doi: 10.1111/apm.12785
9. Zhou Y, Ming J, Deng M, Li Y, Li B, Li J, et al. Berberine-Mediated Up-Regulation of Surfactant Protein D Facilitates Cartilage Repair by Modulating Immune Responses *via* the Inhibition of TLR4/NF-κb Signaling. *Pharmacol Res* (2020) 155:104690. doi: 10.1016/j.phrs.2020.104690
10. Zhou Y, Ming J, Li Y, Du X, Deng M, He B, et al. Surfactant Protein D Attenuates Nitric Oxide-Stimulated Apoptosis in Rat Chondrocyte by Suppressing P38 MAPK Signaling. *Biochem Biophys Res Commun* (2018) 495:526–32. doi: 10.1016/j.bbrc.2017.10.170
11. Saka R, Wakimoto T, Nishiumi F, Sasaki T, Nose S, Fukuzawa M, et al. Surfactant Protein-D Attenuates the Lipopolysaccharide-Induced Inflammation in Human Intestinal Cells Overexpressing Toll-Like Receptor 4. *Pediatr Surg Int* (2016) 32:59–63. doi: 10.1007/s00383-015-3812-y
12. Ohya M, Nishitani C, Sano H, Yamada C, Mitsuzawa H, Shimizu T, et al. Human Pulmonary Surfactant Protein D Binds the Extracellular Domains of Toll-Like Receptors 2 and 4 Through the Carbohydrate Recognition Domain by a Mechanism Different From its Binding to Phosphatidylinositol and Lipopolysaccharide. *Biochemistry* (2006) 45:8657–64. doi: 10.1021/bi060176z
13. Zhang P, Yang M, Chen C, Liu L, Wei X, Zeng S. Toll-Like Receptor 4 (TLR4)/Opioid Receptor Pathway Crosstalk and Impact on Opioid Analgesia, Immune Function, and Gastrointestinal Motility. *Front Immunol* (2020) 11:1455. doi: 10.3389/fimmu.2020.01455
14. Grace PM, Strand KA, Galer EL, Rice KC, Maier SF, Watkins LR. Protraction of Neuropathic Pain by Morphine is Mediated by Spinal Damage Associated Molecular Patterns (Damps) in Male Rats. *Brain Behav Immun* (2018) 72:45–50. doi: 10.1016/j.bbi.2017.08.018
15. Liu CF, Rivere M, Huang HJ, Puzo G, Wang JY. Surfactant Protein D Inhibits Mite-Induced Alveolar Macrophage and Dendritic Cell Activations Through TLR Signalling and DC-SIGN Expression. *Clin Exp Allergy* (2010) 40:111–22. doi: 10.1111/j.1365-2222.2009.03367.x
16. Millerand M, Sudre L, Nefla M, Pène F, Rousseau C, Pons A, et al. Activation of Innate Immunity by 14-3-3 E, a New Potential Alarmin in Osteoarthritis. *Osteoarthritis Cartilage* (2020) 28:646–57. doi: 10.1016/j.joca.2020.03.002
17. Barreto G, Manninen M. Osteoarthritis and Toll-Like Receptors: When Innate Immunity Meets Chondrocyte Apoptosis. *Biol (Basel)* (2020) 9:65. doi: 10.3390/biology9040065.
18. Gómez R, Villalvilla A, Largo R, Gualillo O, Herrero-Beaumont G. TLR4 Signalling in Osteoarthritis–Finding Targets for Candidate Dmoads. *Nat Rev Rheumatol* (2015) 11:159–70. doi: 10.1038/nrrheum.2014.209
19. Hayami T, Pickarski M, Zhuo Y, Wesolowski GA, Rodan GA, Duong LT. Characterization of Articular Cartilage and Subchondral Bone Changes in the Rat Anterior Cruciate Ligament Transection and Meniscectomized Models of Osteoarthritis. *Bone* (2006) 38:234–43. doi: 10.1016/j.bone.2005.08.007
20. Zhou Y, Ming J, Deng M, Li Y, Li B, Li J, et al. Chemically Modified Curcumin (CMC2.24) Alleviates Osteoarthritis Progression by Restoring Cartilage Homeostasis and Inhibiting Chondrocyte Apoptosis. *via NF-κB/HIF-2α Axis J Mol Med (Berl)* (2020) 98:1479–91. doi: 10.1007/s00109-020-01972-1
21. Wang CJ, Huang CY, Hsu SL, Chen JH, Cheng JH. Extracorporeal Shockwave Therapy in Osteoporotic Osteoarthritis of the Knee in Rats: An Experiment in Animals. *Arthritis Res Ther* (2014) 16:R139. doi: 10.1186/ar4601
22. Netea MG, Domínguez-Andrés J, Barreiro LB, Chavakis T, Divangahi M, Fuchs E, et al. Defining Trained Immunity and its Role in Health and Disease. *Nat Rev Immunol* (2020) 20:375–88. doi: 10.1038/s41577-020-0285-6
23. Wang Y, Zhao X, Liu-Bryan R. Role of TLR2 and TLR4 in Regulation of Articular Chondrocyte Homeostasis. *Osteoarthritis Cartilage* (2020) 28:669–74. doi: 10.1016/j.joca.2020.01.011
24. Munk HL, Fakih D, Christiansen L, Tan Q, Christensen AF, Ejstrup L, et al. Surfactant Protein-D, a Potential Mediator of Inflammation in Axial Spondyloarthritis. *Rheumatol (Oxford)* (2018) 57:1861–5. doi: 10.1093/rheumatology/key187
25. Yu J, Ni L, Zhang X, Zhang J, Abdel-Razek O, Wang G. Surfactant Protein D Dampens Lung Injury by Suppressing NLRP3 Inflammasome Activation and NF-κb Signaling in Acute Pancreatitis. *Shock* (2019) 51:557–68. doi: 10.1097/SHK.0000000000001244
26. Zusso M, Lunardi V, Franceschini D, Pagetta A, Lo R, Stifani S, et al. Ciprofloxacin and Levofloxacin Attenuate Microglia Inflammatory Response *via* TLR4/NF-Kb Pathway. *J Neuroinflammation* (2019) 16:148. doi: 10.1186/s12974-019-1538-9
27. Aldapa-Vega G, Moreno-Eutimio MA, Berlanga-Taylor AJ, Jiménez-Uribe AP, Nieto-Velazquez G, López-Ortega O, et al. Structural Variants of Salmonella Typhimurium Lipopolysaccharide Induce Less Dimerization of TLR4/MD-2 and Reduced Pro-Inflammatory Cytokine Production in Human Monocytes. *Mol Immunol* (2019) 111:43–52. doi: 10.1016/j.molimm.2019.03.003

28. Wang Y, Xu J, Zhang X, Wang C, Huang Y, Dai K, et al. TNF-α-Induced LRG1 Promotes Angiogenesis and Mesenchymal Stem Cell Migration in the Subchondral Bone During Osteoarthritis. *Cell Death Dis* (2017) 8:e2715. doi: 10.1038/cddis.2017.129
29. Hsueh MF, Bolognesi MP, Wellman SS, Kraus VB. Anti-Inflammatory Effects of Naproxen Sodium on Human Osteoarthritis Synovial Fluid Immune Cells. *Osteoarthritis Cartilage* (2020) 28:639–45. doi: 10.1016/j.joca.2020.01.013
30. Hu Q, Ecker M. Overview of MMP-13 as a Promising Target for the Treatment of Osteoarthritis. *Int J Mol Sci* (2021) 22:1742. doi: 10.3390/ijms22041742
31. Hartjen N, Bräuer L, Reiß B, Claassen H, Beileke S, Garreis F, et al. Evaluation of Surfactant Proteins a, B, C, and D in Articular Cartilage, Synovial Membrane and Synovial Fluid of Healthy as Well as Patients With Osteoarthritis and Rheumatoid Arthritis. *PloS One* (2018) 13:e0203502. doi: 10.1371/journal.pone.0203502
32. Haraden CA, Huebner JL, Hsueh MF, Li YJ, Kraus VB. Synovial Fluid Biomarkers Associated With Osteoarthritis Severity Reflect Macrophage and Neutrophil Related Inflammation. *Arthritis Res Ther* (2019) 21:146. doi: 10.1186/s13075-019-1923-x
33. Sanchez-Lopez E, Coras R, Torres A, Lane NE, Guma M. Synovial Inflammation in Osteoarthritis Progression. *Nat Rev Rheumatol* (2022) 18:258–75. doi: 10.1038/s41584-022-00749-9
34. Wang D, Jin M, Zhao X, Zhao T, Lin W, He Z, et al. Fgf1$^{(\Delta hbs)}$ Ameliorates Chronic Kidney Disease *via* PI3K/AKT Mediated Suppression of Oxidative Stress and Inflammation. *Cell Death Dis* (2019) 10:464. doi: 10.1038/s41419-019-1696-9
35. Sophia J, Kowshik J, Dwivedi A, Bhutia SK, Manavathi B, Mishra R, et al. Nimbolide, a Neem Limonoid Inhibits Cytoprotective Autophagy to Activate Apoptosis *via* Modulation of the PI3K/Akt/GSK-3β Signalling Pathway in Oral Cancer. *Cell Death Dis* (2018) 9:1087. doi: 10.1038/s41419-018-1126-4
36. Sun LJ, Qiao W, Xiao YJ, Cui L, Wang X, Ren WD. Naringin Mitigates Myocardial Strain and the Inflammatory Response in Sepsis-Induced Myocardial Dysfunction Through Regulation of PI3K/AKT/NF-κb Pathway. *Int Immunopharmacol* (2019) 75:105782. doi: 10.1016/j.intimp.2019.105782
37. Lai JL, Liu YH, Liu C, Qi MP, Liu RN, Zhu XF, et al. Indirubin Inhibits LPS-Induced Inflammation *via* TLR4 Abrogation Mediated by the NF-Kb and MAPK Signaling Pathways. *Inflammation* (2017) 40:1–12. doi: 10.1007/s10753-016-0447-7
38. Feng L, Yang N, Li C, Tian G, Wang J, Dong ZB, et al. Pudilan Xiaoyan Oral Liquid Alleviates LPS-Induced Respiratory Injury Through Decreasing Nitroxidative Stress and Blocking TLR4 Activation Along With NF-κb Phosphorylation in Mice. *J Ethnopharmacol* (2018) 214:292–300. doi: 10.1016/j.jep.2017.07.009
39. Wu X, Gowda NM, Kawasawa YI, Gowda DC. A Malaria Protein Factor Induces IL-4 Production by Dendritic Cells *via* PI3K-Akt-NF-κb Signaling Independent of Myd88/TRIF and Promotes Th2 Response. *J Biol Chem* (2018) 293:10425–34. doi: 10.1074/jbc.AC118.001720
40. Wu Y, Cui J, Zhang X, Gao S, Ma F, Yao H, et al. Pneumococcal Dnaj Modulates Dendritic Cell-Mediated Th1 and Th17 Immune Responses Through Toll-Like Receptor 4 Signaling Pathway. *Immunobiology* (2017) 222:384–93. doi: 10.1016/j.imbio.2016.08.013
41. Xu X, Liu X, Yang Y, He J, Jiang M, Huang Y, et al. Resveratrol Exerts Anti-Osteoarthritic Effect by Inhibiting TLR4/NF-κb Signaling Pathway *via* the TLR4/Akt/Foxo1 Axis in IL-1β-Stimulated SW1353 Cells. *Drug Des Devel Ther* (2020) 14:2079–90. doi: 10.2147/DDDT.S244059
42. Lorenz W, Buhrmann C, Mobasheri A, Lueders C, Shakibaei M. Bacterial Lipopolysaccharides Form Procollagen-Endotoxin Complexes That Trigger Cartilage Inflammation and Degeneration: Implications for the Development of Rheumatoid Arthritis. *Arthritis Res Ther* (2013) 15:R111. doi: 10.1186/ar4291

Conflict of Interest: The authors declare that the research was conducted in the absence of any commercial or financial relationships that could be construed as a potential conflict of interest.

frontiers | Frontiers in Immunology

TYPE Original Research
PUBLISHED 26 August 2022
DOI 10.3389/fimmu.2022.956587

OPEN ACCESS

EDITED BY
Tor Gjøen,
University of Oslo, Norway

REVIEWED BY
Kristen M. Ogden,
Vanderbilt University Medical Center, United States
Jianguo Su,
Huazhong Agricultural University, China
Gailing Yuan,
Huazhong Agricultural University, China

*CORRESPONDENCE
Ming Xian Chang
mingxianchang@ihb.ac.cn
Songying Ouyang
ouyangsy@fjnu.edu.cn

SPECIALTY SECTION
This article was submitted to Comparative Immunology, a section of the journal Frontiers in Immunology

RECEIVED 30 May 2022
ACCEPTED 12 August 2022
PUBLISHED 26 August 2022

CITATION
Zhang J, Li P, Lu R, Ouyang S and Chang MX (2022) Structural and functional analysis of the small GTPase ARF1 reveals a pivotal role of its GTP-binding domain in controlling of the generation of viral inclusion bodies and replication of grass carp reovirus. *Front. Immunol.* 13:956587. doi: 10.3389/fimmu.2022.956587

Structural and functional analysis of the small GTPase ARF1 reveals a pivotal role of its GTP-binding domain in controlling of the generation of viral inclusion bodies and replication of grass carp reovirus

Jie Zhang[1], Pengwei Li[1,2], Riye Lu[3], Songying Ouyang[3]* and Ming Xian Chang[1,2,4]*

[1]State Key Laboratory of Freshwater Ecology and Biotechnology, Institute of Hydrobiology, Chinese Academy of Sciences, Wuhan, China, [2]College of Advanced Agricultural Sciences, University of Chinese Academy of Sciences, Beijing, China, [3]Provincial University Key Laboratory of Cellular Stress Response and Metabolic Regulation, the Key Laboratory of Innate Immune Biology of Fujian Province, Biomedical Research Center of South China, Key Laboratory of OptoElectronic Science and Technology for Medicine of the Ministry of Education, College of Life Sciences, Fujian Normal University, Fuzhou, China, [4]Innovation Academy for Seed Design, Chinese Academy of Sciences, Wuhan, China

Grass carp reovirus (GCRV) is the most pathogenic double-stranded (ds) RNA virus among the isolated aquareoviruses. The molecular mechanisms by which GCRV utilizes host factors to generate its infectious compartments beneficial for viral replication and infection are poorly understood. Here, we discovered that the grass carp ADP ribosylation factor 1 (gcARF1) was required for GCRV replication since the knockdown of gcARF1 by siRNA or inhibiting its GTPase activity by treatment with brefeldin A (BFA) significantly impaired the yield of infectious viral progeny. GCRV infection recruited gcARF1 into viral inclusion bodies (VIBs) by its nonstructural proteins NS80 and NS38. The small_GTP domain of gcARF1 was confirmed to be crucial for promoting GCRV replication and infection, and the number of VIBs reduced significantly by the inhibition of gcARF1 GTPase activity. The analysis of gcARF1-GDP complex crystal structure revealed that the ^{27}AAGKTT^{32} motif and eight amino acid residues (A^{27}, G^{29}, K^{30}, T^{31}, T^{32}, N^{126}, D^{129} and A^{160}), which were located mainly within the GTP-binding domain of gcARF1, were crucial for the binding of gcARF1 with GDP. Furthermore, the ^{27}AAGKTT^{32} motif and the amino acid residue T^{31} of gcARF1 were indispensable for the function of gcARF1 in promoting GCRV replication and infection. Taken together, it is demonstrated that

10.3389/fimmu.2022.956587

the GTPase activity of gcARF1 is required for efficient replication of GCRV and that host GTPase ARF1 is closely related with the generation of VIBs.

KEYWORDS

grass carp reovirus, viral inclusion bodies, nonstructural proteins NS80 and NS38, ADP ribosylation factor 1, gcARF1-GDP complex, GTPase activity

Highlights

1. gcARF1 is indispensable for the formation of VIBs during GCRV infection.
2. GCRV NS80 and NS38 proteins can interact with gcARF1 and recruit gcARF1 into VIBs.
3. The amino acid residues (27AAGKTT32, N126, D129, A160) of gcARF1 are essential for GDP binding and GCRV replication.

Introduction

The ADP ribosylation factors (ARF) belong to the Ras superfamily of small GTPases, which are guanine-nucleotide dependent molecular switches involved in regulating of numerous cellular processes (1). Based on amino-acid sequence identity, mammalian ARF proteins can be divided into 3 classes: ARF1 and ARF3 (class I), ARF4 and ARF5 (class II) and ARF6 (class III) (2). The amino-acid sequences of ARF proteins are well conserved in all eukaryotes, from yeast to humans (3). Like other small GTPases, ARF proteins cycle between their inactive and active conformations, which is achieved by exchanging GTP for GDP *via* guanine nucleotide exchange factors (GEFs) to form active-GTP-bound form and then hydrolyzing GTP to switch back to inactive-GDP-bound form *via* GTPase activating proteins (GAPs) (3–5). ARF proteins play a key role in membrane traffic, mitochondrial architecture, assembly and dynamics of the microtubule and actin cytoskeletons (3, 6).

Among mammalian ARF proteins, ARF1 is a well-studied member, and has a well-established role in the assembly and budding of Golgi coat proteins coatomer (COPI) vesicles at the Golgi (7). Recent research has shown that ARF1 has a role in viral replication and infection. ARF GTPases are required for different steps of cytomegalovirus infection, and the knockdown of ARF1 can abolish the establishment of cytomegalovirus infection (5). During enterovirus infection, ARF1 was recruited to the replication organelles, and co-localized with the viral nonstructural protein 2B and mature virions. Different from other class I and II ARF proteins, only the depletion of ARF1 significantly increased the sensitivity of enterovirus replication to brefeldin A (BFA), a potent inhibitor of viral replication such as many (+) RNA viruses including enteroviruses (8). For hazara nairovirus (HAZV), its replication cycle can be divided into at least two distinct phases. The second phase involved in infectious virus production is highly COPI- and ARF1-dependent (8). For aquatic animal viruses, a study showed that knockdown of ARF1 from giant freshwater prawn *Macrobrachium rosenbergii* decreased the replication level of white spot syndrome virus (9). However the mechanism that ARF1 is involved in the infection and replication of aquatic animal viruses remains unclear.

Grass carp reovirus (GCRV) is recognized as the most pathogenic among the isolated aquareoviruses, which contains a genome of 11 double-stranded (ds) RNA segments enclosed in a core surrounded with a double layered icosahedral capsid (10). The 11 genomic segments encode five nonstructural proteins (NS80, NS38, NS31, NS26 and NS16) and seven structural proteins (VP1 to VP7) (11). Previous review has summarized the known GCRV strains and antiviral immune responses of high-mobility group box proteins (HMGBs), TLRs, RLRs and NLRs signaling pathways in response to GCRV infection (12). Furthermore, it is found that the replication and assembly of GCRV take place in specific intracellular compartments called viral inclusion bodies (VIBs) (13). The nonstructural proteins NS80 and NS38 of GCRV are two main proteins to form the VIBs, and can recruit viral and host factors into VIBs to assist the replication and assembly of GCRV (14–16). Whether viral infections from GCRV recruit ARF proteins to cytoplasmic VIBs remains unclear. Here, we found that grass carp ARF1 (gcARF1) can promote GCRV replication and infection, which is dependent on the GTPase activity of ARF1. The nonstructural proteins NS80 and NS38 of GCRV can interact with the small_GTP domain of gcARF1, and recruit gcARF1 into cytoplasmic VIBs. When the GBF1-mediated activation of ARF1 is blocked by BFA (17), the number of VIBs produced during GCRV infection is significantly reduced. We also resolved the crystal structure of gcARF1 protein, and found the ^{27}AAGKTT^{32} motif and eight amino acid residues (A^{27}, G^{29}, K^{30}, T^{31}, T^{32}, N^{126}, D^{129} and A^{160}) of gcARF1 necessary for

binding to GDP. Furthermore, the ^{27}AAGKTT^{32} motif and the amino acid residue T^{31} of gcARF1 are crucially important for promoting replication and infection of GCRV. Our study thus reveals a new critical function for gcARF1 in generation of VIBs.

Materials and methods

Cells, virus and plasmids

CIK (*Ctenopharyngodon idellus* kidney) cells were grown in minimum essential medium (MEM) supplemented with 10% FBS. Grass carp reovirus (GCRV-873) was propagated in CIK cells using MEM supplemented with 2% FBS. Plasmids used in this study including pTurboGFP vector (Evrogen), p3×FLAG-CMV™-14 Expression Vector (Sigma-Aldrich Co. LLC), and pET28a-SUMO vector were previously prepared and stored in our laboratory. The GenBank accession numbers of gcARF1 is OM567585. gcARF1-GFP was obtained using the primer pairs gcARF1F1/gcARF1R1 and cloned into the pTurboGFP-N vector. gcARF1-FLAG, gcARF1-small_GTP-FLAG, gcARF1 (d27-32aa)-FLAG, and gcARF1(T31N)-FLAG were obtained using the primer pairs gcARF1F/gcARF1R, gcARF1-small_GTPF/gcARF1-small_GTPR, gcARF1(d27-32aa)F/gcARF1(d27-32aa)R, and gcARF1(T31N)F/gcARF1(T31N)R, and cloned into the p3×FLAG-CMV-14 vector, respectively. pET28a-gcARF1 was obtained using the primer pairs gcARF1F2/gcARF1R2, and cloned into the pET28a-SUMO vector. The primers used for plasmid constructs are listed in Table S1.

Antibodies and reagents

The anti-FLAG mouse monoclonal antibody (#F3165), anti-pTurboGFP rabbit polyclonal antibody (#AB513) and anti-GAPDH mouse monoclonal antibody (#60004-1-Ig) were purchased from Sigma-Aldrich, Everogen and Proteintech, respectively. To obtain these antibodies against NS80, NS38, VP3 and VP5 proteins of GCRV, the 2~160 amino acids (aa) of NS38, 500~692 aa of NS80, 2~200 aa of VP3 or 451~ 648 aa of VP5 was inserted into the pET-32a (+) vector (EMD Millipore) for prokaryotic expression. Purified recombinant proteins were used to immunize Japanese White rabbits to acquire the rabbit polyclonal antibodies and mice to acquire the mouse polyclonal antibodies. The antiserum from the rabbit was affinity-purified on antigen-coupled CNBr-activated agarose (GE Healthcare). Goat-anti-mouse Ig-HRP conjugate secondary antibody, Goat-anti-rabbit Ig-HRP conjugate secondary antibody, Alexa Fluor 488-conjugated secondary Ab against mouse IgG, Alexa Fluor 594-conjugated secondary Ab against rabbit IgG, 6-diamidino-2-phenylindole (DAPI), Lipofectamine 2000 and Protease inhibitor cocktail were purchased from Thermo Fisher Scientific. Dimethylsulfoxide (DMSO) and the FLAG® Immunoprecipitation Kit was purchased from Sigma-Aldrich. Brefeldin A (BFA, S7046) was purchased from Selleck. Golgi-tracker red (C1043) was purchased from Beyotime.

Knockdown of gcARF1 by siRNA

Transient knockdown of gcARF1 was achieved by transfection of siRNA targeting gcARF1 mRNA. Three siRNA sequences including siARF1-1 (5′-CGTCACTACTTCCAGAACA-3′), siARF1-2 (5′-GCAGGCAAGAGCTTCTTTA-3′) and siARF1-3 (5′-GCAATGAATGCTGCAGAAA-3′) targeting different regions of gcARF1 were synthesized by RIBOBIO (Guangzhou, China). CIK cells were transfected with siRNA using Lipo 2000 for 24 h. Silencing efficiencies of these three siRNAs were evaluated by qRT-PCR, and results were compared with the control-siRNA provided by the supplier. A preliminary experiment indicated that siARF1-3 possessed the best silencing efficiency at a final concentration of 100 nM, and used for the present study.

Viral infection assays

To investigate the effects of gcARF1 or its mutants in GCRV infection, CIK cells grown in 12-well plates were transfected with 1000 ng FLAG empty plasmid, gcARF1-FLAG, gcARF1-small_GTP-FLAG, gcARF1(d27-32aa)-FLAG, or gcARF1 (T31N)-FLAG respectively. For the effects of gcARF1 knockdown in GCRV infection, CIK cells grown in 12-well plates were transfected with the control-siRNA or siARF1. After 24 h post-transfection, cells were infected with GCRV at an MOI of 1 in serum-free MEM medium at 25°C for 1 h. Following adsorption, cells were washed with PBS to remove non-adsorbed virions. Then, the infected cells were maintained in 2% FBS MEM at 25°C for 24 h.

For inhibition of gcARF1 GTPase activity by BFA, CIK cells were plated in 24-well or 6-well plates, and then the growth medium was replaced with the same medium supplemented with 0.5 μg/ml, 2.5 μg/ml or 10 μg/ml of BFA (stored as a 10 mM/mL stock in DMSO at -80°C), or the equivalent volume of DMSO alone as a control. For BFA pretreatment before GCRV infection, CIK cells were incubated with or without BFA for 1 h, then washed with PBS to remove BFA, and finally infected with GCRV for 1 h. For BFA treatment during virus attachment, CIK cells were infected with GCRV and treated with BFA for 1 h, and then washed with PBS to remove BFA and non-adsorbed virions. For BFA treatment after virus attachment, CIK cells were infected with GCRV for 1 h, then washed with PBS to remove non-adsorbed virions, and finally treated with BFA for another 24 h. For BFA treatment during virus attachment and after virus attachment, CIK cells were infected with GCRV and treated with

BFA for 1 h, then washed with PBS to remove BFA and non-adsorbed virions, and finally treated with BFA for another 24 h.

The cells without BFA treatment and/or GCRV infection were used for the control group. The culture supernatants of infected cells were collected for determination of GCRV titers. The cells in the 24-well plates were used for crystal violet staining. The cells in the 6-well plates were used for protein extraction and Western Blotting.

RNA extraction, reverse transcription and qRT-PCR

For the overexpression of gcARF1, CIK cells seeded overnight in 6-well plates at 1×10^6 cells per well were transiently transfected with 1000 ng FLAG, or gcARF1-FLAG (500 ng or 1000 ng). For the knockdown of gcARF1, CIK cells seeded overnight in 6-well plates at 1×10^6 cells per well were transiently transfected with the control-siRNA or siARF1. At 24 h after transfection, these cells were infected with GCRV at an MOI of 1. Then these cells were collected at 24 hpi, and used for RNA extraction using TRIzol Reagent (Thermo Fisher Scientific). The concentration of total RNA was determined by using the spectrophotometer (NanoDrop 2000; Thermo). RNase-free DNase I (Thermo) was used to remove genomic DNA remnants at 37°C for 30 min. The cDNA was synthesized using the RevertAid^{TM} First Strand cDNA Synthesis Kit (Thermo Fisher Scientific) according to the manufacturer's instructions. qRT-PCR was performed on a BIO-RAD CFX96^{TM} C1000 thermal cycler using iQ^{TM} SYBR Green Supermix (BioRad, Singapore) under the following conditions: 3 min at 95°C, followed by 45 cycles of 10 s at 95°C, 15 s at 60°C and 10 s at 72°C. All reactions were performed in triplicate and the mean value recorded. Those GCRV genes including NS80, NS38, VP1, VP2, VP3, VP4, VP5, VP6, and VP7 were used for qRT-PCR. The housekeeping genes including β-actin, EF-1α and 18S rRNA were used for normalizing cDNA amounts. The fold changes relative to the control group transfected with the FLAG empty plasmid or control-siRNA were calculated using the $2^{-\Delta\Delta Ct}$ method. All primers used for qRT-PCR are shown in Table S1.

Protein purification of gcARF1

The full-length of gcARF1 was cloned from grass carp and inserted into pET28a expression vector. The constructed pET28a-gcARF1 plasmid was transformed into *E. coli* BL21 (DE3) cells. The cells were grown in LB medium at 37°C with constant shaking at 220 rpm about 2.5 h and induced with 0.3 mM isopropyl-b-D-thiogalactopyranoside (IPTG) when the bacteria grew to a density OD_{600} (optical density at 600 nm) = 1.0. The bacteria were cultured for 16 h at 16°C, pelleted by centrifugation, and resuspended in the cold lysis buffer (50 mM Tris-HCl, pH 7.5, 150 mM NaCl). Following lysis by ultrasonication, the cell lysates were centrifuged at 17000 rpm for 30 min at 4°C. The protein with His-SUMO tag was purified by affinity chromatography (Ni^{2+} resin). The His-SUMO tag was removed by SUMO Protease ULP1. The tag-free protein was purified by size-exclusion chromatography using a Superdex 200 Increase column (GE Healthcare) equilibrated with buffer containing 25 mM HEPES, 150 mM NaCl and 2 mM DTT. The purified protein was finally collected and concentrated to A_{280} = 15 for crystallization screen.

Crystallization, data collection and structure determination

Crystallization screens were performed using the hanging-drop vapor diffusion method at 16°C, with drops containing 0.5 µl of protein solution mixed with 0.5 µl of reservoir solution. Diffraction quality of gcARF1 crystals was obtained 0.1 M Sodium citrate tribasic dihydrate, pH 5.5, 22% polyethylene glycol 1000. Crystals were harvested and flash-frozen in liquid nitrogen with the 20% ethylene glycol as a cryoprotectant. Complete X-ray diffraction datasets were collected at BL02U1 beamline of Shanghai Synchrotron Radiation Facility (SSRF). Diffraction images were processed with HKL-200 program. Crystal tructure of gcARF1 was solved by molecular replacement (MR) using Mus musculus ADP-ribosylation factor-like protein 3 as a model (PDB code: 3BH7). Model building and crystallographic refinement were carried out in Coot v0.8.2 and PHENIX v1.10.1 (18, 19). The interactions were analyzed with PyMOL (http://www.pymol.org/), PDBsum and LigPlus. The Figures were generated in PyMOL. The accession number for gcARF1-GDP complex reported in this paper is PDB ID 7WQY.

Immunofluorescence assays

To determine the possible co-localization of gcARF1 with VP3, VP5, NS38 or NS80 of GCRV, CIK cells were plated onto coverslips in 24-well plates, and then transfected with gcARF1-FLAG. After 24 h, CIK cells were infected with GCRV or left untreated. At 24 hpi, the cells were washed twice with PBS and fixed with 4% PFA for 1 h. After being washed three times with PBS, the cells were incubated with anti-FLAG (1:1000), rabbit anti-NS80 or anti-VP5 (1:500) Ab, or mouse anti-NS38 or anti-VP3 (1:500) Ab, followed by incubation with Alexa Fluor 488-conjugated secondary Ab against mouse IgG (1:400) or Alexa Fluor 594-conjugated secondary Ab against rabbit IgG (1:400).

To determine the numbers of VIBs during GCRV infection with or without the BFA treatment, CIK cells were plated onto coverslips in 24-well plates, and then infected with GCRV for 1 h

or left untreated. The cells were washed with PBS to remove non-adsorbed virions. Then, the infected cells were maintained in 2% FBS MEM supplemented with 2.5 μg/ml of BFA, or the equivalent volume of DMSO alone as a control at 25°C for 24 h. At 24 hpi, the cells were washed twice with PBS and fixed with 4% PFA for 1 h. After being washed three times with PBS, the cells were incubated with rabbit anti-NS80 or anti-VP5 (1:500) Ab, or mouse anti-NS38 (1:500) Ab, followed by incubation with Alexa Fluor 488-conjugated secondary Ab against mouse IgG (1:400) or Alexa Fluor 594-conjugated secondary Ab against rabbit IgG (1:400). DAPI staining was applied to detect the cell nucleus. After each incubation step, cells were washed with PBS. Finally, the coverslips were washed and the images were obtained using a SP8 Leica laser confocal microscopy imaging system.

To determine the effects of the depletion of ^{27}AAGKTT^{32} motif or the mutation of T31 residue on the formation and generation of VIBs during GCRV infection, CIK cells were plated onto coverslips in 24-well plates, and then transfected with FLAG, gcARF1-FLAG, gcARF1(d27-32aa)-FLAG or gcARF1(T31N)-FLAG, respectively. After 24 h post-transfection, the cells were infected with GCRV at an MOI of 1 and maintained in MEM containing 2% FBS. At 24 hpi, the cells were washed twice with PBS and fixed with 4% PFA for 1 h. After being washed three times with PBS, the cells were incubated with anti-FLAG (1:1000) and rabbit anti-NS80, followed by incubation with Alexa Fluor 488-conjugated secondary Ab against mouse IgG (1:400) and Alexa Fluor 594-conjugated secondary Ab against rabbit IgG (1:400). DAPI staining was applied to detect the cell nucleus. After each incubation step, cells were washed with PBS. Finally, the coverslips were washed and the images were obtained using a SP8 Leica laser confocal microscopy imaging system. The Image J was used to detect the mean fluorescence intensity of VIBs.

To investigate the effect of BFA on distribution of Golgi apparatus in the presence and absence of GCRV infection, CIK cells plated in 24-well plates were infected with GCRV for 1 h or left untreated. The cells were washed with PBS to remove non-adsorbed virions. Then, the cells were maintained in 2% FBS MEM supplemented with 2.5 μg/ml of BFA or the equivalent volume of DMSO as a control at 25°C for 24 h. The cells were washed with PBS and incubated with Golgi-Tracker Red at 4°C for 30 min. DAPI staining was applied to detect the cell nucleus. Finally, the images were obtained using a SP8 Leica laser confocal microscopy imaging system.

Co-immunoprecipitation assay and western blotting

CIK cells seeded in 10-cm^2 dishes were transfected with various indicated plasmids. After 24 h post-transfection, the cells were infected with GCRV at an MOI of 1 and maintained in 2% FBS MEM at 25°C for another 24 h. Then, the cells were lysed in 600 μl IP lysis buffer containing protease inhibitor cocktail. Cellular debris was removed by centrifugation at 12,000 × g for 10 min at 4°C. Co-IP was performed using the FLAG-tagged Protein Immunoprecipitation Kit according to the manufacturer's manual. The agarose was washed six times with ice-cold washing solution, and protein was eluted with Elution Buffer.

For Western blotting analysis, the whole-cell extracts were subjected to 10% SDS-PAGE and transferred to PVDF membranes, followed by blocking with 5% nonfat milk in Tris-buffered saline-Tween (TBST) for 1 h. The membrane was washed, and then incubated with primary antibody (Ab) overnight at 4°C. The primary Abs including anti-GAPDH (1: 5000), anti-FLAG (1: 5000), anti-pTurboGFP (1: 5000), anti-NS80 (1: 5000), anti-NS38 (1: 5000), anti-VP3 (1: 5000), or anti-VP5 (1: 5000) were used. After washing with TBST, the membrane was next incubated with Goat-anti-mouse Ig-HRP conjugate secondary Ab (1: 5000) or Goat-anti-rabbit Ig-HRP conjugate secondary Ab (1: 5000) for 1 h at room temperature. The bands were detected using Pierce ECL Western Blotting Substrate and ECL Western blot system (LAS-4000mini).

Statistical analysis

Statistical analysis and graphs were performed and produced using Graphpad Prism 7.0 software. Data are presented as mean and SEM. The significance of results was analyzed by Student's t-test and one-way analysis of variance with Bonferroni correction ($^*p < 0.05$, $^{**}p < 0.01$).

Results

ARF1 promotes GCRV replication and infection

To explore the role of gcARF1 in GCRV infection, CIK cells were transfected with gcARF1-FLAG and then infected with GCRV. Compared with the control cells transfected with FLAG empty plasmid, severe cytopathic effect was observed after GCRV infection in the overexpression group (Figure 1A). Cells treated with gcARF1-specific siRNA had efficient reduction in expression of gcARF1 compared with control siRNA with or without GCRV infection (Figure 1B), and siRNA-mediated knockdown of gcARF1 expression showed much more resistant to GCRV infection than the cells transfected with control siRNA (Figure 1C). Consistent with these data, the overexpression of gcARF1 in CIK cells dramatically promoted the GCRV replication with the higher viral titers, and inhibited the GCRV replication by gcARF1-specific siRNA (Figures 1D, E).

Since that we have antibodies against VP3, VP5, NS80 and NS38 proteins of GCRV, the effects of gcARF1 on the protein

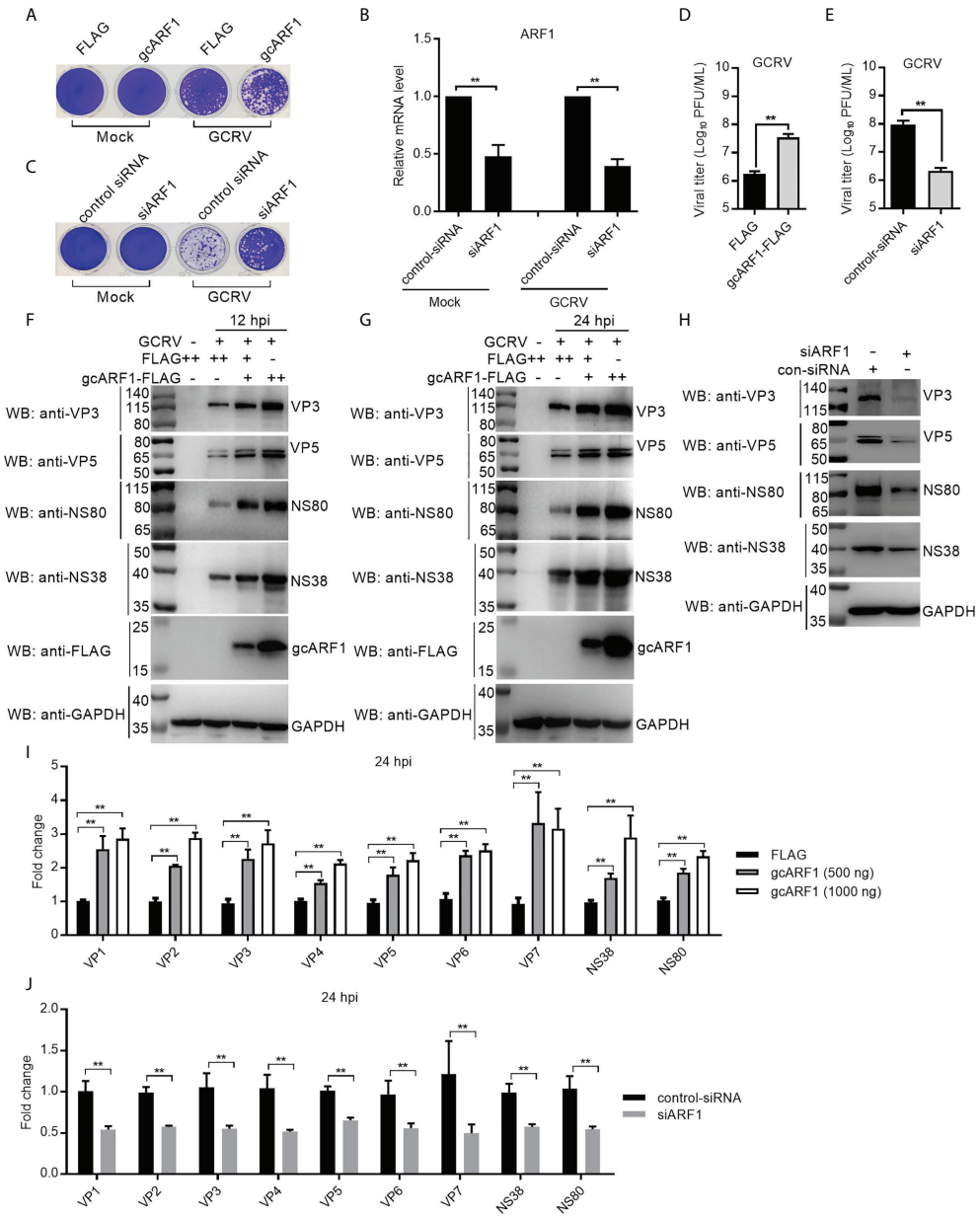

FIGURE 1
gcARF1 promotes GCRV infection. **(A)** Crystal violet staining for overexpression of gcARF1 in CIK cells that were mock infected or infected with GCRV at an MOI of 1 for 24 h. **(B)** The effect of knockdown of gcARF1 on the expression of gcARF1 in CIK cells that were mock infected or infected with GCRV at an MOI of 1 for 24 h. **(C)** Crystal violet staining for knockdown of gcARF1 in CIK cells that were mock infected or infected with GCRV at an MOI of 1 for 24 h. **(D, E)** Virus yield for overexpression and knockdown of gcARF1 in CIK cells infected with GCRV at an MOI of 1 for 24 h. **(F, G)** IB analysis of VP3, VP5, NS80 and NS38 proteins regulated by overexpression of gcARF1 in CIK cells infected with GCRV. CIK cells seeded overnight in 6-well plates were transiently transfected with FLAG vector or gcARF1-FLAG (+: 500 ng, ++: 1000 ng). 24 h later, the cells were infected with the GCRV at an MOI of 1 or left untreated. The cells were collected at 12 **(F)** or 24 dpi **(G)** for protein extraction. **(H)** IB analysis of VP3, VP5, NS80 and NS38 proteins regulated by knockdown of gcARF1 in CIK cells infected with GCRV for 24 h. CIK cells seeded overnight in 6-well plates were transiently transfected with 100 nM control-siRNA or siARF1. After 24 h later, the cells were infected with the GCRV at an MOI of 1 or left untreated. The cells were collected at 24 hpi for protein extraction. **(I)** qRT-PCR analysis of *VP1*, *VP2*, *VP3*, *VP4*, *VP5*, *VP6*, *VP7*, *NS38* or *NS80* expression regulated by overexpression of gcARF1 in CIK cells infected with GCRV. CIK cells seeded overnight in 6-well plates were transiently transfected with FLAG vector or gcARF1-FLAG. After 24 h later, the cells were infected with the GCRV at an MOI of 1. Another 24 h later, these cells were collected and used for RNA extraction and qRT-PCR. **(J)** qRT-PCR analysis of *VP1*, *VP2*, *VP3*, *VP4*, *VP5*, *VP6*, *VP7*, *NS38* or *NS80* expression regulated by knockdown of gcARF1 in CIK cells infected with GCRV for 24 h. CIK cells seeded overnight in 6-well plates were transiently transfected with 100 nM control-siRNA or siARF1. After 24 h later, the cells were infected with the GCRV at an MOI of 1. Another 24 h later, these cells were collected and used for RNA extraction and qRT-PCR. Means ± SEM (n=3) are shown in **(B, D, E, I, J)**. Data were tested for statistical significance, $^{**}p < 0.01$.

expressions of 2 structural proteins and 2 nonstructural proteins of GCRV were examined. Antibody specificity was verified by immunoblotting in the mock-infected and GCRV-infected CIK cells. Using the anti-NS80 polyclonal rabbit antibody, anti-NS38 polyclonal mouse antibody, anti-VP3 polyclonal mouse antibody or anti-VP5 polyclonal rabbit antibody against GCRV-873 strain, a predicated size of approximately 80 kDa (Figure S1A), 40 kDa (Figure S1B), 130 kDa (Figure S1C) or 70 kDa (Figure S1D) was observed in the GCRV-infected CIK cells. The overexpression of gcARF1 increased the protein level of VP3, VP5, NS80 and NS38 in a dose dependent manner both at 12- and 24-hours post-infection (hpi) (Figures 1F, G). The knockdown of gcARF1 significantly decreased the protein level of these structural and nonstructural proteins of GCRV (Figure 1H).

To determine whether the overexpression or knockdown of gcARF1 had a similar effect at the mRNA level, the expression of 9 GCRV genes was examined by qRT-PCR. The overexpression of gcARF1 significantly increased the mRNA level of all tested genes including *VP1*, *VP2*, *VP3*, *VP4*, *VP5*, *VP6*, *VP7*, *NS38* and *NS80* for the transfected gcARF1 in a dose-dependent manner (Figure 1I), and the knockdown of gcARF1 inhibited significantly the expression of all these genes (Figure 1J). Taken together, these results clearly indicate that gcARF1 promotes virus replication and aggravates virus-induced cytopathogenicity in response to GCRV infection.

NS80 and NS38 of GCRV recruit host GTPase gcARF1 to cytoplasmic VIBs through protein-protein interactions

Previous works showed that NS80 and NS38 of GCRV could form cytoplasmic VIBs in the transfected or GCRV infected cells (13, 14, 20). We confirmed that ectopically expressed gcARF1 was diffusely distributed throughout the cytoplasm in the absence of infection, but formed a punctate distribution scattered throughout the cytoplasm in the case of GCRV infection (Figure 2A). The obvious colocalization between gcARF1 and NS80/NS38 was observed, but not for gcARF1 and VP3/VP5 (Figure 2A), which indicated that they were recruited to cytoplasmic VIBs.

To further confirm if gcARF1 was recruited by NS80 and NS38 of GCRV into cytoplasmic VIBs, we used the overexpressed NS80 or NS38 instead of GCRV infection to verify the effect of NS80 or NS38 on the localization of gcARF1. When the CIK cells were co-transfected with gcARF1-FLAG and NS80-GFP or NS38-GFP, gcARF1 was

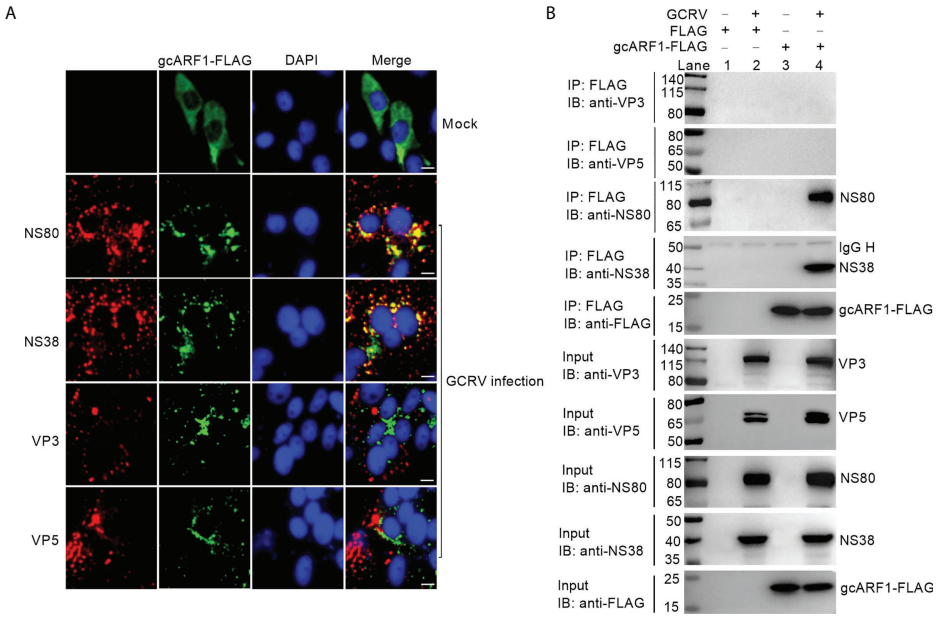

FIGURE 2
The subcellular co-localizations or interactions between gcARF1 and GCRV proteins. **(A)** The subcellular co-localizations between gcARF1 and GCRV proteins. CIK cells plated onto coverslips in 24-well plates were transfected with FLAG-tagged gcARF1. Then the cells were infected with the GCRV at an MOI of 1 or left untreated for another 24 h. Finally, the cells were washed and fixed with 4% PFA for immunofluorescence assays. The images were obtained by Leica confocal microscopy. Scale bars, 10 μm. **(B)** The interactions between gcARF1 and NS80, NS38, VP3 or VP5. CIK cells seeded in 10-cm^2 dishes were transfected with indicated plasmids. After 24 h later, the cells were infected with the GCRV at an MOI of 1 or left untreated for another 24 h. Finally, the cells were harvested and used for protein extraction. Co-IP was performed with anti-FLAG-conjugated agarose beads. The cell lysates and bound proteins were analyzed by immunoblotting with the indicated Abs.

recruited into cytoplasmic VIBs by NS80 and NS38 of GCRV. The subcellular localizations of gcARF1 and NS80 completely overlapped in areas (Figure S2A).

To examine whether gcARF1 also bound to Golgi complex, we used Golgi complex marker to label the localization of Golgi complex. In the absence of infection, the Golgi complex was compact. In GCRV infected cells, Golgi complex became fragmented (Figure S2B), and a small amount of gcARF1 was localized at the Golgi complex (Figure S2C). Furthermore, we also observed that the staining of Golgi complex was not predominantly localized with cytoplasmic VIBs of GCRV (Figure S2D).

Previous studies showed that BFA could disrupt the structure of the Golgi apparatus (21, 22). We next investigated the effects of BFA treatment on the Golgi apparatus in the presence and absence of GCRV infection. The immunofluorescence results showed that both BFA treatment and GCRV infection caused the fragmentation of the Golgi complex. However, the BFA-induced fragmentation of the Golgi complex remained unchanged in the presence of GCRV infection (Figure S2E).

Next, we tested whether NS80 and NS38 of GCRV interacted with gcARF1. CIK cells were transfected with FLAG-tagged gcARF1, and then infected with GCRV or left untreated. The interactions between FLAG and NS80/NS38/VP3/VP5 were examined as the negative controls. As shown in Figure 2B, no NS80, NS38, VP3 or VP5 band was observed (Lane 2), which confirmed that GCRV proteins were not pull-down nonspecifically from the whole protein lysate. However, the anti-FLAG-M2 affinity gel-immunoprecipitated gcARF1 was associated with NS80 (Lane 4 using anti-NS80 antibody for IP product in Figure 2B) and NS38 (Lane 4 using anti-NS38 antibody for IP product in Figure 2B), but not with VP3 (Lane 4 using anti-VP3 antibody for IP product in Figure 2B) and VP5 (Lane 4 using anti-VP5 antibody for IP product in Figure 2B). Sequence analysis revealed that gcARF1 contained a small_GTP domain. A gcARF1 mutant, which only contained a small_GTP domain (Figure S3A), was sufficient for the associations with NS80 and NS38 of GCRV (Figure S3B).

Together, these data demonstrate that the nonstructural proteins NS80 and NS38 of GCRV recruit host gcARF1 to cytoplasmic VIBs through protein-protein interactions.

gcARF1 activation by GBF1 promotes the generation of cytoplasmic VIBs during GCRV infection

BFA inhibits ARF1 activation by targeting the guanine nucleotide exchange factor GBF1 (23, 24). To explore the role of gcARF1 activation in the viral replication cycle, CIK cells were treated with 0.5~10 μg/mL BFA, which had been confirmed to have no significant effect on the viability of CIK cells (Figure S4A). Treatment with BFA before GCRV infection had no obvious effect on the viral cytopathogenicity (Figure 3A), virus proliferation (Figure 3B) and the expressions of VP3, VP5, NS80 and NS38 (Figure 3C). Treatment with BFA during viral attachment inhibited the replication and infection of GCRV in a dose dependent manner. Low concentration of BFA had no obvious effect on the viral cytopathogenicity, virus proliferation and the expressions of viral proteins. However as the concentration of BFA increased, the inhibition of BFA on the viral replication and infection was more obvious (Figures 3D–F). Treatment with BFA after viral attachment significantly led to the inhibition of GCRV replication and infection (Figures 3G–L). These results indicate that gcARF1 activation by GBF1 promotes GCRV replication and infection through facilitating the entry and proliferation of GCRV lifecycle.

Since NS80 and NS38 of GCRV recruit gcARF1 to VIBs by protein-protein interactions, we further investigated the effect of host gcARF1 in the formation or generation of cytoplasmic VIBs in GCRV-infected cells. CIK cell infected by GCRV for 1 h were treated with BFA or DMSO or left untreated. These cells were subsequently fixed and processed for immunofluorescence using antibodies both against NS80 and NS38 of GCRV, which served as protein markers for VIBs of GCRV. Treatment of cells with BFA for 12 or 24 h led to the expected decrease or disappearance of VIBs compared with the untreated cells or DMSO-treated cells (Figure 4). Previous studies have revealed that the outer-capsid proteins of reovirus are responsible for initiating infection. VP5 is the outer-capsid protein of GCRV, and autocleavage of VP5 has been confirmed to be critical for aquareovirus to initiate efficient infection (25). BFA treatment also significantly inhibited the numbers of fluorescent cells expressed with VP5 (Figures S4B–D).

Crystal structures of gcARF1 and gcARF1-GDP complex

The data processed by auto-PROC_XDS is used. The space group is C 1 2 1, each asymmetric unit of the gcARF1 crystal contains two copies of molecules, and the solvent content is 42%. Auto-build and refinement programs from Phenix software were used to reconstruct the structure of gcARF1, with the R-free value of 0.2457 and R-work value of 0.2029. The gcARF1 protein contained a seven-stranded β-sheet surrounded by six α-helices (Figure S5), which indicated that the overall structure of gcARF1 was similar to those of other ARF1 proteins.

During the expression of gcARF1 protein in *E. coli*, we found that the A260 absorbance of gcARF1 protein was unusually high (A260/A280 = 0.82, which was about 0.5 for general proteins), suggesting that gcARF1 might bind to nucleotide or nucleotide analogue when expressed in the *E. coli* system. Meanwhile, the crystal structure of gcARF1 has redundant electron density.

10.3389/fimmu.2022.956587

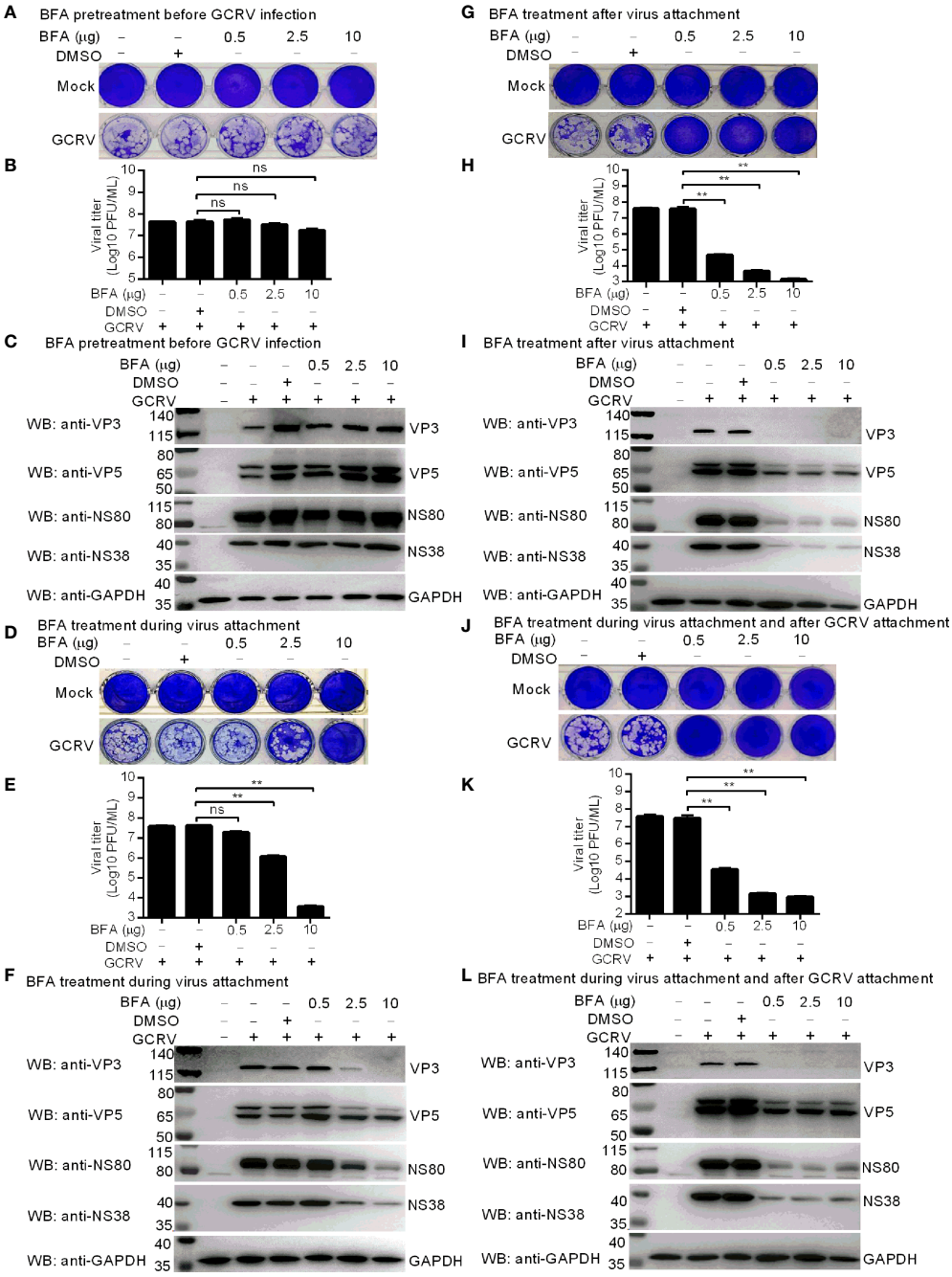

FIGURE 3
Inhibition of gcARF1 activation by BFA impairs GCRV replication and infection. **(A–C)** BFA pretreatment before GCRV infection has no influence on GCRV replication and infection. CIK cells plated in a 24-well or 6-well plates were incubated with BFA using the indicate concentrations or equivalent volume of DMSO for 1 h or left untreated. **(D-F)** BFA treatment during virus attachment suppressed GCRV replication and infection. CIK cells plated in a 24-well or 6-well plates were infected with GCRV and treated with BFA using the indicate concentrations or equivalent volume of DMSO for 1 h or left untreated. Then, the cells were washed with PBS to remove BFA and non-adsorbed virions. **(G–I)** BFA treatment after virus attachment suppressed GCRV replication and infection. CIK cells were infected with GCRV for 1 h, then washed with PBS to remove non-adsorbed virions, and finally treated with BFA using the indicate concentrations or equivalent volume of DMSO for another 24 h or left untreated. **(J–L)** BFA treatment during virus attachment and after virus attachment suppressed GCRV replication and infection. CIK cells were infected with GCRV and treated with BFA for 1 h, then washed with PBS to remove BFA and non-adsorbed virions, and finally treated with BFA for another 24 h. The cells in the 24-well plates were used for crystal violet staining **(A, D, G, J)**, the culture supernatants of infected cells used for determination of GCRV titers **(B, E, H, K)**, and the cells in the 6-well plates used for protein extraction **(C, F, I, L)**. Means ± SEM (n=3) are shown in **(B, E, H, K)**. Data were tested for statistical significance. The asterisk above the bracket indicated statistical significance between the two groups connected by the bracket. $^{**}p < 0.01$; ns, not significant.

10.3389/fimmu.2022.956587

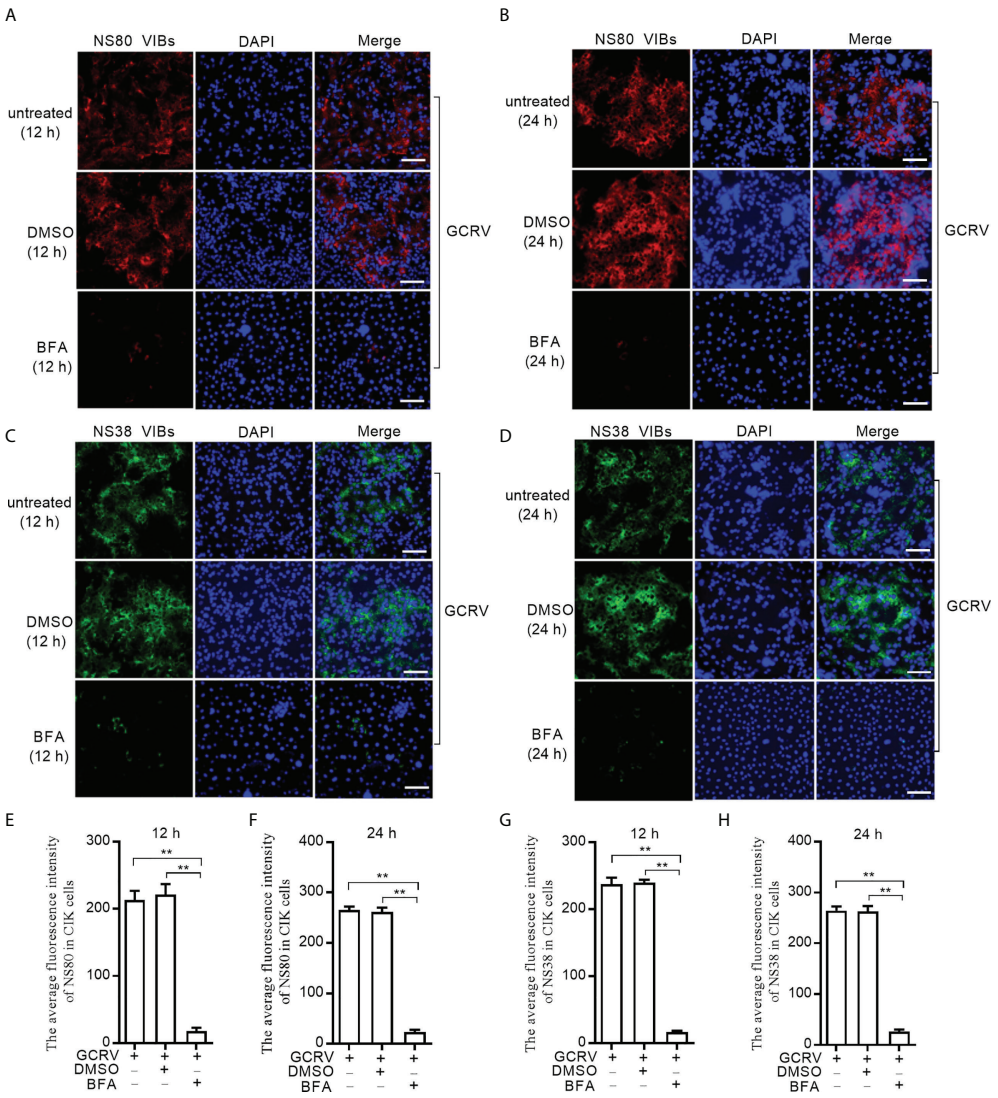

FIGURE 4
BFA treatment reduces the numbers of viral inclusion bodies. **(A)** Immunofluorescence analysis for NS80 in CIK cells that were treated with DMSO or BFA for 12 h or left untreated. Scale bars, 50 μm. **(B)** Immunofluorescence analysis for NS80 in CIK cells that were treated with DMSO or BFA for 24 h or left untreated. Scale bars, 50 μm. **(C)** Immunofluorescence analysis for NS38 in CIK cells that were treated with DMSO or BFA for 12 h or left untreated. Scale bars, 50 μm. **(D)** Immunofluorescence analysis for NS38 in CIK cells that were treated with DMSO or BFA for 24 h or left untreated. Scale bars, 50 μm. **(E)** The average fluorescence intensity of NS80 in CIK cells that were treated with DMSO or BFA for 12 h or left untreated. **(F)** The average fluorescence intensity of NS80 in CIK cells that were treated with DMSO or BFA for 24 h or left untreated. **(G)** The average fluorescence intensity of NS38 in CIK cells that were treated with DMSO or BFA for 12 h or left untreated. **(H)** The average fluorescence intensity of NS38 in CIK cells that were treated with DMSO or BFA for 24 h or left untreated. Means ± SEM (n=3) are shown in **(E-H)**. Data were tested for statistical significance. The asterisk above the bracket indicated statistical significance between the two groups connected by the bracket. $^{**}p < 0.01$.

After repeated refined calculation of the gcARF1 structure, it was confirmed that the excess electron cloud density could match GDP perfectly. The structure of gcARF1-GDP complex was finally confirmed (Figure 5). The structural analysis showed that the groove of gcARF1 binding to GDP mainly consisted of loop between β1 and α2, partial α2, loop between β6 and α5, and loop between β7 and α6. The interaction between gcARF1 and GDP was further analyzed by LigPlus software. Eight amino acid residues (A^{27}, G^{29}, K^{30}, T^{31}, T^{32}, N^{126}, D^{129} and A^{160}) were involved in the binding of GDP with gcARF1. The N^{126}, D^{129} and A^{160} of gcARF1 interacted with guanosine group of GDP by hydrogen bond, which included the carbonyl group of N^{126} side chain interacting with the carbonyl group of GDP guanosine group, the hydrogen atom of the amino group of N^{126} side chain

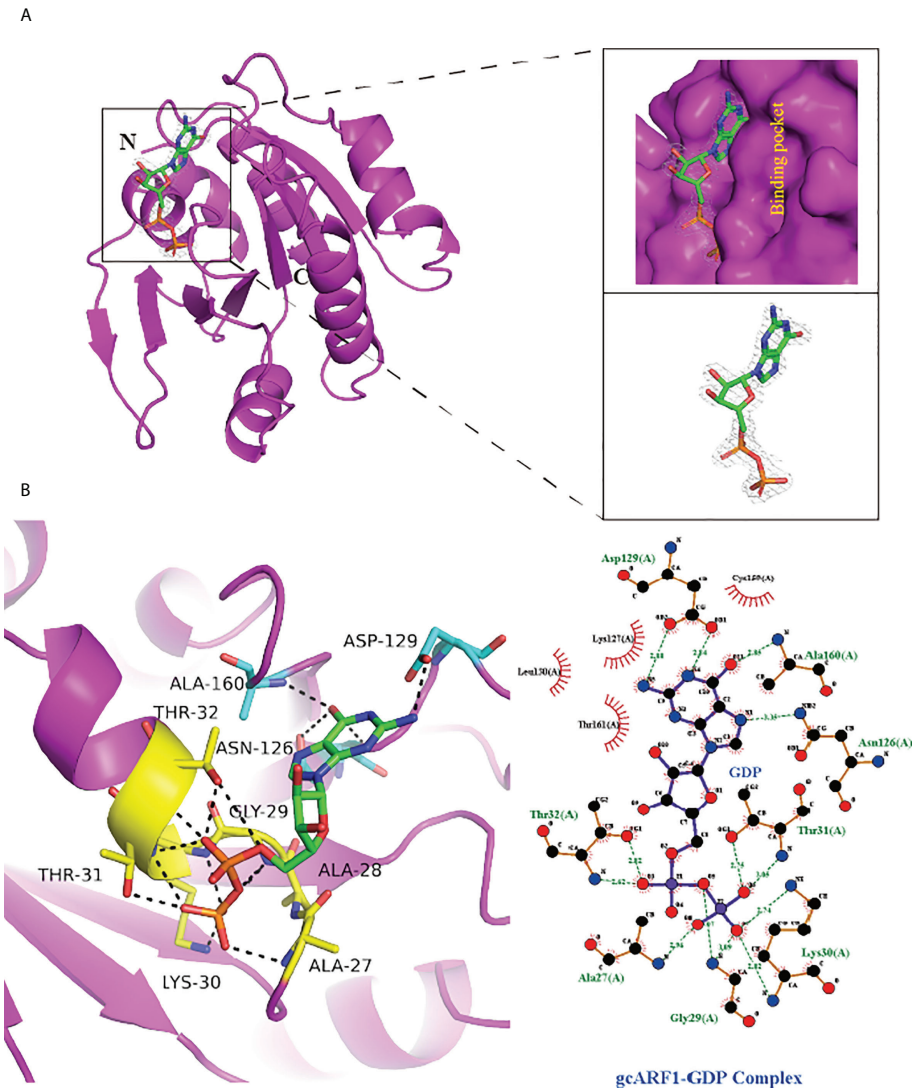

FIGURE 5
Structural analysis of gcARF1-GDP complex. **(A)** The GDP combinative pocket of gcARF1. The surface diagram is shown in the upper right, and the GDP electron density shown in the lower right (level = 2.0). **(B)** The hydrogen bond interaction between GDP and gcARF1. Left: The GDP is shown as green sticks, the AAGKTT motif shown as yellow sticks, the N^{126}, D^{129} and A^{160} shown as cyan sticks, and the hydrogen bonds shown as black dotted line. Right: The interaction between gcARF1 and GDP analyzed by LigPlus software.

interacting with the nitrogen atom of GDP guanosine group, the oxygen atom of the carbonyl group of D^{129} side chain interacting with the amino hydrogen atom of GDP guanosine group, and the amino group of A^{160} main chain interacting with the carbonyl group of GDP guanosine group. Importantly in the ^{27}AAGKTT^{32} motif, the oxygen atom of the T^{32} side chain interacting with the oxygen atom of the first phosphate group of GDP, the hydrogen atom of the K^{30} side chain amino group and the oxygen atom of the T^{31} side chain interacting with the oxygen atom of the second phosphate group of GDP were observed through hydrogen bonds. Therefore, the ^{27}AAGKTT^{32} motif may be crucial for the gcARF1 binding to GDP and the function of gcARF1.

To further investigate whether the AAGKTT motif of ARF1 binding to GDP are conversed among different species, structural comparisons were analyzed using DALI server. The top 5 most similar to gcARF1 structure are *Rattus norvegicus* ARF1 (PDB code: 1RRG), *Homo sapiens* ARF1 (PDB code: 1HUR), *Arabidopsis thaliana* ARF1 (PDB code 3AQ4), *Candida albicans* SC5314 ARF1 (PDB code: 6PTA) and *Homo sapiens* ARF4 (PDB code: 1Z6X) (Figure 6A). Structure alignment analysis suggested that the binding sites between

10.3389/fimmu.2022.956587

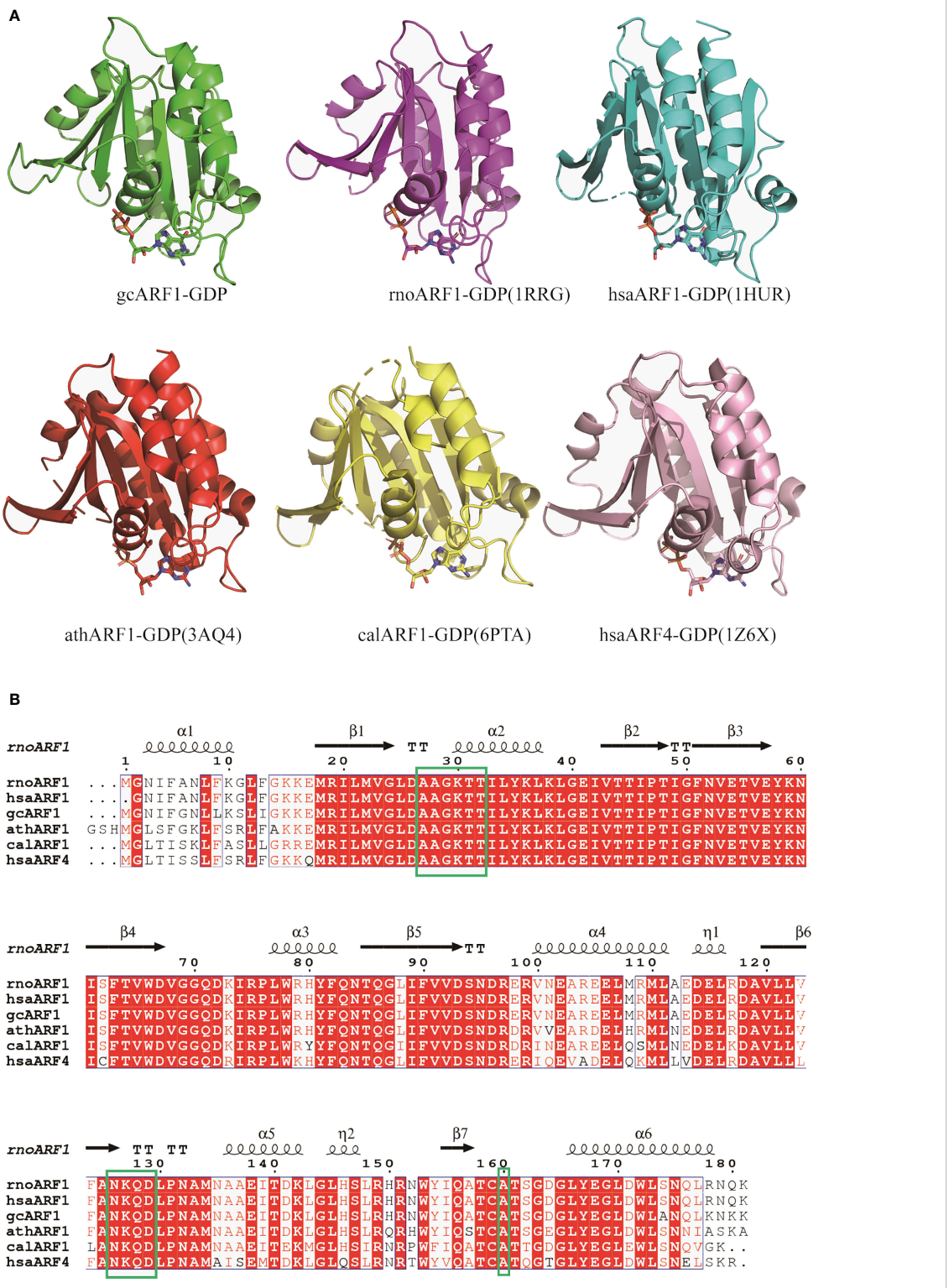

FIGURE 6
Structure and sequence alignments of gcARF1-GDP and ARF-GDP from other species. **(A)** Structure alignments of gcARF1-GDP (green), *Rattus norvegicus* ARF1-GDP (PDB code: 1RRG, purple, RMSD = 0.5), *Homo sapiens* ARF1-GDP (PDB code: 1HUR, cyan, RMSD = 0.6), *Arabidopsis thaliana* ARF1-GDP (PDB code 3AQ4, red, RMSD = 0.8), *Candida albicans* SC5314 ARF1-GDP (PDB code: 6PTA, yellow, RMSD = 0.7) and *Homo sapiens* ARF4-GDP (PDB code: 1Z6X, pink, RMSD = 1.1). **(B)** Sequence alignments of gcARF1 and ARF proteins from other species by Clustal W and ESPript 3.0.

ARF1 and GDP are similar in different species. The AAGKTT motif locating at between TT loop and α2 is also conserved among different species (Figure 6B). All these results suggest that the mechanism of gcARF1 binding to GDP is evolutionarily conservative and the ^{27}AAGKTT^{32} motif is essential for gcARF1 binding to GDP.

The ^{27}AAGKTT^{32} motif and T^{31} residue are required for the function of gcARF1 in promoting GCRV replication and infection

In mammals, ARF1(T31N), a mutant that preferentially binds GDP, is the activation-impaired form of ARF1 (26). Here, crystal structure of gcARF1-GDP complex revealed that the ^{27}AAGKTT^{32} motif was essential for gcARF1 binding to GDP. To determine the pivotal domain, motif and/or residue(s) affecting the function of gcARF1, three mutants included gcARF1-small_GTP-FLAG (Figure S3A), gcARF1(d27-32aa)-FLAG and gcARF1(T31N)-FLAG (Figure 7A) were constructed. We firstly investigated the role of small_GTP domain of gcARF1 in GCRV replication and infection. Similar to gcARF1, overexpression of small_GTP domain of gcARF1 increased the cytopathic effect caused by GCRV infection, with the higher viral titers compared with the control cells transfected with FLAG empty plasmid (Figures S6A, S6B). Overexpression of small_GTP domain of gcARF1 also promoted the expressions of virus-related proteins (Figure S6C). However, the deletion of ^{27}AAGKTT^{32} motif of gcARF1 and the mutation of ARF1 (T31N) significantly inhibited GCRV replication (Figure 7B). Furthermore, the deletion of ^{27}AAGKTT^{32} motif of gcARF1 or the mutation of ARF1(T31N) also inhibited the expressions of virus-related proteins (Figure 7C), which were opposite for the roles of gcARF1 or small_GTP domain of gcARF1 in GCRV infection (Figures 1D-G, Figure S6). All these data suggest that the small_GTP domain of gcARF1 is crucial for GCRV replication and infection, and that the ^{27}AAGKTT^{32} motif and the amino acid residue T31 of gcARF1 are indispensable for the function of gcARF1 in promoting GCRV replication and infection.

Since the above results from Co-IP assays revealed that the small_GTP domain of gcARF1 was sufficient for the association between gcARF1 and NS80 or NS38 protein of GCRV, we further investigated whether the ^{27}AAGKTT^{32} motif and the amino acid residue T^{31} of gcARF1 were essential for protein-protein interactions between gcARF1 and NS80 or NS38 protein of GCRV. We found that the deletion of ^{27}AAGKTT^{32} motif of gcARF1 or the mutation of ARF1(T31N) did not lead to the loss of the interaction with NS80 and NS38 proteins of GCRV (Figure 7D).

The ^{27}AAGKTT^{32} motif and T^{31} residue are required for the generation of VIBs

Given the role of gcARF1 in promoting the generations of cytoplasmic VIBs, we further investigated whether the ^{27}AAGKTT^{32} motif and the amino acid residue T^{31} of gcARF1 were required for the formation and generation of VIBs. In consistent with the fact that the deletion of ^{27}AAGKTT^{32} motif of gcARF1 or the mutation of ARF1(T31N) did not lead to the loss of the interaction with NS80 and NS38 proteins of GCRV, the localization of gcARF1 in cytoplasmic VIBs remained unaffected by the depletion of ^{27}AAGKTT^{32} motif or the mutation of T^{31} residue (Figure 8A). However the total amounts of VIBs were significantly decreased by the depletion of ^{27}AAGKTT^{32} motif or the mutation of T^{31} residue (Figure 8B). All these results suggest that the ^{27}AAGKTT^{32} motif and T^{31} residue are required for the generation of VIBs.

Discussion

During infection, many viruses replicate in cytoplasm of host cells and form viroplasms, viral factories or VIBs, which are often composed of membranous scaffolds, viral and cellular factors. VIBs have multiple functions, including the recruitment of viral and host factors to ensure efficient replication and assembly of virus particles and sequestration of viral nucleic acids and proteins from host innate immune responses (27–29). Previous studies have shown that NS80 of GCRV can form VIBs, and recruit all the inner-capsid proteins (VP1-VP4 and VP6) and NS38 into VIBs (13, 14). Our recent report revealed that NS80 and NS38 of GCRV can hijack grass carp TBK1 and IRF3 into cytoplasmic VIBs for decreasing the formation of TBK1-containing functional complexes and preventing IRF3 translocation into the nucleus, which ultimately leads to the impaired interferon antiviral response (30). Here, we firstly demonstrate that GCRV uses NS80 and NS38 to recruit host GTPase gcARF1 into VIBs to promote GCRV replication and infection. Crystallographic data and functional analysis reveal the pivotal role of ^{27}AAGKTT^{32} motif and T^{31} residue of gcARF1 in the binding to GDP and GCRV replication and infection.

The GCRV genome encodes several non-structural proteins, which do not constitute the nucleocapsids of the virus, but are indispensable for the replication, proliferation, invasion and immune escape of GCRV. NS38 is one of non-structural proteins encoded by GCRV. It has been reported that NS38 interacts with inner-capsid proteins and NS80-RNA complex, and knockdown of NS38 can significantly inhibit the proliferation of GCRV (16). It is speculated that the effects of NS38 on viral protein synthesis are due to its RNA binding characteristics for facilitating interactions with host translational

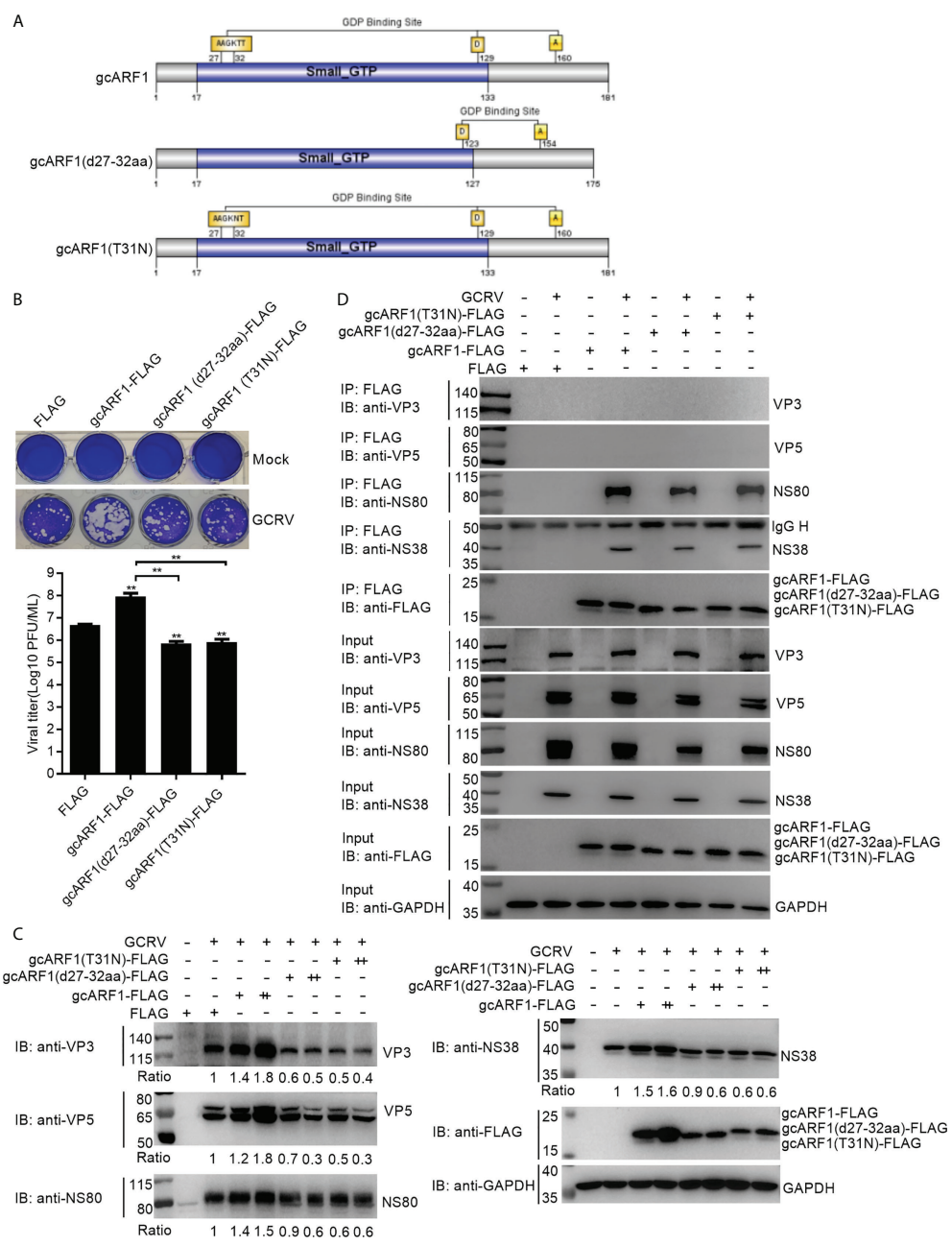

FIGURE 7
The ^{27}AAGKTT^{32} motif and T^{31} residue are required for the function of gcARF1 in promoting GCRV replication and infection. **(A)** Schematic representation of the gcARF1 and its mutants. **(B)** Crystal violet staining and determination of GCRV titers for overexpression of gcARF1 mutants including gcARF1(d27-32aa) and gcARF1(T31N) in CIK cells that were infected with GCRV at an MOI of 1 for 24 h. The asterisk above the error bars indicated statistical significance using the group transfected with FLAG as the control group. The asterisk above the bracket indicated statistical significance between the two groups connected by the bracket. **(C)** IB analysis of VP3, VP5, NS80 and NS38 proteins regulated by overexpression of gcARF1 or gcARF1 mutants including gcARF1(d27-32aa) and gcARF1(T31N) in CIK cells infected with GCRV. CIK cells seeded overnight in 12-well or 6-well plates were transiently transfected with indicated plasmids. After 24 h later, the cells were infected with the GCRV at an MOI of 1 or left untreated. The supernatants in 12-well plates were collected at 24 hpi for viral titer assays, and the cells were fixed and stained with crystal violet **(B)**. The cells in 6-well plates were collected at 24 hpi for protein extraction **(C)**. +: 500 ng, ++: 1000 ng. The expression ratios for viral proteins were quantified by Quantity One. **(D)** The interactions between gcARF1, gcARF1(d27-32aa) or gcARF1(T31N) and viral proteins. CIK cells seeded in 10-cm^2 dishes were transfected with the indicated plasmids. After 24 h later, the cells were infected with or without the GCRV at an MOI of 1. Then the cells were harvested and lysed at 24 hpi. Co-IP was performed with anti-FLAG-conjugated agarose beads. The cell lysates and bound proteins were analyzed by immunoblotting with the indicated Abs.

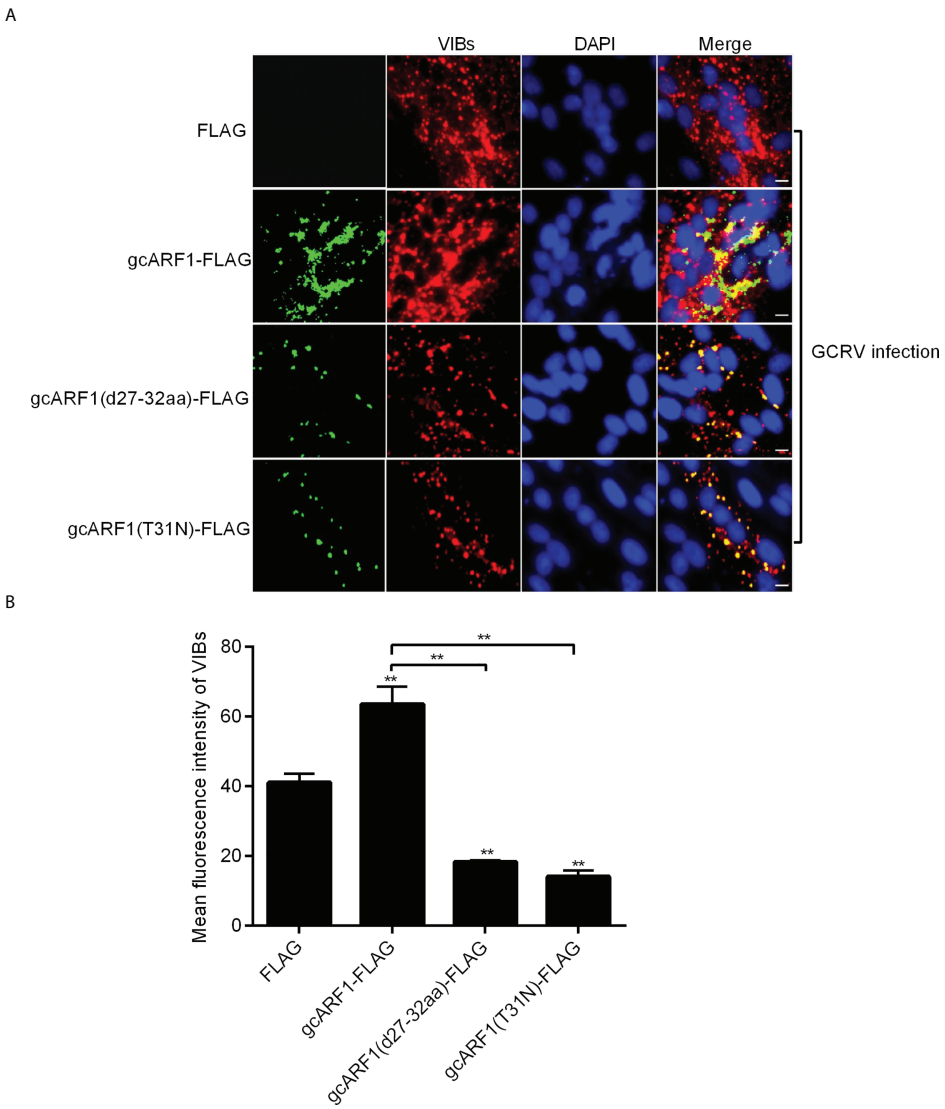

FIGURE 8
The ^{27}AAGKTT^{32} motif and T^{31} residue are required for the generation of VIBs. **(A)** Immunofluorescence analysis for VIBs in CIK cells that were transfected with FLAG, gcARF1-FLAG, gcARF1(d27-32aa)-FLAG or gcARF1(T31N)-FLAG, respectively. Scale bars, 10 μm. **(B)** The average fluorescence intensity of VIBs in CIK cells that were transfected with FLAG, gcARF1-FLAG, gcARF1(d27-32aa)-FLAG or gcARF1(T31N)-FLAG, respectively. Data were tested for statistical significance. $^{**}p < 0.01$. The asterisk above the error bars indicated statistical significance using the group transfected with FLAG as the control group. The asterisk above the bracket indicated statistical significance between the two groups connected by the bracket.

factors such as eIF3A, which is essential for viral translation initiation (16, 31). NS80 is the largest non-structural protein of GCRV. The N-terminal domain of NS80 can recruit NS38, VP1, VP2, VP4 and VP6 into VIBs, and its C-terminal domain is responsible for the formations of VIBs (13, 15, 32, 33). The ARF family is one of five subfamilies of Ras GTPase superfamily, which can cycle between an active GTP-bound state and an inactive GDP-bound state. Previous studies have shown that ARF1 protein can be localized to the Golgi complex, and regulates phosphatidylinositol 4-kinase IIIbeta activity, Golgi transport complex recruitment, architecture of ER-Golgi intermediate compartment, and the formation of bidirectional tubules from Golgi (7, 34, 35). In addition, it has been reported that ARF1 is also involved in the replication process of many viruses, including Hepatitis C virus (HCV), enterovirus 71, white spot syndrome virus (WSSV), and red clover necrotic mosaic virus (RCNMV) (9, 36–38). ARF proteins are also recruited into replication organelles or regulate membrane traffic between ER, ERGIC and Golgi to generate compartments for the replication of viruses (3, 39, 40). In this study, we firstly confirmed that the

piscine ARF1 was recruited by NS80 and NS38 of GCRV into cytoplasmic VIBs *via* protein-protein interactions, and promoted GCRV replication and infection through facilitating the entry and proliferation processes of GCRV lifecycle.

Structure and sequence comparison showed that gcARF1 had high homology with lower eukaryotes (yeast), plants (Arabidopsis), mammals (mouse and human) and other species. GTP-binding domain contains three consensus elements GXXXXGK (S/T), DXXG and NKXD (41). The GXXXXGK (S/T) (where X is any residue) motif is known as a Walker A motif, which is also referred to as 'phosphate-binding loop' and thought to bind to the phosphate groups of GTP (42, 43). The NKXD (where X is any residue) motif can interact with the guanine ring (44). The GXXXXGK (S/T) and NKXD motifs are very conserved for ARF1 proteins from different species, with the same GLDAAGKT sequences for GXXXXGK (S/T) motif and NKQD for NKXD motif. Among eight amino acid residues (A^{27}, G^{29}, K^{30}, T^{31}, T^{32}, N^{126}, D^{129} and A^{160}) involved in the binding of GDP with gcARF1, six amino acid residues locate within the two motifs. Therefore similar to mammal homologues, gcARF1 may act as a molecular switch by switching between an active GTP-bound state and an inactive GDP-bound state and may have undergone conformational changes to change its affinity for substrates through its conserved structural motifs. Furthermore, since the ^{27}AAGKTT^{32} motif and T^{31} residue are essential for gcARF1 binding to GDP, the inhibition on the GCRV replication caused by the deletion of ^{27}AAGKTT^{32} motif of gcARF1 and the mutation of ARF1(T31N) suggest that the GTPase activity of gcARF1 is important for GCRV replication and infection. However, the deletion of ^{27}AAGKTT^{32} motif of gcARF1 and the mutation of ARF1(T31N) did not impair the interaction between gcARF1 and NS80/NS38 protein of GCRV. Based on these data, it is interesting to further resolve the crystal structure of gcARF1-NS80 or gcARF1-NS38 complex and compare the conformational differences between gcARF1 bound to viral protein and bound to GDP, which are helpful for revealing the molecular mechanism by which NS80 and NS38 proteins of GCRV recruit gcARF1 and promote the generation of VIBs.

The GTPase activity of ARF family is regulated by GEFs and GAPs, and lots of inhibitors targeting ARF, ARF-GEF complex, GEFs and GAPs have been reported (1). NAV-2729, which can bind to human ARF6 in the GEF binding region and thus inhibit the interaction of ARF6-GEF, has been used in the treatment of uveal melanoma (1, 45). The most commonly used inhibitor for ARF-GEF binding is BFA, a fungal macrolide that can be embedded in the hydrophobic groove at the binding interface between GEFs (Sec7) and ARF1, thereby inhibiting the GTP/GDP exchange of ARF1 (46). Although the replications of several viruses such as turnip mosaic virus (TuMV), coxsackievirus B3 (CVB3) and EMCV have been shown to be insensitive to BFA (47, 48), BFA treatment has been widely used to inhibit viral replication process in mammals. For example, the enteroviral protein 3A specifically triggers the recruitment of GBF1 to membranes to promote the replication of viral RNA; however BFA can block enterovirus replication by inhibiting the activity of GBF1 (47). For rotavirus, BFA could impair the yield of viral progeny *via* interfering with the synthesis of GBF1 and the virus assembly process (49, 50). During infectious bursal disease virus (IBDV) infection, interfering with GBF1 activity by BFA treatment leads to a dramatic change in the location of viral replication complexes, and significantly reduces the yield of infectious viral progeny (51). The present study revealed that inhibition of gcARF1 activity using BFA disrupted the generation of cytoplasmic VIBs in GCRV-infected cells, and alleviated the replication and infection of GCRV. Furthermore, the mechanisms controlling the GTPase activity of ARF1 may be very conserved, which are revealed by structure and sequence comparison of ARF1 proteins from grass carp and other species. It is interesting to further know whether many other inhibitors targeting ARF-GEF interaction such as AMF-26 can be used for prevention and treatment of grass carp hemorrhagic disease (52).

Several studies have indicated that ARF1 is critical for maintaining Golgi structure and function. The primary localization of mammalian ARF1 in cells is at the Golgi. During its GTP cycle, ARF1 reversibly associates with Golgi membranes, with the ARF1-GTP bound to the membrane and ARF1-GDP being cytosolic (53). Intriguingly, Golgi fragmentation and rearrangement have been observed during viral infections (54, 55). In response to the severe acute respiratory syndrome-associated coronavirus (SARS-CoV) infection, overexpression of ARF1 can restore Golgi morphology (56). Furthermore, many positive-sense RNA (+RNA) viruses form the replication complexes (RCs) for their replication, but ARF1 was hardly recruited to coronavirus RCs (57, 58). Similar to coronavirus mouse hepatitis virus (MHV), GCRV infection also caused Golgi fragmentation and rearrangement. However, gcARF1 was recruited into cytoplasmic VIBs by viral proteins, which was different from the previous report (57). Our results, together with those of others, reveal that ARF1 utilizes distinct means to target different endomembrane recruitment for conferring advantages for viral replication and infection.

In summary, here we demonstrate that gcARF1, which is recruited to cytoplasmic VIBs by NS80 and NS38 of GCRV, promotes GCRV replication and infection through facilitating the entry and proliferation processes of GCRV lifecycle. The AAGKTT motif and the amino acid residue T^{31} located in the small_GTP domain of gcARF1 are indispensable for the function of gcARF1 in viral replication and infection. Further investigations are needed to unravel whether other ARF proteins contribute to the biogenesis of functional VIBs and to GCRV infection.

Data availability statement

The datasets presented in this study can be found in online repositories. The names of the repository/repositories and accession number(s) can be found in the article/Supplementary Material.

Author contributions

JZ, PL, and MC designed the study. JZ performed most of the experiments. PL and RL performed some of the experiments. SO and MC provided reagents or assistance. JZ, PL, and MC analyzed the data and prepared the Figures. JZ, PL, and MC wrote the manuscript. All authors contributed to the article and approved the submitted version.

Funding

This work was supported by Strategic Priority Research Program of the Chinese Academy of Sciences Grant XDA24010308, the National Key Research and Development Program of China (Grant Nos. 2019YFD0900703 and 2021YFC2301403), the National Natural Science Foundation of China (Grant Nos. 82225028 and 82172287), and Fujian Science and Technology Department Project (Grant No. 2020Y4007).

Conflict of interest

The authors declare that the research was conducted in the absence of any commercial or financial relationships that could be construed as a potential conflict of interest.

Publisher's note

All claims expressed in this article are solely those of the authors and do not necessarily represent those of their affiliated organizations, or those of the publisher, the editors and the reviewers. Any product that may be evaluated in this article, or claim that may be made by its manufacturer, is not guaranteed or endorsed by the publisher.

Supplementary material

The Supplementary Material for this article can be found online at: https://www.frontiersin.org/articles/10.3389/fimmu.2022.956587/full#supplementary-material

References

1. Gray JL, von Delft F, Brennan PE. Targeting the small GTPase superfamily through their regulatory proteins. *Angew Chem Int Ed Engl* (2020) 59:6342–66. doi: 10.1002/anie.201900585

2. Kahn RA, Cherfils J, Elias M, Lovering RC, Munro S, Schurmann A. Nomenclature for the human arf family of GTP-binding proteins: ARF, ARL, and SAR proteins. *J Cell Biol* (2006) 172:645–50. doi: 10.1083/jcb.200512057

3. D'Souza-Schorey C, Chavrier P. ARF proteins: roles in membrane traffic and beyond. *Nat Rev Mol Cell Biol* (2006) 7:347–58. doi: 10.1038/nrm1910

4. Donaldson JG. Multiple roles for Arf6: sorting, structuring, and signaling at the plasma membrane. *J Biol Chem* (2003) 278:41573–6. doi: 10.1074/jbc.R300026200

5. Pavisic V, Mahmutefendic Lucin H, Blagojevic Zagorac G, Lucin P. Arf GTPases are required for the establishment of the pre-assembly compartment in the early phase of cytomegalovirus infection. *Life (Basel)* (2021) 11:867. doi: 10.3390/life11080867

6. Fisher S, Kuna D, Caspary T, Kahn RA, Sztul E. ARF family GTPases with links to cilia. *Am J Physiol Cell Physiol* (2020) 319:C404–18. doi: 10.1152/ajpcell.00188.2020

7. Bottanelli F, Kilian N, Ernst AM, Rivera-Molina F, Schroeder LK, Kromann EB, et al. A novel physiological role for ARF1 in the formation of bidirectional tubules from the golgi. *Mol Biol Cell* (2017) 28:1676–87. doi: 10.1091/mbc.E16-12-0863

8. Fuller J, Alvarez-Rodriguez B, Todd E, Mankouri J, Hewson R, Barr JN. Hazara nairovirus requires COPI components in both Arf1-dependent and Arf1-independent stages of its replication cycle. *J Virol* (2020) 94:e00766-20. doi: 10.1128/JVI.00766-20

9. Ding ZF, Ren J, Tan JM, Wang Z, Yin SW, Huang Y, et al. Characterization of two novel ADP ribosylation factors from giant freshwater prawn macrobrachium rosenbergii and their responses to WSSV challenge. *Dev Comp Immunol* (2015) 48:204–9. doi: 10.1016/j.dci.2014.10.006

10. Rangel AAC, Rockemann DD, Hetrick FM, Samal SK. Identification of grass carp haemorrhage virus as a new genogroup of aquareovirus. *J Gen Virol* (1999) 80 (Pt 9):2399–402. doi: 10.1099/0022-1317-80-9-2399

11. Attoui H, Fang Q, Jaafar FM, Cantaloube JF, Biagini P, de Micco P, et al. Common evolutionary origin of aquareoviruses and orthoreoviruses revealed by genome characterization of golden shiner reovirus, grass carp reovirus, striped bass reovirus and golden ide reovirus (genus aquareovirus, family reoviridae). *J Gen Virol* (2002) 83:1941–51. doi: 10.1099/0022-1317-83-8-1941

12. Rao Y, Su J. Insights into the antiviral immunity against grass carp (Ctenopharyngodon idella) reovirus (GCRV) in grass carp. *J Immunol Res* (2015) 2015:670437. doi: 10.1155/2015/670437

13. Shao L, Guo H, Yan LM, Liu H, Fang Q. Aquareovirus NS80 recruits viral proteins to its inclusions, and its c-terminal domain is the primary driving force for viral inclusion formation. *PloS One* (2013) 8:e55334. doi: 10.1371/journal.pone.0055334

14. Yan L, Zhang J, Guo H, Yan S, Chen Q, Zhang F, et al. Aquareovirus NS80 initiates efficient viral replication by retaining core proteins within replication-associated viral inclusion bodies. *PloS One* (2015) 10:e0126127. doi: 10.1371/journal.pone.0126127

15. Zhang J, Guo H, Chen Q, Zhang F, Fang Q. The n-terminal of aquareovirus NS80 is required for interacting with viral proteins and viral replication. *PloS One* (2016) 11:e0148550. doi: 10.1371/journal.pone.0148550

16. Zhang J, Guo H, Zhang F, Chen Q, Chang M, Fang Q. NS38 is required for aquareovirus replication *via* interaction with viral core proteins and host eIF3A. *Virology* (2019) 529:216–25. doi: 10.1016/j.virol.2019.01.029

17. Mossessova E, Corpina RA, Goldberg J. Crystal structure of ARF1*Sec7 complexed with brefeldin a and its implications for the guanine nucleotide exchange mechanism. *Mol Cell* (2003) 12:1403–11. doi: 10.1016/s1097-2765(03)00475-1

18. Adams PD, Afonine PV, Bunkoczi G, Chen VB, Davis IW, Echols N, et al. PHENIX: a comprehensive Python-based system for macromolecular structure

solution. *Acta Crystallogr D Biol Crystallogr* (2010) 66:213–21. doi: 10.1107/S0907444909052925

19. Emsley P, Lohkamp B, Scott WG, Cowtan K. Features and development of coot. *Acta Crystallogr D Biol Crystallogr* (2010) 66:486–501. doi: 10.1107/S0907444910007493

20. Fan C, Shao L, Fang Q. Characterization of the nonstructural protein NS80 of grass carp reovirus. *Arch Virol* (2010) 155:1755–63. doi: 10.1007/s00705-010-0753-6

21. Helms JB, Rothman JE. Inhibition by brefeldin a of a golgi membrane enzyme that catalyses exchange of guanine nucleotide bound to ARF. *Nature* (1992) 360:352–4. doi: 10.1038/360352a0

22. Hidalgo J, Garcia-Navarro R, Gracia-Navarro F, Perez-Vilar J, Velasco A. Presence of golgi remnant membranes in the cytoplasm of brefeldin a-treated cells. *Eur J Cell Biol* (1992) 58:214–27.

23. Niu TK, Pfeifer AC, Lippincott-Schwartz J, Jackson CL. Dynamics of GBF1, a brefeldin a-sensitive Arf1 exchange factor at the golgi. *Mol Biol Cell* (2005) 16:1213–22. doi: 10.1091/mbc.e04-07-0599

24. Viktorova EG, Nchoutmboube J, Ford-Siltz LA, Belov GA. Cell-specific establishment of poliovirus resistance to an inhibitor targeting a cellular protein. *J Virol* (2015) 89:4372–86. doi: 10.1128/JVI.00055-15

25. Yan S, Zhang J, Guo H, Yan L, Chen Q, Zhang F, et al. VP5 autocleavage is required for efficient infection by *in vitro*-recoated aquareovirus particles. *J Gen Virol* (2015) 96:1795–800. doi: 10.1099/vir.0.000116

26. Dascher C, Balch WE. Dominant inhibitory mutants of ARF1 block endoplasmic reticulum to golgi transport and trigger disassembly of the golgi apparatus. *J Biol Chem* (1994) 269:1437–48. doi: 10.1016/S0021-9258(17)42277-0

27. de Castro IF, Volonte L, Risco C. Virus factories: biogenesis and structural design. *Cell Microbiol* (2013) 15:24–34. doi: 10.1111/cmi.12029

28. Tenorio R, Fernandez de Castro I, Knowlton JJ, Zamora PF, Sutherland DM, Risco C, et al. Function, architecture, and biogenesis of reovirus replication neoorganelles. *Viruses* (2019) 11:288. doi: 10.3390/v11030288

29. Papa G, Borodavka A, Desselberger U. Viroplasms: Assembly and functions of rotavirus replication factories. *Viruses* (2021) 13:1349. doi: 10.3390/v13071349

30. Zhang J, Man Wu X, Fang Q, Bi YH, Nie P, Chang MX. Grass carp reovirus nonstructural proteins avoid host antiviral immune response by targeting the RLR signaling pathway. *J Immunol* (2022) 208:707–19. doi: 10.4049/jimmunol.2100723

31. Sun C, Querol-Audi J, Mortimer SA, Arias-Palomo E, Doudna JA, Nogales E, et al. Two RNA-binding motifs in eIF3 direct HCV IRES-dependent translation. *Nucleic Acids Res* (2013) 41:7512–21. doi: 10.1093/nar/gkt510

32. Ke F, He LB, Zhang QY. Nonstructural protein NS80 is crucial in recruiting viral components to form aquareoviral factories. *PloS One* (2013) 8:e63737. doi: 10.1371/journal.pone.0063737

33. Wen D, Yan L, Shao L, Guo H, Li X, Fang Q. Aquareovirus protein VP6 colocalizes with NS80 protein in infected and transfected cells. *Virol J* (2013) 10:133. doi: 10.1186/1743-422X-10-133

34. Haynes LP, Thomas GM, Burgoyne RD. Interaction of neuronal calcium sensor-1 and ADP-ribosylation factor 1 allows bidirectional control of phosphatidylinositol 4-kinase beta and trans-golgi network-plasma membrane traffic. *J Biol Chem* (2005) 280:6047–54. doi: 10.1074/jbc.M413090200

35. Ben-Tekaya H, Kahn RA, Hauri HP. ADP ribosylation factors 1 and 4 and group *VIA* phospholipase A(2) regulate morphology and intraorganellar traffic in the endoplasmic reticulum-golgi intermediate compartment. *Mol Biol Cell* (2010) 21:4130–40. doi: 10.1091/mbc.E10-01-0022

36. Zhang L, Hong Z, Lin W, Shao RX, Goto K, Hsu VW, et al. ARF1 and GBF1 generate a PI4P-enriched environment supportive of hepatitis c virus replication. *PloS One* (2012) 7:e32135. doi: 10.1371/journal.pone.0032135

37. Hyodo K, Mine A, Taniguchi T, Kaido M, Mise K, Taniguchi H, et al. ADP ribosylation factor 1 plays an essential role in the replication of a plant RNA virus. *J Virol* (2013) 87:163–76. doi: 10.1128/JVI.02383-12

38. Wang J, Du J, Jin Q. Class I ADP-ribosylation factors are involved in enterovirus 71 replication. *PloS One* (2014) 9:e99768. doi: 10.1371/journal.pone.0099768

39. Moghimi S, Viktorova E, Zimina A, Szul T, Sztul E, Belov GA. Enterovirus infection induces massive recruitment of all isoforms of small cellular arf GTPases to the replication organelles. *J Virol* (2020) 95:e01629-20. doi: 10.1128/JVI.01629-20

40. Pierini R, Cottam E, Roberts R, Wileman T. Modulation of membrane traffic between endoplasmic reticulum, ERGIC and golgi to generate compartments for the replication of bacteria and viruses. *Semin Cell Dev Biol* (2009) 20:828–33. doi: 10.1016/j.semcdb.2009.03.015

41. Dever TE, Glynias MJ, Merrick WC. GTP-binding domain: three consensus sequence elements with distinct spacing. *Proc Natl Acad Sci U.S.A.* (1987) 84:1814–8. doi: 10.1073/pnas.84.7.1814

42. Greasley SE, Jhoti H, Teahan C, Solari R, Fensome A, Thomas GM, et al. The structure of rat ADP-ribosylation factor-1 (ARF-1) complexed to GDP determined from two different crystal forms. *Nat Struct Biol* (1995) 2:797–806. doi: 10.1038/nsb0995-797

43. Angelis D, Karasmanis EP, Bai X, Spiliotis ET. *In silico* docking of forchlorfenuron (FCF) to septins suggests that FCF interferes with GTP binding. *PloS One* (2014) 9:e96390. doi: 10.1371/journal.pone.0096390

44. Lee CM, Haun RS, Tsai SC, Moss J, Vaughan M. Characterization of the human gene encoding ADP-ribosylation factor 1, a guanine nucleotide-binding activator of cholera toxin. *J Biol Chem* (1992) 267:9028–34.

45. Yamauchi Y, Miura Y, Kanaho Y. Machineries regulating the activity of the small GTPase Arf6 in cancer cells are potential targets for developing innovative anti-cancer drugs. *Adv Biol Regul* (2017) 63:115–21. doi: 10.1016/j.jbior.2016.10.004

46. Renault L, Guibert B, Cherfils J. Structural snapshots of the mechanism and inhibition of a guanine nucleotide exchange factor. *Nature* (2003) 426:525–30. doi: 10.1038/nature02197

47. Lanke KH, van der Schaar HM, Belov GA, Feng Q, Duijsings D, Jackson CL, et al. GBF1, a guanine nucleotide exchange factor for arf, is crucial for coxsackievirus B3 RNA replication. *J Virol* (2009) 83:11940–9. doi: 10.1128/JVI.01244-09

48. Grangeon R, Agbeci M, Chen J, Grondin G, Zheng H, Laliberte JF. Impact on the endoplasmic reticulum and golgi apparatus of turnip mosaic virus infection. *J Virol* (2012) 86:9255–65. doi: 10.1128/JVI.01146-12

49. Mirazimi A, von Bonsdorff CH, Svensson L. Effect of brefeldin a on rotavirus assembly and oligosaccharide processing. *Virology* (1996) 217:554–63. doi: 10.1006/viro.1996.0150

50. Martinez JL, Arnoldi F, Schraner EM, Eichwald C, Silva-Ayala D, Lee E, et al. The guanine nucleotide exchange factor GBF1 participates in rotavirus replication. *J Virol* (2019) 93:e01062-19. doi: 10.1128/JVI.01062-19

51. Gimenez MC, Frontini-Lopez YR, Pocognoni CA, Roldan JS, Garcia Samartino C, Uhart M, et al. Rab1b-GBF1-ARF1 secretory pathway axis is required for birnavirus replication. *J Virol* (2022) 96:e0200521. doi: 10.1128/JVI.02005-21

52. Ohashi Y, Iijima H, Yamaotsu N, Yamazaki K, Sato S, Okamura M, et al. AMF-26, a novel inhibitor of the golgi system, targeting ADP-ribosylation factor 1 (Arf1) with potential for cancer therapy. *J Biol Chem* (2012) 287:3885–97. doi: 10.1074/jbc.M111.316125

53. Donaldson JG, Honda A. Localization and function of arf family GTPases. *Biochem Soc Trans* (2005) 33:639–42. doi: 10.1042/BST0330639

54. Lavi E, Wang Q, Stieber A, Chen Y, Weiss S, Gonatas NK. Fragmentation and rearrangement of the golgi apparatus during MHV infection of l-2 cells. *Adv Exp Med Biol* (1995) 380:103–4. doi: 10.1007/978-1-4615-1899-0_15

55. Lavi E, Wang Q, Weiss SR, Gonatas NK. Syncytia formation induced by coronavirus infection is associated with fragmentation and rearrangement of the golgi apparatus. *Virology* (1996) 221:325–34. doi: 10.1006/viro.1996.0382

56. Freundt EC, Yu L, Goldsmith CS, Welsh S, Cheng A, Yount B, et al. The open reading frame 3a protein of severe acute respiratory syndrome-associated coronavirus promotes membrane rearrangement and cell death. *J Virol* (2010) 84:1097–109. doi: 10.1128/JVI.01662-09

57. Verheije MH, Raaben M, Mari M, Te Lintelo EG, Reggiori F, van Kuppeveld FJ, et al. Mouse hepatitis coronavirus RNA replication depends on GBF1-mediated ARF1 activation. *PloS Pathog* (2008) 4:e1000088. doi: 10.1371/journal.ppat.1000088

58. den Boon JA, Diaz A, Ahlquist P. Cytoplasmic viral replication complexes. *Cell Host Microbe* (2010) 8:77–85. doi: 10.1016/j.chom.2010.06.010

frontiers | Frontiers in Immunology

TYPE Original Research
PUBLISHED 29 September 2022
DOI 10.3389/fimmu.2022.1012594

OPEN ACCESS

EDITED BY
Jason C. O'Connor,
The University of Texas Health Science Center at San Antonio, United States

REVIEWED BY
Juli Bai,
The University of Texas Health Science Center at San Antonio, United States
Lisa Suzanne Robison,
Nova Southeastern University, United States

*CORRESPONDENCE
Eva L. Feldman
efeldman@umich.edu

SPECIALTY SECTION
This article was submitted to Inflammation, a section of the journal Frontiers in Immunology

RECEIVED 05 August 2022
ACCEPTED 16 September 2022
PUBLISHED 29 September 2022

CITATION
Elzinga SE, Henn R, Murdock BJ, Kim B, Hayes JM, Mendelson F, Webber-Davis I, Teener S, Pacut C, Lentz SI and Feldman EL (2022) cGAS/STING and innate brain inflammation following acute high-fat feeding. *Front. Immunol.* 13:1012594. doi: 10.3389/fimmu.2022.1012594

cGAS/STING and innate brain inflammation following acute high-fat feeding

Sarah E. Elzinga[1,2], Rosemary Henn[1,2], Benjamin J. Murdock[1,2], Bhumsoo Kim[1,2], John M. Hayes[1,2], Faye Mendelson[1,2], Ian Webber-Davis[1,2], Sam Teener[1,2], Crystal Pacut[1,2], Stephen I. Lentz[3] and Eva L. Feldman[1,2]*

[1]Department of Neurology, University of Michigan, Ann Arbor, MI, United States, [2]NeuroNetwork for Emerging Therapies, University of Michigan, Ann Arbor, MI, United States, [3]Department of Internal Medicine, Division of Metabolism, Endocrinology and Diabetes, University of Michigan, Ann Arbor, MI, United States

Obesity, prediabetes, and diabetes are growing in prevalence worldwide. These metabolic disorders are associated with neurodegenerative diseases, particularly Alzheimer's disease and Alzheimer's disease related dementias. Innate inflammatory signaling plays a critical role in this association, potentially *via* the early activation of the cGAS/STING pathway. To determine acute systemic metabolic and inflammatory responses and corresponding changes in the brain, we used a high fat diet fed obese mouse model of prediabetes and cognitive impairment. We observed acute systemic changes in metabolic and inflammatory responses, with impaired glucose tolerance, insulin resistance, and alterations in peripheral immune cell populations. Central inflammatory changes included microglial activation in a pro-inflammatory environment with cGAS/STING activation. Blocking gap junctions in neuron-microglial co-cultures significantly decreased cGAS/STING activation. Collectively these studies suggest a role for early activation of the innate immune system both peripherally and centrally with potential inflammatory crosstalk between neurons and glia.

KEYWORDS

cGAS/STING, acute, innate inflammation, microglia, high fat diet

Introduction

Global incidences of obesity, prediabetes, and diabetes are increasing worldwide (1, 2). Obesity rates have burgeoned in recent years, growing to pandemic proportions (3). Global diabetes rates topped 463 million in 2019, with an estimated additional 374 million people having impaired glucose tolerance and prediabetes (1). This alarming rise in the rates of obesity and metabolic disease predispose individuals to complications of

the central nervous system (CNS), including mild cognitive impairment, Alzheimer's disease or Alzheimer's disease related dementias (AD/ADRD) (4–6).

Chronic inflammation and immune system dysregulation are common in individuals with obesity and in individuals who fall along the continuum of metabolic dysfunction from prediabetes to frank type 2 diabetes (7). Previous studies investigating the effects of metabolic dysfunction on the CNS report dysregulation of immune and inflammatory mechanisms, typically increased glial activation and elevated production of CNS pro-inflammatory proteins and mediators (8–10). Specifically, a high-fat diet (HFD) in mice induces an inflammatory phenotype in microglia, the resident immune cells of the CNS (11, 12). Additionally, HFD or other CNS pro-inflammatory events increase trafficking of peripheral immune cells into the brain (13–15), further promoting neuroinflammation.

Although evidence supports a role for CNS inflammation in obesity, prediabetes, and diabetes, previous studies primarily focus on later disease time points, and few have investigated how HFD-induced obesity and prediabetes impact short-term inflammatory changes. Innate inflammatory pathways with an acute response to damage or danger signals may potentially respond to metabolic stress to mediate early CNS responses to HFD. In a dysmetabolic environment, elevated fatty acids can activate innate inflammatory mechanisms and upregulate pro-inflammatory cytokine production (16, 17). This in turn up-regulates downstream feed-forward mechanisms, such as signaling through the interferon-α receptor (18), which further contributes to a pro-inflammatory environment.

One innate inflammatory pathway implicated in the cellular response to metabolic dysfunction is the cGAS/STING (cyclic GMP-AMP/stimulator of interferon genes) pathway (19–21). cGAS/STING is a cytosolic double-stranded DNA (dsDNA) sensing pathway, which responds to viral or bacterial dsDNA as well as self dsDNA, *e.g.*, from damaged nuclei or mitochondria *via* cGAS and working through its adaptor molecule STING and transcription factors interferon regulatory factor 3 (IRF3) and nuclear factor kappa beta (NFkB) to upregulate pro-inflammatory gene expression. In the periphery or peripheral cells, HFD or treatment with the saturated fatty acid palmitate upregulates cGAS/STING signaling (22). cGAS/STING also contributes to pro-inflammatory feed forward mechanisms *via* inflammatory crosstalk between neighboring cells *via* gap junctions (23). Further, cGAS/STING is implicated in the pathology of CNS neurodegenerative diseases, such as AD/ADRD (24–26), Parkinson's disease (27), and amyotrophic lateral sclerosis (28), and may thus constitute a "bridge" between metabolic dysfunction and cognitive impairment.

In the current study, we examined CNS activation of the cGAS/STING pathway in mice fed a high fat diet (HFD) for 3 d. We focused our studies on the primary immune cells of the brain, microglia, capable of inflammatory crosstalk with neurons *via* gap junctions (23). We leveraged our HFD mouse model, which develops obesity and prediabetes along with cognitive impairment upon acute and chronic feeding (29). We observed systemic changes in metabolic and inflammatory responses, with impaired glucose tolerance, insulin resistance, and alterations in peripheral immune cell populations after just 3 d of HFD. We also identified central inflammatory changes, with microglial and cGAS/STING pathway activation. Additionally, in our neuron-microglial co-culture system, reducing cell to cell inflammatory crosstalk by blocking gap junctions significantly reduced cGAS/STING activation. These findings support an early role for cGAS/STING in response to HFD *via* neuron-glial inflammatory crosstalk and suggest a pivotal role for acute activation of innate immune mechanisms in the CNS in response to global metabolic dysfunction.

Materials and methods

Experimental animals and study design

Four-wk-old C57BL/6J male mice obtained from The Jackson Laboratory (catalog # 000664; Bar Harbor, ME). Animals were housed with no more than five littermates per cage in a pathogen free room at 20 ± 2 °C with a 12 h light/dark cycle at the University of Michigan Unit for Laboratory Animal Medicine and monitored daily by veterinary staff. Animals were provided food and water *ad libitum* and a minimum of one enrichment item (nestlet and/or enviropak). Following a 1 or 2 wk acclimation period, animals were assigned randomly to their respective diets (Research Diets, New Brunswick, NJ) as follows: standard diet (SD; 10% calories from fat; catalog # D12450J) or high-fat diet (HFD; 60% calories from fat; catalog # D12492). A subset of animals were used for cognitive phenotyping (see puzzle box), which was performed on day 2 of diet and for a duration of 3d. Animals were sacrificed (detailed below) on the final day of puzzle box (4 d on diet). For all other animals, after 3 d on diet mice underwent glucose tolerance testing (see metabolic phenotyping) and were sacrificed (detailed below) the next day (4 d on diet). Four hours prior to euthanasia, animals were fasted and a subset of animals within both the SD and HFD groups were given intraperitoneal injection of either saline (5 mL/kg body weight [BW]) or lipopolysaccharide (LPS; catalog # tlrl-3pelps, Invivogen, San Diego, CA) at a dose of 500 μg LPS/kg BW in total volume of 5 mL/kg BW saline. At terminal, animals were euthanized *via* intraperitoneal injection of 150 mg/kg pentobarbital (Fatal-Plus, Vortech Pharmaceuticals, Dearborn, MI). Blood was removed from the vena cava and animals were perfused with phosphate buffered saline prior to removal of tissues. Cortex tissue was used to determine *ex vivo* CNS insulin sensitivity using western blotting, plasma and hemi-brains for immunophenotyping using flow cytometry, plasma for inflammatory cytokines using ELISA, hemi-brains for microglial morphology using

immunohistochemistry, and hippocampal tissue for cGAS/STING pathway protein expression using Western blotting (all methods detailed below). The University of Michigan's Institutional Animal Care and Use Committee approved all animal protocols (PRO0010039).

Metabolic phenotyping and immunophenotyping

Glucose tolerance testing (GTT) was performed after 3 d of diet as previously (30, 31). Briefly, 10% D-glucose at 1g glucose/1kg body weight was injected intraperitoneally after a 4 h fast and glucose measurements taken at baseline and 15-, 30-, 60-, and 120-min post injection. Blood glucose levels were determined from a tail blood sample using a glucometer (AlphaTRAK, Abbot Laboratories, Chicago, IL) and appropriate glucose strips (Zoetis, Parsippany, NJ).

After 4 d HFD feeding, immunophenotyping was performed on peripheral blood samples and on CNS tissue using flow cytometry (32) to determine circulating immune cell populations, as previously published (32, 33). Fluorescently labeled leukocytes were classified by staining with antibodies (Biolegend, San Diego, CA) for well-characterized surface markers (Table 1). Briefly, doublets were excluded using forward scatter width (FSC-W) and forward scatter height (FSC-H) where events farther than 10% from the diagonal were excluded. In both tissue types, lymphocytes were characterized as CD45+, SSC-low cells expressing CD3 and either CD4+ or CD8+, while NK cells were characterized as CD45+, SSC-low, CD3–, NK1.1+, and CD49b+. B cells in the periphery were characterized as CD45+, SSC-low, CD3-, and CD19+ and were not detectible in the CNS. Myeloid populations in the blood were characterized as CD45+ and CD11b+: neutrophils were Ly6G+ while monocytes were Ly6G– and either Ly6C– or Ly6C+. In the CNS, myeloid cells were CD45+, CD3–, CD19. Ly6G+ cells were identified as neutrophils, Ly6G-, CD11b+, CD45-high, and Ly6C+ were identified as Ly6C+ monocytes, and Ly6G-, CD11b+, CD45-mid cells were identified as microglia. In both tissue types, monocytes, microglia, and neutrophils were further assessed for F4/80 or CD11c surface expression by their median fluorescent intensity as a proxy for activation state. A FACSAria II (BD Biosciences, San Jose, CA) was used to run samples and FlowJo software (FlowJo, Ashland, OR) to analyze results.

Microglial morphology

As previously (34), we performed analysis of microglial morphology for three regions of the hippocampus, the hilus, molecular layer, and CA1 regions. In brief, hemi-brains were dissected and fixed for 48 h in 4% paraformaldehyde. Following a sucrose gradient (10%, 20%, and 30% for 24 h each), hemi-brains were embedded in OCT and frozen at -80°C. Brains were sectioned (50 μm) and stained (rabbit anti-Iba1, 1:1000; catalog # 019-19741, Wako, Richmond, VA) in 6-well plates in floating tissue sections. Secondary antibody (anti-rabbit Alexa-fluor Plus 594, 1:2000; catalog # A32740, Invitrogen) and Hoechst nuclear stain were applied, and sections were mounted using ProLong Gold (Invitrogen). A Leica Stellaris 8 Falcon Confocal Microscope and a 40X oil immersion objective was used to take Z-stack images (30 μm). Images were processed with Imaris Software (Oxford Instruments) and open microscopy environment TIF files used to analyze microglial territorial volume, cell volume, percent occupied volume, average branch length, maximum branch length, minimum branch length, number of end points, and number of end points using a modified 3DMorph script in MATLAB (MathWorks, Natick, MA), as previously published (34).

TABLE 1 Flow cytometry antibodies for blood and CNS immune cell characterization.

	BV421	FITC	PE	PerCP-5.5	APC	PE-Cy7	APC-Cy7
Lymphoid (Blood and CNS)	CD8	CD3	Nk1.1	CD19	CD45	CD49b	CD4
CD4 T-cells	+	+	–	–	+	–	+
CD8 T-cells	+	+	–	–	+	–	–
NK cells	–	–	+	–	+	+	–
B cells (CNS; not detectible)	–	–	–	+	+	–	–
Myeloid (Blood)	Cd11c	Ly6c	F4/80	CD3/CD19	CD45	Ly6G	CD11b
Neutrophils	MFI	–	MFI	–	+	+	+
Ly6C- Monocytes	MFI	–	MFI	–	+	–	+
Ly6C+ Monocytes	MFI	+	MFI	–	+	–	+
Myeloid (CNS)							
Neutrophils	MFI	–	MFI	–	+	+	+
Ly6C+ Monocytes	MFI	+	MFI	–	+	–	+
Microglia	MFI	–	MFI	–	+/-	–	+

+/- (with/without).

Ex vivo insulin stimulation

On day 4 of diet after sacrifice and perfusion, right cortex was dissected and placed in a 12-well plate containing media (Neruobasal, 5% pen-strep, MN additives (Sigma, St Louis, MO); 10 mg/mL bovine serum albumin, 10 mg/mL apo-transferrin, 0.1 mg/mL biotin, 15 mg/mL D-galactose, 0.63 mg/mL progesterone, 16 mg/mL putrescine, 50 µg/mL selenium, 50 µg/mL β-estradiol, 50 µg/mL hydrocortisone, 16 mg/mL catalase, 2.5 mg/mL SOD). Tissue was finely minced with scissors and split into two microcentrifuge tubes (one for unstimulated control and one for insulin) containing 300 µL media. Tubes were placed into an incubator (37°C, 5% CO_2) for 30 min. Following the 30 min incubation, insulin (20 nM) or an equivalent volume of media was added to the appropriate tubes. Tubes were returned to the incubator for 45 min and inverted several times every 10-15 min. Following the 45 min incubation, tubes were spun down (1 min, 4°C, 17,000 g), media removed, and tissue snap frozen in liquid N_2. Tissue was maintained at -80°C for later Western blot (WB) analysis.

ELISA and WB

On day 4 of diet, blood was collected, and plasma isolated for inflammatory cytokine analysis *via* ELISA. ELISA was performed for TNF-α and MCP-1 by the University of Michigan Rogel Cancer Center Immunology Core. Cortex and hippocampal tissue as well as neuronal and microglia cells were homogenized in RIPA buffer (Pierce, Rockford, IL) with protease inhibitors (Roche Diagnostics, Indianapolis, IN), sonicated, and centrifuged (30 min, 4°C, 13,300 rpm) in preparation for WB, which was performed as previously published (35, 36). All samples were normalized for equal protein concentration prior to loading. Nitrocellulose membranes were blocked (Tris buffered saline [TBS], 0.01% Tween-20, 5% bovine serum albumin [BSA]) for 2 h, primary antibodies (varying concentrations in TBS, 0.01% Tween-20, 5% BSA) were incubated overnight at 4°C, and secondary antibodies (varying concentrations in TBS, 0.01% Tween-20, 5% milk) were incubated for 1.5 h at room temperature. SuperSignal West Femto Maximum Sensitivity Substrate (Pierce, Rockford, IL) or Clarity Max (Biorad, Hercules, CA) was used to visualize signal and images were captured by a ChemiDoc (Biorad) or with x-ray film. Images were analyzed using ImageJ (37) or Image Lab software (Biorad). Insulin signaling primary antibodies were: pAkt (catalog # 4060), Akt (catalog # 4691), pIRS-1 (pSer307, catalog # 2381; pSer636/639, catalog # 2388), IRS-1 (catalog # 3407), all from Cell Signaling Technologies (Danvers, MA) and diluted at 1:1000. cGAS/STING pathway primary antibodies (Cell Signaling Technologies) were: cGAS (catalog # 31659S; 1:1000), STING (catalog # 50494S; 1:1000), pIRF3 (S396; catalog # 4947S; 1:500), total IRF3 (catalog # 4302S; 1:500), and NFκβ (catalog # 8242P; 1:500). Tubulin (catalog # ab6160; 1:20000; AbCam, Cambridge, MA) or histone (catalog # NB 100-56347; Novus Biologicals, Littleton, CO) were used as loading controls. IgG conjugated with horse radish peroxidase secondary antibodies used were anti-rabbit (catalog # 7074), anti-mouse, (catalog # 7076), and anti-rat (catalog # 7077S) all Cell Signaling Technologies.

Cell culture

Partially immortalized human hippocampal neurons (38) and an immortalized human microglia cell line (catalog # T0252; Applied Biological Materials, Richmond, BC, Canada) were used for *in vitro* studies. Cells were maintained in growth media in 6-well plates until 80-85% confluent. Neuron growth media was: N2b medium (customized media from Cytivia, Marlborough, MA) with 0.2 µM beta-estradiol (catalog # E4389; Sigma) and 10 µg/mL fibroblast growth factor basic (catalog # GF003AF; Millipore, Burlington, MA) and 1% heat-inactivated fetal bovine serum (FBS; catalog # MT35016CV; Corning, Corning, NY). Microglia growth media was: PriGroIII (catalog # TM003; Applied Biological Materials, Richmond, BC, Canada) and 10% non-heat inactivated FBS or DMEM (catalog # BW12741F; Lonza, Quakertown, PA) and 10% heat inactivated FBS for cytosolic dsDNA qPCR experiments. At 60-80% confluence, neurons were changed to differentiation media (NSDM, custom media, Cytiva, Global Life Sciences Solutions, Marlborough, MA for 8 d (39)). On differentiation day 9 for neurons and at 80-85% confluence for microglia, media was changed to treatment media (differentiation media without insulin for neurons and growth media without FBS for microglia) 5 h prior to experimental treatments. Following this, cells were treated with either palmitate alone (62.5 µM in microglia or 250 µM in neurons) or palmitate plus insulin (50 nM, both cell types) for 24 h (35, 40). At 24 h, cultures were washed, and cells were fixed for cytosolic dsDNA determination *via* immunocytochemistry or qPCR (below) or isolated for cGAS/STING pathway protein determination by WB (above).

Cytosolic dsDNA *via* qPCR

Cytosolic DNA isolation was performed as previously published (41). In brief, cells were lysed with RIPA buffer (Invitrogen, Waltham, MA), centrifuged (10 min, 4°C, 700*g*), and supernatant used to quantify and normalize protein concentrations. The pelleted nuclei/whole cell fraction was saved for downstream analysis. Normalized protein concentrations of the supernatant were spun further (30 min, 4°C, 10,000*g*) and the pellet (cytosolic fraction) saved. The pelleted nuclei/whole cell fractions and the pelleted cytosolic fractions were used to isolate DNA using a commercially

available kit (catalog # 80004, All prep DNA, RNA, and Protein mini kit; Qiagen, Germantown, MD). Nuclear (18S; 5'-TAG AGG GAC AAG TGG CGT TC-3' [forward] and 5'-CGC TGA GCC AGT CAG TGT-3' [reverse]) and mitochondrial DNA (cytochrome oxidase I; 5'- GCC CCC GAT ATG GCG TTT-3' [forward] and 5'- GTT CAA CCT GTT CCT GCT CC -3' [reverse]) were run on the nuclei/whole cell fractions and pelleted cytosolic fractions using qPCR SYBR green primers (above). Levels of cytosolic DNA were quantified using the ddC_T method (42), with the nuclei fraction used to normalize the cytosolic fraction and the mean ΔC_T of the BSA controls as the calibrator for all samples.

Puzzle box

To assess possible changes in cognition, we performed a modified version of the puzzle box task (43). In this task, mice are intrinsically motivated to move from the light area of the puzzle box into the dark area. On day 2 of diet, puzzle box testing was carried out over a period of 3 d, with a series of three single tasks repeated for a total of three replicates over the first 2 d. The single tasks were then combined into a 'complex' task, which was performed once on day 2 and 24 h later on day 3. Latency to 'escape' or to enter the dark area of the box was recorded for each of the tasks. Animals were allowed 5 min to perform each task. If the mouse was unable to escape the light area of the box after 5 min, it was removed from the box and its time recorded as 5 min.

Statistical analysis

We previously established that a sample size of n=8 per group (30, 44) provides adequate power to detect significant metabolic differences between groups. Statistical analyses were performed using Prism 9 (GraphPad Software, La Jolla, CA) using either t-test or one-way analysis of variance (ANOVA) followed by Tukey's multiple comparisons. Alternatively, analysis of microglial morphology and CNS immunophenotyping data was performed using SAS 9.4 (SAS Institute, Cary, NC) using the Proc Mixed function. Anderson-Darling, D'Agostino-Pearson omnibus, Shapiro-Wilk, and Kolmogorov-Smirnov tests were used to determine normality, and non-normal data was log transformed to achieve normality. Statistical tests and software used for each analysis (glucose tolerance test, immunophenotyping, etc.) and the corresponding results section/figure are detailed in Supplemental Table 1. Statistical significance was defined as $p<0.05$ and trends as $p<0.10$. Unless otherwise indicated, results are presented as mean ± standard error of the mean (SEM).

Results

Acute HFD impairs metabolic but not cognitive responses

We previously showed that chronic HFD induces obesity and prediabetes (29), however little is known about the acute metabolic, inflammatory, and cognitive effects of HFD. Therefore, we examined the impact of acute HFD on both metabolic and cognitive function. To do so, BL6 mice were placed on either a HFD or a sucrose matched 10% fat standard diet (SD) for 4 d. GTT was performed on 3 d and mice were harvested for blood and tissue analysis on 4 d (Figure 1A). Within just 3 d, we observed HFD impaired glucose tolerance, with higher blood glucose levels at all time points of the glucose tolerance test, as well as a higher area under the curve versus SD mice (Figures 1B, C). We and others also previously observed CNS insulin resistance in mice following chronic HFD feeding (29, 45). However, changes in response to acute HFD were unknown. To investigate this, we measured the responsiveness of *ex vivo* brain tissue to insulin by assessing phosphorylation of critical insulin signaling proteins (46, 47). After 3 d of HFD feeding, we observed changes in cortex insulin sensitivity, with decreased phosphorylated protein kinase B (pAkt)/total Akt (Figure 1D; Supplemental Figure S1A) and decreased insulin receptor substrate 1 (IRS1) phosphorylation [pIRS-1(S307)]/total IRS-1 in response to insulin stimulation (Figure 1E; Supplemental Figure S1B).

In addition to metabolic shifts, we and others have shown that chronic HFD also induces cognitive impairment (29, 48, 49), although cognitive changes in response to acute HFD were less clear. Here we performed puzzle box testing, a behavioral task which primarily tests executive function, to assess possible changes in cognition after 3 d on diet. However, we did not detect any differences in behavior between HFD and SD mice (Supplemental Figure S2). Overall, 3 d of HFD induces systemic and central metabolic changes related to glucose tolerance and insulin sensitivity, without a detectable impact on cognition within this timeframe.

Acute HFD alters peripheral and central immune cell populations

We and others have previously reported that chronic HFD also induces changes in circulating inflammatory profiles (33, 48). Using ELISA to examine inflammatory cytokine concentrations and flow cytometry to examine circulating and CNS immune cell populations, we observed changes to plasma inflammatory profiles after 4 d of HFD similar to those seen in long-term HFD feeding (Supplemental Figure S3). Specifically,

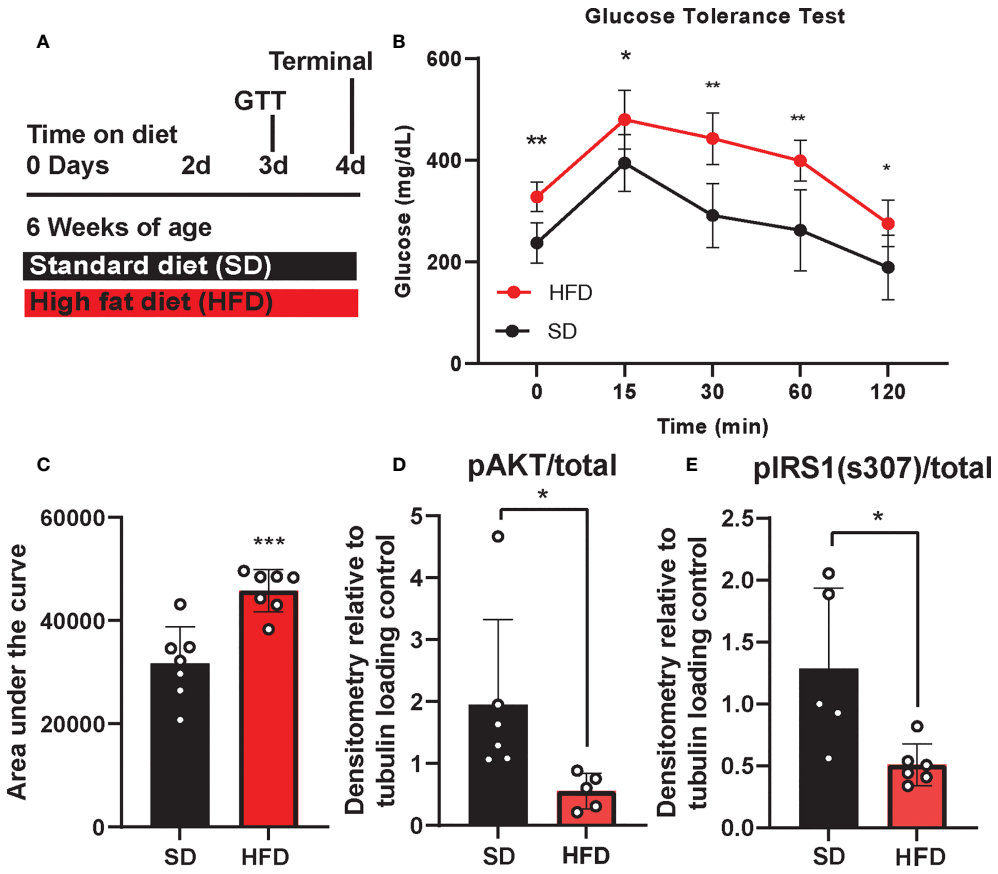

FIGURE 1
Experimental timeline and metabolic phenotyping. Experimental timeline **(A)**, glucose tolerance test, (GTT; **B**), area under the curve **(C)**, and cortex response to insulin stimulation **(D, E)** in male BL/6 mice fed standard diet (SD) or high fat diet (HFD). Protein expression normalized to tubulin and relative to unstimulated control; *p<0.05, **p<0.01, ***p<0.001.

HFD mice had a trending increase in the number of CD4 T-cells (Supplemental Figure S3C), and a significant increase in B-cells (number and % of leukocytes; Supplemental Figures S3F, G) versus SD animals. HFD mice also had a trend for lower Ly6C+ monocytes compared to SD mice (Supplemental Figure S3J). There was no difference due to diet in any of the other measured immune cell populations including CD8 T cells, natural killer cells, Ly6C+ monocytes, Ly6C- monocytes, or neutrophils (Supplemental Figures S3A, B, D, E, G-I, K-S). We also measured plasma inflammatory cytokine levels in HFD and SD mice after injection with either saline or lipopolysaccharide (LPS). LPS robustly increased circulating TNF-α and MCP-1 concentrations (Supplemental Figure S4); there was no effect of diet.

To understand CNS specific changes in immune cell populations, we repeated our experiment in a separate cohort of HFD versus SD mice, both in control treated (saline injection) and in response to immune challenge (LPS injection). When lymphoid populations in the CNS were examined, HFD increased leukocytes (Supplemental Figures S5A, B) and decreased CD8 T-cells (% of leukocytes; Supplemental Figure S5D) versus SD animals and LPS injection had no effect (Supplemental Figure S5). CD4 T-cell levels were low/not detectable and HFD did not impact the numbers or percentages of CNS natural killer cells (Supplemental Figures S5C, E-H). In CNS myeloid cell populations (Figure 2 and Supplemental Figure 6), total immune cell levels and surface marker expression were impacted by 4 d HFD. Neutrophil, microglia, and Ly6C+ monocyte levels were examined as well as expression of CD11c and F4/80, markers of activation and differentiation. HFD mice had more neutrophils (numbers and %; Figures 2A, B) and a greater number of microglia, which also had a trending increase in size as measured by a larger forward side scatter (Figures 2C, I) suggesting activation. There were no differences due to LPS treatment or due to diet for neutrophil or microglial F4/80 or CD11c expression, or for the percentage of microglia (Figures 2C, D, F-H). LPS administration did

10.3389/fimmu.2022.1012594

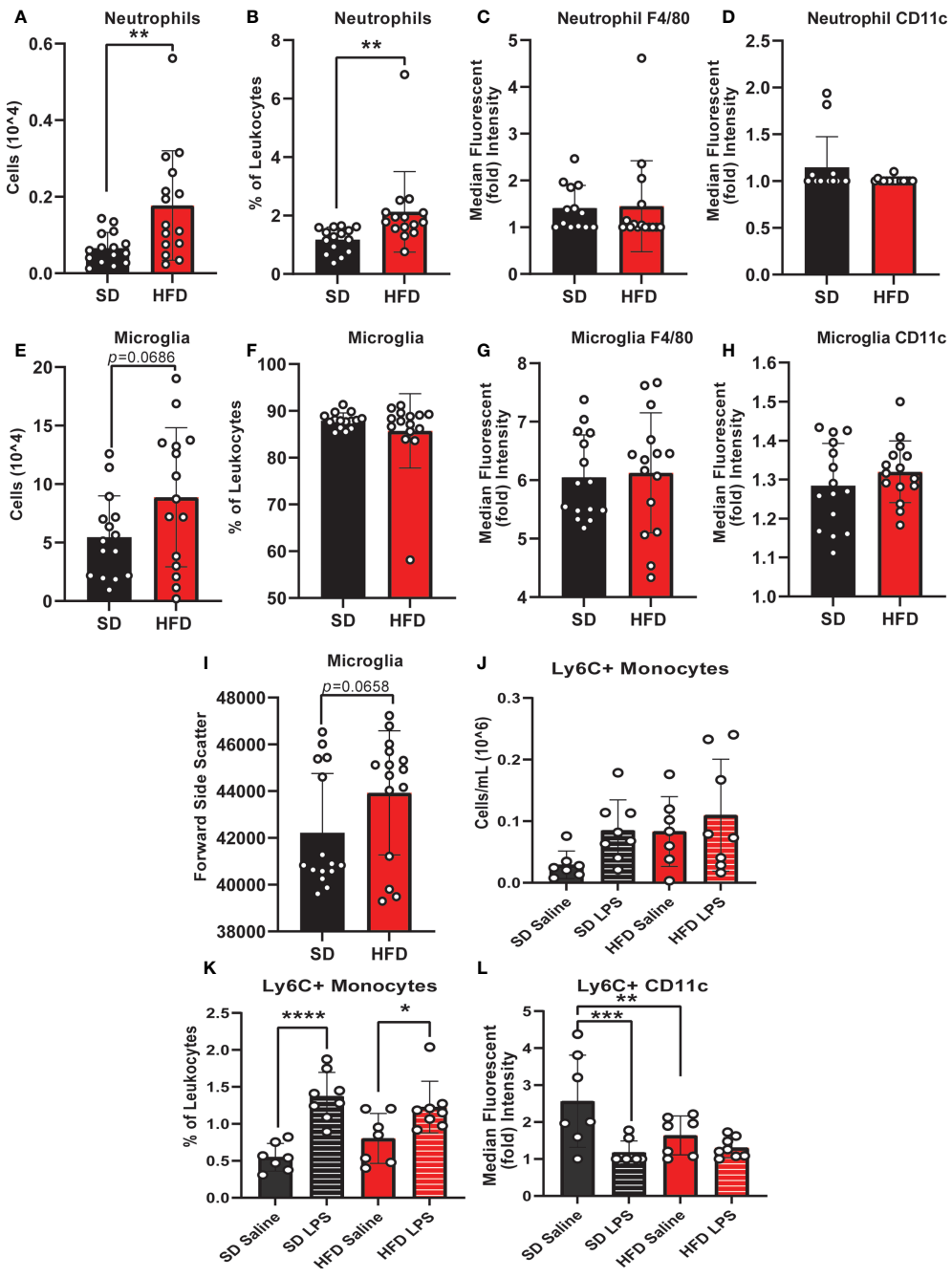

FIGURE 2
CNS immunophenotyping of myeloid cells by flow cytometry. Data represented as neutrophils (number of cells, % of cells, F4/80 expression, and CD11c expression; **A-D**), microglia (number of cells, % of cells, F4/80 expression, CD11c expression, and forward side scatter; **E-I**), and Ly6C + monocytes (number of cells, % of cells, and CD11c expression; **J-L**) in male BL/6 mice fed standard diet (SD) or high fat diet (HFD) who were administered saline or LPS (lipopolysaccharide). In the absence of differences between saline and LPS, data for each dietary group were combined and are presented as SD *vs.* HFD alone; *p<0.05, **p<0.01, ***p<0.001, ****p<0.0001.

impact LyC6+ monocyte numbers and surface expression of CD11c, which was further altered by diet (Figures 2K, L).

Monocyte CD11c expression can indicate a change in monocyte activation, and activation can promote monocyte differentiation into a microglial-like phenotype (32, 50, 51). We observed that LPS increased CNS monocytes in both HFD and SD animals; however, monocyte CD11c expression was lower in response to saline injection in HFD versus SD mice.

In contrast, LPS decreased monocyte CD11c expression in SD but not HFD mice. Increased numbers of microglia and decreased expression of CD11c on monocytes in the absence of increased monocyte numbers likely indicates that HFD promotes monocyte conversion into a more microglial-like phenotype, which LPS fails to further promote. Cumulatively, our findings indicate that acute HFD of only 3 d produces changes in peripheral and central immune cell populations. In this setting, LPS stimulation differentially impacts CNS immune cell dynamics, *i.e.*, monocyte to microglial shifts, in HFD versus SD.

Acute HFD activates hippocampal microglia

Since we observed changes in microglia numbers and size upon 4 d of HFD in our CNS immunophenotyping data, we were interested in further interrogating acute inflammatory microglial changes. We therefore assessed microglial morphology (34) as a proxy of activation in an area of the brain critically important for learning and memory, the hippocampus. Mice were administered HFD or SD with or without LPS stimulation for 4 d, and microglia morphology was examined using confocal microscopy. Three days of HFD shifted the morphology of hippocampal microglia to a state indicative of activation (Figures 3A–D) where microglia of HFD mice given saline (Figure 3C) appeared to have a larger soma size and more ameboid-like shape with fewer and shorter processes compared to microglia of SD mice given saline (Figure 3A). Additionally, microglia in SD (Figure 3B) and HFD (Figure 3D) mice given LPS appeared to take on an activated morphology similar to HFD mice given saline. Indeed, when quantifying these morphological changes, we observed that HFD lowered the ratio of three-dimensional space occupied by the microglia to its perimeter (ramification index; Figure 3E) versus SD mice. Interestingly, administering LPS to SD mice caused the microglia to have a decreased ramification, indicating activation. However, administering LPS to HFD mice did not change their ramification index; this inability of HFD microglia to respond to LPS stimulation may suggest they are activated under basal conditions to such a degree that further stimulation cannot provoke an appropriate immunological response to cellular insult or injury. Like the ramification index, HFD microglia had shorter average branch length (Figure 3F), shorter maximum branch length (Supplemental Figure S7D), and shorter minimum branch length versus SD microglia (Supplemental Figure S7F). LPS stimulation did not affect territorial volume (Supplemental Figure S5A), average branch length (Figure 3F), and maximum branch length (Supplemental Figure S7D). While HFD mice had a greater overall cell volume compared to SD mice, there no effect of LPS (Supplemental Figure S7B). Between groups differences in the number of microglial branch points and end points were varied and dependent upon hippocampal region (Supplemental Figures S7C, E). Thus, acute 3 d HFD activates hippocampal microglia and renders them less able to mount a response to additional stimulation, *e.g.*, to LPS.

Acute HFD activates cGAS/STING signaling

The deleterious role of cGAS/STING inflammatory signaling in obesity and metabolic dysfunction is well established in the periphery, particularly in adipose tissue) (19, 21). However, little is known about its role in this context in the CNS. Therefore, next we wanted to establish the effects of HFD feeding on hippocampal cGAS/STING pathway protein expression (Figure 4; Supplemental Figure S8). To do so, we took hippocampal tissue from SD and HFD animals fed diet for 4 d, homogenized it, and performed Western Blotting. We observed that HFD of only 4 d already acutely upregulated expression in the hippocampus of the dsDNA sensing cGAS and its adaptor molecule STING (Figures 4A, B; Supplemental Figures S8A, B). However, HFD did not promote phosphorylation or change expression of the cGAS/STING pathway transcription factors IRF3 (Figures 4C–E; Supplemental Figures S8C–E) and NFkβ (Figures 4F; Supplemental Figures S8C–E). When activated, IRF3 and NFkβ act as canonical transcription factors and move from the cytosol to the nucleus to induce gene transcription. Therefore, a lack of changes these transcription factors in bulk tissue is perhaps not surprising. Differences in cytosolic *vs.* nuclear localization are likely present, as have been observed by others in culture and in microglia (21, 26). Together, these data further suggest an early upregulated and pro-inflammatory phenotype involving the cGAS/STING pathway after only 3 d on HFD diet.

We previously showed that *in vitro* treatment of neurons with insulin or palmitate for 24 h produces insulin resistance, providing a cell culture model of prediabetes, with the expected changes in cellular signaling pathways (40, 52). We adopted this same approach to establish the contribution of various CNS cell types, namely neurons and microglia, to cGAS/STING pathway activation. Using a partly immortalized human hippocampal cell line and an immortalized human microglial cell line, we first established the presence of cytosolic DNA in response to palmitate and insulin treatment. Our data show a trending increase in cytosolic nuclear DNA (18s) in both neurons and microglia in response to palmitate or combined insulin and palmitate treatment (Figures 5A, C). However, there were no differences in either cell type in response to stimulation for cytochrome oxidase I DNA, a marker of mitochondrial DNA (Figures 5B, D). Of note, only trending differences in cytosolic nuclear DNA and a lack of differences in mitochondrial DNA were likely due to low sample sizes and a high degree of

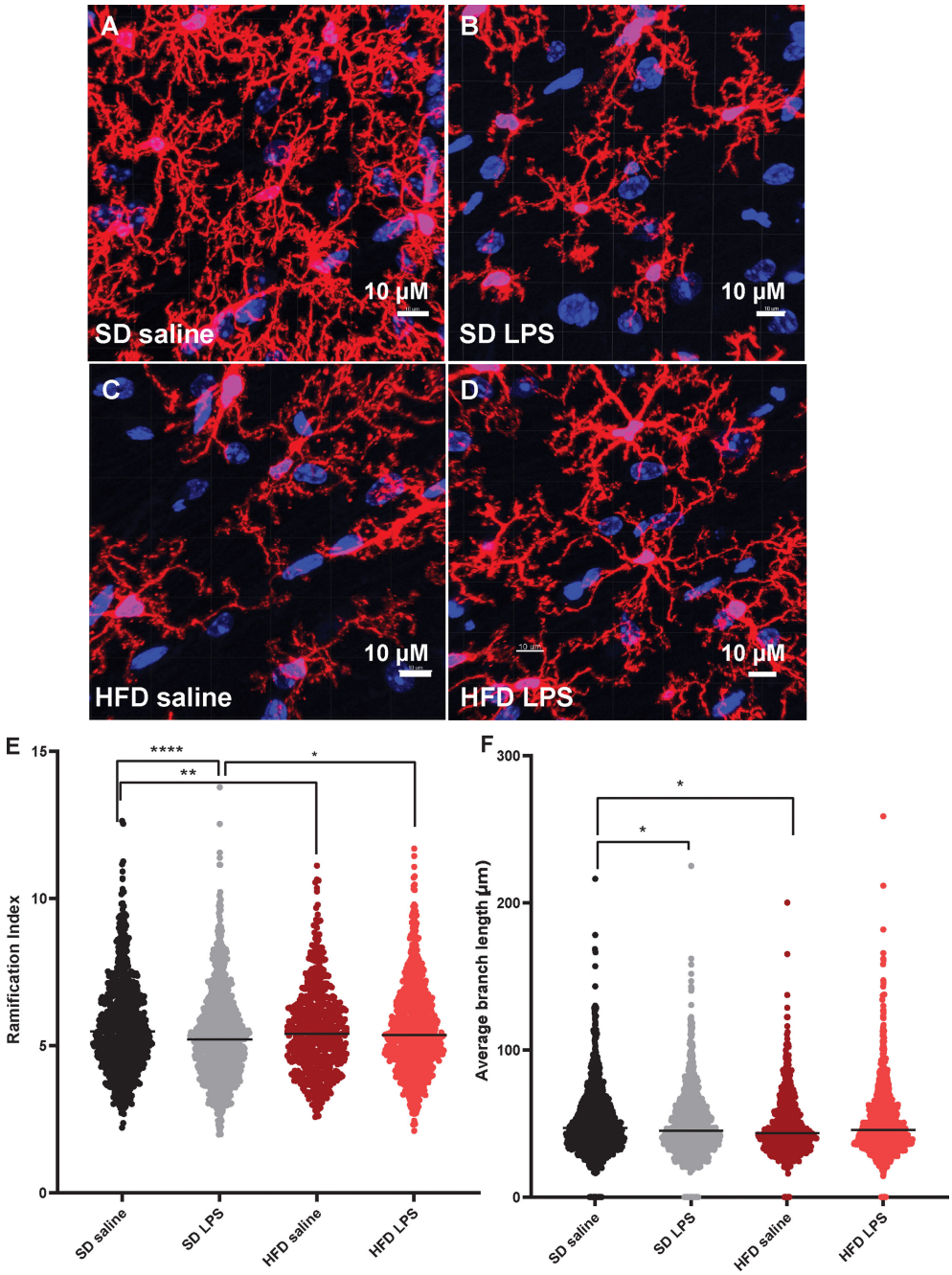

FIGURE 3
Microglial morphology. Representative images of IBA-1 microglia (red stain) in male BL/6 mice fed standard diet (SD) or high fat diet (HFD) who were administered saline or LPS (lipopolysaccharide; **A-D**). Quantification of microglia ramification index **(E)** and average branch length **(F)**. In the absence of differences between saline and LPS, data for each dietary group were combined and are presented as SD *vs.* HFD alone; *p<0.05, **p<0.01, ****p<0.0001.

variability between replicates. Future studies could address how obesogenic conditions might cause genomic damage and the role of mitochondrial *vs.* genomic or nuclear damage on cGAS/STING signaling in the CNS. We next assessed cGAS/STING pathway protein expression in both cell types. There was a robust response in microglia, with a significant increase in STING, pIRF3, and NFκβ, in the presence of either palmitate alone or combined insulin and palmitate for 24 h (Figure 6; Supplemental Figure S9). We also found a trending increase in cGAS protein expression in response to acute treatment for 24 h

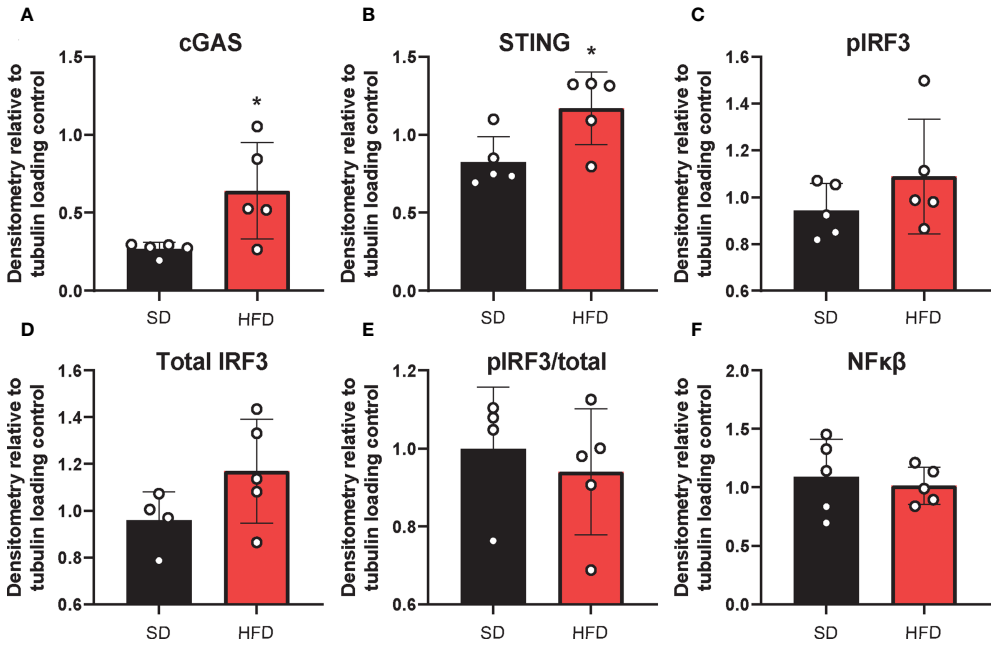

FIGURE 4
Hippocampal cGAS/STING protein expression. Expression in male BL/6 mice fed standard diet (SD) or high fat diet (HFD). Data represented as cGAS **(A)**, STING **(B)**, pIRF3 **(C)**, total IRF3 **(D)**, pIRF3/total **(E)**, and NFκβ **(F)** relative protein expression. Protein expression quantified as average band intensity relative to tubulin loading control; *$p<0.05$.

with either palmitate alone or combined insulin and palmitate in hippocampal neurons (Figure 6A; Supplemental Figure S9A).

Finally, we assessed cGAS/STING pathway activation in co-culture to evaluate the contribution of inflammatory crosstalk on potential pathological mechanisms *via* gap junctions in the CNS. Inflammatory crosstalk (53) is vital for normal intercellular communication (54). However, aberrant inflammatory crosstalk in the CNS (either *via* glia-glia or glia-neuron signaling) may promote pathological inflammatory mechanisms. Indeed, it plays a role in neurodegenerative diseases, such as AD/ADRD (55–57), and gap junctions facilitate transfer between cells of the cGAS/STING second messenger, cyclic GMP-AMP (cGAMP) (23, 56). To determine whether gap junctions mediate inflammatory crosstalk, we co-cultured neurons and microglia in the presence or absence of a gap junction inhibitor (CBX; carbenoxolone). Co-cultures were pre-treated with either the saturated fatty acid palmitate or the combination of insulin to mimic obesogenic prediabetic conditions. Our data (Figure 7; Supplemental Figure S10) show that treating co-cultures with transfection reagent alone did not change cGAS (Figure 7A; Supplemental Figure S10A), STING (Figure 7B; supplemental Figure S10B), or NFκβ protein expression (Figure 7D; Supplemental Figure S10D) in the presence of the gap junction inhibitor, carbenoxolone. However, we observed a significant increase in co-cultures pre-treated with insulin and palmitate for 24 h then stimulated with the dsDNA analog, poly dA:dT (poly deoxyadenylic-deoxythymidylic acid sodium salt), which was completely reversed in the presence of carbenoxolone (Figure 7C; Supplemental Figure S10C). In aggregate, these data suggest that cGAS/STING inflammatory crosstalk between CNS cells, *e.g.*, neurons and microglia, in response to metabolic injury is mediated, at least in part, by gap junctions.

Discussion

Metabolic dysfunction, in the form of chronic obesity, prediabetes, or diabetes, induces peripheral and central inflammation which correlate with cognitive impairment (58, 59). However, early inflammatory events secondary to obesity- or prediabetes that might contribute to cognitive impairment remain uncertain. The innate immune cGAS/STING pathway is dysregulated in cognitive impairment and neurogenerative disease (24, 26) and by responding to excess saturated fatty acids may connect metabolic dysfunction to inflammation in the CNS (19–21). In the current study, we examined the effect of acute HFD on peripheral and CNS inflammation, cognition, and CNS cGAS/STING activation. Our data show that acute HFD for only 3 d causes peripheral and central metabolic and immunologic changes indicative of insulin resistance and an acute pro-inflammatory response,

10.3389/fimmu.2022.1012594

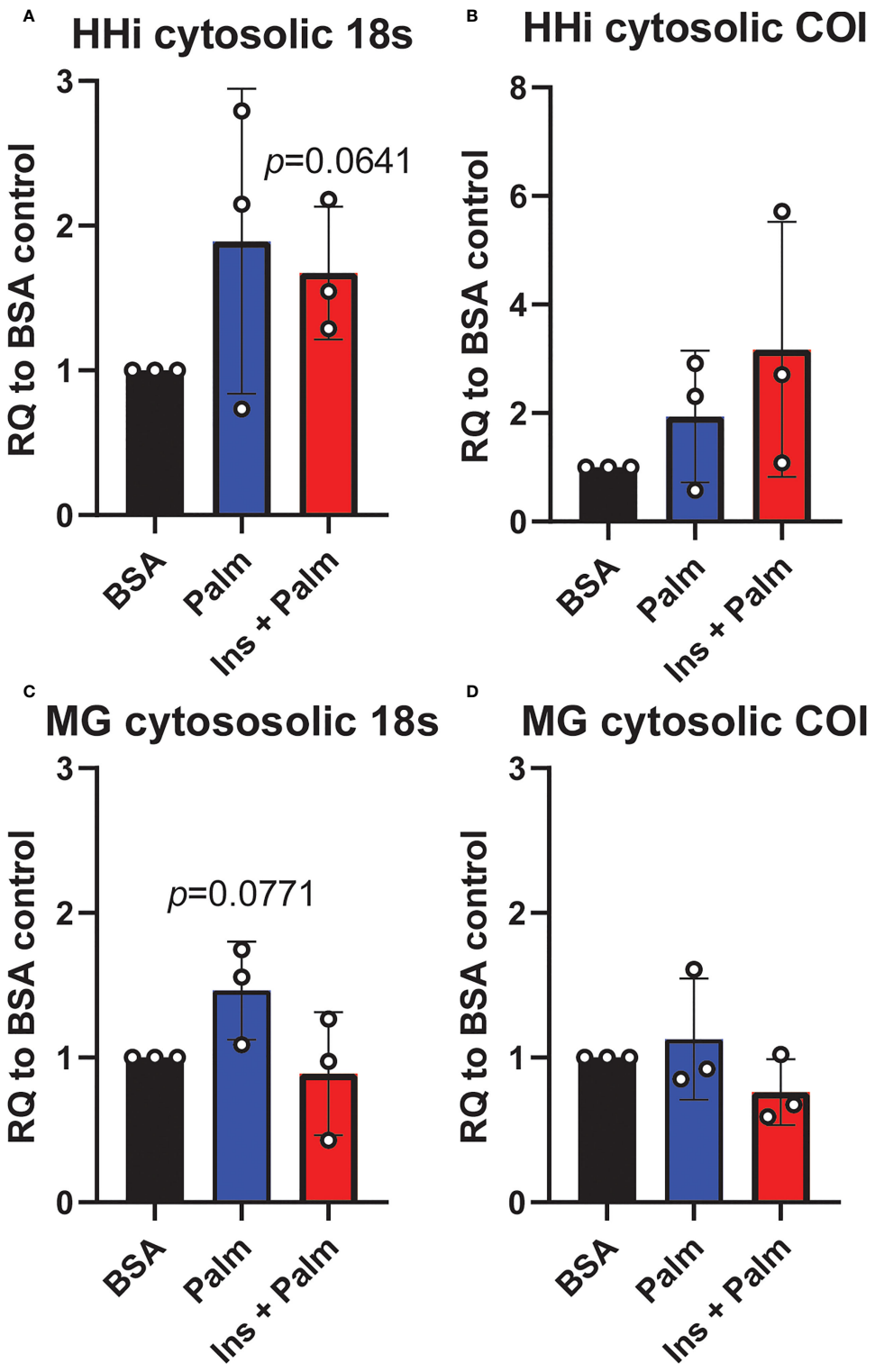

FIGURE 5
Cytosolic DNA concentrations. Relative quantity (RQ) of cytosolic DNA (nuclear and mitochondrial) in partially immortalized human hippocampal neurons (HHi; n=3, **A, B**) and in a human microglial cell line (MG; n=3, **C, D**). Cells treated with palmitate (Palm; HHi=250 µM, microglia=62.5 µM, 24h) or a combination of insulin and palmitate (Ins + Palm; above palmitate concentrations + 50 nM insulin, 24h). Values relative to BSA controls.

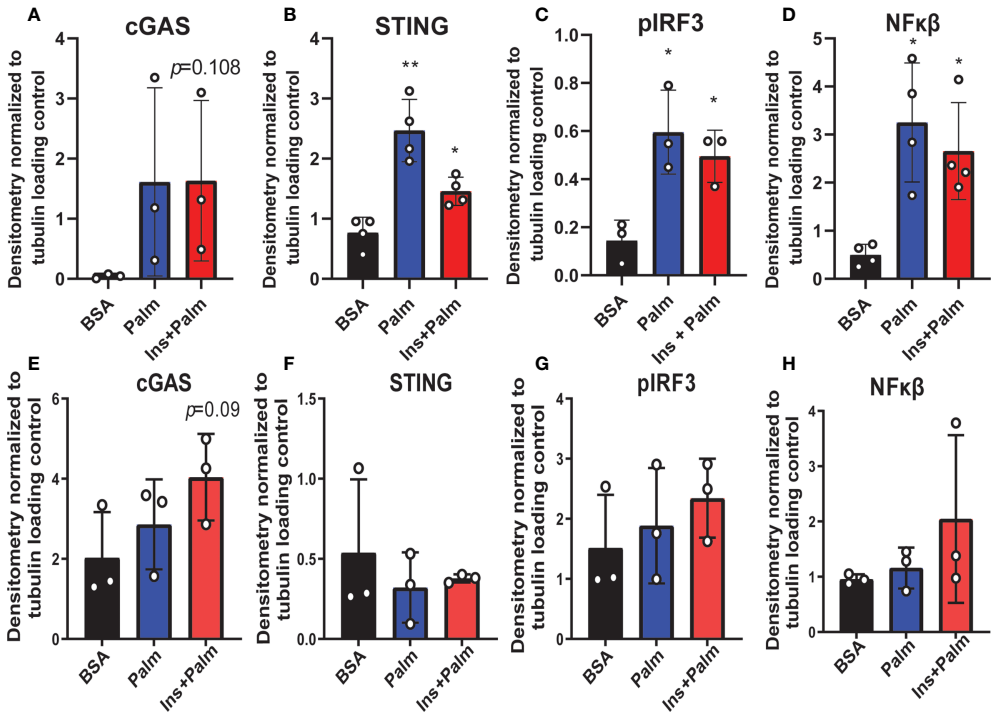

FIGURE 6
Neuronal and microglial cGAS/STING protein expression. Expression in a human microglial cell line (n=3 biological replicates, **A-D**) and a human hippocampal neuronal cell line (n=3 biological replicates, **E-H**) treated with either palmitate alone (Palm; HHi=250 µM, MG=62.5 µM, 24h) or a combination of insulin and palmitate (Ins+Palm; above concentrations of Palm+50nM insulin, 24h). Relative protein expression quantified as average band intensity relative to tubulin loading control; *p<0.05, **p<0.01.

though changes in cognition were not detected. Additionally, acute HFD activates CNS microglia, as measured by changes in cell size and morphology, and promotes cGAS/STING signaling. This immune response was mirrored *in vitro* under conditions of metabolic injury, particularly in microglia, as well as in in neuron-microglia co-culture and was blocked by a gap junction inhibitor. Overall, our findings indicate that inflammation and cGAS/STING activation are early responses to HFD, potentially through direct gap junction-mediated neuron-microglia crosstalk in the CNS.

We found that short-duration HFD induced acute peripheral and CNS metabolic changes in mice, specifically impaired glucose tolerance and insulin resistance. These findings are aligned with another study of 3 d of HFD feeding, which similarly saw impaired glucose homeostasis (60). These changes are also consistent with literature regarding chronic HFD, *i.e.*, of a few to several weeks, that report increases in body weight and impaired glucose tolerance (29, 30). We further show that both peripheral and CNS immune cell populations are dysregulated after only 3 d on HFD. Specifically, HFD increased circulating and CNS lymphocytes and neutrophils. We also observed that acute HFD decreased circulating Ly6C+ monocytes and Ly6C+ monocytes in the CNS had lower CD11c expression. Concurrent with increased CNS microglia, these data suggest that HFD promoted of monocyte recruitment to the CNS and monocyte conversion to a more microglia-like phenotype. Moreover, LPS failed to mount a further immune response in HFD, indicating peripheral and CNS immune cells are activated to such a degree by HFD that LPS is unable to provoke an appropriate response. Our findings are broadly aligned with the acute impact of HFD on the CNS, where others have reported increased levels of inflammatory cytokines after 3 d on diet (12). Furthermore, it is frequently reported that chronic HFD feeding induces an inflammatory phenotype (33, 48, 61).

HFD-induced pro-inflammatory responses through upregulated cGAS/STING signaling in peripheral tissues has been proposed as a potential pathological mechanism in obesity and prediabetes/diabetes (19, 21, 41). As an intracellular pattern recognition receptor, cGAS/STING is widely expressed by innate cells of the CNS, including microglia (62, 63), which canonically senses cytosolic dsDNA of viral or bacterial origin (64). However, the cGAS/STING pathway can also be activated by cytosolic self dsDNA released under conditions of metabolic stress, such as by saturated fatty acid overload (20, 64). Indeed, HFD fed mice have elevated adipose (41) and liver (65) STING levels. In endothelial cultures, the long-chain saturated fatty acid

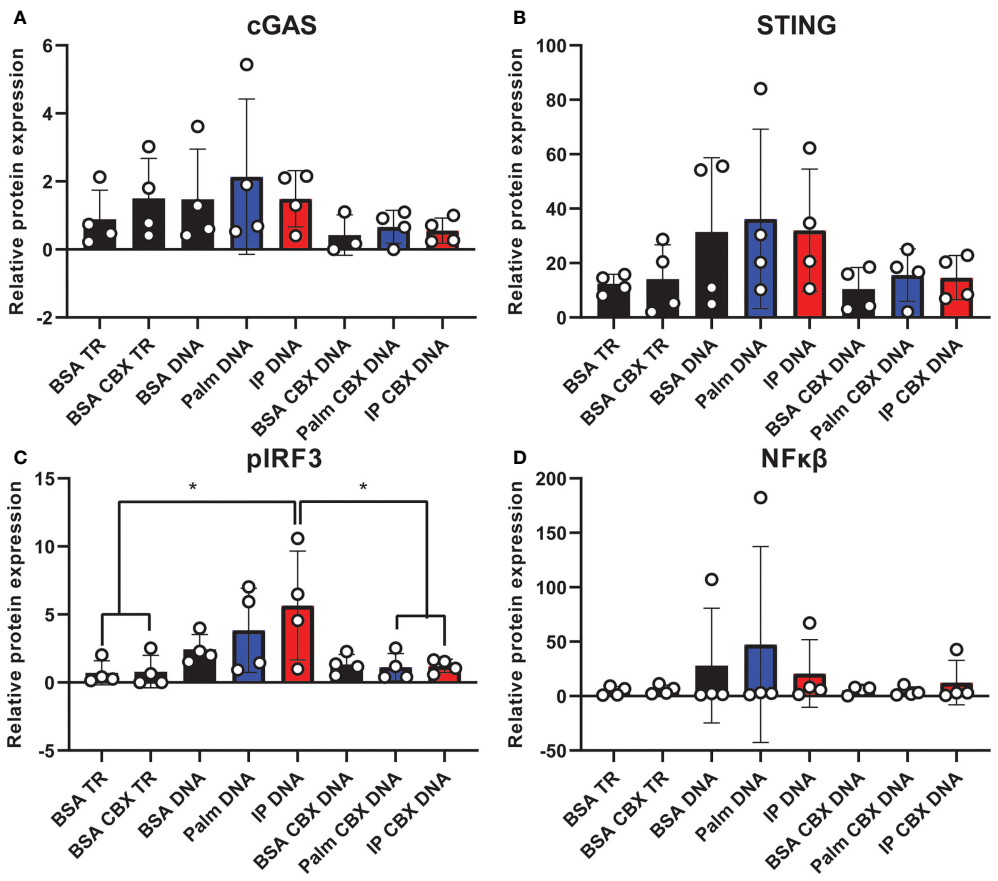

FIGURE 7
Co-culture cGAS/STING protein expression with and without gap junction inhibitor. Expression in a human hippocampal and human microglial cell line co-culture (n=4). Cells pretreated with bovine serum albumin (BSA; 31.25 μM, 24h) as a control, palmitate (Palm; 31.25 μM, 24h), or a combination of insulin and palmitate (IP; 31.25 μM palmitate and 50 nM insulin, 24h) +/- the gap junction inhibitor carbenoxolone (CBX; 150 μM), then stimulated with the dsDNA analog Poly dA:dT (DNA; 1μg/mL). Protein expression of cGAS **(A)**, STING **(B)**, pIRF3 **(C)**, and NFκβ **(D)** quantified quantified as average band intensity relative to histone loading control; *$p<0.05$. TR, transfection reagent.

palmitate activates cGAS/STING and induces inflammation (21, 41). Further, STING deficiency partially reverses HFD-induced weight gain, decreases plasma free fatty acids and adipose macrophage infiltration, and improves impaired insulin sensitivity and glucose tolerance (41).

While there is ample evidence to suggest a role for cGAS/STING in obesity and prediabetes/diabetes in the periphery, the role of cGAS/STING in the brain is less clear. We observed cGAS/STING was upregulated in the hippocampus of HFD animals versus SD controls. We previously established that our HFD feeding paradigm induces obesity, prediabetes and cognitive impairment with chronic HFD in mice (29). While here we did not observe cognitive impairment after only 3 d of HFD, our findings suggest HFD promotes an acute and early CNS pro-inflammatory programming that precedes or initiates the cascade of processes leading up to neurodegeneration and cognitive impairment with chronic HFD. Conversely, others have reported changes in cognition after acute HFD feeding (66–68). Differences may have arisen from variations in model system (mouse versus rat), animal age (5 wk versus 12 wk) or testing modality (puzzle box versus contextual fear conditioning versus radial arm maze) (66–68). Moreover, it is possible that cognitive differences in HFD versus SD animals in only measurable upon additional stimulation, *e.g.*, by LPS (66). Therefore, the temporal evolution of cognitive impairment upon acute HFD requires further study.

In alignment with our findings of early cGAS/STING activation, cGAS/STING is implicated in frank dementia, such as AD/ADRD (24, 26). In the brains of AD models, cGAS/STING is increased and improving DNA damage/repair by NAD+ supplementation normalizes cGAS/STING levels, reduces inflammation, and improves behavioral outcomes (24). Furthermore, cGAS/STING may be involved in AD *via* interaction with one of the key pathological AD proteins, tau. Specifically, tau activates cGAS/STING *via* binding to polyglutamine binding protein 1, which is essential for tau-

mediated cGAS/STING activation, specifically in microglia (26). In a Parkinson's disease mouse model, knocking out cGAS/STING signaling rescues the inflammatory phenotype, prevents loss of dopaminergic neurons, and improves motor deficits (27). In amyotrophic lateral sclerosis, the critical disease protein TDP-43 promotes the release of mitochondrial dsDNA into the cytosol, which subsequently activates the cGAS/STING pathway and promotes neurodegeneration (28).

We observed that acute HFD was sufficient to activate hippocampal microglia, which were unable to respond to additional stimulus in the form of LPS injection. Further, using an established *in vitro* model of metabolic injury, we observed a stronger response of the cGAS/STING pathway in microglia compared to neurons. This was anticipated, as cGAS/STING pathway proteins are highly expressed in microglia (62). Moreover, as we observed, HFD induces an inflammatory phenotype in hippocampal microglia (11, 12), and inflammatory microglia play critical roles in AD/ADRD pathology and related neuroinflammation (69–71). cGAS/STING activation primarily results in type 1 interferons (IFN) pro-inflammatory cytokine production, which acts to further stimulate cytokine release, *e.g.*, of IL-1β, IL-6, TNF-α (72). Excessive cGAS/STING activation contributes to pathological mechanisms, often mediated in the CNS by microglia (72, 73). This cGAS/STING activation and subsequent IFN release structurally and functionally injures neurons (72). Our findings indicate that microglia may be constituently activated under HFD conditions in the hippocampus, are less able to respond to inflammatory stimulus, and may contribute to CNS neuroinflammation, neurodegeneration, and eventual cognitive decline.

The immune system has multiple functions, including to induce inflammation, recruit immune cells, initiate protective cellular programs (including metabolic processes), preserve homeostasis, and maintain tissue functions (74). To perform these functions, it partly relies on inflammatory crosstalk, such as gap junctions (53), for intercellular communication (54). This crosstalk may become dysregulated upon chronic inflammatory activation, such as occurs in obesity and prediabetes, and thus is a potential mechanism promoting disease progression. In our co-culture model of human hippocampal neurons and microglia, we showed activation of the cGAS/STING pathway is strongly reduced in the presence of a gap junction inhibitor. These data show that gap junction mediated cGAS/STING crosstalk is a mechanism by which cGAS/STING inflammatory signaling can be promoted in the CNS in the presence of metabolic insults. In fact, gap junctions are relevant to neurodegenerative diseases, such as AD. Gap junctions are elevated near Aβ plaques (75, 76), and their blockade slows disease progression (55). Further, immune responses and cytokines can regulate gap junctions during insult, infection, or injury (77, 78). cGAS/STING has been shown to utilize gap junctions as an inflammatory crosstalk mechanisms in HEK cells and murine fibroblasts (23). Specifically, in response to cytosolic dsDNA, cGAS triggers production of its second messenger, cGAMP (20), which can travel to neighboring cells *via* gap junctions and stimulate downstream cytokine production by activating STING and pIRF3 (23). This represents a source of direct cell-to-cell crosstalk, contributing to inflammatory activation in neighboring cells, possibly furthering pathological processes. While our data support a role for gap junctions in promoting inflammatory crosstalk, it is unclear which cell types are the primary source of this inflammation. Future studies using single cell sequencing and cGAS cell specific knock out models are currently underway to better understand how different cell types contribute to this inflammation and the downstream effects they might have on cognition.

However, our study had some limitations. First it was carried out in male animals only. We (79) and others (80) have shown that male and female animals have sexually dimorphic responses to high fat diet feeding, particularly early in the paradigm. Additionally, there are known differences between males and females in terms of immune function and inflammation (81, 82), including in microglia (83). These differential effects also potentially impact cognition, as some have shown a differential effect of sex on cognitive outcomes (84). As mentioned above, no differences were observed between groups for puzzle box performance. However, motivation to escape in the puzzle box task is primarily driven by the animal's fear and anxiety in brightly lit spaces (85). Additional non-cognitive tasks that more directly measure anxiety under a similar motivation, such as the open field task (86), would allow for discrimination between a lack of cognitive deficits *vs.* overall anxiety in the animals and should be considered for future studies.

Overall, our data indicate that acute HFD feeding promotes early dysregulated glucose and insulin metabolism in the periphery and CNS. HFD feeding also causes an acute pro-inflammatory response, including microglial and innate inflammatory cGAS/STING pathway activation in the brain. Our *in vitro* data in neurons and microglia further point to a critical role for microglia in promoting this pro-inflammatory phenotype and indicate that gap junction may, at least in part, mediate cGAS/STING signaling, participating in inflammatory spread in the CNS.

Data availability statement

The original contributions presented in the study are included in the article/Supplementary Material. Further inquiries can be directed to the corresponding author.

Ethics statement

The animal study was reviewed and approved by The University of Michigan's Institutional Animal Care and Use Committee approved all animal protocols (PRO0010039).

Author contributions

SE, RH, and EF designed the studies. IW-D, ST, and BM performed the immunophenotyping. BK, JH, FM, IW-D, ST, RH, and SE contributed to the tissue processing. BK and SE performed the *ex vivo* insulin stimulation and western blotting. IW-D sectioned and stained the images for microglial morphology. SE and RH imaged and analyzed the microglial morphology data. CP and SE performed the cell culture and subsequent PCR and western blotting. SE performed statistical analyses. SE wrote the manuscript. RH, EF, BK, and BM edited the manuscript. All authors contributed to the article and approved the submitted version.

Funding

Funding was provided by the NIH (U01AG057562, U24DK115255, R01DK130913, T32DK007245), the Sinai Medical Staff Foundation Research Fund for Studying Diet and Brain Health, the Robert and Katherine Jacobs Environmental Health Initiative, the Robert E. Nederlander Sr. Program for Alzheimer's Research, the Andrea and Lawrence A. Wolfe Brain Health Initiative Fund, the A. Alfred Taubman Medical Research Institute, and the NeuroNetwork for Emerging Therapies. SE is supported by an Edith Briskin/SKS Foundation NeuroNetwork Emerging Scholar Fund, the Michigan Alzheimer's Disease Research Center early career investigator mentorship program (supported by the NIH/NIA funded by the Michigan Alzheimer's Disease Research Center (P30AG072931) and the University of Michigan Alzheimer's Disease Center), and NIA K99/R00 (1K99AG071667-01A1).

Acknowledgments

Authors are grateful to the University of Michigan flow cytometry core and Rogel Cancer Center immunology core for assistance with flow cytometry and ELISA, as well as the University of Michigan Unit for Laboratory Animal Medicine for their care of the animals used for this work.

Conflict of interest

The authors declare that the research was conducted in the absence of any commercial or financial relationships that could be construed as a potential conflict of interest.

Publisher's note

Supplementary material

The Supplementary Material for this article can be found online at: https://www.frontiersin.org/articles/10.3389/fimmu.2022.1012594/full#supplementary-material

SUPPLEMENTARY FIGURE 1
Representative insulin signaling western blot images. Representative unaltered images of western blots quantified in main figure 1 (w/link color) for cortex insulin signaling protein expression of AKT (pAKT and total AKT; **A**) and IRS-1 (pIRS-1(pS307) and IRS-1; **B**) in male BL/6 mice fed standard diet (SD) or high fat diet (HFD) and +/- acute insulin treatment.

SUPPLEMENTARY FIGURE 2
Cognition as measured by puzzle box testing. Data represented as single tasks **(A-D)**, and the combination of the single tasks into a complex task **(E)** in male BL6 mice fed high-fat diet (HFD) versus standard diet (SD).

SUPPLEMENTARY FIGURE 3
Peripheral immunophenotyping by flow cytometry. Data represented as leukocytes (number of cells **A**), CD4 T-cells (% of cells or number of cells; **B, C**), CD8 T-cells (% of cells or number of cells; **D, E**), B-cells (% of cells or number of cells; **F, G**), natural killer cells (% of cells or number of cells; **H, I**), Ly6C+ monocytes (% of cells or number of cells; **J, K**), Ly6C- monocytes (% of cells or number of cells; **L, M**), neutrophils (% of cells or number of cells; **N, O**), Ly6C+ monocytes CD11c expression (median fluorescent (fold) intensity; **P**), Ly6C+ monocytes F4/80 expression (median fluorescent (fold) intensity; **Q**), Ly6C- monocytes CD11c expression (median fluorescent (fold) intensity; **R**), and Ly6C- monocytes F4/80 expression (median fluorescent (fold) intensity; **S**) in male BL6 mice fed high-fat diet (HFD) versus standard diet (SD); *p<0.05.

SUPPLEMENTARY FIGURE 4
Plasma inflammatory cytokines as measured by ELISA. Data represented as plasma TNF-α (pg/mL; **A**) and plasma MCP-1 (pg/mL; **B**) concentrations in male BL6 mice fed high-fat diet (HFD) versus standard diet (SD), administered either saline or lipopolysaccharide (LPS); **p<0.01, ****p<0.0001.

SUPPLEMENTARY FIGURE 5
CNS immunophenotyping of lymphoid cells by flow cytometry. Data represented as leukocytes (number of cells or % of cells; **A, B**), CD8 T-cells (number of cells or % of cells; **C, D**), CD4 T-cells (number of cells or % of cells; **E, F**), and natural killer cells (number of cells or % of cells; **G, H**) in male BL6 mice fed high-fat diet (HFD) versus standard diet (SD). There were no differences between animals administered saline *vs.* lipopolysaccharide (LPS), therefore SD and LPS animals were combined within their appropriate dietary groups; *p<0.05.

SUPPLEMENTARY FIGURE 6
Representative flow cytometry panels for CNS myeloid cells. Data represented as CD11c or F4/80 surface expression on neutrophils **(A)**, microglia **(B)**, and monocytes **(C)** in male BL6 mice fed high-fat diet (HFD; black) versus standard diet (SD; red) given saline. For monocytes, solid lines represent mice given saline and dashed lines represent mice given lipopolysaccharide. Grey peaks represent IgG control antibody.

SUPPLEMENTARY FIGURE 7
Microglial morphology. Quantification of microglial territorial volume (μm^3; **A**), cell volume (μm^3; **B**), number of end points **(C)**, maximum

branch length (μm; **D**), number of end points **(E)**, and minimum branch length (μm; **F**) in male BL6 mice fed high-fat diet (HFD) versus standard diet (SD) administered saline or LPS (lipopolysaccharide; **A-D**). Quantification of microglia percentage occupied volume **(E)** and average branch length **(F)**. For A, B, D, and F quantification was performed on individual cells per image (n=3 images for the CA1 and molecular layers of the hippocampus and n=2 images for the hilus). For C and E quantification was performed by combing all images per hippocampal region. In the absence of differences between saline and LPS, data for each dietary group were combined and are presented as SD *vs.* HFD alone; *$p<0.05$, **$p<0.01$, *** $p<0.001$, ****$p<0.0001$.

SUPPLEMENTARY FIGURE 8

Representative hippocampal cGAS/STING western blot images. Representative unaltered images of western blots quantified in main figure 4 (w/link color) for hippocampal cGAS/STING pathway protein expression of cGAS **(A)**, STING **(B)**, pIRF3 **(C)**, IRF3 **(D)**, NFκβ **(E)**, and tubulin **(F)** in male BL/6 mice fed standard diet (SD) or high fat diet (HFD).

SUPPLEMENTARY FIGURE 9

Representative neuron and microglia cGAS/STING western blot images. Representative unaltered images of western blots quantified in main figure 6 (w/link color) for cGAS/STING pathway protein expression of cGAS **(A)**, STING **(B)**, pIRF3 **(C)**, NFκβ **(D)**, and tubulin **(F)** in palmitate (Palm) and insulin (Ins) stimulated neuronal and microglial cell lines. Conditions in bold are those used for analysis.

SUPPLEMENTARY FIGURE 10

Representative co-culture cGAS/STING western blot images. Representative unaltered images of western blots quantified in main figure 7 (w/link color) for cGAS/STING pathway protein expression of cGAS **(A)**, STING **(B)**, pIRF3 **(C)**, NFκβ **(D)**, and histone **(F)** in in palmitate (Palm) and insulin and palmitate (IP) stimulated neuronal and microglial cell line co-culture +/- the gap junction inhibitor carbenoxolone (CBX; 150 μM). Co-cultures were further stimulated with the dsDNA analog Poly dA:dT (DNA; 1μg/mL). Conditions in bold are those used for analysis. TR; transfection reagent.

References

1. Saeedi P, Petersohn I, Salpea P, Malanda B, Karuranga S, Unwin N, et al. Global and regional diabetes prevalence estimates for 2019 and projections for 2030 and 2045: Results from the international diabetes federation diabetes atlas, 9(th) edition. *Diabetes Res Clin Pract* (2019) 157:107843. doi: 10.1016/j.diabres.2019.107843

2. Fryar CD, Carroll MD, Ogden CL. *Prevalence of overweight, obesity, and severe obesity among adults aged 20 and over: 1960–1962 through 2015–2016*. National Center for Health Statistics (Health E-Stats), Division of Health and Nutrition Examination Surveys, United states (2018).

3. Blüher M. Obesity: global epidemiology and pathogenesis. *Nat Rev Endocrinol* (2019) 15(5):288–98. doi: 10.1038/s41574-019-0176-8

4. Biessels GJ, Despa F. Cognitive decline and dementia in diabetes mellitus: mechanisms and clinical implications. *Nat Rev Endocrinol* (2018) 1:591–604. doi: 10.1038/s41574-018-0048-7

5. Geijselaers SL, Sep SJ, Claessens D, Schram MT, Van Boxtel MP, Henry RM, et al. The role of hyperglycemia, insulin resistance, and blood pressure in diabetes-associated differences in cognitive performance–the maastricht study. *Diabetes Care* (2017) 40(11):dc170330. doi: 10.2337/dc17-0330

6. O'Brien PD, Hinder LM, Callaghan BC, Feldman EL. Neurological consequences of obesity. *Lancet Neurol* (2017) 16(6):465–77. doi: 10.1016/S1474-4422(17)30084-4

7. Esser N, Legrand-Poels S, Piette J, Scheen AJ, Paquot N. Inflammation as a link between obesity, metabolic syndrome and type 2 diabetes. *Diabetes Res Clin Pract* (2014) 105(2):141–50. doi: 10.1016/j.diabres.2014.04.006

8. Henn RE, Noureldein MH, Elzinga SE, Kim B, Savelieff MG, Feldman EL. Glial-neuron crosstalk in health and disease: A focus on metabolism, obesity, and cognitive impairment. *Neurobiol Dis* (2022) 105766. doi: 10.1016/j.nbd.2022.105766

9. Wanrooy BJ, Kumar KP, Wen SW, Qin CX, Ritchie RH, Wong CH. Distinct contributions of hyperglycemia and high-fat feeding in metabolic syndrome-induced neuroinflammation. *J Neuroinflamm* (2018) 15(1):1–13. doi: 10.1186/s12974-018-1329-8

10. Söderbom G, Zeng B-Y. The NLRP3 inflammasome as a bridge between neuro-inflammation in metabolic and neurodegenerative diseases. *Int Rev Neurobiol* (2020) 154:345–91. doi: 10.1016/bs.irn.2020.03.023

11. Butler MJ, Cole RM, Deems NP, Belury MA, Barrientos RM. Fatty food, fatty acids, and microglial priming in the adult and aged hippocampus and amygdala. *Brain Behav Immun* (2020) 89:145–58. doi: 10.1016/j.bbi.2020.06.010

12. Nakandakari SCBR, Muñoz VR, Kuga GK, Gaspar RC, Sant'Ana MR, Pavan ICB, et al. Short-term high-fat diet modulates several inflammatory, ER stress, and apoptosis markers in the hippocampus of young mice. *Brain Behav Immun* (2019) 79:284–93. doi: 10.1016/j.bbi.2019.02.016

13. Fakih W, Zeitoun R, AlZaim I, Eid AH, Kobeissy F, Abd-Elrahman KS, et al. Early metabolic impairment as a contributor to neurodegenerative disease: Mechanisms and potential pharmacological intervention. *Obesity* (2022) 30(5):982–93. doi: 10.1002/oby.23400

14. Herrada AA, Olate-Briones A, Rojas A, Liu C, Escobedo N, Piesche M. Adipose tissue macrophages as a therapeutic target in obesity-associated diseases. *Obes Rev* (2021) 22(6):e13200. doi: 10.1111/obr.13200

15. Butler MJ. The role of Western diets and obesity in peripheral immune cell recruitment and inflammation in the central nervous system. *Brain Behav Immunity-Health* (2021) 16:100298. doi: 10.1016/j.bbih.2021.100298

16. Zhou H, Urso C, Jadeja V. Saturated fatty acids in obesity-associated inflammation. *J Inflammation Res* (2020) 13:1. doi: 10.2147/JIR.S229691

17. Li B, Leung JC, Chan LY, Yiu WH, Tang SC. A global perspective on the crosstalk between saturated fatty acids and toll-like receptor 4 in the etiology of inflammation and insulin resistance. *Prog Lipid Res* (2020) 77:101020. doi: 10.1016/j.plipres.2019.101020

18. Ivashkiv LB, Donlin LT. Regulation of type I interferon responses. *Nat Rev Immunol* (2014) 14(1):36–49. doi: 10.1038/nri3581

19. Bai J, Cervantes C, Liu J, He S, Zhou H, Zhang B, et al. DsbA-l prevents obesity-induced inflammation and insulin resistance by suppressing the mtDNA release-activated cGAS-cGAMP-STING pathway. *Proc Natl Acad Sci* (2017) 114(46):201708744. doi: 10.1073/pnas.1708744114

20. Bai J, Liu F. The cGAS-cGAMP-STING pathway: A molecular link between immunity and metabolism. *Diabetes* (2019) 68(6):1099–108. doi: 10.2337/dbi18-0052

21. Yuan L, Mao Y, Luo W, Wu W, Xu H, Wang XL, et al. Palmitic acid dysregulates the hippo-YAP pathway and inhibits angiogenesis by inducing mitochondrial damage and activating the cytosolic DNA sensor cGAS-STING-IRF3 signaling. *J Biol Chem* (2017) 292(36): 804005. doi: 10.1074/jbc.M117.804005

22. Gui X, Yang H, Li T, Tan X, Shi P, Li M, et al. Autophagy induction *via* STING trafficking is a primordial function of the cGAS pathway. *Nature* (2019) 567(7747):262–6. doi: 10.1038/s41586-019-1006-9

23. Ablasser A, Schmid-Burgk JL, Hemmerling I, Horvath GL, Schmidt T, Latz E, et al. Cell intrinsic immunity spreads to bystander cells *via* the intercellular transfer of cGAMP. *Nature* (2013) 503(7477):530. doi: 10.1038/nature12640

24. Hou Y, Wei Y, Lautrup S, Yang B, Wang Y, Cordonnier S, et al. NAD+ supplementation reduces neuroinflammation and cell senescence in a transgenic mouse model of alzheimer's disease *via* cGAS–STING. *Proc Natl Acad Sci* (2021) 118(37):e2011226118. doi: 10.1073/pnas.2011226118

25. Sanders OD, Rajagopal L, Rajagopal JA. Does oxidatively damaged DNA drive amyloid-β generation in alzheimer's disease? a hypothesis. *J Neurogenet* (2021) 35(4):1–7. doi: 10.1080/01677063.2021.1954641

26. Jin M, Shiwaku H, Tanaka H, Obita T, Ohuchi S, Yoshioka Y, et al. Tau activates microglia *via* the PQBP1-cGAS-STING pathway to promote brain inflammation. *Nat Commun* (2021) 12(1):1–22. doi: 10.1038/s41467-021-26851-2

27. Sliter DA, Martinez J, Hao L, Chen X, Sun N, Fischer TD, et al. Parkin and PINK1 mitigate STING-induced inflammation. *Nature* (2018) 561(7722):258–62. doi: 10.1038/s41586-018-0448-9

28. Yu C-H, Davidson S, Harapas CR, Hilton JB, Mlodzianoski MJ, Laohamonthonkul P, et al. TDP-43 triggers mitochondrial DNA release *via* mPTP to activate cGAS/STING in ALS. *Cell* (2020) 183(3):636–49. e18. doi: 10.1016/j.cell.2020.09.020

29. Sims-Robinson C, Bakeman A, Bruno E, Jackson S, Glasser R, Murphy GG, et al. Dietary reversal ameliorates short-and long-term memory deficits induced by high-fat diet early in life. *PloS One* (2016) 11(9):e0163883. doi: 10.1371/journal.pone.0163883

30. Hinder LM, O'Brien PD, Hayes JM, Backus C, Solway AP, Sims-Robinson C, et al. Dietary reversal of neuropathy in a murine model of prediabetes and metabolic syndrome. *Dis Model Mech* (2017) 10(6):717–25. doi: 10.1242/dmm.028530

31. O'Brien PD, Hinder LM, Rumora AE, Hayes JM, Dauch JR, Backus C, et al. Juvenile murine models of prediabetes and type 2 diabetes develop neuropathy. *Dis Models Mech* (2018) 11(12):dmm037374. doi: 10.1242/dmm.037374

32. Figueroa-Romero C, Guo K, Murdock BJ, Paez-Colasante X, Bassis CM, Mikhail KA, et al. Temporal evolution of the microbiome, immune system and epigenome with disease progression in ALS mice. *Dis Models Mech* (2020) 13(2): dmm041947. doi: 10.1241/dmm.041947

33. Elzinga S, Murdock BJ, Guo K, Hayes JM, Tabbey MA, Hur J, et al. Toll-like receptors and inflammation in metabolic neuropathy; a role in early versus late disease? *Exp Neurol* (2019) 320:112967. doi: 10.1016/j.expneurol.2019.112967

34. York EM, LeDue JM, Bernier L-P, MacVicar BA. 3DMorph automatic analysis of microglial morphology in three dimensions from ex vivo and *In vivo* imaging. *eNeuro* (2018) 5(6):ENEURO.0266–18.2018. doi: 10.1523/ENEURO.0266-18.2018

35. Kim B, Elzinga SE, Henn RE, McGinley LM, Feldman EL. The effects of insulin and insulin-like growth factor I on amyloid precursor protein phosphorylation in in vitro and *in vivo* models of alzheimer's disease. *Neurobiol Dis* (2019) 132:104541. doi: 10.1016/j.nbd.2019.104541

36. Kim B, Figueroa-Romero C, Pacut C, Backus C, Feldman EL. Insulin resistance prevents AMPK-induced tau dephosphorylation through akt-mediated increase in AMPKSer485 phosphorylation. *J Biol Chem* (2015) 290(31):19146–57. doi: 10.1074/jbc.M115.636852

37. Schneider CA, Rasband WS, Eliceiri KW. NIH Image to ImageJ: 25 years of image analysis. *Nat Methods* (2012) 9(7):671–5. doi: 10.1038/nmeth.2089

38. Sims-Robinson C, Bakeman A, Glasser R, Boggs J, Pacut C, Feldman EL. The role of endoplasmic reticulum stress in hippocampal insulin resistance. *Exp Neurol* (2016) 277:261–7. doi: 10.1016/j.expneurol.2016.01.007

39. McGinley LM, Sims E, Lunn JS, Kashlan ON, Chen KS, Bruno ES, et al. Human cortical neural stem cells expressing insulin-like growth factor-I: A novel cellular therapy for alzheimer's disease. *Stem Cells Trans Med* (2016) 5(3):379–91. doi: 10.5966/sctm.2015-0103

40. Kim B, McGinley LM, Elzinga SE, Mendelson FE, Savelieff MG, Feldman EL. Palmitate increases amyloid precursor protein exosome secretion: A missing link between metabolic syndrome and alzheimer's disease. *Submitted* (2020) 90: S93–S93.

41. Mao Y, Luo W, Zhang L, Wu W, Yuan L, Xu H, et al. STING-IRF3 triggers endothelial inflammation in response to free fatty acid-induced mitochondrial damage in diet-induced obesity. *Arterioscler Thromb Vasc Biol* (2017) 37(5):920–9. doi: 10.1161/ATVBAHA.117.309017

42. Livak KJ, Schmittgen TD. Analysis of relative gene expression data using real-time quantitative PCR and the 2– ΔΔCT method. *methods* (2001) 25(4):402–8. doi: 10.1006/meth.2001.1262

43. Williams A, Lowry T, Sims-Robinson C. The development of a cognitive rehabilitation task for mice. *Neurobiol Learn Memory* (2020) 175:107296. doi: 10.1016/j.nlm.2020.107296

44. Vincent AM, Hayes JM, McLean LL, Vivekanandan-Giri A, Pennathur S, Feldman EL. Dyslipidemia-induced neuropathy in mice: The role of oxLDL/LOX-1. *Diabetes* (2009) 58(10):2376–85. doi: 10.2337/db09-0047

45. De Souza CT, Araujo EP, Bordin S, Ashimine R, Zollner RL, Boschero AC, et al. Consumption of a fat-rich diet activates a proinflammatory response and induces insulin resistance in the hypothalamus. *Endocrinology* (2005) 146 (10):4192–9. doi: 10.1210/en.2004-1520

46. Kim B, Feldman EL. Insulin resistance in the nervous system. *Trends Endocrinol Metab* (2012) 23(3):133–41. doi: 10.1016/j.tem.2011.12.004

47. Kim B, Feldman EL. Insulin resistance as a key link for the increased risk of cognitive impairment in the metabolic syndrome. *Exp Mol Med* (2015) 47(3):e149. doi: 10.1038/emm.2015.3

48. Denver P, Gault VA, McClean PL. Sustained high-fat diet modulates inflammation, insulin signalling and cognition in mice and a modified xenin peptide ameliorates neuropathology in a chronic high-fat model. *Diabetes Obes Metab* (2018) 20(5):1166–75. doi: 10.1111/dom.13210

49. Miranda CL, Johnson LA, De Montgolfier O, Elias VD, Ullrich LS, Hay JJ, et al. Non-estrogenic xanthohumol derivatives mitigate insulin resistance and cognitive impairment in high-fat diet-induced obese mice. *Sci Rep* (2018) 8(1):1–17. doi: 10.1038/s41598-017-18992-6

50. Martin E, Boucher C, Fontaine B, Delarasse C. Distinct inflammatory phenotypes of microglia and monocyte-derived macrophages in alzheimer's disease models: Effects of aging and amyloid pathology. *Aging Cell* (2017) 16 (1):27–38. doi: 10.1111/acel.12522

51. Kapellos TS, Bonaguro L, Gemünd I, Reusch N, Saglam A, Hinkley ER, et al. Human monocyte subsets and phenotypes in major chronic inflammatory diseases. *Front Immunol* (2019) 10:2035. doi: 10.3389/fimmu.2019.02035

52. Kim B, Sullivan KA, Backus C, Feldman EL. Cortical neurons develop insulin resistance and blunted akt signaling: A potential mechanism contributing to enhanced ischemic injury in diabetes. *Antioxid Redox Signaling* (2011) 14 (10):1829–39. doi: 10.1089/ars.2010.3816

53. Orellana JA, Martinez AD, Retamal MA. Gap junction channels and hemichannels in the CNS: Regulation by signaling molecules. *Neuropharmacology* (2013) 75:567–82. doi: 10.1016/j.neuropharm.2013.02.020

54. Stubbington MJ, Rozenblatt-Rosen O, Regev A, Teichmann SA. Single-cell transcriptomics to explore the immune system in health and disease. *Science* (2017) 358(6359):58–63. doi: 10.1126/science.aan6828

55. Takeuchi H, Mizoguchi H, Doi Y, Jin S, Noda M, Liang J, et al. Blockade of gap junction hemichannel suppresses disease progression in mouse models of amyotrophic lateral sclerosis and alzheimer's disease. *PloS One* (2011) 6(6):e21108. doi: 10.1371/journal.pone.0021108

56. Orellana JA, Sáez PJ, Shoji KF, Schalper KA, Palacios–Prado N, Velarde V, et al. Modulation of brain hemichannels and gap junction channels by pro-inflammatory agents and their possible role in neurodegeneration. *Antioxid Redox Signaling* (2009) 11(2):369–99. doi: 10.1089/ars.2008.2130

57. Angeli S, Kousiappa I, Stavrou M, Sargiannidou I, Georgiou E, Papacostas SS, et al. Altered expression of glial gap junction proteins Cx43, Cx30, and Cx47 in the 5XFAD model of alzheimer's disease. *Front Neurosci* (2020) 14:1060. doi: 10.3389/fnins.2020.582934

58. Wang Q, Yuan J, Yu Z, Lin L, Jiang Y, Cao Z, et al. FGF21 attenuates high-fat diet-induced cognitive impairment *via* metabolic regulation and anti-inflammation of obese mice. *Mol Neurobiol* (2018) 55(6):4702–17. doi: 10.1007/s12035-017-0663-7

59. Yaffe K, Kanaya A, Lindquist K, Simonsick EM, Harris T, Shorr RI, et al. The metabolic syndrome, inflammation, and risk of cognitive decline. *Jama* (2004) 292 (18):2237–42. doi: 10.1001/jama.292.18.2237

60. Haley MJ, Krishnan S, Burrows D, de Hoog L, Thakrar J, Schiessl I, et al. Acute high-fat feeding leads to disruptions in glucose homeostasis and worsens stroke outcome. *J Cereb Blood Flow Metab* (2019) 39(6):1026–37. doi: 10.1177/0271678X17744718

61. Avtanski D, Pavlov VA, Tracey KJ, Poretsky L. Characterization of inflammation and insulin resistance in high-fat diet-induced male C57BL/6J mouse model of obesity. *Anim Models Exp Med* (2019) 2(4):252–8. doi: 10.1002/ame2.12084

62. Jeffries AM, Marriott I. Human microglia and astrocytes express cGAS-STING viral sensing components. *Neurosci Lett* (2017) 658:53–6. doi: 10.1016/j.neulet.2017.08.039

63. Chin AC. Neuroinflammation and the cGAS-STING pathway. *J Neurophysiol* (2019) 121(4):1087–91. doi: 10.1152/jn.00848.2018

64. Chen Q, Sun L, Chen ZJ. Regulation and function of the cGAS–STING pathway of cytosolic DNA sensing. *Nat Immunol* (2016) 17(10):1142. doi: 10.1038/ni.3558

65. Qiao JT, Cui C, Qing L, Wang LS, He TY, Yan F, et al. Activation of the STING-IRF3 pathway promotes hepatocyte inflammation, apoptosis and induces metabolic disorders in nonalcoholic fatty liver disease. *Metabolism* (2018) 81:13–24. doi: 10.1016/j.metabol.2017.09.010

66. Sobesky JL, D'Angelo HM, Weber MD, Anderson ND, Frank MG, Watkins LR, et al. Glucocorticoids mediate short-term high-fat diet induction of neuroinflammatory priming, the NLRP3 inflammasome, and the danger signal HMGB1. *eNeuro* (2016) 3(4). doi: 10.1523/ENEURO.0113-16.2016

67. Spencer SJ, D'Angelo H, Soch A, Watkins LR, Maier SF, Barrientos RM. High-fat diet and aging interact to produce neuroinflammation and impair hippocampal-and amygdalar-dependent memory. *Neurobiol Aging* (2017) 58:88–101. doi: 10.1016/j.neurobiolaging.2017.06.014

68. Kanoski SE, Davidson TL. Different patterns of memory impairments accompany short-and longer-term maintenance on a high-energy diet. *J Exp Psychol: Anim Behav Processes* (2010) 36(2):313. doi: 10.1037/a0017228

69. Keren-Shaul H, Spinrad A, Weiner A, Matcovitch-Natan O, Dvir-Szternfeld R, Ulland TK, et al. A unique microglia type associated with restricting development of alzheimer's disease. *Cell* (2017) 169(7):1276–90. e17. doi: 10.1016/j.cell.2017.05.0

70. Leng F, Edison P. Neuroinflammation and microglial activation in Alzheimer disease: where do we go from here? *Nat Rev Neurol* (2021) 17 (3):157–72. doi: 10.1038/s41582-020-00435-y

71. Hickman S, Izzy S, Sen P, Morsett L, El Khoury J. Microglia in neurodegeneration. *Nat Neurosci* (2018) 21(10):1359–69. doi: 10.1038/s41593-018-0242-x

72. Paul BD, Snyder SH, Bohr VA. Signaling by cGAS-STING in neurodegeneration, neuroinflammation, and aging. *Trends Neurosci* (2021) 44 (2):83–96. doi: 10.1016/j.tins.2020.10.008

73. Tanaka Y, Takahashi A. Senescence-associated extracellular vesicle (SA-EV) release plays a role in senescence-associated secretory phenotype (SASP) in age-associated diseases. *J Biochem* (2020) 169(2):147–53. doi: 10.1093/jb/mvaa109

74. Chavan SS, Pavlov VA, Tracey KJ. Mechanisms and therapeutic relevance of neuro-immune communication. *Immunity* (2017) 46(6):927–42. doi: 10.1016/j.immuni.2017.06.008

75. Mei X, Ezan P, Giaume C, Koulakoff A. Astroglial connexin immunoreactivity is specifically altered at β-amyloid plaques in β-amyloid precursor protein/presenilin1 mice. *Neuroscience* (2010) 171(1):92–105. doi: 10.1016/j.neuroscience.2010.08.001

76. Giaume C, Sáez JC, Song W, Leybaert L, Naus CC. Connexins and pannexins in alzheimer's disease. *Neurosci Lett* (2019) 695:100–5. doi: 10.1016/j.neulet.2017.09.006

77. Eugenin EA. Role of connexin/pannexin containing channels in infectious diseases. *FEBS Lett* (2014) 588(8):1389–95. doi: 10.1016/j.febslet.2014.01.030

78. Valdebenito S, Barreto A, Eugenin EA. The role of connexin and pannexin containing channels in the innate and acquired immune response. *Biochim Biophys Acta (BBA)-Biomembranes* (2018) 1860(1):154–65. doi: 10.1016/j.bbamem.2017.05.015

79. Elzinga SE, Savelieff MG, O'Brien PD, Mendelson FE, Hayes JM, Feldman EL. Sex differences in insulin resistance, but not peripheral neuropathy, in a diet-induced prediabetes mouse model. *Dis Models Mech* (2021) 14(4):dmm048909. doi: 10.1242/dmm.048909

80. Salinero AE, Anderson BM, Zuloaga KL. Sex differences in the metabolic effects of diet-induced obesity vary by age of onset. *Int J Obes* (2018) 42(5):1088–91. doi: 10.1038/s41366-018-0023-3

81. Klein SL, Flanagan KL. Sex differences in immune responses. *Nat Rev Immunol* (2016) 16(10):626–38. doi: 10.1038/nri.2016.90

82. Taneja V. Sex hormones determine immune response. *Front Immunol* (2018) 9:1931. doi: 10.3389/fimmu.2018.01931

83. Robison LS, Albert NM, Camargo LA, Anderson BM, Salinero AE, Riccio DA, et al. High-fat diet-induced obesity causes sex-specific deficits in adult hippocampal neurogenesis in mice. *eNeuro* (2020) 7(1):ENEURO.0391–19.2019. doi: 10.1523/ENEURO.0391-19.2019

84. Gannon OJ, Robison LS, Salinero AE, Abi-Ghanem C, Mansour FM, Kelly RD, et al. High-fat diet exacerbates cognitive decline in mouse models of alzheimer's disease and mixed dementia in a sex-dependent manner. *J Neuroinflamm* (2022) 19(1):1–20. doi: 10.1186/s12974-022-02466-2

85. Nada M-B, Fuss J, Trusel M, Galsworthy MJ, Bobsin K, Colacicco G, et al. The puzzle box as a simple and efficient behavioral test for exploring impairments of general cognition and executive functions in mouse models of schizophrenia. *Exp Neurol* (2011) 227(1):42–52. doi: 10.1016/j.expneurol.2010.09.008

86. Eltokhi A, Kurpiers B, Pitzer C. Behavioral tests assessing neuropsychiatric phenotypes in adolescent mice reveal strain-and sex-specific effects. *Sci Rep* (2020) 10(1):1–15. doi: 10.1038/s41598-020-67758-0

frontiers | Frontiers in Immunology

TYPE Original Research
PUBLISHED 13 October 2022
DOI 10.3389/fimmu.2022.1021384

OPEN ACCESS

EDITED BY
Brian J. Ferguson,
University of Cambridge,
United Kingdom

REVIEWED BY
Jing Zou,
Xiangya Hospital, Central South University, China
Qiang Liu,
University of Saskatchewan, Canada
Yong Huang,
Northwest A&F University, China

*CORRESPONDENCE
Jianzhong Zhu
jzzhu@yzu.edu.cn

†These authors have contributed equally to this work

SPECIALTY SECTION
This article was submitted to Molecular Innate Immunity, a section of the journal Frontiers in Immunology

RECEIVED 17 August 2022
ACCEPTED 28 September 2022
PUBLISHED 13 October 2022

CITATION
Xia N, Zheng W, Jiang S, Cao Q, Luo J, Zhang J, Xu Y, Sun S, Zhang K, Chen N, Meurens F and Zhu J (2022) Porcine cGAS-STING signaling induced autophagy inhibits STING downstream IFN and apoptosis. *Front. Immunol.* 13:1021384. doi: 10.3389/fimmu.2022.1021384

Porcine cGAS-STING signaling induced autophagy inhibits STING downstream IFN and apoptosis

Nengwen Xia[1,2,3,4†], Wanglong Zheng[1,2,3,4†], Sen Jiang[1,2,3,4], Qi Cao[1,2,3,4], Jia Luo[1,2,3,4], Jiajia Zhang[1,2,3,4], Yulin Xu[1,2,3,4], Shaohua Sun[1,2,3,4], Kaili Zhang[1,2,3,4], Nanhua Chen[1,2,3,4], François Meurens[5,6] and Jianzhong Zhu[1,2,3,4*]

[1]Comparative Medicine Research Institute, Yangzhou University, Yangzhou, China, [2]College of Veterinary Medicine, Yangzhou University, Yangzhou, China, [3]Joint International Research Laboratory of Agriculture and Agri-Product Safety, Yangzhou, China, [4]Jiangsu Co-innovation Center for Prevention and Control of Important Animal Infectious Diseases and Zoonoses, Yangzhou University, Yangzhou, China, [5]Unit of Biology, Epidemiology and Risk Analysis in Animal Health (BIOEPAR), French National Institute for Agriculture, Food, and Environment (INRAE), Oniris, Nantes, France, [6]Department of Veterinary Microbiology and Immunology, Western College of Veterinary Medicine, University of Saskatchewan, Saskatoon, SK, Canada

The innate immune DNA sensing cGAS-STING signaling pathway has been widely recognized for inducing interferons (IFNs) and subsequent antiviral state. In addition to IFN, the cGAS-STING pathway also elicits other cell autonomous immunity events including autophagy and apoptosis. However, the downstream signaling events of this DNA sensing pathway in livestock have not been well defined. Here, we systematically analyzed the porcine STING (pSTING) induced IFN, autophagy and apoptosis, revealed the distinct dynamics of three STING downstream events, and established the IFN independent inductions of autophagy and apoptosis. Further, we investigated the regulation of autophagy on pSTING induced IFN and apoptosis. Following TBK1-IRF3-IFN activation, STING induced Atg5/Atg16L1 dependent autophagy through LIR motifs. In turn, the autophagy likely promoted the pSTING degradation, inhibited both IFN production and apoptosis, and thus restored the cell homeostasis. Therefore, this study sheds lights on the molecular mechanisms of innate immunity in pigs.

KEYWORDS

cGAS-STING pathway, porcine, interferon, autophagy, apoptosis, regulation

Introduction

Innate immune response is the first barrier for the host to resist pathogen invasion. It recognizes pathogen associated molecular patterns (PAMPs) or damage associated molecular patterns (DAMPs) through pattern recognition receptors (PRRs), to trigger downstream signaling cascades and exert strong immune responses (1). The innate DNA receptor cGAS recognizes self and non-self double stranded DNA and synthesizes the second messenger 2'3'-cGAMP, which binds STING on endoplasmic reticulum (ER) and triggers the STING translocation from ER. Next, the STING recruits TBK1 which activates IRF3 and NF-κB transcriptions (2, 3). The gene transcriptions generate downstream interferons (IFNs), IFN stimulated genes (ISGs), and proinflammatory cytokines, playing an important antiviral role in virus infections (2, 3). Recently, accumulating evidences have shown that cGAS-STING pathway is involved not only in the IFN induction, but also in autophagy and cell death, which also have anti-virus and/or anti-tumor functions (4, 5).

Autophagy is a primary protective mechanism that allows cells to cope with a series of stressors and to maintain cellular and physiological homeostasis (6). The cGAS-STING pathway has been proved to induce autophagy in mammals, fruit flies and sea anemones, and this function was identified earlier than IFN during evolution (7, 8). Both cGAS and STING induce canonical autophagy as well as non-canonical autophagy (9). STING induces canonical autophagy through ER stress and mammalian target of rapamycin (mTOR) signaling pathway (10). Additionally, STING also induces non-canonical autophagy through the interaction with microtubule associated protein I light chain 3 (LC3) protein (7, 11, 12). STING induced autophagy is usually independent of TBK1 and IRF3 activation, but dependent on Atg5, Atg16L1 and Atg7 (11–13).

STING has been reported to be involved in regulating several types of cell death, including apoptosis, necroptosis, pyroptosis, ferroptosis and so on (4, 14). Apoptosis, also known as the non-inflammatory type of programmed cell death, is one of the most widely studied cell death pathways (15). At present, the mechanism of STING induced apoptosis is not clear; nevertheless, most studies point to ER stress (16–20). Under different conditions including agonist stimulation, gain-of-function mutation, bacterial infection or ethanol treatment, STING and ER stress are linked to trigger apoptosis, through an evolutionarily conserved unfolded protein response (UPR) motif (18). Alternatively, STING may induce apoptosis through downstream IRF3 or NF-κB (16, 17, 21, 22), where STING mainly mediates the phosphorylation of IRF3 and triggers the formation of IRF3-Bax complex (16, 17, 21).

Although the cGAS-STING induced autophagy and apoptosis in humans and mice have been extensively studied, the mechanisms in an important animal species such as the pig are still unknown or unclear. Further, as the STING downstream signaling events, IFN, autophagy and apoptosis all play a role in anti-virus or anti-tumor immunity, it is thus necessary to clarify the relationships between all these events induced by STING. In this study, we found that porcine STING (pSTING) signaling activates IFN, autophagy and apoptosis with the peak levels appearing in sequence, with autophagy and apoptosis inductions independently of IFN. In addition, autophagy inhibited both IFN production and apoptosis occurrence, restoring the cell homeostasis.

Materials and methods

Chemical reagents and antibodies

TRIpure Reagent for RNA extraction was obtained from Aidlab (Beijing, China). 2×Taq Master Mix (Dye plus) were from Vazyme Biotech Co.,Ltd (Nanjing, China). Poly I:C-LMW, 2'3'-cGAMP and poly dA:dT were bought from InvivoGen (Hong Kong, China). The Golden Star T6 Super PCR mix polymerase was from Tsingke (Nanjing, China) and the KOD plus neo polymerase was from Toyobo (Shanghai, China). Annexin V/propidium iodide (PI) were purchased from Becton Dickinson Company (BD; Franklin Lakes, NJ, USA).

The rabbit mAbs of HA (3724S), LC3I/II (3868), cleaved caspase3 (Asp175) (9664S), TBK1 (3504S), p-TBK1 (5483S), IRF3 (11904S), FLAG (14793), GFP (2956) and β-actin (5057) were acquired from Cell Signaling Technology (Boston, MA, USA). The phosphorylated-IRF3 (Ser396) rabbit mAb (MA5-14947), Goat anti-rabbit IgG (H+L) cross-adsorbed 488 (35553) were from ThermoFisher Scientific (Shanghai, China), The mCherry rabbit pAb (ab183628) and Goat anti-mouse IgG H&L Alexa Fluor®594 (ab150120) were acquired from Abcam (Cambridge, UK). The STING rabbit pAb (19851-1-AP), Bax rabbit pAb (50599-2-lg), Bcl2 mouse mAb (60178-1-lg), Atg5 rabbit pAb (10181-2-AP), Atg16L1 mouse mAb (67943-1-Ig), were all purchased from ProteinTech (Wuhan, China). The HA mouse mAb, GFP mouse mAb, HRP anti-mouse IgG (HS201), and HRP anti-rabbit IgG (HS101) were all acquired from Transgen Biotech (Beijing, China).

Cells and cell transfection

HEK293T was cultured in DMEM (Hyclone Laboratories, USA) containing 10% fetal bovine serum (FBS) and 100 IU/mL of penicillin plus 100 mg/ml streptomycin. Porcine alveolar macrophages (3D4/21, ATCC CRL-2843™) were cultured in RPMI (Hyclone Laboratories) containing 10% FBS with penicillin/streptomycin. All cells were maintained at 37°C with 5% CO2 in a humidified incubator. Cell transfection was

performed by using the Lipofectamine 2000 (ThermoFisher Scientific, Shanghai, China) following the manufacturer's instructions. The Vesicular Stomatitis Virus (VSV-GFP) and Herpes Simplex Virus-1 (HSV-1-GFP) were both provided by Dr. Tony Wang in SRI International USA, and used as we described previously (23).

STING molecular cloning and gene mutations

The HA tagged pcDNA DEST^{47} plasmids of pcGAS and pSTING were previously constructed and have been used in our laboratory (24). The pSTING was PCR amplified from pcDNA DEST^{47}-pSTING-2HA using 2×Taq Master Mix (Dye plus) and the designed primers as presented in Supplementary Table S1. The PCR product was cloned into the *Bgl* II and *EcoR* I sites of pmCherry-C1 vector. The mutation PCR primers of pSTING were designed by QuickChange Primer Design method (https://www.agilent.com) and shown in Supplementary Table S1. The mutation PCR was performed with KOD plus neo polymerase and pcDNA-DEST^{47}-pSTING-2HA or pmCherry-C1-pSTING as the templates. The PCR products were transformed into competent DMT *E.coli* after *Dpn* I digestion, and the resultant mutants were sequence confirmed.

Preparation of homozygous KO 3D4/21 cell clones by CRISPR-Cas9 approach

The CRISPR gRNAs targeting porcine Atg5 and Atg16L1 were designed using the web tool from Benchling (www.benchling.com). For each gene, two pairs of gRNAs were selected according to the prediction score. The DNA sequences encoding all gRNA are shown in Supplementary Table S2. The annealed gRNA encoding DNA sequences were cloned into the *Bbs*I site of pX458-EGFP and the recombinant pX458-gRNA plasmids were sequence confirmed. 3D4/21 cells grown in 6-well plates (6-8×10^5 cells/well) were co-transfected with each pX458-gRNA using Lipofectamine 2000. Twenty four hours later, the GFP positive cells were sorted by flow cytometry and grown in 96-well plates by limiting dilution for monoclonal growth. The single clones of 3D4/21 cells were used to detect the protein expression of Atg5 or Atg16L1 by Western blotting. All 3D4/21 cell clones were detected for genomic DNA editing by PCR using primers shown in Supplementary Table S2. Specifically, the genomic PCR products were cloned into T vector using pClone007 versatile simple vector kit (TsingKe Biological Technology, Beijing, China) and inserted fragments were sequenced and analyzed for base insertion and deletion (ins/del) mutations. Finally, homologous KO cell clones were obtained for both Atg5 and Atg16L1, respectively.

RNA extraction and reverse transcription-quantitative PCR

Total RNA was extracted using TRIpure reagent following the manufacturer's suggestions. The extracted RNA was reverse transcribed into cDNA using HiScript 1st strand cDNA synthesis kit, and then the target gene expressions were measured by quantitative PCR with SYBR qPCR master Mix (Vazyme, Nanjing, China) in StepOne Plus equipment (Applied Biosystems). The qPCR program is denaturation at 94°C for 30 s followed by 40 cycles of 94°C for 5 s and 60°C for 30 s. The relative mRNA levels were normalized to β-actin mRNA levels, and calculated using $2^{-\Delta\Delta CT}$ method. The sequence of qPCR primers used are shown in Supplementary Table S3.

Western blotting detection

Whole cell proteins were extracted with an RIPA lysis buffer. Then, the concentration of lysate protein was analyzed and adjusted using the BCA protein assay kit (Beyotime Institute of Biotechnology, Shanghai, China). The protein samples were mixed at the ratio of 3:1 with 4 × loading buffer and boiled for 10 min. The protein supernatants were run by SDS-PAGE, and then the proteins in the gel were transferred to PVDF membranes. The membranes were incubated with 5% skim milk solution at room temperature (RT) for 2 h, probed with the indicated primary antibodies at 4°C overnight, washed, and then incubated with secondary antibodies for 1 h at RT. The protein signals were detected by ECL detection substrate and imaging system.

Cell apoptosis analysis

The level of cell apoptosis was examined using the Annexin V-fluorescein isothiocyanate (FITC) apoptosis detection kit. Briefly, after treatment, the cells were harvested and washed with the binding buffer, and then resuspended in the binding buffer. The staining solutions of Annexin V-FITC and PI were added one by one. The cells were incubated at RT for 15 min in the dark, and the stained cells immediately detected using flow cytometry. The ratios of Annexin positive cells including PI negative and positive were calculated as the levels of apoptotic cells.

Confocal microscopy

3D4/21 cells grown on 15 mm glass bottom cell culture dish (NEST, Wuxi, China) were transfected with pSTING-HA or pSTING mutants and pCMV-GFP-LC3II (D2815, Beyotime,

Shanghai, China), using Lipofectamine 2000. Twenty-four hours later, the cells were fixed with 4% paraformaldehyde at RT for 30 min, and permeabilized with 0.5% Triton X-100 for 20 min. After washing with PBS, the cells were sequentially incubated with primary LC3I/II rabbit pAb (1:200) and HA mouse mAb (1:200), and next secondary Donkey anti-rabbit IgG Alexa Fluor 488 (1:800), Goat anti-mouse IgG H&L Alexa Fluor 594 (1:800). The stained cells were counter-stained for cell nucleus with 0.5mg/mL 4',6-diamidino-2-phenylindole (DAPI, Beyotime, China) at 37°C for 15 min. Lastly, cells were visualized under laser-scanning confocal microscope (LSCM, Leica SP8, Solms, Germany) at the excitation wavelengths 488 nm and 594 nm, respectively.

Statistical analysis

All of the experiments were representative of two or three similar experiments. The results were analyzed by using SPSS and presented as the mean ± standard deviation (SD) of triplicate samples (n=3). Statistical analysis was performed by using Student's *t*-test and *ANOVA*. * denotes $p < 0.05$, ** denotes $p < 0.01$ and $p < 0.05$ is considered statistically significant.

Results

Activation of porcine cGAS-STING signaling pathway induces autophagy

First, we expressed porcine cGAS (pcGAS) and porcine STING (pSTING) in transfected 293T cells and the various cell signaling pathways were examined by Western blotting (Figure 1A and Figure S1). The expression of pSTING but not pcGAS activated the phosphorylation of TBK1 (p-TBK1), indicating an IFN response, and the co-expression of pcGAS intensified the pSTING activated p-TBK1 (Figure 1A). Similarly, the ectopic pSTING expression induced autophagy as evidenced by the conversion of LC3I to LC3II, the indicator of LC3 lipidation and the co-expression of pcGAS further enhanced the LC3 lipidation (Figure 1A). In addition, pSTING activated both p-TBK1 and LC3 lipidation in a pSTING dose dependent manner (Figure 1B and Figure S1).

Second, porcine macrophages 3D4/21 were stimulated by the transfection of STING specific agonist 2'3'-cGAMP (Figure 1C and Figure S1) or cGAS agonist poly dA:dT (Figure 1D and Figure S1), and the p-TBK1 and LC3 lipidation were examined. The 2'3'-cGAMP activated p-TBK1

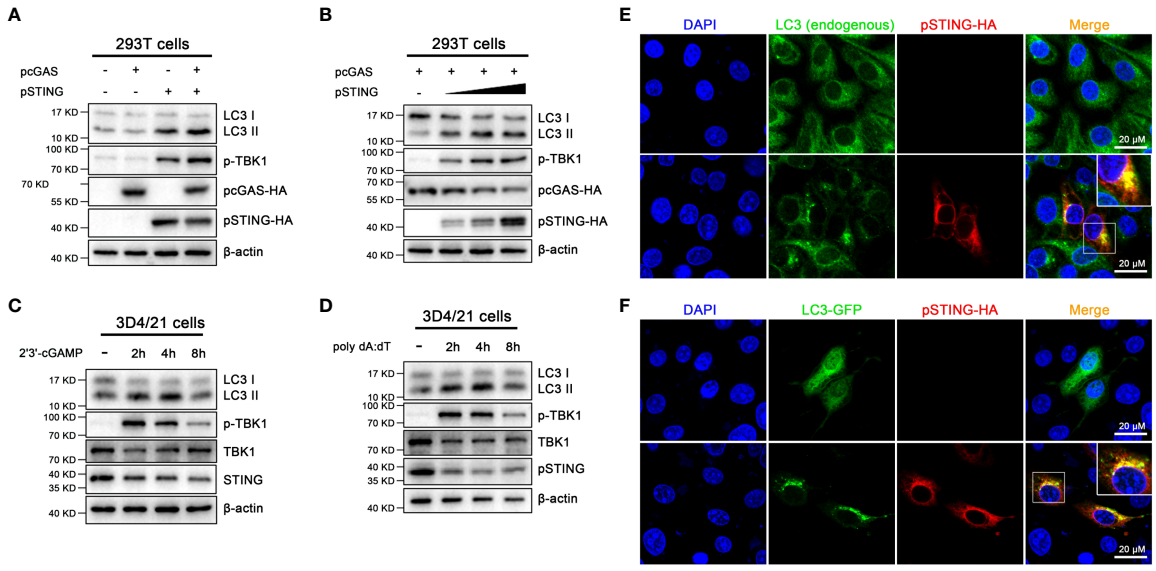

FIGURE 1
Activation of porcine cGAS-STING signal causes autophagy. **(A)** 293T cells were transfected with the indicated pcDNA encoded pcGAS (0.5 μg), pSTING (0.5 μg) with HA tags. **(B)** 293T cells were co-transfected with pcGAS (0.5 μg) and pSTING at different amounts (0, 0.125, 0.25 and 0.5 μg) for 24 h **(C, D)** 3D4/21 cells were stimulated by transfection of 2'3'-cGAMP or poly dA:dT (1 μg/mL) for the indicated times. Western blotting were performed to detect the LC3I/II protein expressions. **(E)** 3D4/21 cells were transfected with the pcDNA-pSTING-2HA (1 μg) for 24 h **(F)** 3D4/21 cells were co-transfected with pcDNA-pSTING-2HA and LC3-GFP for 24 h The confocal microscope was used to analyze the formations of endogenous and exogenous LC3 puncta, indicators of phagosomes. The small insets are magnified on the up-right corner. Scale bar: 20 μm.

with peaking level at 2 h post stimulation, whereas the LC3 lipidation peaked at 4 h post stimulation (Figure 1C). Similarly, poly dA:dT activated p-TBK1 and LC3 lipidation with peak levels at 2 and 4 h post stimulation, respectively (Figure 1D).

Third, the autophagy induction was further validated by observation for LC3 autophagosome formations under fluorescence microscopy (Figures 1E, F). In normal 3D3/21 cells, both endogenous and exogenous LC3 were diffusely distributed in cytoplasm; upon ectopic pSTING expression, both endogenous and exogenous LC3 presented as puncta indicative of autophagosome formations, which were also co-localized with ectopic pSTING (Figures 1E, F).

Activation of porcine cGAS-STING signaling pathway induces apoptosis

We found that the activation of porcine cGAS-STING signaling pathway seriously affected cell growth; therefore, the effects of cGAS-STING signaling on cell apoptosis in 293T and 3D4/21 cells were analyzed using annexin V staining followed by flow cytometry. As shown in Figures 2A, B, the ratios of cell apoptosis in pcGAS and pSTING co-transfected 293T cells was significantly higher relative to control transfected cells. Further, the apoptosis levels increased in the pSTING concentration dependent manner (Figures 2C, D). In 3D4/21 cells, both 2'3'-cGAMP and poly dA:dT stimulations triggered significantly higher levels of apoptosis, with poly dA:dT stimulating more potent apoptosis (Figures 2E, F).

Bcl2 family plays a key role in apoptosis (25), and it is composed of pro-apoptotic members such as Bax and anti-apoptotic members such as Bcl2. The Bax and Bcl2 regulate the mitochondrial outer membrane permeabilization (MOMP), which is the key to induce intrinsic apoptosis (26). Caspase 3, one of the important members of caspase family, is the executor of apoptosis (26). Western blotting showed that the cleaved caspase 3 and the proportion of Bax/Bcl2 markedly increased in a pSTING dose dependent manner in pcGAS/pSTING co-transfected 293T cells (Figure 2G and Figure S2). In 3D4/21 cells, both 2'3'-cGAMP and poly dA:dT stimulations activated the cleaved caspase 3, with the peak levels at 8 h post stimulation, following those of p-IRF3 indicative of IFN induction (2 h post stimulation) and LC3 lipidation indicative of autophagy (4 h post stimulation) (Figures 2H, I and Figure S2).

Porcine STING is essential for autophagy and apoptosis inductions

To check the role of pSTING in the inductions of IFN, autophagy and apoptosis, the STING$^{-/-}$ 3D4/21 cells were used and stimulated with various agonists including 2'3'-cGAMP for STING, poly dA:dT and HSV1 for cGAS, and poly I:C for RIG-I/MDA5, and the downstream cell events were examined by Western blotting (Figure 3 and Figure S3). Consistently, in normal 3D4/21 cells, the IFN response reflected by p-TBK1 appeared and peaked at 2 h post stimulations with 2'3'-cGAMP (Figure 3A) or poly dA:dT (Figure 3B); the autophagy induction evidenced by LC3 lipidation peaked at 4 h post stimulations with 2'3'-cGAMP (Figure 3A) or poly dA:dT (Figure 3B); the apoptosis induction indicated by cleaved caspase 3 peaked at 8 h post stimulations with 2'3'-cGAMP (Figure 3A) or poly dA:dT (Figure 3B). Whereas in STING$^{-/-}$ 3D4/21 cells, the p-TBK1, LC3 lipidation and cleaved caspase 3 all disappeared with both 2'3'-cGAMP and poly dA:dT stimulations (Figures 3A, B). The results of flow cytometry further showed that 2'3'-cGAMP and poly dA:dT induced apoptosis in STING$^{-/-}$ 3D4/21 cells were largely reduced relative to normal 3D4/21 cells (Figures 3C, D).

HSV1 activated cGAS-STING to induce p-TBK1, LC3 lipidation and cleaved caspase 3 in normal 3D4/21 cells, and the three cell events all disappeared in STING$^{-/-}$ 3D4/21 cells (Figure 3E). However, the poly I:C, as control agonist to activate RNA sensors RIG-I and/or MDA5, induced p-TBK1, LC3 lipidation and cleaved caspase 3 in both normal 3D4/21 cells and STING$^{-/-}$ 3D4/21 cells (Figure 3F). Taken together, these results suggest that porcine cGAS-STING signaling pathway induces IFN, autophagy and apoptosis with different dynamics, and pSTING is essential for the inductions of three cellular events.

The pSTING induced apoptosis and autophagy are both IFN independent

It has been known that STING is able to induced IFN independent autophagy (7), and previous studies showed that STING regulates apoptosis through downstream IRF3, but with dispute on the involvement of IFN (16, 27, 28). It has been reported that human STING serine 366 and leucine 374 (equivalent to pSTING S365 and L373) are critical sites for its recruitment and activation of IRF3 and TBK1, respectively, and thus important for subsequent IFN induction (29, 30). The C-terminal tail (CTT) of STING (pSTING residues 340-378), contains both IRF3 and TBK1 recruitment and activation motifs (Figure 4A), are critical for IFN induction (31).

In order to explore whether the inductions of autophagy and apoptosis by STING requires the participation of IFN, we constructed pSTING mutants STING S365A, L373A and ΔCTT, and examined the cellular events in transfected 293T cells by Western blotting (Figure 4B and Figure S4). Consistent with the results in humans and mice, pSTING S365A could not phosphorylate IRF3, but still phosphorylated TBK1, whereas

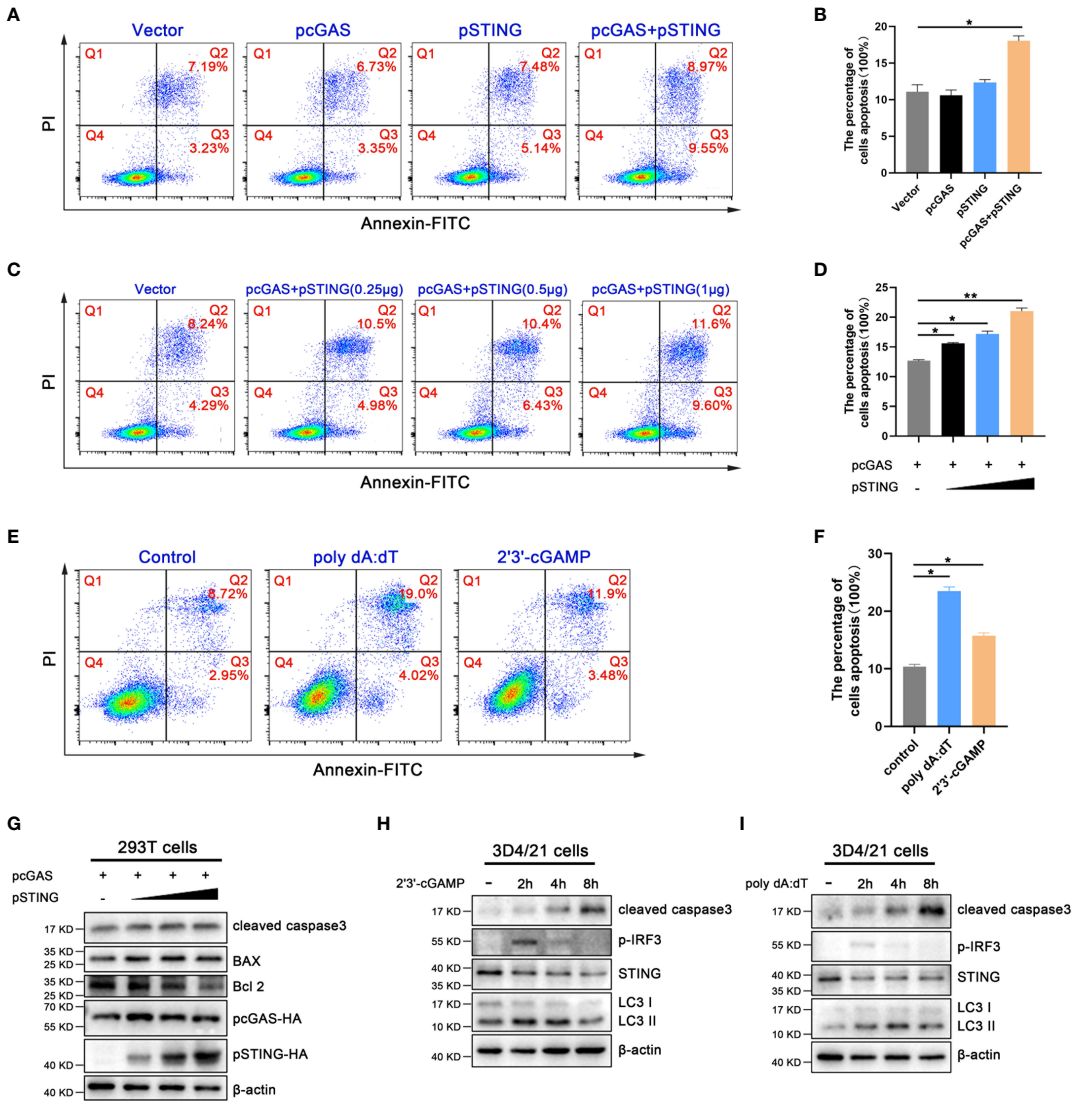

FIGURE 2
Activation of porcine cGAS-STING signal induces apoptosis. **(A, B)** 293T cells were transfected with pcDNA encoded pcGAS (0.5 μg), pSTING (0.5 μg) as indicated. **(C, D)** 293T cells were co-transfected with pcGAS (0.5 μg) plus pSTING at different amounts (0, 0.125, 0.25 and 0.5 μg). **(E, F)** 3D4/21 cells were stimulated by transfection of 2′3′-cGAMP (1 μg/mL) or poly dA:dT (1 μg/mL) for 16 h. Cells were stained with Annexin V and PI followed by flow cytometry analysis. The percentages of cells in each quadrants of dot blots were indicated and apoptotic cell levels were presented in graphs. *$p < 0.05$ and **$p < 0.01$. **(G)** 293T cells were co-transfected with pcGAS (0.5 μg) plus pSTING at different amounts (0, 0.125, 0.25 and 0.5 μg) for 24 h. **(H, I)** 3D4/21 cells were stimulated with 2′3′-cGAMP or poly dA:dT (1 μg/mL) for the indicated times. Cells were analyzed by Western blotting for cleaved caspase 3 expressions.

L373A and ΔCTT could phosphorylate neither one (Figure 4B). On the contrary, all three IFN defective pSTING mutants was able to induce autophagy indicated by LC3 lipidation (Figure 4B). In the meantime, these IFN defective pSTING mutants induced similar levels of apoptosis to wild type pSTING as shown by flow cytometry (Figures 4C, D). Together, these results suggest that pSTING induced autophagy and apoptosis are both IFN independent.

The pSTING exerts IFN independent antiviral effect, likely *via* autophagy and/or apoptosis

It was reported that STING induced autophagy mediate antiviral function (8), and we were curious to know whether the IFN defective pSTING mutants exert antiviral function. In 293T cells, the pSTING mutants S365A, L373A and

10.3389/fimmu.2022.1021384

ΔCTT were co-transfected with pcGAS into 293T cells and subsequently infected by HSV1 or VSV. Surprisingly, all the IFN defective pSTING mutants exhibited similar antiviral effects against HSV1 (Figures 5A, B) and VSV (Figures 5C, D) as wild type pSTING, which was evidenced by viral GFP fluorescence microscopy (Figures 5A, C), viral GFP intensity in flow cytometry (Figures 5A, C), and GFP immunoblotting (Figures 5B, D and Figure S5). The IFN defective pSTING mutants did not induce p-TBK and/or p-IRF3, again confirming the absence of IFN response, whereas these pSTING mutants exhibited normal inductions of LC3 lipidation and cleaved caspase 3 (Figures 5B, D). These results suggest that pSTING exerts its antiviral function likely *via* autophagy and/or apoptosis.

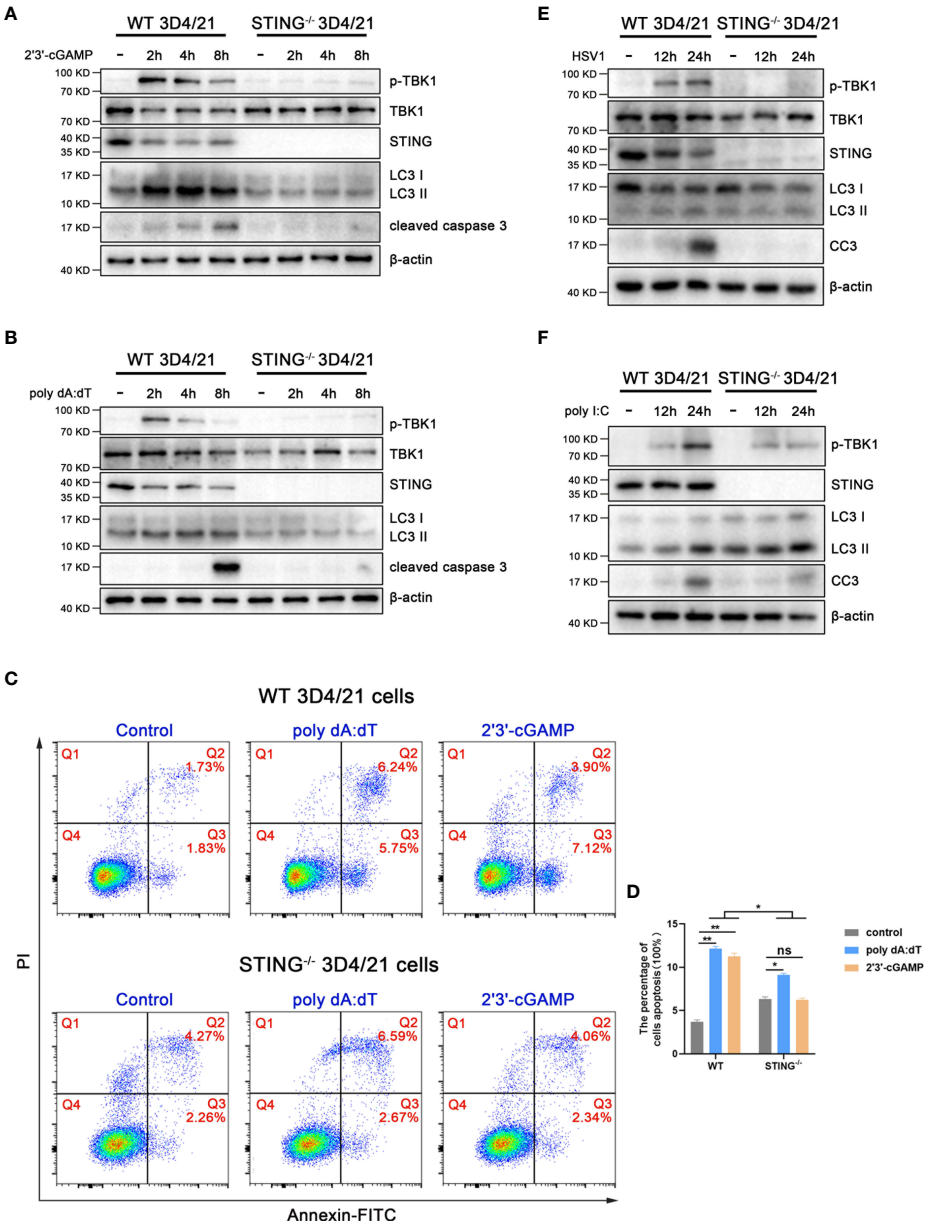

FIGURE 3
STING is essential for autophagy and apoptosis. STING$^{-/-}$ and wild type 3D4/21 cells were stimulated by 2'3'-cGAMP (1 μg/mL) **(A)**, poly dA:dT (1 μg/mL) **(B)**, HSV1 (MOI=0.01) **(E)** or poly I:C (1 μg/mL) **(F)**, respectively. Cells were harvested at the indicated times and analyzed by Western blotting. The abbreviations CC3 in **(E)**, **(F)** and subsequent Figures all denote cleaved caspase 3. **(C, D)** Cells were stimulated with 2'3'-cGAMP or poly dA:dT for 16 h, and the stimulated cells were stained with annexin V and PI followed by flow cytometry for cell apoptosis analysis. ns, not significant; *$p < 0.05$ and **$p < 0.01$.

The pSTING induced autophagy suppresses its IFN response

In order to study the influence of pSTING induced autophagy on IFN response, we constructed two autophagy related gene knockout cells, Atg5$^{-/-}$ and Atg16L1$^{-/-}$ 3D4/21 cells, respectively (Figure S9). Previous studies have shown that STING induced autophagy is Atg5 and Atg16L1 dependent (7, 11, 12), and our results showed that 2'3'-cGAMP stimulated LC3 lipidation disappeared in both Atg5$^{-/-}$ 3D3/21 cells (Figure 6A and Figure S6) and Atg16L1$^{-/-}$ 3D4/21 cells (Figure 6B and Figure S6). In contrast, the levels of p-TBK, p-IRF3 and downstream ISG56 were all upregulated in both gene knockout macrophages (Figures 6A, B), suggesting the negative regulation of IFN response by autophagy.

Further, the mRNA transcriptions of IFNβ and co-regulated genes were examined by RT-qPCR. Upon 2'3'-cGAMP stimulation, the activated IFNβ, ISG15 and CXCL10 mRNA levels were significantly upregulated in both Atg5$^{-/-}$ 3D3/21 cells and Atg16L1$^{-/-}$ 3D4/21 cells relative to those in wild type 3D4/21 cells (Figure 6C). Upon HSV1 infection, the activated IFNβ, ISG15 and TNFα mRNA levels were also significantly upregulated in both Atg5$^{-/-}$ 3D3/21 cells and Atg16L1$^{-/-}$ 3D4/21 cells relative to those in wild type 3D4/21 cells (Figure 6D). These results suggest that pSTING induced autophagy plays a negative regulatory role in its IFN response.

The pSTING induced autophagy inhibits its apoptosis activity

In order to analyze the effect of pSTING activated autophagy on apoptosis, we first examined the caspase 3 cleavage in Atg5$^{-/-}$ 3D4/21 cells by Western blotting (Figures 7A, B and Figure S7). The levels of cleaved caspase 3 were greatly upregulated in Atg5$^{-/-}$ 3D4/21 cells upon 2'3'-cGAMP stimulation (Figure 7A) or HSV1 infection (Figure 7B). Similarly, both poly dA:dT and 2'3'-cGAMP induced cell apoptosis were significantly

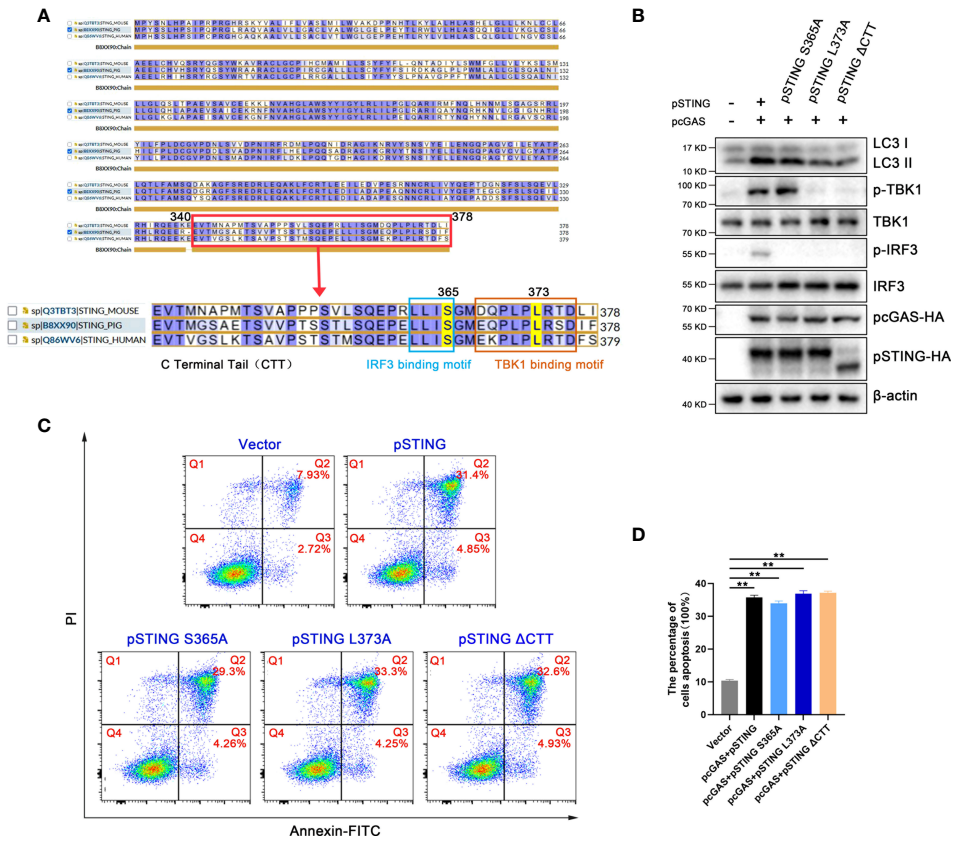

FIGURE 4
The apoptosis and autophagy induced by STING signaling are both IFN independent. **(A)** The alignment of human, mouse and porcine STING with CTT domain enlarged, IRF and TBK1 recruitment motifs box marked. The pSTING S365 in IRF recruitment motif and L373 in TBK1 recruitment motif are also indicated. **(B, D)** 293T cells were co-transfected with pcDNA-pcGAS-2HA (0.5 μg) plus pcDNA-pSTING-2HA, pSTING S365A, pSTING L373A or pSTING ΔCTT (each 0.5 μg) for 24 h, followed by Western blotting **(B)** and flow cytometry **(C, D)**. $^{**}p < 0.01$.

upregulated in Atg5$^{-/-}$ 3D3/21 cells analyzed by flow cytometry (Figures 7C, D).

Simultaneously, the levels of cleaved caspase 3 were also obviously upregulated in Atg16L1$^{-/-}$ 3D3/21 cells upon 2'3'-cGAMP stimulation (Figure 7E and Figure S7). Further, both poly dA:dT and 2'3'-cGAMP induced cell apoptosis were significantly upregulated in Atg16L1$^{-/-}$ 3D4/21 cells as observed by flow cytometry (Figures 7F, G). These results suggest that pSTING induced autophagy plays a negative regulatory role in its apoptosis activity.

LIR motifs participate in pSTING mediated autophagy induction and regulation

A recent study identified STING as an autophagy receptor, which interacts with LC3 through LIR motifs (11). LIR, called LC3 interaction region, is a typical linear amino acid motif, with conserved sequence W/YxxL/I (32). Using the iLIR server to predict potential LIR motifs in the porcine STING protein (33), we identified five hypothetical LIR motifs, with LIRs 1-3 in the transmembrane region of pSTING and LIR4 and 5 in the cyclic dinucleotide-binding domain (CBD) (Figure 8A). To verify the roles of LIR motifs in pSTING induced autophagy, we constructed five LIR motif mutants of pSTING, with the first residue W/Y and the fourth residue L/I in each LIR motif mutated into A, and verified the protein expressions. Western blotting showed that the pcDNA recombinant pSTING LIR4 and LIR5 mutants had very poor protein expressions in transfected 293T cells (Figure 8B and Figure S8). We expressed the pSTING with different doses and ensured the comparable protein expressions of pSTING to various LIR mutants (Figure 8C and Figure S8). Based on comparable protein expression levels, it was concluded that pSTING LIR4 and LIR5 motifs are important for pSTING induced autophagy

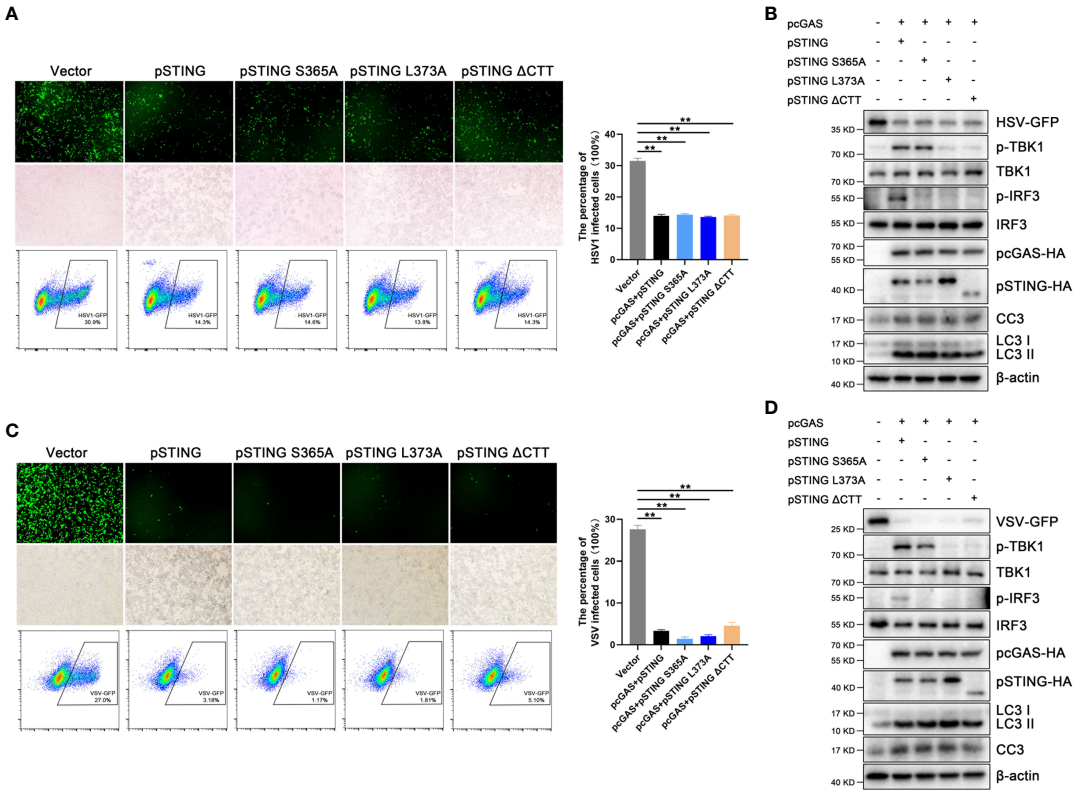

FIGURE 5
STING exerts antiviral effects independent of IFN. **(A, B)** 293T cells were co-transfected with pcDNA-pcGAS-2HA (0.5 μg) plus pcDNA-pSTING-2HA or various mutants (each 0.5 μg) for 24 h, followed by HSV1 (MOI=0.01) infection for another 12 h. $^{**}p < 0.01$. **(C, D)** 293T cells were co-transfected with pcDNA-pcGAS-2HA (0.5 μg) and pcDNA-pSTING-2HA or various mutants (each 0.5 μg) for 24 h, followed by VSV (MOI=0.001) infection for another 8 h. Cells were analyzed for viral GFP signal by fluorescence microscopy, viral GFP intensity by flow cytometry and protein expressions by Western blotting. $^{**}p < 0.01$.

as indicated by LC3 lipidation (Figure 8C and Figure S8). The pmCherry recombinant pSTING LIR mutants further supported the hypothesis that LIR4 and LIR5 motifs are important for pSTING induced autophagy (Figure 8D and Figure S8). Accordingly, the laser confocal microscopy results showed that the accumulations of LC3 puncta in 3D4/21 cells were greatly reduced in LIR4 or LIR5 mutant relative to wild type pSTING. (Figure 8E). Importantly, we found that both LIR4 and LIR5 mutants induced significantly heightened apoptosis relative to wild type pSTING in transfected 293T cells when the pSTING transfection amount was reduced to ensure the equal protein expression as LIR4 and LIR5 mutants (Figures 8F, G), which is consistent with the results from Agt5$^{-/-}$ and Atg16L1$^{-/-}$ macrophages (Figure 7), suggesting that pSTING induced autophagy negatively regulates apoptosis.

Discussion

In this study, we first found that porcine cGAS-STING signaling activation not only induces TBK1-IRF3 mediated IFN response, but also activates Atg5/Atg16L1 dependent autophagy and caspase3 cleavage mediated apoptosis. The IFN, autophagy and apoptosis downstream of pSTING peak in a sequential order. Second, both autophagy and apoptosis inductions are IFN independent, suggesting no regulation of IFN signaling on autophagy and apoptosis. Third, pSTING activated Atg5/Atg16L1 dependent autophagy is LIR motif related and exerts a negative regulation on IFN and apoptosis. Thus, we define the pSTING downstream IFN, autophagy and apoptosis, and are able to make a conclusion for the interrelationship of pSTING downstream IFN, autophagy and

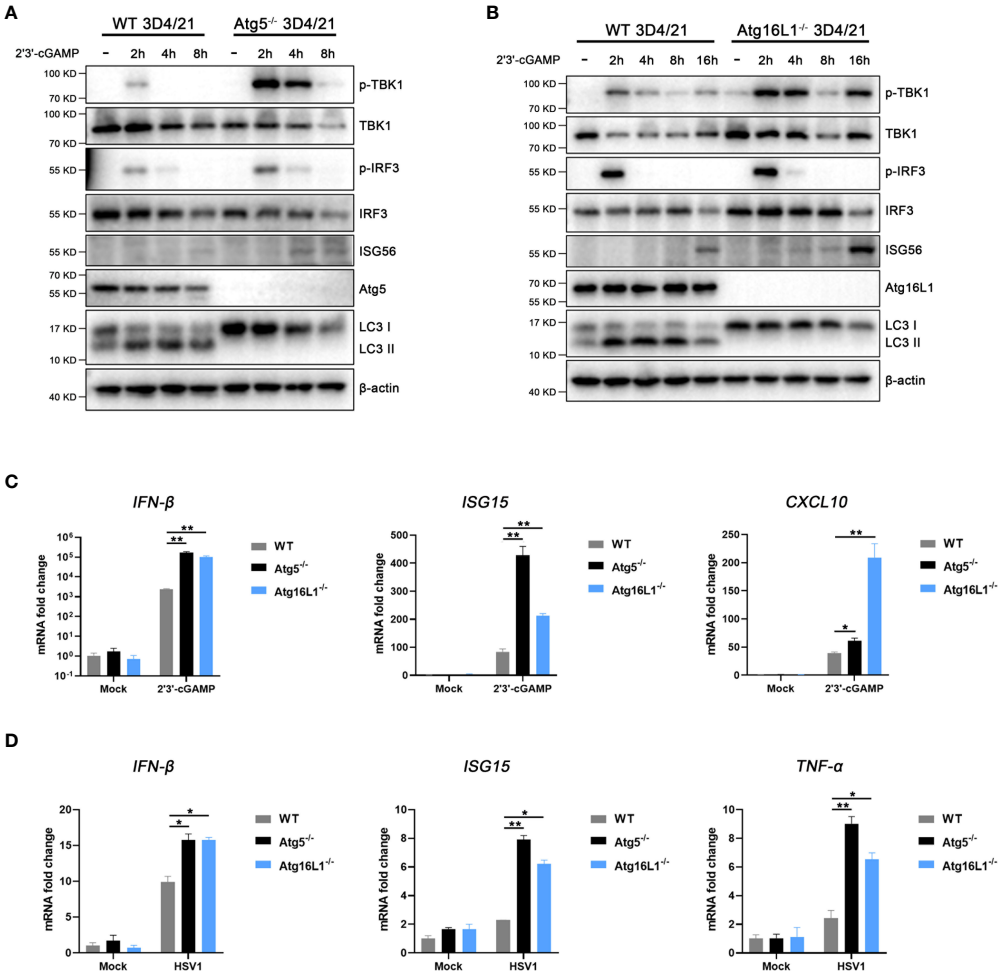

FIGURE 6
STING induced autophagy suppresses IFN signaling. **(A, B)** Wild type and Atg5$^{-/-}$ 3D4/21 cells **(A)** or Atg16L1$^{-/-}$ 3D4/21 cells **(B)** were stimulated by transfection of 2'3'-cGAMP (1 μg/mL) for the indicated times, and cell lysates were analyzed by Western blotting with the indicated antibodies. **(C, D)** Wild-type, Atg5$^{-/-}$ and Atg16L1$^{-/-}$ 3D4/21 cells were stimulated with 2'3'-cGAMP (1 μg/mL) for 4h **(C)** or infected with HSV1 (0.01 MOI) for 8 h **(D)**. The harvested cells were analyzed by RT-qPCR for downstream gene expressions as indicated. *$p < 0.05$ and **$p < 0.01$.

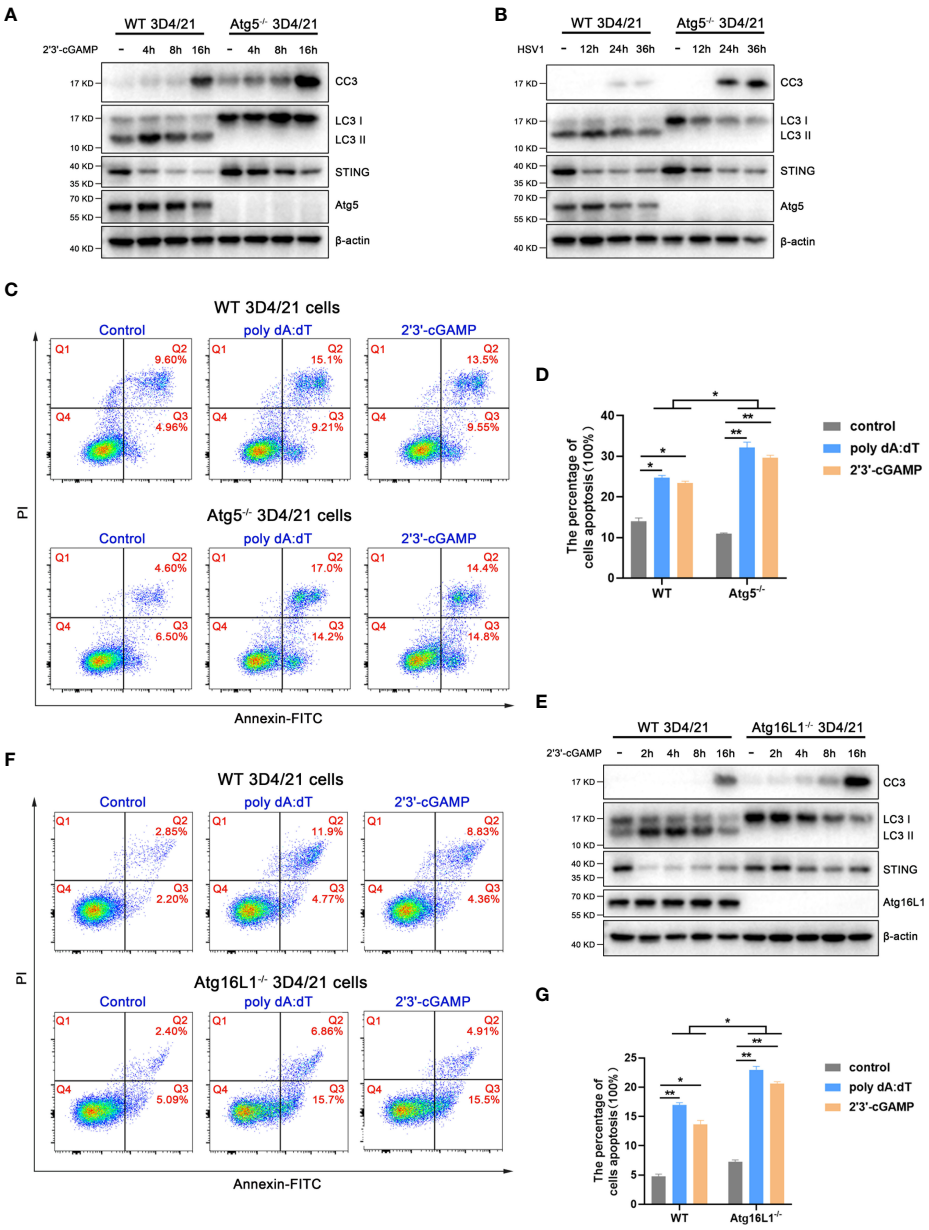

FIGURE 7
STING induced autophagy promotes STING degradation and inhibits apoptosis. **(A, B)** Wild type and Atg5$^{-/-}$ 3D4/21 cells were stimulated by 2'3'-cGAMP (1 μg/mL) **(A)** or HSV1 (0.01 MOI) **(B)** for the indicated times, followed by Western blotting. **(C, D)** Wild type and Atg5$^{-/-}$ 3D4/21 cells were stimulated by poly dAdT or 2'3'-cGAMP (each 1 μg/mL) for 16 h, followed by flow cytometry analysis of cell apoptosis. *$p < 0.05$ and **$p < 0.01$. **(E)** Wild type and Atg16L1$^{-/-}$ 3D4/21 cells were stimulated by 2'3'-cGAMP (1 μg/mL) for the indicated times, followed by Western blotting. **(F, G)** Wild type and Atg16L1$^{-/-}$ 3D4/21 cells were stimulated by poly dA:dT or 2'3'-cGAMP (each 1 μg/mL) for 16 h, followed by flow cytometry analysis of cell apoptosis. *$p < 0.05$ and **$p < 0.01$.

apoptosis, i.e. IFN does not regulate autophagy and apoptosis, and autophagy can negatively regulate IFN and apoptosis.

It is known that STING induces autophagy independently of TBK1-IRF3 activation and IFN signaling (7, 10–12, 34). We confirmed the IFN independent induction of autophagy by pSTING (Figure 4). There are 7 LIR motifs in human STING and LIR4, LIR6 and LIR7 are important for STING autophagy (11). Although only 5 predicted LIR motifs exist in pSTING with LIR1 unique to pSTING, we found that LIR4 and LIR5 in pSTING are associated with autophagy (Figure 8) which

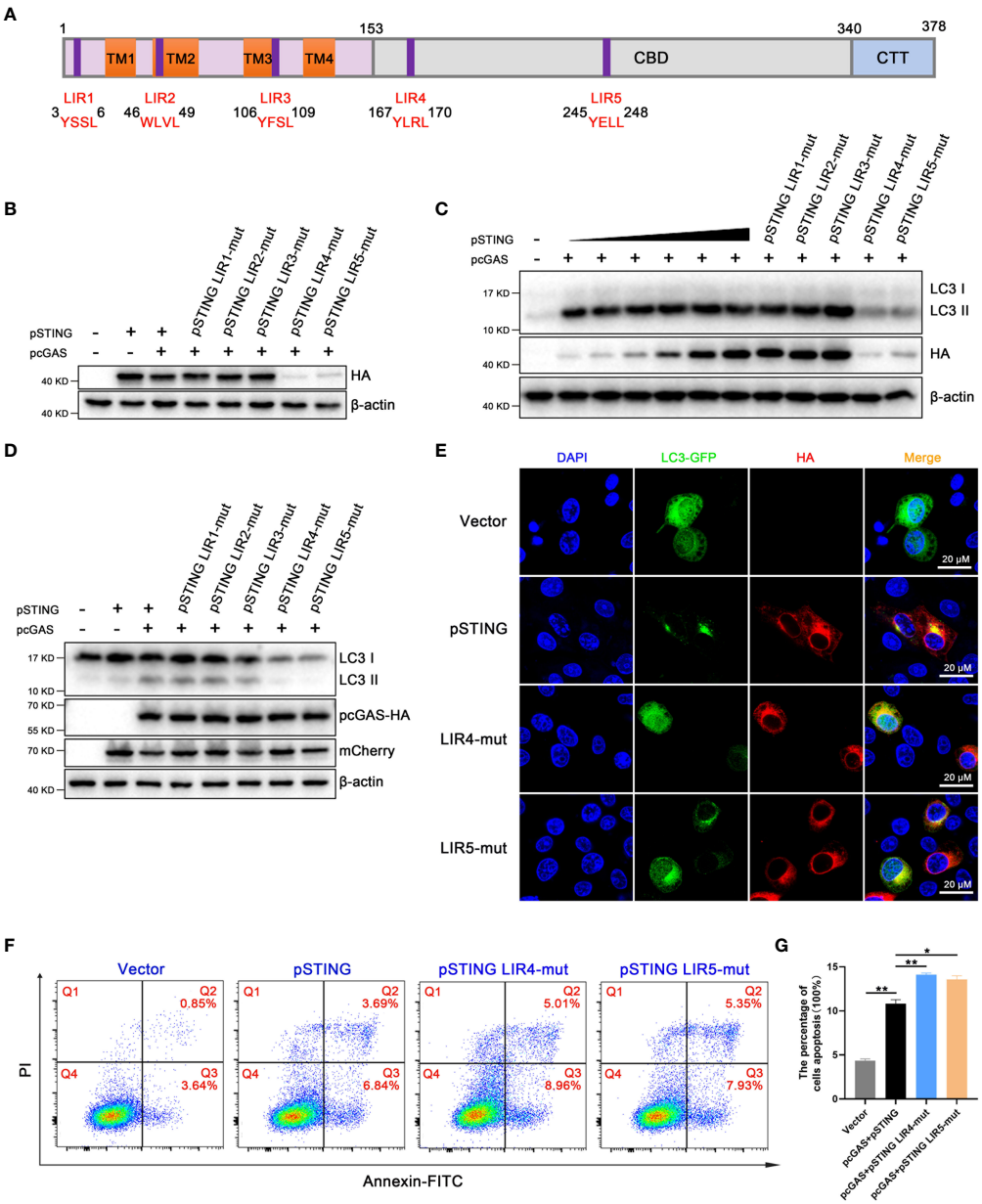

FIGURE 8
LIRs as important motifs participate in STING mediated autophagy regulation. **(A)** Graphical representation of the pSTING showing the five potential LIR motifs. The N-terminal domain contains 4 transmembrane regions (TM1-4), the CBD is c-di-GMP binding domain, and the C-terminal tail (CTT) contains the cytoplasmic tail. The amino acid sequences of the predicted LIR motifs are indicated. **(B)** 293T cells were transfected with pcDNA-pSTING-2HA or corresponding LIR mutants (1μg each) for 24 h, followed by Western blotting. **(C)** 293T cells were co-transfected with pcDNA-pcGAS-2HA (0.5 μg) and pcDNA-pSTING-2HA (0, 0.05, 0.1, 0.2, 0.3, 0.4, 0.5 μg) or corresponding LIR mutants (each 0.5 μg) for 24 h, followed by Western blotting. **(D)** 293T cells were co-transfected with pcDNA-pcGAS-2HA (0.5 μg) plus pmCherry-C1-pSTING or corresponding LIR mutants (0.5 μg) for 24 h, followed by Western blotting. **(E)** 3D4/21 cells were co-transfected with LC3-GFP (0.5 μg) and pSTING-2HA or LIR4-mut or LIR5-mut (0.5 μg each) for 24 h. Images of LC3 and pSTING were then captured by confocal microscopy. Scale bar: 20 μm. **(F, G)** 293T cells were co-transfected with pcGAS-HA (0.5 μg) plus pSTING-HA (0.05 μg), LIR4-mut or LIR5-mut (0.5 μg) for 24 h, and the Annexin V positive cells were detected by flow cytometry. *$p < 0.05$ and **$p < 0.01$.

correspond to LIR 4 and LIR7 in hSTING. The coincident results reflect the conserved function between pigs and human STING.

Whether STING induces apoptosis independently of TBK1-IRF3 activation and IFN signaling is unknown (16–21). Some studies suggested that ER stress is related with STING induced apoptosis (16–20), whereas others showed that the activation of TBK1-IRF3 is required (16, 17, 21). Our results using several IFN defective pSTING mutants including S365A, L373A and ΔCTT clearly showed that the apoptosis induced by pSTING is also independent of TBK1-IRF3 phosphorylation and activation (Figure 4). However, the pSTING induced apoptosis in TBK1$^{-/-}$ and IRF3$^{-/-}$ 3D4/21 cells are largely decreased, suggesting the presence of TBK1 and IRF3 is necessary for the apoptosis (data not shown). The exact mechanism of pSTING induced apoptosis deserves further investigation. Since pSTING induced autophagy and apoptosis are both IFN independent (Figure 4), autophagy and/or apoptosis likely mediate the IFN independent antiviral function of pSTING (Figure 5). Our separate study further showed pSTING exerts an antiviral function independently of both IFN and autophagy, therefore, the antiviral activity of STING appears complex.

Autophagy is originally a self-protection measure for cells to cope with harsh environments such as hunger, stress or pathogen infections (35, 36). Our data showed that it plays a negative regulatory role in the pSTING induced activations of TBK1 and IRF3, and IFN response at early stage of STING activation, as well as in the pSTING induced apoptosis at the late stage of STING activation, thus maintaining cell homeostasis after STING activation. STING has multiple negative feedback regulation mechanisms after activation, including ubiquitin proteasome pathway (37, 38), lysosomal degradation pathway (39) and autophagy mediated degradation (40, 41). Here we observed the pSTING degradation post stimulations, which is accompanied by autophagy (Figures 1 - 3 and Figure 7). Further, under the autophagy knockout conditions, the pSTING degradation weakened, which might be responsible for the heightened IFN response and apoptosis (Figure 6 and 7). Therefore, autophagy may exert homeostatic role by promoting pSTING degradation.

In summary, our work suggests that STING triggered IFN independent activity including autophagy and apoptosis have significant regulatory roles in STING signaling activity. Autophagy plays a negative regulatory role in STING signaling activity by promoting STING degradation. As for the regulatory role of apoptosis in STING signaling activity including IFN and autophagy, it will be investigated in our future study.

Data availability statement

The raw data supporting the conclusions of this article will be made available by the authors, without undue reservation.

Author contributions

JZZ and WZ conceived and designed the experiments; NX, WZ, SJ, QC, JL, JJZ, YX, SS, KZ performed the experiments; WZ, NC, FM, JZZ analyzed the data; NX, WZ and JZZ wrote the paper. All authors contributed to the article and approved the submitted version.

Funding

The work was partly supported by the National Natural Science Foundation of China (32202818; 32172867; 31872450), and A Project Funded by the Priority Academic Program Development of Jiangsu Higher Education Institutions (PAPD).

Conflict of interest

The authors declare that the research was conducted in the absence of any commercial or financial relationships that could be construed as a potential conflict of interest.

The reviewer QL declared a shared affiliation with the author FM to the handling editor at the time of review.

Publisher's note

Supplementary material

The Supplementary Material for this article can be found online at: https://www.frontiersin.org/articles/10.3389/fimmu.2022.1021384/full#supplementary-material

SUPPLEMENTARY FIGURE 1–8
The densitometry analysis of the protein blots in, Figures 1A–D, 2G–I, 3A, B, 3E, F, 4B, 5B, 5D, 6A-B, 7A, B, 7E and 8B-D were presented in Figure S1, Figure S2–S8, respectively. *p < 0.05 and **p < 0.01.

SUPPLEMENTARY FIGURE 9
The genomic DNA sequencing results of porcine Atg5 and Atg16L1 knockout cell clones. The Atg5 **(A–D)** and Atg16L1 **(E–G)** genomic PCR products of 3D4/21 clones were cloned into T vectors and the multiple cloned sequences were aligned with the corresponding Atg genome templates for analysis of base insertion/deletion (ins/del) mutations. For each cell clones, two typical sequences were shown for alignment, with the base ins (+) and del (-) indicated on the right. The red boxed Atg KO cell clones were selected for subsequent experiments.

References

1. Takeuchi O, Akira S. Pattern recognition receptors and inflammation. *Cell* (2010) 140:805–20. doi: 10.1016/j.cell.2010.01.022

2. Sun L, Wu J, Du F, Chen X, Chen ZJ. Cyclic GMP-AMP synthase is a cytosolic DNA sensor that activates the type I interferon pathway. *Science* (2013) 339:786–91. doi: 10.1126/science.1232458

3. Hopfner KP, Hornung V. Molecular mechanisms and cellular functions of cGAS-STING signalling. *Nat Rev Mol Cell Biol* (2020) 21:501–21. doi: 10.1038/s41580-020-0244-x

4. Zhang R, Kang R, Tang D. The STING1 network regulates autophagy and cell death. *Signal Transduct Target Ther* (2021) 6:208. doi: 10.1038/s41392-021-00613-4

5. Wu J, Yan N. No longer a one-trick pony: STING signaling activity beyond interferon. *J Mol Biol* (2022) 434:167257. doi: 10.1016/j.jmb.2021.167257

6. Jin M, Zhang Y. Autophagy and inflammatory diseases. *Adv Exp Med Biol* (2020) 1207:391–400. doi: 10.1007/978-981-15-4272-5_26

7. Gui X, Yang H, Li T, Tan X, Shi P, Li M, et al. Autophagy induction *via* STING trafficking is a primordial function of the cGAS pathway. *Nature* (2019) 567:262–6. doi: 10.1038/s41586-019-1006-9

8. Delorme-Axford E, Klionsky DJ. Inflammatory-dependent sting activation induces antiviral autophagy to limit zika virus in the drosophila brain. *Autophagy* (2019) 15:1–3. doi: 10.1080/15548627.2018.1539585

9. Zheng W, Xia N, Zhang J, Chen N, Meurens F, Liu Z, et al. How the innate immune DNA sensing cGAS-STING pathway is involved in autophagy. *Int J Mol Sci 22* (2021) 22:13232. doi: 10.3390/ijms222413232

10. Moretti J, Roy S, Bozec D, Martinez J, Chapman JR, Ueberheide B, et al. STING senses microbial viability to orchestrate stress-mediated autophagy of the endoplasmic reticulum. *Cell* (2017) 171:809–23.e13. doi: 10.1016/j.cell.2017.09.034

11. Liu D, Wu H, Wang C, Li Y, Tian H, Siraj S, et al. STING directly activates autophagy to tune the innate immune response. *Cell Death Differ* (2019) 26:1735–49. doi: 10.1038/s41418-018-0251-z

12. Fischer TD, Wang C, Padman BS, Lazarou M, Youle RJ. STING induces LC3B lipidation onto single-membrane vesicles *via* the V-ATPase and ATG16L1-WD40 domain. *J Cell Biol* (2020) 219:e202009128. doi: 10.1083/jcb.202009128

13. Yang J, Tang X, Nandakumar KS, Cheng K. Autophagy induced by STING, an unnoticed and primordial function of cGAS. *Cell Mol Immunol* (2019) 16:683–4. doi: 10.1038/s41423-019-0240-2

14. Sun F, Liu Z, Yang Z, Liu S, Guan W. The emerging role of STING-dependent signaling on cell death. *Immunol Res* (2019) 67:290–6. doi: 10.1007/s12026-019-09073-z

15. Xiong Y, Tang YD, Zheng C. The crosstalk between the caspase family and the cGAS–STING signaling pathway. *J Mol Cell Biol* (2021) 13:739–47. doi: 10.1093/jmcb/mjab071

16. Petrasek J, Iracheta-Vellve A, Csak T, Satishchandran A, Kodys K, Kurt-Jones EA, et al. STING-IRF3 pathway links endoplasmic reticulum stress with hepatocyte apoptosis in early alcoholic liver disease. *Proc Natl Acad Sci U.S.A.* (2013) 110:16544–9. doi: 10.1073/pnas.1308331110

17. Cui Y, Zhao D, Sreevatsan S, Liu C, Yang W, Song Z, et al. Mycobacterium bovis induces endoplasmic reticulum stress mediated-apoptosis by activating IRF3 in a murine macrophage cell line. *Front Cell Infect Microbiol* (2016) 6:182. doi: 10.3389/fcimb.2016.00182

18. Wu J, Chen YJ, Dobbs N, Sakai T, Liou J, Miner JJ, et al. STING-mediated disruption of calcium homeostasis chronically activates ER stress and primes T cell death. *J Exp Med* (2019) 216:867–83. doi: 10.1084/jem.20182192

19. Larkin B, Ilyukha V, Sorokin M, Buzdin A, Vannier E, Poltorak A. Cutting edge: Activation of STING in T cells induces type I IFN responses and cell death. *J Immunol* (2017) 199:397–402. doi: 10.4049/jimmunol.1601999

20. Tang CH, Zundell JA, Ranatunga S, Lin C, Nefedova Y, Del Valle JR, et al. Agonist-mediated activation of STING induces apoptosis in malignant b cells. *Cancer Res* (2016) 76:2137–52. doi: 10.1158/0008-5472.CAN-15-1885

21. Sze A, Belgnaoui SM, Olagnier D, Lin R, Hiscott J, van Grevenynghe J. Host restriction factor SAMHD1 limits human T cell leukemia virus type 1 infection of monocytes *via* STING-mediated apoptosis. *Cell Host Microbe* (2013) 14:422–34. doi: 10.1016/j.chom.2013.09.009

22. Guo Q, Chen X, Chen J, Zheng G, Xie C, Wu H, et al. STING promotes senescence, apoptosis, and extracellular matrix degradation in osteoarthritis *via* the NF-κB signaling pathway. *Cell Death Dis* (2021) 12:13. doi: 10.1038/s41419-020-03341-9

23. Li S, Yang J, Zhu Y, Ji X, Wang K, Jiang S, et al. Chicken DNA sensing cGAS-STING signal pathway mediates broad spectrum antiviral functions. *Vaccines (Basel)* (2020) 8:369. doi: 10.3390/vaccines8030369.

24. Jiang S, Luo J, Zhang Y, Cao Q, Wang Y, Xia N, et al. The porcine and chicken innate DNA sensing cGAS-STING-IRF signaling axes exhibit differential species specificity. *J Immunol* (2022) 209:412–26. doi: 10.4049/jimmunol.2101212

25. Czabotar PE, Lessene G, Strasser A, Adams JM. Control of apoptosis by the BCL-2 protein family: implications for physiology and therapy. *Nat Rev Mol Cell Biol* (2014) 15:49–63. doi: 10.1038/nrm3722

26. Galluzzi L, Kepp O, Kroemer G. Mitochondrial regulation of cell death: a phylogenetically conserved control. *Microb Cell* (2016) 3:101–8. doi: 10.15698/mic2016.03.483

27. Li C, Liu W, Wang F, Hayashi T, Mizuno K, Hattori S, et al. DNA Damage-triggered activation of cGAS-STING pathway induces apoptosis in human keratinocyte HaCaT cells. *Mol Immunol* (2021) 131:180–90. doi: 10.1016/j.molimm.2020.12.037

28. Reinert LS, Rashidi AS, Tran DN, Katzilieris-Petras G, Hvidt AK, Gohr M, et al. Brain immune cells undergo cGAS/STING-dependent apoptosis during herpes simplex virus type 1 infection to limit type I IFN production. *J Clin Invest* (2021) 131:e136824. doi: 10.1172/JCI136824

29. Zhang C, Shang G, Gui X, Zhang X, Bai XC, Chen ZJ. Structural basis of STING binding with and phosphorylation by TBK1. *Nature* (2019) 567:394–8. doi: 10.1038/s41586-019-1000-2

30. Liu S, Cai X, Wu J, Cong Q, Chen X, Li T, et al. Phosphorylation of innate immune adaptor proteins MAVS, STING, and TRIF induces IRF3 activation. *Sci* (2015) 347:aaa2630. doi: 10.1126/science.aaa2630

31. Tanaka Y, Chen ZJ. STING specifies IRF3 phosphorylation by TBK1 in the cytosolic DNA signaling pathway. *Sci Signal* (2012) 5:ra20. doi: 10.1126/scisignal.2002521

32. Birgisdottir Å B, Lamark T, Johansen T. The LIR motif - crucial for selective autophagy. *J Cell Sci* (2013) 126:3237–47. doi: 10.1242/jcs.126128

33. Jacomin AC, Samavedam S, Promponas V, Nezis IP. iLIR database: A web resource for LIR motif-containing proteins in eukaryotes. *Autophagy* (2016) 12:1945–53. doi: 10.1080/15548627.2016.1207016

34. Yum S, Li M, Fang Y, Chen ZJ. TBK1 recruitment to STING activates both IRF3 and NF-kappaB that mediate immune defense against tumors and viral infections. *Proc Natl Acad Sci USA* (2021) 118:e2100225118. doi: 10.1073/pnas.2100225118

35. Deretic V, Saitoh T, Akira S. Autophagy in infection, inflammation and immunity. *Nat Rev Immunol* (2013) 13:722–37. doi: 10.1038/nri3532

36. Deretic V, Levine B. Autophagy balances inflammation in innate immunity. *Autophagy* (2018) 14:243–51. doi: 10.1080/15548627.2017.1402992

37. Zhong B, Zhang L, Lei C, Li Y, Mao AP, Yang Y, et al. The ubiquitin ligase RNF5 regulates antiviral responses by mediating degradation of the adaptor protein MITA. *Immunity* (2009) 30:397–407. doi: 10.1016/j.immuni.2009.01.008

38. Wang Y, Lian Q, Yang B, Yan S, Zhou H, He L, et al. TRIM30α is a negative-feedback regulator of the intracellular DNA and DNA virus-triggered response by targeting STING. *PloS Pathog* (2015) 11:e1005012. doi: 10.1371/journal.ppat.1005012

39. Gonugunta VK, Sakai T, Pokatayev V, Yang K, Wu J, Dobbs N, et al. Trafficking-mediated STING degradation requires sorting to acidified endolysosomes and can be targeted to enhance anti-tumor response. *Cell Rep* (2017) 21:3234–42. doi: 10.1016/j.celrep.2017.11.061

40. Konno H, Konno K, Barber GN. Cyclic dinucleotides trigger ULK1 (ATG1) phosphorylation of STING to prevent sustained innate immune signaling. *Cell* (2013) 155:688–98. doi: 10.1016/j.cell.2013.09.049

41. Prabakaran T, Bodda C, Krapp C, Zhang BC, Christensen MH, Sun C, et al. Attenuation of cGAS-STING signaling is mediated by a p62/SQSTM1-dependent autophagy pathway activated by TBK1. *EMBO J* (2018) 37:e97858. doi: 10.15252/embj.201797858

frontiers | Frontiers in Immunology

TYPE Mini Review
PUBLISHED 08 December 2022
DOI 10.3389/fimmu.2022.1075192

OPEN ACCESS

EDITED BY
Hyun Ho Park,
Chung-Ang University, Republic of Korea

REVIEWED BY
Hyung Ho Lee,
Seoul National University, Republic of Korea

*CORRESPONDENCE
Sunghark Kwon
naritsuru@kku.ac.kr

SPECIALTY SECTION
This article was submitted to Molecular Innate Immunity, a section of the journal Frontiers in Immunology

RECEIVED 20 October 2022
ACCEPTED 22 November 2022
PUBLISHED 08 December 2022

CITATION
Kwon S (2022) Molecular dissection of Janus kinases as drug targets for inflammatory diseases.
Front. Immunol. 13:1075192.
doi: 10.3389/fimmu.2022.1075192

Molecular dissection of Janus kinases as drug targets for inflammatory diseases

Sunghark Kwon*

Department of Biotechnology, Konkuk University, Chungju, Chungbuk, Republic of Korea

The Janus kinase (JAK) family enzymes are non-receptor tyrosine kinases that phosphorylate cytokine receptors and signal transducer and activator of transcription (STAT) proteins in the JAK-STAT signaling pathway. Considering that JAK-STAT signal transduction is initiated by the binding of ligands, such as cytokines to their receptors, dysfunctional JAKs in the JAK-STAT pathway can lead to severe immune system-related diseases, including autoimmune disorders. Therefore, JAKs are attractive drug targets to develop therapies that block abnormal JAK-STAT signaling. To date, various JAK inhibitors have been developed to block cytokine-triggered signaling pathways. However, kinase inhibitors have intrinsic limitations to drug selectivity. Moreover, resistance to the developed JAK inhibitors constitutes a recently emerging issue owing to the occurrence of drug-resistant mutations. In this review, we discuss the role of JAKs in the JAK-STAT signaling pathway and analyze the structures of JAKs, along with their conformational changes for catalysis. In addition, the entire structure of the murine JAK1 elucidated recently provides information on an interaction mode for dimerization. Based on updated structural information on JAKs, we also discuss strategies for disrupting the dimerization of JAKs to develop novel JAK inhibitors.

KEYWORDS

janus kinase, signal transducer and activator of transcription, cytokine, autoimmune disorder, kinase inhibitor

Introduction

The Janus kinase (JAK)-signal transducer and activator of transcription (STAT) signaling pathway is involved in various cellular phenomena, such as cell division, apoptosis, inflammatory reactions, and carcinogenesis (1–8). The initial reaction in the JAK-STAT signaling pathway is triggered by binding of extracellular ligands, such as cytokines, to transmembrane type I and II cytokine receptors, which causes receptor dimerization. This multimeric state induces access of JAKs to the dimeric receptor, resulting in autophosphorylation of JAKs. Activated JAKs add phosphate groups to their

receptors, enabling STATs to recognize the phosphorylated receptors. The binding of STATs to their receptors facilitates STAT phosphorylation by JAKs. These activated STATs form dimers and translocate to the cell nucleus. Finally, STATs bind to specific DNA regions, causing transcription of target genes. Because these target genes are associated with many cellular processes, including immunity, the JAK-STAT signaling pathway plays a vital role in immune response (2, 6–8).

JAK proteins are non-receptor tyrosine kinases that are classified into four groups: JAK1, JAK2, JAK3, and tyrosine kinase2 (TYK2) (9, 10). While JAK1, JAK2, and TYK2 are produced in most cell types, JAK3 is produced only in hematopoietic and lymphoid cells (11). Regardless of JAK isoforms, however, JAKs are responsible for immune responses including interferon signaling (12, 13). To perform their biological functions, JAKs form homodimers or heterodimers by binding to the same isoform or other forms. The binary combination of JAKs differs depending on specific receptors that bind their own ligands (7, 14). Each dimeric JAK is involved in specific biological functions, most of which correspond to immune response (7, 14). Accordingly, dysfunctional JAKs can cause severe immune disorders by precluding normal downstream signaling in the JAK-STAT pathway.

Owing to their importance in the JAK-STAT pathway, JAKs have been attractive drug targets to develop inhibitors that block cytokine signaling. Starting with ruxolitinib approved in 2011 (15, 16), numerous JAK inhibitors have been approved and launched in the global pharmaceutical market (17–32). They target one or more than one kinases among JAK1, JAK2, JAK3, and TYK2, accordingly aiming at different indications such as myelofibrosis, rheumatoid arthritis, atopic dermatitis, and psoriasis (13, 14, 33). Several review papers provide valuable information on JAKs and their inhibitors in the treatment of specific indications. Roskoski Jr. introduced JAK inhibitors with a focus on the treatment of neoplastic and inflammatory disorders, along with depiction of structural features of JAKs (13). Huang et al. summarized JAK inhibitors in clinical trials of COVID-19 (14). Inhibition of JAK activities constitutes an effective treatment strategy, in that JAKs are key molecules associated with upstream signal transduction in the JAK-STAT pathway. They also have diverse isoforms and dimeric combinations, depending on specific ligands, including cytokines. In particular, JAK3 can be a suitable drug target to treat adaptive immune disorders, considering that JAK3 kinases are produced in specific cells such as hematopoietic cells and lymphocytes (11).

Although various inhibitors targeting JAKs have been approved and launched, JAK inhibitors have two intrinsic limitations as therapeutic agents, i.e., a lack of selectivity and potential drug resistance. These issues have commonly been raised with other kinase inhibitors (34, 35). Considering that all kinases require an ATP molecule as one of their two substrates, assuming that spatial features of the ATP-binding site are shared to some extent among kinases is reasonable. Indeed, approved JAK inhibitors competitively bind to the ATP-binding site (36–39), which signifies that JAK inhibitors can target not only JAKs but also other kinases. Moreover, mutations in *JAK* genes can create structurally altered JAK proteins, leading to drug resistance to JAK inhibitors by weakening the affinity of JAK inhibitors. Therefore, understanding the mode of inhibition of JAK inhibitors and structural features of JAKs is indispensable for developing novel and specific JAK inhibitors. In addition, the entire structure of murine JAK1 was elucidated recently. This structure showed a unique dimerization mode of JAK1. This structural information can lead to a new approach to the development of JAK inhibitors.

In this review, we describe previously known structures of JAKs to obtain structural insight into their inhibitory mechanisms. We also discuss conformational changes of JAKs for catalysis. Based on updated structural information on JAKs including the entire structure of murine JAK1, the potential inhibitor-binding sites of JAKs are explored to develop novel and specific inhibitors. This review enables us to profoundly understand the molecular biology of JAKs, which can ultimately lead to the development of novel anti-inflammatory agents.

Architecture of JAKs

In general, JAKs consist of seven JAK homology (JH1-7) domains from the C terminus to N terminus (2, 40, 41). The JH1 and JH2 domains correspond to kinase and pseudokinase domains, respectively. The JH3-5 domains form an Src homology 2 (SH2) domain, and the JH6-7 domains correspond to a band-4.1 protein, ezrin, radixin, and moesin (FERM) domain. The SH2 and FERM domains are directly involved in the binding of JAKs to cytokine receptors.

Recently, the entire structure of murine JAK1 in complex with part of the interferon lambda receptor (IFNλR) was determined as a homodimeric form using cryo-electron microscopy (PDB ID: 7T6F) (Figure 1A) (42). Although JAK1 was known to form a heterodimer with other types of JAKs such as JAK2, JAK3, and TYK2 in the cellular environment (14, 43), this dimeric structure provides valuable information on the entire architecture of JAK1 as a snapshot of its active form.

Of the seven domains of JAKs, the JH1 and JH2 domains are directly associated with catalytic function as kinases, although they exhibit different catalytic activities (10, 44, 45). These two domains are structurally similar, along with similarities in amino acid sequences (46). Since all four JAK family members (JAK1-3 and TYK2) are kinases, they share structural features common with those of all kinases. The structure of the JH2 domain of JAK2 (PDB ID: 5I4N) (47) containing an ATP molecule (one of its two substrates) at the active site provides structural information on the ATP-binding mode. The JH2 domain consists of two parts: a small N-terminal lobe and a large

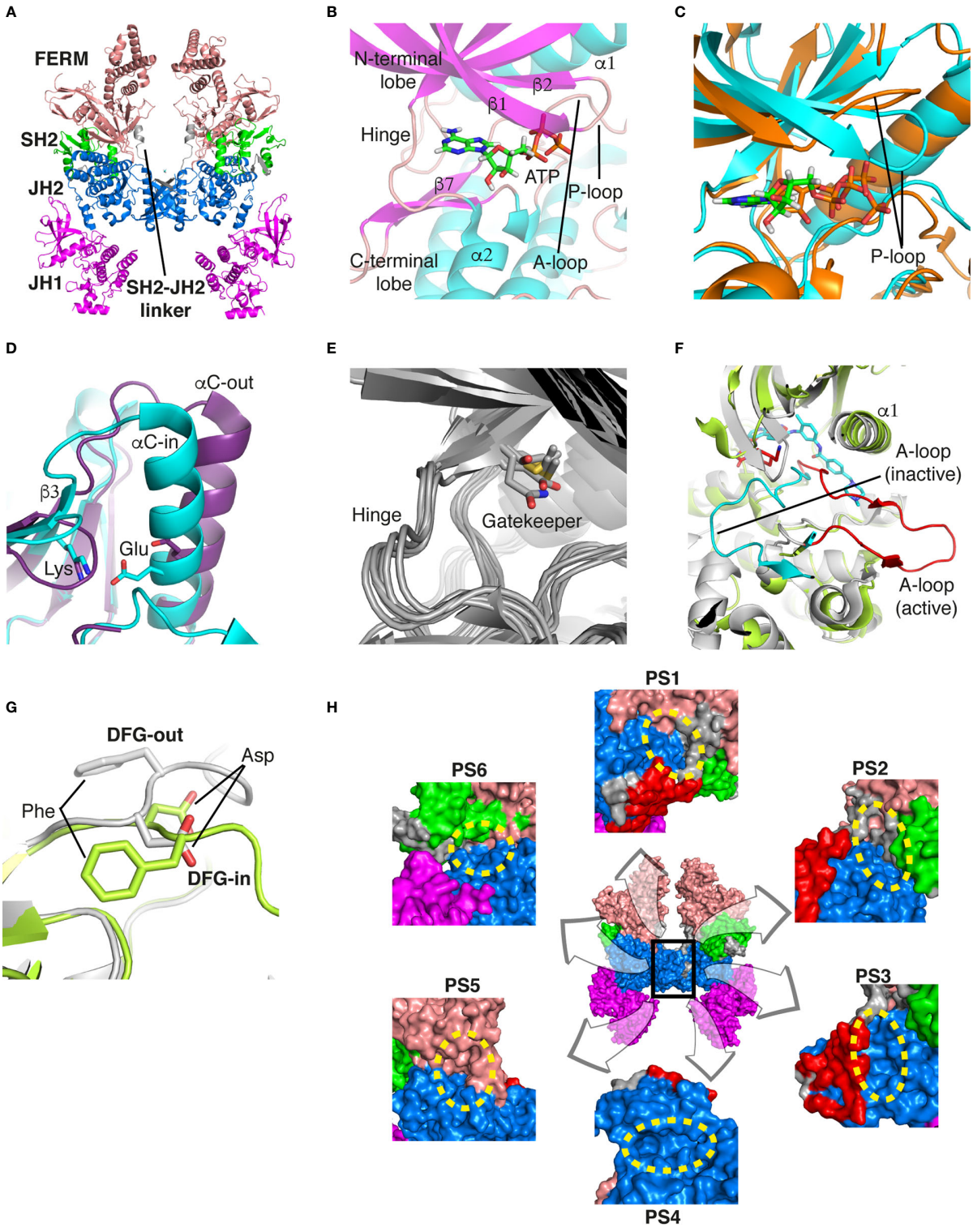

FIGURE 1 (Continued)

FIGURE 1 (Continued)
Structural analysis of JAK. **(A)** The entire structure of murine JAK1 as a dimeric form (PDB ID: 7T6F) is represented as cartoon. IFNΛR is omitted for clarity. The JH1 (magenta), JH2 (marine), SH2 (green), and FERM (salmon) domains are shown. The SH2-JH2 linker is located between the JH2 and SH2 domains. **(B)** The ATP-binding site of the JH2 structure of JAK2 (PDB ID: 5I4N). The JH2 domain is divided into the N- and C-terminal lobes. The ATP molecule is depicted as sticks. **(C)** Different conformations of the P-loop. The ATP-bound form (cyan; PDB ID: 5I4N) is superimposed onto the ADP-bound form (brown; PDB ID: 4GVJ). The adenosine moiety of ATP and ADP is colored green and gray, respectively. **(D)** Two conformations of the C-helix. The αC-in state form (cyan; PDB ID: 5CSW) is superimposed onto the αC-out state form (violet; PDB ID: 5L3A). **(E)** Gatekeeper residues. The four JH1 (PDB ID: 6HZU, 6X8G, 7Q6H, and 7REE) and three JH2 (PDB ID: 4L01, 7AX4, and 7JYQ) domain structures are superimposed onto each other. Met and the other residues are colored yellow and gray, respectively. **(F)** Two conformations of the A-loop: active (red) and inactive (cyan) conformations. The structure of the JH1 domain of JAK1 (limon; PDB ID: 6HZU) is superimposed onto that of an ABL kinase (gray; PDB ID: 1IEP). The A-loops of JAK1 and ABL are colored red and cyan, respectively. Imatinib is represented as sticks. **(G)** Two conformations of the DFG-motif. The DFG-in form (limon; PDB ID: 1IEP) is superimposed onto the DFG-out form (gray; PDB ID: 5L3A). **(H)** Potential inhibitor-binding sites of JAKs. The entire structure of murine JAK1 as a dimeric form is shown in the center, and represented as

C-terminal lobe. The N-terminal lobe is linked to the C-terminal lobe by a hinge region (Figure 1B). These two lobes create a cleft in the linkage region, which constitutes the active site (Figure 1B).

An ATP molecule binds to the active site, which is surrounded by a β-sheet in the N-terminal lobe and the α2 helix in the C-terminal lobe (Figure 1B). A loop connecting the β1 and β2 strands is located next to the α1 helix (Figure 1B). This loop is known as P-loop or G-loop (i.e., a Gly-rich loop). The α1 helix in the N-terminal lobe is called the C-helix (αC) (Figure 1B). The β7 strand in the C-terminal lobe is linked to a relatively long loop (Figure 1B). This loop is called A-loop (i.e., an activation loop). The A-loop can adopt different conformations, including a helical form, in response to substrates binding to the active site.

Conformational changes of JAKs for catalysis

As other kinases have several flexible regions in the proximity of active sites, the active sites of JAKs are also surrounded by several loops along with the C-helix, which undergo conformational changes in response to their substrates or inhibitors. The P-loop is directly associated with positioning of the phosphate groups of ATP. Specifically, the Gly554, Thr555, and Thr557 residues in the P-loop form hydrogen bonds with phosphates. However, owing to the substantial flexibility of this loop, this region appears disordered in several crystal structures. Compared with the ATP-bound form (PDB ID: 5I4N) (47), the P-loop opens outwards in the ADP-bound form (PDB ID: 4GVJ) (48) (Figure 1C). Namely, the P-loop residues do not interact with ADP as tightly as that with ATP. This structural difference seems reasonable, in that ADP, as a product of catalysis needs to be released from the active site.

The C-helix also plays an important role in JAK catalysis. A Lys residue of the conserved AXK motif (X = any amino acid) in the β3 strand can form a salt bridge with a Glu residue in the C-helix at an appropriate position (αC-in state) (Figure 1D; cyan). The Lys residue is a key residue in JAK catalysis, which corresponds to K908 (JAK1), K882 (JAK2), K855 (JAK3), and K930 (TYK2). However, spatial distortion of the C-helix gives rise to a deviation from the C-helix-in state, thereby disrupting the salt bridge (αC-out state) (Figure 1D; violet). Therefore, the C-helix-in state facilitates catalysis by rendering correct position of the Lys residue.

A residue in the β5 strand adjacent to the hinge region is called 'gatekeeper'. The gatekeeper plays a vital role in controlling the access of ATP or inhibitors to the hydrophobic backpocket. This residue varies depending on the type and domain of JAKs. Specifically, JH1 domains of all four JAKs (JAK1, JAK2, JAK3, and TYK2) retain a Met residue as the gatekeeper (Figure 1E). In contrast, Glu (JAK1), Gln (JAK2), and Thr (TYK2) residues are assigned to the same position in JH2 domains (Figure 1E). This gatekeeper is critical for sensitivity to inhibitors. Mutation of the gatekeeper to other residues, such as bulkier residues, can decrease the affinity of inhibitors by causing steric hindrance to inhibitor binding (49).

Remarkably, the A-loop shows two distinct conformations. In the ATP-bound form, the A-loop is located distantly from the P-loop (active conformation) (Figure 1F). This conformation renders the active site constructed, thereby facilitating the binding of ATP and its target protein substrate to the active site. Because this conformation provides the architecture of the ATP-binding pocket, numerous inhibitors have been developed to bind to the ATP-binding site in this active conformation (49). In contrast, in the "rest period" of kinases, the A-loop exhibits a form moved towards the P-loop (inactive conformation) (Figure 1F). However, JAK structures in the inactive conformation have not yet been determined. The inactive conformation of Abl, a tyrosine-protein kinase (PDB ID: 1IEP) (50), is described in this review (Figure 1F). This conformation does not form an ATP-binding pocket. Alternatively, this inactive conformation renders the space between the A-loop and C-helix wider, which implies that this region can be another target site for inhibitors. Indeed, the structure of Abl shown here (PDB ID: 1IEP) contains imatinib as an inhibitor in the inactive conformation (50) (Figure 1F). Consequently, the conformational change in the A-loop is the most striking

structural phenomenon concerning kinase catalysis, which is noteworthy in that this structural information can lead to the development of novel JAK inhibitors.

The conserved DFG-motif is another significant part of the conformational changes involved in catalysis (49). This motif is located at the N terminus of the A-loop. In the active conformation, the Asp residue of the DFG-motif orients inward the ATP-binding site and coordinates with a Mg ion (DFG-in) (Figure 1G; gray). In the inactive conformation, the Asp residue orients outwards from the ATP-binding site, where it cannot coordinate with a Mg ion in the ATP-binding site (DFG-out) (Figure 1G; limon). Therefore, the DFG-motif regulates the catalytic activity of kinases by suitably adopting their respective conformations.

Development strategies for novel JAK inhibitors

In general, kinase inhibitors are classified into six types depending on their binding sites and kinase conformations (types I-VI) (51). Type I inhibitors bind to the ATP binding site in the active conformation (DFG-in and αC-in). Type $I^{1/2}$ inhibitors bind to the same site in an incomplete and inactive conformation (DFG-in and αC-out). Type II inhibitors bind in the inactive conformation (DFG-out and αC-out). In contrast to types I and II, the binding site of type III inhibitors is located near the ATP binding site. Type IV inhibitors bind to an allosteric site far from the ATP binding site. Accordingly, type III and IV inhibitors target allosteric sites, in that they do not bind to the ATP binding site. Type V inhibitors bind to the ATP-binding or allosteric site. Lastly, type VI inhibitors covalently bind to the ATP binding or allosteric site.

To date, all JAK inhibitors launched into the pharmaceutical market are type I inhibitors, except for inhibitors unidentified in the PDB (13). Information on launched JAK drugs is summarized in Table 1. However, type I inhibitors compete with ATP for the same binding site. This signifies that type I inhibitors can bind to other unintended kinases which have ATP-binding sites. Nonspecific binding usually results in unexpected side effects. Therefore, discovering target sites other than the ATP-binding site is of recent interest in developing new inhibitors for a specific kinase. Accordingly, although the current JAK drugs are type I inhibitors, other types of JAK inhibitors can be designed and developed to enhance JAK-binding specificity.

Notably, two monomeric JAKs also form a dimer when two monomeric cytokine receptors form a dimer upon binding a cytokine (13, 14, 43). The resulting JAK dimer facilitates the *trans*-phosphorylation of its counterpart (13, 14, 43). Dimerization of JAKs is a prerequisite for JAK-STAT signaling transfer; therefore disturbing JAK dimerization may constitute a novel strategy for blocking the JAK-STAT signaling pathway at the upstream level. Hubbard proposed a putative mechanism for JAK2 activation (52). In this review, the author explained JAK2 activation with vast conformational changes. According to this hypothesis, monomeric JAK2 exists in the inactive conformation in the equilibrium state (52). Namely, the JH1 domain is attached to the JH2 domain, thereby maintaining the autoinhibited state. When a cytokine binds to its receptor, dimerization of the receptor by the cytokine induces JAK2 dimerization. V617F, a JAK2 mutant in the JH2 domain, which causes myeloproliferative neoplasms, has been previously identified (53–56). This mutant may induce a substantial conformational change in the JH1 domain, resulting in the active conformation of JAK2, despite the absence of a cytokine (52). Moreover, the V617F mutant may reinforce the interface between monomers owing to the bulkier side chain. Consequently, the V617F mutant leads to abnormal JAK-STAT signaling by maintaining its active dimeric form without external stimuli.

The V617 residue of human JAK2 corresponds to the V660 residue of the murine JAK1, which is associated with the dimerization of murine JAK1. The substitution of V660 with Phe presumably increases the hydrophobic interaction between the two Phe residues through π- π stacking. However, determining the extent to which this hydrophobic interaction affects the dimerization is challenging.

As JAK dimerization is a critical step for the *trans*-phosphorylation of the JH1 domain, blocking the dimerization of JAKs may constitute a new paradigm for developing JAK inhibitors. The entire structure of JAK1 (PDB ID: 7T6F) (42) provides structural insight into potential inhibitor-binding sites to block dimerization. However, this structure is that of murine JAK1, not human JAK. Several clefts (PS1-6), which could be novel inhibitor-binding sites, were identified between the JH2 domain and adjacent domains (Figure 1H). The PS1 and PS2 clefts comprise part of the FERM, SH2-JH2 linker, and JH2 domains, whereas the PS3 cleft consists of part of SH2-JH2 linker and JH2. The PS4 cleft corresponds to the ATP-binding site of the JH2 domain. The PS5 cleft, which comprises part of the FERM and JH2 domains, is located at the rear of the JH2 interface. Lastly, the PS6 cleft consists of part of FERM, SH2, SH2-JH2 linker, and JH2. These clefts appear relatively large and sufficiently deep to accept small molecules. Furthermore, all clefts except PS3 are located at the interface of the domains. This implies that the binding of suitable small compounds to the PS clefts might trigger a conformational change in the JH2 domain, thereby affecting and obstructing its dimerization. However, whether these sites induce significant conformational changes remains to be determined.

Discussion

To date, several JAK inhibitors have been approved and launched in the pharmaceutical market. Structures of the

TABLE 1 Human JAK inhibitor profiles[a].

Generic name	Brand name	Target	Type	First Approval year	Approval country	PDB ID[b]	Chemical structure
Ruxolitinib	Jakafi/Jakavi	JAK1, JAK2, JAK3, TYK2	I	2011	US	6VGL	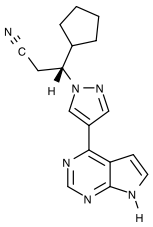
Tofacitinib	Xeljanz	JAK1, JAK2, JAK3, TYK	I	2012	US	3EYG, 3FUP, 3LXK, 3LXN	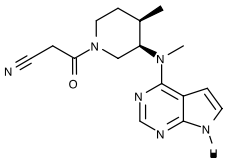
Baricitinib	Olumiant	JAK1, JAK2, TYK2	I	2017/2022	EU/US	6WTO	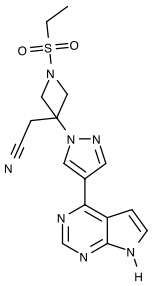
Peficitinib	Smyraf	JAK1, JAK2, JAK3, TYK2	I	2019	Japan	6AAH, 6AAJ, 6AAK, 6AAM	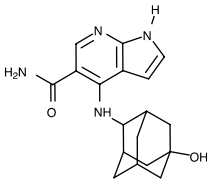
Fedratinib	Inrebic	JAK2	I	2019	US	6VNE	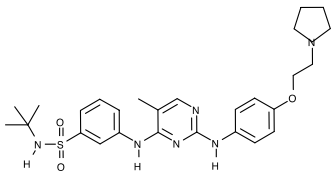
Upadacitinib	Rinvoq	JAK1	–	2019	US	–	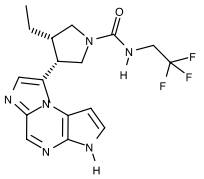
Filgotinib	Jyseleca	JAK1	I	2020	US/Japan	4P7E, 5UT5	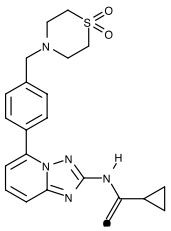

(Continued)

TABLE 1 Continued

Generic name	Brand name	Target	Type	First Approval year	Approval country	PDB ID[b]	Chemical structure
Delgocitinib	Corectim	JAK1, JAK2, JAK3, TYK2	I	2021	Japan	7C3N	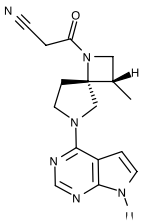
Abrocitinib	Cibinqo	JAK1	I	2021/2022	EU/US	6BBU, 6BBV	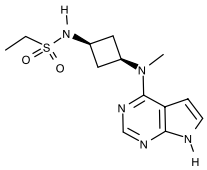
Pacritinib	Vonjo	JAK2	–	2022	US	–	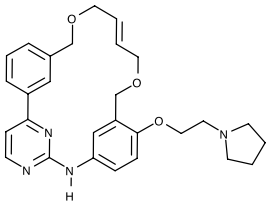

[a] Ref. (13, 14, 33).
[b] Inhibitor-complex structure.

JAK-inhibitor complexes have also been reported (36–39). Such structural information provides insight into the inhibitor-binding modes. However, considering that the affinity of many kinase inhibitors has decreased owing to the occurrence of drug resistance (49), the inhibitory ability of the JAK drugs may also reduce eventually.

The mutation of key residues in the active site of kinases is one of the most prevalent molecular mechanisms underlying inhibitor resistance (49). One of the most common mutation sites is the gatekeeper residue. The size and shape of the gatekeeper residue regulate the access of a molecule binding to the hydrophobic back pocket; therefore mutations in the gatekeeper residue can reduce the affinity of kinase inhibitors to the ATP-binding site. Gatekeeper mutations have also been identified in several kinases (57–60). The A-loop is another mutation site for kinase inhibitor resistance (49). Mutations in the A-loop are more variable than those in gatekeeper mutations. Such mutations affect the binding of inhibitors to kinases in the inactive conformation of the A-loop (49). Mutations in the A-loop typically lower the affinity of the inhibitors for the inhibitor-binding site in the inactive conformation by maintaining the active conformation of the A-loop. Therefore, mutations in the A-loop appear to be critically related to the conformation.

Natural JAK-related mutations associated with inhibitor resistance in patients have not been reported. However, a recent study indicated that several mutations in JAK2 induce resistance to ruxolitinib at the cellular level (61). In this study, the authors reported that the Y931C, L983F, and G993A mutants of murine JAK2 cause acquired resistance to ruxolitinib (61). These residues were associated with the ATP/ruxolitinib binding site. Although these residues may not constitute naturally occuring mutation sites for resistance to ruxolitinib, these *in vitro* results may provide valuable information for developing novel JAK2-inhibitors.

The entire structure of murine JAK1, which was recently elucidated (42), helped us understand the detailed molecular mechanisms of its receptor binding and dimerization. Notably, the dimerization mode of the JH2 domain suggests novel strategies for JAK-inhibitor development. In the JAK-STAT signaling pathway, diverse heterodimers of JAKs except for the JAK2 homodimer are associated with downstream signaling. These combinations include JAK1-JAK2, JAK1-JAK3, and JAK1-TYK2. Although these heterodimeric structures have not been determined, the respective JH2 domains are probably involved in dimerization. If each dimerization mode is the same as in the murine JAK1, the dimerization mode of murine JAK1 may be generalized to all JAK heterodimers. This assumption means that strategies for disrupting dimerization can be applied to these heterodimers. However, the potential inhibitor-binding sites discussed in the previous section are based on the premise that such binding induces significant conformational changes in the JH2 domain to destabilize dimerization. Therefore, future studies should focus on the

discovery of potential inhibitor-binding sites and factors that affect conformational changes to obstruct dimerization.

Author contributions

The author confirms being the sole contributor of this work and has approved it for publication.

Funding

This work was supported by the National Research Foundation of Korea (NRF) grant funded by the Korean Government (MSIT) (2022R1F1A1074928).

Conflict of interest

The author declares that the research was conducted in the absence of any commercial or financial relationships that could be construed as a potential conflict of interest.

Publisher's note

References

1. Garrido-Trigo A, Salas A. Molecular structure and function of janus kinases: Implications for the development of inhibitors. *J Crohns Colitis* (2020) 14 (Supplement_2):S713–24. doi: 10.1093/ecco-jcc/jjz206

2. Villarino AV, Gadina M, O'Shea JJ, Kanno Y. SnapShot: Jak-STAT signaling II. *Cell* (2020) 181:1696–6. doi: 10.1016/j.cell.2020.04.052

3. Katz M, Amit I, Yarden Y. Regulation of MAPKs by growth factors and receptor tyrosine kinases. *Biochim Biophys Acta* (2007) 1773:1161–76. doi: 10.1016/j.bbamcr.2007.01.002

4. Lee JY, Chiu YH, Asara J, Cantley LC. Inhibition of PI3K binding to activators by serine phosphorylation of PI3K regulatory subunit p85alpha src homology-2 domains. *Proc Natl Acad Sci U.S.A.* (2011) 108:14157–62. doi: 10.1073/pnas.1107747108

5. Gadina M, Gazaniga N, Vian L, Furumoto Y. Small molecules to the rescue: Inhibition of cytokine signaling in immune-mediated diseases. *J Autoimmun* (2017) 85:20–31. doi: 10.1016/j.jaut.2017.06.006

6. Mertens C, Darnell JEJr. SnapShot: JAK-STAT signaling. *Cell* (2007) 131:612. doi: 10.1016/j.cell.2007.10.033

7. O'Shea JJ, Plenge R. JAK and STAT signaling molecules in immunoregulation and immune-mediated disease. *Immunity* (2012) 36:542–50. doi: 10.1016/j.immuni.2012.03.014

8. Xin P, Xu X, Deng C, Liu S, Wang Y, Zhou X, et al. The role of JAK/STAT signaling pathway and its inhibitors in diseases. *Int Immunopharmacol* (2020) 80:106210. doi: 10.1016/j.intimp.2020.106210

9. Wilks AF. Two putative protein-tyrosine kinases identified by application of the polymerase chain reaction. *Proc Natl Acad Sci U.S.A.* (1989) 86:1603–7. doi: 10.1073/pnas.86.5.1603

10. Yamaoka K, Saharinen P, Pesu M. Holt VE 3rd, silvennoinen O, O'Shea JJ. the janus kinases (Jaks). *Genome Biol* (2004) 5:253. doi: 10.1186/gb-2004-5-12-253

11. Kawamura M, McVicar DW, Johnston JA, Blake TB, Chen YQ, Lal BK, et al. Molecular cloning of l-JAK, a janus family protein-tyrosine kinase expressed in natural killer cells and activated leukocytes. *Proc Natl Acad Sci U.S.A.* (1994) 91:6374–8. doi: 10.1073/pnas.91.14.6374

12. Hu X, Li J, Fu M, Zhao X, Wang W. The JAK/STAT signaling pathway: from bench to clinic. *Signal Transduct Target Ther* (2021) 6:402. doi: 10.1038/s41392-021-00791-1

13. Roskoski RJr. Janus kinase (JAK) inhibitors in the treatment of neoplastic and inflammatory disorders. *Pharmacol Res* (2022) 183:106362. doi: 10.1016/j.phrs.2022.106362

14. Huang J, Zhou C, Deng J, Zhou J. JAK inhibition as a new treatment strategy for patients with COVID-19. *Biochem Pharmacol* (2022) 202:115162. doi: 10.1016/j.bcp.2022.115162

15. Verstovsek S, Kantarjian H, Mesa RA, Pardanani AD, Cortes-Franco J, Thomas DA, et al. Safety and efficacy of INCB018424, a JAK1 and JAK2 inhibitor, in myelofibrosis. *N Engl J Med* (2010) 363:1117–27. doi: 10.1056/NEJMoa1002028

16. Verstovsek S, Mesa RA, Gotlib J, Levy RS, Gupta V, DiPersio JF, et al. A double-blind, placebo-controlled trial of ruxolitinib for myelofibrosis. *N Engl J Med* (2012) 366:799–807. doi: 10.1056/NEJMoa1110557

17. Deeks ED, Duggan S. Abrocitinib: First approval. *Drugs* (2021) 81:2149–57. doi: 10.1007/s40265-021-01638-3

18. Coricello A, Mesiti F, Lupia A, Maruca A, Alcaro S. Inside perspective of the synthetic and computational toolbox of JAK inhibitors: Recent updates. *Molecules* (2020) 25:3321. doi: 10.3390/molecules25153321

19. Markham A. Baricitinib: First global approval. *Drugs* (2017) 77:697–704. doi: 10.1007/s40265-017-0723-3

20. Rubin R. Baricitinib is first approved COVID-19 immunomodulatory treatment. *JAMA* (2022) 327:2281. doi: 10.1001/jama.2022.9846

21. Blair HA. Fedratinib: First approval. *Drugs* (2019) 79:1719–25. doi: 10.1007/s40265-019-01205-x

22. Pettit K, Rezazadeh A, Atallah EL, Radich J. Management of myeloproliferative neoplasms in the molecular era: From research to practice. *Am Soc Clin Oncol Educ Book* (2022) 42:1–19. doi: 10.1200/EDBK_349615

23. Mascarenhas J, Hoffman R. Ruxolitinib: the first FDA approved therapy for the treatment of myelofibrosis. *Clin Cancer Res* (2012) 18:3008–14. doi: 10.1158/1078-0432.CCR-11-3145

24. Raedler LA. Jakafi (Ruxolitinib): First FDA-approved medication for the treatment of patients with polycythemia Vera. *Am Health Drug Benefits* (2015) 8 (Spec Feature):75–9.

25. Yang W, Zhu G, Qin M, Li Z, Wang B, Yang J, et al. The effectiveness of ruxolitinib for Acute/Chronic graft-versus-Host disease in children: A retrospective study. *Drug Des Devel Ther* (2021) 15:743–52. doi: 10.2147/DDDT.S287218

26. Ayala-Aguilera CC, Valero T, Lorente-Macías Á, Baillache DJ, Croke S, Unciti-Broceta A. Small molecule kinase inhibitor drugs (1995-2021): Medical indication, pharmacology, and synthesis. *J Med Chem* (2022) 65:1047–131. doi: 10.1021/acs.jmedchem.1c00963

27. Kostik MM, Raupov RK, Suspitsin EN, Isupova EA, Gaidar EV, Gabrusskaya TV, et al. The safety and efficacy of tofacitinib in 24 cases of pediatric rheumatic diseases: Single centre experience. *Front Pediatr* (2022) 10:820586. doi: 10.3389/fped.2022.820586

28. Mohanakrishnan R, Beier S, Deodhar A. Tofacitinib for the treatment of active ankylosing spondylitis in adults. *Expert Rev Clin Immunol* (2022) 18:273–80. doi: 10.1080/1744666X.2022.2038134

29. Duggan S, Keam SJ. Upadacitinib: First approval. *Drugs* (2019) 79:1819–28. doi: 10.1007/s40265-019-01211-z

30. Muensterman E, Engelhardt B, Gopalakrishnan S, Anderson JK, Mohamed MF. Upadacitinib pharmacokinetics and exposure-response analyses of efficacy and safety in psoriatic arthritis patients - analyses of phase III clinical trials. *Clin Transl Sci* (2022) 15:267–78. doi: 10.1111/cts.13146

31. Narla S, Silverberg JI. The suitability of treating atopic dermatitis with janus kinase inhibitors. *Expert Rev Clin Immunol* (2022) 18:439–59. doi: 10.1080/1744666X.2022.2060822

32. Napolitano M, D'Amico F, Ragaini E, Peyrin-Biroulet L, Danese S. Evaluating upadacitinib in the treatment of moderate-to-Severe active ulcerative colitis: Design, development, and potential position in therapy. *Drug Des Devel Ther* (2022) 16:1897–913. doi: 10.2147/DDDT.S340459

33. Shawky AM, Almalki FA, Abdalla AN, Abdelazeem AH. Gouda AM. *A Compr Overview Globally Approved JAK Inhibitors. Pharmaceutics* (2022) 14:1001. doi: 10.3390/pharmaceutics14051001

34. Szakács G, Paterson JK, Ludwig JA, Booth-Genthe C, Gottesman MM. Targeting multidrug resistance in cancer. *Nat Rev Drug Discovery* (2006) 5:219–34. doi: 10.1038/nrd1984

35. Fabbro D, Cowan-Jacob SW, Möbitz H, Martiny-Baron G. Targeting cancer with small-molecular-weight kinase inhibitors. *Methods Mol Biol* (2012) 795:1–34. doi: 10.1007/978-1-61779-337-0_1

36. Williams NK, Bamert RS, Patel O, Wang C, Walden PM, Wilks AF, et al. Dissecting specificity in the janus kinases: the structures of JAK-specific inhibitors complexed to the JAK1 and JAK2 protein tyrosine kinase domains. *J Mol Biol* (2009) 387:219–32. doi: 10.1016/j.jmb.2009.01.041

37. Davis RR, Li B, Yun SY, Chan A, Nareddy P, Gunawan S, et al. Structural insights into JAK2 inhibition by ruxolitinib, fedratinib, and derivatives thereof. *J Med Chem* (2021) 64:2228–41. doi: 10.1021/acs.jmedchem.0c01952

38. Chang Y, Min J, Jarusiewicz JA, Actis M, Yu-Chen Bradford S, Mayasundari A, et al. Degradation of janus kinases in CRLF2-rearranged acute lymphoblastic leukemia. *Blood* (2021) 138:2313–26. doi: 10.1182/blood.2020006846

39. Vazquez ML, Kaila N, Strohbach JW, Trzupek JD, Brown MF, Flanagan ME, et al. Identification of n-{cis-3-[Methyl(7H-pyrrolo[2,3-d]pyrimidin-4-yl)amino] cyclobutyl}propane-1-sulfonamide (PF-04965842): A selective JAK1 clinical candidate for the treatment of autoimmune diseases. *J Med Chem* (2018) 61:1130–52. doi: 10.1021/acs.jmedchem.7b01598

40. Tangye SG, Pelham SJ, Deenick EK, Ma CS. Cytokine-mediated regulation of human lymphocyte development and function: Insights from primary immunodeficiencies. *J Immunol* (2017) 199:1949–58. doi: 10.4049/jimmunol.1700842

41. Clark JD, Flanagan ME, Telliez JB. Discovery and development of janus kinase (JAK) inhibitors for inflammatory diseases. *J Med Chem* (2014) 57:5023–38. doi: 10.1021/jm401490p

42. Glassman CR, Tsutsumi N, Saxton RA, Lupardus PJ, Jude KM, Garcia KC. Structure of a janus kinase cytokine receptor complex reveals the basis for dimeric activation. *Science* (2022) 376:163–9. doi: 10.1126/science.abn8933

43. Xu P, Shen P, Yu B, Xu X, Ge R, Cheng X, et al. Janus kinases (JAKs): The efficient therapeutic targets for autoimmune diseases and myeloproliferative disorders. *Eur J Med Chem* (2020) 192:112155. doi: 10.1016/j.ejmech.2020.112155

44. Saharinen P, Takaluoma K, Silvennoinen O. Regulation of the Jak2 tyrosine kinase by its pseudokinase domain. *Mol Cell Biol* (2000) 20:3387–95. doi: 10.1128/MCB.20.10.3387-3395.2000

45. Meyer SC, Levine RL. Molecular pathways: molecular basis for sensitivity and resistance to JAK kinase inhibitors. *Clin Cancer Res* (2014) 20:2051–9. doi: 10.1158/1078-0432.CCR-13-0279

46. Liau NPD, Laktyushin A, Morris R, Sandow JJ, Nicola NA, Kershaw NJ, et al. Enzymatic characterization of wild-type and mutant janus kinase 1. *Cancers (Basel)* (2019) 11:1701. doi: 10.3390/cancers11111701

47. Leroy E, Dusa A, Colau D, Motamedi A, Cahu X, Mouton C, et al. Uncoupling JAK2 V617F activation from cytokine-induced signalling by modulation of JH2 αC helix. *Biochem J* (2016) 473:1579–91. doi: 10.1042/BCJ20160085

48. Liang J, Tsui V, Van Abbema A, Bao L, Barrett K, Beresini M, et al. Lead identification of novel and selective TYK2 inhibitors. *Eur J Med Chem* (2013) 67:175–87. doi: 10.1016/j.ejmech.2013.03.070

49. Fabbro D, Cowan-Jacob SW, Moebitz H. doi: 10.1111/bph.13096

50. Nagar B, Bornmann WG, Pellicena P, Schindler T, Veach DR, Miller WT, et al. Crystal structures of the kinase domain of c-abl in complex with the small molecule inhibitors PD173955 and imatinib (STI-571). *Cancer Res* (2002) 62:4236–43.

51. Roskoski RJr. Classification of small molecule protein kinase inhibitors based upon the structures of their drug-enzyme complexes. *Pharmacol Res* (2016) 103:26–48. doi: 10.1016/j.phrs.2015.10.021

52. Hubbard SR. Mechanistic insights into regulation of JAK2 tyrosine kinase. *Front Endocrinol (Lausanne)* (2018) 8:361. doi: 10.3389/fendo.2017.00361

53. Baxter EJ, Scott LM, Campbell PJ, East C, Fourouclas N, Swanton S, et al. Acquired mutation of the tyrosine kinase JAK2 in human myeloproliferative disorders. *Lancet* (2005) 365:1054–61. doi: 10.1016/S0140-6736(05)71142-9

54. James C, Ugo V, Le Couédic JP, Staerk J, Delhommeau F, Lacout C, et al. A unique clonal JAK2 mutation leading to constitutive signalling causes polycythaemia vera. *Nature* (2005) 434:1144–8. doi: 10.1038/nature03546

55. Kralovics R, Passamonti F, Buser AS, Teo SS, Tiedt R, Passweg JR, et al. A gain-of-function mutation of JAK2 in myeloproliferative disorders. *N Engl J Med* (2005) 352:1779–90. doi: 10.1056/NEJMoa051113

56. Levine RL, Wadleigh M, Cools J, Ebert BL, Wernig G, Huntly BJ, et al. Activating mutation in the tyrosine kinase JAK2 in polycythemia vera, essential thrombocythemia, and myeloid metaplasia with myelofibrosis. *Cancer Cell* (2005) 7:387–97. doi: 10.1016/j.ccr.2005.03.023

57. Gorre ME, Mohammed M, Ellwood K, Hsu N, Paquette R, Rao PN, et al. Clinical resistance to STI-571 cancer therapy caused by BCR-ABL gene mutation or amplification. *Science* (2001) 293:876–80. doi: 10.1126/science.1062538

58. Heinrich MC, Corless CL, Demetri GD, Blanke CD, von Mehren M, Joensuu H, et al. Kinase mutations and imatinib response in patients with metastatic gastrointestinal stromal tumor. *J Clin Oncol* (2003) 21:4342–9. doi: 10.1200/JCO.2003.04.190

59. Bishop AC. A hot spot for protein kinase inhibitor sensitivity. *Chem Biol* (2004) 11:587–9. doi: 10.1016/j.chembiol.2004.05.002

60. Katayama R, Shaw AT, Khan TM, Mino-Kenudson M, Solomon BJ, Halmos B, et al. . doi: 10.1126/scitranslmed.3003316

61. Downes CEJ, McClure BJ, Bruning JB, Page E, Breen J, Rehn J, et al. Acquired JAK2 mutations confer resistance to JAK inhibitors in cell models of acute lymphoblastic leukemia. *NPJ Precis Oncol* (2021) 5:75. doi: 10.1038/s41698-021-00215-x

frontiers | Frontiers in Immunology

TYPE Original Research
PUBLISHED 20 June 2023
DOI 10.3389/fimmu.2023.1190943

OPEN ACCESS

EDITED BY
Hyun Ho Park,
Chung-Ang University, Republic of Korea

REVIEWED BY
Jinghua Lu,
National Institute of Allergy and Infectious Diseases (NIH), United States
József Dobó,
Hungarian Academy of Sciences (MTA), Hungary

*CORRESPONDENCE
M. Cristina Vega
cvega@cib.csic.es
Francisco J. Fernández
fjfernandez@abvance.com

RECEIVED 21 March 2023
ACCEPTED 30 May 2023
PUBLISHED 20 June 2023

CITATION
Navas-Yuste S, de la Paz K, Querol-García J, Gómez-Quevedo S, Rodríguez de Córdoba S, Fernández FJ and Vega MC (2023) The structure of *Leptospira interrogans* GAPDH sheds light into an immunoevasion factor that can target the anaphylatoxin C5a of innate immunity.
Front. Immunol. 14:1190943.
doi: 10.3389/fimmu.2023.1190943

The structure of *Leptospira interrogans* GAPDH sheds light into an immunoevasion factor that can target the anaphylatoxin C5a of innate immunity

Sergio Navas-Yuste[1], Karla de la Paz[1,2], Javier Querol-García[1,2], Sara Gómez-Quevedo[1,3], Santiago Rodríguez de Córdoba[1,4], Francisco J. Fernández[1,2*] and M. Cristina Vega[1*]

[1]Centro de Investigaciones Biológicas Margarita Salas, Consejo Superior de Investigaciones Científicas (CSIC), Madrid, Spain, [2]Abvance Biotech Srl, Madrid, Spain, [3]Universidad Europea, Madrid, Spain, [4]Centro de Investigación Biomedica en Red sobre Enfermedades Raras (CIBERER), Madrid, Spain

Leptospirosis is a neglected worldwide zoonosis involving farm animals and domestic pets caused by the Gram-negative spirochete *Leptospira interrogans*. This bacterium deploys a variety of immune evasive mechanisms, some of them targeted at the complement system of the host's innate immunity. In this work, we have solved the X-ray crystallographic structure of *L. interrogans* glyceraldehyde-3-phosphate dehydrogenase (GAPDH) to 2.37-Å resolution, a glycolytic enzyme that has been shown to exhibit moonlighting functions that potentiate infectivity and immune evasion in various pathogenic organisms. Besides, we have characterized the enzyme's kinetic parameters toward the cognate substrates and have proven that the two natural products anacardic acid and curcumin are able to inhibit *L. interrogans* GAPDH at micromolar concentration through a noncompetitive inhibition modality. Furthermore, we have established that *L. interrogans* GAPDH can interact with the anaphylatoxin C5a of human innate immunity in vitro using bio-layer interferometry and a short-range cross-linking reagent that tethers free thiol groups in protein complexes. To shed light into the interaction between *L. interrogans* GAPDH and C5a, we have also carried out cross-link guided protein-protein docking. These results suggest that *L. interrogans* could be placed in the growing list of bacterial pathogens that exploit glycolytic enzymes as extracellular immune evasive factors. Analysis of the docking results indicates a low affinity interaction that is consistent with previous evidence, including known binding modes of other α-helical proteins with GAPDH. These findings allow us to propose *L. interrogans* GAPDH as a potential immune evasive factor targeting the complement system.

KEYWORDS

structural biology, innate immunity, complement system, C5a anaphylatoxin, GAPDH – glyceraldehyde 3-phospate dehydrogenase, leptospirosis, moonlighting proteins

1 Introduction

The complement system is a central part of the innate immune defense against pathogens (1). It comprises about forty soluble and membrane-associated proteins, which survey the blood and interstitial fluids for pathogens, immune complexes, and apoptotic cell debris. Those stimuli can activate the complement system very swiftly through three main activation pathways: the alternative (AP), classical (CP), and lectin (LP) pathways. Normal complement activation on surfaces involves a self-amplification cascade where the so-called C3 convertases proteolytically cleave C3, the most abundant complement factor, to yield C3b, which remains attached to the activating surface, and C3a. Surface-attached C3b can assemble C3-convertase enzyme complexes, propagating C3b deposition in a process known as opsonization. C3b can be quickly cleaved by factor I into iC3b (2). On densely opsonized surfaces like those of pathogens and other foreign or damaged surfaces, C3b-containing enzyme complexes can cleave C5 into C5b and soluble C5a, a 74-amino-acid anaphylatoxin (3). The former remains bound to surfaces and nucleate the assembly of the so-called membrane attack complex (MAC) (4), which can lyse targeted cells directly through osmotic shock in a process known as terminal pathway. Like C3a, C5a is a soluble factor that diffuses away from the site of activation and acts as one of the most powerful chemoattractants of innate immunity. Once liganded to its cognate receptor (C5aR1/CD88), C5a stimulates proinflammatory responses like chemotaxis and vascular permeability, which result in the recruitment of inflammatory neutrophils and macrophages to the sites of activation (5). On self-cells, however, complement activation is strongly suppressed by self-protective fluid-phase regulators such as factor H and C4b binding protein (C4BP), both involved in the inactivation of iC3b on opsonized cell surfaces, and membrane regulators such as MCP and DAF, which disassemble C3 convertases to prevent further deposition of C3b (6).

Leptospirosis is a widespread zoonotic disease caused by the highly motile Gram-negative spirochete *Leptospira* (7, 8). *Leptospira* colonizes a range of hosts including humans, domestic and farm animals, and some wild animal species such as mice, rats, and bats, which typically serve as reservoirs of infection (9). In humans, leptospirosis typically presents with mild fever and flu-like symptoms, but in its more severe forms it can lead to fatal multi-organ failure. Leptospirosis causes about 1 million severe cases in humans every year with 60,000 fatalities (10). In cattle and swine, leptospirosis causes veterinary and economic damage through reproductive failure, abortion, still-births, fetal mummification, weak calves/piglets, and agalactia (8, 11). Its prevalence has surged in recent years due to global warming, intensive farming, and other geographic and socioeconomic factors (12). Globally, leptospirosis represents an increasing public and veterinary health threat, as evidenced by growing incidence rates and multiple outbreaks around the world, compounded by frequent misdiagnosis.

Pathogenic *Leptospira* produces the activation of all three complement activation pathways and, not surprisingly, it has evolved sophisticated immune evasion mechanisms to escape it (13). The deployment of *Leptospira*'s complement-targeting molecular weaponry accelerates the decay of the three complement activation pathways and inhibits the terminal pathway, thereby promoting the pathogen's dissemination and infection. Examples of immunoevasion strategies deployed by *Leptospira* include: 1) acquisition *via* surface evasion molecules of host's soluble complement regulators like factor H and C4BP (molecular mimicry) (14); 2) terminal pathway inhibition either through the direct interaction of surface pathogenic proteins with C9 or through the indirect interaction with vitronectin, an inhibitor of C5b7 complex formation and C9 polymerization; 3) plasminogen binding to and cleavage of C3b, C4b, and C5 (mixed molecular mimicry/proteolytic cleavage) (15); and 4) direct proteolytic degradation of complement proteins C2, C3, C4, and factor B. Several *Leptospira* virulence factors comprising extracellular enzymes and cell-surface proteins have been demonstrated to play key roles in host-cell adherence and immunoevasion. To date, two *Leptospira* proteins displaying moonlighting functions have been found: elongation factor-thermal unstable (EF-Tu), shown to interact with host extracellular membrane (ECM) molecules, plasminogen, and factor H, and the glycolytic enzyme α-enolase, described to interact with plasminogen, factor H, and C4BP.

We and others have proposed that the ubiquitous glycolytic enzyme glyceraldehyde-3-phosphate dehydrogenase (GAPDH; E.C. 1.2.1.12) from pathogenic bacteria may double as an innate immune evasive factor when it is found in the extracellular environment (16). To perform these moonlighting functions, GAPDH must be relocated to the extracellular space by cell lysis (e.g., *via* streptococcal lysins) (16), secretion (e.g., type-3 secretion systems in enteropathogenic *Escherichia coli*) (17), or outer membrane shedding (e.g., *Francisella tularensis*, *Mycobacterium tuberculosis*, *Staphylococcus aureus*, *Atopobium vaginae*, and *Leptospira interrogans*). Some of the infectivity enhancing functions attributed to moonlighting GAPDH are mostly targeted at the innate immunity and, specifically, the complement system. Examples of these mechanisms include sequestering nascent C5a as it is being generated by C5 cleavage, a mechanism described for Gram-positive bacteria such as *Streptococcus pneumoniae*, *S. pyogenes*, *A. vaginae*, and *Clostridium perfringens* (16, 18, 19); binding complement factors like C3 and C1q (20, 21); and increasing pathogen dissemination by binding to ECM components as plasminogen to help to degrade tissue barriers, basement membranes, and fibrin clots (13, 22).

In this work, we set out to characterize the structure and function of GAPDH from the Gram-negative spirochete *L. interrogans* and investigate whether it could operate as a virulence factor by binding to C5a. We have characterized *Li*GAPDH's enzymatic activity and inhibition by curcumin and anacardic acid, two natural products, and we have solved its crystal structure at 2.37-Å resolution complete with its NAD^+ cofactor. Furthermore, we have shown by bio-layer interferometry and controlled cross-linking experiments that *Li*GAPDH can bind C5a, a property shared by GAPDH enzymes from other pathogenic bacteria that might contribute to immune evasion in the mammalian host. To shed light into the C5a recognition mechanism, we have performed cross-link guided protein-protein docking.

2 Materials and methods

2.1 Cloning, expression, and purification of *Li*GAPDH

The gene encoding full-length *Li*GAPDH (UniProt Accession No. Q72QM3_LEPIC) was amplified by PCR from *L. interrogans* serovar Copenhageni strain Fiocruz L1-130 genomic DNA (ATCC) and cloned into the pETM-11 expression vector by restriction-ligation after digesting the PCR fragment with BsaI-XhoI and the pETM-11 expression vector with NcoI-XhoI, conferring an N-terminal hexahistidine tag and a tobacco etch virus cleavage (TEV) site in frame with the *Li*GAPDH gene. The expression plasmid was verified by sequencing the entire ORF. For protein expression, the *Li*GAPDH construct was transformed into Rosetta (DE3) chemically competent cells. An overnight starter culture was used to inoculate a 2.5-L expression culture at 37 °C. The culture was allowed to grow at 37 °C in Luria-Bertani medium supplemented with 50 µg/ml kanamycin and 34 µg/ml chloramphenicol to an absorbance of 0.6 at 590 nm and then induced with 1 m*M* isopropyl β-D-thiogalactopyranoside (IPTG) for 20 h. Cell pellet was lysed by sonication in IMAC-A buffer (50 m*M* Tris-HCl (pH 8.0), 500 m*M* NaCl, 20 m*M* imidazole) supplemented with 1 mM phenylmethylsulfonyl fluoride (PMSF) and one tablet of EDTA-free protease inhibitor cocktail. Supernatant was collected upon centrifugation for 20 min at 4 °C. The sample was clarified further by filtration through a 0.22 µm membrane and loaded on a HisTrap column (Cytiva) pre-equilibrated in IMAC-A buffer and eluted in IMAC-A buffer with 250 m*M* imidazole. Peak fractions were analyzed by SDS-PAGE and fractions containing *Li*GAPDH were pooled and dialyzed against a buffer containing 10 m*M* HEPES-NaOH (pH 7.4), 150 m*M* NaCl, 3.4 m*M* EDTA. Then, *Li*GAPDH was subjected to size exclusion chromatography on a HiLoad 16/60 Superdex 200 pg (Cytiva) pre-equilibrated in the same buffer. Comparison of the elution volume of *Li*GAPDH with a calibration curve constructed using high and low molecular weight calibration kits (Cytiva) revealed that the quaternary structure of *Li*GAPDH corresponds to a tetrameric oligomeric state. Finally, *Li*GAPDH was concentrated to 10 mg/ml, dispensed in 50-µl aliquots, snap-frozen in liquid nitrogen and stored at −80 °C until use. The yield was ~2 mg *Li*GAPDH/l of culture, showing a >95% purity on a Coomassie brilliant blue-stained SDS-PAGE gel.

2.2 Enzyme kinetics

The *Li*GAPDH enzyme activity was followed spectrophotometrically by the change in absorbance at 340 nm due to NADH formation (ϵ = 6220 M^{-1} cm^{-1}), adapted from a previously described method (23). Temperature controlled assays were performed in an Eppendorf BioSpectrometer spectrophotometer at 25 °C. One unit of enzyme activity was defined as the amount of GAPDH that converts 1 µmol/min of NAD^+ to NADH at 25 °C. A standard assay was carried out in a final volume of 0.15 ml using 40 m*M* Tris-HCl (pH 8.5), 2 m*M* EDTA, 10 n*M* *Li*GAPDH, and indicated concentrations of the different substrates: nicotinamide adenine dinucleotide (NAD^+), glyceraldehyde 3-phosphate (G3P), and inorganic phosphate (P_i). NAD^+ concentration was varied between 0.02 and 1.62 m*M* while keeping fixed G3P at 2 m*M* and P_i at 5 m*M*; G3P concentration between 0.14 and 11.7 m*M* at 2 m*M* NAD^+ and 5 m*M* Pi; and P_i concentration between 0.38 and 31.5 m*M* at 2 m*M* NAD^+ and 2 m*M* G3P. The reaction was initiated by adding 0.56 µg of enzyme. Michaelis-Menten parameters were obtained by non-linear regression fitting of the kinetic data using SigmaPlot 14.5 (Systat Software Inc.).

2.3 Inhibition by curcumin and anacardic acid

Inhibition assays were performed with two natural compounds, anacardic acid and curcumin. Four inhibitor concentrations each were tested for anacardic acid (10, 24, 64, and 160 µ*M*) and curcumin (10, 25, 62.5, and 150 µ*M*). To ascertain the inhibition modality with respect to G3P and NAD^+, initial velocity measurements at each inhibitor concentration were carried out varying G3P concentration (0.06-1.56 m*M* G3P for both inhibitors) while maintaining a saturating concentration of 2 m*M* NAD^+; or varying NAD^+ concentration (0.02-1.1 m*M* NAD^+ for both inhibitors) while maintaining a saturating concentration of 2 m*M* G3P. In either case, potassium phosphate was kept at a saturating concentration of 5 m*M*. The software SigmaPlot 14.5 (Systat Software Inc.) was used to analyze the data.

2.4 Crystallization and X-ray diffraction data collection

To find the optimal crystallization conditions, we performed extensive scans of crystallization conditions from commercial screenings by Hampton Research and Molecular Dimensions (Crystal Screening 1 and 2, Salt Screening 1 and 2, JSCG+ 1 and 2). The best results were obtained with Bis-Tris buffer at different concentrations of PEG 3350 as precipitant. The crystals presented a form of elongated prisms with a dimension of 150-300 µm in their longest axis. For freezing, 20% (v/v) glycerol was used as cryoprotectant. Crystals were mounted on Micromount loops (MiTeGen) and frozen in liquid nitrogen. The crystals were diffracted at the BL13-XALOC beamline of the ALBA synchrotron (Barcelona) (24). The maximum observable resolution was 2.37 Å with unit cell dimensions of a = 79.8 Å, b = 82.0 Å, c = 123.2 Å, α = 94.0°, β = 95.1°, and γ = 112.5° and *P*1 space group. The data was processed with *XDS* (25) and scaled and merged with *Aimless* (26).

2.5 Structure determination

The crystallographic structure of *Li*GAPDH was solved by molecular replacement using *PHASER* (27) in the *PHENIX* suite (28) with the structure of *Av*GAPDH as a model (PDB ID 5LD5; http://doi.org/10.2210/pdb5LD5/pdb) (18). The crystal structure

10.3389/fimmu.2023.1190943

contained two tetramers in the asymmetric unit. The difference map (F_o-F_c) showed a clear position and conformation for an NAD^+ cofactor in the active site of all the monomers from the two tetramers. Refinement cycles with phenix.refine (29) of the *PHENIX* suite were interspersed with cycles of manual construction (placing first NAD^+ and then solvent molecules) and validation cycles with *Coot* (30). Non-crystallographic symmetry was applied as a constraint on the main-chain dihedral angles during the initial refinement, but they were removed during the later stages of refinement. At the end of the refinement, the *Li*GAPDH model obtained a R_{work}/R_{free} of 0.19/0.23 with an r.m.s.d. of 0.011 Å and 1.31° for distance and bond angles, respectively. The final model consists of 2674 amino acid residues, eight NAD^+ molecules, 380 water molecules, 4 phosphate anions, and 33 glycerol molecules from the cryoprotectant solution. The crystallographic refinement statistics are summarized in Table 1.

The coordinate and structure factors files have been deposited with the Protein Data Bank (PDB) with PDB ID 8OHA (http://doi.org/10.2210/pdb8OHA/pdb).

2.6 Small angle X-ray scattering

SAXS experiments were carried out at the B21 beamline (31) from the Diamond Light Source synchrotron (DLS, UK). To improve sample purity and monodispersity, we collected SAXS data using continuous flow in HPLC-SAXS mode (620 images/3 s) at 9 °C. Sample *Li*GAPDH at 7 mg/ml in 10 m*M* HEPES-NaOH (pH 7.4), 150 m*M* NaCl, 3.4 m*M* EDTA, 2 m*M* TCEP, 3% (v/v) glycerol were injected on a Shodex KW-403 size-exclusion column (theoretical separation range 10-700 kDa, 4.6-ml column volume), previously equilibrated in the same buffer. Individual 2D data images were radially averaged to produce 1D diffraction profiles $I(q)$ *vs.* q without subtracting buffer. For the final data reduction process, statistical checks were performed to rule out images affected by radiation damage or systematic scaling errors (32). The data were averaged, buffer subtracted, and combined to produce the final SAXS profile covering the transfer momentum range 0.0026 to 0.3400 $Å^{-1}$. The *ATSAS* 3.0 software package (33) was used to extract structural information and perform an *ab initio* shape restoration of *Li*GAPDH. Firstly, the number of Shannon channels and the maximum usable q were estimated with *SHANUM* (34). Next, the direct diffraction extrapolated to zero angle $I(0)$ and the R_g were evaluated using the Guinier approximation (35) and the pairwise distance distribution function in real space ($P(r)$ *vs.* r) computed with *GNOM* (36). From the $P(r)$ profile it was possible to evaluate the maximum dimension (D_{max}) of the particle. Additionally, two different concentration-independent methods were used to estimate the molecular mass of *Li*GAPDH: the correlation volume (V_C) and the empirical Porod volume (V_P) correction (37), implemented in the *ATSAS* toolsets called *DATMOW*, *DATVC*, and *DATPOROD*. With *DATCLASS*, the

TABLE 1 Data collection and refinement statistics (molecular replacement).

	*Li*GAPDH
Data collection	
Space group	*P*1
Cell dimensions	
a, *b*, *c* (Å)	79.80, 82.04, 123.19
α, β, γ (°)	94.02, 95.15, 112.52
Resolution (Å)	45.5–2.37 (2.43–2.37)*
No. total reflections	401,101 (27,157)
No. unique reflections	109,875 (7248)
Mean $I/\sigma I$	8.10 (0.91)
R_{merge}	0.1077 (1.356)
R_{meas}	0.1262 (1.581)
CC1/2	0.996 (0.401)
Completeness (%)	94.76 (87.31)
Redundancy	3.6 (3.7)
Refinement	
No. reflections	109,875 (7248)
No. reflections in test set	2008 (131)
R_{work}/R_{free}	0.1923/0.2322
No. residues	2674
No. atoms	21,539
Protein	20,540
Ligand/ion	619
Water	380
B-factors ($Å^2$)	61.12
Protein	61.32
Ligand/ion	57.95
Water	55.49
R.m.s. deviations	
Bond lengths (Å)	0.011
Bond angles (°)	1.31
Ramachandran plot	
Favored (%)	97.84
Allowed (%)	1.82
Outliers (%)	0.34
Rotamer outliers (%)	1.00
Clashscore	6.00

The structure was determined from a single crystal.
* Values in parentheses are for the highest-resolution shell.

shape of *Li*GAPDH derived from the SAXS data was classified as compact and potentially unique (38). *Ab initio* shape restoration was performed using a dummy bead model of 50 independent runs with *DAMMIF* (39), which were superimposed, averaged, and clustered with *DAMAVER* (40), and further refined with *DAMMIN* (41) to create the final *ab initio* shape. The most representative cluster contained >90% of all bead models with a normalized spatial discrepancy (NSD) threshold of 0.55 (42). The resolution was estimated from the Fourier shell correlation (FSC) at FSC = 0.5 (43). The fit of the crystal structure of *Li*GAPDH to the SAXS data was evaluated using *CRYSOL* (44).

2.7 Bio-layer interferometry

Bio-layer interferometry (BLI) studies were performed on a BLItz instrument (ForteBio) at 25 °C with shaking at 2200 rpm. BLI assay buffer consisted of 10 m*M* HEPES-NaOH (pH 7.4), 50 m*M* NaCl, 0.34 m*M* EDTA, 0.02% (v/v) polysorbate 20 (P20), which was 0.22-µm filtered. Before use, (anti-biotin) streptavidin (SA) biosensors (ForteBio 18-5019) were hydrated in BLI assay buffer for 10 min. All samples for BLI measurements were prepared in 4.5 µl. The BLI assay was as follows: baseline (30 s) (Equilibration), loading (300 s) (BLI assay buffer for nonspecific binding or biotinylated-C5a (34 µg/ml) (Abvance Biotech ABVC5ARBIO1), stabilization (300 s) (BLI assay buffer), baseline (30 s) (Equilibration), association (300 s) (230 µM *Li*GAPDH), and dissociation (300 s) (BLI assay buffer). Loading of biotinylated-C5a for 300 s onto SA sensor tips resulted in a wavelength shift signal of ~2.75 nm. Loading of *Li*GAPDH for 300 s onto either the mock SA sensor tips or the biotinylated-C5a SA sensor tips resulted in wavelength shift signals of 0.5 and 4.5 nm, respectively.

2.8 Cross-linking

Specific cross-linking assays were performed with bis (maleimido)ethane (BMOE; Pierce 22322), a 7-atom, 8.0-Å short spacer arm cross-linking reagent that generates non-cleavable cross-links between sulfhydryl groups that are in proximity (< 8 Å apart). Cross-linking reactions were carried out by mixing 10 µg *Li*GAPDH with 0.5, 1.0, 2.0, 4.0, or 5.0 µg human recombinant C5a (ABVC5A, Abvance Biotech) in assay buffer (10 m*M* HEPES-NaOH (pH 7.4), 150 m*M* NaCl, 3.4 m*M* EDTA) containing 0.3 m*M* BMOE, and incubating the reaction mixtures for 2 h at 4 °C. The C5a:*Li*GAPDH molar ratio for these assays was 0.27, 0.53, 1.07, 2.13, or 2.67; and the BMOE:*Li*GAPDH molar ratio was 1.44. To control for nonspecific cross-linking, we treated identical amounts of *Li*GAPDH (10 µg) and C5a (5 µg) with 0.3 m*M* BMOE and without BMOE. We followed the appearance of cross-linked products by 12% SDS-PAGE gel electrophoresis and Coomassie-Brilliant Blue (CBB) staining. A second SDS-PAGE gel was run with one-fourth of the cross-linking reactions under otherwise identical conditions and transferred onto a nitrocellulose membrane (1 h at 80 V) for Western blotting. The membrane was incubated 1 h at RT with blocking solution (5% (w/v) BSA in TBST), probed with an anti-C5a primary antibody (1:6000, 1 h at 37 °C) and a Goat anti-Rabbit HRP secondary antibody (1:2000, 30 min at 37 °C), developed with luminol and water peroxide, and imaged on a ChemiDoc Imaging System (Bio-Rad). Afterwards, the same blot was treated with Restore Stripping buffer (ThermoFisher Scientific 21059) for 30 min at 37 °C, reblocked, reprobed with an anti-His HRP antibody (1:3000, 1 h at RT), developed with luminol and water peroxide, and imaged.

2.9 Cross-link guided docking protocol

We applied a cross-link guided protein-protein docking protocol to predict *Li*GAPDH-C5a complexes using the standard *ROSETTA* docking protocol (45), with modifications. Receptor (*Li*GAPDH) and ligand (C5a) were first relaxed and then subjected to cross-link guided docking using the known length of the BMOE cross-link as restraint. The protocol filters and ranks the protein-protein docking poses by the sequential application of Xwalk (46) to simulate cross-links on protein surfaces, FreeSASA (47) and *PISA* (48) to calculate the size of predicted binding interfaces, and an energy-based clustering approach implemented in *ROSETTA* (49).

2.10 Electrostatic potential calculations

Electrostatic potential surfaces of *Li*GAPDH and C5a were calculated with the APBS (Adaptive Poisson-Boltzmann Solver) (50) software as a plugin in PyMOL (51) using default parameters.

3 Results

3.1 Crystallographic structure of *Li*GAPDH

We have determined the first crystal structure of *Li*GAPDH at 2.37-Å resolution (Figure 1). The crystal structure corresponds to the holoenzyme with an NAD^+ molecule tightly bound into the active site (Figure 1). We solved the structure by molecular replacement using *Atopobium vaginae* GAPDH as a model (*Av*GAPDH; PDB ID 5LD5; http://doi.org/10.2210/pdb5LD5/pdb) (18). There are two independent tetramers in the asymmetric unit that are nearly identical, with an r.m.s.d. of 0.30 Å. This remarkable similarity is mirrored by the structure of the individual subunits, which can be superimposed with an r.m.s.d. of 0.26 Å on average. Crystallographic data processing and refinement and validation statistics are reported in Table 1.

The quaternary structure of *Li*GAPDH consists in a homotetramer with O, P, Q, and R subunits related by a 222/*D*2 molecular symmetry, which gives rise to three non-equivalent interfaces related by three mutually perpendicular axes referred to as P, Q, and R (Figure 1A). The monomers are composed of two domains: an *N*-terminal domain that contains the NAD^+ binding

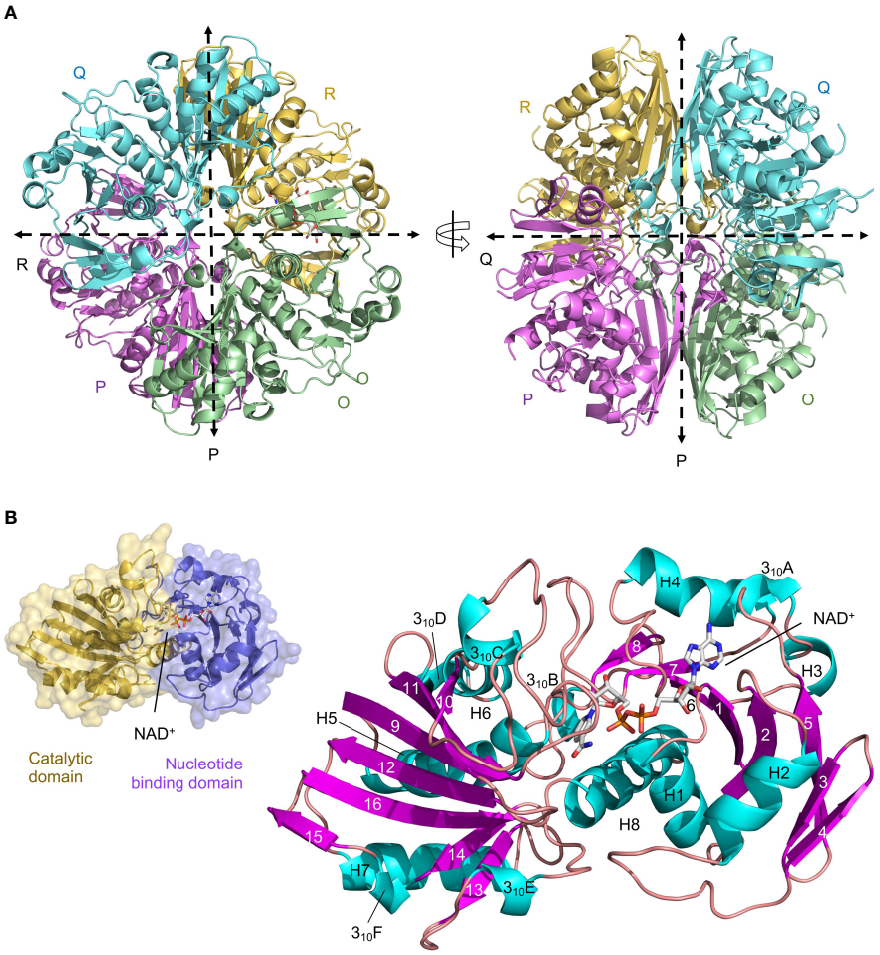

FIGURE 1
Crystal structure of *Li*GAPDH. **(A)** Overall tetrameric structure of *Li*GAPDH in cartoon representation with chain colors (O in green, P in violet, Q in cyan, and R in yellow). Crossing dashed lines indicate the directions of the two molecular symmetry axes on the plane of the figure. The NAD^+ cofactor is shown in sticks and CPK colors. Two views of the *Li*GAPDH tetramer are shown down the Q-axis or the R-axis, which are perpendicular to the plane of the figure. **(B)** Cartoon representation of the *Li*GAPDH subunit structure color coded according to secondary structure: helices in cyan, β-strands in violet, and irregular segments and loops in salmon. Secondary structural elements and the NAD^+ are annotated. In the inset (top left corner) we show the same monomer in molecular surface representation, color according to the domain: the *N*-terminal nucleotide-binding domain is in violet and the *C*-terminal catalytic domain in gold.

pocket (residues 1-152), and a catalytic *C*-terminal domain spanning residues 153-335 (Figure 1B). The *N*-terminal domain adopts an α/β/α Rossmann fold characterized by the classic α/β nucleotide binding pocket, which typically contains a central 7-stranded β-sheet and a tightly bound NAD^+ cofactor occupying the active site. In *Li*GAPDH there are 8 β-strands (β1 to β8) because the canonical seventh β-strand is split into two smaller β-strands (β7 and β8) by a small irregular segment of extended conformation. Small helices are inserted between consecutive β-strands in this domain, which is further stabilized by packing against the *C*-terminal H8 helix. The *C*-terminal domain contains an 8-stranded β-sheet (β9 to β16), with helices inserted between β9-β10 (3_{10}C), β10-β11 (H6 and 3_{10}D), β12-β13 (H7), and β13-β14 (3_{10}E). Helix H8 is the last secondary structural motif of *Li*GAPDH.

The main interfaces through which each *Li*GAPDH monomer interacts with its two neighboring chains within the tetramer are not equivalent and have different surface areas (Figure 1A and Supplementary Figures 1, 2). First, the interface between the O-P subunits is the most extensive, with an average surface area of 1901 $Å^2$ (Supplementary Figure 1). Nine H-bonds and 19 salt bridges stabilize the O-P interface. Second, the O-R interface, with an average surface area of 1412 $Å^2$, has up to 13 H-bonds (Supplementary Figure 2A). Finally, the smallest intersubunit interface lies between the O-Q subunits, with an average surface area of 492 $Å^2$, 10 H-bonds, and 2 salt bridges (Supplementary Figure 2B).

Another key structural feature of *Li*GAPDH is the *S* loop, an extended and irregular segment comprising residues Ala180-Ile207 that inserts itself between the NAD^+-binding site and the adjacent subunit (Figure 1B and Supplementary Figure 2). The *S* loop contains residues lying between two of the catalytic triad residues His179 and Arg234 that are important for catalysis, cofactor-binding, and dimerization.

3.2 Solution SAXS shape of *Li*GAPDH

We analyzed the size and other hydrodynamic properties of *Li*GAPDH by solution small-angle X-ray scattering (SAXS) at the B21 beamline of the Diamond Light Synchrotron (DLS) (31). SAXS parameters are reported in Table 2 and Supplementary Table 1. Results indicated that *Li*GAPDH is a fairly spherical homotetramer with a well-folded structure (Figures 2A, B), with a radius of gyration R_g of 34.8 Å and a maximum dimension D_{max} of 90.9 Å (Figure 2C). These hydrodynamic parameters match well those obtained from the crystallographic structure (R_g 32.5 Å, D_{max} 99.6 Å). Indeed, direct comparison of the theoretical scattering calculated with *CRYSOL*, and the experimental scattering confirmed the excellent agreement with a χ^2 = 1.5 (Figure 2A). *Ab initio* shape reconstruction of *Li*GAPDH using dummy-bead models as implemented in *DAMMIF* resulted in a family of volumes with a consistent shape and a calculated resolution for the consensus reconstruction of 28.3 Å (Supplementary Figure 3). Attempts to rigid-body fit the crystallographic model of *Li*GAPDH into the *ab-initio* SAXS shape showed a close agreement between the crystal and solution structures (Figure 2D). From these observations, we concluded that the overall organization of *Li*GAPDH in solution is preserved in the crystal lattice.

3.3 Active site of *Li*GAPDH

The active site of *Li*GAPDH is a large cavity covered by a lid spanning about 50 amino acid residues (residues 114-164). At the bottom of the groove, the NAD^+ cofactor occupies an elongated binding site between the central β-sheet of the *N*-terminal domain and helices H1-H5, where it makes contacts with the main-chain atoms of Asn32 (from β2), Glu76, and Arg77 (from the β5-3_{10}A loop) (Figure 3). The catalytic Cys152 residue is located at the intersection between the *N*-terminal and *C*-terminal domains, where it interacts with the side chains of His179 and Arg234, the two other catalytic triad residues, responsible for lowering the pK_a of the Cys152 thiol nucleophile. Arg234, in turn, interacts with Thr182 and Gln185. *Li*GAPDH lacks an aspartic acid residue between Thr182 and Gln185, unlike other GAPDH sequences like those of *C. perfringens* and *S. pyogenes* (19).

In contrast to other GAPDH structures, in *Li*GAPDH, well-ordered electron density was found for the residues responsible for binding the inorganic phosphate moieties of substrates and products, the so-called P_s and P_i binding sites (Figure 3). Inspection of the eight active sites in the crystal structure revealed that some of them had the P_s and P_i sites occupied by phosphate anions from the purification buffers or glycerol molecules from the cryoprotectant solution, which acted as substrates or substrate analogs. These ligands corroborated the relevance of the observed active-site configuration, which remained unchanged with or without substrate analogs across all subunits. The P_s site is formed by residues Thr182, Thr184, and Gln185, and the P_i site by residues Ser151, Thr153, His179, Thr211, and Gly212. The catalytic triad residue Arg234 interacts with both phosphate sites, thereby it belongs to the P_s and P_i sites.

TABLE 2 Small-angle X-ray scattering (SAXS) parameters.

SAXS parameters	
Molecular mass *M* from composition (Da)[1,2]	36 648 (*p.s.*)
Molecular mass *M* for a tetramer (Da)	146 592
Guinier analysis	
R_g (Å)	35.70 ± 0.09
Quality-of-fit parameter (r^2 fit)	0.84
***P*(*r*) analysis**	
R_g (Å)	34.79 ± 0.03
D_{max} (Å)	90.9
M (Da) from *I*(*0*) (ratio to expected value)	143 866 (0.98)
Volume (V_P/V_C)	264 297/744
Structural modeling	
Symmetry/anisotropy assumptions	*P*222/unknown
χ^2 value/range	0.957–0.976
Model resolution (Å)	28.3

[1] ProtParam, Expasy web server at https://web.expasy.org/cgi-bin/protparam/protparam.
[2] Theoretical molecular mass calculated from the primary sequence (p.s.).

3.4 *Li*GAPDH kinetic parameters

Besides carrying out moonlighting functions in the extracellular space, *Li*GAPDH is a glycolytic enzyme located in the cytoplasm. We have measured its enzymatic activity using a well-established assay that reports on the reduction of the NAD^+ cofactor to NADH at 25 °C and pH 8.5 (18, 19). In these assays, the kinetic parameters for the direct reaction catalyzed by *Li*GAPDH were determined by systematically varying NAD^+, G3P, and P_i concentrations. While we observed a classic hyperbolic dependence of the catalytic activity for G3P/P_i at low substrate concentration (Michaelis-Menten model), with excess of either G3P or P_i the enzyme exhibited significant substrate inhibition with inhibitory constants K_{SS} larger though within one order of magnitude of the corresponding K_m values (Supplementary Figure 4). Kinetic parameters are reported in Table 3.

3.5 Inhibition of *Li*GAPDH by two natural compounds

Next, we examined the inhibitory effect of two natural compounds, anacardic acid and curcumin, which have previously shown efficacy against GAPDH from the Gram-positive bacterial pathogens *A. vaginae* (18) and *S. pyogenes* (19), and, in the case of anacardic acid, *Trypanosoma cruzi* (52). The safety of these compounds for use in humans makes them attractive lead compounds in repositioning campaigns for leptospirosis.

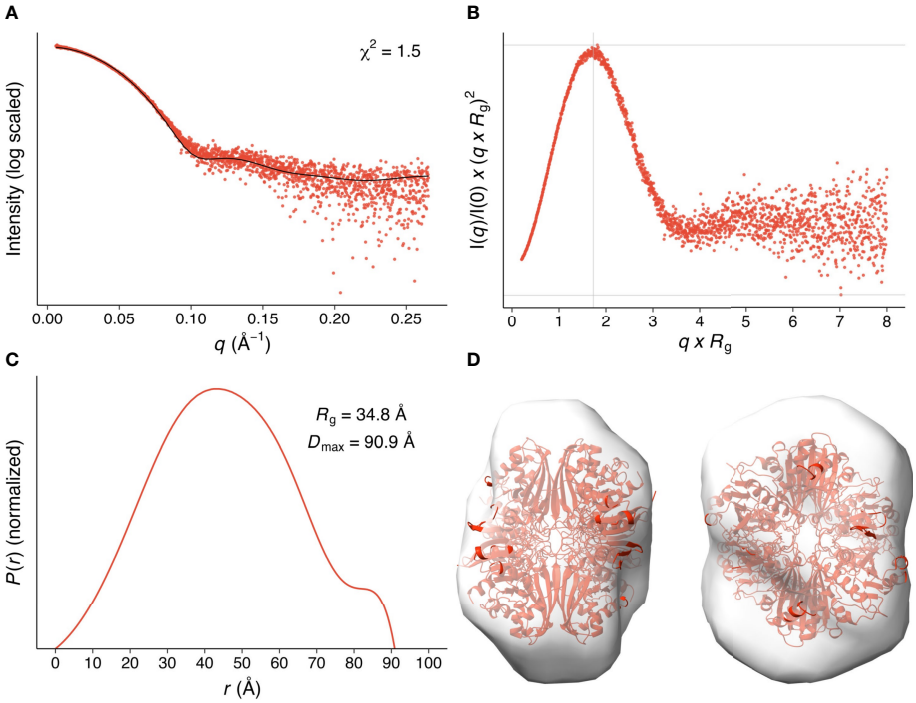

FIGURE 2
SAXS hydrodynamic properties and shape restoration for *Li*GAPDH. **(A)** 1D diffraction intensity of *Li*GAPDH plotted as a function of the diffraction momentum transfer *q*. Experimental data shown as a scatter plot (red circles). The black line corresponds to the average of the theoretical scattering profile of the two *Li*GAPDH tetramers in the asymmetric unit (χ^2 = 1.5). **(B)** Dimensionless Kratky representation showing the degree of protein folding in solution. The experimental pattern is shown as a scatter plot (red circles). The cross (gray lines) marks the so-called Guinier-Kratky point (1.732, 1.1), i.e., where the position of the main peak for globular proteins would be located. **(C)** Pair distance distribution function *P*(*r*) plotted as a function of *r*. The experimental pattern is shown as a solid line (red color). The value of D_{max} is the largest non-negative value that the distribution function supports. **(D)** Cartoon representation of *Li*GAPDH (in red) fitted inside the *ab initio* shape calculated with *DAMMIF*. Two orientations 90° apart are shown.

We obtained comparable results after testing the two natural compounds in the range 10-160 µ*M* (anacardic acid) and 10-150 µ*M* (curcumin) while varying the concentrations of either the G3P substrate or the NAD^+ cofactor (Table 4; Figure 4; Supplementary Figures 5, 6). Both anacardic acid and curcumin behaved as micromolar non-competitive inhibitors of *Li*GAPDH with respect to G3P and NAD^+. Not only was the inhibitory modality the same for both natural products, but also the magnitude of the inhibition constants was comparable: $K_i^{ana/G3P}$ = 135 µ*M vs.* $K_i^{cur/G3P}$ = 148 µ*M* and $K_i^{ana/NAD}$ = 41 µ*M vs.* $K_i^{cur/NAD}$ = 59 µ*M*.

3.6 Interaction between C5a and *Li*GAPDH

It has been reported that C5a can interact with immune evasive factors like GAPDH on the pathogen's surface through weak, transient interactions, which might be enhanced by the high local concentration of surface associated GAPDH (16, 18, 19). To reveal a potential interaction between natively folded *Li*GAPDH and C5a *in vitro*, we performed bio-layer interferometry experiments with streptavidin (SA) biosensors loaded with biotinylated-C5a. At a high *Li*GAPDH concentration (230 µ*M*, ~9 mg/mL), we observed a clear binding event with immobilized C5a characterized by a low kinetic association constant (k_{on} estimated at 37.3 ± 0.2 M^{-1} s^{-1}) and a slow dissociation constant, which could not be accurately determined (Figure 5A). Binding to the unmodified SA biosensors was far lower at the same concentration of *Li*GAPDH, ruling out strong nonspecific interactions between the biosensor and the analyte.

To provide independent evidence for the interaction, we resorted to the highly specific cross-linker reagent BMOE. BMOE covalently tethers the free sulfhydryl groups of Cys residues that lie in close proximity, typically at a distance of 8 Å apart. This stringent condition discriminates nonspecific interactions from meaningful though weak interactions, at the risk of missing some authentic but little populated complexes or those that would have required a longer tether. As shown in Figure 5B, SDS-PAGE electrophoresis of BMOE-treated mixtures of *Li*GAPDH and C5a revealed the appearance of a band corresponding to cross-linked *Li*GAPDH-C5a complexes, clearly discernable already at substoichiometric C5a:*Li*GAPDH molar ratios (between 0.53-1.07). The molecular mass of this cross-linked band (~10 kDa greater than monomeric *Li*GAPDH) coincided with the expected mass increment due to C5a (molecular mass ~9 kDa) (Figure 5B, indicated by an asterisk). The intensity of this band depended on the amount of C5a in the cross-linking reaction, thus proving that a native, though weak interaction is likely to exist between *Li*GAPDH and C5a. We could identify proteins bands simultaneously containing C5a and hexahistidine-

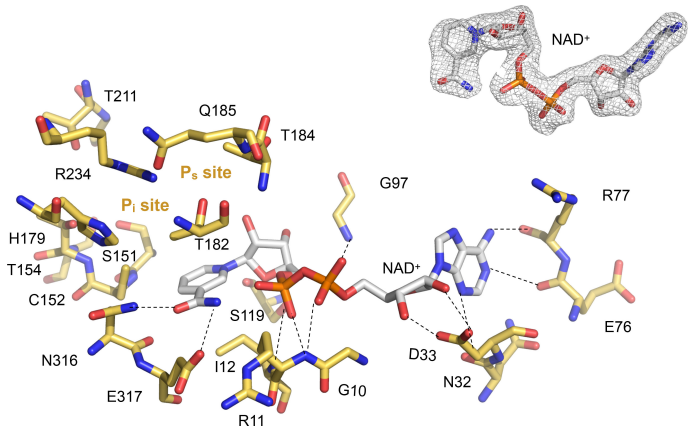

FIGURE 3
Close-up into the active site of *Li*GAPDH. Catalytic residues are shown in sticks in CPK colors (non-C atoms) or gold (C atoms). The NAD^+ cofactor is shown in sticks in CPK colors. Dashed lines represent polar interactions (H-bonds). The P_s and P_i sites are annotated. Inset (top right) shows the quality of the experimental electron density surrounding the cofactor.

tagged *Li*GAPDH by Western blotting with anti-C5a and anti-His antibodies (Figures 5C, D, indicated by asterisks), demonstrating the formation of *Li*GAPDH:C5a cross-linked complexes. This interaction necessarily involves protein surfaces containing a free Cys residue. The only free Cys in C5a (Cys704 in C5 numbering, Cys27 in C5a numbering) must therefore mediate this interaction. Based on previous evidence (16) we hypothesize that the catalytic Cys residue (Cys152 in *Li*GAPDH) participates in this interaction. Cys152 is the most reactive Cys residue in *Li*GAPDH since the nucleophilicity of its thiol moiety is enhanced by the catalytic environment. The specificity of the reaction was corroborated by the observation that no cross-linked bands developed in samples containing only C5a until later than the *Li*GAPDH-C5a cross-linked complexes, nor did they spontaneously appear on samples not treated with BMOE (Figure 5B).

To shed light on the structure of the *Li*GAPDH-C5a binary complexes, we carried out cross-link guided protein-protein docking with *ROSETTA*, as distance restraints from chemical cross-linking experiments can guide protein-protein docking calculations and significantly improve the accuracy of the simulations (45). All the calculated docking poses were clustered and filtered according to binding energy, compliance with distance restraints derived from the cross-linker, and the buried surface area. After analyzing the 10 most populated clusters of binary complexes (Supplementary Figure 7), the most likely docking pose was identified (Figure 6A). In this pose, C5a approximates the *Li*GAPDH deep groove at the interface between chains Q and P, making polar interactions with residues from both chains (shown in aquamarine and violet, respectively, in Figures 6A, B). Residues from C5a implicated in binding include residues near Cys27 (residues 23-36) and also from the *N*- and the *C*-terminal helices (Figure 6C, color coded as in Figures 6A, B). As far as the electrostatic potential is concerned, the face of C5a that comes closest to *Li*GAPDH bears a slightly negative charge, which is complementary to the long and positively charged cavity of the active site and neighboring residues (Figures 6D, E). The *C*-terminal helix of C5a tilts at an angle that allows it to slide out of the binding site. This orientation is consistent with known facts about the interaction of GAPDH from various organisms with mostly α-helical proteins of small size (53–55).

Other high-ranking docking poses exploited the same or very similar docking surfaces as the top-ranking pose, differing mainly in the angle with which C5a approximated *Li*GAPDH (Supplementary Figure 7). Using the most representative poses, which differ minimally in the binding site, we can describe a consensus binding interface (Figure 7). Concerning *Li*GAPDH, the surface residues that mediate most contacts with C5a belong to the *N*- and *C*-terminal domains and to two chains, Q and P. On subunit Q, the three identified patches comprise residues 75-81 (patch 1Q), 183-185 (patch 2Q), and 192-196 (patch 3Q); and, on subunit P, residues 36-38 (patch 1P), 7 and 96-97 (patch 2P), and 182-186 and 191-196 (patch 3P) (Figure 7A). Reciprocally, the C5a residues that consistently contributed to the docking interface in the top-ranking docking solutions comprised residues surrounding Cys27

TABLE 3 *Li*GAPDH kinetic parameters.

	V_{max} (m*M* min^{-1})	K_m (m*M*)	K_{SS} (m*M*)	k_{cat} (s^{-1})	k_{cat}/K_m (mM^{-1} s^{-1})
G3P	$(4.2 \pm 0.4) \times 10^{-2}$	0.6 ± 0.1	2.0 ± 0.3	70 ± 7	121 ± 24
NAD^+	$(2.65 \pm 0.05) \times 10^{-2}$	0.081 ± 0.006	–	44.2 ± 0.9	543 ± 44
P_i	$(6.6 \pm 0.4) \times 10^{-2}$	1.2 ± 0.1	10 ± 1	110 ± 7	91 ± 13

TABLE 4 Inhibition of *Li*GAPDH by anacardic acid and curcumin.

Inhibitor	Mode	Substrate	V_{max} (m*M* min^{-1})	K_m (m*M*)	K_i (μ*M*)	k_{cat} (s^{-1})	k_{cat}/K_m (mM^{-1} s^{-1})
Anacardic acid	NC[1]	G3P	$(3.18 \pm 0.09) \times 10^{-2}$	0.65 ± 0.04	135 ± 8	53 ± 1	82 ± 6
		NAD^+	$(2.79 \pm 0.06) \times 10^{-2}$	0.076 ± 0.005	41 ± 2	46.5 ± 0.9	612 ± 43
Curcumin	NC	G3P	$(3.22 \pm 0.09) \times 10^{-2}$	0.66 ± 0.04	148 ± 9	54 ± 2	81 ± 6
		NAD^+	$(2.76 \pm 0.04) \times 10^{-2}$	0.072 ± 0.004	59 ± 3	46 ± 1	637 ± 33

[1] NC, noncompetitive inhibition.

and from the two long helices (Figure 7B); the end of the *C*-terminal helix was pointing out of the docking site in most poses. The generally polar nature of the interface of most docking poses and the relatively wide range of compatible tilts for C5a (within the same small docking area) are compatible with a weak interaction between C5a and *Li*GAPDH, which could be enhanced in the biological context through electrostatic and avidity effects as previously described for GAPDH from Gram-positive pathogens (18, 19).

4 Discussion

Vertebrate innate immunity has evolved to prevent and fight infections by recognizing features of pathogens that are broadly shared such as plasma membrane lipids and cell-wall composition, called pathogen-associated molecular patterns (PAMPs). The complement system is one of the oldest and most efficient branches of our innate immunity. It therefore makes evolutionary sense that many pathogens have evolved sophisticated molecular weaponry to circumvent, inactivate, or mimic components of the complement system. Bacteria (and many eukaryotic parasites) rely on multiple complement-evasive strategies, often deployed simultaneously. One of these complement-targeting strategies consists in the neutralization of the C5a anaphylatoxin, which bacteria have learned to do in two separate but complementary ways: by proteolytic inactivation and by direct binding (sequestration). Proteases that can cleave C5a are deployed by pathogenic bacteria (56) as diverse as *Pseudomonas aeruginosa* (the alkaline protease ArpA and elastase B LasB) (57) and all sequenced serotypes of Group B streptococci (streptococcal cell-wall C5a peptidase) (58, 59).

Besides the direct proteolytic cleavage of C5a, some pathogens have also evolved the capacity to bind and retain C5a close to the

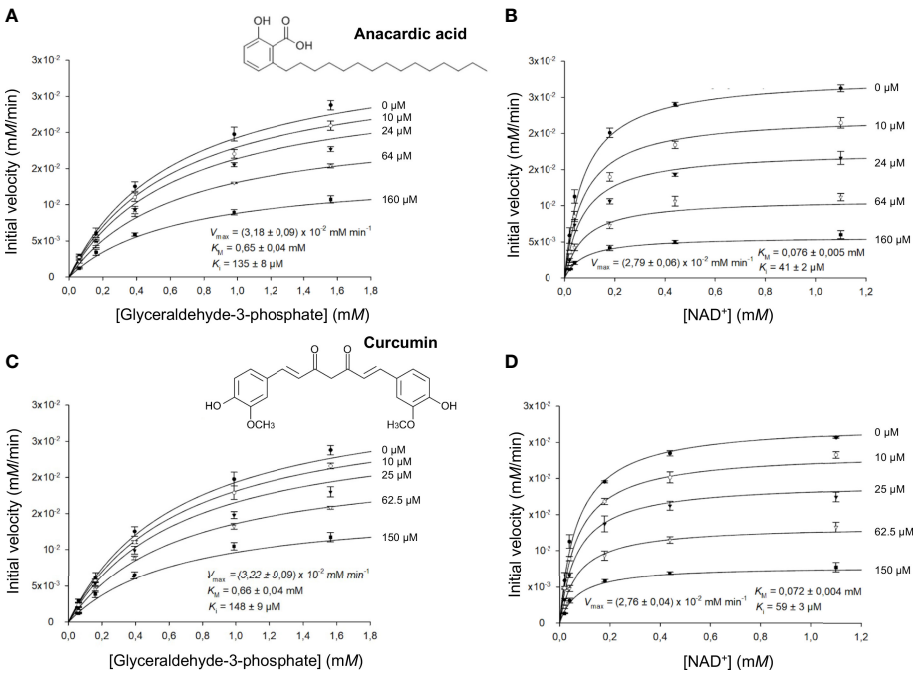

FIGURE 4
LiGAPDH can be inhibited by natural products. Initial rate of reaction plotted in the presence of various concentrations of anacardic acid (10-160 μ*M*) against the concentration of **(A)** glyceraldehyde-3-phosphate (G3P) or **(B)** NAD^+, and in the presence of curcumin (10-150 μ*M*) against the concentration of **(C)** glyceraldehyde-3-phosphate (G3P) or **(D)** NAD^+. Each experimental data point represents the mean and the errors are standard deviations of the mean (SEM) from three independent experiments. Nonlinear regression to a Michaelis-Menten hyperbolic model with noncompetitive inhibition was carried out with SigmaPlot 14.5 (R^2 = 0.98).

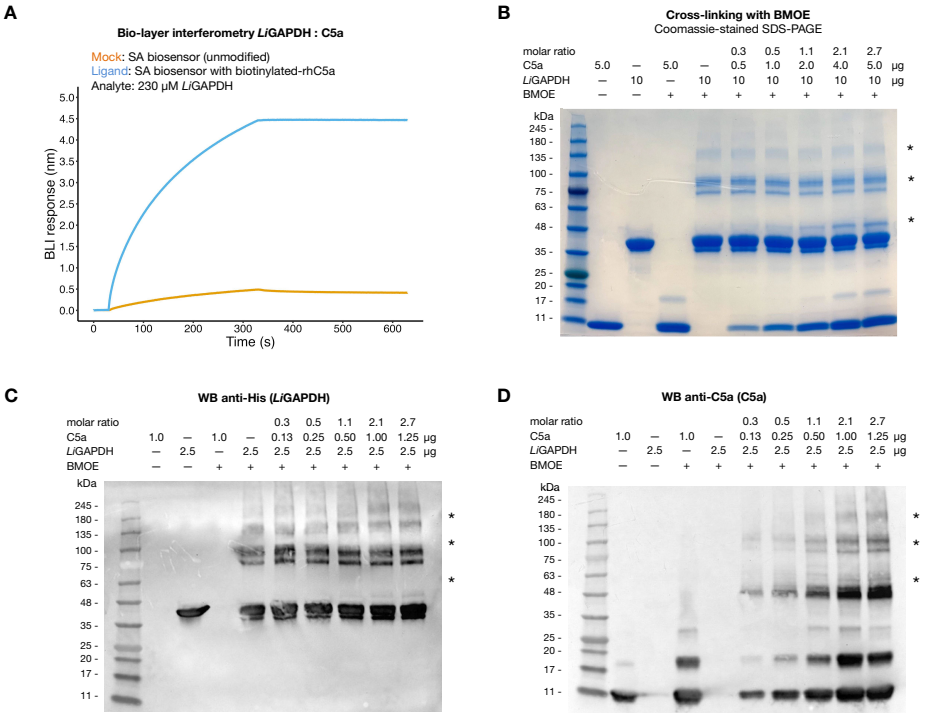

FIGURE 5
Interaction of *Li*GAPDH-C5a. **(A)** Bio-layer interferometry sensorgrams showing the wavelength shift length or BLI response (nm) obtained by incubating streptavidin (SA) biosensors previously loaded with biotinylated-C5a (blue line) or unmodified (orange line) with 230 µ*M Li*GAPDH. **(B)** SDS-PAGE electrophoretic separation of cross-linking reactions of *Li*GAPDH and C5a with BMOE. Gel loaded with mock-treated control samples and BMOE-treated samples (increasing concentrations of C5a for a fixed concentration of *Li*GAPDH). The first two lanes with added BMOE represent internal controls for C5a (maximum load) and *Li*GAPDH without added C5a. **(C)** Western blotting of the same samples in **(A)** revealed with an anti-His HRP antibody. **(D)** Like **(C)** with an anti-C5a primary antibody **(D)**. Asterisks indicate protein bands containing cross-linked *Li*GAPDH:C5a complexes.

site of infection, thereby precluding the anaphylatoxin (or, at least, slowing it down) from recruiting neighboring phagocytes. One of the virulence factors is the moonlighting protein GAPDH. Intracellularly, GAPDH is the well-known glycolytic enzyme; however, outside the cell, GAPDH can bind C5a (and, in some microorganisms, C3). In *S. pneumoniae*, GAPDH remains associated with the cell wall, indicating that bound C5a remains attached to the pathogen cells (16). Reciprocally, in clinical isolates of *S. pyogenes*, added C5a binds the cells in a dose-dependent fashion (19). These two complementary views show that streptococcal cells have the ability to "soak in" C5a, effectively shielding it from macrophages. Other cell-wall components might help to retain C5a besides GAPDH, further enhancing the immune evasive effect.

L. interrogans is a Gram-negative pathogen with an impressive array of immune evasive mechanisms, including many targeted at complement factors (13, 60). Several of the best characterized immune evasion mechanisms of *L. interrogans* include recruiting endogenous complement regulators such as FH and C4BP (13, 61, 62). However, complement-targeting immune evasion mechanisms directly interfering with C5a had not been demonstrated. In this work, we have shown that C5a binding and sequestration through *Li*GAPDH can provide an additional immune evasive mechanism to an already impressive weaponry. In support of this view, other metabolic and glycolytic enzymes have been shown to perform similar functions, such as enolase (22), EF-Tu (63), and the chaperonin GroEL (64). The *in vivo* relevance of these interactions for the pathogen's survival in the host is still a matter of debate, further complicated by the essential nature of the bacterial genes encoding most moonlighting proteins, which precludes the analysis of gene deletion phenotypes, and the high concentrations found for these proteins in both the bacterial cytosol and exoproteome. Another difficulty for dissecting the relevance of specific moonlighting/virulence factors arises from the multiplicity of redundant and nonredundant immune evasive strategies that appear to contribute to the adaptation of *L. interrogans* and other bacterial pathogens to their hosts.

To better understand the unconventional roles of *Li*GAPDH, we have solved the crystal structure of the holoenzyme to 2.37-Å resolution. The crystallographic structure agrees with the solution SAXS data, suggesting that the crystal lattice has trapped the native conformation. The structural information it provides contributes to a significant pool of GAPDH structures available at the PDB. This information can be used for purposes such as drug discovery and repurposing campaigns in cases where GAPDH has a role in completely expressing pathogen's virulence. This unconventional

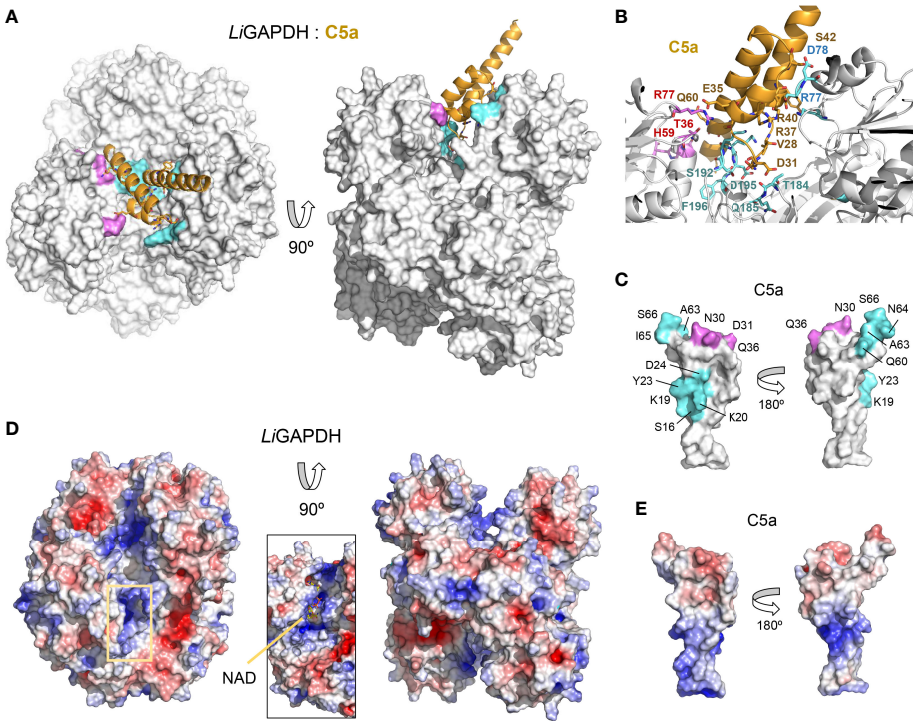

FIGURE 6
*Li*GAPDH-C5a complex by guided docking. **(A)** Two views 90° apart of the top-ranking *Li*GAPDH-C5a docking pose, shown in molecular surface representation (*Li*GAPDH, in white) and in cartoon (C5a, in orange). *Li*GAPDH residues engaged in polar interactions with C5a are shown in aquamarine (Q subunit) or violet (P subunit). **(B)** Zoom into the binding interface with interacting residues shown in sticks and annotated, color coded as in **(A)**. **(C)** Two orientations 180° apart of C5a shown in molecular surface representation, with residues engaged in interactions with the Q and P subunits of *Li*GAPDH colored in aquamarine and violet, respectively. **(D)** Electrostatic potential surface of *Li*GAPDH mapped onto the same two orientations shown in **(A)**. The inset zooms into the NAD^+ binding site, highlighting the positively charged residues in the neighboring area. **(E)** Electrostatic potential surface of C5a mapped onto the same two orientations shown in **(C)**. It can be noted that the region around Cys27 is slightly negatively charged.

role appears to be rather prevalent as phylogenetically diverse Gram-negative and Gram-positive bacteria (and at least one eukaryotic parasite too) exhibit it (16, 18–21, 56). In this light, the kinetic characterization that we have performed on *Li*GAPDH shows that the enzyme is susceptible to inhibition by natural products such as anacardic acid and curcumin. Given the favorable safety profile of these natural products, they represent promising starting points for further drug development.

In the context of leptospirosis, extracellular *Li*GAPDH may play a virulence role by binding to C5a generated by the activation of complement's terminal pathway. Indeed, *Li*GAPDH has been shown to be one of the twenty most abundant proteins in the extracellular proteome of pathogenic *L. interrogans* strains (11). Although not yet known, *Li*GAPDH could be exported to the cellular exterior by type I or II secretion systems or *via* extracellular vesicles, two of the most common secretion mechanisms characterized in *L. interrogans*.

In this work, we have shown by bio-layer interferometry and cross-linking experiments that *Li*GAPDH and C5a can form a specific complex at a sufficiently high concentration to overcome an intrinsically slow kinetic association constant. Initially, a weak interaction between nascent C5a (generated *in situ* on the surface of opsonized bacteria) and *Li*GAPDH could delay C5a diffusion long enough to be proteolytically degraded by nonspecific proteases from the pathogen or dearginated by serum carboxypeptidases; in fact, deargination of anaphylatoxins C5a and C3a *in vivo* is a fast and irreversible process that dampens the chemotactic response. In either scenario, neutrophil recruitment to the site of infection would be much reduced. The cross-link guided docking protocol that we have explored in this work produces *Li*GAPDH-C5a complexes that are compatible with the known facts about the interaction: proximity between C5a Cys27, the only free Cys residue in C5a, and the highly reactive catalytic Cys152 residue; structural and electrostatic complementarity at the docking site; a considerable buried interface (>2000 $Å^2$); a predominantly electrostatic nature; and a variety of compatible poses differing in the overall tilt of C5a inside the interfacial groove between *Li*GAPDH Q-P subunits.

As our structural knowledge of the molecular machinery of the host's innate immunity and the pathogens' immune evasion factors expands and refines, our tools to fight recalcitrant infections will likely become more efficient and sophisticated. In the face of the dwindling efficacy of antibiotics and the looming medical and humanitarian crisis unleashed by global warming, further

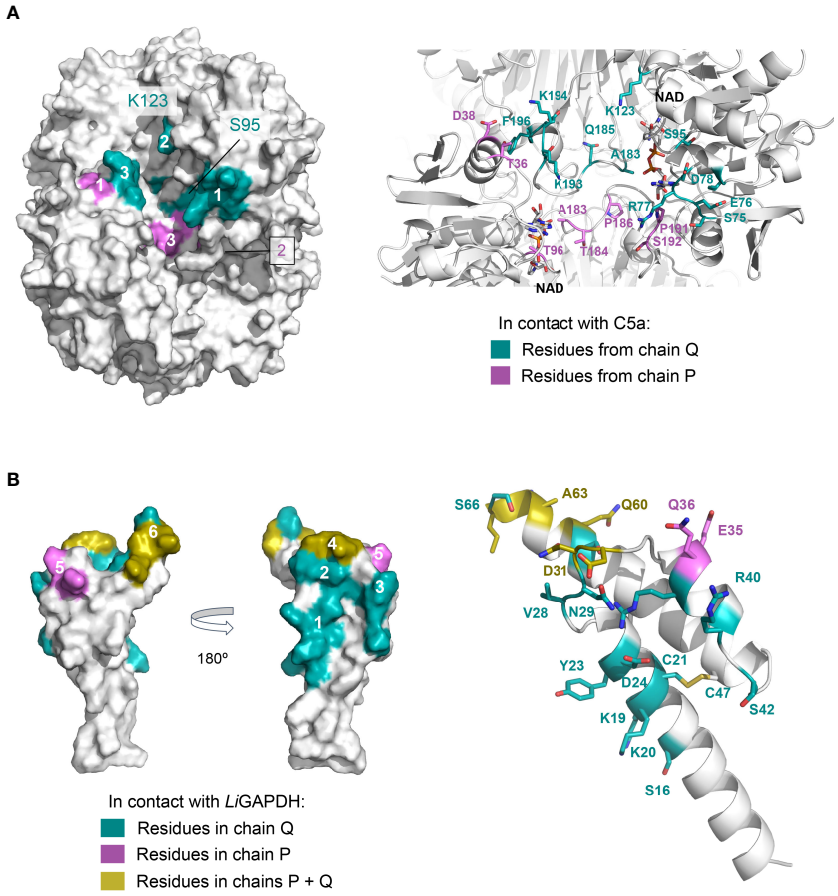

FIGURE 7
Consensus docking surfaces for *Li*GAPDH-C5a. **(A)** Molecular surface representation of *Li*GAPDH (in white). Surface areas that interact with C5a in most of the top-ranking docking poses (consensus docking surfaces) are highlighted in aquamarine if the residues come from the Q subunit, and violet if they come from the P subunit. Spatially close residues define up to three interaction patches on chains Q and P. The inset shows a zoom into the area containing the consensus docking residues (shown in sticks with the same color coding); *Li*GAPDH is shown in cartoon (in white). **(B)** Likewise, for C5a. Two orientations 180° apart are shown for the molecular surface representation. Residues in aquamarine interact with the Q subunit and in violet with the P subunit of *Li*GAPDH; the few residues that interact with both the Q and P subunits are colored yellow. Patches are numbered 1 through 6. Patches 4 and 6 (in yellow) pivot between binding the Q or the P subunits depending on the specific pose. In addition, C5a is shown in cartoons with the residues predicted to interact with *Li*GAPDH shown in sticks and with the same color coding.

research is sorely needed to generate new approaches to curb infectious diseases through the combination of structural information from the host's innate immune system and the pathogens' virulence factors.

Data availability statement

The datasets presented in this study can be found in online repositories. The names of the repository/repositories and accession number(s) can be found in the article/Supplementary Material.

Author contributions

FJF and MCV contributed to the conception of the study and the design of all the experiments. SNY and KdlP expressed and purified the protein samples for biochemical and structural analysis. SNY, KdlP, and SGQ performed kinetics experiments. SNY performed the BLI experiments. JQG carried out the cross-linking experiments, FJF and MCV ran the cross-link guide docking calculations and analyses. FJF and MCV collected the diffraction data. SNY, FJF and MCV solved and refined the crystal structure and the SAXS shape. FJF and MCV wrote the manuscript. SRdC read the manuscript critically. All authors contributed to the article and approved the submitted version.

Funding

This work was funded by Spanish Ministerio de Ciencia, Innovación y Universidades-FEDER grants RTI2018-102242-B-I00 (to MCV) and PID2019-104912RB-I00 (to SRdC); and the Spanish Ministerio de Ciencia e Innovación-Recovery, Transformation and Resilience Plan (PRTR) grant PDC2022-

133713-I00. It was also funded by Grants S2017/BMD-3673 and S2022/BMD-7278 of the Regional Government of Madrid and the European Commission – NextGenerationEU through CSIC's Global Health Platform ("PTI Salud Global") (SGL2103020) (to SRdC and MCV), and the CSIC Special Intramural Grant PIE-201620E064 (to MCV). It was additionally supported by the Research Network on Complement in Health and Disease (RED2022-134750-T). SRdC was also supported by the CIBER de Enfermedades Raras. KdlP was supported by an Industrial PhD grant (IND2018-010094) awarded by the Spanish Ministerio de Economía y Competitividad.

Acknowledgments

The authors acknowledge the ALBA synchrotron light source (Barcelona, Spain) for the provision of synchrotron radiation facilities at the BL13-XALOC beamline and the Diamond Light Source (Leeds, UK) for access to the BioSAXS B21 beamline under Proposal SM28015. SNY and KdlP acknowledge the support of the PhD program in Biochemistry, Molecular Biology and Biomedicine of the Universidad Complutense de Madrid (UCM).

Conflict of interest

Abvance Biotech slr provided salaries for KdlP, JQG and FJF.

The remaining authors declare that the research was conducted in the absence of any commercial or financial relationships that could be construed as a potential conflict of interest.

Publisher's note

Supplementary material

The Supplementary Material for this article can be found online at: https://www.frontiersin.org/articles/10.3389/fimmu.2023.1190943/full#supplementary-material

References

1. Walport MJ. Complement. first of two parts. *N Engl J Med* (2001) 344:1058–66. doi: 10.1056/NEJM200104053441406

2. Medicus RG, Melamed J, Arnaout MA. Role of human factor I and C3b receptor in the cleavage of surface-bound C3bi molecules. *Eur J Immunol* (1983) 13:465–70. doi: 10.1002/eji.1830130607

3. Rawal N, Pangburn MK. Structure/function of C5 convertases of complement. *Int Immunopharmacol* (2001) 1:415–22. doi: 10.1016/s1567-5769(00)00039-4

4. Xie CB, Jane-Wit D, Pober JS. Complement membrane attack complex: new roles, mechanisms of action, and therapeutic targets. *Am J Pathol* (2020) 190:1138–50. doi: 10.1016/j.ajpath.2020.02.006

5. Guo R-F, Ward PA. Role of C5a in inflammatory responses. *Annu Rev Immunol* (2005) 23:821–52. doi: 10.1146/annurev.immunol.23.021704.115835

6. Merle NS, Church SE, Fremeaux-Bacchi V, Roumenina LT. Complement system part I – molecular mechanisms of activation and regulation. *Front Immunol* (2015) 6:262. doi: 10.3389/fimmu.2015.00262

7. Bharti AR, Nally JE, Ricaldi JN, Matthias MA, Diaz MM, Lovett MA, et al. Leptospirosis: a zoonotic disease of global importance. *Lancet Infect Dis* (2003) 3:757–71. doi: 10.1016/s1473-3099(03)00830-2

8. Adler B, de la Peña Moctezuma A. Leptospira and leptospirosis. *Vet Microbiol* (2010) 140:287–96. doi: 10.1016/j.vetmic.2009.03.012

9. Putz EJ, Nally JE. Investigating the immunological and biological equilibrium of reservoir hosts and pathogenic leptospira: balancing the solution to an acute problem? *Front Microbiol* (2020) 11:2005. doi: 10.3389/fmicb.2020.02005

10. Costa F, Hagan JE, Calcagno J, Kane M, Torgerson P, Martinez-Silveira MS, et al. Global morbidity and mortality of leptospirosis: a systematic review. *PloS Negl Trop Dis* (2015) 9:e0003898. doi: 10.1371/journal.pntd.0003898

11. Eshghi A, Pappalardo E, Hester S, Thomas B, Pretre G, Picardeau M. Pathogenic leptospira interrogans exoproteins are primarily involved in heterotrophic processes. *Infect Immun* (2015) 83:3061–73. doi: 10.1128/IAI.00427-15

12. Goarant C. Leptospirosis: risk factors and management challenges in developing countries. *Res Rep Trop Med* (2016) 7:49–62. doi: 10.2147/RRTM.S102543

13. Fraga TR, Isaac L, Barbosa AS. Complement evasion by pathogenic leptospira. *Front Immunol* (2016) 7:623. doi: 10.3389/fimmu.2016.00623

14. Barbosa AS, Abreu PAE, Vasconcellos SA, Morais ZM, Gonçales AP, Silva AS, et al. Immune evasion of leptospira species by acquisition of human complement regulator C4BP. *Infect Immun* (2009) 77:1137–43. doi: 10.1128/IAI.01310-08

15. Cosate MR, Siqueira GH, de Souza GO, Vasconcellos SA, Nascimento ALTO. Mammalian cell entry (Mce) protein of leptospira interrogans binds extracellular matrix components, plasminogen and beta2 integrin. *Microbiol Immunol* (2016) 60:586–98. doi: 10.1111/1348-0421.12406

16. Terao Y, Yamaguchi M, Hamada S, Kawabata S. Multifunctional glyceraldehyde-3-phosphate dehydrogenase of streptococcus pyogenes is essential for evasion from neutrophils. *J Biol Chem* (2006) 281:14215–23. doi: 10.1074/jbc.M513408200

17. Aguilera L, Ferreira E, Giménez R, Fernández FJ, Taulés M, Aguilar J, et al. Secretion of the housekeeping protein glyceraldehyde-3-phosphate dehydrogenase by the LEE-encoded type III secretion system in enteropathogenic escherichia coli. *Int J Biochem Cell Biol* (2012) 44:955–62. doi: 10.1016/j.biocel.2012.03.002

18. Querol-García J, Fernández FJ, Marin AV, Gómez S, Fullà D, Melchor-Tafur C, et al. Crystal structure of glyceraldehyde-3-Phosphate dehydrogenase from the gram-positive bacterial pathogen a. vaginae, an immunoevasive factor that interacts with the human C5a anaphylatoxin. *Front Microbiol* (2017) 8:541. doi: 10.3389/fmicb.2017.00541

19. Gómez S, Querol-García J, Sánchez-Barrón G, Subias M, González-Alsina À, Franco-Hidalgo V, et al. The antimicrobials anacardic acid and curcumin are not-competitive inhibitors of gram-positive bacterial pathogenic glyceraldehyde-3-Phosphate dehydrogenase by a mechanism unrelated to human C5a anaphylatoxin binding. *Front Microbiol* (2019) 10:326. doi: 10.3389/fmicb.2019.00326

20. Terrasse R, Tacnet-Delorme P, Moriscot C, Pérard J, Schoehn G, Vernet T, et al. Human and pneumococcal cell surface glyceraldehyde-3-phosphate dehydrogenase (GAPDH) proteins are both ligands of human C1q protein. *J Biol Chem* (2012) 287:42620–33. doi: 10.1074/jbc.M112.423731

21. Sahoo S, Murugavel S, Devi IK, Vedamurthy GV, Gupta SC, Singh BP, et al. Glyceraldehyde-3-phosphate dehydrogenase of the parasitic nematode haemonchus contortus binds to complement C3 and inhibits its activity. *Parasite Immunol* (2013) 35:457–67. doi: 10.1111/pim.12058

22. Nogueira SV, Backstedt BT, Smith AA, Qin J-H, Wunder EA, Ko A, et al. Leptospira interrogans enolase is secreted extracellularly and interacts with plasminogen. *PloS One* (2013) 8:e78150. doi: 10.1371/journal.pone.0078150

23. Ferdinand W. The isolation and specific activity of rabbit-muscle glyceraldehyde phosphate dehydrogenase. *Biochem J* (1964) 92:578–85. doi: 10.1042/bj0920578

24. Juanhuix J, Gil-Ortiz F, Cuní G, Colldelram C, Nicolás J, Lidón J, et al. Developments in optics and performance at BL13-XALOC, the macromolecular crystallography beamline at the alba synchrotron. *J Synchrotron Radiat* (2014) 21:679–89. doi: 10.1107/S160057751400825X

25. Kabsch W. XDS. In: *International tables for crystallography* (2012). (International Union of Crystallography). 11.6, 304–10. doi: 10.1107/97809553602060000835

26. Evans PR, Murshudov GN. How good are my data and what is the resolution? *Acta Crystallogr D Biol Crystallogr* (2013) 69:1204–14. doi: 10.1107/S0907444913000061

27. McCoy AJ, Grosse-Kunstleve RW, Adams PD, Winn MD, Storoni LC, Read RJ. Phaser crystallographic software. *J Appl Crystallogr* (2007) 40:658–74. doi: 10.1107/S0021889807021206

28. Adams PD, Afonine PV, Bunkóczi G, Chen VB, Davis IW, Echols N, et al. PHENIX: a comprehensive Python-based system for macromolecular structure solution. *Acta Crystallogr D Biol Crystallogr* (2010) 66:213–21. doi: 10.1107/S0907444909052925

29. Afonine PV, Grosse-Kunstleve RW, Echols N, Headd JJ, Moriarty NW, Mustyakimov M, et al. Towards automated crystallographic structure refinement with phenix.refine. *Acta Crystallogr Sect Biol Crystallogr* (2012) 68:352–67. doi: 10.1107/S0907444912001308

30. Emsley P, Lohkamp B, Scott WG, Cowtan K. Features and development of coot. *Acta Crystallogr Sect Biol Crystallogr* (2010) 66:486–501. doi: 10.1107/S0907444910007493

31. Cowieson NP, Edwards-Gayle CJC, Inoue K, Khunti NS, Doutch J, Williams E, et al. Beamline B21: high-throughput small-angle X-ray scattering at diamond light source. *J Synchrotron Radiat* (2020) 27:1438–46. doi: 10.1107/S1600577520009960

32. Franke D, Jeffries CM, Svergun DI. Correlation map, a goodness-of-fit test for one-dimensional X-ray scattering spectra. *Nat Methods* (2015) 12:419–22. doi: 10.1038/nmeth.335

33. Manalastas-Cantos K, Konarev PV, Hajizadeh NR, Kikhney AG, Petoukhov MV, Molodenskiy DS, et al. ATSAS 3.0: expanded functionality and new tools for small-angle scattering data analysis. *J Appl Crystallogr* (2021) 54:343–55. doi: 10.1107/S1600576720013412

34. Konarev PV, Svergun DI. A posteriori determination of the useful data range for small-angle scattering experiments on dilute monodisperse systems. *IUCrJ* (2015) 2:352–60. doi: 10.1107/S2052252515005163

35. Guinier A. La diffraction des rayons X aux très petits angles: application à l'étude de phénomènes ultramicroscopiques. *Ann Phys* (1939) 11:161–237. doi: 10.1051/anphys/193911120161

36. Svergun DI. Determination of the regularization parameter in indirect-transform methods using perceptual criteria. *J Appl Crystallogr* (1992) 25:495–503. doi: 10.1107/S0021889892001663

37. Petoukhov MV, Franke D, Shkumatov AV, Tria G, Kikhney AG, Gajda M, et al. New developments in the ATSAS program package for small-angle scattering data analysis. *J Appl Crystallogr* (2012) 45:342–50. doi: 10.1107/S0021889812007662

38. Petoukhov MV, Svergun DI. Ambiguity assessment of small-angle scattering curves from monodisperse systems. *Acta Crystallogr Sect D* (2015) 71:1051–8. doi: 10.1107/S1399004715002576

39. Franke D, Svergun DI. DAMMIF, a program for rapid ab-initio shape determination in small-angle scattering. *J Appl Crystallogr* (2009) 42:342–6. doi: 10.1107/S0021889809000338

40. Volkov VV, Svergun DI. Uniqueness of ab initio shape determination in small-angle scattering. *J Appl Crystallogr* (2003) 36:860–4. doi: 10.1107/S0021889803000268

41. Svergun DI. Restoring low resolution structure of biological macromolecules from solution scattering using simulated annealing. *Biophys J* (1999) 76:2879–86. doi: 10.1016/S0006-3495(99)77443-6

42. Kozin MB, Svergun DI. Automated matching of high- and low-resolution structural models. *J Appl Crystallogr* (2001) 34:33–41. doi: 10.1107/S0021889800014126

43. Tuukkanen AT, Kleywegt GJ, Svergun DI. Resolution of ab initio shapes determined from small-angle scattering. *IUCrJ* (2016) 3:440–7. doi: 10.1107/S2052252516016018

44. Svergun D, Barberato C, Koch MHJ. CRYSOL – a program to evaluate X-ray solution scattering of biological macromolecules from atomic coordinates. *J Appl Crystallogr* (1995) 28:768–73. doi: 10.1107/S0021889895007047

45. Kahraman A, Herzog F, Leitner A, Rosenberger G, Aebersold R, Malmström L. Cross-link guided molecular modeling with ROSETTA. *PloS One* (2013) 8:e73411. doi: 10.1371/journal.pone.0073411

46. Kahraman A, Malmström L, Aebersold R. Xwalk: computing and visualizing distances in cross-linking experiments. *Bioinformatics* (2011) 27:2163–4. doi: 10.1093/bioinformatics/btr348

47. Mitternacht S. FreeSASA: an open source c library for solvent accessible surface area calculations. *F1000Research* (2016) 5:189. doi: 10.12688/f1000research.7931.1

48. Krissinel E. Macromolecular complexes in crystals and solutions. *Acta Crystallogr Sect Biol Crystallogr* (2011) 67:376–85. doi: 10.1107/S0907444911007232

49. Hosseinzadeh P, Bhardwaj G, Mulligan VK, Shortridge MD, Craven TW, Pardo-Avila F, et al. Comprehensive computational design of ordered peptide macrocycles. *Science* (2017) 358:1461–6. doi: 10.1126/science.aap7577

50. Jurrus E, Engel D, Star K, Monson K, Brandi J, Felberg LE, et al. Improvements to the APBS biomolecular solvation software suite. *Protein Sci* (2018) 27:112–28. doi: 10.1002/pro.3280

51. *The PyMOL molecular graphics system, version 2.0*. Available at: https://pymol.org/2/support.html?#citing (Accessed December 9, 2022).

52. Pereira JM, Severino RP, Vieira PC, Fernandes JB, da Silva MFGF, Zottis A, et al. Anacardic acid derivatives as inhibitors of glyceraldehyde-3-phosphate dehydrogenase from trypanosoma cruzi. *Bioorg Med Chem* (2008) 16:8889–95. doi: 10.1016/j.bmc.2008.08.057

53. Matsumura H, Kai A, Maeda T, Tamoi M, Satoh A, Tamura H, et al. Structure basis for the regulation of glyceraldehyde-3-Phosphate dehydrogenase activity via the intrinsically disordered protein CP12. *Structure* (2011) 19:1846–54. doi: 10.1016/j.str.2011.08.016

54. McFarlane CR, Shah NR, Kabasakal BV, Echeverria B, Cotton CAR, Bubeck D, et al. Structural basis of light-induced redox regulation in the Calvin–Benson cycle in cyanobacteria. *Proc Natl Acad Sci* (2019) 116:20984–90. doi: 10.1073/pnas.1906722116

55. Yu A, Xie Y, Pan X, Zhang H, Cao P, Su X, et al. Photosynthetic phosphoribulokinase structures: enzymatic mechanisms and the redox regulation of the Calvin-Benson-Bassham cycle. *Plant Cell* (2020) 32:1556–73. doi: 10.1105/tpc.19.00642

56. Fernández FJ, Gómez S, Vega MC. Pathogens' toolbox to manipulate human complement. *Semin Cell Dev Biol* (2019) 85:98–109. doi: 10.1016/j.semcdb.2017.12.001

57. Mateu-Borrás M, González-Alsina A, Doménech-Sánchez A, Querol-García J, Fernández FJ, Vega MC, et al. Pseudomonas aeruginosa adaptation in cystic fibrosis patients increases C5a levels and promotes neutrophil recruitment. *Virulence* (2022) 13:215–24. doi: 10.1080/21505594.2022.2028484

58. Cheng Q, Stafslien D, Purushothaman SS, Cleary P. The group b streptococcal C5a peptidase is both a specific protease and an invasin. *Infect Immun* (2002) 70:2408–13. doi: 10.1128/IAI.70.5.2408-2413.2002

59. Lynskey NN, Reglinski M, Calay D, Siggins MK, Mason JC, Botto M, et al. Multi-functional mechanisms of immune evasion by the streptococcal complement inhibitor C5a peptidase. *PloS Pathog* (2017) 13:e1006493. doi: 10.1371/journal.ppat.1006493

60. Alves da Silva PYO, Midon LM, Heinemann MB, de Moraes Vasconcelos D, Barbosa AS, Isaac L. Contribution of complement system pathways to the killing of leptospira spp. *Microbes Infect* (2020) 22:550–7. doi: 10.1016/j.micinf.2020.07.005

61. Castiblanco-Valencia MM, Fraga TR, da SLB, Monaris D, Abreu PAE, Strobel S, et al. Leptospiral immunoglobulin-like proteins interact with human complement regulators factor h, FHL-1, FHR-1, and C4BP. *J Infect Dis* (2012) 205:995–1004. doi: 10.1093/infdis/jir875

62. Meri T, Murgia R, Stefanel P, Meri S, Cinco M. Regulation of complement activation at the C3-level by serum resistant leptospires. *Microb Pathog* (2005) 39:139–47. doi: 10.1016/j.micpath.2005.07.003

63. Wolff DG, Castiblanco-Valencia MM, Abe CM, Monaris D, Morais ZM, Souza GO, et al. Interaction of leptospira elongation factor tu with plasminogen and complement factor h: a metabolic leptospiral protein with moonlighting activities. *PloS One* (2013) 8:e81818. doi: 10.1371/journal.pone.0081818

64. Ho JD, Takara LEM, Monaris D, Gonçalves AP, Souza-Filho AF, de Souza GO, et al. GroEL protein of the leptospira spp. interacts with host proteins and induces cytokines secretion on macrophages. *BMC Microbiol* (2021) 21:99. doi: 10.1186/s12866-021-02162-w

frontiers | Frontiers in Immunology

TYPE Original Research
PUBLISHED 29 August 2023
DOI 10.3389/fimmu.2023.1254415

OPEN ACCESS

EDITED BY
Payam Behzadi,
Islamic Azad University, ShahreQods, Iran

REVIEWED BY
Jean-philippe Herbeuval,
UMR8601 Laboratoire de Chimie et Biochimie Pharmacologiques et Toxicologiques, France
Shuobing Chen,
Columbia University, United States
Naoyuki Kondo,
Kansai Medical University, Japan

*CORRESPONDENCE
Hyun Ho Park
xrayleox@cau.ac.kr

RECEIVED 07 July 2023
ACCEPTED 11 August 2023
PUBLISHED 29 August 2023

CITATION
Ha HJ, Kim JH, Lee GH, Kim S and Park HH (2023) Structural basis of IRGB10 oligomerization by GTP hydrolysis. *Front. Immunol.* 14:1254415. doi: 10.3389/fimmu.2023.1254415

Structural basis of IRGB10 oligomerization by GTP hydrolysis

Hyun Ji Ha[1], Ju Hyeong Kim[1,2], Gwan Hee Lee[1,2], Subin Kim[1,2] and Hyun Ho Park[1,2]*

[1]College of Pharmacy, Chung-Ang University, Seoul, Republic of Korea, [2]Department of Global Innovative Drugs, Graduate School of Chung-Ang University, Seoul, Republic of Korea

Immunity-related GTPase B10 (IRGB10) is a crucial member of the interferon (IFN)-inducible GTPases and plays a vital role in host defense mechanisms. Following infection, IRGB10 is induced by IFNs and functions by liberating pathogenic ligands to activate the inflammasome through direct disruption of the pathogen membrane. Despite extensive investigation into the significance of the cell-autonomous immune response, the precise molecular mechanism underlying IRGB10–mediated microbial membrane disruption remains elusive. Herein, we present two structures of different forms of IRGB10, the nucleotide-free and GppNHp-bound forms. Based on these structures, we identified that IRGB10 exists as a monomer in nucleotide-free and GTP binding states. Additionally, we identified that GTP hydrolysis is critical for dimer formation and further oligomerization of IRGB10. Building upon these observations, we propose a mechanistic model to elucidate the working mechanism of IRGB10 during pathogen membrane disruption.

KEYWORDS

crystal structure, GTPase, innate immunity, IRG proteins, oligomerization

1 Introduction

Pathogen invasion triggers various immune responses in living organisms, the production of interferon through the immune response representing one such example (1, 2). The produced interferon triggers an intracellular signal to induce immune response-related gene expression, and the resulting proteins then contribute to proper host defense through various ways (3–5). In the event that these defense processes fail, various diseases, including immunodeficiency, can occur (6, 7). Interferon (IFN)-inducible GTPase is one of the main immune response-related proteins induced by interferons. IFN-inducible GTPases are characterized by the ability to protect the host by eliminating pathogens using their GTPase activity (8, 9). The GTPase family is divided into four groups, including Mx GTPase, very large inducible GTPase (VLIG), guanylate-binding protein (GBP), and immunity-related GTPase (IRG), according to the type of inducer interferon and physical-molecular mass of the proteins (8, 10–12). Type 1 interferons (alpha and beta) induce Mx

GTPases (72–82 kDa) (13), while type 2 interferon (gamma) induces VLIG (molecular weight: 200–285 kDa) (14), GBP (molecular weight: 65–73 kDa) (15), and IRG (molecular weight: 21–47 kDa) (16) GTPases.

The IRG family, also called p47 GTPases, comprise IFN-inducible GTPases, which are involved in the early immune response. In mice, a total of 23 genes (*IRGA 1–8, IRGB 1–10, IRGC, IRGD, IRGM 1–3*) have been identified as IRG family, while only a single full-length IRGC and truncated IRGM have been identified as human IRG family (8, 17). Similar to other GTPases, the IRG family possesses a GTPase domain containing a highly conserved P-loop to which GTP binds. The IRG family is divided into two classes, the GKS class and GMS class, according to the P-loop sequence (18). The IRG family GKS class contains a conserved G-x(4)-GKS pattern in the P-loop, while the GMS class contains a G-x(4)-GMS sequence pattern in the P-loop. All IRG families except IRGM (GMS class) are included in the GKS class (17, 18). The IRG family is known to contribute to cell-autonomous immune responses against invasion by various pathogens (19, 20).

Although their detailed working mechanisms are unclear, several studies on IRGB10, an IRG family member, have indicated that the IRG family mediates pathogen membrane disruption in collaboration with the GBP family, which is critical for the host defense mechanism (20). During this pathogen membrane disruption stage, pathogenic products, such as DNA and lipopolysaccharide (LPS), are released from the pathogen and induce the formation of inflammasomes to further promote the host immune response (20). In the case of IRGA6 and IRGB6, IRGA6 directly binds to the pathogen membrane using N-terminal myristoylation, whereas IRGB6 is not involved in the membrane disruption. However, it remains unclear whether other IRG family proteins can also directly interact with pathogens and contribute to pathogen membrane disruption similar to IRGB10 and IRGA6 (20–24). The various IRG families may have their own action mechanism for the immune system.

Among the IRG family, the structures of IRGA6 (25), IRGB6 (24), and IRGB10 (26) have been elucidated, with several studies revealing that they share similar structures, comprising two distinct domains, a helical domain, and a GTPase domain. The IRG family usually forms a unique head-to-head dimer, as well as a further oligomer during pathogen membrane disruption (26, 27). To form head-to-head dimers, IRGA6 uses the P-loop and switch I region of the GTPase domain, whereas IRGB10 uses one of the helices of the GTPase domain (26, 27). Without clear experimental data, we previously suggested a structural model of pathogen membrane disruption by IRGB10 using the elucidated GDP-bound dimeric IRGB10 structure (26). Additionally, we speculated that the structure of IRGB10 is altered by GTP hydrolysis similar to that of other GTPase proteins, such as Atlastin1, which is structurally related to the IRG families. We also speculated that GTP hydrolysis and the presence or absence of nucleotides impact the function of IRGB10. Although these assumptions were made based on the GDP-bound structure of IRGB10 in our previous study, several unanswered questions remain regarding the functional mechanism of IRGB10. First, how does nucleotide binding affect the structure and function of IRGB10? Second, is GTP hydrolysis critical for the oligomerization of IRGB10? Lastly, how can IRGB10 make pores in the pathogen membrane? To answer these questions, in this study, we elucidated two more IRGB10 structures, including nucleotide-free and GppNHp-bound forms. Additionally, we reveal that GTP hydrolysis is critical for dimer formation and further oligomerization of IRGB10. Based on the current structural, biochemical, and biophysical studies, we provide a model of IRGB10-mediated pore formation on pathogen membranes in a step-by-step manner.

2 Methods

2.1 Expression and purification of GDP-bound IRGB10

The purification details of GDP-bound IRGB10 were introduced in a previous study (26). Briefly, the plasmid containing the *IRGB10* gene was transformed into *Escherichia coli* BL21 (DE3) competent cells. Subsequently, the cells were coated onto plates containing Luria-Bertani (LB) agar and incubated overnight at 37°C. A single colony was inoculated into 5–10 mL of LB medium, transferred to 1 L of LB medium, and incubated at 37°C until the optical density (OD) reached ~0.7. Subsequently, 0.5 mM isopropyl β-D-thiogalactopyranoside was added to the medium to induce protein expression, and the cells were incubated overnight at 20°C. After overnight incubation, cells expressing IRGB10 were collected by centrifugation and suspended in 16 mL of lysis buffer (20 mM Tris-HCl pH 8.0, 500 mM NaCl, and 5 mM imidazole). Subsequently, the cells were disrupted by sonication on ice. The cell lysates were centrifuged at 10,000 g for 30 min at 4°C to remove the cell debris, and the supernatant was incubated with nickel-nitrilotriacetic acid (Ni-NTA) affinity resin (Qiagen, Hilden, Germany). After incubation, the supernatant was loaded onto a gravity-flow column (Bio-Rad, Hercules, CA, USA) and the resin was washed with 50 mL of washing buffer (20 mM Tris-HCl pH 8.0, 500 mM NaCl, and 25 mM imidazole) to remove impurities. The target protein was eluted from the resin in the column using elution buffer (20 mM Tris-HCl pH 8.0, 500 mM NaCl, and 250 mM imidazole). The eluted protein was further purified with size-exclusion chromatography (SEC) using SEC buffer (20 mM Tris-HCl pH 8.0, and 150 mM NaCl). The target protein was eluted at around 13 mL, concentrated to 10–12 mg/mL, and stored for structural and biochemical studies.

2.2 Expression and purification of nucleotide-free IRGB10

The same IRGB10 expression clone that was used for the expression and purification of GDP-bound IRGB10 was used for the expression and purification of nucleotide-free IRGB10. The expression in *E. coli* and affinity chromatography was performed using the same method as that used for the purification of GDP-bound IRGB10. During the washing step, the resin was washed with 30 mL of the first washing buffer (20 mM Tris-HCl pH 8.0, 500 mM

NaCl), before transferring the washed Ni-NTA resin to 50 mL of the second washing buffer (20 mM Tris-HCl pH 8.0, 1.5 M NaCl) and incubating for 30 min at room temperature. Subsequently, the incubated Ni-NTA resin was reloaded into a gravity column and washed again with 30 mL of the third washing buffer (20 mM Tris-HCl pH 8.0, 500 mM NaCl, 25 mM imidazole). The target protein was eluted using 3 mL elution buffer applied onto the column, and the eluted proteins were loaded onto the SEC column. A Superdex 200 Increase 10/300 GL column (GE Healthcare, Chicago, USA), which had been pre-equilibrated with the SEC buffer, was used in the SEC experiment. The absence of nucleotides was checked by UV absorbance (A260/A280), as outlined in a previous study (28).

2.3 Multi-angle light scattering

The molar masses of nucleotide-free IRGB10, GppNHp-bound IRGB10, and K81A mutant IRGB10 were determined by multi-angle light scattering (MALS). The purified target protein was injected into a Superdex 200 HR 10/30 gel-filtration column (GE Healthcare) that had been pre-equilibrated in buffer containing 20 mM Tris-HCl pH 8.0 and 150 mM NaCl. The chromatography system was coupled to a MALS detector (mini-DAWN TREOS) and a refractive index detector (Optilab DSP) (Wyatt Technology). The data were collected every 0.5 s at a flow rate of 0.4 mL/min and then analyzed using the ASTRA program.

2.4 Crystallization and data collection

Crystallization of nucleotide-free IRGB10 was performed at 20°C using the hanging drop vapor diffusion method. Initial crystals were screened using a crystallization screening kit from molecular Dimensions, Hampton Research. The crystals were grown on plates by equilibrating a mixed drop of 1 µL protein solution (8–9 mg/mL protein in SEC buffer) and 1 µL reservoir solution containing 0.1 M Tris-HCl pH 7.0, 2.0 M $(NH_4)_2SO_4$, and 0.2 M Li_2SO_4 against 0.3 mL reservoir solution. The crystallization conditions were further optimized by experimenting with various concentrations and pH values of $(NH_4)_2SO_4$. The optimized crystals appeared in the presence of 0.1 M Tris-HCl pH 7.2, 1.8 M $(NH_4)_2SO_4$, and 0.2 M Li_2SO_4.

Crystallization of the GppNHp-bound IRGB10 was performed at 20°C using the hanging drop vapor diffusion method. Just before crystallization, 10 mM GppNHp and 2 mM $MgCl_2$ were added to 11 mg/mL nucleotide-free IRGB10 protein sample and incubated for 20 min. After incubation, the mixture was screened using a crystallization screening kit. Initial crystals were grown on a reservoir solution containing 0.1 M Tris-HCl pH 8.5, 20% (w/v) polyethylene glycol (PEG), 2,000 monomethyl ether (MME), and 0.2 M trimethylamine n-oxide. The diffraction data sets were collected at the BL-5C beamline of Pohang Accelerator Laboratory (PAL) (Pohang, Republic of Korea). Data processing and scaling were conducted using the HKL2000 package.

2.5 Structure determination and analysis

The structures of nucleotide-free and GppNHp-bound IRGB10 were determined by the molecular-replacement (MR) phasing method using the Phaser program in the PHENIX program (29). The previously solved IRGB10 GDP-bound structure (PDB ID: 7C3K) was used as the search model. Model building and refinement were conducted by COOT (30) and Refmac5 (31), respectively. Water molecules were added using the ARP/wARP function in Refmac5. The geometry was inspected using PROCHECK and was found to be acceptable. The quality of the model was confirmed using MolProbity (32). All structure figures were created using PyMOL (33).

2.6 Oligomerization measurement

Oligomerization of IRGB10 was assessed using turbidity measurement (34, 35). Assembly of the IRGB10 oligomer was determined by measuring the absorbance at 350 nm UV using a Nanophotometer NP80 (IMPLEN, Munich, Germany) at 37°C. Purified proteins were concentrated to 100 µM ~ 500 µM and placed in quartz cuvettes. The protein only was placed in cuvettes before starting the measurement. After 500 s, 10 µL of the GTP and $MgCl_2$ mixture was added. After finishing the measurement, the protein samples were centrifuged at 10,000 g for 10 min at 4°C to remove aggregates. The remaining solution was loaded onto a SEC column, which had been pre-equilibrated with buffer containing 20 mM Tris-HCl pH 8.0, 150 mM to determine the dimer form of IRGB10.

2.7 Native-PAGE

Self-oligomerization of IRGB10 due to GTPase activity was monitored by native-PAGE using a Phast system (GE Healthcare). Pre-made 8%–25% acrylamide gradient gels (GE Healthcare) were used for this experiment. The shifted bands on the gel were stained with Coomassie Brilliant Blue. Purified nucleotide-free IRGB10 was mixed and incubated with different concentrations of GTP and $MgCl_2$ mixtures at 37°C for 30 min, before loading the mixture onto native gels.

2.8 Circular dichroism measurements

A tentative structural change of IRGB10 caused by GTPase activity was detected using CD measurements. A J-1500 spectropolarimeter at the Korea Basic Science Institute (Osong, South Korea) was used for the CD experiment. The spectra were obtained from 200 to 260 nm at 25°C in a 1-mm pathlength quartz cuvette using a bandwidth of 1.0 nm, a 100 nm/min speed, and a 5-s response time. Three scans were accumulated and averaged. The concentration of nucleotide-free IRGB10 and K81A mutant

IRGB10 in the SEC buffer was 0.3–0.4 mg/mL. Next, 2 mM GTP and 0.2 mM $MgCl_2$ mixture was added to the protein to generate a nucleotide-free IRGB10 + GTP sample. The mixture was incubated at 25°C for 30 min just before injecting the sample into the spectropolarimeter.

2.9 Accession codes

The atomic coordinates and structure factors of nucleotide-free and GppNHp-bound IRGB10 were deposited in the Protein Data bank under accession numbers 8JQY and 8JQZ, respectively.

3 Results

3.1 Nucleotide-free IRGB10 is a monomer in solution

Many GTPases, including the GTPase domain-containing dynamin family, function appropriately by altering their structure and stoichiometry dependent on their GTP/GDP binding state and GTPase activity (36, 37). To reveal the accurate working mechanism of IRGB10 in the process of pathogen membrane disruption, whose function might be dependent on the state of nucleotide binding and hydrolysis capacity, we attempted to solve the structures of the nucleotide-free IRGB10 and IRGB10/GTP complexes. As we observed that endogenous GDP in *E. coli* was automatically incorporated into IRGB10 during the purification step, we used an additional high-salt washing step during an affinity chromatography step, which has been used previously to remove nucleotides from binding proteins, to obtain nucleotide-free IRGB10 (38). The absence of nucleotides was checked by UV absorbance (A260/A280), as has been outlined previously (28). This experiment showed that the absorbance value of nucleotide-free IRGB10 was 0.67~0.64, while that for GDP-bound IRGB10 was 1.02~1.36, indicating that GDP was washed out during the purification step (Supplementary Figure 1). Next, purified nucleotide-free IRGB10 was applied to SEC, with a GDP-bound IRGB10 sample used for size control. Comparison of the SEC profiles indicated that the main elution peak of nucleotide-free IRGB10 was moved to the monomer size position, although the overall generated peaks on the SEC profiles were similar (Figure 1A). The molecular size of nucleotide-free IRGB10 was accurately determined by MALS, which was then used to calculate the absolute molecular mass of the protein particle. The results of MALS showed that the molecular weight of the tentative monomeric peak from nucleotide-free IRGB10 was 53.65 kDa (± 0.7%), whereas the molecular mass of the dimeric GDP-bound IRGB10 was 102.72 (± 1.8%) (Figure 1B). These results indicated that the dimeric GDP-bound IRGB10 became monomeric when IRGB10 lost its GDP. Purified nucleotide-free IRGB10 was successfully crystallized, which allowed the structure of the monomeric nucleotide-free IRGB10 to be solved. The crystallographic data and refinement statistics are summarized in Table 1. Unlike dimeric GDP-bound IRGB10, a single molecule of IRGB10 was detected in the crystallographic asymmetric unit (ASU). The overall structure of monomeric nucleotide-free IRGB10 was almost identical to that of GDP-bound IRGB10, which was composed of a helical domain formed by N-terminal, C-terminal, and GTPase domains, which is a typical domain composition of the IRG family (Figures 1C, D). The GTPase domain consisted of six β-sheets (S1–S6) and six α-helices (H4–H9), while the helical domain consisted of eleven α-helices, including H1~H3 from the N-terminus region and H10~H17 from the C-terminus region. The model of nucleotide-free IRGB10 was constructed from residue 16 to residue 406. The LEH residues at the C-terminus, which were from the plasmid construct, were included in the final model. The electron density of the N-terminus residues and several loops, including switches I and II in the GTPase domain, were not visible in the model (Figure 1C). These parts of the structure could not be constructed due to poor electron density. The unconstructed N-terminus and several loops in the GTPase domains around these structures were also observed in structural studies of IRGA6 and dimeric GDP-bound IRGB10; this indicates that the N-terminus loop, containing around 13–15 residues, and several loops, including switches I and II at the GTPase domain, are extremely flexible and unstructured regions (25). As we removed GDP from IRGB10 during the purification step and found that nucleotide-free IRGB10 became a monomer in solution, using the current structure, we first sought to investigate whether GDP or GTP is in the GTPase domain. The electron density search revealed no traceable electron density for GDP in the typical nucleotide-binding site of the GTPase domain (Figure 1E).

Next, we compared the structure of the nucleotide-free IRGB10 to that of the GDP-bound IRGB10 (PDB ID: 7C3K) to analyze any structural changes that might occur by the loss of nucleotides in IRGB10. Pair-wise structural alignments between nucleotide-free and GDP-bound IRGB10 showed that the overall structures were similar to each other, with a RMSD between the two structures of 1.3 Å (Figure 1F). However, close-up analysis showed that the H2 and H3 helical domains formed by the N-terminal part of IRGB10 were dislocated from the positions of the H2 and H3 regions of GDP-bound IRGB10 (Figure 1G). In contrast, the last part of the helical domain that was constructed by the C-terminal part of IRGB10 was identical to that in GDP-bound IRGB10, indicating that binding nucleotide or GTP hydrolysis causes a slight structural alteration of IRGB10. Although the structures of the GTPase domain of each structure were almost identical, the positions of several loops were not. The structures of switches I and II, both of which are critical for GTPase activity, were unconstructed in nucleotide-free IRGB10, while only switch I was unconstructed in GDP-bound IRGB10 (Figure 1H). Interestingly, the P-loop, which is critical for nucleotide binding and GTP hydrolysis, was well constructed in both structures, indicating that the formation and location of the proper positioning of the P-loop is independent of nucleotide binding, contrary to what we have argued in a previous structural study of GDP-bound IRGB10 (26).

10.3389/fimmu.2023.1254415

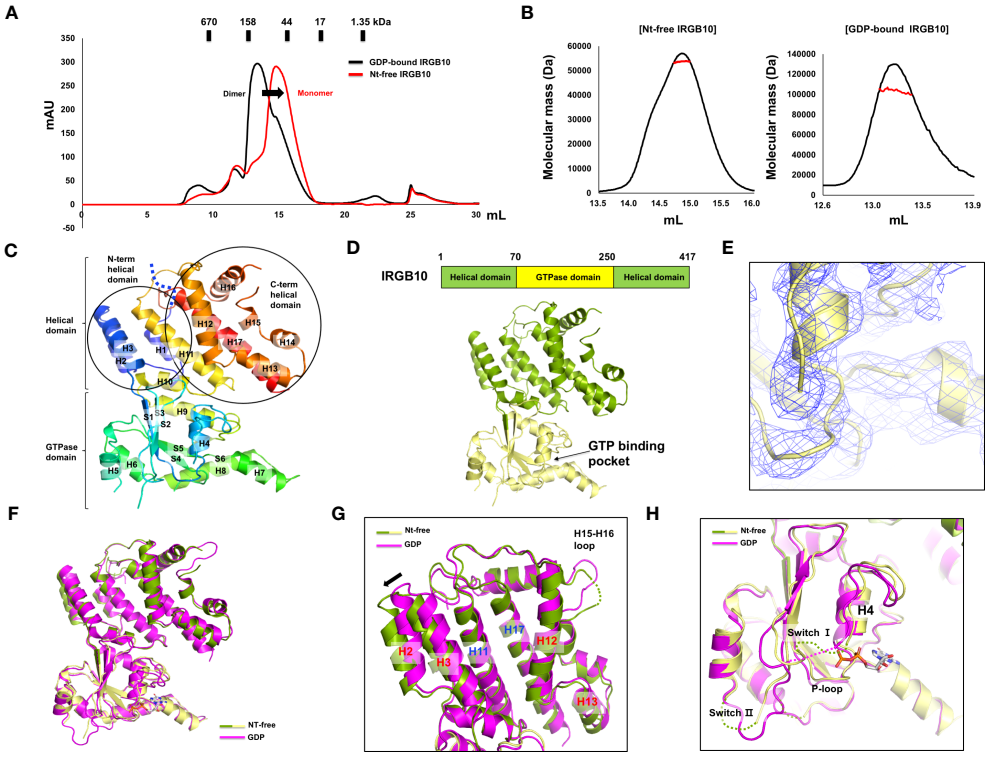

FIGURE 1
Structure of nucleotide-free IRGB10. **(A)** Profiles of the size-exclusion chromatography (SEC) of GDP-bound IRGB10 (black line) and nucleotide-free IRGB10 (red-line). The shifted peak is indicated by the black arrow. **(B)** Multi-angle light scattering (MALS) profiles derived from the SEC peak from the nucleotide-free IRGB10 (left panel) and GDP-bound IRGB10 (right panel). Red line indicates the experimental molecular mass. **(C)** Overall structure of nucleotide-free IRGB10. The rainbow-colored cartoon representation of monomeric nucleotide-free IRGB10 is shown. The chain from the N- to C-terminus is colored blue to red. Helices and sheets are labeled with H and S, respectively. The missing N-terminal loop in indicated by the blue dotted line. **(D)** The domain boundary and overall structure of IRGB10. The relative positions of the helical domain and the GTPase domains are shown in the bar diagram at the top. **(E)** Close-up view of the nucleotide binding pocket in the GTPase domain of IRGB10. The *2Fo-Fc* electron density map contoured at the 1σ level is indicated by the blue mesh. **(F)** Structural comparison of nucleotide-free IRGB10 (mixed green and yellow) with GDP-bound IRGB10 (magenta) by structural superposition. **(G)** Close-up view of the helical domains from panel **(F)** The structurally misaligned region is indicated by the black arrow. **(H)** Close-up view of the GTPase domain from panel **(F)** Missing, unconstructed loops in the model are indicated by dotted lines.

3.2 GTP hydrolysis causes dimerization and further oligomerization of IRGB10

Indeed, as we observed that nucleotide binding affects the stoichiometry change of IRGB10, we also investigated the effect of GTPase activity and GTP binding on any oligomeric and structural changes of IRGB10. To accomplish this, we first performed a turbidity assay that has been used previously to analyze the oligomerization of IRGA6 (34). The oligomerization of IRGB10 was detected by checking the absorbance of 350 nm UV light. After adding the GTP/$MgCl_2$ mixture to GDP-bound IRGB10, UV absorbance was not detected for 1200 s (Figure 2A). However, when the GTP/$MgCl_2$ mixture was added to nucleotide-free IRGB10, a considerable increase in UV absorbance was detected 600 s after GTP addition (Figure 2B). This UV absorbance was not detected when a non-hydrolysable GTP analog (GppNHp) was supplied to nucleotide-free IRGB10 (Supplementary Figure 2). The results of these turbidity assays indicated that GTP hydrolysis caused the oligomerization of IRGB10. Moreover, visible IRGB10 oligomeric particles were detected in the tube containing nucleotide-free IRGB10 following GTP addition. After removing those oligomeric particles by centrifugation, the solution was loaded onto SEC to determine the remnants in the solution. As GTPase hydrolyzes GTP to GDP, we speculated that the dimeric form of GDP-bound IRGB10 would be observed if the hydrolyzed product of GDP was incorporated into IRGB10 after hydrolysis. As expected, the SEC profile showed that the last portion of IRGB10 after GTP hydrolysis was a dimeric size and was eluted around the 13–14 position where dimeric GDP-bound IRGB10 was eluted (Figure 2C). When the non-hydrolysable GTP analog GppNHp was added to nucleotide-free IRGB10, no oligomeric particles were observed in the tube and the SEC profile showed a monomeric size (Figure 2C), indicating that GTP hydrolysis is critical for the dimerization and further oligomerization of IRGB10. The effect of GDP addition on the nt-free IRGB10 was also assessed by performing the same turbidity (Supplementary Figure 3). As shown at the S3 Figure, GDP addition did not produce oligomeric peak although a little absorbance was detected at 200 sec point after addition of GDP/$MgCl_2$. This indicated that GTP hydrolysis is critical step for IRGB10 oligomerization. The GTP

TABLE 1 Data collection and refinement statistics.

	Nucleotide-free	GppNHp-bound
Data collection		
Space group	*P* 3_2 2 1	*P* 1 2_1 1
Unit cell parameter		
a, *b*, *c* (Å) *α*, *β*, *γ* (°) Resolution range (Å) Total reflections Unique reflections Multiplicity[1] Completeness (%)[1] Mean *I*/σ (*I*)[1] R_{merge} (%)[1,2] Wilson *B*-factor (Å^2)	190.24, 190.24, 38.88 90, 90, 120 29.59–3.68 184231 8893 20.7 (21.9) 99.66 (100.00) 18.54 (1.84) 18.04 (215.1) 138.93	62.64, 62.44, 119.23 90, 99.52, 90 29.43–3.05 116108 17524 6.6 (6.8) 99.44 (99.43) 12.86 (1.80) 13.13(111.3) 84.19
Refinement		
Resolution range (Å) Reflections R_{work} (%)[1] R_{free} (%)[1] No. of molecules in ASU[3] No. of non-hydrogen atoms Macromolecules	29.59–3.68 8892 24.94 (34.29) 27.19 (36.96) 1 3032 3032	29.43–3.05 17494 23.19 (35.46) 26.50 (35.74) 2 6137 6073
Ligands		64
Average *B*-factor values (Å^2) Macromolecules	155.45 155.45	93.03 92.35
Ligands		158.07
Ramachandran plot:		
favored/allowed/outliers (%) Rotamer outliers (%) Clashscore RMSD bonds (Å)/angles (°)	97.26/2.74/0.00 0.00 11.35 0.003/0.58	98.77/1.23/0.00 0.00 5.54 0.003/0.92

[1] Values for the outermost resolution shell are shown in parentheses.
[2] $R_{merge} = \Sigma_h \Sigma_i |I(h)_i - \langle I(h)\rangle| / \Sigma_h \Sigma_i I(h)_i$, where I(h) is the observed intensity of reflection h, and <I(h)> is the average intensity obtained from multiple measurements.
[3] Crystallographic Asymmetric Unit.

hydrolysis-mediated oligomerization of IRGB10 was confirmed by native PAGE, which is another oligomerization detection assay. As shown in Figure 2D, the newly formed oligomeric band was detected by the addition of GTP, indicating that GTP addition caused IRGB10 oligomerization, which was observed in the turbidity assay. Finally, we attempted to confirm whether GTP hydrolysis of IRGB10 is essential for dimer formation and further oligomer formation by constructing mutants that cannot hydrolyze GTP. To perform this experiment, K81, a catalytically important residue identified from previous study (19), was mutated to alanine to produce the K81A mutant, which is the GTP-locked form of IRGB10. Using this GTP-locked form of IRGB10, we performed a turbidity assay and SEC-MALS. Unlike wildtype IRGB10, K81A did not produce visible oligomeric particles following the addition of GTP. Additionally, K81A did not produce a dimeric peak on the SEC profile when GTP was added to K81A (Figure 2E). All three SEC samples, including nucleotide-free K81A, K81A with GTP, and K81A with GppNHp, were eluted at the monomer position at SEC-MALS (Figures 2E, F). In addition, K81A did not produced dimeric peak in the presence of GDP (Supplementary Figure 4). These additional experiments confirmed that GTP hydrolysis is essential for dimer formation and further oligomerization of IRGB10, which may be critical for pathogen membrane disruption. Finally, we elucidated the role of the dimer PPI of IRGB10 on the oligomerization of IRGB10. To evaluate this, we used dimer PPI disrupting mutant D185R, which has been identified by our previous study as PPI interfering mutant. The turbidity assay showed that nt-free D185R mutant failed to produce oligomeric peak after addition of GTP/$MgCl_2$ (Supplementary Figure 5). Based on this experiment, we concluded that dimerization is a seed of further oligomerization of IRGB10.

3.3 GppNHp-bound IRGB10 is a monomer in solution

The mimetic structure of the GTP-bound form of IRGB10 was also solved using GppNHp, which is a non-hydrolyzable GTP

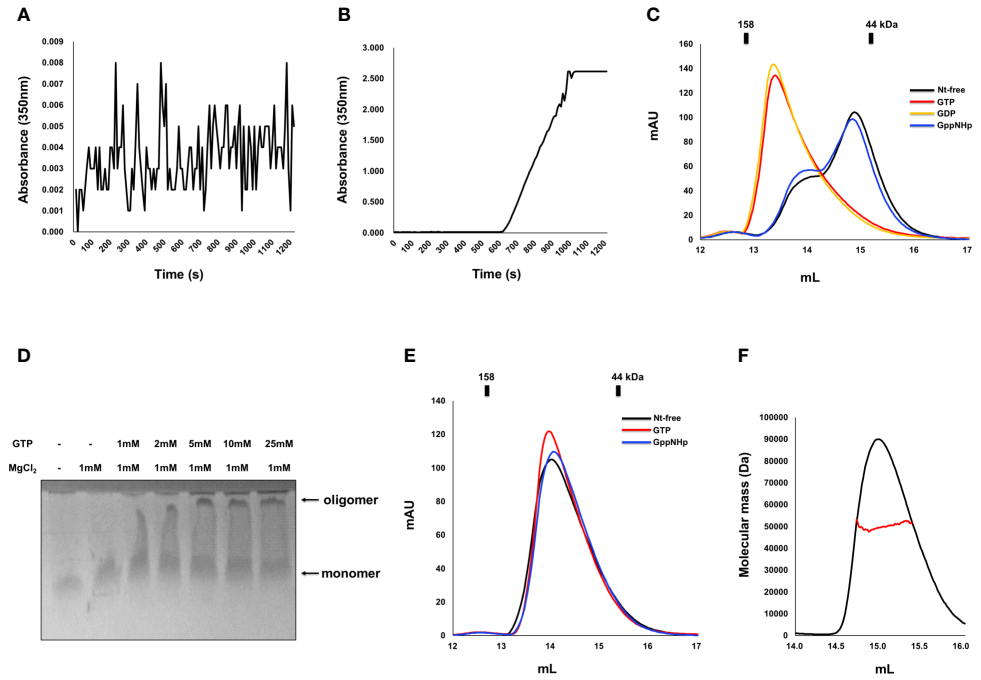

FIGURE 2
Dimerization and further oligomerization of IRGB10 by GTP hydrolysis. **(A, B)** Assembly of the IRGB10 oligomer as measured by turbidity changes. Turbidity changes of solutions containing nucleotide-free IRGB10 were measured upon addition of water for control **(A)** and GTP/$MgCl_2$ **(B)**. **(C)** SEC profiles of nucleotide-free (Nt-free) IRGB10 (black line), GTP-added IRGB10 (red line), GDP-added IRGB10 (yellow line), and GppNHp-added IRGB10 (blue line). **(D)** Native-PAGE of IRGB10 incubated with various concentrations of GTP in the presence or absence of $MgCl_2$. The concentrations of GTP incubated with IRGB10 are indicated. **(E)** SEC profiles of K81A mutant IRGB10. **(F)** MALS profile derived from the SEC peak from the K81A mutant IRGB10. Red line indicates the experimental molecular mass.

analog. The crystallographic data and refinement statistics are summarized in Table 1. The overall structure and numbers of α-helices and β-sheets were similar to previously revealed nucleotide-free and GDP-bound IRGB10 structures. We detected a clear electron density map at the nucleotide-binding site in the GTPase domain responsible for GppNHp (Figure 3A). The P-loop was stably fixed in GppNHp-bound IRGB10, while switches I and II remained unstructured (Figure 3A). Additionally, the crystallographic asymmetric unit comprised two identical IRGB10 molecules, molecule A and B (Figure 3B). As the stoichiometric and structural changes of the IRG family of GTPases are critical for understanding the working mechanism of the IRG family, we next analyzed the stoichiometry of GppNHp-bound IRGB10 in the solution using MALS. The experimentally calculated molecular weight of GppNHp-bound IRGB10 was 48.93 kDa (± 3.941%), indicating that GppNHp-bound IRGB10 is a monomer in the solution (Figure 3C), indicating that GTP bound-IRGB10 without GTP hydrolysis is still a monomer in solution.

To comprehend any structural change caused by nucleotide binding and GTPase activity, we next compared the GppNHp structure with nucleotide-free (Figure 3D) and GDP-bound (Figure 3E) IRGB10 structures by structural superposition analysis. The results of this structural comparison indicated that the overall GppNHp structure is almost identical to that of the nucleotide-free and GDP-bound forms of IRGB10, with RMSDs of 0.8 Å and 1.2 Å, respectively. However, upon closer examination of the helical domain, the locations of several helices were not identical. Indeed, H2 and H3 of the GppNHp-bound form were tilted by approximately 5° compared to those of the nucleotide-free form of IRGB10 (Figure 3F). Moreover, compared to the helical domain of the GDP-bound form, H13 and H14 of the GppNHp-bound form were tilted by approximately 8° compared to those of the GDP-bound form of IRGB10 (Figure 3G). The largest structural alteration was detected in the nucleotide binding site (Figure 3H). Although no structural changes were detected when the GppNHp-bound structure was compared to the nucleotide-free form (Figure 3I), distinct movements of the H4 and H4 connecting loops were detected when the GppNHp-bound structure was superposed with the GDP-bound form (Figure 3J). Moreover, by conducting a structural comparison of the GTPase domain of the GppNHp-bound IRGB10 with the GDP-bound form, we found that the loops of the GppNHp-bound form were very flexible and unfixed, and the position of H4 connected to the switch I loop in the GDP-bound form was different from that of the GppNHp-bound form (Figures 3H, J). All P-loops structures, which are important for nucleotide binding, of the three structures were identical. Finally, we evaluated the far UV circular dichroic (CD) spectra to determine the tentative structural changes of IRGB10

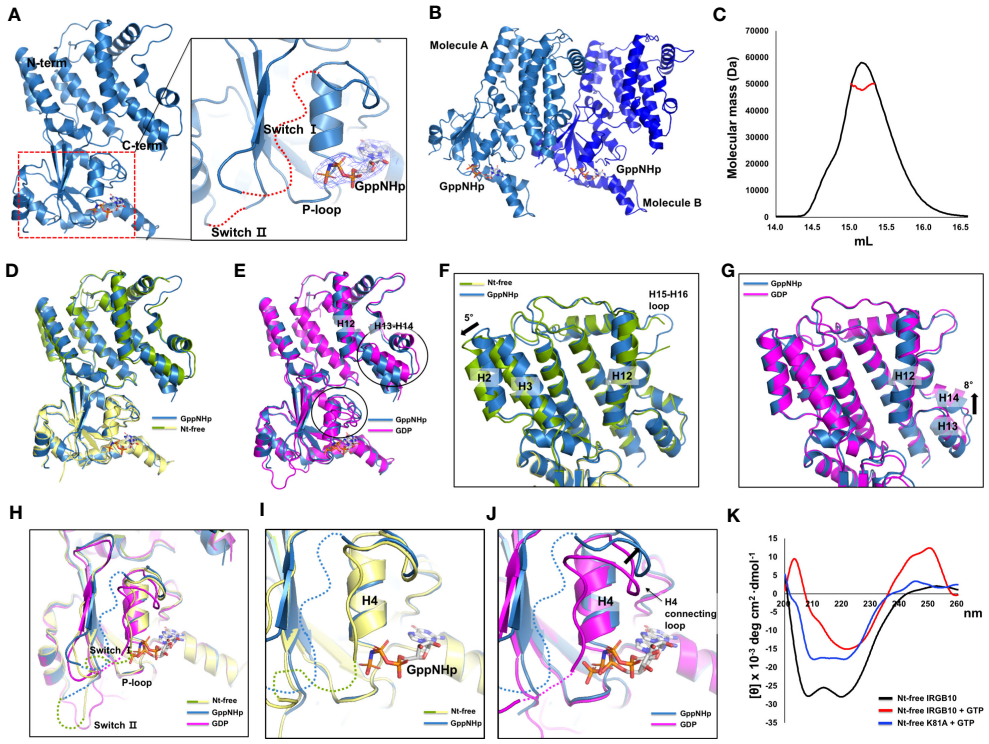

FIGURE 3
Structure of GppNHp-bound IRGB10. **(A)** Overall structure of GppNHp-bound IRGB10. Close-up view of the nucleotide binding pocket in the GTPase domain of IRGB10 shown in the right panel. The missing unconstructed switch I and II loops are indicated by red dotted lines. The *2Fo-Fc* electron density map contoured at the 1σ level around GppNHp is indicated by blue mesh. **(B)** A cartoon representation of two GppNHp-bound IRGB10s presented in an asymmetric unit. **(C)** Multi-angle light scattering (MALS) profiles derived from the SEC peak from GppNHp-bound IRGB10. Red line indicates the experimental molecular mass. **(D)** Structural comparison of GppNHp-bound IRGB10 (metal blue) with nucleotide-free IRGB10 (mixed green and yellow) by structural superposition. **(E)** Structural comparison of GppNHp-bound IRGB10 (metal blue) with GDP-bound IRGB10 (magenta) by structural superposition. Two structurally misaligned regions are indicated by black circles. **(F)** Close-up view of the helical domains from panel **(D)**. The structurally misaligned region is indicated by a black arrow. **(G)** Close-up view of the helical domains from panel **(E)**. The structurally misaligned region is indicated by a black arrow. **(H)** Structural comparison of the GTPase domains of GppNHp-bound IRGB10 (metal blue) with GDP-bound IRGB10 (magenta) and nucleotide-free IRGB10 (mixed green and yellow) by structural superposition. **(I)** Close-up view of the nucleotide pocket from panel H showing GppNHp-bound IRGB10 and nucleotide-free IRGB10. **(J)** Close-up view of the nucleotide pocket from panel H showing GppNHp-bound IRGB10 and GDP-bound IRGB10. The structurally misaligned region and H4 and H4 connecting loop are indicated. **(k)** Circular dichroic spectra of nucleotide-free (Nt-free) IRGB10 (black line), Nt-free IRGB10 provided GTP (red-line), and Nt-free K81A mutant IRGB10 provided GTP (blue line).

during GTP hydrolysis. The results of this experiment showed that the spectrum patterns were different when nucleotide-free IRGB10 was treated with GTP (Figure 3K). The nucleotide-free IRGB10 alone sample produced a typical CD spectrum pattern of α-helical proteins, exhibiting two pronounced minima at 208 nm and 222nm and a maxima at 200 nm. This pattern was not observed when GTP was provided. Moreover, these changes in the CD pattern were not observed when the GTPase activity defect K81A mutant was treated with GTP. In addition, GDP or GppNHp addition also produced a typical CD spectrum pattern produced by wildtype IRGB10 (Supplementary Figure 6). These CD experiments indicate that GTP hydrolysis might lead to structural changes in IRGB10.

4 Discussion

Given the importance of the field of study and understanding the mechanism underlying membrane disruption, several structures of the IRG family, including IRGA6, IRGB6, and IRGB10, have been revealed so far. Despite this, the functionally important filament-like structures of the IRG family, which are formed for membrane disruption, remain to be elucidated. To better understand the working mechanism of the IRG family, we initially solved the structure of the dimeric GDP-bound form of IRGB10 (26). Although GDP was not included in the protein sample preparation steps, endogenous bacterial GDP was incorporated in the GTPase domain of IRGB10. As the IRG family has a higher affinity for GDP than GTP, the natural production of GDP-bound IRGB10 was not extraordinary (25, 39). We established a method for purification of the nucleotide-free form of IRGB10 and revealed the structures of the nucleotide-free and GppNHp-bound forms of IRGB10 to establish the structural basis of membrane pore formation. Our results showed that IRGB10 existed as a monomer in the nucleotide-free state and became a dimeric form through GTP hydrolysis. During GTPase activation, the GTPase domain was flexible, and several helices underwent structural changes.

Following GTP addition, visible IRGB10 oligomeric particles were detected in the tube containing nucleotide-free IRGB10, which may be aggregates that can be formed due to the absence of membrane. After GTP hydrolysis, IRGB10 is supposed to work on the membrane; however, due to the absence of a membrane or binding partner such as GBP5, oligomeric IRGB10 became aggregated in solution. After removing all of the higher oligomeric particles (or aggregates), the remaining IRGB10 was detected as a dimer in solution, suggesting that the dimeric form is the main functional building block used by the IRG family for membrane disruption of pathogens.

Structural comparison of the three structures of IRGB10, including nucleotide-free, GDP-bound, and GppNHp-bound, indicated that the structure of the monomeric nucleotide-free form was almost identical to that of the monomeric GppNHp-bound IRGB10. However, the structure of IRGB10 changed if it experienced GTP hydrolysis. Although we observed a limited structural change at both the helical domain and GTPase domain of IRGB10, we expected huge structural changes in the helical domain of IRGB10, which were not observed in our study. In a previous study, although the bacterial dynamin-like protein (BDLP), a member of the IRG-like GTPase dynamin family in bacteria, had a closed conformation in the crystal structures of the nucleotide-free and GDP-bound states (36), this dynamin-like GTPase underwent huge structural changes at the helical domain when GTP was hydrolyzed. This structural change induced by forming the extended helical domain conferred BDLP with the capability to wrap the membrane by further oligomerization in the presence of lipid membrane, as evidence by cryo-EM structure analysis (40). Assuming that IRGB10 works in a manner similar to that of BDLP, GTP hydrolysis-mediated power generation, structural changes to the extended helical domain using generated power, and further oligomerization–mediated membrane disruption may occur, which may be achieved only in the presence of a phospholipid membrane. The possibility of huge strycyral change of IRGB10 during GTP hydrolysis was indicated by our CD experiments. Although dramatic change of CD profile was detected when IRGB10 was incubated with GTP, this change might be not due to the structural changes but due to the oligomerization of IRGB10 induced by GTP addition. This should be investigated further in near future. Taken together, based on the results of our structural, biochemical, and biophysical studies, we propose a model of IRGB10-mediated pathogen membrane pore formation (Figure 4). Initially, IRGB10 without nucleotide forms an inactive monomeric conformation. Once GTP is loaded into the GTPase domain of IRGB10, a minimal structural change, especially at the helical domain, occurs to prepare IRGB10 for action. During the GTP-hydrolysis step, IRGB10 may undergo huge structural changes, which may be critical for the membrane association of IRGB10, dimerization, and further oligomerization for pore formation (Figure 4). As we cannot capture the moment at which structural changes of IRGB10 are induced, the types of structural changes that occur during GTP hydrolysis remains an open question.

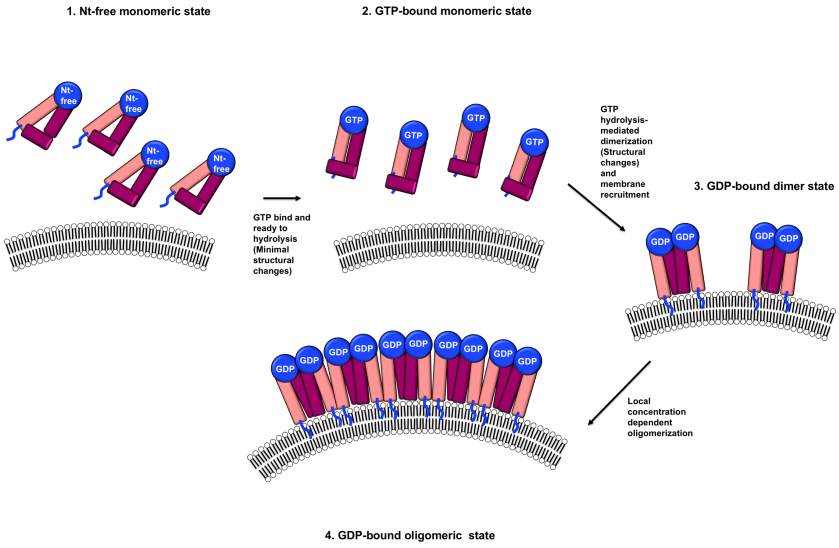

FIGURE 4
Putative model of a nucleotide and its hydrolysis-mediated membrane pore formation by IRGB10. The blue lines indicate the N-terminus loops where myristoylation occurs.

Data availability statement

The datasets presented in this study can be found in online repositories. The names of the repository/repositories and accession number(s) can be found in the article/Supplementary Material.

Author contributions

HH: data curation, investigation, writing – original draft. JK: data curation, writing – original draft. GL: data curation, writing – original draft. SK: data curation, writing – original draft. HP: conceptualization, data curation, funding acquisition, project administration, supervision, writing – review & editing, writing – original draft.

Funding

This work was supported by the National Research Foundation of Korea (NRF) grant funded by the Korea government (MSIT) (NRF-2021R1A2C3003331, NRF-2018R1A4A1023822, and NRF-2021R1A6A3A13044844) This research is a part of the project titled 'Development of potential antibiotic compounds using polar organism resources (KOPRI Grant PM22030)', funded by the Ministry of Oceans and Fisheries, Korea.

Conflict of interest

The authors declare that the research was conducted in the absence of any commercial or financial relationships that could be construed as a potential conflict of interest.

Publisher's note

Supplementary material

The Supplementary Material for this article can be found online at: https://www.frontiersin.org/articles/10.3389/fimmu.2023.1254415/full#supplementary-material

References

1. Chaplin DD. Overview of the immune response. *J Allergy Clin Immunol* (2010) 125:S3–23. doi: 10.1016/j.jaci.2009.12.980

2. Barber GN. Host defense, viruses and apoptosis. *Cell Death Differ* (2001) 8:113–26. doi: 10.1038/sj.cdd.4400823

3. Broz P, Dixit VM. Inflammasomes: mechanism of assembly, regulation and signalling. *Nat Rev Immunol* (2016) 16:407–20. doi: 10.1038/nri.2016.58

4. Hoss F, Budden CF, Latz E. IRGB10 exposes bacteria's intimate secrets. *Dev Cell* (2016) 39:7–8. doi: 10.1016/j.devcel.2016.09.026

5. MacMicking JD. Interferon-inducible effector mechanisms in cell-autonomous immunity. *Nat Rev Immunol* (2012) 12:367–82. doi: 10.1038/nri3210

6. Malhotra S, Hayes D Jr., Wozniak DJ. Cystic fibrosis and pseudomonas aeruginosa: the host-microbe interface. *Clin Microbiol Rev* (2019) 32:e00138–18. doi: 10.1128/CMR.00138-18

7. Tretina K, Park ES, Maminska A, MacMicking JD. Interferon-induced guanylate-binding proteins: guardians of host defense in health and disease. *J Exp Med* (2019) 216:482–500. doi: 10.1084/jem.20182031

8. Pilla-Moffett D, Barber MF, Taylor GA, Coers J. Interferon-inducible GTPases in host resistance, inflammation and disease. *J Mol Biol* (2016) 428:3495–513. doi: 10.1016/j.jmb.2016.04.032

9. Kim BH, Shenoy AR, Kumar P, Bradfield CJ, MacMicking JD. IFN-inducible GTPases in host cell defense. *Cell Host Microbe* (2012) 12:432–44. doi: 10.1016/j.chom.2012.09.007

10. Li G, Zhang JY, Sun Y, Wang H, Wang YQ. The evolutionarily dynamic IFN-inducible GTPase proteins play conserved immune functions in vertebrates and cephalochordates. *Mol Biol Evol* (2009) 26:1619–30. doi: 10.1093/molbev/msp074

11. MacMicking JD. IFN-inducible GTPases and immunity to intracellular pathogens. *Trends Immunol* (2004) 25:601–9. doi: 10.1016/j.it.2004.08.010

12. Martens S, Howard J. The interferon-inducible GTPases. *Annu Rev Cell Dev Biol* (2006) 22:559–89. doi: 10.1146/annurev.cellbio.22.010305.104619

13. Staeheli P, Haller O, Boll W, Lindenmann J, Weissmann C. Mx protein: constitutive expression in 3T3 cells transformed with cloned Mx cDNA confers selective resistance to influenza virus. *Cell* (1986) 44:147–58. doi: 10.1016/0092-8674(86)90493-9

14. Klamp T, Boehm U, Schenk D, Pfeffer K, Howard JC. A giant GTPase, very large inducible GTPase-1, is inducible by IFNs. *J Immunol* (2003) 171:1255–65. doi: 10.4049/jimmunol.171.3.1255

15. Cheng YS, Colonno RJ, Yin FH. Interferon induction of fibroblast proteins with guanylate binding activity. *J Biol Chem* (1983) 258:7746–50. doi: 10.1016/S0021-9258(18)32242-7

16. Taylor GA, Feng CG, Sher A. Control of IFN-gamma-mediated host resistance to intracellular pathogens by immunity-related GTPases (p47 GTPases). *Microbes Infect* (2007) 9:1644–51. doi: 10.1016/j.micinf.2007.09.004

17. Bekpen C, Hunn JP, Rohde C, Parvanova I, Guethlein L, Dunn DM, et al. The interferon-inducible p47 (IRG) GTPases in vertebrates: loss of the cell autonomous resistance mechanism in the human lineage. *Genome Biol* (2005) 6:R92. doi: 10.1186/gb-2005-6-11-r92

18. Boehm U, Guethlein L, Klamp T, Ozbek K, Schaub A, Futterer A, et al. Two families of GTPases dominate the complex cellular response to IFN-gamma. *J Immunol* (1998) 161:6715–23. doi: 10.4049/jimmunol.161.12.6715

19. Haldar AK, Piro AS, Pilla DM, Yamamoto M, Coers J. The E2-like conjugation enzyme Atg3 promotes binding of IRG and Gbp proteins to Chlamydia- and Toxoplasma-containing vacuoles and host resistance. *PloS One* (2014) 9:e86684. doi: 10.1371/journal.pone.0086684

20. Man SM, Karki R, Sasai M, Place DE, Kesavardhana S, Temirov J, et al. IRGB10 liberates bacterial ligands for sensing by the AIM2 and caspase-11-NLRP3 inflammasomes. *Cell* (2016) 167:382–96. doi: 10.1016/j.cell.2016.09.012

21. Hunn JP, Koenen-Waisman S, Papic N, Schroeder N, Pawlowski N, Lange R, et al. Regulatory interactions between IRG resistance GTPases in the cellular response to Toxoplasma gondii. *EMBO J* (2008) 27:2495–509. doi: 10.1038/emboj.2008.176

22. Martens S, Pavanova I, Zerrahn J, Griffiths G, Schell G, Reichmann G, et al. Disruption of Toxoplasma gondii parasitophorous vacuoles by the mouse p47-resistance GTPases. *PloS Pathog* (2005) 1:e24. doi: 10.1371/journal.ppat.0010024

23. Yamada H, Abe T, Nagaoka H, Takashima E, Nitta R, Yamamoto M, et al. Recruitment of Irgb6 to the membrane is a direct trigger for membrane deformation. *Front Cell Infect Microbiol* (2022) 12:992198. doi: 10.3389/fcimb.2022.992198

24. Saijo-Hamano, Sherif AA, Pradipta A, Sasai M, Sakai N, Sakihama Y, et al. Structural basis of membrane recognition of Toxoplasma gondii vacuole by Irgb6. *Life Sci Alliance* (2022) 5:e202101149. doi: 10.1101/2021.07.01.450801

25. Ghosh A, Uthaiah R, Howard J, Herrmann C, Wolf E. Crystal structure of IIGP1: a paradigm for interferon-inducible p47 resistance GTPases. *Mol Cell* (2004) 15:727–39. doi: 10.1016/j.molcel.2004.07.017

26. Ha HJ, Chun HL, Lss SY, Jeong J, Kim Y, Park HH. Molecular basis of IRGB10 oligomerization and membrane association for pathogen membrane disruption. *Commun Biol* (2021) 4:92. doi: 10.1038/s42003-020-01640-7

27. Schulte K, Pawlowski N, Faelber K, Frohlich C, Howard J, Daumke O. The immunity-related GTPase Irga6 dimerizes in a parallel head-to-head fashion. *BMC Biol* (2016) 14:14. doi: 10.1186/s12915-016-0236-7

28. Glasel JA. Validity of nucleic acid purities monitored by 260nm/280nm absorbance ratios. *Biotechniques* (1995) 18:62–3.

29. McCoy AJ. Solving structures of protein complexes by molecular replacement with Phaser. *Acta Crystallogr D Biol Crystallogr* (2007) 63:32–41. doi: 10.1107/S0907444906045975

30. Emsley P, Cowtan K. Coot: model-building tools for molecular graphics. *Acta Crystallogr D Biol Crystallogr* (2004) 60:2126–32. doi: 10.1107/S0907444904019158

31. Vagin AA, Steiner RA, Lebedev AA, Potterton L, Mcnocholas S, Long F, et al. REFMAC5 dictionary: organization of prior chemical knowledge and guidelines for its use. *Acta Crystallogr D Biol Crystallogr* (2004) 60:2184–95. doi: 10.1107/S0907444904023510

32. Chen VB, Arendall WB, Headd JJ, Keedy DA, Immormino RM, Kapral GJ, et al. MolProbity: all-atom structure validation for macromolecular crystallography. *Acta Crystallogr D* (2010) 66:12–21. doi: 10.1107/S0907444909042073

33. DeLano WL, Lam JW. PyMOL: a communications tool for computational models. *Abstr Pap Am Chem S* (2005) 230:U1371–U2.

34. Reese ML, Shah N, Boothroyd JC. The Toxoplasma pseudokinase ROP5 is an allosteric inhibitor of the immunity-related GTPases. *J Biol Chem* (2014) 289:27849–58. doi: 10.1074/jbc.M114.567057

35. Wang L, Barylko B, Byers C, Ross JA, Jameson DM, Albanesi JP. Dynamin 2 mutants linked to centronuclear myopathies form abnormally stable polymers. *J Biol Chem* (2010) 285:22753–7. doi: 10.1074/jbc.C110.130013

36. Low HH, Lowe J. A bacterial dynamin-like protein. *Nature* (2006) 444:766–9. doi: 10.1038/nature05312

37. Byrnes LJ, Sondermann H. Structural basis for the nucleotide-dependent dimerization of the large G protein atlastin-1/SPG3A. *Proc Natl Acad Sci USA* (2011) 108:2216–21. doi: 10.1073/pnas.1012792108

38. Ariza A, Tanner SJ, Walter CT, Dent KC, Shepherd DA, Wu W, et al. Nucleocapsid protein structures from orthobunyaviruses reveal insight into ribonucleoprotein architecture and RNA polymerization. *Nucleic Acids Res* (2013) 41:5912–26. doi: 10.1093/nar/gkt268

39. Praefcke GJ, McMahon HT. The dynamin superfamily: universal membrane tubulation and fission molecules? *Nat Rev Mol Cell Biol* (2004) 5:133–47. doi: 10.1038/nrm1313

40. Low HH, Sachse C, Amos LA, Lowe J. Structure of a bacterial dynamin-like protein lipid tube provides a mechanism for assembly and membrane curving. *Cell* (2009) 139:1342–52. doi: 10.1016/j.cell.2009.11.003

frontiers | Frontiers in Immunology

TYPE Review
PUBLISHED 11 September 2023
DOI 10.3389/fimmu.2023.1239146

OPEN ACCESS

EDITED BY
Hyun Ho Park,
Chung-Ang University, Republic of Korea

REVIEWED BY
Laure Yatime,
UMR5235 Laboratoire des Interactions Pathogène Hôte (LPHI), France
Brandon L. Garcia,
East Carolina University, United States

*CORRESPONDENCE
Francisco J. Fernández
fjfernandez@abvance.com
M. Cristina Vega
cvega@cib.csic.es

†These authors have contributed equally to this work

RECEIVED 12 June 2023
ACCEPTED 16 August 2023
PUBLISHED 11 September 2023

CITATION
Santos-López J, de la Paz K, Fernández FJ and Vega MC (2023) Structural biology of complement receptors.
Front. Immunol. 14:1239146.
doi: 10.3389/fimmu.2023.1239146

Structural biology of complement receptors

Jorge Santos-López[1†], Karla de la Paz[1,2†], Francisco J. Fernández[2*] and M. Cristina Vega[1*]

[1]Centro de Investigaciones Biológicas Margarita Salas, Consejo Superior de Investigaciones Científicas (CSIC), Madrid, Spain, [2]Research & Development, Abvance Biotech SL, Madrid, Spain

The complement system plays crucial roles in a wide breadth of immune and inflammatory processes and is frequently cited as an etiological or aggravating factor in many human diseases, from asthma to cancer. Complement receptors encompass at least eight proteins from four structural classes, orchestrating complement-mediated humoral and cellular effector responses and coordinating the complex cross-talk between innate and adaptive immunity. The progressive increase in understanding of the structural features of the main complement factors, activated proteolytic fragments, and their assemblies have spurred a renewed interest in deciphering their receptor complexes. In this review, we describe what is currently known about the structural biology of the complement receptors and their complexes with natural agonists and pharmacological antagonists. We highlight the fundamental concepts and the gray areas where issues and problems have been identified, including current research gaps. We seek to offer guidance into the structural biology of the complement system as structural information underlies fundamental and therapeutic research endeavors. Finally, we also indicate what we believe are potential developments in the field.

KEYWORDS

complement, complement receptors, structural biology, CR1/CR2, CR3/CR4, CRIg, C5aR1/C5L2/C3aR, host-pathogen interactions

1 Introduction to the complement receptors

The currently accepted list of complement receptors includes four broad structural classes of transmembrane proteins: complement control protein (CCP)/short consensus repeat (SCR) domain modular single-pass transmembrane receptors (CR1, CR2), β_2 integrins (CR3, CR4), complement receptor of the immunoglobulin family (CRIg), and G-protein coupled receptors (GPCR) (C5aR1, C5aR2, C3aR) (Table 1). Various aspects of their sequence, function, structure, localization, regulation, activation, and implications for infection, pathogenesis, and therapy have been reviewed elsewhere (1–19). Complement receptors recognize either the C3 proteolytically activated fragments C3b, iC3b, and C3dg deposited on opsonized surfaces (CR1 to CR4 and CRIg) or the soluble anaphylatoxins

TABLE 1 Complement receptors and membrane-associated regulators.

Complement receptor[1]	Structural class	Ligands[2]	PDB ID[3]
CR1 CD35	Single-pass (bitopic) membrane protein CCP/SCR mosaic protein 30 CCP domains (~220 kDa) Other spliced isoforms contain 23, 37, or 44 CCP domains	C3b / C4b AP / CP C3 convertase C5 convertase Other ligands: C1q, MBL, and iC3b/C3d(g) with low affinity	sCR1 (SAXS: 2Q7Z) CCPs 1-2 (NMR: 2MCZ) CCPs 2-3 (NMR: 2MCY) CCP16 (NMR: 1PPQ) CCPs 16-17 (NMR: 1GKG) CCPs 15-17 (NMR: 1GKN) CCPs 15-17:C3b (XRD: 5FO9)
CR2 CD21	Single-pass (bitopic) membrane protein CCP/SCR mosaic protein 15 CCP domains (~145 kDa)	iC3b C3d(g) Other ligands: IFNα, Low-affinity IgE receptor CD23	sCR2 (SAXS: 2GSX) CCPs 1-2 (XRD: 1LY2; NMR: 1W2R) CCPs 1-2:C3d (XRD: 1W2S, 3OED)
CR3[4] CD11b+CD18 $\alpha_M\beta_2$ Mac-1	Heterodimer of single-pass (bitopic) subunits Integrin superfamily 170 kDa (α_M) + 95 kDa (β_2)	iC3b C3d(g) C3(H_2O) Other ligands: ICAMs, Fibrinogen, Plasminogen, LPS (many others)	α_MI (XRD: 1BHO, 1BHQ, 1IDN, 1IDO, 1JLM, 1M1U, 1MF7, 1N9Z, 1NA5) Cytoplasmic domain (NMR: 2LKE, 2LKJ) CR3 headpiece (XRD: 7P2D) CR3 ectodomain (cEM: 7USM) α_MI:C3d (XRD: 4M76) α_MI:iC3b (XRD: 7AKK)
CR4[4] CD11c+CD18 $\alpha_X\beta_2$ p150/95	Heterodimer of single-pass (bitopic) subunits Integrin superfamily 150 kDa (α_X) + 95 kDa (β_2)	iC3b Other ligands: ICAM-1, VCAM-1, Fibrinogen, LPS, Heparin (others)	α_XI (XRD: 1N3Y) Cytoplasmic domain (NMR: 2LUV) CR4 ectodomain (closed) (XRD: 3K71, 3K72, 3K6S, 5ES4) CR4 ectodomain (metastable) (XRD: 4NEN, 4NEH)
Only CD18[4]			I-EGF2-3 (NMR: 1LY3) PSI/Hybrid/I-EGF1 (XRD: 1YUK, 5E6V) + I-EGF2 (XRD: 2P26, 5E6W) + I-EGF3 (XRD: 2P28, 5E6X) β_2 TM helix (NMR: 5ZAZ)
CRIg VSIG4 Z39Ig	Single-pass (bitopic) membrane protein Ig-like superfamily ~42 kDa	C3b iC3b	V-set Ig-like 1 (XRD: 2ICC) V-set Ig-like 1:C3c (XRD: 2ICE) V-set Ig-like 1:C3b (XRD: 2ICF) CRIg (AlphaFold AF-Q9Y279-F1)
C5aR1 CD88	G-protein coupled receptor ~39 kDa	C5a $C5a^{desArg}$ Other ligands: C3a, ribosomal protein S19	C5aR1:NDT9513727 (XRD: 5O9H) C5aR1:PMX53:NDT9513727 (XRD: 6C1Q) C5aR1:PMX53:Avacopan (XRD: 6C1R) C5aR1:G_i:C5a (cEM: 7Y64) C5aR1:G_i:$C5a^{pep}$ (cEM: 7Y65) C5aR1:G_i:BM213 (cEM: 7Y66) C5aR1(I116A):G_i:C089 (cEM: 7Y67)
C5aR2 C5L2 GPR77	Class A (Rhodopsin) G-protein coupled receptor 36 ~kDa	C5a $C5a^{desArg}$	No structure available
C3aR C3aR1	Class A (Rhodopsin) G-protein coupled receptor ~53 kDa	C3a Other ligands: C5a	C3aR:G_i (cEM: 8HK3) C3aR:G_i:C3a (cEM: 8HK2) C3aR:G_i:C5a (cEM: 8HK5)

[1] The name of the complement receptor used in this review appears in bold. Alternative names and CD nomenclature (if available) are also indicated.
[2] Main (canonical) ligands are given first. Other ligands are listed, although no attempt has been made to classify them according to their physiological relevance. Viral proteins that hijack complement receptors to gain entry to the target cell have not been included.
[3] The list of PDB entries is not meant to be exhaustive. In choosing among available structures, we have placed the emphasis in those that have contributed crucial information to the understanding of the architecture of the receptors. Accordingly, we have omitted a few structures featuring only short peptides derived from complement receptors (e.g., for CR4) or when they represent antibody/small-molecule complexes that do not significantly alter our structural understanding of the receptor (e.g., CR3 α_MI).
[4] For the integrin receptors (CR3/CR4), we have arranged the PDB IDs of structures containing CD11b/α_M chain sequences under CR3, those containing CD11c/α_X chain sequences under CR4, and those containing exclusively CD18/β_2 chain sequences under "Only CD18".

released during alternative pathway activation (C3aR) or terminal pathway activation (C5aR1/C5aR2). The pattern of cellular expression and compartmentalization of the complement receptors underlies their various functions: leukocyte recruitment and migration, phagocytosis, and inflammation. A fascinating function of complement receptors is connecting the effector responses of the innate and adaptive branches of the immune system.

The membrane-bound negative complement regulators membrane cofactor protein (MCP/CD46) and decay accelerating

factor (DAF/CD55) are structurally related to CR1 and CR2 as they contain tandem repetitions of the CCP/SCR domain (20). However, they are not commonly considered complement receptors as their main function is to accelerate convertase decay or act as cofactor of complement factor I (FI) to prevent unregulated complement deposition on self-cell surfaces, and will not be discussed further (but see (21, 22) regarding MCP as a complement receptor in T-cell lymphocytes). Likewise, we will not cover three proteins that have been proposed as C1q receptors: C1qRp/CD93, cC1qR/calreticulin (CR), and gC1qbp. CD93, also known as C1q receptor protein (C1qRp), promotes cell adhesion, migration, and angiogenesis; however, its main ligand appears to be multimerin-2, not C1q (23, 24). cC1qR is a 62-kDa form of ecto-calreticulin that can bind the collagen domain in C1q with the assistance of other membrane proteins including β_1 integrins, CD91, and the KDEL docking receptor (25). Finally, gC1qR is a 33-kDa binding protein for the globular head of C1q (gC1qbp) found in both the intracellular and cell surface compartments, where it can bind various proteins including vitronectin, thrombin, and fibrinogen; the location of gC1qR is mainly in the mitochondria, where its leader peptide is processed (24).

The renewed interest in the pharmacological modulation of the complement system (26–31) has contributed to a recent surge of structural information on the structure and function of complement receptors, especially CR3 (32–34) and the anaphylatoxin receptors C5aR1 and C3aR (35, 36). This review aims to inform and guide structurally aware basic and clinical research by providing an up-to-date synthesis of our current understanding of the structural biology of complement receptors.

An exciting topic that we will not cover in this review is the intracellular complement system, the complosome, despite the breadth of attributed effector functions and the important associations uncovered with prevalent diseases (reviewed in (37)). We have decided to leave the complosome outside the scope of this review as the available structural information is not specific to the intracellular location of complosome components (e.g., C3aR/C5aR1).

2 Highly modular complement receptors based on the CCP/SCR domain

2.1 The building block: CCP/SCR domain

The complement receptors CR1 and CR2 and the negative complement regulators FH, FH-related (FHR) proteins, C4b binding protein (C4BP), MCP, and DAF are all mosaic proteins comprised of several independently-folded modules known as the short consensus repeat (SCR), complement control protein (CCP), or Sushi domain (20, 38). Other complement factors that bind C3b or C4b, like FB or FI, also contain CCP domains and other structural and catalytic domains. Conversely, CCP domains are also found in complement factors lacking the ability to bind C3b or C3b, like the complement proteases C1r and C1s (39).

The dimensions of the CCP domain are approximately 1 nm in width and 3.6 nm in length (Figure 1A). Each CCP (61 amino acids) contains a hydrophobic core composed of up to eight-stranded antiparallel β-sheet stabilized by two conserved disulfide bridges (Cys1-Cys3 and Cys2-Cys4) and a buried conserved Trp residue (40) (Figure 1A). Individual CCP domains in mosaic sequences start with the first conserved Cys (Cys1) and end with the last conserved Cys (Cys4); the two-to-eight residues between Cys4 in the preceding CCP domain and Cys1 in the following CCP domain are denoted as inter-CCP linking regions. A structurally important feature of the inter-CCP linkers is that they allow a wide range of inter-domain orientations, thus adding to the structural variability of the mosaic proteins that contain them (41). CCP domains have been structurally classified into nine distinct groups (from A to I) according to sequence and structural features (42). This classification is intended to help the systematic structural analysis and the accurate homology modeling of CCP domain-containing proteins.

2.2 Complement receptor 1

Complement receptor 1 (CR1, CD35, C3b/C4b receptor) is a type I transmembrane glycoprotein from the Regulators of Complement Activity (RCA) family. CR1 acts as a receptor for C3b/C4b, C1q (43), the mannan-binding lectin (MBL) (44), and as an immune adherence receptor (45). The biological functions of CR1 rely on its ability to bind to C3b and C4b reversibly, components of the C3 convertase of the alternative pathway (C3bBb) or the classical pathway (C4b2a), inactivating the C3 and C5 convertases, and promoting the dissociation of the catalytic subunits C3a or Bb (decay-accelerating activity) (46). CR1 also serves as a necessary cofactor for FI-mediated proteolytic cleavage of C3b and C4b to the breakdown products iC3b/C3dg and iC4b/C4dg, respectively (cofactor activity) (46). The cellular location of CR1 influences its biological functions. CR1 is mainly found on the surface of erythrocytes, where it is responsible for the Knops blood group (York and McCoy antigens), and on antigen-presenting (APC) cells (47). While in erythrocytes CR1 contributes to the clearance of complement-fixed immune complexes, in leukocytes its main role seems to be channeling the immune response to foreign antigens to other immune cell types bearing CR2, CR3, and CR4 receptors. In addition, CR1 acts as a B-cell receptor (BCR) inhibitor to prevent B cell activation (48). A soluble version of CR1 (sCR1) has also been identified with anti-inflammatory properties (43).

2.2.1 Structure of the largest complement receptor, CR1

CR1 is the largest member of the RCA family. In the most common allelic form, the extra-cellular component of CR1 (sCR1) contains 30 CCP domains and 14 occupied *N*-linked glycosylation sites; other allelic forms have 23, 37, or 44 CCP domains. The 30 CCP domains of CR1 are organized as four long homologous repeat regions spanning seven CCP domains (LHR-A to LHR-D) plus two

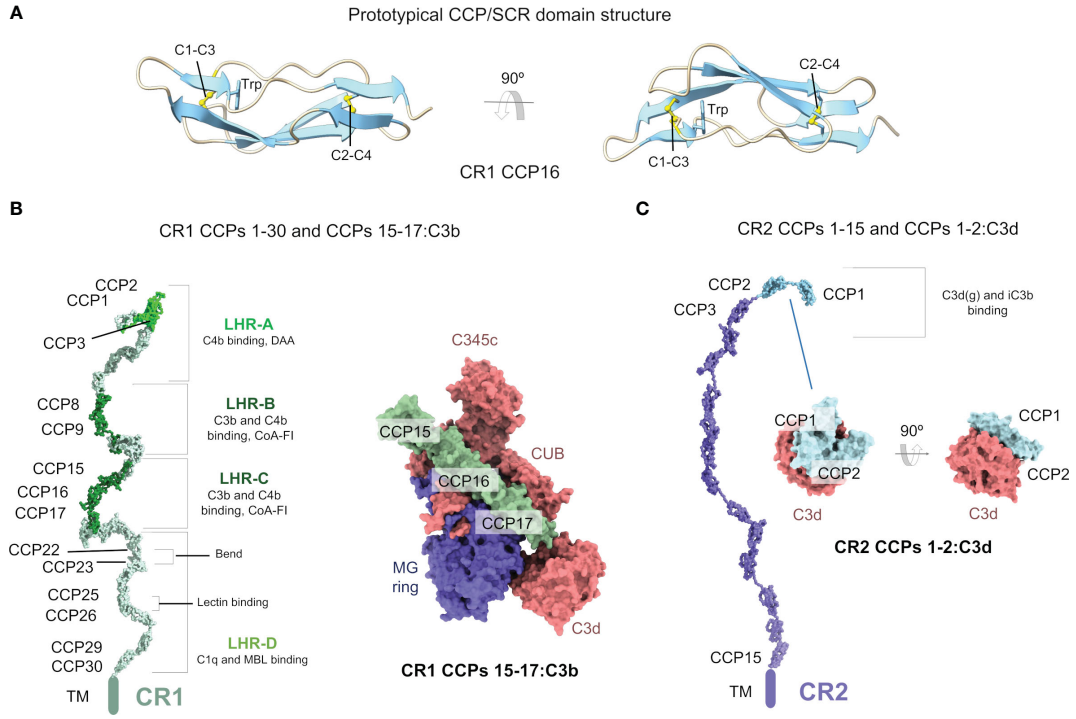

FIGURE 1
Complement receptors CR1 and CR2 are mosaic proteins built from CCP/SCR modules. **(A)** Structure of a prototypical CCP/SCR domain, the CR1 CCP16, taken from the structure of CR1 CCPs 15-17:C3b (PDB ID 5FO9). The domain is shown in cartoons in two orientations. The two most conserved features of CCP domains, the disulfide bonds between four conserved cysteine residues (C1-C3 and C2-C4) and a conserved tryptophan (W) residue, are shown in sticks and CPK atom colors. **(B)** Structure of the CR1 ectodomain (left) comprising CCPs 1-30 modeled from SAXS data (PDB ID 2Q7Z), with C3b/C4b interacting CCP domains colored in lime (C4b) and dark green (C3b/C4b). Structure of the CR1 CCPs 15-17:C3b (right) (PDB ID 5FOB) in molecular surface representation. C3b is colored according to chain (the α′ chain in red, the β chain in blue), and CR1 CCPs 15-17 is colored in dark green. **(C)** Structure of the CR2 ectodomain (left) comprising CCPs 1-15 modeled from SAXS data (PDB ID 2GSX), with C3b interacting CCP domains colored in cyan. Structure of the CR2 CCPs 1-2:C3d (right) (PDB ID 3OED) in molecular surface representation. C3d is colored in red, and CR2 CCPs 1-2 is colored in cyan.

C-terminal CCP domains. Three functionally relevant sites have been identified in CR1: Site 1 in CCPs 1-3 in LHR-A binds C4b and is the site harboring the decay-accelerating activity toward the classical and alternative pathway C3 convertases; site 2 in CCPs 8-10 in LHR-B and site 3 in CCPs 15-17 in LHR-C bind C3b and C4b and are the main sites for the FI cofactor activity.

Given the membrane location, size, glycosylation, and highly modular and flexible structure, obtaining high-resolution structural information about CR1 has been challenging. The first structural information about sCR1 was obtained by negative staining electron microscopy (NS-EM). Those early electron micrographs exposed the elongated structure of sCR1 in various CCP structural arrangements (49). However, the most comprehensive structural description of sCR1 has thus far been obtained by solution small-angle X-ray scattering (SAXS) coupled with biophysical techniques like analytical ultracentrifugation (AUC) and constrained computational modeling.

Even though at a moderate resolution, this approach has revealed critical structural features of CCP repeat proteins like FH (50), CR2 (51), and CR1 (52). Strikingly, sCR1, as FH and sCR2, does not adopt a fully extended structure, which would stick out of the cellular surfaces harboring it by a maximum theoretical length of 108 nm (compared with 17 nm for C3b/C4b). In contrast, SAXS data analysis revealed that sCR1 structure folds back onto itself to yield a more densely packed molecule with a maximum dimension D_{max} = 55 nm and a radius of gyration R_G = 13.4 nm (52) (PDB ID 2Q7Z) (Figure 1B). In comparison, FH has a D_{max} = 40 nm instead of the maximum theoretical length of 73 nm, and sCR2 has a D_{max} = 38 nm instead of the theoretically maximum length of 54 nm. Analysis of the SAXS cross-sectional radii of gyration for sCR1 (R_{XS-1} = 4.7 nm and R_{XS-2} = 1.2 nm) in combination with the R_G and the frictional ratio R_G/R_0 = 3.76 provided further confirmation of the folded-back structure of sCR1, which resembles that of FH more closely than that of sCR2. For CCP-containing proteins, R_{XS-1} reports on the averaged medium-range folding back and R_{XS-2} on the averaged short-range inter-CCP orientation between adjacent CCP domains (50). Equilibrium sedimentation experiments with sCR1 resulted in a sedimentation coefficient $s°_{20,w}$ = 5.84, and a frictional coefficient anisotropy ratio f/f_0 = 2.3 (compared to 1.25 for globular proteins), which agree with the extended but folded-back structural model derived from SAXS measurements.

SAXS-constrained modeling of the three-dimensional structure of sCR1 has shown that sCR1 can be best described as a family of partly folded-back CCP structural arrangements with a moderate degree of flexibility around the CCP inter-linking regions. SAXS and other biophysical techniques have comprehensively sampled the

translational and rotational average structural ensemble. SAXS-constrained modeling has suggested that the four-residue linker between CCP22 and CCP23 might be responsible for the main bend in sCR1. Still, this inference awaits experimental corroboration as SAXS alone cannot prove where the kink occurs. A kink at CCP22-CCP23 would introduce an angle between the LHR-C and LHR-D regions, apparently without implications for ligand recognition, as the C3b/C4b binding sites are in the LHR-A, LHR-B, and LHR-C regions. This observation contrasts with the oft-cited statement that the folded-back structure of CR1 facilitates binding to multiple ligands on the surface of pathogens or immune complexes.

Higher resolution structures of unliganded CR1 domains are only available for a subset of CCP domains. The earliest structures were determined by multinuclear NMR for the three CCP domain tandem constructs CCPs 1-3, CCPs 8-10, and CCPs 22-24 (41), and the CCPs 15-16 (PDB ID 1GKN) and CCPs 16-17 (PDB ID 1GKG) domain pairs in site 3 of CR1 (53). The NMR structure of an individual CCP domain was also published for CCP16 (PDB ID 1PPQ) (54). The NMR structure of the N-terminal CCP domain pairs CCPs 1-2 (PDB ID 2MCZ) and CCPs 2-3 (PDB ID 2MCY) (55).

2.2.2 CR1 dampens C3 and C5 convertase activities, and transports opsonized cargo

CR1 uses CCP binding sites in LHR-A, LHR-B, and LHR-C to recognize and bind C3b and C4b. CR1 ligands include both monomeric ligands such as C3b, C4b, or the C3 convertase (C3bBb or C4b2a) and the bivalent C5 convertases, which contain a back-to-back arrangement of either C3b-C3b dimers (alternative pathway) or C3b-C4b dimers (classical pathway) (56, 57). This bivalent recognition sets CR1 apart from all other RCA proteins and it explains the 10-fold tighter binding affinity of CR1 for C5 convertases over C3 convertases (58).

Recent structural data have shed light on how CR1 recognizes its cognate ligand C3b (59). The crystallographic structure of C3b: CR1 CCPs 15-17 (PDB ID 5FO9) has shown how CR1 exploits a similar binding mode to FH CCPs 1-4 to exert cofactor activity (60) (Figure 1C). C3b domains engaged in this interaction include MG7, MG6, CUB, MG2, MG1, and TED, and the α'NT region over a region spanning ~100 Å with ~1910 Å^2 buried surface area.

In contrast to C3b/C4b ligands, CR1 uses the LHR-D homologous repeat to recognize and bind C1q and MBL. Therefore, C1q and MBL must compete for binding to CR1. A structural characterization of the interaction between CR1 and C1q/MCP awaits further investigation.

2.2.3 Implications of CR1 structure for disease and immune evasion

sCR1 has been proposed for therapeutic use based on its anti-inflammatory properties and low immunogenicity. Possible applications include controlling inflammatory tissue damage in myocardial infarction (49), tissue damage suppression in complement-dependent autoimmune diseases (46), and the treatment of pemphigus foliaceus (61).

CR1 is also known as a receptor for various pathogens, including *Plasmodium falciparum*, the malaria agent, through direct interaction with erythrocyte membrane protein 1 (PfEMP1) and reticulocyte-binding homolog protein 4 (PfRh4) (55, 62–66). The interaction with PfEMP1 causes red blood cells to become "sticky" and rigid, displaying the parasite phenotype known as "rosetting" or adhesion of infected erythrocytes to uninfected erythrocytes, which maintains infected red blood cells in the microvasculature, and avoiding destruction in the spleen and liver. At the structural level, rosetting depends on C3b-binding sites on LHR-B and LHR-C homologous repeats, even though it does not involve C3b. In contrast, PfRh4 interacts with CR1 CCP1 inhibiting the decay-accelerating activity without affecting C3b/C4b binding (55).

2.3 Complement receptor 2

Complement receptor 2 (CR2, CD21) is a type I membrane glycoprotein found on the cell surface of mature B cells, follicular dendritic cells, epithelial cells, and some T cells. CR2 contains 15-16 CCP domains depending on alternative splicing (67), which makes it the third largest CCP repeat protein within the RCA proteins after CR1 and FH. CR2 is the only RCA protein lacking complement regulatory functions; instead, CR2 links the innate and adaptive immune response during the activation of B cells through binding to its primary ligand, C3d, in a complex with CD19, CD81, and mIgM, which is thought to reduce the threshold of immune activation. Besides C3d and the C3d-containing opsonin iC3b (but not C3b) (68, 69), CR2 has three known ligands: IFNα (70, 71), the low-affinity IgE receptor CD23 (72), the glycoprotein gp350 of the Epstein-Barr virus (73, 74).

2.3.1 CR2: a dynamic structure to bind opsonized surfaces

As sCR1 and FH, the structure of sCR2 has been studied by various structural and biophysical methods. The first images of sCR2's elongated structure were obtained by electron microscopy (75). More detailed structural information has been obtained by a combination of SAXS and AUC (76). In solution, sCR2 has an R_G = 11.5 nm (R_G/R_0 = 4.1), $R_{XS\text{-}2}$ = 1.2 nm (and no $R_{XS\text{-}1}$), and a D_{max} = 38 nm (SAXS) and $s^0_{20,w}$ = 4.2 nm (f/f_0 = 2) (AUC). In contrast to sCR1 and FH, the CCP overall structural arrangement of sCR2 is more extended (although not fully extended) and only folds back partially onto itself (PDB ID 2GSX) (Figure 1C). Accordingly, the D_{max} derived from SAXS comes nearer to the theoretically maximum length of 54 nm. Another feature of CR2 concerns the length of the inter-CCP linkers, which is longer compared with CR1 and FH; in CR2, there are several inter-CCP linkers from four to eight amino-acid long. The greater length of the inter-CCP linkers gives CR2 a higher degree of flexibility, allowing it to reach a larger overall length than structurally similar proteins.

Isolated CR2 CCP domains have also been studied at the structural level. CCPs 1-2 have been shown to adopt a V-shaped structure by X-ray crystallography with implications for C3d/iC3b ligand binding (Figure 1C). Although the crystal structure of unbound CR2 CCPs 1-2 (PDB ID 1LY2) suggested a compact V-shaped arrangement with substantial flexibility at the junction

between CCP1 and CCP2 domains (77), the solution NMR structures calculated for the same domains have shown a more open, but equally kinked, structure (PDB ID 1W2R) (78–80).

2.3.2 Ligand binding at the interface between innate and adaptive immunity

The CR2 structure binds three relatively small protein ligands: C3d, gp350, and IFNα at CCPs 1-2, while a fourth ligand, CD23, binds both CCPs 1-2 and CCPs 5-8. The maximum dimensions of these ligands are 6.0 nm (C3d), 10.2 nm (gp350), 5.3 nm (IFNα), and 6.8 nm (CD23). Although CD23 is not much larger than C3d, CR2 uses two sets of CCP binding sites to latch onto it, a process likely favored by the flexibility of CR2. Therefore, CR2 can bind to antigen-C3d complexes on the B-cell surface and CD23 to bring the N-terminal tip of CR2 closer to membrane-bound IgE molecules on the B-cell surface (76).

The first crystal structure of CR2 CCPs 1-2 in complex with C3d showed a compact V-shaped structure where only CCP2 interacts with C3d (81). This was later disputed by constrained molecular modeling in 50 m*M* NaCl and mutagenesis data in 137 m*M* NaCl, which provided compelling evidence that both the CCP1 and CCP2 domains bind to the surface of C3d in a kinked conformation (PDB ID 1W2S) (79, 82). Later, a new crystal structure was published for CR2 CCPs 1-2:C3d, revealing a V-shaped conformation for CR2 CCPs 1-2 with a more extensive interface comprising residues from both CCP domains (PDB ID 3OED) (Figure 1C) (83). Although the conformation of CR2 CCPs 1-2 is similar in the two C3d complexes (RMSD 1.2-1.5 Å), the region of C3d involved in the interaction with CR2 CCPs 1-2 found in the crystal structure is more consistent with available functional and mutagenesis data.

The first structural glimpse into the CR2:C3d complex, indeed, into any large CCP-containing protein and its ligand, was obtained by SAXS and AUC (51). While sCR2 structure and oligomeric state remained unchanged in 50-137 m*M* NaCl, unbound C3d was shown to exist as monomers only in 137 m*M* NaCl; in 50 m*M* NaCl, C3d exists in monomer-dimer and monomer-trimer equilibria. Interestingly, the sCR2:C3d complex could be analyzed by AUC only in 50 m*M* NaCl, where the sedimentation coefficient shifted from 4.0 S (sCR2 alone) to 4.5 S (sCR2:C3d). The models put forward to rationalize the CR2:C3d complex (PDB ID 1W2R, PDB ID 1W2S) provide a solid foundation for future work, even if the details of the C3d binding interface may be better captured by the CR2 CCPs 1-2:C3d crystallographic structure (PDB ID 3OED) (76, 83).

Several features of the interaction between CR2 and C3d are worth remembering. Firstly, the extended, flexible, and relatively fold-back structure of CR2 and the V-shaped arrangement of CCPs 1-2 that is ideally positioned to interact with C3d-antigen complexes. Secondly, the constellation of weak and electrostatically modulated interactions between CR2 and C3d becomes physiologically significant only by avidity effects driven by receptor clustering. This weak summation of specific interactions appears discriminatory for B cells to respond only to antigens presented as multimeric C3d molecules clustered through surface-bound CR2 molecules. This parallels the weak CR1 interaction with C3b/C4b molecules on neutrophils, which is enhanced by the polymerization or multimerization of the ligand and receptor clustering. Other examples of this structural principle will be seen later.

2.3.3 Implications of CR2 structure for diseases and immune evasion

CR2 was recognized as a receptor for the Epstein-Barr virus (EBV) very early on, mapping the CR2 binding region to the first two CCP domains and thereby in competition with C3d (68, 74). The gp350 protein on the surface of the viral membrane envelope interacts with CR2 during the first steps of EBV entry. Another virus that exploits CR2 as a receptor for viral entry is the human immunodeficiency virus 1 (HIV-1) (84). HIV-1 can infect B cell lymphocytes in a complement/C3-dependent and CD4-independent manner, thus facilitating viral dispersion and access to lymphoid organs (85). Besides viruses, the pathogenic yeast *Cryptococcus neoformans* has been shown to use an extracellular factor, the antiphagocytic protein 1 (App1), to bind to CR2 (and also CR3) and avoid complement-mediated phagocytosis by alveolar macrophages (86).

2.4 CR1 and CR2 are structurally selective receptors

CR1 and CR2 both recognize C3 activated fragments tethered to a biological surface by using a common structural framework, yet they accomplish a remarkable degree of selectivity through distinct binding modes and cell localization. As already seen, CR1's main ligands are C3b, C4b, the AP/CP C3 convertases (monovalent binding sites), and the C5 convertases (bivalent binding sites), all markers of active complement opsonization. In contrast, CR2's ligands are iC3b and C3d(g), both monovalent binding sites and markers of halted complement activation.

Although at face value CR1 and CR2 recognize distinct ligand sets, the fact that C3b, iC3b, and C3d(g) share the TED domain could potentially lead to overlapping binding sites. In fact, CR1 is known to bind iC3b and C3d with low affinity (87) in addition to the higher affinity binding to C3b/C4b. The solution to this apparent problem has been revealed by the X-ray crystal structures of CR1 CCPs 15-17:C3b (PDB ID 5FO9) (59) (Figure 1B) and CR2 CCPs 1-2:C3d (PDB ID 3OED) (83) (Figure 1C). By comparing these two complexes, which reflect the tightest receptor-ligand interactions (2 μ*M* for CR1 CCPs 15-17:C3b (59) and 22 n*M* for CR2 CCPs 1-2:C3d (78)), it is straightforward to see that the molecular surfaces recognized by either receptor are rather distinct. A small overlap is, however, created by CR1 CCPs 15-17 interacting weakly with the CUB-TED domains in C3b (59), interactions that are likely lost in iC3b. Furthermore, interaction of CR2 with C3d occurs through surfaces that are partially occluded in C3b, but sterically unimpeded in iC3b/C3d(g).

3 Integrin receptors

Integrins link the extracellular matrix (ECM) to the cellular cytoskeleton and associated signal transduction pathways and

mediate cell-cell, cell-ECM, and cell-pathogen adhesion (88). Integrin-mediated interactions participate in cytoskeletal remodeling, phagocytosis, and cell migration (89). Complement receptors 3 (CR3) and 4 (CR4) belong to the integrin superfamily of type I transmembrane heterodimers (90). CR3 and CR4 are co-expressed in myeloid cells like neutrophil granulocytes, monocytes, macrophages, activated T and B lymphocytes, and lymphoid natural killer cells (91). They mediate immune adhesion-dependent processes such as adhesion to endothelium, phagocytosis of opsonized foreign particles, and other activation events that promote the innate and adaptive branches of the immune system (92).

These leukocyte-specific receptors bind multiple ligands like iC3b (93–95), ICAMs (96), fibrinogen (97), or lipopolysaccharide (LPS) (98). Despite their sequence homology, structural similarities, and overlapping ligands, CR3 and CR4 are functionally specialized, presenting a "division of labor" that makes them nonredundant receptors (34, 99).

Integrin signaling involves bidirectional communication between the extracellular environment and the intracellular cytoskeleton and signal transduction pathways, and the most accepted mechanism invokes an "inside-out" signaling precedence (100, 101). In the resting state, integrins adopt a bent, "closed", ligand-free inactive state; signals initiated in the actin cytoskeleton can trigger a dramatic conformational change in the extracellular region of integrins, which become extended, "open", ready to engage the ligand if available. When appropriate ligands are nearby, they can engage the receptors, initiating signaling processes from the "outside-in".

3.1 The overall structure of the β_2 integrins

Integrins are comprised of two noncovalently-associated protein chains: the α subunit (150-172 kDa) and the smaller β subunit (95 kDa), which is glycosylated. The cytoplasmic regions of integrins are very small compared to the large ectodomains. CR3 and CR4 share the same β_2 chain (CD18) and belong to the β_2 integrin family of adhesion receptors (90, 102), differing in their α chain, which is α_M in CR3 and α_X in CR4. The full CR3 heterodimer is also known as Mac-1 (Macrophage-1 antigen), CD11b/CD18, or integrin $\alpha_M\beta_2$, and the CR4 heterodimer is also known as p150,95, CD11c/CD18, or integrin $\alpha_X\beta_2$.

CD18/β_2 integrins are restricted to leukocytes, and except for mast cells, which lose CD18 expression during differentiation, all leukocytes express one or more CD18 integrins (91). CR3 and CR4 have found utility in biomedicine as their expression in NK cells enables complement-dependent cytotoxicity toward anti-CD20 (rituximab)-coated cancer B cells, contributing to the treatment's efficacy (103). CR3 and CR4 belong to the class of inserted (I) domain-carrying receptors. Fittingly, the N-terminal end of the α chain contains the iC3b-binding von Willebrand type A (VWA) domain or α chain inserted domain (αI), a specialized region characterized by a modified Rossman-fold architecture and a metal ion (Mg^{2+})-dependent adhesion site (MIDAS) motif (7). This relatively small domain is inserted between β-sheets (blades) 2 and 3 of the next domain in the α chain, a seven-bladed β-propeller domain, which allows the relative orientation of the αI and β-propeller to adjust flexibly (104). The aptly named Thigh, Calf-1, and Calf-2 domains complete the α chains. The α_M and α_X chains are homologous, with an overall sequence identity of ~60% (~47% in the αI domain). The functional discrimination of ligands by CR3 and CR4 is even more intriguing because most of the ligand recognition seems to be mediated by the 320-amino-acid αI domain, with the crucial involvement of the Mg^{2+} in the MIDAS. A comparison of the nature of known ligands suggests that strongly negatively charged molecules tend to be recognized by CR3, whereas CR4 tends to bind positively charged species (7). CR3 and CR4 are also homologous to two additional β_2 integrins, the lymphocyte function-associated antigen 1 (LFA1, CD11a/CD18, $\alpha_L\beta_2$) and $\alpha_D\beta_2$ (CD11d/CD18).

The sequence of domains of the β_2 chain from the N to the C terminus includes I-like, Hybrid, plexin-semaphorin-integrin (PSI), integrin epidermal growth factor (I-EGF) 1-4, and β tail (BT) domains. The β_2-chain I-like domain interacts with the α-chain β-propeller domain to form a broad platform that supports the ligand-binding αI domain. The overall structure of the β_2 chain domains contributing to the headpiece will be discussed later with available structural data for CR3 and CR4. As for the stalk region of the β_2 chain, there is structural data for a substantial part, even if piecemeal.

The crystal structure of the PSI/Hybrid domain/I-EGF1 segment from the human integrin β_2 chain was solved by X-ray crystallography at 1.8-Å resolution (PDB ID 1YUK) (105). The structure of this first part of the stalk revealed an elongated molecule with a rigid architecture stabilized by nine disulfide bonds. The PSI domain is wedged between the Hybrid and I-EGF1 domains, with extensive interfaces stabilized by contacts between conserved arginine and tryptophan residues. Soon after, there appeared two additional structures containing the PSI/Hybrid domain/I-EGF1 and additional I-EGF modules, I-EGF2 (PDB ID 2P26) and I-EGF2 and I-EGF3 (PDB ID 2P28) (106). The I-EGF is a cysteine-rich repeat module with a nosecone shape; four copies are located in the stalk region, where they relay activation signals to the ligand-binding headpiece. In the first structure, there was a prominent kink between the I-EGF1 and I-EGF2 modules, whereas, in the second structure, the three I-EGF modules adopted an extended conformation. The NMR structure for I-EGF3 and the NMR analysis of the interface contacts between I-EGF2 and I-EGF3 had been previously studied (PDB ID 1LY3) (107). The interdomain contacts between I-EGF domains 2 and 3 could be measured by NMR and were interpreted in terms of an approximate two-fold screw axis. In the NMR structure, the I-EGF domains 2 and 3 adopt an extended conformation connected by the "genu", a highly flexible linker that allows extreme bending. Based on these data, the authors posited that the release of contacts of the headpiece with I-EGF modules 2 and 3 could trigger a switchblade-like opening motion springing the integrin into its extended, active conformation. Reanalysis of these structures in the context of the structure of the $\alpha_L\beta_2$ headpiece in the closed conformation confirmed previous results while stressing the importance of proper disulfide pairing in the cysteine-rich I-EGF modules (PDB ID 5E6V, 5E6W, 5E6X) (108).

The structure of the single transmembrane helix of the β_2 chain has been shown by NMR to use a membrane-snorkeling lysine residue (Lys702) to interact with acidic phospholipids in the membrane bilayer to stabilize the bent closed conformation (PDB ID 5ZAZ) (109). This interaction can be modulated by intracellular Ca^{2+}, disrupting it and facilitating the acquisition of the extended open conformation. As this mechanism seems independent from the "inside-out" integrin signaling in T cell lymphocytes, it suggests a more prominent role for direct interactions of the β_2 chain, membrane phospholipids, and Ca^{2+} in regulating integrin structure and conformational changes.

3.2 Complement receptor 3

The initial work on the structure of CR3 was carried out by negative-staining electron microscopy on the headpiece (110) and by X-ray crystallography on the ligand-binding α_MI domain, which has been most thoroughly characterized (111–113). More recently, the crystal structure of the CR3 headpiece (33) and the cryoelectron microscopy structure of the CR3 ectodomain (114) have advanced the field significantly (Figure 2A, B).

Crystal structures of the α_MI domain in the open (PDB ID 1IDO) (112) and closed (PDB ID 1JLM) (113) conformations revealed the overall structure of the MIDAS motif and a ligand-binding regulatory mechanism whereby helix α_7 plays a crucial role in the closed form by restricting access to negatively charged ligand residues. While in the open state a glutamic acid residue from a neighboring α_MI domain completed the Mg^{2+} coordination sphere, in the closed form it was a key aspartic acid in helix α_7 that played the role. Two other crystallographic structures of the α_MI with the antagonist simvastatin (PDB ID 4XW2) (115) and with a ligand-mimicking antibody (PDB ID 3QA3) (116) have strengthened this idea by showing binding interfaces where the ligand contributes an acidic side chain to complete the metal coordination sphere.

CR3 and other β_2 integrins show homotypic interactions or, at least, a tendency to form homotypic interactions. Tellingly, NS-EM studies on the CR3 headpiece showed large numbers of dimers (110). Even the α_MI domain in the open conformation formed weak homodimeric interactions with crystallographic lattice neighboring molecules (112). Homotypic interactions may be desirable for β_2 integrins as they must accommodate large concentrations during receptor clustering or result from the loose ligand specificity. The first structure of a β_2 integrin with a complement factor ligand was

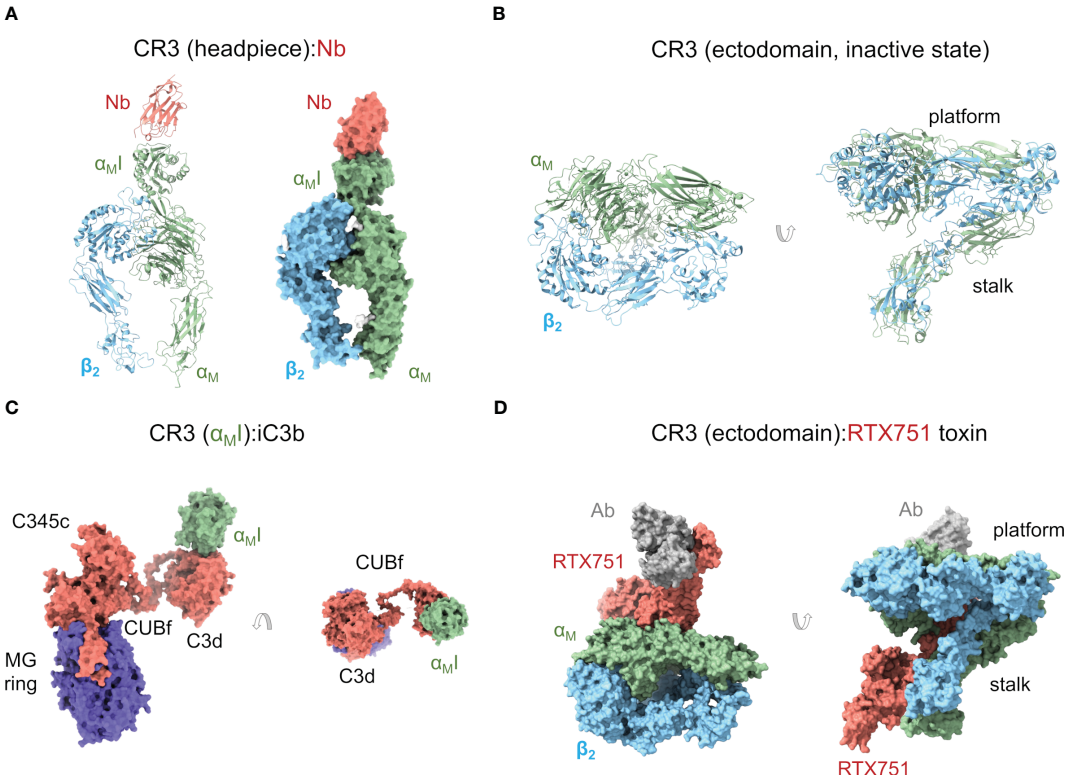

FIGURE 2
Complement receptor CR3. **(A)** Cartoon and molecular surface representations of the X-ray crystallographic structure of the CR3 headpiece in complex with a nanoantibody (Nb) (PDB ID 7P2D). The α_MI domain is in the inactive, closed conformation. **(B)** Cartoon representation of the cryoelectron microscopy structure of the CR3 ectodomain (except for the α_MI domain) in an inactive, closed conformation (PDB ID 7USM). **(C)** X-ray crystallographic structure of a complex between iC3b and CR3 α_MI domain (PDB ID 7AKK) where iC3b adopts an extended conformation. The interaction between the TED/C3d domain of iC3b and CR3 α_MI is shown in two orientations related by a 90° rotation. **(D)** Molecular surface representation of the cryoelectron microscopy structure of the CR3 ectodomain (except for the α_MI domain) in complex with *B. pertussis* RTX751 toxin (PDB ID 7USL). In this structure, the CR3 ectodomain adopts a more extended conformation than in **(B)** through interactions with the toxin.

that of CR3 α_MI in complex with C3d (PDB ID 4M76), the main ligand for CR3 (111). This structure revealed the binding mode of C3d to α_MI, characterized by an aspartate side chain of C3d chelating the MIDAS motif of α_MI, which was occupied by a non-physiologic Ni^{2+} cation from the crystallization condition. Although the buried surface area is relatively small, the interaction is strong enough (affinity (K_D) is in the micromolar range) to stabilize the complex and is comparable in area and affinity to other integrin complexes. A key insight from this structure showed that the C3d surface engaged by α_MI is masked in C3b by a well-folded CUB domain, effectively ruling out the possibility of an α_MI interaction with C3b. In iC3b, however, the cleavage by FI inside the CUB domain causes it to unfold, making the α_MI binding motif accessible.

Another fascinating insight from the α_MI:C3d structure was its compatibility with the binding of C3d by CR2 through its CCPs 1-2 domains (7). This hypothetical α_MI:C3d:CR2 complex was interpreted as a hand-over or transfer of C3d-opsonized antigens from CR3-bearing macrophages to CR2-bearing B lymphocytes. This process might act like an MHC-independent antigen presentation mechanism bridging the innate and adaptive branches of immunity. It would be interesting to characterize the hand-over in more cellular structural detail as the involvement of three distinct surfaces (macrophages, B cells, and opsonized particles) renders the entire process challenging.

A recent structure by our group has shown a complex between the entire iC3b and the α_MI domain (PDB ID 7AKK) (Figure 2C) (34). In this structure, the MIDAS motif of α_MI was fully charged with Mg^{2+}. The interaction between α_MI and the TED domain of iC3b was identical to the interaction previously observed between α_MI and C3d (111). More interestingly, the structure of CR3 α_MI:iC3b revealed two potential interfaces for the α_MI domain on the MG ring of the C3c fragment. This is relevant because the C3c moiety has been known to contribute to CR3 binding in interaction assays (111) and, perhaps more importantly, because iC3b-opsonized surfaces are phagocytosed by CR3-expressing macrophages at much lower opsonin concentration than C3d-opsonized surfaces (117), begging the question about what the role of C3c in CR3 binding might be. In one of these α_MI:C3c interfaces involving C3c MG1-2 domains, the C3c moiety of iC3b would conserve an "original" orientation with respect to the surface-anchored TED domain ("upright"), while in the other one, involving the C3c MG3-4 domains, the C3c moiety would be required to turn around and lie "upside-down" with respect to the TED domain. Surface plasmon resonance (SPR) binding experiments and site-directed mutagenesis of interfacial residues on the α_MI domain indicated that both interfaces may be relevant *in vivo*. Additional evidence will be necessary to clarify the physiological role of the C3c moiety of iC3b for CR3 recognition. Meanwhile, an enticing hypothesis is that iC3b behaves as a modular platform comprising a surface-anchored C3d and a more detached C3c moiety that collaborate to bind the CR3 ectodomain in the highly concentrated environment of the cell-particle interface. A modular iC3b would facilitate binding by increasing the number of low-affinity contacts (avidity effect), restricting the angular spread of CR3:C3d complexes to increase CR3:iC3b packing efficiency (alignment effect), and making it possible for C3d(g) and C3c moieties from the same or different iC3b molecules to collaborate in CR3 binding.

Although the role of CR3 as a complement receptor is well-attested, the capacity of CR3 (and CR4) to recognize and bind to a wide variety of other ligands remains puzzling. CR3, for example, interacts with many macromolecular components of the coagulation system (e.g., fibrinogen, fibrin, kininogen, plasminogen, heparin), denatured proteins, and oxidative and degrative products of lipids and glycans (7). Analysis of the electrostatic properties of the ligand-facing molecular surface has shown that it is a markedly negatively charged surface, which is in line with the preference of CR3 for cationic ligands like the intrinsically unstructured myelin basic protein (MBP) (118) and the antimicrobial peptide LL-37 (119), as long as they also have a carboxylate moiety. These properties have been used to justify including CR3 and CR4 as scavenging receptors, i.e., those receptors like CD36 and the receptor for advanced glycation end products (RAGE) that enable cellular removal of decayed macromolecules in extracellular space (7). With its preference for cationic ligands that can interact with cell membranes, CR3 could function as a receptor for clearing cellular debris associated with membrane damage. CR3's multitude of ligands and the fact that its outside-in signaling dampens inflammatory responses are in line with this proposal; CR4, instead, lacks anti-inflammatory signaling, suggesting that it may be functionally distinct from CR3 in this context (7).

More recently, the crystal structure of the CR3 headpiece has been determined in complex with a nanoantibody at 3.2-Å resolution (PDB ID 7P2D) (33) (Figure 2A). This structure provides the first high-resolution structure of CR3 beyond the α_MI domain. In this structure, the CR3 headpiece adopts the closed conformation, which resembles those of LFA1 and CR4 in the same state. The nanoantibody used for crystallization could sterically block C3d binding in an Mg^{2+}-independent manner but, surprisingly, acted as an agonist for cell-bound $\alpha_M\beta_2$, thus apparently increasing affinity for the iC3b ligand. These seemingly contradictory observations could be reconciled by proposing that additional conformational flexibility on the integrin and iC3b might permit interactions in cell surface-bound integrin that are not observed in solution or binding experiments *in vitro*. Indeed, the current understanding of both $\alpha_M\beta_2$ and iC3b structures suggests that they can interact in complex, heterogeneous environments using multiple domains in the crowded cell surface environment (32, 34).

Within a few months of the publication of the previous structure, the cryoelectron microscopy structure of the CR3 ectodomain at 2.7-Å resolution was published (PDB ID 7USM), along with the structure of a complex with an adenylate cyclase toxin RTX751 from *Bordetella pertussis* and a stabilizing Fab (PDB ID 7USL) (114) (Figure 2D). While the unbound $\alpha_M\beta_2$ adopts the closed conformation seen for the CR3 headpiece and closed CR4 ectodomain (see below), RTX751-bound $\alpha_M\beta_2$ was able to achieve a more extended conformation through stabilizing interactions with RTX751, closely resembling the conformations of extended $\alpha_X\beta_2$ ectodomains (120, 121). The closed and extended conformations of

CR3 were related by a hinge motion of the headpiece relative to the tailpiece, pivoting between the Thigh/β-propeller in the α_M headpiece with the Calf-2 domain in the tailpiece. The observation of a partially extended conformation in the RTX751 complex suggests that CR3 must be able to spontaneously sample more extended conformations by built-in flexibility around the headpiece-tailpiece hinge angle, which is consistent with previous observations (107).

3.3 Complement receptor 4

Earlier structural work on the CR4 headpiece by NS-EM showed an overall structure like that of other integrins, particularly very similar to that of CR3 (120). Maintaining the inactive state of the α_XI domain requires the correct pairing of the α_X and β_2 chains, as shown by several experimental approaches (e.g., 122). When CR4 adopts an extended conformation, an α-helix in the I-like domain exerts a pull on the α_XI domain that opens it up for binding.

The α_XI domain was the first αI domain to be elucidated by X-ray crystallography (121). The crystallographic structure of the α_XI shows a similar overall fold to that of CR3. Studies of CR4 revealed the flexible connection of the α_XI domain with the β-propeller domain, suggesting that rotational freedom was required for efficient ligand binding (108). This property might also be necessary for binding structurally diverse ligands since the chelation of acidic ligand groups by the core cation in the MIDAS motif is likely to restrict ligand movement to pivoting around the Mg^{2+} cation.

NS-EM micrographs of the CR4 headpiece bound to iC3b revealed up to two independent CR4 α_XI binding sites on the iC3b MG ring (110). The dominant site, present in all complexes, was located close to the macroglobulin domains MG3-4, and a secondary site, less frequently occupied, was found near the C345c domain. Interestingly, the two α_XI binding sites do not overlap with the MG binding sites identified for α_MI (34), suggesting that the two receptors saturate all potential binding sites on the MG ring of iC3b without directly competing. This does not imply the potential for simultaneous binding of iC3b by CR4 and CR3, which would be sterically impeded, but it shows that the αI domains have some degree of selectivity in ligand binding.

A structural chemical feature of CR4 α_XI is the presence of a "ridge" of positively charged residues on the ligand-facing molecular surface (7). The electrostatic properties of α_XI are markedly distinct from those of the homologous α_MI and α_LI domains (7, 34). This property has been invoked to explain why CR4 can selectively bind polyanionic molecules more efficiently than CR3 (7). Indeed, highly negatively charged polymers/molecules like heparin, nucleic acids, LPS, and osteopontin are proficient ligands for CR4. In parallel to the potential role of CR3 as a scavenger receptor for polycationic species, a receptor like CR4 with a strong preference for polyanionic species could serve complementary functions as a scavenger receptor by clearing excessive amounts of negatively charged proteins, detecting the presence of the negatively charged bacterial cell wall and LPS-rich membranes, and potentially alerting the immune system about their presence.

The structure of the complete CR4 ectodomain has been solved by X-ray crystallography in a bent, resting state (PDB ID 3K71, 3K72, 3K6S, 5ES4) (121) and a metastable, transition state (PDB ID 4NEN, 4NEH) (120) (Figures 3A, B). In the resting structure, the α_XI domain is in the inactive conformation, as expected for the ectodomain's inactive state. Surprisingly, the α_XI domain shows a high degree of flexibility around the loops connecting it to the β-propeller domain. This suggests a more dynamic coupling between the αI domain with implications for the allosteric transmission of information along the integrin's body. The second set of structures of the $\alpha_X\beta_2$ ectodomain represents an intermediate or transition state from the bent, closed, to the open, extended conformations, with a crystal lattice contact stabilizing the α_XI domain in an open conformation. A key feature of this structure consists in the unwinding of much of α_X α_7 helix and its insertion into the interface between the β-propeller and the βI domains. The elevation (lift-off) of the α_XI domain above the headpiece's platform facilitates large-scale extensional and rotational motions of sufficient amplitude to communicate allosteric changes across the length of CR4.

4 Complement receptor of the immunoglobulin family

The complement receptor of the immunoglobulin (Ig) family (CRIg) is a type I transmembrane Ig superfamily member first cloned during a search for homologs of the junctional adhesion molecule (JAM) family (123). CRIg is also known as V-set and immunoglobulin domain-containing protein 4 (VSIG4), Z39Ig, UNQ317, and PRO362. In humans, there are three spliced isoforms of CRIg. The most common allelic form contains 399 amino acids and is known as huCRIg(L), whereas isoforms 2 and 3 are shorter, with 274 and 296 amino acids, respectively. Isoform 3 is also known as huCRIg(S). Full-length CRIg contains a signal peptide, a V-type Ig-like 1 domain, a C2-type Ig-like 2 domain, several potential *O*-glycosylation sites, and an intracellular domain with two potential phosphorylation sites, and is structurally related to the B7 family of immune regulatory proteins (124). Whereas huCRIg(L) comprises both Ig-like domains, huCRIg(S) contains only the V-type Ig-like 1 domain.

CRIg is expressed in tissue-resident and sinusoidal macrophages like the Kupffer cells, the resident macrophages in the liver, and it mediates phagocytosis of particles opsonized by any of its two ligands, C3b and iC3b (125). Besides stimulating pathogen opsonophagocytosis, CRIg is also known to be a potent inhibitor of the activation of the C3 convertase of the alternative pathway by binding to C3b, acting as a negative regulator of complement activation. In contrast to the other C3 fragment receptors (CR1 to CR4), CRIg is found on a constitutive recycling pool of membrane vesicles where it participates in the internalization of C3-opsonized particles from the bloodstream by Kupffer cells. Instead, CR1, CR3, and CR4 are located on secretory vesicles that fuse with the plasma membrane upon cytokine stimulation of the cells and internalize ligands through a macropinocytotic process only after receptor

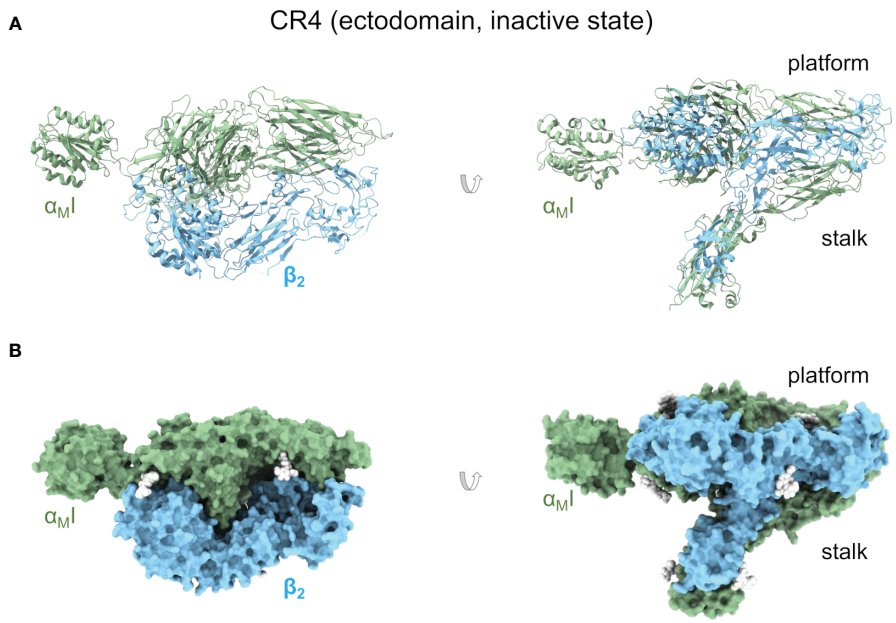

FIGURE 3
Complement receptor CR4. **(A)** Cartoon representation of an X-ray crystallographic structure of the CR4 ectodomain in an inactive but metastable structure that anticipates activation (PDB ID 4NEH). Two orientations related by a 90° rotation are shown. **(B)** As in **(A)** but as a molecular surface representation. Native glycan moieties are shown as white spheres.

cross-linking (126). Besides its localization in the liver, CRIg is also abundantly expressed in resident macrophages from several fetal and adult tissues, with the highest expression attained in the lung and placenta. The main function of CRIg is to act as a potent negative regulator of T-cell proliferation and IL-2 production (127).

4.1 CRIg has two consecutive Ig-like domains

CRIg contains two Ig domains known as Ig-like 1 and Ig-like 2 domains. The crystallographic structure of Ig-like 1 (residues 19-137) was determined to 1.2-Å resolution, showing a V-set Ig-like fold that resembles the antibody variable domain, responsible for providing the binding specificity (PDB ID 2ICC) (128) (Figure 4A). Subsequent crystal structures of the same V-set Ig-like 1 domain from human and mouse have been determined in complex with a nanoantibody that blocks binding with C3c and C3b (PDB ID 5IMK, 5IML, 5IMM, 5IMO) (129).

In contrast, the structure of Ig-like 2 (residues 143-226) has not been solved, although sequence homology has identified its fold as a C2-type Ig-like domain reminiscent of constant antibody domains that provide the effector functions. The AlphaFold model corresponding to full-length CRIg contains the predicted structure of the Ig-like 2 domain (AlphaFold AF-Q9Y279-F1) with a very high degree of confidence (Figure 4B).

The Ig-like domain consists of antiparallel β-strands arranged into two sheets linked by a disulfide bond. V-set domains can be distinguished from C2-type domains because they show the variability associated with antigen/ligand recognition, and the domain is longer with two extra strands tucked into the middle of the domain (C' and C"). The first β-sheet in Ig-like 1 comprises β-strands A', G, F, C, C', and C", and the second one of β-strands B, E, and D (Figures 3A, B).

4.2 CRIg binds to the β-chain of C3b and iC3b

C3b and iC3b are the main ligands of CRIg. Other C3 proteolytic fragments have been tested for CRIg binding, including C3, C3a, and C3d, and other homologous complement factors like C4 and C5, all with negative results (125).

The structures of CRIg Ig-like 1 domain bound to C3c (PDB ID 2ICE) and C3b (PDB ID 2ICF) (Figure 4C) have been determined by X-ray crystallography at 3.1-Å and 4.1-Å resolution, respectively (128). Since C3d is not a ligand for CRIg, the C3c moiety shared by C3b/iC3b becomes the most likely binding site for CRIg Ig-like 1 domain. Furthermore, C3c and C3b differ essentially in the lost TED domain (C3dg) while they share most of their structural core with minimal deviation: ~0.6 Å root mean square distance over 479 Cαs of the α-chain and 642 Cαs of the β-chain.

CRIg Ig-like 1 domain binds to C3c or C3b identically without restructuring or inducing conformational changes in the ligand. Residues from β-strands A', F, G, C', and C" from one of the β-sheets and β-strand B from the second β-sheet are engaged in the interaction, with β-strands C' and C" contributing most of the interactions. The hairpin loop between β-strands C' and C" sticks into the cavity in the center of the keyring-shaped β-chain of C3b.

The binding site is quite large (2,670 $Å^2$ of solvent-accessible surface). It overlaps the cavity inside the C3c macroglobulin ring, crossing it diagonally and ending at the interfaces between

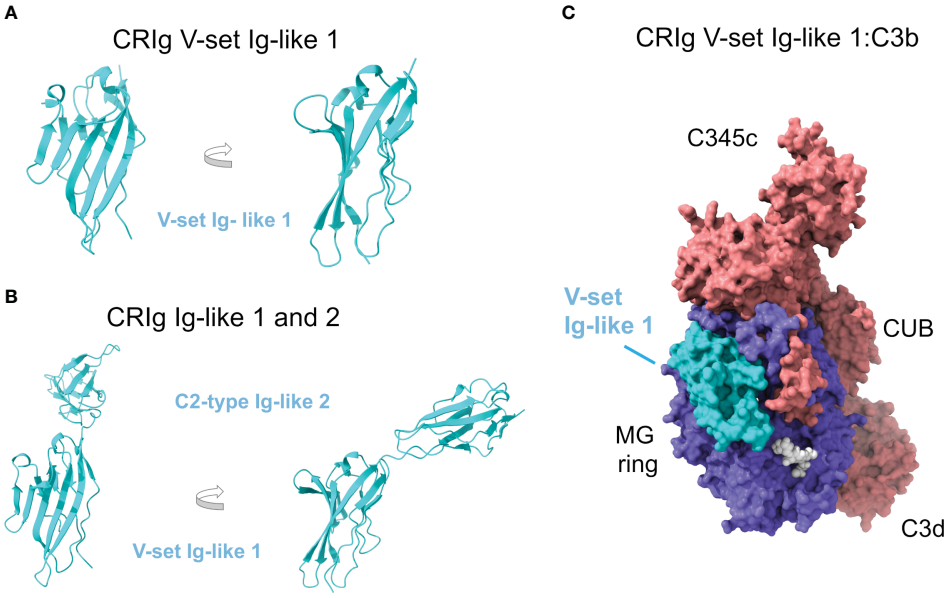

FIGURE 4
Complement receptor CRIg consists of two Ig-like domains and binds the β-chain of C3b. **(A)** Crystallographic structure of the V-set Ig-like 1 domain of CRIg, in cartoon representation and two orientations (PDB ID 2ICC). **(B)** AlphaFold predicts with high confidence the structural model of the C2-type Ig-like 2 domain of CRIg (AlphaFold AF-Q9Y279-F1). The consecutive Ig-like 1 and 2 domains are shown in cartoon representation and two orientations; the orientation of the V-set Ig-like 1 matches panel A for comparison. **(C)** Structure of CRIg V-set Ig-like 1:C3b (PDB ID 2ICF) in molecular surface representation. C3b is colored according to chain (the α chain in red, the β chain in blue), and CRIg V-set Ig-like 1 domain is in cyan. Native glycan chains in C3b are shown in white spheres.).

consecutive MG domains MG3-MG4 and MG5-MG6 (Figure 3C). This binding site places CRIg on the opposite side of the surface-anchored C3dg/TED domain, a sterically accessible location facilitating binding. The most extensive contributions to binding are made by MG3 and MG6, supplemented by MG4, MG5, and LNK. Compared to C3, in C3c and C3b MG3 has rotated by 15° and there is a movement of the helical section in the LNK region, which appear to be necessary to form the CRIg binding site and thereby explain why CRIg cannot bind to C3.

The V-set Ig-like 1 domain of CRIg is sufficient for high-affinity binding to C3b/iC3b, even though this domain alone binds iC3b more strongly than to C3b. Although the presence of the C2-type Ig-like 2 domain is not required for binding, it restores high-affinity binding to C3b to the same level observed for iC3b (125). Interestingly, dimeric C3b ($C3b_2$) (130) is bound more tightly to CRIg than monomeric C3b, a relevant result because multimeric C3b is supposed to represent the physiologic state of C3b on opsonized surfaces.

Significantly, CRIg binding to C3b inhibits the C3 and C5 convertases of the alternative pathway since CRIg blocks the generation of C3a and C3b by C3 convertase and C5b by C5 convertase. In a series of elegant experiments, site-directed mutations introduced in CRIg residues in contact with C3b MG3, MG5, or MG6 at the center, periphery, or outside the CRIg:C3b interface led to a strong, weak, or negligible effect on CRIg-mediated inhibition of the C3 convertase, evaluated in hemolytic assays with rabbit red blood cells (128). This proved that CRIg inhibition of the C3 convertase depended on its interaction with C3b.

In contrast to other complement negative regulators, CRIg does not inhibit the alternative pathway convertases by dissociating the catalytic subunit Bb (decay accelerating activity) or promoting C3b degradation by FI (cofactor activity). In contrast, it appears that CRIg, once bound to the β-chain of C3b, can sterically hamper association with the C3 and C5 alternative pathway convertases. Remarkably, CRIg fails to inhibit the C3 and C5 classical pathway convertases, indicating that the functional effect is confined to C3b and the alternative pathway.

4.3 Implications for diseases and immune evasion

CRIg is an essential receptor for the clearance of complement-opsonized particles, which are recognized and phagocytosed by Kupffer cells in the liver. Pathogens and immune complexes are shuttled in the circulation by CR1-bearing erythrocytes and handed over to CRIg-expressing Kupffer cells in the liver in a dynamic process relying on immune adherence that prevents systemic inflammation and immune complex diseases associated with aberrant vascular deposition (8). This extremely efficient mechanism of blood-borne pathogen clearance can catch Gram-positive and Gram-negative bacteria (8) and eukaryotic parasites (131).

5 Anaphylatoxin G-protein coupled receptors

The anaphylatoxins C5a and C3a, generated by the proteolytic activation of C5 and C3, respectively, are potent chemoattractants

and pro-inflammatory mediators. The cognate receptors of C5a are C5aR1 (C5aR/CD88) and C5aR2 (C5L2/GPR77), and the cognate receptor of C3a is C3aR (C3aR). The analogous "anaphylatoxin" released by proteolytic activation of the C3-homologous zymogen C4, C4a, has thus far defied a functional description and, perhaps significantly, lacks a specific receptor (132, 133).

C5aR1/C5aR2 and C3aR belong to the G-protein coupled receptor (GPCR) family and, more precisely, to the rhodopsin family and class A, two equivalent groupings at the highest hierarchy level of the two main GPCR ordering systems (134–136). Based on sequence homology and functional similarity of GPCR, the three receptors are classified into the complement peptide group inside class A (135). In contrast, within the rhodopsin family defined by the phylogenetic classification of human GPCR, C5aR1/C5aR2 are members of the chemokine cluster of γ-group, while C3aR belongs to the purine receptor cluster of δ-group (134).

The three anaphylatoxin receptors share structural features common to all GPCR. They are comprised of an extracellular N-terminal region, seven transmembrane α-helices (TM1-7), connected sequentially by intracellular (ICL) or extracellular (ECL) loops, and an intracellular C-terminal region (137–139). To refer to TM residues, we will follow the Ballesteros-Weinstein numbering (140), and for the remaining residues, we will use the name of the containing motif (ECL, ICL, N-ter, or C-ter) as superscripts.

The anaphylatoxin receptors are widely expressed in immune cells from the myeloid and lymphoid lineages and nonimmune cells like epithelial cells and neurons (141). By binding their cognate ligands, the receptors are implicated in diverse cellular functions, physiological processes, and pathologies, mainly related to the immunological system (141–148).

The clinical relevance of these receptors in different acute and chronic disorders, mainly with an inflammatory etiology, has triggered a great interest in developing specific and effective modulators (149). In this context, an exhaustive investigation has aimed to reveal insights into the structure-function of these receptors to increase the understanding of how they carry out their functions and to support the finding of modulators with clinical potential.

5.1 Complement receptor 5a 1

5.1.1 Structure of C5aR1

C5aR1 was discovered in 1978 (150), and the coding sequence of its 350 amino acids was cloned and determined in 1991 (151, 152). While the unliganded receptor has defied structural determination, recently published high-resolution X-ray crystal (PDB ID 5O9H, 6C1Q, 6C1R) and cryoelectron microscopy (PDB ID 7Y64, 7Y65, 7Y66, 7Y67) structures (Figure 5A) have provided insights into the structural features of this receptor.

The structure of the core transmembrane region is conserved with other class A GPCR (138, 139, 153) including the overall helical arrangement and kinks, the placement of TM3 at the center of C5aR1 with a lower tilt-angle with respect to the plane of the lipid bilayer, $W^{6.48}$ ($W255^{6.48}$) near $P^{6.50}$ ($P257^{6.50}$), the PIF motif ($P214^{5.50}$, $I124^{3.40}$, $F251^{6.44}$), an intrahelical sodium coordination site ($D82^{2.50}$, $N292^{7.45}$, $N296^{7.49}$) at the cytoplasmic side, the NPXXY motif ($N296^{7.49}$, $P297^{7.50}$, $I298^{7.51}$, $I299^{7.52}$, $Y300^{7.53}$) and the DRY/F motif ($D133^{3.49}$, $R134^{3.50}$, and $F135^{3.51}$). On the extracellular side, C5aR1 presents a conserved disulfide bond ($C109^{3.25}$ and $C188^{ECL2}$) and a β-hairpin conformation in ECL2 that resembles other peptide binding receptors (138, 154, 155).

At the intracellular region, the ICL2 exhibits a two-turn α-helical structure, and some C-terminal residues form the conserved eighth amphipathic α-helix (H8) of three turns long (35, 138, 154, 155). C5aR1 can oligomerize *in vivo*, forming homodimers and perhaps higher-order homo-oligomers (156, 157) and heterodimers with CCR5 (158) and C5aR2 (159).

Other post-translational modifications observed in C5aR1 are an *N*-glycosylation at N5 (160), tyrosine sulfation at Y11 and Y14 (161) at the N terminus, and serine phosphorylation at S314, S317, S327, S332, S334, and S338 in the C terminus (162); albeit to a lesser degree, threonine residues can also be phosphorylated (158).

5.1.2 C5a-binding orthosteric site

The cognate ligands of C5aR1 are the anaphylatoxin C5a and its dearginated product $C5a^{desArg}$, which have been extensively researched (163, 164). Other ligands of the C5aR1 have been recently discovered (165).

The high-resolution structures of liganded C5aR1 have revealed an orthosteric and an allosteric binding site (35, 36, 154, 155). The orthosteric binding site consists of an interhelical solvent-exposed amphipathic cavity located at the extracellular side of the receptor (35, 36, 155) (Figure 5A). This site can be divided into a polar region and a hydrophobic cage. The polar region spans from the outer edge to one side of the binding site and comprises hydrophilic and charged residues recruited from TM3-7 and the membrane-proximal part of ECL2. The hydrophobic cage is mainly formed by hydrophobic residues from TM1-3, TM7, and ECL1, which extend from one side to the bottom of the binding site. The orthosteric site can bind peptide ligands of up to eight residues (amino acid positions numbered P1-P8) with various pharmacological effects, including C5a, BM213, $C5a^{pep}$, PMX53, and C089. Water molecules can be involved in ligand binding, forming a polar network connecting the ligand to residues from the polar surface (155). The allosteric binding site is an extra-helical hydrophobic cleft formed by residues from the middle regions of TM3, TM4, and TM5, which bind non-peptide ligands such as NDT9513727 or Avacopan through shape complementarity, hydrophobic interactions, and a key hydrogen bond with $W213^{5.49}$ (154, 155). The N terminus and the turn region of the ECL2 can also participate in binding orthosteric ligands (35, 36).

The structures of C5aR1 in complex with C5a and the G_i protein show that C5a binds in a C-terminus-inside mode, and the receptor interacts with three distinct regions of the anaphylatoxin (35) (Figure 5A). Firstly, an amphipathic stretch of the receptor's N terminus (L22-D27) interacts with a cavity between C5a α-helices H2 and H4 and the H3-H4 loop. Secondly, the orthosteric site accommodates the last eight residues of C5a. Inside the orthosteric site, the C5a C terminus adopts a hook-shaped

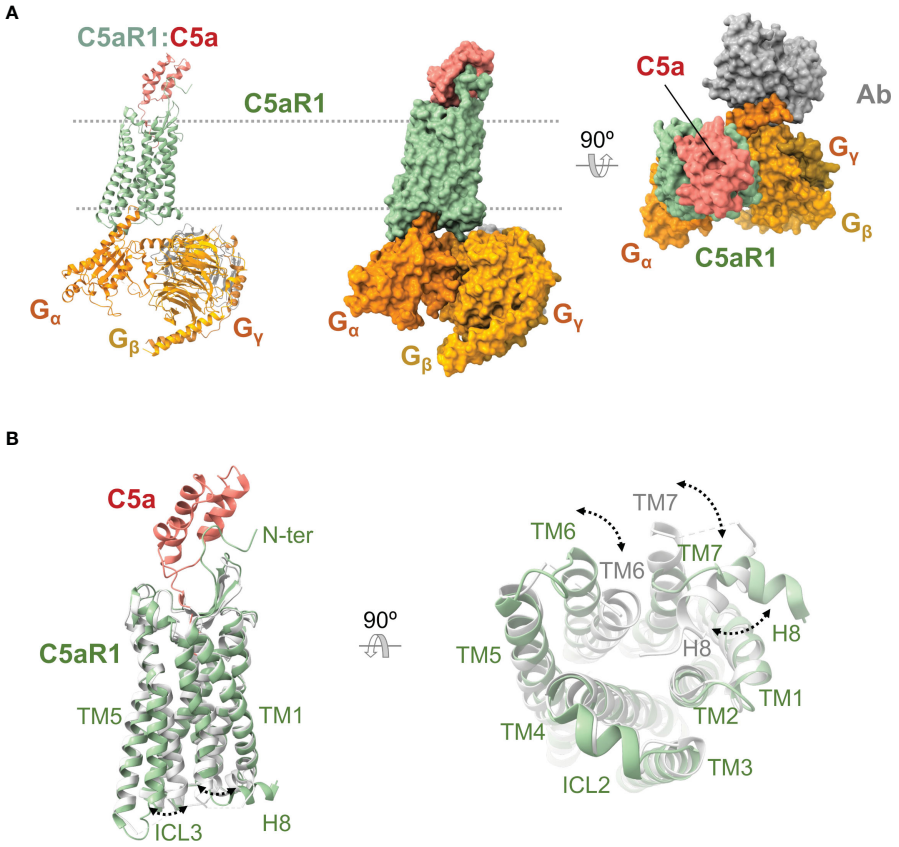

FIGURE 5
Anaphylatoxin receptor C5aR1 in complex with C5a and conformational changes underlying activation. **(A)** Cryoelectron microscopy structure of C5aR1:C5a bound to heterotrimeric G protein comprising the Gα, Gβ, and Gγ subunits (shown in orange, yellow, and gold), and a stabilizing antibody (shown in gray) (PDB ID 7l65). C5aR1 is shown in green, and C5a in red. The same view is shown of the cartoon and molecular surface representations of the complex. We show a 90° rotated view of the complex on the right in molecular surface representation. **(B)** Superposition of the active conformation of the C5aR1:C5a complex (PDB ID 7l65) (C5aR1 in green, C5a in red) and an inactive reference structure (PDB ID 6C1Q) (C5aR1 in grey; the antagonist PMX53 is not shown for clarity). Side (left) and bottom (right) views are shown. Conformational changes are indicated by dashed lines between and labeling of structural elements that occupy distinct positions in the active *versus* inactive conformations.

conformation, establishing strong interactions with residues at the polar surface while accommodating inside the hydrophobic cage. In this orientation, the side chain of C5a L^{P6} interacts with a triad of receptor residues denominated IWI region ($I91^{2.59}$, $W102^{ECL1}$, $I116^{3.32}$) (35, 36). Finally, the amphipathic turn region of ECL2 ($E180^{ECL2}$-$P183^{ECL2}$) makes contact with C5a in a cleft assembled by α-helices H1, H2, and H4 and the H2-H3 loop.

Other C5aR1 ligand peptides occupy the orthosteric binding site in a similar fashion to the C5a C terminus (35). The main differences in binding mode between C5a and these peptides have been observed in the hydrophobic cage of the orthosteric site, particularly in the interactions established between the peptides' P6 and P7 positions and the IWI region and surrounding residues (e.g., $L92^{2.60}$, $S95^{2.63}$, $H100^{ECL1}$, $P113^{3.29}$, and $V286^{7.39}$) (35, 155). A unique feature of the cyclic peptide PMX53 is a hydrogen bond between W^{P5} and $P113^{3.29}$ (155).

The recent flurry of C5aR1 structures has made important contributions to understanding the structure-function relationship of C5aR1 and how C5a binds and activates the receptor. However, a few questions remain unanswered. For example, receptor aspartic acid residues upstream of L22 (166, 167) and the sulfated Y11 and Y14 (161) had been shown to play important roles in C5a binding. Still, current structures have not revealed any direct interactions between these residues and the ligand. Therefore, how these residues contribute to C5a binding has not been explained. They may establish direct interactions with C5a (168) or be required for the structural conformation of the binding site (169).

The recent structural evidence agrees with a two binding sites model previously proposed (170). In this model, the first binding event with C5a engages a site 1 in C5aR1 composed of the N terminus and the ECL2, which directly contacts the helical core of C5a; this binding event favors a conformational change of C5a that promotes binding to the site 2, composed of the orthosteric pocket, which interacts with C5a C terminus. In support of this model, kinetic and thermodynamic analyses by atomic force microscopy of the binding interaction have confirmed that both sites 1 and 2 contribute to the high-affinity binding of C5aR1:C5a through a cooperative mechanism (171). The markedly different conformation adopted by bound C5a with respect to the free form lends further support to this model. In the bound conformation, C5a shows a rearrangement of the C terminus and the helical bundle, which changes from a 1.5-turn helix form placed

near the helical bundle (as seen in free C5a) to an unfolded conformation in bound C5a (35). These changes have been rationalized as a bi-directional information flow between C5a and C5aR1 (166). According to this view, the first binding event would be characterized by C5aR1 site 1 promoting or favoring a conformational change in C5a, and the second binding event in a fully extended conformation of C5a inside site 2 would then activate the receptor.

Orthosteric ligands vary widely in their binding affinity for C5aR1. While C5a interacts with C5aR1 with a dissociation constant K_D = 1-5 n*M* (151, 167, 172, 173), its dearginated version C5a^{desArg}, which only differs from C5a in the last amino acid, R74 (174), has a 10 to 100-fold lower binding affinity. However, peptides derived from the C-terminal end of C5a show modest binding affinities, suggesting that the engagement of the receptor N terminus and the ligand coupling to the orthosteric site (35, 175) are important features for the strong binding of C5a. The lower affinity of C5aR1 for C5a^{desArg} could be explained by the putative lack of interactions between R74 at P8 in the orthosteric site (35).

5.1.3 C5a-mediated activation of C5aR1

C5aR1 is activated by orthosteric agonists (170, 175–177), which cause rearrangements in the extracellular, transmembrane, and intracellular regions of the receptor (35, 36) (Figure 5B), leading to a conformation in which it can trigger intracellular signaling pathways by recruiting transducers (138, 139, 153). At the extracellular region, the N terminus appears not to be involved in the C5aR1 conformational changes since this stretch is not required for receptor activity (161, 166, 175, 177). The ECL1 and especially its WXFG motif perform a critical role in C5aR1 activation (178). The ECL2 accomplishes a striking function in ligand-mediated activation of C5aR1 beyond its role in ligand binding (35, 179). In contrast to ECL1 and ECL2, ECL3 seems not to be involved in C5aR1 activation (178). Other residues essential for C5aR1 activation were found at the core of the transmembrane helix bundle and inter-helical interfaces (178, 180, 181).

In line with the common mechanism of class A GPCR (153, 182), an activation mechanism has been proposed for C5aR1 based on the receptor conformational changes observed between an active state (bound to C5a and G_i) and an inactive state (bound to PMX53 and Avacopan), and the currently available receptor structure-function data (35, 36, 155). Initially, the coupling of C5a into the orthosteric site causes TM displacements that loosen a hydrophobic zipper formed by I116$^{3.32}$, M120$^{3.36}$, W255$^{6.48}$, and Y290$^{7.43}$ at the extracellular side of C5aR1. This zipper is proposed to act as a lock tethering TM3, TM6, and TM7 in an inactive configuration, and movements key for loosening it are an upward rotation of the extracellular region of TM3 and a TM6 downward displacement, which may be caused by the engagement of C5a L^{P6} by the IWI region and the R^{P8}-Y258$^{6.51}$ interaction, respectively. Next, TM shifts keep taking place disturbing the PIF motif at the hydrophobic core. Sequentially, the reorganization of the helical bundle core cause conformational changes at the cytoplasmic side of C5aR1 that include a pronounced outward displacement of the intracellular section of TM6, an H8 swing from its location between TM1 and TM7 oriented toward the receptor's center to a classic conformation near to the lipid bilayer, alterations of NPXXY and DRY/F motifs, the sodium coordination site collapse, and the opening of an interhelical water-accessible cavity (Figure 5B). Eventually, the rearrangements promote receptor-transducer interactions and, ultimately, intracellular signaling (35, 36).

Other remarkable conformational changes associated with C5aR1 activation by C5a include an uncommon placement of Y300$^{7.53}$ that may be important for the particular H8 reorientation, TM3 and TM7 distancing their extracellular sides and approaching their intracellular segments, and rearrangements of clusters of water molecules located into the interhelical cavities that are separated by W255$^{6.48}$ and I116$^{3.32}$ at the helical core of the receptor (35, 36, 155).

5.1.4 Modulation and selectivity of C5aR1 activity

C5aR1 exhibits functional selectivity as it triggers distinct downstream signaling and cellular responses in a ligand and cell-type-dependent fashion. The ability of C5aR1 to activate different transducers and the variety of mechanisms by which its activity can be modulated contribute to this functional selectivity. Agonist-activated C5aR1 can signal through heterotrimeric guanine nucleotide-binding proteins (G-proteins) with α-subunits of the $G_{i/o}$ and $G\alpha_{16}$ families (183–187). Coupling the $G\alpha_{i1}$ subunit involves C5aR1 residues from ICL2, ICL3, TM3, TM5, and TM6, and $G\alpha_{i1}$ residues from the β_2-β_3 loop, β_6 strand, and α_5 helix. Remarkably, the α_5 helix of $G\alpha_{i1}$ inserts into the receptor intracellular cavity taking up part of the space filled by H8 in the inactive C5aR1 (35, 36). The receptor segments involved in G-protein signaling include the DRY/F and NPXXY motifs, particularly the ICL3 (180, 188, 189).

The G-protein specificity of C5aR1 seems to lie in the three ICLs and particularly the receptor C terminus, which could work together to restrict the receptor interaction with G-proteins (188). Noteworthy, C5aR1 can bind G_i even in the absence of agonist stimulation, suggesting that, although G-protein pre-coupling to C5aR1 is not essential for ligand binding, the pre-coupling could increase the receptor affinity for ligands as C5a:C5aR1 binding fosters the G-protein coupling to the receptor (190–192).

The main phosphorylation sites identified in C5aR1 include serine (S314, S317, S327, S332, S334, and S338) and threonine residues at the C terminus (158, 162, 193). A likely PKC phosphorylation site has also been identified in the ICL3 (194). C5aR1 phosphorylation seems hierarchical as the initial modification of S332/S334 or S334/S338 is required for the efficient phosphorylation of the remaining sites (195). Several kinases, including GRK (GRK2, GRK3, GRK5, and GRK6) and PKC (PKCβ), can be implicated in C5aR1 phosphorylation (193, 196, 197). GRK2 can be translocated to the plasma membrane in response to C5a, and the receptor ICL3 is the intracellular stretch preferentially bound by GRK2 and PKCβII (198). Receptor phosphorylation is involved in β-arrestin recruitment (158, 193, 199), receptor internalization (158, 194, 199, 200), and desensitization (193, 195). Although the precise roles of these

phosphorylation sites have not yet been elucidated, one or several of the C-terminal serine residues (S327, S332, S334, and S338) appear to be the most relevant phosphorylation sites for β-arrestin recruitment and C5aR1 internalization and desensitization (193). $L318^{H8}$ plays an important role in the receptor conformation that can be efficiently phosphorylated and internalized (201).

Activated C5aR1 can recruit β-arrestins 1 and 2 (199). GRK 2, 3, 5, and 6 have all been shown to facilitate the recruitment of β-arrestins 1 and 2 to C5aR1 (187, 202). β-arrestins 1 and 2 recruitment by C5aR1 may be followed by receptor internalization and downstream signaling (199, 203). The C terminus of C5aR1 is required for efficient homologous receptor internalization (194). C5aR1 internalization has been observed as a clathrin-dependent process that is associated with the β-arrestin recruitment by the receptor. C5aR1 internalized in early endosomes can be targeted to lysosomes for degradation or recycled to the cell membrane. The trafficking of C5aR1 through these pathways appears to depend on the cell type (199–201). Recycling of C5aR1 likely requires its dephosphorylation by several phosphatases, including protein phosphatase 1 (PP1) (193, 200). Although a structure of C5aR1 binding to β-arrestins is lacking, impaired β-arrestin binding by different phosphorylation-deficient C5aR1 mutants indicates that a stable association between C5aR1 and β-arrestin likely requires a certain degree of receptor phosphorylation (158, 193, 199). C5aR1 can also couple with the Wiskott-Aldrich syndrome protein (WASP), which binds to the receptor's C terminus (204).

Agonist-induced and unliganded C5aR1 receptor oligomerization have been observed (205). Oligomerization likely plays important functional or regulatory roles *in vivo*, but little is known about how C5aR1 assembles into oligomers and the implications for receptor activity. Structurally, TM1, 2, and 4 may be involved in C5aR1 dimerization (157, 181), while neither the N nor the C terminus is required for C5aR1 dimerization (205). Only in one of the solved structures with the extra-helical antagonist NDT9513727 (PDB ID 5O9H), C5aR1 has been observed in a non-crystallographic homodimeric organization, although this arrangement might not be physiologically relevant (154, 155); structural comparison with the homodimer of the smoothened (SMO) receptor (206) has lent support to the C5aR1 homodimer arrangement. Remarkably, the agonist activation of C5aR1 homodimers and phosphorylation of only a monomer can lead to the internalization of these dimers (205).

C5aR1 activity can also be modulated by antagonists and inverse agonists that bind to its orthosteric or allosteric site (154, 155). These allosteric modulators trap the receptor in the inactive state by stabilizing the network of hydrophobic interactions that maintain the receptor in the inactive state or by sterically hindering the helical rearrangements required for receptor activation. The structures of PMX53:C5aR1 (PDB ID 6C1Q, 6C1R) reveal how the cyclic peptide PMX53 sits in the orthosteric site, interacting with residues of the polar surface that interact with C5a and inserting the side chains of the d-cyclohexyl alanine ($dCha^{P4}$) and W^{P5} in the vicinity to the IWI region (155). In the allosteric site, NDT9513727 (PDB ID 6C1Q) and Avacopan (PDB ID 6C1R) establish interactions with the hydrophobic core of the transmembrane region, including the PIF motif (155).

Several C5aR1 agonists display ligand bias, i.e., differences in receptor signaling via G-protein signaling and β-arrestin recruitment (35, 207, 208). Ligand bias may depend on interactions between the agonist and ECL2 and between the ligand P6 and the IWI region, which are important for C5a-mediated β-arrestin recruitment. Interestingly, C5aR1 inhibitors display ligand bias effects: while PMX53 preferentially inhibits G-protein coupling over β-arrestin recruitment, Avacopan shows the opposite trend (35).

5.2 Complement receptor 5a 2

5.2.1 Structural features of C5aR2

The gene encoding human C5aR2 (*HsC5L2*) was cloned and sequenced many years after *HsC5aR1* (209), and what its specific functions may be is still an active research area. In particular, the structure of C5aR2 has not been elucidated experimentally. As C5aR1, C5aR2 belongs to the class A GPCR superfamily and therefore shares the overall structure of the model GPCR. Although the sequence identity and similarity with C5aR1 are relatively high (~36.4% and 57.1%, 128 identical and 73 similar residues), the difference is sufficiently extensive to make us cautious about extrapolating structural facts about C5aR1 onto C5aL2 without critical assessment.

The following putative and potential structural features have been recognized by sequence homology. Firstly, the seven transmembrane helical core that is a hallmark of all GPCR. Secondly, the N terminus contains an *N*-glycosylation site at N3 (143). Thirdly, the presence of a disulfide bond between $C107^{3.25}$-$C186^{ECL2}$. Fourthly, serine and threonine phosphorylation sites in the ICL3 and C terminus. And, finally, a remarkably shorter ICL3 compared with C5aR1 and other related GPCR.

As far as differences are concerned, C5aR2 lacks a canonical DRY/F motif at the end of TM3, which is substituted for by the sequence $D131^{3.49}$, $L132^{3.50}$, and $C133^{3.51}$, thereby resulting in the obligate uncoupling of C5aR2 from heterotrimeric G proteins (210). It also lacks an S/T-X-R/K phosphorylation site in ICL3. Finally, the NPXXY motif in TM7 lacks the tyrosine residue, which has been replaced by $F291^{7.53}$ (209, 211).

5.2.2 C5aR2 binds C5a and $C5a^{desArg}$

C5aR2 has two high-affinity ligands: C5a and $C5a^{desArg}$. Like C5aR1, C5aR2 exhibits a higher affinity for C5a over $C5a^{desArg}$. While the affinity for C5a is similar for C5aR1 and C5aR2, the affinity of C5aR2 for $C5a^{desArg}$ is one order of magnitude tighter than C5aR1 (210, 211). This, together with the slower dissociation rates of C5a from C5aR2 (210), has motivated the proposal that the primary physiological role of C5aR2 may be modulating the activation through C5aR1.

C5aR2 does not seem to share the exact binding mechanism for orthosteric ligands proposed for C5aR1. Indeed, C5a and $C5a^{desArg}$ display distinct binding modes to C5aR2. The C5aR2 N terminus plays crucial roles in $C5a^{desArg}$ binding, especially through the acidic and tyrosine residues and the tyrosine sulfation posttranslational modification (212).

Underscoring this differential recognition of C5a by C5aR1 and C5aR2, two partial agonists (P32 and P59) that are selective for C5aR2 over C5aR1/C3aR have been discovered (213). Conversely, the well-characterized C5aR1 antagonist PMX53 is perfectly selective toward C5aR1 and biased toward G_i signaling and does not bind C5aR2 (159).

Besides the two cognate ligands, there has been some controversy over the possibility that C3a, $C3a^{desArg}$ (ASP), and C4a could also bind to C5aR2 (211). Although enticing, this proposal has not been supported by recent data. None of the three proteins activates the receptor (211, 214); it seems none binds to it (210, 213).

5.2.3 C5aR2: a C5a receptor that recruits β-arrestin

There are striking differences between C5aR2 and C5aR1 concerning localization, phosphorylation, internalization, and regulation.

To begin with, C5aR2 is mainly localized inside the cell rather than in the plasma membrane and does not show a rapid internalization in response to C5a binding (210, 215). The internalization mechanism of C5aR2 appears to be different from that of C5aR1 and is only clathrin-dependent. In fact, internalized C5aR2 can also be constitutively recycled to the plasma membrane by a clathrin-dependent process (215). These processes suggest that C5aR2-bearing cells can uptake C5a and $C5a^{desArg}$ and either keep them intracellularly, target them for degradation, or release them back into the extracellular environment. Since C5aR2 exhibits a greater efficiency in ligand uptake and processing than C5aR1, C5aR2 can be posited as the main receptor involved in internalizing, retaining, and degrading C5a in natively expressing C5aR2 cells (215).

Regarding phosphorylation status, C5aR2 is phosphorylated to a lesser degree than C5aR1 in response to C5a binding (210). C5aR2 can recruit β-arrestin 1 and 2 in an agonist-dependent manner (187, 213, 214), a process involving phosphorylation sites introduced by GRKs 5-6 (187). Besides C5a-mediated recruitment, C5aR2 can also pre-couple both β-arrestins in the absence of agonist (187, 216). The direct interaction of C5aR2 with β-arrestin 1 has been shown by NS-EM (187). Interestingly, both β-arrestins exhibit different conformations bound to C5aR2 than those bound to C5aR1 (187). In contrast with C5aR1, C5aR2 showed a greater β-arrestin 2 recruitment stimulated by C5a/$C5a^{desArg}$ that was equally strong for the two anaphylatoxins (214, 216).

An intriguing aspect of C5a receptors is that C5aR2 can form heterodimers with C5aR1 constitutively and also in an agonist-dependent manner (159). It has been hypothesized that through heterodimerization, C5aR2 might regulate C5aR1 activity and cooperate functionally (159, 216).

C5aR2 does not signal through the heterotrimeric G proteins (187, 210), and grafting the C5aR1 motifs that engage with G proteins such as the DRY/F motif, ICL3, and the NPXXY motif does not complement C5aR2 (215). The inability of C5aR2 to couple with G proteins explains that C5aR2 plays a much smaller role in intracellular signaling than C5aR1 (210, 214).

Based on the lack of G-protein signaling, clearing of extracellular C5a/$C5a^{desArg}$, and β-arrestin recruitment and internalization properties, C5aR2 has been proposed to be a recycling decoy receptor (215). Although this is an attractive theory, C5aR2 still contributes to intracellular signaling processes in a variety of roles, including modulation of the phosphorylation state of several transducers (e.g., p90RSK and ERK1/2) and intracellular calcium mobilization (187, 217). Different functions attributed to C5aR2 consist in the modulation of other immunological receptors, like C5aR1, C3aR, chemokine-like receptor 1 (CMKLR1), or different pattern recognition receptors (PRRs) (217). Through these functions, C5aR2 is involved in regulating complex cellular responses, such as releasing cytokines from macrophages (213, 217).

5.3 Complement receptor 3a

5.3.1 Structure of C3aR

Like the other anaphylatoxin receptors, C3aR was classified as a GPCR when the encoding gene was cloned and its primary sequence determined (218, 219). Analysis of the primary sequence revealed a distinctive structural feature of C3aR: an unusually long ECL2 of about 172 amino acids, predicted to be highly flexible, with a disulfide bond formed between $C95^{3.25}$ and $C172^{ECL2}$. In contrast, its N terminus is shorter than that of C5aR1.

C3aR has several posttranslational modifications, including *N*- and *O*-glycosylations and tyrosine sulfations (220). $S266^{ECL2}$ is *O*-glycosylated (221), and $N9^{N\text{-}ter}$ and $N194^{ECL2}$ have been predicted to be *N*-glycosylated. Y174, Y184, Y188, Y317, and Y318 in the ECL2 can carry sulfations. The ICL3 and C terminus of C3aR contain serine and threonine residues that can be phosphorylated (197).

The cryoelectron microscopy structures of C3a-free (PDB ID 8HK3) and C3a-bound C3aR coupled to a G_i heterotrimeric protein (PDB ID 8HK2) (Figure 6A) have only recently become available, representing a striking leap ahead in the field (36). As suspected, the long ECL2 loop is highly flexible, and only the first 16 residues (V159-K175) were resolved, adopting a β-hairpin conformation.

5.3.2 C3a last five amino acids are critical for C3aR interaction

The cognate ligand of C3aR is the C3a anaphylatoxin, which binds with high affinity (~1 n*M*) (218, 219, 222). Compared to C5aR1, C3aR does not bind $C3a^{desArg}$ (223). C3a recognition by C3aR has been proposed to follow a mechanism like that of C5aR1 with some differences. Like C5aR1, a two binding site model has been proposed (36, 222).

The primary or effector binding site (orthosteric site) consists of an interhelical amphipathic pocket found in the extracellular region of the receptor and formed by residues from TM3, TM5-7, and ECL2 (Figure 6A). The orthosteric site of C3aR is smaller than that of C5aR1, and it can only accommodate the last five residues of C3a (P1-P5). The C-terminal end of C3a inside the binding site adopts a hook-shaped conformation enabling multiple interactions with the amino acids in the cavity, including ionic and hydrophobic

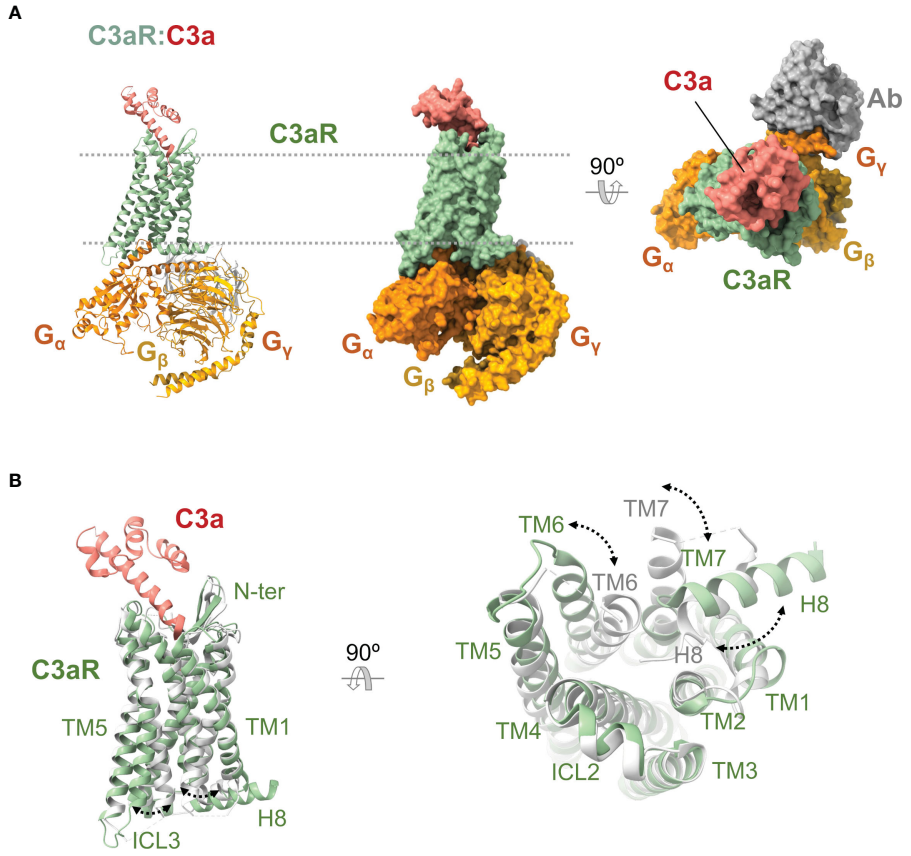

FIGURE 6
Anaphylatoxin receptor C3aR in complex with C3a and conformational changes underlying activation. **(A)** Cryoelectron microscopy structure of C3aR:C3a bound to heterotrimeric G protein comprising the Gα, Gβ, and Gγ subunits (shown in orange, yellow, and gold), and a stabilizing antibody (shown in gray) (PDB ID 8HZ2). C3aR is shown in green, and C3a in red. The same view is shown of the cartoon and molecular surface representations of the complex. We show a 90° rotated view of the complex on the right in molecular surface representation. **(B)** Superposition of the active conformation of the C3aR:C3a complex (PDB ID 8HZ2) (C3aR in green, C3a in red) and an inactive reference structure (PDB ID 6C1Q) (C5aR1 in grey; the antagonist PMX53 is not shown for clarity). Side (left) and bottom (right) views are shown. Conformational changes are indicated by dashed lines between and labeling of structural elements that occupy distinct positions in the active *versus* inactive conformations.

interactions and hydrogen bonds. Remarkably, R77 of C3a establishes some of the critical interactions, which include a salt bridge with $D417^{7.35}$, a cation-π interaction with $Y393^{6.51,}$ and two hydrogen bonds with $Y174^{ECL2}$ and $R340^{5.42}$ (36).

The secondary binding site encompasses residues from the outermost segments of ECL2 and ECL3 that still make contact with the α_4 helix of C3a. Even though this secondary binding site plays a less important role in engaging C3a, some functionally relevant contacts have been found in this region, e.g., the salt bridge between C3aR $D404^{ECL3}$ and C3a R65 (36).

While the C3aR N terminus has shown little implication in C3a binding (36, 222, 224), its ECL2 plays an important role in the anaphylatoxin coupling. Site-directed mutagenesis studies have established that aspartic acid residues along the N-terminal and C-terminal ends of ECL2 (D183, D186, D325, D326, and D327) and sulfation of Y174 are required for high-affinity binding of C3a (36, 220, 222). Besides mediating C3a binding, the ECL2 appears vital for arranging the helical bundle functionally (224).

The selectivity toward their cognate anaphylatoxin ligands of C3aR and C5aR1 is in part due to the amino acid composition of the C terminal tails; in particular, C3a G74 seems to be essential for C3aR selectivity (36). Furthermore, the N terminus of these receptors also has shown a significant contribution to this selectivity, so the amino terminus of C3aR appears to hinder C5a binding (224). This is in accordance with the composition and implication of these N termini in the anaphylatoxin binding.

5.3.3 Activation of C3aR

Once liganded, C3aR can couple and signal by different heterotrimeric G proteins with α subunits from the $G_{i/o}$ and G_q families (164). C3aR recognizes residues in the β_2-β_3 loop, β_6 strand, and α_5 helix of the $G\alpha_i$ subunit through residues from TM3-6, ICL2, and ICL3. The coupling to the heterotrimeric G_i to C3aR is similar to C5aR1, although the α_5 helix of the $G\alpha_i$ subunit is inserted more deeply, TM6 is displaced by ~1.5 Å, and the ICL3 displays a distinct topology and broader interaction with $G\alpha_i$ (36) (Figure 6B).

C3a stimulation leads to C3aR phosphorylation on Ser and Thr residues in a dose-dependent manner by GRKs 2/3/5/6 and PKC

(197). Removal of the C3a stimulus is followed by C3aR dephosphorylation. GRKs have shown different functions over C3aR signaling in mast cells. While GRK2/3 are involved in agonist-induced desensitization, GRK5/6 are implicated in cell degranulation (225). Phosphorylation at $Ser459^{C\text{-}ter}$, $Thr463^{C\text{-}ter}$, $Ser465^{C\text{-}ter}$, $Thr466^{C\text{-}ter}$, and $Ser470^{C\text{-}ter}$ is involved in β-arrestin 2 recruitment at C3aR and receptor desensitization in mast cells (226). $Thr463^{C\text{-}ter}$, $Ser465^{C\text{-}ter}$, $Thr466^{C\text{-}ter}$, and $Ser470^{C\text{-}ter}$ have important roles in C3aR internalization, which occurs in an agonist-dependent manner (227). Agonist-induced phosphorylation of C3aR performs an important role in signal transduction from the receptor. In C3a-stimulated mast cells, phosphorylation is required for CCL2 production, but these modifications seem to attenuate a degranulation response (228).

C3aR activity can be modulated by β-arrestins 1 and 2. β-arrestins can inhibit C3a-induced ERK1/2 phosphorylation and perform other regulatory activities. For example, in mast cells, β-arrestin 2 is involved in C3aR desensitization, internalization, and inhibition of the C3a-induced NF-kB activation and CCL4 generation; β-arrestin 1 contributes mainly to cell degranulation (229).

6 Concluding remarks

The progressive recognition of the complement system as a driver of inflammatory and autoimmune diseases (11, 27, 28, 30, 31) has incentivized the functional and structural study of the complement system and, in particular, of the complement receptors, their ligands, and their complexes.

Work over many years has established the existence of at least four structurally distinct classes of complement receptors: the CCP/SCR mosaic receptors CR1 and CR2 (along with the negative regulators MCP and DAF), the Ig superfamily receptor CRIg, the β_2 (CD18) integrin receptors CR3 and CR4, and the anaphylatoxin GPCR receptors C5aR1, C5aR2, and C3aR. This diversity likely reflects the enormous span of evolutionary time over which cellular immunity has coevolved with the complement system (230–232).

Although the diversity of functions carried out by the complement system and immune cells defies classification, specific unifying themes can be recognized.

Firstly, CCP/SCR mosaic receptors (CR1 and CR2) are long and flexible molecules that can survey considerable distances both in the plane of the membrane and above it to find their main ligands: C3b/C4b and C3 and C5 convertases (CR1) and C3d and iC3b (CR2). CR1 downregulates complement activation through the well-known decay-accelerating and cofactor activities, also exerted by the negative regulators MCP and DAF (membrane-bound) and FH and C4BP (fluid phase). In contrast, CR2 lacks complement regulatory activities but it has a more specialized role in bridging innate immunity with adaptive immunity by handing over complement-opsonized pathogens from macrophages to antigen-presenting cells in the spleen and other lymphoid organs.

Secondly, CRIg recognizes C3b (and iC3b) but does it with a structurally unrelated fold (Ig-like) and targets the β-chain of the proteolytically activated C3 fragments. Its unique binding mode is used by the tissue-resident macrophages that express it (mostly, Kupffer cells in the liver) to snatch complement-opsonized pathogens and cellular debris and facilitate their clearance by phagocytosis.

Thirdly, the β_2 integrin receptors CR3 and CR4 have played an important role in establishing the structural basis for activation (e.g., the transition from a bent, closed, inactive conformation to an extended, open, active state) and ligand recognition by integrin receptors. Besides binding to iC3b (and to C3d in the case of CR3), these receptors have remarkable ligand promiscuity, employing a small but versatile domain (the αI domain) to recognize them. Their study has highlighted the degree to which surface concentration effects (the so-called 2D concentration, through avidity, compartmentalization, and clustering) and diversity in the structural presentation of ligands can influence the outcome of their interaction.

Fourthly, the anaphylatoxin GPCR receptors have aroused considerable interest as C5a and C3a have been associated with inflammatory diseases, and agonists/antagonists are available. Although the first structures of C5aR1 were obtained by X-ray crystallography, cryoelectron microscopy has allowed the determination of high-resolution structures of C5aR1:C5a and C3aR:C3a complexes within a short time. This acceleration promises a revolution in the structural understanding of anaphylatoxin receptors, how anaphylatoxins are recognized, and how binding triggers receptor activation and signal transduction. The detailed structural knowledge of receptor:anaphylatoxin complexes will also allow better agonists and antagonists to be engineered and validated as therapeutics.

The applications of the structural inquiry of the complement receptors and their ligands are important. Knowledge about the structural organization of the receptors and the ligand complexes advances a fundamental understanding of the immune system. It often results in unexpected and fascinating results, like the proposal that CR2 can hand over iC3b/C3d-opsonized surfaces from macrophages to antigen-presenting cells to stimulate (prime) adaptive immunity. More pragmatically, the structures of ligand complexes often make it possible to elucidate the mechanism of action of known (or suspected) receptor agonists and antagonists, with implications for developing more efficient treatments. It also paves the way for the rational or semi-rational discovery of new agonists and antagonists, increasing their utility, selectivity, and safety. For example, discovering new allosteric inhibitors/antagonists of the anaphylatoxin receptors could result in new treatments.

What are the challenges for the future regarding the structural biology of complement receptors?

The structural catalog of complement receptors is still incomplete. Although state-of-the-art protein structure prediction methods like AlphaFold (233) are filling in the gaps with enticing structural hypotheses (e.g., the C2-type domain of CRIg), it is important to elucidate the structures of receptors, ligands, ligand complexes, and complexes involving them and other immune system components and the host-pathogen machinery. In connection with this central endeavor, developing new methods

for protein production and the characterization of protein-protein and protein-ligand complexes will continue to play a significant role as enabling technologies (234, 235).

Much remains to be elucidated regarding structural diversity and modularity, especially in 2D surfaces, highly concentrated clusters of receptors and ligands, and cell-cell interactions. The role of cryoelectron microscopy in advancing the field of structural biology of transmembrane receptors cannot be denied, and the trend is likely to strengthen further (236). A goal for the future should be to integrate cellular structural biology approaches (237) to gain insights into how complement receptors (and complement regulators, membrane-bound or otherwise) function in the physiological and pathological context.

As extracellular pathogens have evolved a seemingly endless repertoire of complement-evasive factors (238, 239), intracellular pathogens have evolved molecular mechanisms to hijack all the non-GPCR complement receptors, MCP, and DAF to gain entry to the cell (240, 241). Strategies aimed at restricting pathogen entry into their host cells targeting the virulence factors or their cognate complement receptors would greatly benefit from a complete understanding of the structural determinants of the interaction.

Finally, these advances should also result in a more subtle and precise appreciation of the differences between the various animal models in use in the field of complement. Applying structural methods and tools to the complement factors and complement receptors of mice, rats, and other animal models beside humans will allow a more informed understanding of the differences in the complement biology between these animals, with important implications for developing disease models and therapies.

Author contributions

FJF and MCV conceived the study. JS-L wrote the first draft of the sections on anaphylatoxin receptors. KdlP wrote the first draft of the sections on complement integrin receptors. FJF and MCV wrote the sections on CR1, CR2, and CRIg with support from KdlP. FJF and MCV wrote the final version of the manuscript. All authors contributed to manuscript revision, read, and approved the submitted version.

Funding

This work was funded by Grants PDC2022-133713-I00 of the Spanish Ministerio de Ciencia e Innovación-Recovery, Transformation and Resilience Plan (PRTR), S2022/BMD-7278 of the Regional Government of Madrid, and the European Commission – NextGenerationEU through CSIC's Global Health Platform ("PTI Salud Global") (SGL2103020) (to MCV), and the CSIC Special Intramural Grant PIE-201620E064 (to MCV). It was additionally supported by the Network of Excellence Complement in Health and Disease (RED2022-134750-T). KdlP was supported by the Industrial Ph.D. Doctorate (DIN2018-010094) of the Spanish Ministry of Economy and Innovation.

Acknowledgments

JS-L acknowledges the support of the Ph.D. program in Molecular Biosciences of the Universidad Autónoma de Madrid (UAM) and the Ministry of Education, Culture and Sports of Spain (FPU Grant 17/06090). KdlP acknowledges the Ph.D. program in Biochemistry, Molecular Biology, and Biomedicine of the Universidad Complutense de Madrid (UCM).

Conflict of interest

Abvance Biotech SL provided salaries for KdlP and FJF.

The remaining authors declare that the research was conducted in the absence of any commercial or financial relationships that could be construed as a potential conflict of interest.

Publisher's note

References

1. Brown EJ. Complement receptors and phagocytosis. *Curr Opin Immunol* (1991) 3:76–82. doi: 10.1016/0952-7915(91)90081-B

2. Erdei A, Kovács KG, Nagy-Baló Z, Lukácsi S, Mácsik-Valent B, Kurucz I, et al. New aspects in the regulation of human B cell functions by complement receptors CR1, CR2, CR3 and CR4. *Immunol Lett* (2021) 237:42–57. doi: 10.1016/j.imlet.2021.06.006

3. Lamers C, Plüss CJ, Ricklin D. The promiscuous profile of complement receptor 3 in ligand binding, immune modulation, and pathophysiology. *Front Immunol* (2021) 12:662164. doi: 10.3389/fimmu.2021.662164

4. Vandendriessche S, Cambier S, Proost P, Marques PE. Complement receptors and their role in leukocyte recruitment and phagocytosis. *Front Cell Dev Biol* (2021) 9:624025. doi: 10.3389/fcell.2021.624025

5. Zarantonello A, Revel M, Grunenwald A, Roumenina LT. C3-dependent effector functions of complement. *Immunol Rev* (2023) 313:120–38. doi: 10.1111/imr.13147

6. Ghebrehiwet B, Geisbrecht BV, Xu X, Savitt AG, Peerschke EIB. The C1q Receptors: Focus on gC1qR/p33 (C1qBP, p32, HABP-1). *Semin Immunol* (2019) 45:101338. doi: 10.1016/j.smim.2019.101338

7. Vorup-Jensen T, Jensen RK. Structural immunology of complement receptors 3 and 4. *Front Immunol* (2018) 9:2716. doi: 10.3389/fimmu.2018.02716

8. Van Lookeren Campagne M, Verschoor A. Pathogen clearance and immune adherence "revisited": Immuno-regulatory roles for CRIg. *Semin Immunol* (2018) 37:4–11. doi: 10.1016/j.smim.2018.02.007

9. Marin AV, Cárdenas PP, Jiménez-Reinoso A, Muñoz-Ruiz M, Regueiro JR. Lymphocyte integration of complement cues. *Semin Cell Dev Biol* (2019) 85:132–42. doi: 10.1016/j.semcdb.2018.02.005

10. Dustin ML. Complement receptors in myeloid cell adhesion and phagocytosis. *Microbiol Spectr* (2016) 4:4.6.04. doi: 10.1128/microbiolspec.MCHD-0034-2016

11. Holers VM. Complement and its receptors: new insights into human disease. *Annu Rev Immunol* (2014) 32:433–59. doi: 10.1146/annurev-immunol-032713-120154

12. Kemper C, Köhl J. Novel roles for complement receptors in T cell regulation and beyond. *Mol Immunol* (2013) 56:181–90. doi: 10.1016/j.molimm.2013.05.223

13. Erdei A, Isaák A, Török K, Sándor N, Kremlitzka M, Prechl J, et al. Expression and role of CR1 and CR2 on B and T lymphocytes under physiological and autoimmune conditions. *Mol Immunol* (2009) 46:2767–73. doi: 10.1016/j.molimm.2009.05.181

14. Roozendaal R, Carroll MC. Complement receptors CD21 and CD35 in humoral immunity. *Immunol Rev* (2007) 219:157–66. doi: 10.1111/j.1600-065X.2007.00556.x

15. Van Lookeren Campagne M, Wiesmann C, Brown EJ. Macrophage complement receptors and pathogen clearance. *Cell Microbiol* (2007) 9:2095–102. doi: 10.1111/j.1462-5822.2007.00981.x

16. Villiers CL, Perrin-Cocon L, Marche PN, Villiers M-B. Complement receptors and B lymphocytes. *Crit Rev Immunol* (2004) 24:14. doi: 10.1615/CritRevImmunol.v24.i6.50

17. Carroll MC. The role of complement and complement receptors in induction and regulation of immunity. *Annu Rev Immunol* (1998) 16:545–68. doi: 10.1146/annurev.immunol.16.1.545

18. Ember JA, Hugli TE. Complement factors and their receptors. *Immunopharmacology* (1997) 38:3–15. doi: 10.1016/S0162-3109(97)00088-X

19. Krych M, Atkinson JP, Michael Holers V. Complement receptors. *Curr Opin Immunol* (1992) 4:8–13. doi: 10.1016/0952-7915(92)90116-V

20. Soares DC, Barlow PN. Complement control protein modules in the regulators of complement activation. In: *Structural biology of the complement system*. Boca Raton, FL CRC Press (2005).

21. Arbore G, West EE, Spolski R, Robertson AAB, Klos A, Rheinheimer C, et al. T helper 1 immunity requires complement-driven NLRP3 inflammasome activity in $CD4^+$ T cells. *Science* (2016) 352:aad1210. doi: 10.1126/science.aad1210

22. Arbore G, West EE, Rahman J, Le Friec G, Niyonzima N, Pirooznia M, et al. Complement receptor CD46 co-stimulates optimal human CD8+ T cell effector function via fatty acid metabolism. *Nat Commun* (2018) 9:4186. doi: 10.1038/s41467-018-06706-z

23. Norsworthy PJ, Fossati-Jimack L, Cortes-Hernandez J, Taylor PR, Bygrave AE, Thompson RD, et al. Murine CD93 (C1qRp) contributes to the removal of apoptotic cells *in vivo* but is not required for C1q-mediated enhancement of phagocytosis. *J Immunol* (2004) 172:3406–14. doi: 10.4049/jimmunol.172.6.3406

24. McGreal EP, Ikewaki N, Akatsu H, Morgan BP, Gasque P. Human C1qRp is identical with CD93 and the mNI-11 antigen but does not bind C1q. *J Immunol* (2002) 168:5222–32. doi: 10.4049/jimmunol.168.10.5222

25. Ghebrehiwet B. cC1q-R (calreticulin) and gC1q-R/p33: ubiquitously expressed multi-ligand binding cellular proteins involved in inflammation and infection. *Mol Immunol* (2004) 41:173–83. doi: 10.1016/j.molimm.2004.03.014

26. Kemper C, Ferreira VP, Paz JT, Holers VM, Lionakis MS, Alexander JJ. Complement: the road less traveled. *J Immunol* (2023) 210:119–25. doi: 10.4049/jimmunol.2200540

27. Zelek WM, Xie L, Morgan BP, Harris CL. Compendium of current complement therapeutics. *Mol Immunol* (2019) 114:341–52. doi: 10.1016/j.molimm.2019.07.030

28. Holers VM. Complement therapeutics are coming of age in rheumatology. *Nat Rev Rheumatol* (2023) 19:470–85. doi: 10.1038/s41584-023-00981-x

29. Lamers C, Ricklin D, Lambris JD. Complement-targeted therapeutics: An emerging field enabled by academic drug discovery. *Am J Hematol* (2023) 98, S29, S76-7. doi: 10.1002/ajh.26875

30. Ricklin D, Lambris JD. New milestones ahead in complement-targeted therapy. *Semin Immunol* (2016) 28:208–22. doi: 10.1016/j.smim.2016.06.001

31. Ricklin D, Lambris JD. Complement-targeted therapeutics. *Nat Biotechnol* (2007) 25:1265–75. doi: 10.1038/nbt1342

32. Jensen RK, Bajic G, Sen M, Springer TA, Vorup-Jensen T, Andersen GR. Complement receptor 3 forms a compact high-affinity complex with iC3b. *J Immunol* (2021) 206:3032–42. doi: 10.4049/jimmunol.2001208

33. Jensen RK, Pedersen H, Lorentzen J, Laursen NS, Vorup-Jensen T, Andersen GR. Structural insights into the function-modulating effects of nanobody binding to the integrin receptor αMβ2. *J Biol Chem* (2022) 298:102168. doi: 10.1016/j.jbc.2022.102168

34. Fernández FJ, Santos-López J, Martínez-Barricarte R, Querol-García J, Martín-Merinero H, Navas-Yuste S, et al. The crystal structure of iC3b-CR3 alphaI reveals a modular recognition of the main opsonin iC3b by the CR3 integrin receptor. *Nat Commun* (2022) 13:1955. doi: 10.1038/s41467-022-29580-2

35. Feng Y, Zhao C, Deng Y, Wang H, Ma L, Liu S, et al. Mechanism of activation and biased signaling in complement receptor C5aR1. *Cell Res* (2023) 33:312–24. doi: 10.1038/s41422-023-00779-2

36. Wang Y, Liu W, Xu Y, He X, Yuan Q, Luo P, et al. Revealing the signaling of complement receptors C3aR and C5aR1 by anaphylatoxins. *Nat Chem Biol* (2023). doi: 10.1038/s41589-023-01339-w

37. West EE, Kemper C. Complosome — the intracellular complement system. *Nat Rev Nephrol* (2023) 19:426–39. doi: 10.1038/s41581-023-00704-1

38. Barlow PN, Baron M, Norman DG, Day AJ, Willis AC, Sim RB, et al. Secondary structure of the complement control protein module by two-dimensional proton NMR. *Biochemistry* (1991) 30:997–1004. doi: 10.1021/bi00218a016

39. Almitairi JOM, Venkatraman Girija U, Furze CM, Simpson-Gray X, Badakshi F, Marshall JE, et al. Structure of the C1r–C1s interaction of the C1 complex of complement activation. *Proc Natl Acad Sci* (2018) 115:768–73. doi: 10.1073/pnas.1718709115

40. Saunders RE, Abarrategui-Garrido C, Frémeaux-Bacchi V, Goicoechea de Jorge E, Goodship THJ, López Trascasa M, et al. The interactive Factor H-atypical hemolytic uremic syndrome mutation database and website: update and integration of membrane cofactor protein and Factor I mutations with structural models. *Hum Mutat* (2007) 28:222–34. doi: 10.1002/humu.20435

41. Perkins SJ, Gilbert HE, Aslam M, Hannan J, Holers VM, Goodship THJ. Solution structures of complement components by X-ray and neutron scattering and analytical ultracentrifugation. *Biochem Soc Trans* (2002) 30:996–1001. doi: 10.1042/bst0300996

42. Soares DC, Gerloff DL, Syme NR, Coulson AFW, Parkinson J, Barlow PN. Large-scale modelling as a route to multiple surface comparisons of the CCP module family. *Protein Eng Des Sel* (2005) 18:379–88. doi: 10.1093/protein/gzi039

43. Klickstein LB, Barbashov SF, Liu T, Jack RM, Nicholson-Weller A. Complement receptor type 1 (CR1, CD35) is a receptor for C1q. *Immunity* (1997) 7:345–55. doi: 10.1016/s1074-7613(00)80356-8

44. GhIran I, Barbashov SF, Klickstein LB, Tas SW, Jensenius JC, Nicholson-Weller A. Complement receptor 1/cd35 is a receptor for mannan-binding lectin. *J Exp Med* (2000) 192:1797–808. doi: 10.1084/jem.192.12.1797

45. Nelson RA. The immune-adherence phenomenon: an immunologically specific reaction between microorganisms and erythrocytes leading to enhanced phagocytosis. *Science* (1953) 118:733–7. doi: 10.1126/science.118.3077.733

46. Krych-Goldberg M, Atkinson JP. Structure-function relationships of complement receptor type 1: Active sites of CR1. *Immunol Rev* (2001) 180:112–22. doi: 10.1034/j.1600-065X.2001.1800110.x

47. Khera R, Das N. Complement Receptor 1: Disease associations and therapeutic implications. *Mol Immunol* (2009) 46:761–72. doi: 10.1016/j.molimm.2008.09.026

48. Kremlitzka M, Polgár A, Fülöp L, Kiss E, Poór G, Erdei A. Complement receptor type 1 (CR1, CD35) is a potent inhibitor of B-cell functions in rheumatoid arthritis patients. *Int Immunol* (2013) 25:25–33. doi: 10.1093/intimm/dxs090

49. Weisman HF, Bartow T, Leppo MK, Marsh HC, Carson GR, Concino MF, et al. Soluble human complement receptor type 1: *in vivo* inhibitor of complement suppressing post-ischemic myocardial inflammation and necrosis. *Science* (1990) 249:146–51. doi: 10.1126/science.2371562

50. Aslam M, Perkins SJ. Folded-back solution structure of monomeric factor H of human complement by synchrotron X-ray and neutron scattering, analytical ultracentrifugation and constrained molecular modelling. *J Mol Biol* (2001) 309:1117–38. doi: 10.1006/jmbi.2001.4720

51. Li K, Okemefuna AI, Gor J, Hannan JP, Asokan R, Holers VM, et al. Solution structure of the complex formed between human complement C3d and full-length complement receptor type 2. *J Mol Biol* (2008) 384:137–50. doi: 10.1016/j.jmb.2008.08.084

52. Furtado PB, Huang CY, Ihyembe D, Hammond RA, Marsh HC, Perkins SJ. The partly folded back solution structure arrangement of the 30 SCR domains in human complement receptor type 1 (CR1) permits access to its C3b and C4b ligands. *J Mol Biol* (2008) 375:102–18. doi: 10.1016/j.jmb.2007.09.085

53. Smith BO, Mallin RL, Krych-Goldberg M, Wang X, Hauhart RE, Bromek K, et al. Structure of the C3b binding site of CR1 (CD35), the immune adherence receptor. *Cell* (2002) 108:769–80. doi: 10.1016/s0092-8674(02)00672-4

54. O'Leary JM, Bromek K, Black GM, Uhrinova S, Schmitz C, Wang X, et al. Backbone dynamics of complement control protein (CCP) modules reveals mobility in binding surfaces. *Protein Sci* (2004) 13:1238–50. doi: 10.1110/ps.03582704

55. Park HJ, Guariento M, Maciejewski M, Hauhart R, Tham W-H, Cowman AF, et al. Using mutagenesis and structural biology to map the binding site for the plasmodium falciparum merozoite protein pfRh4 on the human immune adherence receptor. *J Biol Chem* (2014) 289:450–63. doi: 10.1074/jbc.M113.520346

56. Takata Y, Kinoshita T, Kozono H, Takeda J, Tanaka E, Hong K, et al. Covalent association of C3b with C4b within C5 convertase of the classical complement pathway. *J Exp Med* (1987) 165:1494–507. doi: 10.1084/jem.165.6.1494

57. Kinoshita T, Takata Y, Kozono H, Takeda J, Hong KS, Inoue K. C5 convertase of the alternative complement pathway: covalent linkage between two C3b molecules within the trimolecular complex enzyme. *J Immunol Baltim Md 1950* (1988) 141:3895–901. doi: 10.4049/jimmunol.141.11.3895

58. Krych-Goldberg M, Hauhart RE, Subramanian VB, Yurcisin BM, Crimmins DL, Hourcade DE, et al. Decay accelerating activity of complement receptor type 1 (CD35). *J Biol Chem* (1999) 274:31160–8. doi: 10.1074/jbc.274.44.31160

59. Forneris F, Wu J, Xue X, Ricklin D, Lin Z, Sfyroera G, et al. Regulators of complement activity mediate inhibitory mechanisms through a common C3b-binding mode. *EMBO J* (2016) 35:1133–49. doi: 10.15252/embj.201593673

60. Wu J, Wu Y-Q, Ricklin D, Janssen BJC, Lambris JD, Gros P. Structure of complement fragment C3b–factor H and implications for host protection by complement regulators. *Nat Immunol* (2009) 10:728–33. doi: 10.1038/ni.1755

61. Oliveira LC, Kretzschmar GC, Dos Santos ACM, Camargo CM, Nisihara RM, Farias TDJ, et al. Complement receptor 1 (CR1, CD35) polymorphisms and soluble CR1: A proposed anti-inflammatory role to quench the fire of "Fogo selvagem" Pemphigus foliaceus. *Front Immunol* (2019) 10:2585. doi: 10.3389/fimmu.2019.02585

62. Krych-Goldberg M, Moulds JM, Atkinson JP. Human complement receptor type 1 (CR1) binds to a major malarial adhesin. *Trends Mol Med* (2002) 8:531–7. doi: 10.1016/S1471-4914(02)02419-X

63. Tham W-H, Wilson DW, Lopaticki S, Schmidt CQ, Tetteh-Quarcoo PB, Barlow PN, et al. Complement receptor 1 is the host erythrocyte receptor for *Plasmodium falciparum* PfRh4 invasion ligand. *Proc Natl Acad Sci* (2010) 107:17327–32. doi: 10.1073/pnas.1008151107

64. Reiling L, Richards JS, Fowkes FJI, Wilson DW, Chokejindachai W, Barry AE, et al. The Plasmodium falciparum Erythrocyte Invasion Ligand Pfrh4 as a Target of Functional and Protective Human Antibodies against Malaria. *PloS One* (2012) 7: e45253. doi: 10.1371/journal.pone.0045253

65. Prajapati SK, Borlon C, Rovira-Vallbona E, Gruszczyk J, Menant S, Tham W-H, et al. Complement Receptor 1 availability on red blood cell surface modulates Plasmodium vivax invasion of human reticulocytes. *Sci Rep* (2019) 9:8943. doi: 10.1038/s41598-019-45228-6

66. Jensen AR, Adams Y, Hviid L. Cerebral Plasmodium falciparum malaria: The role of PfEMP1 in its pathogenesis and immunity, and PfEMP1-based vaccines to prevent it. *Immunol Rev* (2020) 293:230–52. doi: 10.1111/imr.12807

67. Prodinger WM. Complement receptor type two (CR2,CR21): A target for influencing the humoral immune response and antigen-trapping. *Immunol Res* (1999) 20:187–94. doi: 10.1007/BF02790402

68. Lowell CA, Klickstein LB, Carter RH, Mitchell JA, Fearon DT, Ahearn JM. Mapping of the Epstein-Barr virus and C3dg binding sites to a common domain on complement receptor type 2. *J Exp Med* (1989) 170:1931–46. doi: 10.1084/jem.170.6.1931

69. Carel JC, Myones BL, Frazier B, Holers VM. Structural requirements for C3d,g/Epstein-Barr virus receptor (CR2/CD21) ligand binding, internalization, and viral infection. *J Biol Chem* (1990) 265:12293–9. doi: 10.1016/S0021-9258(19)38344-9

70. Delcayre AX, Salas F, Mathur S, Kovats K, Lotz M, Lernhardt W. Epstein Barr virus/complement C3d receptor is an interferon alpha receptor. *EMBO J* (1991) 10:919–26. doi: 10.1002/j.1460-2075.1991.tb08025.x

71. Asokan R, Hua J, Young KA, Gould HJ, Hannan JP, Kraus DM, et al. Characterization of human complement receptor type 2 (CR2/CD21) as a receptor for IFN-α: A potential role in systemic lupus erythematosus. *J Immunol* (2006) 177:383–94. doi: 10.4049/jimmunol.177.1.383

72. Aubry J-P, Pochon S, Graber P, Jansen KU, Bonnefoy J-Y. CD21 is a ligand for CD23 and regulates IgE production. *Nature* (1992) 358:505–7. doi: 10.1038/358505a0

73. Fingeroth JD, Weis JJ, Tedder TF, Strominger JL, Biro PA, Fearon DT. Epstein-Barr virus receptor of human B lymphocytes is the C3d receptor CR2. *Proc Natl Acad Sci* (1984) 81:4510–4. doi: 10.1073/pnas.81.14.4510

74. Nemerow GR, Wolfert R, McNaughton ME, Cooper NR. Identification and characterization of the Epstein-Barr virus receptor on human B lymphocytes and its relationship to the C3d complement receptor (CR2). *J Virol* (1985) 55:347–51. doi: 10.1128/jvi.55.2.347-351.1985

75. Moore MD, DiScipio RG, Cooper NR, Nemerow GR. Hydrodynamic, electron microscopic, and ligand-binding analysis of the epstein-barr virus/C3dg receptor (CR2). *J Biol Chem* (1989) 264:20576–82. doi: 10.1016/S0021-9258(19)47101-9

76. Gilbert HE, Asokan R, Holers VM, Perkins SJ. The 15 SCR flexible extracellular domains of human complement receptor type 2 can mediate multiple ligand and antigen interactions. *J Mol Biol* (2006) 362:1132–47. doi: 10.1016/j.jmb.2006.08.012

77. Prota AE, Sage DR, Stehle T, Fingeroth JD. The crystal structure of human CD21: Implications for Epstein–Barr virus and C3d binding. *Proc Natl Acad Sci* (2002) 99:10641–6. doi: 10.1073/pnas.162360499

78. Guthridge JM, Rakstang JK, Young KA, Hinshelwood J, Aslam M, Robertson A, et al. Structural studies in solution of the recombinant N-terminal pair of short consensus/complement repeat domains of complement receptor type 2 (CR2/CD21) and interactions with its ligand C3dg. *Biochemistry* (2001) 40:5931–41. doi: 10.1021/bi0101749

79. Gilbert HE, Eaton JT, Hannan JP, Holers VM, Perkins SJ. Solution structure of the complex between CR2 SCR 1-2 and C3d of human complement: an X-ray scattering and sedimentation modelling study. *J Mol Biol* (2005) 346:859–73. doi: 10.1016/j.jmb.2004.12.006

80. Gilbert HE, Aslam M, Guthridge JM, Holers VM, Perkins SJ. Extended flexible linker structures in the complement chimaeric conjugate CR2-ig by scattering, analytical ultracentrifugation and constrained modelling: implications for function and therapy. *J Mol Biol* (2006) 356:397–412. doi: 10.1016/j.jmb.2005.11.050

81. Szakonyi G, Guthridge JM, Li D, Young K, Holers VM, Chen XS. Structure of complement receptor 2 in complex with its C3d ligand. *Science* (2001) 292:1725–8. doi: 10.1126/science.1059118

82. Hannan JP, Young KA, Guthridge JM, Asokan R, Szakonyi G, Chen XS, et al. Mutational analysis of the complement receptor type 2 (CR2/CD21)–C3d interaction reveals a putative charged SCR1 binding site for C3d. *J Mol Biol* (2005) 346:845–58. doi: 10.1016/j.jmb.2004.12.007

83. Van Den Elsen JMH, Isenman DE. A crystal structure of the complex between human complement receptor 2 and its ligand C3d. *Science* (2011) 332:608–11. doi: 10.1126/science.1201954

84. Montefiori DC, Stewart K, Ahearn JM, Zhou J, Zhou J. Complement-mediated binding of naturally glycosylated and glycosylation-modified human immunodeficiency virus type 1 to human CR2 (CD21). *J Virol* (1993) 67:2699–706. doi: 10.1128/jvi.67.5.2699-2706.1993

85. Montefiori DC, Zhou J, Shaff DI. CD4-independent binding of HIV-1 to the B lymphocyte receptor CR2 (CD21) in the presence of complement and antibody. *Clin Exp Immunol* (2008) 90:383–9. doi: 10.1111/j.1365-2249.1992.tb05855.x

86. Stano P, Williams V, Villani M, Cymbalyuk ES, Qureshi A, Huang Y, et al. App1: an antiphagocytic protein that binds to complement receptors 3 and 2. *J Immunol* (2009) 182:84–91. doi: 10.4049/jimmunol.182.1.84

87. Medof ME, Iida K, Mold C, Nussenzweig V. Unique role of the complement receptor CR1 in the degradation of C3b associated with immune complexes. *J Exp Med* (1982) 156:1739–54. doi: 10.1084/jem.156.6.1739

88. Bajtay Z. Biologia Futura: stories about the functions of β2-integrins in human phagocytes. *Biol Futura* (2021) 72:7–13. doi: 10.1007/s42977-020-00063-z

89. Hynes RO. Integrins. *Cell* (2002) 110:673–87. doi: 10.1016/S0092-8674(02)00971-6

90. Springer TA. Adhesion receptors of the immune system. *Nature* (1990) 346:425–34. doi: 10.1038/346425a0

91. Kishimoto TK, Larson RS, Corbi AL, Dustin ML, Staunton DE, Springer TA. The leukocyte Integrins. In: *Advances in Immunology*:Academic Press, New York. Elsevier (1989). p. 149–82. doi: 10.1016/S0065-2776(08)60653-7

92. Ley K, Laudanna C, Cybulsky MI, Nourshargh S. Getting to the site of inflammation: the leukocyte adhesion cascade updated. *Nat Rev Immunol* (2007) 7:678–89. doi: 10.1038/nri2156

93. Rosen H, Law SKA. The Leukocyte Cell Surface Receptor(s) for the iC3b Product of Complement. In: Lambris JD, editor. *The Third Component of Complement. Current Topics in Microbiology and Immunology*. Berlin, Heidelberg: Springer Berlin Heidelberg (1990). p. 99–122. doi: 10.1007/978-3-642-74977-3_6

94. Ross GD, Větvička V. CR3 (CD11b, CD18): a phagocyte and NK cell membrane receptor with multiple ligand specificities and functions. *Clin Exp Immunol* (2008) 92:181–4. doi: 10.1111/j.1365-2249.1993.tb03377.x

95. Myones BL, Dalzell JG, Hogg N, Ross GD. Neutrophil and monocyte cell surface p150,95 has iC3b-receptor (CR4) activity resembling CR3. *J Clin Invest* (1988) 82:640–51. doi: 10.1172/JCI113643

96. Diamond MS, Garcia-Aguilar J, Bickford JK, Corbi AL, Springer TA. The I domain is a major recognition site on the leukocyte integrin Mac-1 (CD11b/CD18) for four distinct adhesion ligands. *J Cell Biol* (1993) 120:1031–43. doi: 10.1083/jcb.120.4.1031

97. Lishko VK, Yakubenko VP, Hertzberg KM, Grieninger G, Ugarova TP. The alternatively spliced αEC domain of human fibrinogen-420 is a novel ligand for leukocyte integrins αMβ2 and αXβ2. *Blood* (2001) 98:2448–55. doi: 10.1182/blood.V98.8.2448

98. Wright SD, Jong MT. Adhesion-promoting receptors on human macrophages recognize Escherichia coli by binding to lipopolysaccharide. *J Exp Med* (1986) 164:1876–88. doi: 10.1084/jem.164.6.1876

99. Erdei A, Lukácsi S, Mácsik-Valent B, Nagy-Baló Z, Kurucz I, Bajtay Z. Non-identical twins: Different faces of CR3 and CR4 in myeloid and lymphoid cells of mice and men. *Semin Cell Dev Biol* (2019) 85:110–21. doi: 10.1016/j.semcdb.2017.11.025

100. Springer TA, Dustin ML. Integrin inside-out signaling and the immunological synapse. *Curr Opin Cell Biol* (2012) 24:107–15. doi: 10.1016/j.ceb.2011.10.004

101. Wen L, Lyu Q, Ley K, Goult BT. Structural basis of β2 integrin inside—Out activation. *Cells* (2022) 11:3039. doi: 10.3390/cells11193039

102. Whittaker CA, Hynes RO. Distribution and evolution of von willebrand/integrin A domains: widely dispersed domains with roles in cell adhesion and elsewhere. *Mol Biol Cell* (2002) 13:3369–87. doi: 10.1091/mbc.e02-05-0259

103. Lee C-H, Romain G, Yan W, Watanabe M, Charab W, Todorova B, et al. IgG Fc domains that bind C1q but not effector Fcγ receptors delineate the importance of complement-mediated effector functions. *Nat Immunol* (2017) 18:889–98. doi: 10.1038/ni.3770

104. Springer TA. Folding of the N-terminal, ligand-binding region of integrin α-subunits into a β-propeller domain. *Proc Natl Acad Sci* (1997) 94:65–72. doi: 10.1073/pnas.94.1.65

105. Shi M, Sundramurthy K, Liu B, Tan S-M, Law SKA, Lescar J. The crystal structure of the plexin-semaphorin-integrin domain/hybrid domain/I-EGF1 segment from the human integrin β2 subunit at 1.8-Å Resolution. *J Biol Chem* (2005) 280:30586–93. doi: 10.1074/jbc.M502525200

106. Shi M, Foo SY, Tan S-M, Mitchell EP, Law SKA, Lescar J. A structural hypothesis for the transition between bent and extended conformations of the leukocyte β2 integrins. *J Biol Chem* (2007) 282:30198–206. doi: 10.1074/jbc.M701670200

107. Beglova N, Blacklow SC, Takagi J, Springer TA. Cysteine-rich module structure reveals a fulcrum for integrin rearrangement upon activation. *Nat Struct Biol* (2002) 9:282–7. doi: 10.1038/nsb779

108. Sen M, Springer TA. Leukocyte integrin $\alpha_L\beta_2$ headpiece structures: The αI domain, the pocket for the internal ligand, and concerted movements of its loops. *Proc Natl Acad Sci* (2016) 113:2940–5. doi: 10.1073/pnas.1601379113

109. Guo J, Zhang Y, Li H, Chu H, Wang Q, Jiang S, et al. Intramembrane ionic protein–lipid interaction regulates integrin structure and function. *PloS Biol* (2018) 16: e2006525. doi: 10.1371/journal.pbio.2006525

110. Xu S, Wang J, Wang J-H, Springer TA. Distinct recognition of complement iC3b by integrins αXβ2 and αMβ2. *Proc Natl Acad Sci* (2017) 114:3403–8. doi: 10.1073/pnas.1620881114

111. Bajic G, Yatime L, Sim RB, Vorup-Jensen T, Andersen GR. Structural insight on the recognition of surface-bound opsonins by the integrin I domain of complement receptor 3. *Proc Natl Acad Sci U.S.A.* (2013) 110:16426–31. doi: 10.1073/pnas.1311261110

112. Lee J-O, Rieu P, Arnaout MA, Liddington R. Crystal structure of the A domain from the a subunit of integrin CR3 (CD11 b/CD18). *Cell* (1995) 80:631–8. doi: 10.1016/0092-8674(95)90517-0

113. Baldwin ET, Sarver RW, Bryant GL, Curry KA, Fairbanks MB, Finzel BC, et al. Cation binding to the integrin CD11b I domain and activation model assessment. *Structure* (1998) 6:923–35. doi: 10.1016/S0969-2126(98)00093-8

114. Goldsmith JA, DiVenere AM, Maynard JA, McLellan JS. Structural basis for non-canonical integrin engagement by Bordetella adenylate cyclase toxin. *Cell Rep* (2022) 40:111196. doi: 10.1016/j.celrep.2022.111196

115. Jensen MR, Bajic G, Zhang X, Laustsen AK, Koldsø H, Skeby KK, et al. Structural basis for simvastatin competitive antagonism of complement receptor 3. *J Biol Chem* (2016) 291:16963–76. doi: 10.1074/jbc.M116.732222

116. Mahalingam B, Ajroud K, Alonso JL, Anand S, Adair BD, Horenstein AL, et al. Stable coordination of the inhibitory ca2+ Ion at the metal ion-dependent adhesion site in integrin CD11b/CD18 by an antibody-derived ligand aspartate: implications for integrin regulation and structure-based drug design. *J Immunol* (2011) 187:6393–401. doi: 10.4049/jimmunol.1102394

117. Gaither TA, Vargas I, Inada S, Frank MM. The complement fragment C3d facilitates phagocytosis by monocytes. *Immunology* (1987) 62:405–11.

118. Stapulionis R, Pinto Oliveira CL, Gjelstrup MC, Pedersen JS, Hokland ME, Hoffmann SV, et al. Structural insight into the function of myelin basic protein as a ligand for integrin αMβ2. *J Immunol* (2008) 180:3946–56. doi: 10.4049/jimmunol.180.6.3946

119. Zhang X, Bajic G, Andersen GR, Christiansen SH, Vorup-Jensen T. The cationic peptide LL-37 binds Mac-1 (CD11b/CD18) with a low dissociation rate and promotes phagocytosis. *Biochim Biophys Acta BBA - Proteins Proteomics* (2016) 1864:471–8. doi: 10.1016/j.bbapap.2016.02.013

120. Sen M, Yuki K, Springer TA. An internal ligand-bound, metastable state of a leukocyte integrin, αXβ2. *J Cell Biol* (2013) 203:629–42. doi: 10.1083/jcb.201308083

121. Xie C, Zhu J, Chen X, Mi L, Nishida N, Springer TA. Structure of an integrin with an αI domain, complement receptor type 4. *EMBO J* (2010) 29:666–79. doi: 10.1038/emboj.2009.367

122. Bilsland CA, Diamond MS, Springer TA. The leukocyte integrin p150,95 (CD11c/CD18) as a receptor for iC3b. Activation by a heterologous beta subunit and localization of a ligand recognition site to the I domain. *J Immunol Baltim Md 1950* (1994) 152:4582–9. doi: 10.1101/gr.1293003

123. Clark HF, Gurney AL, Abaya E, Baker K, Baldwin D, Brush J, et al. The secreted protein discovery initiative (SPDI), a large-scale effort to identify novel human secreted and transmembrane proteins: A bioinformatics assessment. *Genome Res* (2003) 13:2265–70. doi: 10.1101/gr.1293003

124. Smith DK, Xue H. Sequence profiles of immunoglobulin and immunoglobulin-like domains. *J Mol Biol* (1997) 274:530–45. doi: 10.1006/jmbi.1997.1432

125. Helmy KY, Katschke KJ, Gorgani NN, Kljavin NM, Elliott JM, Diehl L, et al. CRIg: A macrophage complement receptor required for phagocytosis of circulating pathogens. *Cell* (2006) 124:915–27. doi: 10.1016/j.cell.2005.12.039

126. Carpentier JL, Lew DP, Paccaud JP, Gil R, Iacopetta B, Kazatchkine M, et al. Internalization pathway of C3b receptors in human neutrophils and its transmodulation by chemoattractant receptors stimulation. *Cell Regul* (1991) 2:41–55. doi: 10.1172/JCI25673

127. Vogt L, Schmitz N, Kurrer MO, Bauer M, Hinton HI, Behnke S, et al. VSIG4, a B7 family-related protein, is a negative regulator of T cell activation. *J Clin Invest* (2006) 116:2817–26. doi: 10.1172/JCI25673

128. Wiesmann C, Katschke KJ, Yin J, Helmy KY, Steffek M, Fairbrother WJ, et al. Structure of C3b in complex with CRIg gives insights into regulation of complement activation. *Nature* (2006) 444:217–20. doi: 10.1038/nature05263

129. Wen Y, Ouyang Z, Schoonooghe S, Luo S, De Baetselier P, Lu W, et al. Structural evaluation of a nanobody targeting complement receptor Vsig4 and its cross reactivity. *Immunobiology* (2017) 222:807–13. doi: 10.1016/j.imbio.2016.11.008

130. Arnaout MA, Melamed J, Tack BF, Colten HR. Characterization of the human complement (c3b) receptor with a fluid phase C3b dimer. *J Immunol Baltim Md 1950* (1981) 127:1348–54. doi: 10.1073/pnas.1913443116

131. Liu G, Fu Y, Yosri M, Chen Y, Sun P, Xu J, et al. CRIg plays an essential role in intravascular clearance of bloodborne parasites by interacting with complement. *Proc Natl Acad Sci* (2019) 116:24214–20. doi: 10.1073/pnas.1913443116

132. Barnum SR. C4a: an anaphylatoxin in name only. *J Innate Immun* (2015) 7:333–9. doi: 10.1159/000371423

133. Han X, de la Fuente M, Nieman MT. Complement factor C4a does not activate protease-activated receptor 1 (PAR1) or PAR4 on human platelets. *Res Pract Thromb Haemost* (2021) 5:104–10. doi: 10.1002/rth2.12459

134. Fredriksson R, Lagerström MC, Lundin L-G, Schiöth HB. The G-protein-coupled receptors in the human genome form five main families. Phylogenetic analysis, paralogon groups, and fingerprints. *Mol Pharmacol* (2003) 63:1256–72. doi: 10.1124/mol.63.6.1256

135. Alexander SPH, Christopoulos A, Davenport AP, Kelly E, Mathie A, Peters JA, et al. THE CONCISE GUIDE TO PHARMACOLOGY 2021/22: G protein-coupled receptors. *Br J Pharmacol* (2021) 178, S27-156. doi: 10.1111/bph.15538

136. Kolakowski LF. GCRDb: a G-protein-coupled receptor database. *Receptors Channels* (1994) 2:1–7. doi: 10.1038/nrm908

137. Pierce KL, Premont RT, Lefkowitz RJ. Seven-transmembrane receptors. *Nat Rev Mol Cell Biol* (2002) 3:639–50. doi: 10.1038/nrm908

138. Venkatakrishnan AJ, Deupi X, Lebon G, Tate CG, Schertler GF, Babu MM. Molecular signatures of G-protein-coupled receptors. *Nature* (2013) 494:185–94. doi: 10.1038/nature11896

139. Weis WI, Kobilka BK. The molecular basis of G protein–coupled receptor activation. *Annu Rev Biochem* (2018) 87:897–919. doi: 10.1146/annurev-biochem-060614-033910

140. Ballesteros JA, Weinstein H. Integrated methods for the construction of three-dimensional models and computational probing of structure-function relations in G protein-coupled receptors. In: *Methods in Neurosciences*:Academic Press, New York. Elsevier (1995). p. 366–428. doi: 10.1016/S1043-9471(05)80049-7

141. Laumonnier Y, Karsten CM, Köhl J. Novel insights into the expression pattern of anaphylatoxin receptors in mice and men. *Mol Immunol* (2017) 89:44–58. doi: 10.1016/j.molimm.2017.05.019

142. Klos A, Tenner AJ, Johswich K-O, Ager RR, Reis ES, Köhl J. The role of the anaphylatoxins in health and disease. *Mol Immunol* (2009) 46:2753–66. doi: 10.1016/j.molimm.2009.04.027

143. Zhang T, Garstka MA, Li K. The controversial C5a receptor C5aR2: its role in health and disease. *J Immunol Res* (2017) 2017:1–16. doi: 10.1155/2017/8193932

144. Wang Y, Zhang H, He Y-W. The complement receptors C3aR and C5aR are a new class of immune checkpoint receptor in cancer immunotherapy. *Front Immunol* (2019) 10:1574. doi: 10.3389/fimmu.2019.01574

145. Gao S, Cui Z, Zhao M. The complement C3a and C3a receptor pathway in kidney diseases. *Front Immunol* (2020) 11:1875. doi: 10.3389/fimmu.2020.01875

146. Giorgio C, Zippoli M, Cocchiaro P, Castelli V, Varrassi G, Aramini A, et al. Emerging role of C5 complement pathway in peripheral neuropathies: current treatments and future perspectives. *Biomedicines* (2021) 9:399. doi: 10.3390/biomedicines9040399

147. Ruocco A, Sirico A, Novelli R, Iannelli S, Van Breda SV, Kyburz D, et al. The role of C5a-C5aR1 axis in bone pathophysiology: A mini-review. *Front Cell Dev Biol* (2022) 10:957800. doi: 10.3389/fcell.2022.957800

148. Schanzenbacher J, Köhl J, Karsten CM. Anaphylatoxins spark the flame in early autoimmunity. *Front Immunol* (2022) 13:958392. doi: 10.3389/fimmu.2022.958392

149. Hawksworth OA, Li XX, Coulthard LG, Wolvetang EJ, Woodruff TM. New concepts on the therapeutic control of complement anaphylatoxin receptors. *Mol Immunol* (2017) 89:36–43. doi: 10.1016/j.molimm.2017.05.015

150. Chenoweth DE, Hugli TE. Demonstration of specific C5a receptor on intact human polymorphonuclear leukocytes. *Proc Natl Acad Sci* (1978) 75:3943–7. doi: 10.1073/pnas.75.8.3943

151. Gerard NP, Gerard C. The chemotactic receptor for human C5a anaphylatoxin. *Nature* (1991) 349:614–7. doi: 10.1038/349614a0

152. Boulay F, Mery L, Tardif M, Brouchon L, Vignais P. Expression cloning of a receptor for C5a anaphylatoxin on differentiated HL-60 cells. *Biochemistry* (1991) 30:2993–9. doi: 10.1021/bi00226a002

153. Hilger D. The role of structural dynamics in GPCR-mediated signaling. *FEBS J* (2021) 288:2461–89. doi: 10.1111/febs.15841

154. Robertson N, Rappas M, Doré AS, Brown J, Bottegoni G, Koglin M, et al. Structure of the complement C5a receptor bound to the extra-helical antagonist NDT9513727. *Nature* (2018) 553:111–4. doi: 10.1038/nature25025

155. Liu H, Kim HR, Deepak RNVK, Wang L, Chung KY, Fan H, et al. Orthosteric and allosteric action of the C5a receptor antagonists. *Nat Struct Mol Biol* (2018) 25:472–81. doi: 10.1038/s41594-018-0067-z

156. Floyd DH, Geva A, Bruinsma SP, Overton MC, Blumer KJ, Baranski TJ. C5a receptor oligomerization. *J Biol Chem* (2003) 278:35354–61. doi: 10.1074/jbc.M305607200

157. Klco JM, Lassere TB, Baranski TJ. C5a receptor oligomerization. *J Biol Chem* (2003) 278:35345–53. doi: 10.1074/jbc.M305606200

158. Hüttenrauch F, Pollok-Kopp B, Oppermann M. G protein-coupled receptor kinases promote phosphorylation and β-arrestin-mediated internalization of CCR5 homo- and hetero-oligomers. *J Biol Chem* (2005) 280:37503–15. doi: 10.1074/jbc.M500535200

159. Croker DE, Halai R, Fairlie DP, Cooper MA. C5a, but not C5a-des Arg, induces upregulation of heteromer formation between complement C5a receptors C5aR and C5L2. *Immunol Cell Biol* (2013) 91:625–33. doi: 10.1038/icb.2013.48

160. Pease JE, Barker MD. N-linked glycosylation of the C5a receptor. *Biochem Mol Biol Int* (1993) 31:719–26. doi: 10.1084/jem.193.9.1059

161. Farzan M, Schnitzler CE, Vasilieva N, Leung D, Kuhn J, Gerard C, et al. Sulfated tyrosines contribute to the formation of the C5a docking site of the human C5a anaphylatoxin receptor. *J Exp Med* (2001) 193:1059–66. doi: 10.1084/jem.193.9.1059

162. Giannini E, Brouchon L, Boulay F. Identification of the major phosphorylation sites in human C5a anaphylatoxin receptor in vivo. *J Biol Chem* (1995) 270:19166–72. doi: 10.1074/jbc.270.32.19166

163. Monk PN, Scola A-M, Madala P, Fairlie DP. Function, structure and therapeutic potential of complement C5a receptors. *Br J Pharmacol* (2007) 152:429–48. doi: 10.1038/sj.bjp.0707332

164. Klos A, Wende E, Wareham KJ, Monk PN. International union of basic and clinical pharmacology. LXXXVII. Complement peptide C5a, C4a, and C3a receptors. *Pharmacol Rev* (2013) 65:500–43. doi: 10.1124/pr.111.005223

165. Pandey S, Maharana J, Li XX, Woodruff TM, Shukla AK. Emerging insights into the structure and function of complement C5a receptors. *Trends Biochem Sci* (2020) 45:693–705. doi: 10.1016/j.tibs.2020.04.004

166. DeMartino JA, Van Riper G, Siciliano SJ, Molineaux CJ, Konteatis ZD, Rosen H, et al. The amino terminus of the human C5a receptor is required for high affinity C5a binding and for receptor activation by C5a but not C5a analogs. *J Biol Chem* (1994) 269:14446–50. doi: 10.1016/S0021-9258(17)36643-7

167. Mery L, Boulay F. The NH2-terminal region of C5aR but not that of FPR is critical for both protein transport and ligand binding. *J Biol Chem* (1994) 269:3457–63. doi: 10.1016/S0021-9258(17)41884-9

168. Hagemann IS, Narzinski KD, Floyd DH, Baranski TJ. Random mutagenesis of the complement factor 5a (C5a) receptor N terminus provides a structural constraint for C5a docking. *J Biol Chem* (2006) 281:36783–92. doi: 10.1074/jbc.M607686200

169. Chen Z, Zhang X, Gonnella NC, Pellas TC, Boyar WC, Ni F. Residues 21–30 within the extracellular N-terminal region of the C5a receptor represent a binding domain for the C5a anaphylatoxin. *J Biol Chem* (1998) 273:10411–9. doi: 10.1074/jbc.273.17.10411

170. Siciliano SJ, Rollins TE, DeMartino J, Konteatis Z, Malkowitz L, Van Riper G, et al. Two-site binding of C5a by its receptor: analternative binding paradigm for G protein-coupled receptors. *Proc Natl Acad Sci* (1994) 91:1214–8. doi: 10.1073/pnas.91.4.1214

171. Dumitru AC, Deepak RNVK, Liu H, Koehler M, Zhang C, Fan H, et al. Submolecular probing of the complement C5a receptor–ligand binding reveals a cooperative two-site binding mechanism. *Commun Biol* (2020) 3:786. doi: 10.1038/s42003-020-01518-8

172. Pease JE, Burton DR, Barker MD. Generation of chimeric C5a/formyl peptide receptors: towards the identification of the human C5a receptor binding site. *Eur J Immunol* (1994) 24:211–5. doi: 10.1002/eji.1830240133

173. Gerard C, Gerard NP. C5A anaphylatoxin and its seven transmembrane-segment receptor. *Annu Rev Immunol* (1994) 12:775–808. doi: 10.1146/annurev.iy.12.040194.004015

174. Bokisch VA, Müller-Eberhard HJ. Anaphylatoxin inactivator of human plasma: its isolation and characterization as a carboxypeptidase. *J Clin Invest* (1970) 49:2427–36. doi: 10.1172/JCI106462

175. Kawai M, Quincy DA, Lane B, Mollison KW, Or YS, Luly JR, et al. Structure-function studies in a series of carboxyl-terminal octapeptide analogs of anaphylatoxin C5a. *J Med Chem* (1992) 35:220–3. doi: 10.1021/jm00080a004

176. Kawai M, Quincy DA, Lane B, Mollison KW, Luly JR, Carter GW. Identification and synthesis of a receptor binding site of human anaphylatoxin C5a. *J Med Chem* (1991) 34:2068–71. doi: 10.1021/jm00111a022

177. Higginbottom A, Cain SA, Woodruff TM, Proctor LM, Madala PK, Tyndall JDA, et al. Comparative agonist/antagonist responses in mutant human C5a receptors define the ligand binding site *. *J Biol Chem* (2005) 280:17831–40. doi: 10.1074/jbc.M410797200

178. Klco JM, Nikiforovich GV, Baranski TJ. Genetic analysis of the first and third extracellular loops of the C5a receptor reveals an essential WXFG motif in the first loop. *J Biol Chem* (2006) 281:12010–9. doi: 10.1074/jbc.M600548200

179. Klco JM, Wiegand CB, Narzinski K, Baranski TJ. Essential role for the second extracellular loop in C5a receptor activation. *Nat Struct Mol Biol* (2005) 12:320–6. doi: 10.1038/nsmb913

180. Baranski TJ, Herzmark P, Lichtarge O, Gerber BO, Trueheart J, Meng EC, et al. C5a receptor activation. *J Biol Chem* (1999) 274:15757–65. doi: 10.1074/jbc.274.22.15757

181. Geva A, Lassere TB, Lichtarge O, Pollitt SK, Baranski TJ. Genetic mapping of the human C5a receptor. *J Biol Chem* (2000) 275:35393–401. doi: 10.1074/jbc.M005602200

182. Zhou Q, Yang D, Wu M, Guo Y, Guo W, Zhong L, et al. Common activation mechanism of class A GPCRs. *eLife* (2019) 8:e50279. doi: 10.7554/eLife.50279

183. Amatruda TT, Gerard NP, Gerard C, Simon MI. Specific interactions of chemoattractant factor receptors with G-proteins. *J Biol Chem* (1993) 268:10139–44. doi: 10.1016/S0021-9258(18)82183-4

184. Buhl AM, Eisfelder BJ, Worthen GS, Johnson GL, Russell M. Selective coupling of the human anaphylatoxin C5a receptor and α_{16} in human kidney 293 cells. *FEBS Lett* (1993) 323:132–4. doi: 10.1016/0014-5793(93)81464-B

185. Vanek M, Hawkins LD, Gusovsky F. Coupling of the C5a receptor to Gi in U-937 cells and in cells transfected with C5a receptor cDNA. *Mol Pharmacol* (1994) 46:832–9. doi: 10.1006/bbrc.1995.1327

186. Shum JK, Allen RA, Wong YH. The human chemoattractant complement C5a receptor inhibits cyclic AMP accumulation through gi and gz proteins. *Biochem Biophys Res Commun* (1995) 208:223–9. doi: 10.1006/bbrc.1995.1327

187. Pandey S, Kumari P, Baidya M, Kise R, Cao Y, Dwivedi-Agnihotri H, et al. Intrinsic bias at non-canonical, β-arrestin-coupled seven transmembrane receptors. *Mol Cell* (2021) 81:4605–4621.e11. doi: 10.1016/j.molcel.2021.09.007

188. Matsumoto ML, Narzinski K, Kiser PD, Nikiforovich GV, Baranski TJ. A comprehensive structure-function map of the intracellular surface of the human C5a receptor. *J Biol Chem* (2007) 282:3105–21. doi: 10.1074/jbc.M607679200

189. Auger GA, Smith BM, Pease JE, Barker MD. The use of membrane translocating peptides to identify sites of interaction between the C5a receptor and downstream effector proteins. *Immunology* (2004) 112:590–6. doi: 10.1111/j.1365-2567.2004.01919.x

190. Siciliano SJ, Rollins TE, Springer MS. Interaction between the C5a receptor and Gi in both the membrane-bound and detergent-solubilized states. *J Biol Chem* (1990) 265:19568–74. doi: 10.1016/S0021-9258(17)45409-3

191. Wennogle LP, Conder L, Winter C, Braunwalder A, Vlattas S, Kramer R, et al. Stabilization of C5a receptor-G-protein interactions through ligand binding. *J Cell Biochem* (1994) 55:380–8. doi: 10.1002/jcb.240550316

192. Raffetseder U, Roper D, Mery L, Gietz C, Klos A, Grotzinger J, et al. Site-directed mutagenesis of conserved charged residues in the helical region of the human C5a receptor. Arg206 determines high-affinity binding sites of C5a receptor. *Eur J Biochem* (1996) 235:82–90. doi: 10.1111/j.1432-1033.1996.00082.x

193. Pollok-Kopp B, Hüttenrauch F, Rethorn S, Oppermann M. Dynamics of protein kinase C-mediated phosphorylation of the complement C5a receptor on serine 334. *J Biol Chem* (2007) 282:4345–53. doi: 10.1074/jbc.M601317200

194. Bock D, Martin U, Gärtner S, Rheinheimer C, Raffetseder U, Arseniev L, et al. The C terminus of the human C5a receptor (CD88) is required for normal ligand-dependent receptor internalization. *Eur J Immunol* (1997) 27:1522–9. doi: 10.1002/eji.1830270631

195. Christophe T, Rabiet M-J, Tardif M, Milcent M-D, Boulay F. Human complement 5a (C5a) anaphylatoxin receptor (CD88) phosphorylation sites and their specific role in receptor phosphorylation and attenuation of G protein-mediated responses. *J Biol Chem* (2000) 275:1656–64. doi: 10.1074/jbc.275.3.1656

196. Tardif M, Mery L, Brouchon L, Boulay F. Agonist-dependent phosphorylation of N-formylpeptide and activation peptide from the fifth component of C (C5a) chemoattractant receptors in differentiated HL60 cells. *J Immunol Baltim Md 1950* (1993) 150:3534–45. doi: 10.1002/(SICI)1521-4141(199909)29:09<3035::AID-IMMU3035>3.0.CO;2-Z

197. Langkabel P, Zwirner J, Oppermann M. Ligand-induced phosphorylation of anaphylatoxin receptors C3aR and C5aR is mediated by G protein-coupled receptor kinases. *Eur J Immunol* (1999) 29:3035–46. doi: 10.1002/(SICI)1521-4141(199909)29:09<3035::AID-IMMU3035>3.0.CO;2-Z

198. Suvorova ES, Gripentrog JM, Oppermann M, Miettinen HM. Role of the carboxyl terminal di-leucine in phosphorylation and internalization of C5a receptor. *Biochim Biophys Acta BBA - Mol Cell Res* (2008) 1783:1261–70. doi: 10.1016/j.bbamcr.2008.02.004

199. Braun L, Christophe T, Boulay F. Phosphorylation of key serine residues is required for internalization of the complement 5a (C5a) anaphylatoxin receptor via a β-arrestin, dynamin, and clathrin-dependent pathway. *J Biol Chem* (2003) 278:4277–85. doi: 10.1074/jbc.M210120200

200. Naik N, Giannini E, Brouchon L, Boulay F. Internalization and recycling of the C5a anaphylatoxin receptor: evidence that the agonist-mediated internalization is modulated by phosphorylation of the C-terminal domain. *J Cell Sci* (1997) 110:2381–90. doi: 10.1242/jcs.110.19.2381

201. Suvorova ES, Gripentrog JM, Miettinen HM. Different endocytosis pathways of the C5a receptor and the N-formyl peptide receptor: different targeting of activated C5aR vs. *FPR Traffic* (2005) 6:100–15. doi: 10.1111/j.1600-0854.2004.00256.x

202. Drube J, Haider RS, Matthees ESF, Reichel M, Zeiner J, Fritzwanker S, et al. GPCR kinase knockout cells reveal the impact of individual GRKs on arrestin binding and GPCR regulation. *Nat Commun* (2022) 13:540. doi: 10.1038/s41467-022-28152-8

203. Wu K-C, Condon ND, Hill TA, Reid RC, Fairlie D, Lim J. Ras related protein Rab5a regulates complement C5a receptor trafficking, chemotaxis and chemokine secretion in human macrophages. *J Innate Immun* (2023) 15, (1): 468–84. doi: 10.1159/000530012

204. Tardif M, Brouchon L, Rabiet M-J, Boulay F. Direct binding of a fragment of the Wiskott-Aldrich syndrome protein to the C-terminal end of the anaphylatoxin C5a receptor. *Biochem J* (2003) 372:453–63. doi: 10.1042/bj20021803

205. Rabiet M-J, Huet E, Boulay F. Complement component 5a receptor oligomerization and homologous receptor down-regulation. *J Biol Chem* (2008) 283:31038–46. doi: 10.1074/jbc.M805260200

206. Wang C, Wu H, Katritch V, Han GW, Huang X-P, Liu W, et al. Structure of the human smoothened receptor bound to an antitumour agent. *Nature* (2013) 497:338–43. doi: 10.1038/nature12167

207. Pandey S, Li XX, Srivastava A, Baidya M, Kumari P, Dwivedi H, et al. Shukla AK. Partial ligand-receptor engagement yields functional bias at the human complement receptor, C5aR1. *J Biol Chem* (2019) 294:9416–29. doi: 10.1074/jbc.RA119.007485

208. Gorman DM, Li XX, Lee JD, Fung JN, Cui CS, Lee HS, et al. Development of potent and selective agonists for complement C5a receptor 1 with *in vivo* activity. *J Med Chem* (2021) 64:16598–608. doi: 10.1021/acs.jmedchem.1c01174

209. Ohno M, Hirata T, Enomoto M, Araki T, Ishimaru H, Takahashi TA. A putative chemoattractant receptor, C5L2, is expressed in granulocyte and immature dendritic cells, but not in mature dendritic cells. *Mol Immunol* (2000) 37:407–12. doi: 10.1016/S0161-5890(00)00067-5

210. Okinaga S, Slattery D, Humbles A, Zsengeller Z, Morteau O, Kinrade MB, et al. C5L2, a nonsignaling C5A binding protein. *Biochemistry* (2003) 42:9406–15. doi: 10.1021/bi034489v

211. Cain SA, Monk PN. The orphan receptor C5L2 has high affinity binding sites for complement fragments C5a and C5a des-arg74. *J Biol Chem* (2002) 277:7165–9. doi: 10.1074/jbc.C100714200

212. Scola A-M, Higginbottom A, Partridge LJ, Reid RC, Woodruff T, Taylor SM, et al. The role of the N-terminal domain of the complement fragment receptor C5L2 in ligand binding. *J Biol Chem* (2007) 282:3664–71. doi: 10.1074/jbc.M609178200

213. Croker DE, Monk PN, Halai R, Kaeslin G, Schofield Z, Wu MC, et al. Discovery of functionally selective C5aR2 ligands: novel modulators of C5a signalling. *Immunol Cell Biol* (2016) 94:787–95. doi: 10.1038/icb.2016.43

214. Van Lith LHC, Oosterom J, Van Elsas A, Zaman GJR. C5a-stimulated recruitment of β-arrestin2 to the nonsignaling 7-transmembrane decoy receptor C5L2. *SLAS Discovery* (2009) 14:1067–75. doi: 10.1177/1087057109341407

215. Scola A-M, Johswich K-O, Morgan BP, Klos A, Monk PN. The human complement fragment receptor, C5L2, is a recycling decoy receptor. *Mol Immunol* (2009) 46:1149–62. doi: 10.1016/j.molimm.2008.11.001

216. Croker DE, Halai R, Kaeslin G, Wende E, Fehlhaber B, Klos A, et al. C5a2 can modulate ERK1/2 signaling in macrophages via heteromer formation with C5a1 and β-arrestin recruitment. *Immunol Cell Biol* (2014) 92:631–9. doi: 10.1038/icb.2014.32

217. Li XX, Clark RJ, Woodruff TM. C5aR2 activation broadly modulates the signaling and function of primary human macrophages. *J Immunol* (2020) 205:1102–12. doi: 10.4049/jimmunol.2000407

218. Ames RS, Li Y, Sarau HM, Nuthulaganti P, Foley JJ, Ellis C, et al. Molecular cloning and characterization of the human anaphylatoxin C3a receptor. *J Biol Chem* (1996) 271:20231–4. doi: 10.1074/jbc.271.34.20231

219. Crass T, Raffetseder U, Martin U, Grove M, Klos A, Köhl J, et al. Expression cloning of the human C3a anaphylatoxin receptor (C3aR) from differentiated U-937 cells. *Eur J Immunol* (1996) 26:1944–50. doi: 10.1002/eji.1830260840

220. Gao J, Choe H, Bota D, Wright PL, Gerard C, Gerard NP. Sulfation of tyrosine 174 in the human C3a receptor is essential for binding of C3a anaphylatoxin. *J Biol Chem* (2003) 278:37902–8. doi: 10.1074/jbc.M306061200

221. Halim A, Rüetschi U, Larson G, Nilsson J. LC–MS/MS characterization of O-glycosylation sites and glycan structures of human cerebrospinal fluid glycoproteins. *J Proteome Res* (2013) 12:573–84. doi: 10.1021/pr300963h

222. Chao T-H, Ember JA, Wang M, Bayon Y, Hugli TE, Ye RD. Role of the second extracellular loop of human C3a receptor in agonist binding and receptor function. *J Biol Chem* (1999) 274:9721–8. doi: 10.1074/jbc.274.14.9721

223. Wilken H-C, Götze O, Werfel T, Zwirner J. C3a(desArg) does not bind to and signal through the human C3a receptor. *Immunol Lett* (1999) 67:141–5. doi: 10.1016/S0165-2478(99)00002-4

224. Crass T, Ames RS, Sarau HM, Tornetta MA, Foley JJ, Köhl J, et al. Chimeric receptors of the human C3a receptor and C5a receptor (CD88). *J Biol Chem* (1999) 274:8367–70. doi: 10.1074/jbc.274.13.8367

225. Guo Q, Subramanian H, Gupta K, Ali H. Regulation of C3a receptor signaling in human mast cells by G protein coupled receptor kinases. *PloS One* (2011) 6:e22559. doi: 10.1371/journal.pone.0022559

226. Gupta K, Subramanian H, Klos A, Ali H. Phosphorylation of C3a receptor at multiple sites mediates desensitization, β-arrestin-2 recruitment and inhibition of NF-κB activity in mast cells. *PloS One* (2012) 7:e46369. doi: 10.1371/journal.pone.0046369

227. Settmacher B, Rheinheimer C, Hamacher H, Ames RS, Wise A, Jenkinson L, et al. Structure-function studies of the C3a-receptor: C-terminal serine and threonine residues which influence receptor internalization and signaling. *Eur J Immunol* (2003) 33:920–7. doi: 10.1002/eji.200323293

228. Ahamed J, Haribabu B, Ali H. Cutting edge: differential regulation of chemoattractant receptor-induced degranulation and chemokine production by receptor phosphorylation. *J Immunol* (2001) 167:3559–63. doi: 10.4049/jimmunol.167.7.3559

229. Vibhuti A, Gupta K, Subramanian H, Guo Q, Ali H. Distinct and shared roles of β-arrestin-1 and β-arrestin-2 on the regulation of C3a receptor signaling in human mast cells. *PloS One* (2011) 6:e19585. doi: 10.1371/journal.pone.0019585

230. Ramirez MD, Pairett AN, Pankey MS, Serb JM, Speiser DI, Swafford AJ, et al. The last common ancestor of most bilaterian animals possessed at least nine opsins. *Genome Biol Evol* (2016) 8:3640–52. doi: 10.1093/gbe/evw248

231. Elvington M, Liszewski MK, Atkinson JP. Evolution of the complement system: from defense of the single cell to guardian of the intravascular space. *Immunol Rev* (2016) 274:9–15. doi: 10.1111/imr.12474

232. Nonaka M. Evolution of the complement system. *Subcell Biochem* (2014) 80:31–43. doi: 10.1007/978-94-017-8881-6_3

233. Jumper J, Evans R, Pritzel A, Green T, Figurnov M, Ronneberger O. Highly accurate protein structure prediction with AlphaFold. *Nature* (2021) 596:583–9. doi: 10.1038/s41586-021-03819-2

234. Fernández FJ, Vega MC. Technologies to keep an eye on: alternative hosts for protein production in structural biology. *Curr Opin Struct Biol* (2013) 23:365–73. doi: 10.1016/j.sbi.2013.02.002

235. Fernández FJ, Vega MC. Choose a suitable expression host: A survey of available protein production platforms. In: Vega MC, editor. *Advanced Technologies for Protein Complex Production and Characterization. Advances in Experimental Medicine and Biology*. Cham: Springer International Publishing (2016). p. 15–24. doi: 10.1007/978-3-319-27216-0_2

236. García-Nafría J, Tate CG. Cryo-electron microscopy: moving beyond X-ray crystal structures for drug receptors and drug development. *Annu Rev Pharmacol Toxicol* (2020) 60:51–71. doi: 10.1146/annurev-pharmtox-010919-023545

237. Ito Y, Selenko P. Cellular structural biology. *Curr Opin Struct Biol* (2010) 20:640–8. doi: 10.1016/j.sbi.2010.07.006

238. Querol-García J, Fernández FJ, Marin AV, Gómez S, Fullà D, Melchor-Tafur C, et al. Crystal structure of glyceraldehyde-3-phosphate dehydrogenase from the gram-positive bacterial pathogen A. vaginae, an immunoevasive factor that interacts with the human C5a anaphylatoxin. *Front Microbiol* (2017) 8:541. doi: 10.3389/fmicb.2017.00541

239. Gómez S, Querol-García J, Sánchez-Barrón G, Subias M, González-Alsina À, Franco-Hidalgo V, et al. The antimicrobials anacardic acid and curcumin are not-competitive inhibitors of gram-positive bacterial pathogenic glyceraldehyde-3-phosphate dehydrogenase by a mechanism unrelated to human C5a anaphylatoxin binding. *Front Microbiol* (2019) 10:326. doi: 10.3389/fmicb.2019.00326

240. Lambris JD, Ricklin D, Geisbrecht BV. Complement evasion by human pathogens. *Nat Rev Microbiol* (2008) 6:132–42. doi: 10.1038/nrmicro1824

241. Fernández FJ, Gómez S, Vega MC. Pathogens' toolbox to manipulate human complement. *Semin Cell Dev Biol* (2019) 85:98–109. doi: 10.1016/j.semcdb.2017.12.001

Frontiers in Immunology

Explores novel approaches and diagnoses to treat immune disorders.

The official journal of the International Union of Immunological Societies (IUIS) and the most cited in its field, leading the way for research across basic, translational and clinical immunology.

Discover the latest Research Topics

See more →

Frontiers

Avenue du Tribunal-Fédéral 34
1005 Lausanne, Switzerland
frontiersin.org

Contact us

+41 (0)21 510 17 00
frontiersin.org/about/contact